



XA9846730

IAEA-TECDOC-996

# ***Waterside corrosion of zirconium alloys in nuclear power plants***



INTERNATIONAL ATOMIC ENERGY AGENCY

**IAEA**

January 1998

*D*  
**29 - 15**

The IAEA does not normally maintain stocks of reports in this series.  
However, microfiche copies of these reports can be obtained from

INIS Clearinghouse  
International Atomic Energy Agency  
Wagramerstrasse 5  
P.O. Box 100  
A-1400 Vienna, Austria

Orders should be accompanied by prepayment of Austrian Schillings 100,—  
in the form of a cheque or in the form of IAEA microfiche service coupons  
which may be ordered separately from the INIS Clearinghouse.

The originating Section of this publication in the IAEA was:

Nuclear Fuel Cycle and Materials Section  
International Atomic Energy Agency  
Wagramer Strasse 5  
P.O. Box 100  
A-1400 Vienna, Austria

WATERSIDE CORROSION OF ZIRCONIUM ALLOYS IN  
NUCLEAR POWER PLANTS

IAEA, VIENNA, 1998

IAEA-TECDOC-996

ISSN 1011-4289

© IAEA, 1998

Printed by the IAEA in Austria  
January 1998

## FOREWORD

Technically the study of corrosion of zirconium alloys in nuclear power reactors is a very active field and both experimental work and understanding of the mechanisms involved are going through rapid changes. As a result, the lifetime of any publication in this area is short. Because of this it has been decided to revise IAEA-TECDOC-684 — Corrosion of Zirconium Alloys in Nuclear Power Plants — published in 1993. This updated, revised and enlarged version includes major changes to incorporate some of the comments received about the first version.

Since this review deals exclusively with the corrosion of zirconium and zirconium based alloys in water, and another separate publication is planned to deal with the fuel-side corrosion of zirconium based fuel cladding alloys, i.e. stress corrosion cracking, it was decided to change the original title to Waterside Corrosion of Zirconium Alloys in Nuclear Power Plants.

The rapid changes in the field have again necessitated a cut-off date for incorporating new data. This edition incorporates data up to the end of 1995; including results presented at the 11 International Symposium on Zirconium in the Nuclear Industry held in Garmisch-Partenkirchen, Germany, in September 1995.

The IAEA wishes to express its thanks to all the authors, both of this updated review and of IAEA-TECDOC-684 on which it was based. The IAEA staff member responsible for this publication was I.G. Ritchie of the Division of Nuclear Power and the Fuel Cycle.



### ***EDITORIAL NOTE***

*In preparing this publication for press, staff of the IAEA have made up the pages from the original manuscripts as submitted by the authors. The views expressed do not necessarily reflect those of the IAEA, the governments of the nominating Member States or the nominating organizations.*

*Throughout the text names of Member States are retained as they were when the text was compiled.*

*The use of particular designations of countries or territories does not imply any judgement by the publisher, the IAEA, as to the legal status of such countries or territories, of their authorities and institutions or of the delimitation of their boundaries.*

*The mention of names of specific companies or products (whether or not indicated as registered) does not imply any intention to infringe proprietary rights, nor should it be construed as an endorsement or recommendation on the part of the IAEA.*

## CONTENTS

1. INTRODUCTION .....	9
2. METALLURGY OF ZIRCONIUM ALLOYS .....	11
2.1. Processing .....	11
2.2. Microstructure .....	12
2.2.1. Pure zirconium .....	12
2.2.2. Alloys and alloying elements .....	12
2.3. Heat treatments and resultant microstructure .....	19
2.4. Deformation and texture .....	23
3. OXIDATION THEORY .....	27
3.1. Microcrystalline nature of the oxide .....	28
3.2. Electrical resistivity of zirconia .....	29
3.3. Effects of electric fields on the oxidation kinetics .....	29
3.4. Effect of impurities and alloying elements .....	34
4. CORROSION IN THE ABSENCE OF IRRADIATION .....	37
4.1. Introduction .....	37
4.2. Uniform oxide formation .....	37
4.2.1. Oxidation kinetics .....	40
4.2.2. Pre-transition oxidation mechanism .....	57
4.2.3. Mechanism of oxide breakdown on the Zircalloys .....	67
4.2.4. Mechanism of oxide breakdown in Zr-Nb alloys .....	78
4.2.5. Post-transition growth .....	78
4.3. Non-uniform (nodular) oxide formation .....	84
4.3.1. Nodular oxide formation .....	85
4.3.2. Mechanism of nodule formation .....	88
4.3.3. Simulating nodular corrosion in high temperature water .....	90
5. HYDROGEN ABSORPTION .....	91
5.1. Hydrogen absorption mechanism .....	91
5.1.1. Hydrogen uptake during corrosion .....	92
5.1.2. Absorption of hydrogen gas .....	104
5.1.3. Hydrogen absorption via metallic contacts .....	111
5.1.4. Hydrogen uptake during cathodic polarisation .....	114
5.2. Effects of hydrogen content on oxidation .....	116
6. FACTORS AFFECTING THE CORROSION OF ZIRCONIUM ALLOYS IN REACTORS ..	124
6.1. Alloy compositions for nuclear applications .....	124
6.1.1. Alloy types .....	124
6.1.2. Alloy development programmes .....	126

6.2. Metallurgical variables	136
6.2.1. Precipitate size	136
6.2.2. Influence of quenching conditions	145
6.2.3. Influence of final annealing	145
6.2.4. Influence of cold work and deformation sequence	150
6.2.5. Initiation of nodular corrosion in BWR materials	150
6.2.6. Effect of metallurgical conditions on the corrosion of Zr-Nb alloys	150
6.3. Surface conditions	152
6.4. Coolant chemistry	154
6.4.1. PWR chemistry	155
6.4.2. BWR chemistry	161
6.4.3. WWR chemistry	162
6.4.4. PHWR (CANDU) chemistry	164
6.5. Effect of temperature	164
6.5.1. High temperature oxidation of Zircaloy alloys	165
6.5.2. High temperature oxidation of Zr-1%Nb alloys.	165
6.6. Effect of heat flux	165
<b>7. MODELLING OF IN-REACTOR CORROSION OF ZIRCONIUM ALLOY FUEL CLADDING</b>	<b>170</b>
7.1. Introduction	170
7.2. Calculation of oxide-metal interface temperatures	171
7.2.1. Single phase coolants	171
7.2.2. Two phase coolants	173
7.2.3. Oxide thermal conductivity	174
7.3. Semi-empirical models for Zircaloy corrosion in PWRs	175
7.3.1. Generic formulation for semi-empirical models	178
7.3.2. Individual models of simple generic form	179
7.3.3. Individual models incorporating additional effects	188
7.4. Mechanistic models	189
7.4.1. Cox's model	189
7.4.2. Russian models for Zr-1%Nb cladding	191
7.5. Summary of PWR corrosion modelling	195
<b>8. IRRADIATION EFFECTS ON CORROSION</b>	<b>198</b>
8.1. Irradiation damage	198
8.1.1. Fast neutron damage in the metals	198
8.1.2. Displacement damage in other structures	199
8.1.3. Effect of irradiation on microstructures	203
8.2. Radiation chemistry	212
8.2.1. Radiolysis in the bulk water	212
8.2.2. Radiolysis near metal surfaces or in the pores surrounded by metal oxides	218
8.2.3. "Thick oxide film effects"	221
8.2.4. Localised corrosion and dissimilar metals	224
8.3. Crud deposition and heat transfer effects	225
8.3.1. PWR crud deposition	225

8.3.2. WWER crud deposition .....	236
8.3.3. BWR crud deposition .....	236
8.4. Metallurgical and chemical variables .....	238
8.4.1. Behaviour of alloying additions .....	238
8.4.2. Electrochemical effects .....	239
8.5. Corrosion of Zr-1%Nb cladding .....	242
9. PRESENT STATUS OF THE MECHANISTIC UNDERSTANDING .....	249
9.1. Current understanding of the out-reactor oxidation mechanism .....	249
9.1.1. Mobile species .....	249
9.1.2. Evolution of oxide morphology .....	250
9.1.3. The development and nature of oxide porosity .....	256
9.1.4. Oxide barrier layers .....	261
9.1.5. Effect of some variables on the oxide structure .....	264
9.2. Empirical correlations of effects of irradiation .....	265
9.2.1. Development of irradiation corrosion mechanisms .....	266
9.2.2. Open questions on micromechanisms for in-reactor corrosion .....	277
9.2.3. Present status of mechanistic studies .....	278
9.2.4. Recommendations for future work .....	278
APPENDIX .....	279
REFERENCES .....	281
BIBLIOGRAPHY .....	311
LIST OF CONTRIBUTORS .....	313

**NEXT PAGE(S)**  
**left BLANK**

## 1. INTRODUCTION

The original version of this TECDOC [1] was written at a time when major programmes on fuel cladding improvement were under way in most countries with active nuclear power programmes, but few of the results of these programmes had been published. The references on which this first version was based were cut off essentially prior to the Portland IAEA Conference [2], whose Proceedings were not then available, and the Kobe Zirconium Conference [3] respectively in September 1989 and November 1990, although a few references to these meetings were subsequently added. The contents of this version, therefore, rapidly became dated. The original version had been targeted at the relatively limited audience of those professionals actively working on some aspect of the research and development of corrosion resistant zirconium alloys, but in practice a large fraction of the demand came from those involved in the nuclear fuel cycle at the utility level. This has been taken into account in the new version.

Zirconium alloys continue to be the major structural materials employed within the fuelled region of all water cooled nuclear power reactors. Thus, they are invariably used as fuel cladding, fuel channels (boxes, wrappers), pressure tubes and calandria tubes and often as fuel spacer grids. Other structural metals appear in this region of the reactor core mainly as minor components such as grid springs and garter springs (spacers between pressure and calandria tubes in CANDUs). The performance of zirconium alloys in service has been generally satisfactory, although the pressures to achieve higher fuel burnups and higher reactor thermal efficiencies have pushed the historically used alloys to the limits of their capabilities. Evidence that these limits were being reached was the primary driving force for the major new alloy development programmes already mentioned. A further driving force has been the acknowledgement that debris fretting had become the primary cause of fuel failures, and that primary failures from this cause could lead to unexpectedly severe secondary failures, especially for zirconium barrier cladding developed to protect against pellet-cladding interaction (stress-corrosion cracking) failures as a primary defect mechanism.

In PWRs, therefore, there is a general desire to reduce oxidation rates in order to achieve higher fuel burnup and rating. However, because of the temperature feedback loop (section 7.2.3) at the end of life, the corrosion rate (and the associated hydrogen uptake rate) accelerates rapidly. Other factors may also increase the corrosion rate under these conditions, including the precipitation of hydrides (section 5.2), dissolution of precipitates and the concentration of lithium hydroxide. There is a need to understand the potential effects of concentrating lithium hydroxide under these conditions because they are linked to the ability to reduce circuit activation, and hence personnel radiation exposures, that could result from the use of increased LiOH concentrations. In BWRs, the infrequent secondary degradation failures that led to serious operational consequences as a result of rapid increases in off-gas radiation levels, are also the target of a major research and development effort.  $\beta$ -quenched cladding amongst other changes has eliminated serious episodes of nodular corrosion induced (Crud Induced Localised Corrosion-CILC) failures, but a reduction in end-of-life uniform oxide thickness is still a desirable objective.

As in any system where the consequences of minor changes in materials or operating conditions can have major impacts on the economics of the system if they lead to forced outages, it is vitally important that the consequences of any changes be thoroughly explored and understood. Decisions on whether to make operational changes (e.g. increased Li) can often be beset with conflicting requirements which have to be balanced before a decision can be made. It is hoped that this review will provide sufficient background and information on the factors controlling zirconium alloy corrosion and hydrogen uptake in-reactor to permit such decisions to be made on a sound basis.

The revised format of the review now includes

- Introductory chapters on basic zirconium metallurgy and oxidation theory,
- A revised chapter discussing the present extent of our knowledge of the corrosion mechanism based on laboratory experiments,

- A separate and revised chapter discussing hydrogen uptake,
- A completely reorganised chapter summarising the phenomenological observations of zirconium alloy corrosion in reactors,
- A new chapter on modelling in-reactor corrosion,
- A revised chapter devoted exclusively to the manner in which irradiation might influence the corrosion process,
- Finally, a summary of our present understanding of the corrosion mechanisms operating in reactor

Although much new information has become available in the last five years, there are still blocks of data that have not been linked together in an understandable manner. Thus, much of the early corrosion data was obtained from non-heat transfer specimens in in-reactor loops, whereas virtually all of the recent in-reactor data comes from high heat flux fuel cladding. Only minor amounts of recent data come from non-heat transfer surfaces such as oxide thicknesses on plena, spacer grids, pressure tubes, water rods or guide tubes. As a result, it remains difficult to extrapolate conclusions drawn from the early loop tests to the behaviour of current fuel cladding or pressure tubes.

Great strides have been made recently in delineating the impact of variations in fabrication route and of careful control of impurity and alloying additions on the in-reactor behaviour of fuel-cladding. As a result most fuel vendors have moved to some version of "optimised" Zircaloy cladding, as precursor to the introduction of new cladding alloys lying outside the range of the Zircaloy specifications. The introduction of such new alloys has been greatly facilitated by the demonstration of both the production and satisfactory performance of duplex cladding tubes. These are in the form of duplex tubes ~90% of the wall thickness of which is standard Zircaloy-4, with the outer ~10% of the tube made of the new alloy. This requires similar technology to that which puts unalloyed (or low alloyed) zirconium barriers on the inside of fuel cladding tubes for BWR applications. The advantage of this duplex tube technology is that alloys that could not be considered for fuel cladding use in a monotube form, because of inadequate, or inadequately known, mechanical properties, can be introduced in the form of duplex tubes with minimal regulatory limitations.

Another area where major changes have been apparent since the original review was written is in the availability of much evidence on the behaviour of Zr-1%Nb cladding in KOH/ammonia or hydrazine water chemistries typical of Russian designed reactors. This information has been incorporated wherever possible to provide a comparison with the observations on Zircaloy-4 in LiOH water chemistry. The low oxide thicknesses still present on Zr-1%Nb cladding after high burnup in KOH/ammonia water chemistry (where thermal hydraulic conditions have been comparable to those in a high temperature PWR, i.e.  $T_{\text{sat}} \geq 345^{\circ}\text{C}$  with sub-channel boiling) call for some comparative testing of Zircaloy-4 under these conditions so that any contribution of LiOH to current in-reactor experience can be properly evaluated.

This revision of the review should increase its value to a wider range of readership than was aimed for in the original.

## 2. METALLURGY OF ZIRCONIUM ALLOYS

In the process of selecting new structural alloys for water reactors, zirconium and its alloys were chosen because of the conjunction of the following properties: low thermal neutron capture cross section, high resistance to corrosion in high temperature water and relatively high mechanical strength. The main properties of Zr and the Zr alloys are given in Table 2.1. It should be noted that one of the main reasons for selecting Zr as a nuclear material is its low thermal neutron capture cross section which is about 30 times less than that of stainless steel giving a better neutron efficiency in water reactors.

The main characteristics of Zr metallurgy come from its high reactivity with oxygen, from the different type of chemical interactions with the alloying elements (complete solubility or intermetallic compound formation) and from its strongly anisotropic hexagonal crystal structure, the latter leading to the development of a textured material after thermo-mechanical processing.

Table 2.1. Physical Properties of the Zr Alloys

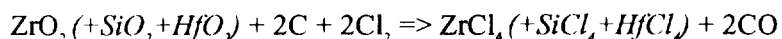
	Unit	Average	[11 $\bar{2}$ 0] direction	[0 0 01] direction
Specific mass	kg·m <sup>-3</sup>	6,500		
Thermal expansion	K <sup>-1</sup>	6.7×10 <sup>-6</sup>	5.2×10 <sup>-6</sup>	10.4×10 <sup>-6</sup>
Young's Modulus	GPa		99	125
Lattice parameter	nm		a = 0.323	c = 0.515
Thermal conductivity	W·m <sup>-1</sup> ·K <sup>-1</sup>	22		
Specific heat capacity	J·kg <sup>-1</sup> ·K <sup>-1</sup>	276		
Thermal neutron capture cross section, $\sigma$	barn (10 <sup>-28</sup> m <sup>2</sup> )	0.185		

### 2. 1. PROCESSING

The element zirconium is commonly found in nature associated with its lower row counterpart in Mendeleev's table, hafnium. Most of the common Zr ores contain between 1.5 and 2.5% Hf. Due to its high thermal neutron capture cross section ( $\sigma = 105 \pm 5$  barns for the natural mixture of isotopes), Hf needs to be removed from Zr for nuclear applications [4].

The most frequently used ore is zircon (ZrSiO<sub>4</sub>) with a world-wide production of about one million metric tons per year. Most of the zircon is used in its original form or in the form of zirconia (ZrO<sub>2</sub>) as foundry die sands, abrasive materials or high temperature ceramics. Only 5% is processed into Zr metal and alloys.

The processing of Zr alloy industrial components is rather difficult because of the high reactivity of this metal with oxygen. The first step is to convert the zircon into ZrCl<sub>4</sub>, through a carbo-chlorination process performed in a fluidized bed furnace at 1,200°C. The reaction scheme is the following:



After this step, Zr and Hf are separated using one of the two following processes:

- (i) After a series of chemical reactions to obtain Zr as a solution of hafnium-zirconium-thiocyanate (Zr, Hf)O(SCN)<sub>2</sub>, a liquid-liquid extraction is performed with methyl-isobutyl-ketone (MIBK, gives the name to the process). Because of the high quantities of chemical wastes induced by this process, the tendency is to use a direct separation method:
- (ii) A vapour phase distillation, at 350°C, within a mixture of KCl-AlCl<sub>3</sub>, where the liquid phase is enriched in Zr [5].

Zr metal is obtained by the reduction of  $\text{ZrCl}_4$  in gaseous form by liquid magnesium, at about 850°C in an oxygen-free environment, giving the sponge cake. This is the base product for alloy ingot preparation.

For industrial alloys, a lot of sponge pieces is compacted with the alloying elements - O (in the form of  $\text{ZrO}_2$ ), Sn, Fe, Cr, Ni and Nb - at the desired composition. It is melted in a consumable electrode vacuum furnace, usually three times. These vacuum meltings reduce the gas content and increase the homogeneity of the ingot. Typical ingot diameters range between 50 and 80 cm, for a mass of 3 to 8 metric tons.

Industrial use of Zr alloys requires either tube- or plate-shaped material. The first step in mechanical processing is forging or hot rolling in the  $\beta$  phase, at a temperature close to 1,050°C, or lower in the  $\alpha+\beta$  range. Hot extrusion followed by one cold reduction step is used to obtain tube shells or TREX (tube reduced extrusions), while hot rolling is used for flat products. Further reduction in size is obtained by cold rolling either on standard or pilger-rolling mills. Low temperature (500-700°C) recrystallization is performed between the various size reduction steps.

## 2.2 MICROSTRUCTURE

### 2.2.1 Pure zirconium

Pure zirconium crystallizes at ambient temperatures in the hexagonal close packed system, with a  $c/a$  ratio of 1.593. Lattice parameters are  $a = 0.323$  nm and  $c = 0.515$  nm [6]. The thermal expansion coefficients have been measured on single crystals. The difference in thermal expansion coefficients between the  $a$  and  $c$  directions (see Table 2.1.) implies that the  $c/a$  ratio tends towards the ideal ratio at higher temperatures.

At 865°C, Zr undergoes an allotropic transformation from the low temperature hexagonal close packed (hcp)  $\alpha$  phase to body centred cubic (bcc)  $\beta$  phase. On cooling, the transformation is either martensitic or bainitic, depending on the cooling rate. An epitaxy of the new  $\alpha$  platelets on the old  $\beta$  grains such as  $(0001)\alpha // \{110\}\beta$  and  $\langle 1120 \rangle \alpha // \langle 111 \rangle \beta$ , gives a microstructure in which a set of crystallographic orientations is found in the same former  $\beta$  grain, leading to a basket weave or parallel plate microstructure. The melting of pure Zr occurs at 1,860°C, and thus, Zr can be considered as a slightly refractory metal.

Among the different physical properties listed in Table 2.1, particular attention should be given to its strongly anisotropic behaviour. For instance, regarding the thermo-elastic properties, the differences in thermal expansion and Young's modulus along the main directions of the hexagonal lattice induce the development of internal stresses after any heat treatment due to grain-to-grain thermal expansion incompatibilities, after annealing at 500°C and cooling to room temperature, the  $\langle c \rangle$  planes are in tension at a stress level up to 100 MPa [7].

### 2.2.2 Alloys and alloying elements

The relative solubility of the various alloying elements in the  $\alpha$  and  $\beta$  phases is one of the bases for the choice of additions as well as heat treatments. Due to the impact of minor additions upon neutron physics performance, the high absorption species have chemical specifications in the range of a few ppm.

The zirconium alloys in use today for nuclear applications are limited in number. Besides pure Zirconium, grade R 60001, only four alloys are currently listed in the ASTM standard B 353 (Table 2.2). The first three are used for cladding and structural materials, such as guide tubes in PWRs, water channel boxes in BWRs and structural materials in CANDU reactors, while the last one, grade R 60904, is used in pressure tubes for CANDU or RBMK reactors.



Table 2.2. ASTM Specifications for Zr and Zr Alloys in Nuclear Industry

ASTM REF.	R 60001	R 60802	R 60804	R 60901	R 60904
Common Name	Pure Zr	Zircaloy 2	Zircaloy 4	Zr - Nb	Zr - Nb
Alloying Elements Mass %					
Sn		1.2-1.7	1.2-1.7	-	-
Fe		0.07-0.20	0.18-0.24	-	-
Cr		0.05-0.15	0.07-0.13	-	-
Ni		0.03-0.08	-	-	-
Nb		-	-	2.4-2.8	2.5-2.8
O		TBS*	TBS*	0.09-0.13	TBS*
Impurities (Max. ppm)					
Al	75	75	75	75	75
B	0.5	0.5	0.5	0.5	0.5
Cd	0.5	0.5	0.5	0.5	0.5
C	270	270	270	270	150
Cr	200	-	-	200	100
Co	20	20	20	20	20
Cu	50	50	50	50	50
Hf	100	100	100	100	50
H	25	25	25	25	25
Fe	1500	-	-	1,500	650
Mg	20	20	20	20	20
Mn	50	50	50	50	50
Mo	50	50	50	50	50
Ni	70	-	70	70	35
N	80	80	80	80	65
Pb					50
Si	120	120	120	120	120
Sn	50	-	-	50	100
Ta	-	-	-	-	100
Ti	50	50	50	50	50
U	3.5	3.5	3.5	3.5	3.5
V					50
W	100	100	100	100	100

\* To be specified on ordering, usually 1000-1400 ppm for the Zircaloys

For cladding tubes, only Zircaloy-2 and -4 are listed in ASTM B 811. Other alloys have been developed during the early history of nuclear power, but except for the Zr-1%Nb alloy used for cladding in Russian PWRs (WWERs) and BWRs (RBMKs), none are in current use any more, except for specialized applications such as the Zr-Nb-Cu alloy used in garter springs for CANDU pressure tubes. The needs for better performance of nuclear fuel assemblies and structural parts, mainly with regard to corrosion resistance, has led metallurgists and fuel designers to intensive R&D efforts in order to improve the properties of the Zr alloys by advanced compositions and thermo-mechanical processing, and to optimize the microstructure. Some of them are listed in Tables 6.1. and 6.2.

Since the specifications for Zr alloys have a rather large composition range, and since minor changes in chemical composition or microstructure have large impacts on properties, each fuel producer is developing a specific set of alloy compositions and heat treatments for advanced fuel design. The main directions for such alloy development can be found in the recent publications presented at the most recent ASTM symposia on Zr in nuclear industry or at the ANS and ENS conferences on nuclear fuel behaviour (see Bibliography). Some of those developments are presented in this document.

The following alloying elements are considered as the most important

**Oxygen** is to be considered as an alloying element, rather than an impurity. It is added to the compacts before melting as small additions of  $\text{ZrO}_2$  powder. Oxygen is an  $\alpha$ -stabilizer, expanding the  $\alpha$  region of the phase diagram by formation of an interstitial solid solution. The usual oxygen content is in the range of 800-1,600 ppm and its purpose is to increase the yield strength by solution strengthening: a 1,000 ppm oxygen addition increases the yield strength by 150 MPa at room temperature. The effect is less pronounced above 250°C.

The Zr-O phase diagram is given in Figure 2.1 a). At high concentrations, oxygen stabilizes the  $\alpha$  phase up to liquid temperatures. During high temperature oxidation, simulating a reactor accident, a layer of oxygen-stabilized  $\alpha$ -zirconium is found between the  $\beta$ -quenched structure and the zirconia. At normal operating temperatures, where the oxidation discussed in this document occurs, the oxygen diffusion layer ahead of the oxide front is very limited in thickness (below one micron at 400°C).

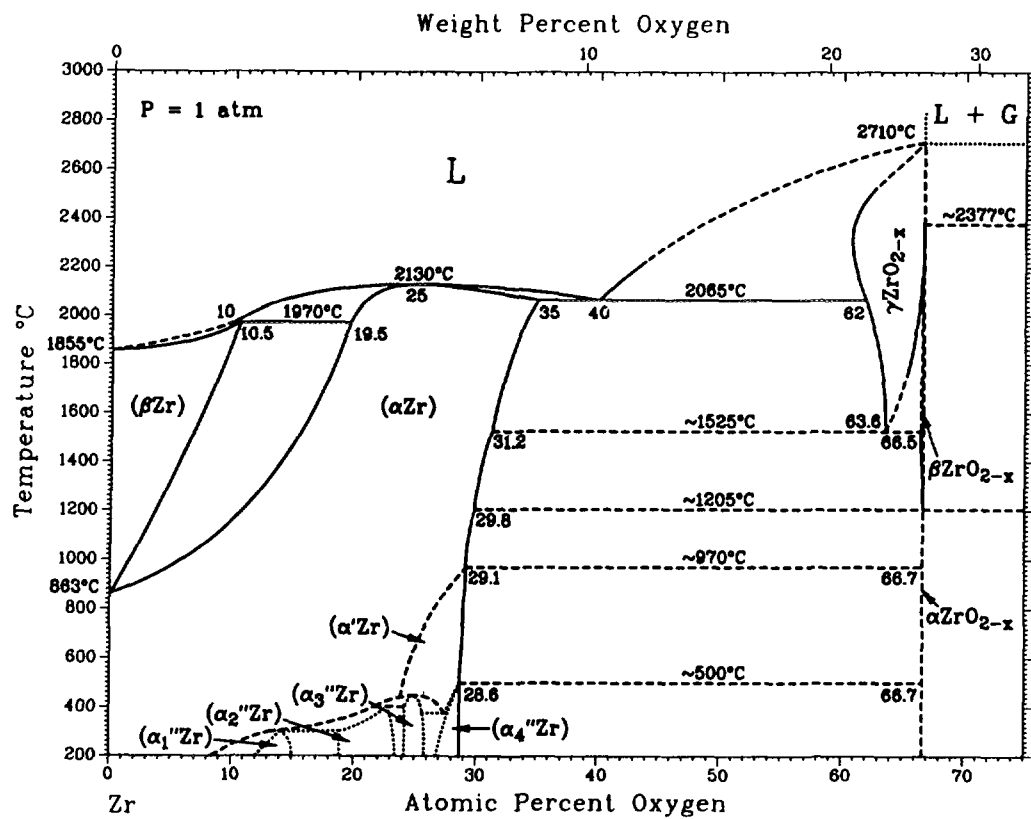
**Tin**, is also an  $\alpha$  stabilizer. It forms, in the  $\alpha$  and  $\beta$  phases, a substitutional solid solution. The Zr-Sn phase diagram is given in Figure 2.1 b). Sn, at a concentration of 1.2-1.7%, was originally added to increase the corrosion resistance, especially by mitigating the deleterious effects of nitrogen in deteriorating the corrosion resistance. Due to a better control of processing parameters, and consequently of nitrogen content, it is now possible, if desired, to reduce the tin contents in the current alloys for PWRs. Tin, however, has also an impact on the mechanical properties and therefore its concentration should not be excessively reduced, without specific consideration of this effect.

**Iron, Chromium and Nickel** are considered as " $\beta$ -eutectoids", because, in their phase diagrams, these elements give a eutectoid decomposition of the  $\beta$  phase (Figure 2.2a to 2.2c). They were added to the early binary Sn alloys after an "accidental pollution" of a melt, by a stainless steel coupon, showed an enhancement in corrosion resistance, leading to the Zircaloy-2 to -4 family.

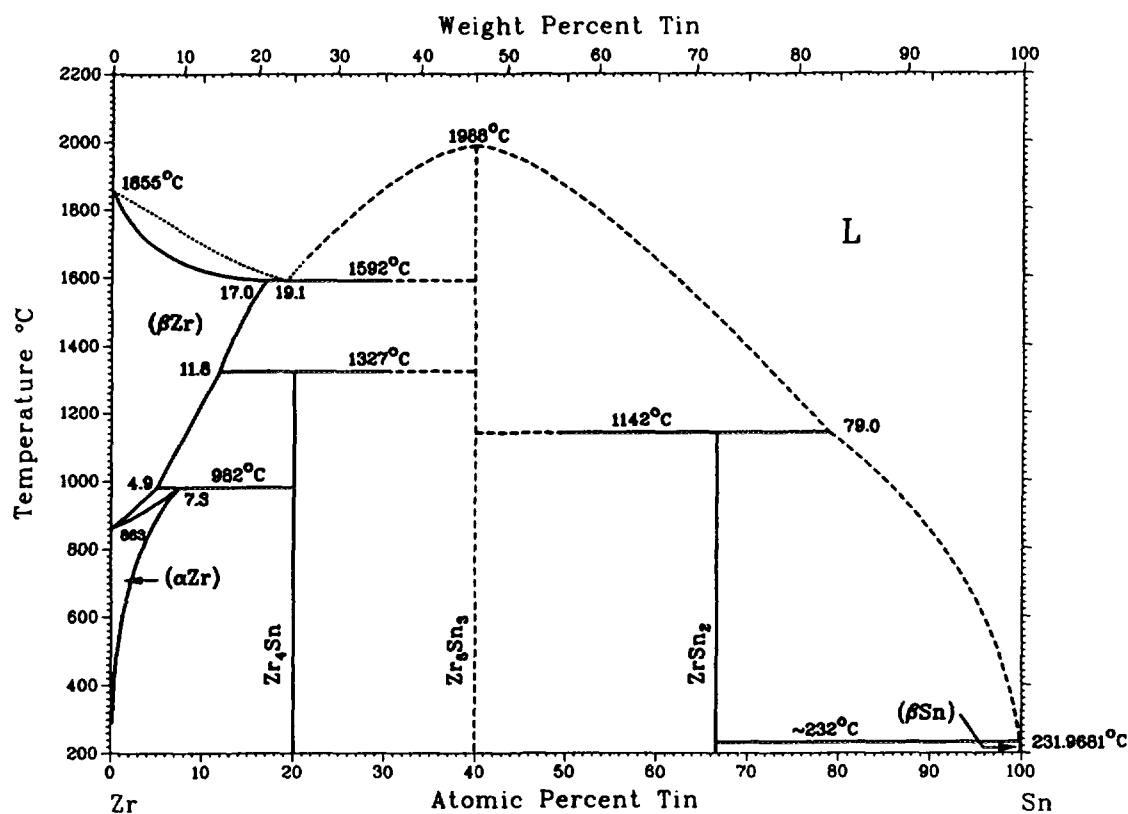
At their usual concentrations, these elements are fully soluble in the  $\beta$  phase. This temperature of dissolution is in the range of 835-845°C, i.e., in the upper  $\alpha+\beta$  range. In the  $\alpha$  phase their solubility is very low: in the region of 120 ppm for Fe and 200 ppm for Cr at the maximum solubility temperature [8]. For the Zr-Cr and Zr-Ni binary alloys, the stable forms of the second phase are  $\text{Zr}_2\text{Ni}$  or  $\text{ZrCr}$ . In the Zircalloys, the Fe substitutes for the corresponding transition metal and the intermetallic compounds found in Zircaloy are  $\text{Zr}_2(\text{Ni}, \text{Fe})$  and  $\text{Zr}(\text{Cr}, \text{Fe})$ . In Zircaloy-4, the Fe/Cr ratio of those precipitates is the same as the nominal composition of the alloy. In Zircaloy-2 alloys, the partitioning of Fe between the two types of intermetallic phases leads to a more complex relationship between nominal composition and precipitate composition, giving a broad range of Fe/Cr ratios in  $\text{Zr}(\text{Cr}, \text{Fe})$ , and Fe/Ni in  $\text{Zr}_2(\text{Fe}, \text{Ni})$  [9].

The  $\text{Zr}(\text{Cr}, \text{Fe})$  precipitates are either hcp or fcc, - both structures are Laves phases - depending on composition and heat treatment, and usually show the characteristic stacking faults as seen in Figure 2.3. The equilibrium crystallographic structure is dependent upon the Fe/Cr ratio, cubic fcc (structure type C15) below 0.1 and above 0.9, and hexagonal hcp (C14) in between. In common alloys, both types of structure are found, even in the same sample, with random probabilities of occurrences of each. The  $\text{Zr}_2(\text{Ni}, \text{Fe})$  precipitates are a Zintl phase with the body centred tetragonal (C16) structure.

The size of these precipitates is of importance for the properties of the alloys, especially the corrosion rate. Better uniform corrosion resistance is obtained for Zircalloys used in PWRs if they contain large precipitates, while better resistance to localized forms of corrosion is seen in BWRs in materials that have finely distributed small precipitates. Section 6.2 describes in detail the thermomechanical treatments required to control the precipitate size distribution and their impact on corrosion.



a)



b)

FIG. 2.1. a) the Zirconium-Oxygen phase diagram and b) the Zirconium-Tin phase diagram.

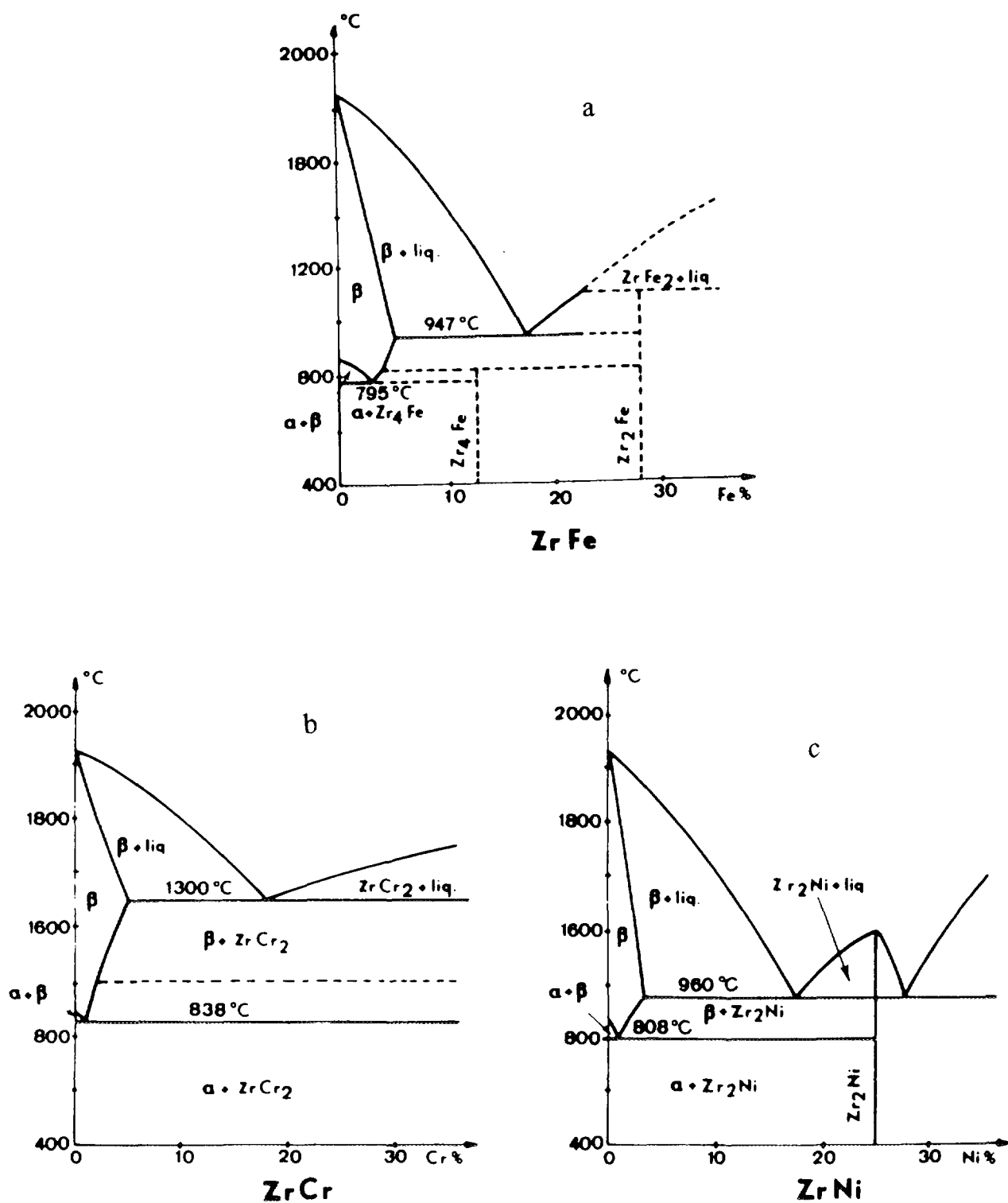


FIG. 2.2. The Zirconium eutectoid phase diagrams (a-Fe, b-Cr, c-Ni).



*FIG. 2-3 Microstructure of the Zr (Fe, Cr) precipitates with characteristic stacking faults*

**Niobium** (columbium) is a  $\beta$  stabilizer. From pure  $\beta$ -Zr to pure Nb there exists complete substitutional solid solution at high temperature (Figure 2.4). A monotectoid transformation occurs at about 620°C and around 18.5 at% Nb. By water quenching from the  $\beta$  or upper  $\alpha+\beta$  regions, the  $\beta$  Nb-rich grains transform by martensitic decomposition into an  $\alpha'$  supersaturated hcp phase; subsequent heat treatment below the monotectoid temperature leads to the precipitation of  $\beta'$  Nb precipitates at twin boundaries of  $\alpha'$  needles [10]. In addition a metastable  $\omega$  phase can be obtained from the  $\beta$  phase by slow cooling or ageing of a quenched structure. In the Zr-1%Nb or Zr-2.5%Nb alloys, the very small amount of Fe impurity present is usually not found in the  $\alpha$ -phase, most of it being in the remaining  $\beta$ -phases, in metastable solid solution.

**Other minor constituents** are often found in the form of precipitates. Among them are the carbide fcc-ZrC and silicides or phosphides of various stoichiometries ( $\text{Zr}_3\text{Si}$ ,  $\text{ZrSi}_2$ ,  $\text{ZrP}$ ,  $\text{Zr}_3\text{P}$ ). Silicon tends to segregate in the  $\text{Zr}_3(\text{Ni}, \text{Fe})$  precipitates. It has recently been found that C and Si have a clear impact on the corrosion behaviour of the alloys in reactor operation. Therefore, most of the fuel vendors now add specific requirements on these elements for the new alloys.

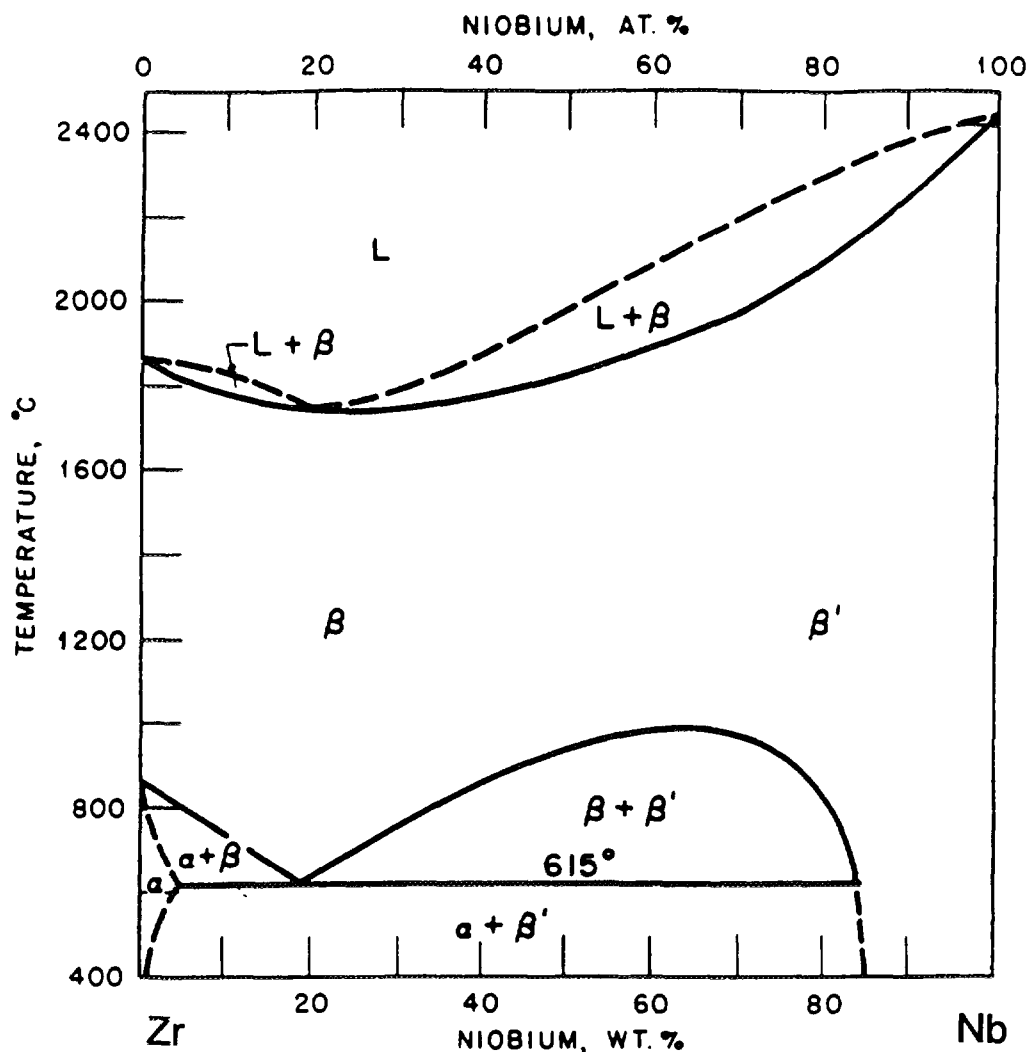


FIG. 2.4. The Zirconium-Niobium phase diagram.

## 2. 3. HEAT TREATMENTS AND RESULTANT MICROSTRUCTURE

After ingot melting, the thermo-mechanical processing commonly used for industrial alloys is the following:

- Hot forging in the  $\beta$  range (1,000 to 1,050°C);
- Water quenching from the homogeneous  $\beta$  phase (above 1,000°C);
- Intermediate temperature (upper  $\alpha$ ) forging and rolling, or extrusion for tubes;
- A series of cold temperature rollings followed by intermediate anneals in vacuum furnaces.

Homogenization in the  $\beta$  phase leads to the complete dissolution of all the second phase particles, but gives rise to significant grain growth. After 30 minutes at 1,050°C, grain size may reach several millimetres. During the water quench, the  $\beta$  grains transform into  $\alpha$  needles by bainitic transformation due to the slow cooling rate of the large ingots involved. The  $\beta$ -eutectoid elements are repelled by the transformation front and precipitate at the boundaries of those needles (Figure 2.5). This  $\beta$  quench is a reference state for further processing. The cold working steps and intermediate recrystallizations allow further control of the precipitate size distribution.

After each cold working step of plate or tube material, an annealing treatment is mandatory to restore ductility. It is usually performed in the range of 530-600°C to obtain the fully recrystallized material (RX). The resultant microstructure is an equiaxed geometry of the Zr grains with the precipitates located at the  $\alpha$ -grain boundaries (they are obtained there not by intergranular precipitation, but because they pin the grain boundaries during grain growth) and within the grains (Figure 2.6). These different heat treatments contribute to the control of the cumulative annealing parameter to be described in section 6. 2. For better mechanical properties of the final product, the temperature of the last annealing treatment can be reduced to avoid complete recrystallization. This is the stress-relieved (SR) state, characterized by elongated grains and a high density of dislocations, and thus a greater mechanical strength.

In the case of Zr-2.5%Nb alloys,  $\beta$  quenching in water of small pieces leads to the precipitation of  $\alpha'$  martensite supersaturated in Nb. Tempering at an intermediate temperature results in  $\beta$ -Nb precipitation at the lath boundaries and at twin boundaries within the lath [10], followed by transformation of  $\alpha'$  into  $\alpha$ . When quenching is performed from an  $\alpha+\beta$  region, a uniform distribution of  $\alpha$  and  $\beta$  grains is obtained, and the Nb-rich  $\beta$  phase does not transform. In this latter case, however, the texture is less uniform along the length of the tube than in  $\beta$  quenching. After rolling or extrusion, the Nb-rich  $\beta$  grains tend to align and the resultant microstructure is shown in Figure 2.7. By ageing, at temperatures in the region of 500°C, the metastable Nb-rich  $\beta$  phase can be decomposed into an hcp  $\omega$  phase. This gives a sharp increase in mechanical strength due to the fine microstructure obtained by the  $\beta \rightarrow \omega$  transformation [11]. In the usual form of the Zr-2.5%Nb used in the CANDU pressure tubes, the cold worked condition after  $\alpha+\beta$  extrusion and air cooling, the microstructure consists of Zr grains with layers of Nb rich  $\beta$ -Zr phase (close to the eutectoid composition). Due to the affinity of Fe for the  $\beta$  phase, most of this element is found in the minor  $\beta$  grains. These  $\beta$  grains are metastable and decompose upon aging into a mixture of  $\alpha$ -Zr and  $\beta$ -Nb. For the amount of Nb remaining, the  $\alpha$ -Zr phase itself is metastable and an irradiation-induced precipitation from the slightly supersaturated Nb solid solution can occur, which is believed to improve corrosion resistance [12].

The general procedure for tube fabrication is similar for different Zr-based alloys. For the production of Zr tubing in Russia it is mandatory to provide a structure close to the equilibrium one (phase composition, recrystallization). The structure of Zr-2.5%Nb pressure tubes used in boiling water reactors (RBMKs) is not fully recrystallized; the recrystallized fraction increases with temperature. The final anneal is usually carried out at 550-560°C (Figure 2.8a).

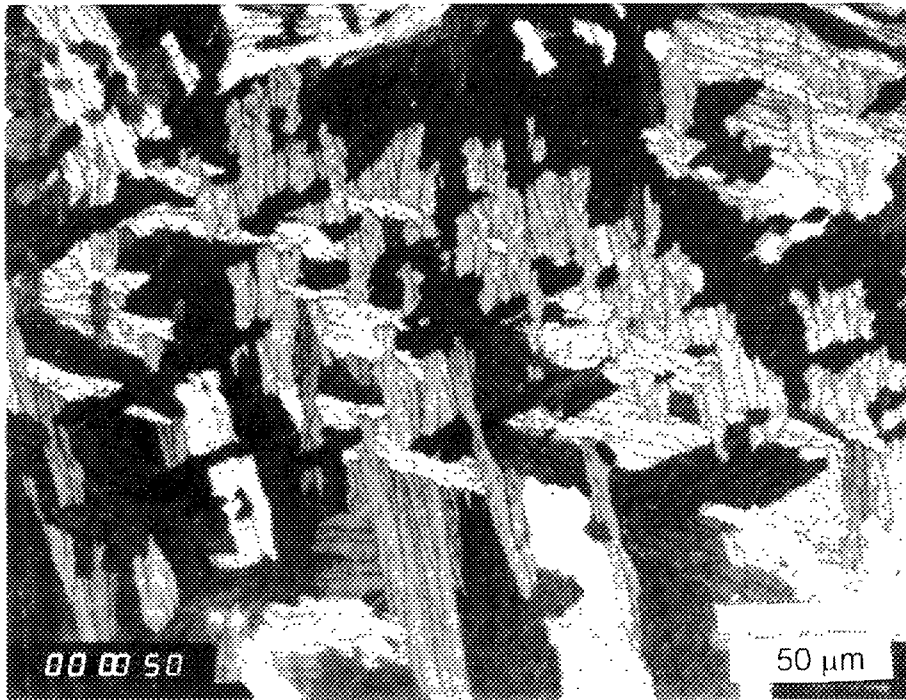


FIG. 2.5. Typical microstructure of  $\beta$ -quenched Zr alloy with precipitates present at former  $\beta$  grain boundaries.

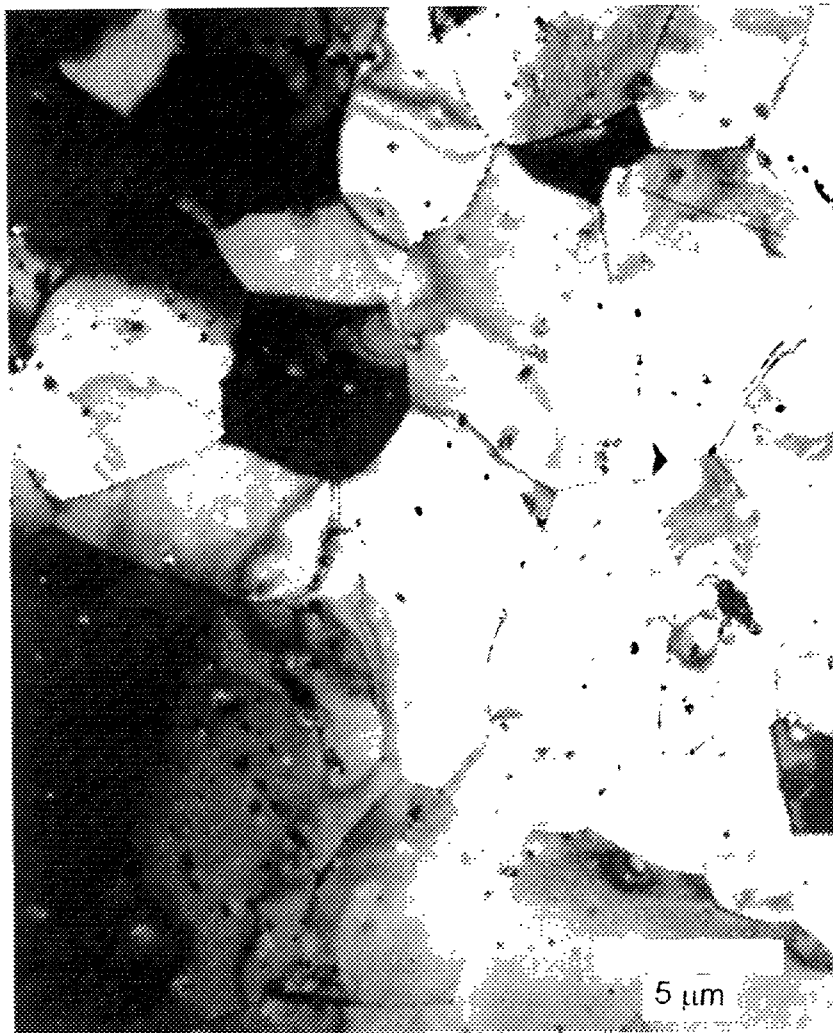


FIG. 2.6. TEM observation of recrystallized Zircaloy-4 cladding tube with  $\text{Zr}(\text{Fe}, \text{Cr})_2$  precipitates.



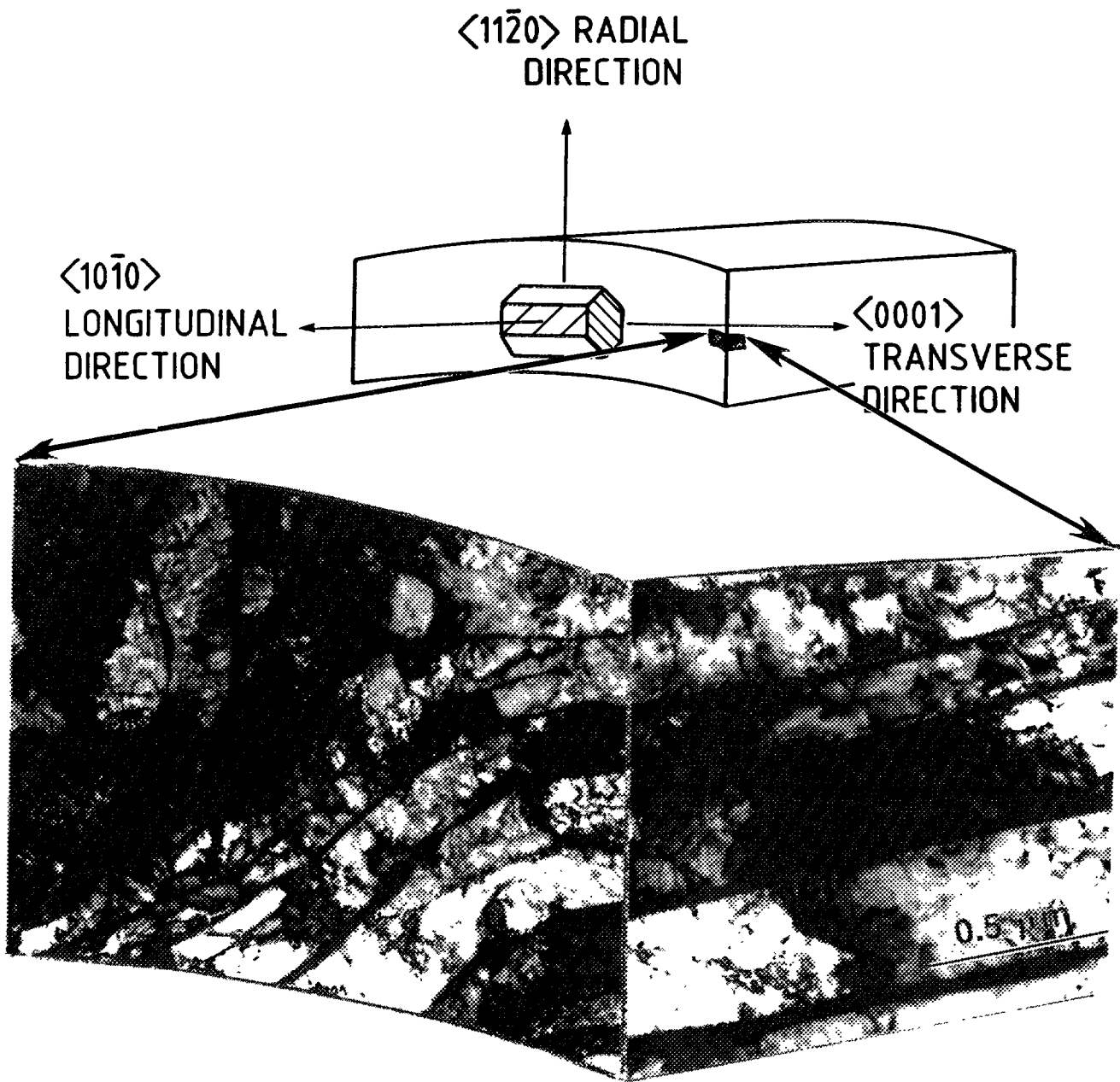


FIG. 2.7. Typical microstructure of Zr-2.5%Nb pressure tubes.

During the anneal, the  $\beta$ -Zr interlayer precipitates, which are disposed along the  $\alpha$ -Zr grain boundaries, decompose to form  $\beta$ -Nb particles containing 85-90% Nb. Prior to final cold reduction it is possible to use quenching from the temperature of ( $\alpha$ + $\beta$ ) or  $\beta$  phases (Figure 2.9): this results in dissolution of  $\beta$ -Zr interlayers and promotes, during subsequent thermo-mechanical treatment, the precipitation of uniformly distributed finely dispersed  $\beta$ -Nb particles. This improves, to some extent, corrosion resistance under irradiation.

In Zr-1%Nb alloys used for cladding material, the  $\alpha$ -Zr structure is close to fully recrystallized after the final anneal at 580°C. The structure of the tubes reveals finely dispersed  $\beta$ -Nb precipitates along boundaries of  $\alpha$ -Zr grains and in the matrix (Figure 2.10a). This structure, and the phase distribution not containing  $\beta$ -Zr, provide the high corrosion resistance of tubes.

The multi-component Zr-1.0%Nb-1.3%Sn-0.4%Fe alloy proposed as cladding and pressure tube material has a higher corrosion resistance than the Zircalloys in specific environments. This is caused by the availability of intermetallic particles containing Zr, Nb, Fe in the form of  $Zr(Nb, Fe)$  or  $(Zr, Nb)_2Fe$  types. For use as a pressure tube material, the alloy in the partially recrystallized state was studied and recommended, while as cladding material the alloy must be fully recrystallized (Figures 2.8b and 2.10b).

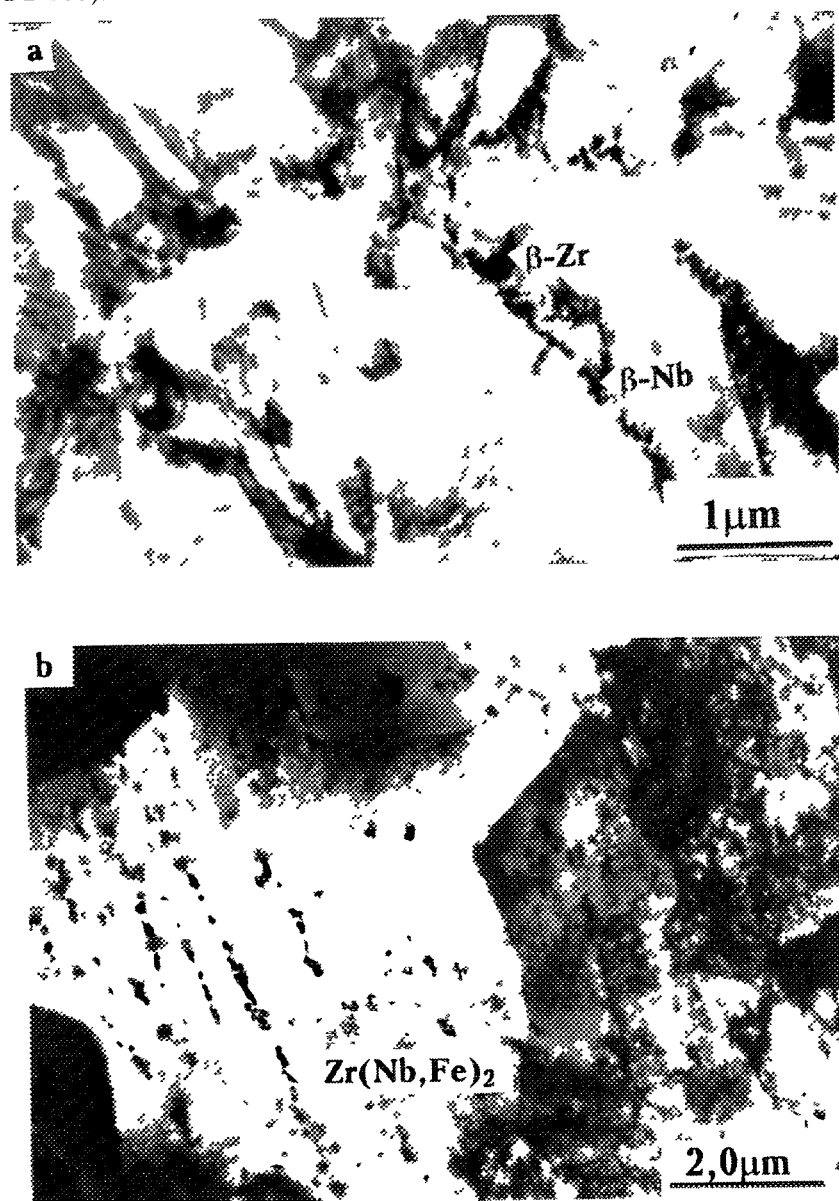


FIG. 2.8. Microstructure of pressure tubes. a) partially recrystallized Zr-2.5%Nb, b) partially recrystallized Zr-1Nb-1.3Sn-0.4Fe (E635) alloy

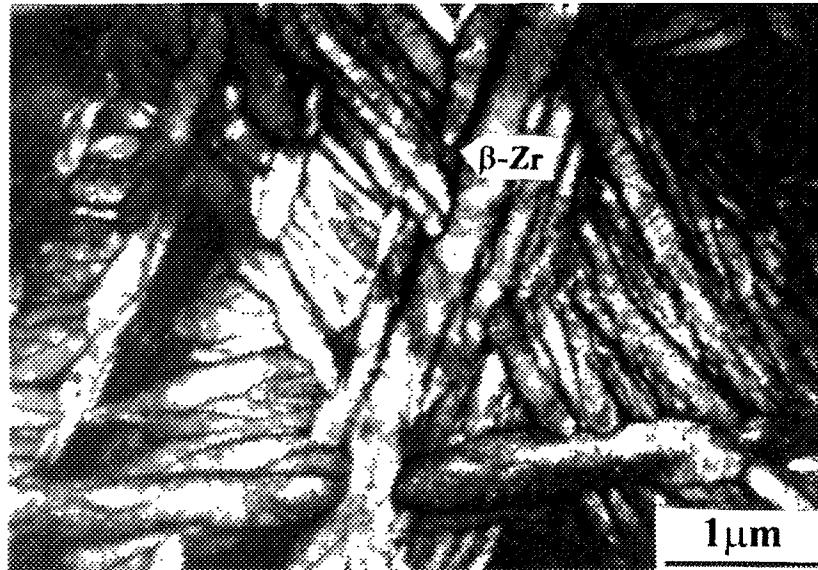


FIG. 2.9. Microstructure of  $\beta$ -quenched Zr-2.5%Nb alloy and  $\alpha'$  martensite.

#### 2. 4. DEFORMATION AND TEXTURE

Plastic deformation of Zr alloys is obtained either by dislocation slip, mostly on prism planes or by twinning during cold rolling [13]. In addition, at high deformations and as the temperature is increased,  $(c + a)$  type slip is activated on pyramidal planes [14]. At room temperature the twinning is activated on several systems: for tensile stress in the  $c$  direction  $\{10\bar{1}2\}\langle 1011\rangle$  twins are the most frequent, while the  $\{11\bar{2}2\}\langle \bar{1}\bar{1}23\rangle$  system is observed when compression is applied in the  $c$  direction.

At the large strains obtained during mechanical processing, steady state interactions occur between the twin and slip systems. The result is a tendency to align the basal planes parallel to the direction of the main deformation for rolling and pilgering and perpendicular to that direction for extruding [13]. The final texture may change with the specific conditions of the processing mechanisms chosen. For cold rolled materials (sheets or tubes), the textures are such that the majority of the grains have their  $c$ -axis tilted 30-40 degrees away from the normal of the sheet towards the transverse direction, as can be seen in the (0002) pole figure shown in Figure 2.11. During tube pilgering, the spread of the texture can be reduced by control of the ratio of the wall thickness to diameter reduction (Q factor): a reduction in wall thickness higher than the reduction in diameter gives a more radial texture, i.e., a texture with the  $c$  poles closer to the radial direction as illustrated in Figure 2.12 [9]. After cold processing and stress relief treatment, the  $\langle 1010\rangle$  direction is parallel to the rolling direction, and during recrystallization, a 30-degree rotation occurs around the  $c$  direction and the rolling direction is then aligned with the  $\langle 11\bar{2}0\rangle$  direction.

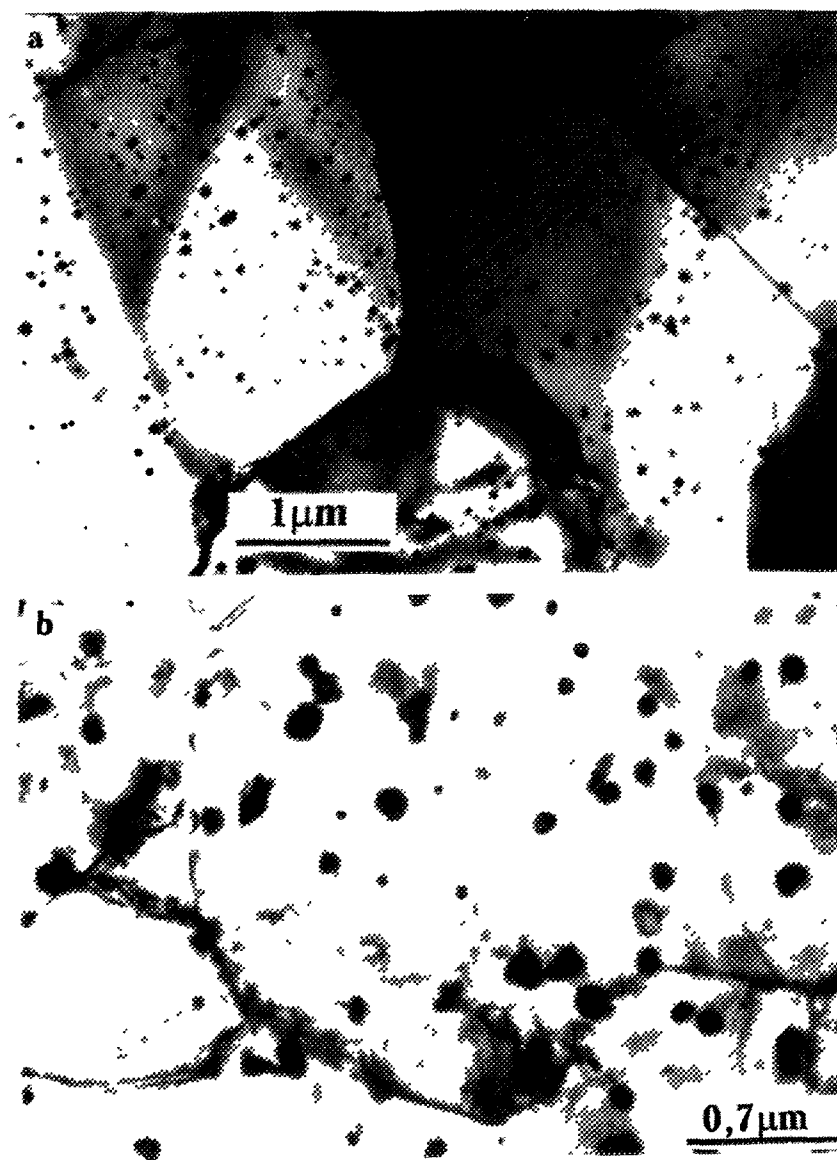
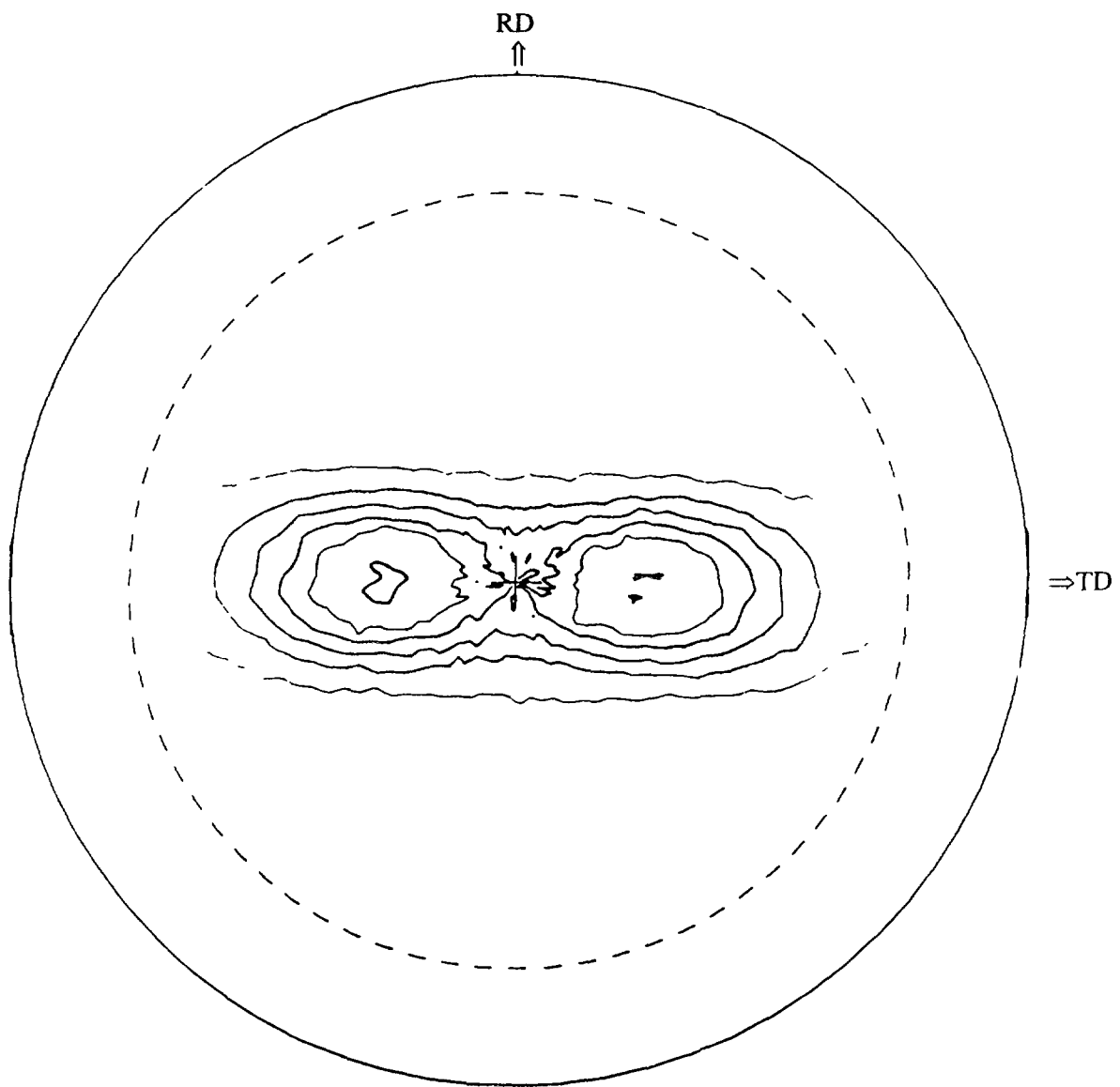


FIG. 2 10. Microstructure of fuel cladding tubes: a) recrystallized Zr-1%Nb alloy, with uniform distribution of  $\beta$ -Nb precipitates in the matrix and at grain boundaries, b) recrystallized Zr-1Nb-1.3Sn-0.4Fe (E635) alloy with  $Zr(Nb, Fe)_2$ .



*FIG. 2.11. (0002) Pole figure of cold rolled Zircaloy-4 sheet.*

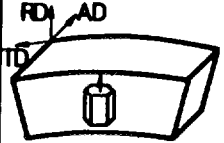
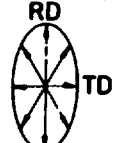
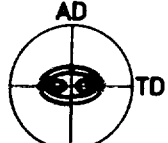
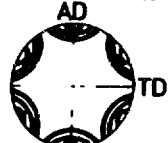
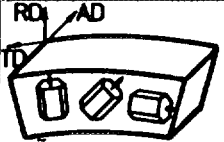
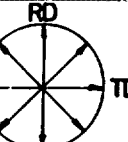
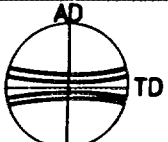

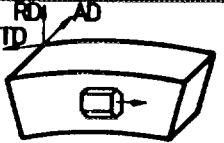
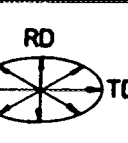

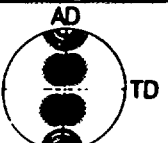
TYPE OF DEFORMATION	TUBE	STRAIN ELLIPSE IN THE PLANE PERPENDICULAR TO THE DIRECTION OF DEFORMATION	DEFORMATION TEXTURE	
			(0002) POLE FIGURE	$\{10\bar{1}0\}$ POLE FIGURE
TUBE REDUCTION WITH $\frac{R_W}{R_D} > 1$				
$\frac{R_W}{R_D} = 1$				
$\frac{R_W}{R_D} < 1$				

FIG. 2.12. Type of deformation, resulting strain ellipse and the derived basal pole figure for different tube reduction values (schematically) (a)  $R_W/R_D > 1$ , (b)  $R_W/R_D \cong 1$  and  $R_W/R_D < 1$  (ASTM-STP-754, p. 14).

### 3. OXIDATION THEORY

It is intended here to present a simplified introduction to the various theories of the oxidation of metals, and to consider to what extent the zirconium alloy oxidation system satisfies the boundary conditions required by these theories. There have been many books and reviews of this topic, and more detailed descriptions of the various derivations can be found, inter alia, in the works of Cabrera and Mott [15], Hauffe [16] and Fromhold [17].

If we start with an oxygen free single crystal surface of a metal and allow the initial stages of gas phase oxidation - collision of oxygen molecules with the surface, adsorption, dissociation of the adsorbed molecules, and place exchange of oxygen and metal atoms to form a layer of oxide - to go to completion, then we start with a thin parallel sided layer of oxide that may also be without grain boundaries. The mechanism of thickening of this layer may then be considered. As a result of the thermodynamics of the oxidation system being considered and the environment and temperature to which the material is exposed, defect concentrations will be established at the two interfaces of the oxide layer. If we neglect, for simplicity, the presence of an electric field across the oxide, and of any space charge either locally or in layers near the interfaces, then it will be the differences in the defect concentrations across the oxide film that will provide the driving force for the diffusion of the various possible species across the oxide film. These mobile species will be some combination of cation interstitials or vacancies, anion interstitials or vacancies and electrons or holes. In any particular system the most probable migrating species can be established from studies of the defect structure of the phases observed in the oxide film. If this is known, then the concentration gradients of the various defect species across the oxide film can be estimated from the oxygen partial pressures ( $p_{O_2}$ ,  $p_{O_2}$ ) at the oxide/environment surface and the oxide/metal interface respectively.

The rate of diffusion of each defect species can then be estimated from the concentration of each species ( $C_1, C_2, \dots, C_n$ ) and its diffusion coefficient in the oxide. Although in theory the diffusion coefficient of a species can be calculated from the difference between its equilibrium and saddle-point free energies (activation energy) during each jump in the diffusion process and the lattice dynamics, in practice diffusion coefficients cannot be calculated from first principles and must be measured experimentally. If this diffusion coefficient ( $D_i$ ) is known, then the flux of a particular defect ( $J_i$ ) at any position ( $x$ ) in the oxide (where the  $x$  direction lies in the thickness direction and  $y$  and  $z$  lie in the plane of the oxide/metal interface) is given by Fick's 1<sup>st</sup> Law:

$$J_i = -D_i dC_i/dx \quad (3.1)$$

Given the boundary conditions of no field in the oxide and no local space charge, this would be the only migration process transporting matter through the oxide. It is also assumed that the partial oxidation reactions occur only at one or other of the oxide surfaces and not within the oxide. The flux of each species must, therefore, be constant throughout the oxide. It is also usually assumed that the diffusion coefficient ( $D_i$ ) is constant throughout the oxide, but we will see later that there can be situations where this is not the case. If the difference in the concentration of each species between the oxide/metal interface ( $C_i^l$ ) and the oxide surface ( $C_i^s$ ) is given as  $\Delta C_i$ , then, when the oxide has a thickness  $l$ , the flux is given by:

$$J_i = -D_i \Delta C_i / l \quad (3.2)$$

In many oxidation systems both anions and cations are mobile during oxidation, and the fluxes of both must be summed to obtain the total oxidation flux. However, during zirconium alloy oxidation only the oxygen anions are mobile, so we should expect

$$f(dl/dt) = K^1 J_o = K/l \quad (3.3)$$

Where  $K^1$  is a constant (the partial specific volume) that relates the amount of oxide formed by a given flux of the mobile species, and  $K$  (the parabolic rate constant) =  $K^1 D \Delta C$ .

The integrated form of this is

$$l_t^2 - l_0^2 = 2Kt \quad (3.4)$$

the parabolic growth law first observed experimentally by Tammann [18]

This is the zero field approximation which is valid, strictly speaking, only for the migration of uncharged species down the concentration gradient. This difficulty is overcome in the Wagner-Hauffe theory [16] by requiring local electroneutrality at all times. This process, called "ambipolar diffusion", is seen as a coupling between ionic and electronic defect migration on a local scale in order to avoid the creation of space charge, and is one of the boundary conditions that must be met for the application of the Wagner-Hauffe theory. A further pre-requisite for the Wagner-Hauffe theory is that cation and anion diffusion are equally likely.

Thus, we have a number of boundary conditions that must be met if the Wagner-Hauffe theory is to be applied

- Both metal and oxide should be homogeneous in the yz plane (i.e., ideally both should be monocrystalline)
- Only diffusional transport should be rate-determining
- Ionic and electronic transport must be coupled to maintain local electroneutrality
- Cation and anion diffusion should be equally likely

These conditions are obviously most likely to be met at high temperatures and for electrically conducting oxides. They will also be most applicable to the growth of thick oxide films where any space charge layers that are present at the oxide interfaces will have the least influence on the overall diffusion processes. Fromhold [17] gives a lower limit for the possible attainment of such conditions as  $\sim 0.1 \mu\text{m}$ , and the upper limit for the possible modification of diffusion by space charge effects as  $\sim 10 \mu\text{m}$ .

If we consider the applicability of these boundary conditions to zirconium alloy oxidation we find that

- Even on a zirconium single crystal face the zirconia crystallite size is very small (5-20 nm) when a thin oxide is formed at reactor temperatures
- Until very high temperatures are reached, coherent oxide films on zirconium alloys seldom exceed 2-3  $\mu\text{m}$ , and so break down before they exceed a thickness at which space charge effects would be expected to cease to influence diffusion
- Zirconia is an electrical insulator with the electronic current flowing at locally conducting defect sites. It is not clear that local electroneutrality can be maintained in such a material
- Only anion diffusion has been detected, so far, during zirconium oxidation

Most of these aspects of zirconium alloy oxidation will be discussed in more detail later but it may be appropriate to consider, at present, how these departures from the required boundary conditions might affect the expected oxidation kinetics.

### 3.1 MICROCRYSTALLINE NATURE OF THE OXIDE

If the small oxide crystallite size was the only point at which zirconium oxidation failed to meet the boundary conditions required for the application of the Wagner-Hauffe theory, then this might be simply accommodated by using a composite diffusion coefficient in the parabolic rate equation. This would allow for the observation that crystallite boundary diffusion in zirconia films is much faster than bulk diffusion [19,20], and for the significant fraction of grain boundary area



represented by the very small crystallite size. This was the route taken in many early studies of zirconium oxidation in oxygen. Even when the oxidation kinetics, in relatively short oxidation experiments, could not be well fitted to parabolic plots, an effective diffusion coefficient for the oxide was often calculated. Examples of such results are given in Figure 3.1 and 3.2 [21].

For such an approach to be meaningful the mean crystallite size (and hence the volume fraction of crystallite boundary material) must remain constant throughout the experiment. This seemed to be the case only for short experiments or low temperature oxidation. However, when much longer experiments were done the rate law changed from parabolic (at short times) to cubic (at long times). An example of such a curve is shown in Figure 3.3 [22]. It was soon determined [23] that the most probable cause of this change in kinetics was the development of large columnar oxide grains in thick films from an initial state where the oxide crystallite size in the thin oxide is isotropic and much smaller than the oxide thickness at transition (see section 9.1.2). This results in a decrease in crystallite boundary area as one progresses towards the oxide-metal interface, which translates into a decrease in the effective diffusion coefficient as one progresses through the film. Since the flux of oxygen has to remain constant through the oxide, this results in a non-linear vacancy concentration gradient and a lower average growth rate than predicted by the parabolic rate law. There is also, of course, a decreasing average diffusion coefficient in such oxides as a function of time (or oxide thickness) so that the change in the exponent of the oxidation kinetics with increasing time actually measures the kinetics of oxide crystallite growth as the oxide thickens.

There are two main hypotheses for this crystallite growth, and for the development of a texture in the oxide [24,25], since the columnar crystallites always grow normal to the oxide/metal interface. The first argues that the compressive stresses in the oxide drive the preferential growth of specific crystallite orientations since the orientations of the columnar crystallites that are observed are those that most effectively minimise the stress in the oxide [26], while the second predicts that the stress build-up has a direct effect on the effective vacancy volume and so affects the diffusion coefficient directly [27]. Crystallite growth then becomes a consequence of this. The latter hypothesis appears to be the less probable in view of the predominantly crystallite boundary diffusion process that is occurring during the growth of zirconia films. A more detailed discussion of this can be found in section 4.2.1.1.

### 3.2 ELECTRICAL RESISTIVITY OF ZIRCONIA

Zirconia is a very good electrical insulator when pure, and it might be argued that the much lower effective resistivity of oxide films on zirconium alloys resulted from doping of the oxide by impurities and alloying elements. This would lead to a relatively homogeneous increase in oxide conductivity which might still allow the "ambipolar diffusion" criterion to be met. However, experimentation has shown that in most oxide films on zirconium alloys, the electrical conductivity is localised at the sites of second phase particles (formed as a result of the insolubility in zirconium of many impurities and alloying elements). Thus, the migration routes for ionic and electronic transport may become quite widely separated. Since overall electrical neutrality must be maintained, only a "coupled current" approach, such as that proposed by Fromhold [17], seems to satisfactorily fit the situation. This allows for the net negative and positive charge currents to be zero in the oxide, and for the electric fields to be perturbed in the oxide, without requiring a rigid electroneutrality criterion at every point in the oxide. The other consequence of a relatively wide separation of ionic and electronic conduction routes will be the probable presence of large internal electric fields and inhomogeneous space charge distributions. The effect of such phenomena on the kinetics will be considered next.

### 3.3 EFFECTS OF ELECTRIC FIELDS ON THE OXIDATION KINETICS

We have seen that control of oxidation solely by diffusion, with local electroneutrality maintained, gives rise to the parabolic rate law. If a constant electric field,  $E$ , is imposed across the

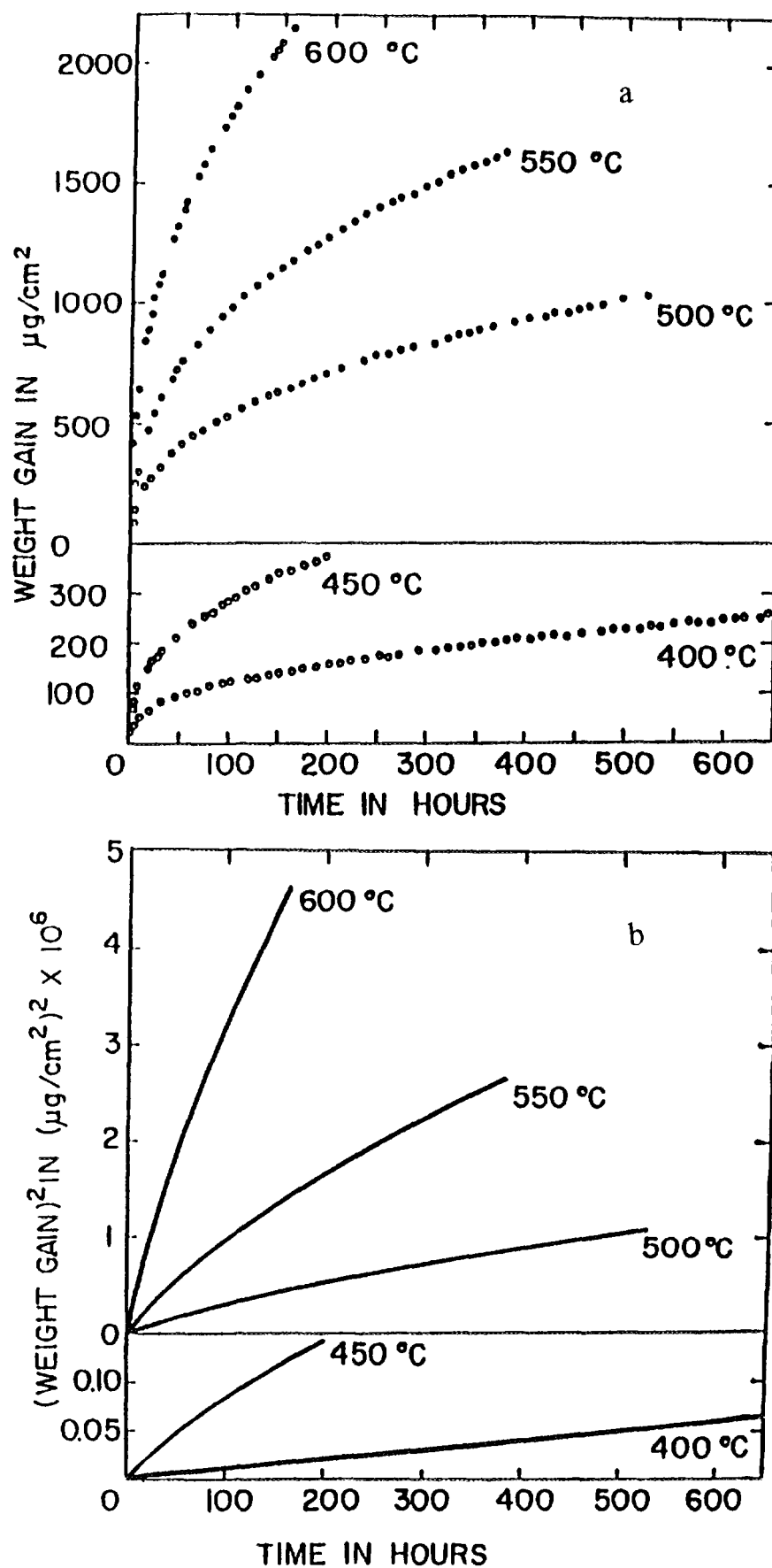


FIG. 3.1. Oxidation of zirconium at 400-600°C in oxygen at 10 cm Hg pressure. a. linear plot, b. parabolic plot [21].

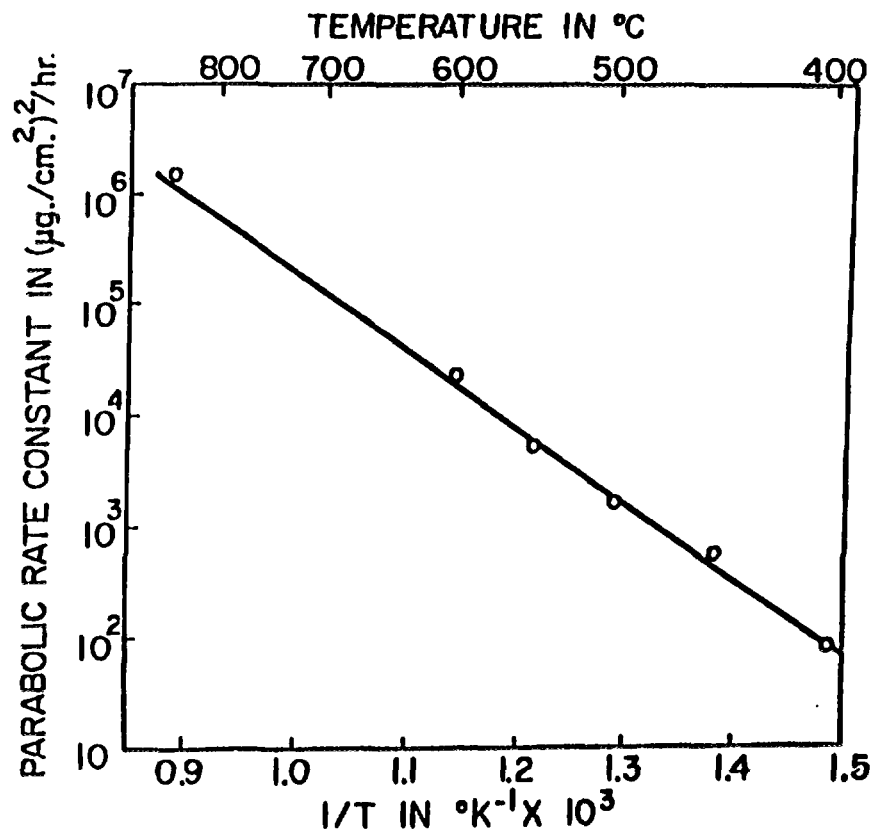


FIG. 3.2. Variation of the parabolic oxidation rate constant with temperature fitted to the data in Figure 3.1. [21].

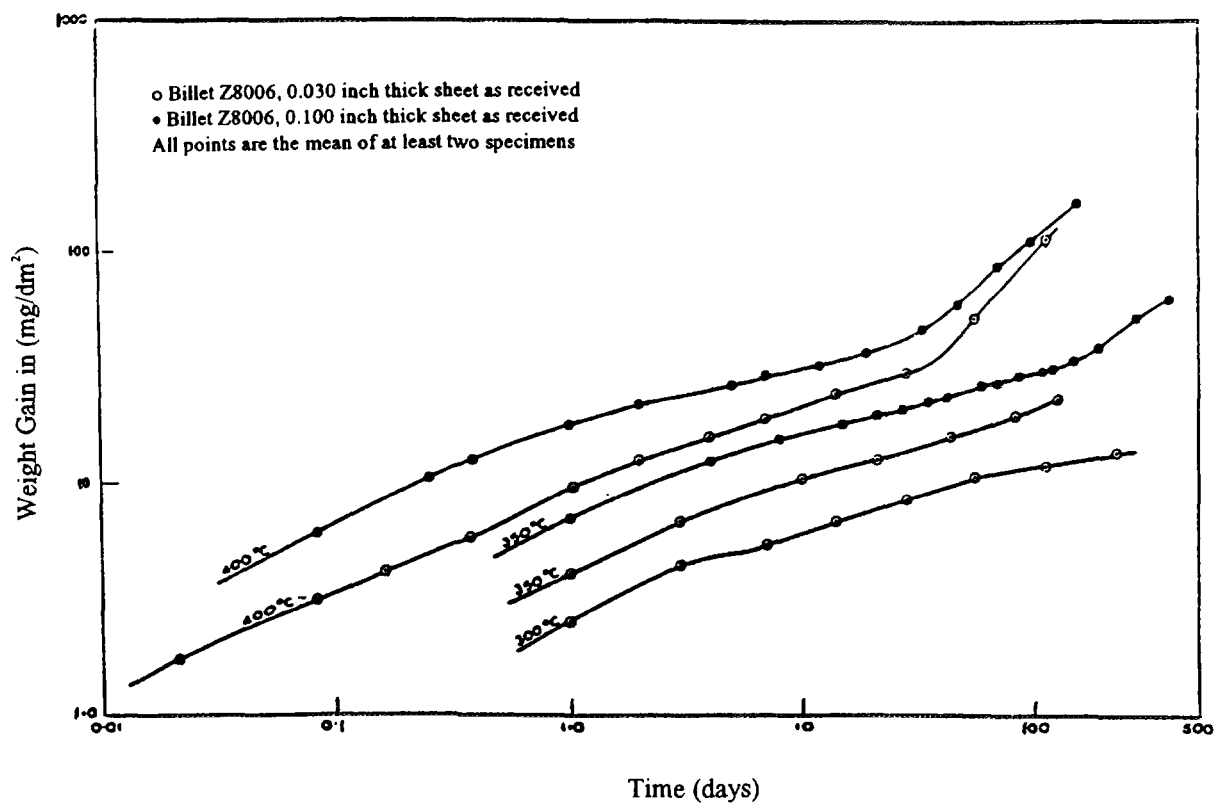


FIG. 3.3. Oxidation of Zircaloy-2 (billet Z8006) in steam at 300-400°C, 1 atm. pressure [22].

oxide during growth then, if the oxide is considered to be a homogeneous electrolyte, each electrically charged species in the oxide will have a characteristic ionic mobility ( $\mu_i, \mu^-$ ). The flux of any charged mobile species having a concentration in the oxide,  $C$ , will be given by

$$J^i = \mu EC \quad (3.5)$$

if these concentrations are sufficiently low that they do not perturb the average electrical field

If the contribution to the particle flux from both diffusion and electrolysis can be considered to be independent and additive, then the total flux of a given charged species, if reactions take place only at the interfaces will be

$$J = J^D + J^E \quad (3.6)$$

and if there is only one mobile species

$$J = -D(dC/dx) + \mu EC \quad (3.7)$$

Fromhold [17] has provided a solution to this

$$J = \mu E [DC \exp(\mu E/D)]/[1 - \exp(\mu E/D)] \quad (3.8)$$

and an approximate integration to give the oxidation kinetics

$$1 + \beta t = e^{\alpha} - \alpha l \quad (3.9)$$

where

$$\alpha = |\mu E/D|$$

$$\beta = |\alpha K^1 \mu E C_{max}|$$

and  $C_{max}$  is the maximum concentration of the mobile species at whichever interface of the oxide this occurs

In practice few, if any, oxidation experiments have ever been carried out in which a constant field has been maintained across the oxide. It is difficult to make uniformly good contact with the outer surface of an oxide film during gaseous oxidation without interfering with the reactions at the environment/oxide surface. These contact problems can be overcome in oxidising fused salts or high temperature aqueous electrolytes, but since the oxide thickness at any point in time is difficult to monitor during such experiments the tendency has been to maintain a constant voltage during the experiment [28-29]. The alternative of maintaining a constant current [30-31] is fraught with danger in a system where electrical conduction is localised and very high local current densities may be reached if all the applied current flows at only a few sites.

For the situation where a constant voltage is applied and the electric field decreases as the oxide thickens Fromhold [17] has also provided an approximate expression for this situation with an applied voltage  $V$

$$l - l_0 = -2K^1 \mu V t [(C^1 - C) \exp(-\mu V/D)]/[1 - \exp(-\mu V/D)] \quad (3.10)$$

this reduces to the zero-field form (3.4) as  $V \rightarrow 0$  or as the oxide thickens to the point where the field tends to zero and only the diffusional component of film growth ( $J^D$ ) remains

In instances where experiments of this nature have been carried out on zirconium during oxidation [28,29-31], it is surprising to find that in many experiments cathodic polarisation of the

metal substrate has resulted in small **increases** in the initial oxidation rate (Figure 3.4), while in another experiment, where Zircaloy specimens were cathodically polarised in steam at constant current [30], it appeared that an increased incidence of nodular corrosion occurred. In at least one of these instances it appears that the enhanced oxidation resulted from a large uptake of cathodic hydrogen [31].

For very thin films, and relatively low temperature oxidation, the perturbation of the field in the oxide by space-charge layers near the interfaces must also be taken into account. Here it may be that the model of Cabrera and Mott is most applicable [15]. In this model the electrons are considered to be capable of migrating through the oxide film much more easily than any ionic species. As a result of this a potential (the Mott potential) is set up which slows down electron migration and accelerates ionic diffusion until the two are equal. The electron migration processes considered were tunnelling, for very thin oxides, and thermionic emission for somewhat thicker oxides. The large electric field that results was considered to lower the energy barrier for ionic motion even at temperatures where thermally activated ionic diffusion would be slow. Thus, in many ways the electric field resulting from the Mott potential can be considered to drive the ionic migration by a process similar to that resulting in anodic oxide growth, which is sometimes referred to as nonlinear diffusion [17].

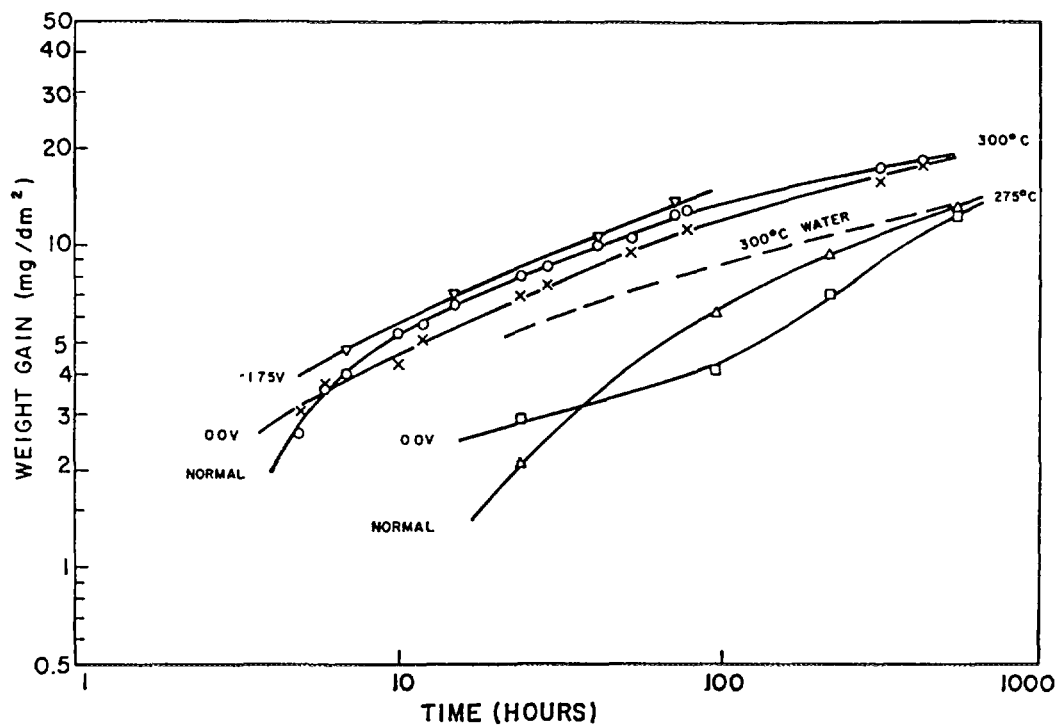


FIG 3.4. Weight gain versus time curves for Zircaloy-2 specimens biased during oxidation in fused salt at 275 and 300°C [29]. Normal refers to open circuit, 0.0 V to short circuit and -1.75 V refers to the metal negative with respect to the oxide.

The ionic flux generated by this field is given by

$$J_i = 2n_i v_i \exp(-W_i/k_B T) \sinh(-q_i a V_m / k_B T) \quad (3.11)$$

where

$V_m$  is the Mott potential  
 $n_i$  is the number of mobile ions per unit volume  
 $W$  is the rate-limiting energy barrier  
 $v$  is the ionic jump frequency  
 $2a$  is the ionic jump distance  
 $q_i$  is the charge on the mobile ionic species  
 $k_B$  is Boltzmann constant, and  
 $T$  is the absolute temperature

This mechanism, with electron tunnelling as the controlling process, is probably applicable to the growth of the air-formed oxide on zirconium alloys, while a similar mechanism, with thermionic emission as the electron transport process, may be applicable to the growth of thin interference colour oxides at low temperatures ( $\sim 573\text{K}$ ). These models should lead to an inverse, rather than a direct, logarithmic rate law for oxidation, that has the form

$$I^{-1} = A - B \ln(t) \quad (3.12)$$

It has been suggested that the pretransition oxidation kinetics of the Zircalloys at temperatures  $\leq 573\text{K}$  can be fitted to the sum of two such processes representing different rate controlling mechanisms [32]. Studies of the electron conduction through thin zirconia films have shown that Schottky emission, a form of thermionic emission, is the common conduction process [33].

### 3.4 EFFECT OF IMPURITIES AND ALLOYING ELEMENTS

Treatments of the effect of alloying additions on the growth of thick oxides by the parabolic Wagner-Hauffe model derive ultimately from Wagner's formulation [34] of the effects of oxygen pressure. This was later simplified by Jost [35] to give the following expression -

$$dw/dt = T T_e K A n (p_i^{1/n} - p_m^{1/n}) 8.91 \times 10^{-10} / l Z \quad (3.13)$$

where

$w$  is the number of gram equivalents of oxide formed,  
 $t$  is the time in seconds,  
 $T, T_e$  are the transference numbers for ions and electrons,  
 $K$  is the specific conductivity of the oxide at  $pO = 1$  atm in  $(\text{ohm cm})^{-1}$ ,  
 $A$  is the specimen area in  $\text{cm}^2$ ,  
 $1/n$  is the exponent in the equation for the pressure dependence of the rate controlling species (assumed to be oxygen ion vacancies for Zr, whence  $[ ] = K p^{1/n}$ ),  
 $T$  is the absolute temperature,  
 $p, p_m$  are the partial pressures of oxygen in atmospheres at the gas/oxide and oxide/metal interfaces respectively,  
 $l$  is the oxide thickness in cm, and  
 $Z$  is the numerical charge on the oxygen ion

If it is assumed that the anion vacancy concentration in the oxide is equal to the oxygen deficiency at any position, then the mole fraction of vacancies is equal to half that of the free electrons from the reaction



By the Law of Mass Action

$$[\square^{\circ}]^2 [e^-]^4 p(O_2) / [O^{2-}]^2 = \text{const.} \quad (3.15)$$

Since the concentration of oxygen ions is always very much larger than the concentration of oxygen vacancies (and especially so in  $ZrO_2$  where the limit of non-stoichiometry does not usually exceed  $ZrO_{1.96}$ ), then by substituting for the relation between oxygen ion vacancies and electrons in equation (3.14)

$$[\square^{\circ}] \propto p(O_2)^{1/6} \quad (3.16)$$

As the oxygen partial pressure at the oxide/metal interface at any temperature is set by the thermodynamics of the system (for zirconium/zirconia at a temperature of 573K,  $p_{m}O_2 \sim 10^{-90}$  atm), the oxidation rate of zirconium given by equation (3.13) should be proportional to  $p_{s}O_2^{1/6}$  [36].

An extension of this approach for mixed oxides containing large concentrations of vacancies was followed by investigators studying the conductivity of stabilized zirconia as a high temperature electrolyte [37,38]. The basis for this was the assumption that the stabilising elements (e.g.  $Ca^{2+}$ ,  $Y^{3+}$ ) would occupy substitutional positions in the  $ZrO_2$  lattice, and would adopt their normal valencies while present. Thus, equations can be written relating the concentration of aliovalent (i.e. an element having a normal valency different from that of the host) additive to the vacancy concentration that is created. For example

$$[Ca^{2+}] = [\square^{\circ}] \quad (3.17)$$

in calcia stabilized zirconia. With local charge compensation there should be a net two negative charges at a site occupied by a calcium ion and two positive charges on the oxygen ion vacancy. With the relatively large vacancy concentrations introduced in materials such as calcia stabilised zirconia, the probable presence of vacancy ordering and vacancy/addition-ion clusters must also be considered

This approach may be acceptable for ceramic electrolytes which are usually sintered at high temperatures in atmospheres with a  $pO_2$  close to 1 atm. Thus, there is a high probability that the aliovalent addition will occupy substitutional sites, that vacancy concentrations will be uniform throughout the resulting ceramic, and that the normal valency of the addition will be adopted. However, the same approach has been applied to the oxidation of zirconium alloys [39]. The perils of such an approach include the following unestablished factors:-

- There is usually no evidence that the alloying (or impurity) elements occupy substitutional positions in the  $ZrO_2$  lattice at low temperatures; if they do not, then an analysis based on their disturbing the oxygen vacancy concentration is invalid.
- Although alloying elements and impurities may adopt their normal valence states close to oxide surface, most of them should be thermodynamically incapable of oxidising close to the oxide/metal interface in a barrier oxide film because of the low effective oxygen partial pressure there.
- Most alloying additions and impurities have very low solubilities in zirconium and are present as second phase particles. These must be treated separately in any analysis and their local effects on the oxide considered individually.

It was demonstrated early that the oxidation rates for zirconium alloys in oxygen did not follow the pattern that would be expected if the alloying additions occupied substitutional sites in the oxide with their normal valence states [40,41]. In the early work where oxidation rates were measured in gaseous oxygen, the pre-transition rate constants varied very little for 1-5% additions of a large number of additives (Table 3.1.). The primary effect of the additives was on the time to transition and the post-transition oxidation rate. Recent work has tended to demonstrate that elements such as iron do not oxidise close to the metal oxide interface, as would be expected thermodynamically [42,43].

Table 3.1. Oxidation of Zirconium Alloys which Followed the Cubic Rate Law With no Transition up to 1400 Minutes (700°C and 200 mm Oxygen) [41]

Alloy Composition Atomic and Weight (%)			Cubic Rate Constant ( $10^4(\text{mg}/\text{dm}^2)^3\text{Min}^{-1}$ )	Duration of Run (Min)	Weight Gain ( $\text{mg}/\text{dm}^2$ )	Colour and Character of Oxide Film
Unalloyed Zr			1.6	1300	260	Blue-gray; adherent
a/o		w/o				
0.90	Be	0.09	1.2	1400	250	Blue (gold tinge); adherent
4.23	Be	0.44	1.1	1400	240	Black with white raised edges; adherent
0.65	C	0.086	2.5	1400	330	Silver-gold with white edges and spots;
0.86	Co	0.55	1.6	1285	270	Gray-black; adherent
3.72	Co	2.44	2.2	1150	285	Gray (gold tinge); adherent
0.77	Cr	0.44	1.7	1400	270	Black; adherent
3.61	Cr	2.05	1.7	1400	280	Black; adherent
1.08	Cu	0.75	1.1	1400	240	Black; adherent
3.60	Cu	2.53	0.78	1400	240	Black; adherent
1.09	Fe	0.67	3.0	520	250	Gold-gray; adherent
3.95	Fe	2.46	2.4	1400	320	Gray; adherent
1.03	Hf	2.00	1.4	1400	270	Black with raised edges; adherent
4.08	Hf	7.65	1.4	1400	260	Black with raised edges; adherent
1.03	Mo	1.08	2.5	1400	340	Black with raised edges and white spots;
0.91	Ni	0.59	1.5	1400	260	Black; adherent
4.22	Ni	2.75	1.0	1400	240	Gray (gold tinge); adherent
1.08	Pt	2.28	1.5	1400	270	Black; adherent
0.80	Si	0.25	3.4	1400	340	Gray with white specks on faces; adherent
0.89	U	2.30	3.2	1400	240	Black with raised edges; 2 faces gold flaky oxide
0.68	W	1.34	1.9	3000	390	Black; adherent
1.96	W	3.87	3.6	1400	370	Black with yellow adherent oxide at flaws in metal; adherent



## 4. CORROSION IN THE ABSENCE OF IRRADIATION

### 4. 1. INTRODUCTION

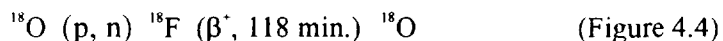
Under most conditions of temperature and environment the oxidation and corrosion of zirconium and its alloys results in the growth of uniform oxide films, especially in the early protective oxidation stage. Only in two isolated regions of temperature and environment,  $\sim 300^\circ\text{C}$  boiling (or oxygenated) water in-reactor and high temperature, high pressure ( $\geq 450^\circ\text{C}$ ,  $\geq 5\text{MPa}$ ) steam, does a very local form of oxidation called nodular corrosion occur. Typical nodules are round lenticular cross-section patches of thick oxide, although this characteristic appearance is not always evident, especially for batches of alloy showing very poor nodular corrosion resistance. Although no universally accepted mechanism for nodular corrosion is available, it is clear that nodular corrosion obeys different rules from uniform corrosion with respect to dependence on metallurgical and other variables and, for this reason, uniform and nodular corrosion will be treated separately.

### 4. 2. UNIFORM OXIDE FORMATION

The thermodynamics of the Zr-O system (Figure 4.1) show that oxygen is more stable when dissolved in the metal phase than when present as an oxide film [44]. As a result of this, the first 1/2 monolayer of oxygen that reacts with a clean zirconium surface goes into subsurface sites, even at liquid nitrogen temperature [45]. As more oxygen reacts, oxygen physisorbed on the surface becomes evident, and with further reaction this is converted into a thin oxide film. This oxide grows until it is limited by the ability of electrons to tunnel through it. The thickness at this point is variously measured at between  $\sim 2$  nm (from XPS studies [46]) and  $\sim 5$  nm (from NRA studies [47]). All zirconium alloy surfaces bear at least this thickness of oxide, the so-called air-formed film, unless great efforts are made to eliminate it. Again, because of the thermodynamics of the system, this can only be readily achieved by dissolving the oxide in the metal at high temperature in a good vacuum ( $<10^{-3}$  Pa), or by continuously sputtering the oxide off the surface at low temperature in an even better vacuum ( $<10^{-6}$  Pa).

Thus, at elevated temperatures in an oxidising environment, where thermally activated thickening of the initial oxide film occurs [26], not all the oxygen that reacts forms oxide, some of the oxygen dissolves in the metal matrix. The dissolved oxygen profiles can be measured by microhardness traverses (Figure 4.2) or by a nuclear reaction of oxygen (Figure 4.3). The fraction of the oxygen that dissolves depends upon a balance between the kinetics of oxide growth and the kinetics of oxygen diffusion into the metal. Since dissolution in the metal seems to vary much less from alloy to alloy than the oxide growth kinetics, rapidly oxidising alloys should have shallower diffusion profiles than more slowly oxidising alloys at all temperatures. At temperatures close to reactor operating temperatures, however, the ability to measure these diffusion profiles is very limited. Any change in the oxidation rate, such as occurs at the transition in the oxidation kinetics, will result either in an increase or a decrease in the depth of the oxygen diffusion profile under the oxide film.

The fraction of oxygen dissolving in the metal is not well known even at high temperatures where it is largest because the activation energy for dissolution is higher than the activation energy for oxide growth [26]. Most of the evidence for the magnitude of the dissolved oxygen fraction comes from experiments in oxygen, because few measurements have been made for oxides grown in steam or water. The fraction of the oxygen reacting with zirconium that dissolves in the metal decreases from  $\sim 50\%$  at  $900^\circ\text{C}$ , to  $\sim 20\%$  at  $600^\circ\text{C}$ , and  $<10\%$  at  $400^\circ\text{C}$ . At temperatures lower than  $400^\circ\text{C}$  neither the fraction dissolved nor its distribution is well known. Dissolution is known to be localised at temperatures less than  $600^\circ\text{C}$ , where preferential oxygen dissolution along metal grain boundaries has been demonstrated by imaging autoradiographically the nuclear reaction:



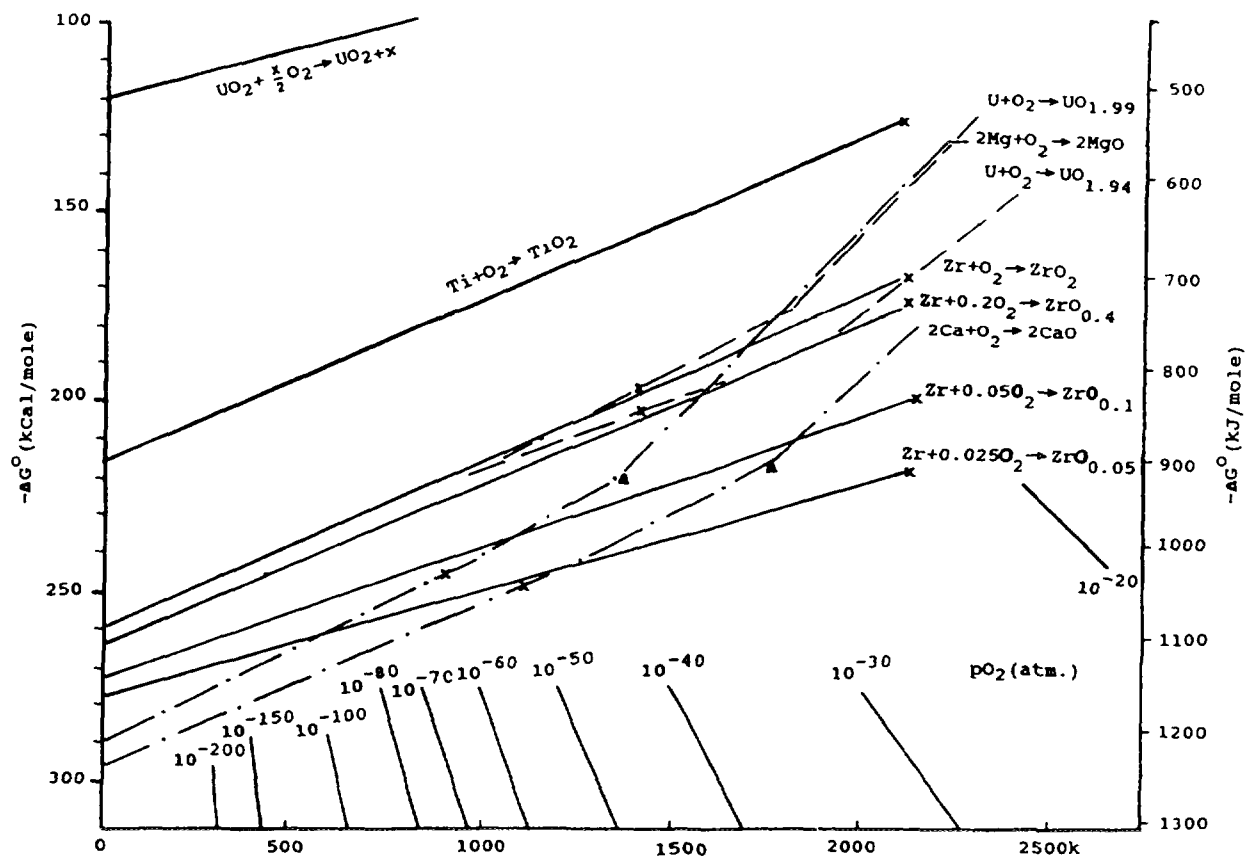


FIG. 4.1. Ellingham diagram of thermodynamics of Zr/O and other relevant systems[44].

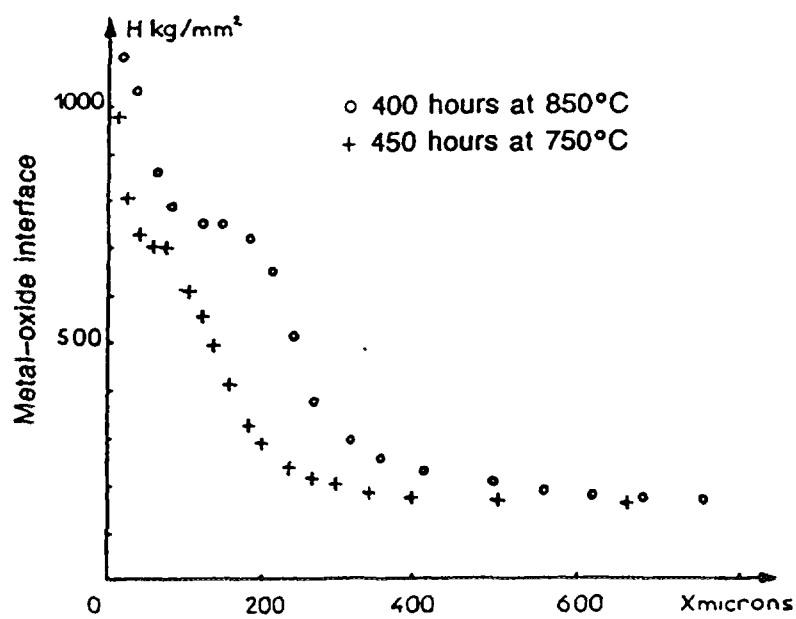


FIG. 4.2. Variation in the microhardness as a function of depth of penetration of oxygen in zirconium (50 g. load) [26].

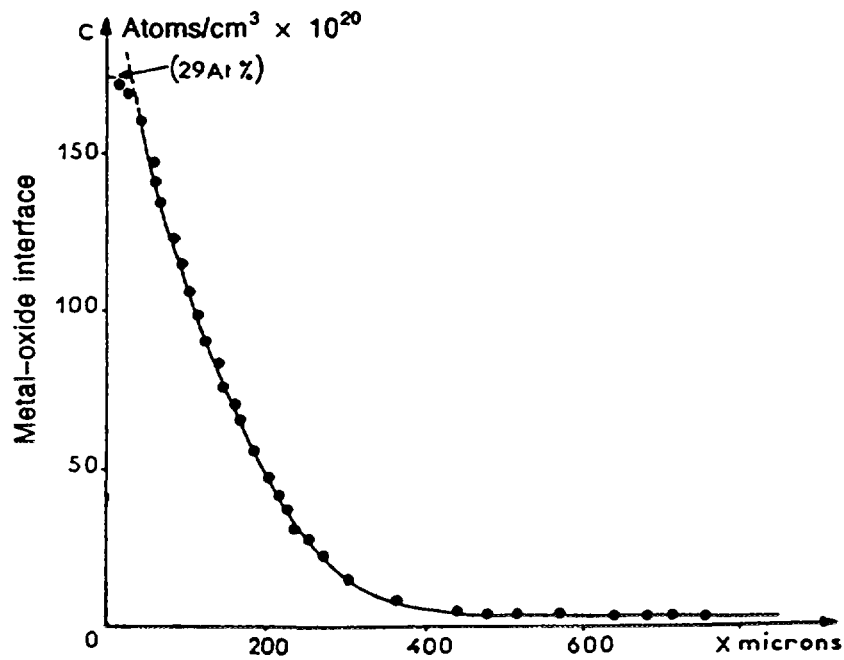


FIG 4 3 Curve for the penetration of oxygen, established using the  $^{16}\text{O}(d, p)^{17}\text{O}^*$  nuclear reaction with  $E_d$  900 keV, and compared with a calculated curve (error function complement) for a zirconium specimen oxidized at  $850^\circ\text{C}$  for 400 hours [26]

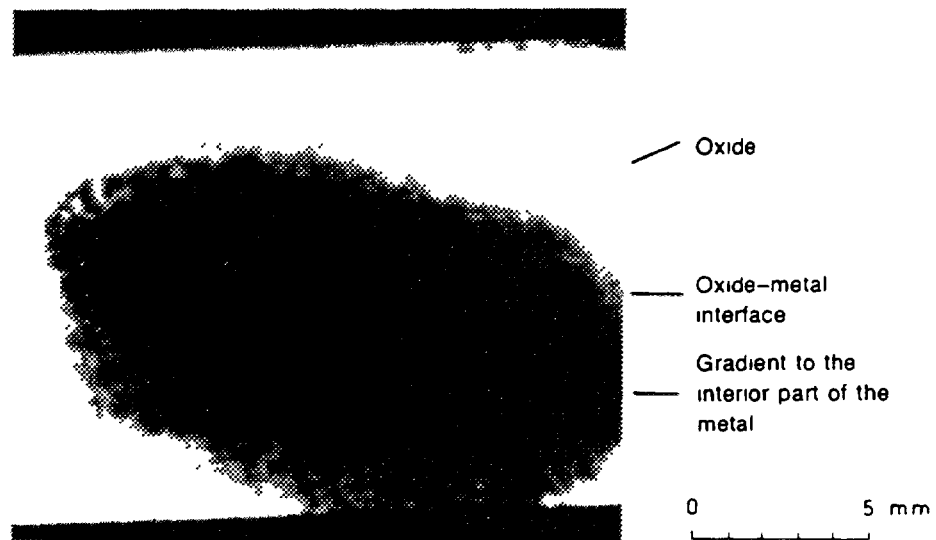


FIG 4 4 Oxygen distribution in the region between the oxide-metal interface and the metal interior (darkest part) of zirconium oxidized in oxygen-18 at  $600^\circ\text{C}$  for  $2.7 \times 10^5$  s [48]

and these observations have been confirmed by microhardness studies using very low loads [48] (Figure 4 5) At lower temperatures there even appear to be preferred sites along the metal grain boundaries where preferential diffusion into the metal occurs (see section 5 2 1 and Figure 5 20)

The difference between the total  $O_2$  reacting (accurately known) and the amount dissolving (not well known) causes problems with calibrating other physical methods for establishing the oxide thickness (e.g., impedance, interferometry) so that errors in such calibrations at low temperature (300-400°C) may be equal to the range of values for the fraction of oxygen dissolving (0-10%) and add to the difficulties caused by variations in the local oxide growth from grain to grain (Figure 4 6) [49], variations in the oxide thickness at grain boundaries (Figure 4 7) and variations over an individual grain surface (Figure 4 8) so as to render accurate knowledge of oxide growth kinetics impossible, based on present evidence [50]

The oxide growth kinetics are usually derived from the weight gain kinetics (the amount of  $O_2$  reacting), assuming that all the oxide formed remains on the specimen, converted directly to an oxide thickness (assumed to be uniform) using the theoretical density of  $ZrO_2$  (not known to be accurate) This conversion, in the light of the above, can only be approximate (1  $\mu m$  oxide  $\sim 15$  mg/dm<sup>2</sup> oxygen weight gain) The only merit that such an approach has is that if used in a standardized manner, it permits a comparison of the kinetic behaviour of different alloys The dissolution of oxygen in the metal is thought (but not known) to be insensitive to alloying variability

#### 4 2 1 Oxidation kinetics

##### 4 2 1 1 Zircalloys

For the present discussion we will accept the fiction that the above conversion of weight gain to oxide thickness gives the oxide growth kinetics but we reemphasize the following caveats

- Oxide films are assumed, but not known, to have the theoretical  $ZrO_2$  density
- No correction has been made for local dissolution of oxygen in the metal
- Unless the amount of oxygen reacting ( $\Delta O$ ), rather than the weight gain ( $\Delta w$ ) is quoted, the experimental results will not have been corrected for the amount of hydrogen absorbed, if the reaction was with  $H_2O$
- It is assumed that no loss of oxide occurs by any process (e.g. spalling, dissolution), and that all the weight change measured is from the oxygen reacted (e.g. no carbon from  $CO$ , or other species are weighed)

The weight gain kinetics for zirconium and its alloys usually fall into two periods colloquially referred to as pre- and post-transition (Figure 4 9) [6,51,52] The initial, pre-transition period is characterized by a decreasing rate of weight gain which is usually closer to a cubic or a quartic growth kinetic curve than to the parabolic kinetics predicted by the Wagner/Hauffe theory It is believed that the departures from parabolic kinetics arise because the diffusion process controlling oxide growth is not a homogeneous one occurring in a uniform solid (as required by this theory) but is heavily localized at crystallite boundaries within the oxide [19,20] Electron microscopy shows that the oxide is microcrystalline (Figure 4 10) and that the mean crystallite size increases initially as the oxide thickens [53] Details of this phenomenon are not completely agreed upon Differences of opinion as to whether some initial crystallite orientations grow at the expense of others, or whether successive layers of crystallites initiate and grow to different extents remain to be resolved The oxide forms under compression because of its formation entirely by inward diffusion of oxygen and because of the high Pilling-Bedworth ratio (the ratio of the oxide volume to the volume of metal from which it formed) of  $\sim 1.56$ , which depends on the value used for the density of the oxide film

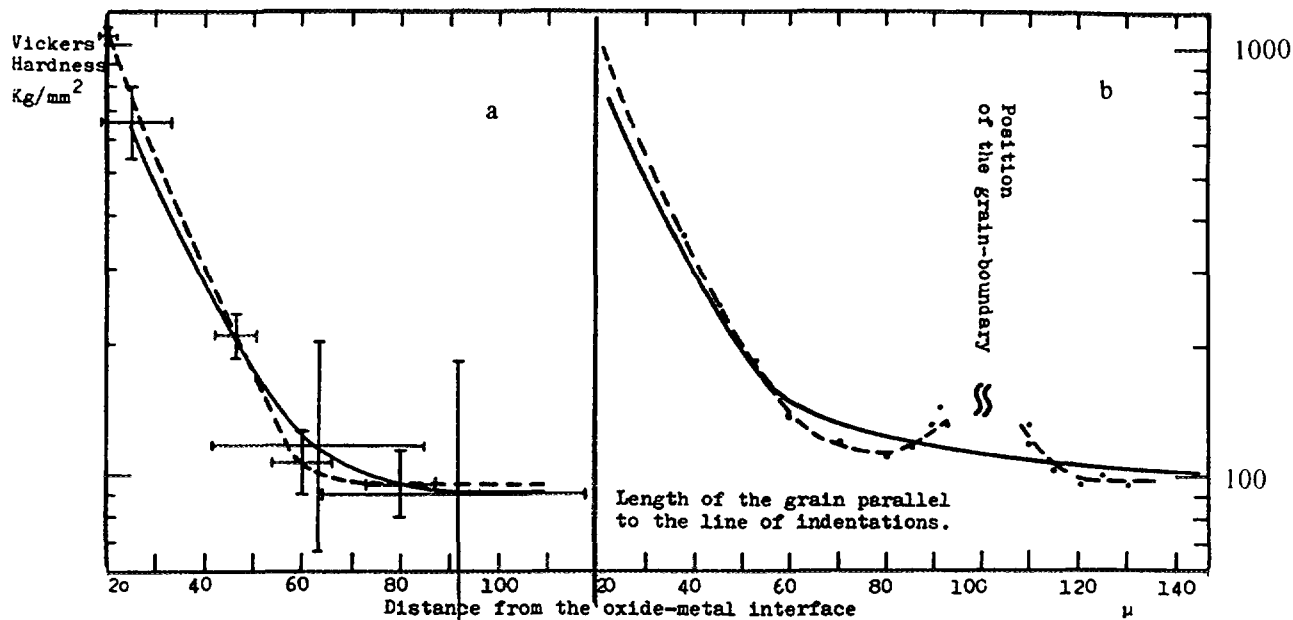


FIG. 4.5. Effect of the load used in microhardness testing on zirconium oxidized at 600°C for  $1.8 \times 10^6$  s. Dashed lines, 15 g. load; solid lines, 130 g. load. a. Variations in the size of the indentations, b. Effect on the results in the neighbourhood of a grain boundary: the size of the metal grains was small compared to the depth of penetration of oxygen [48].

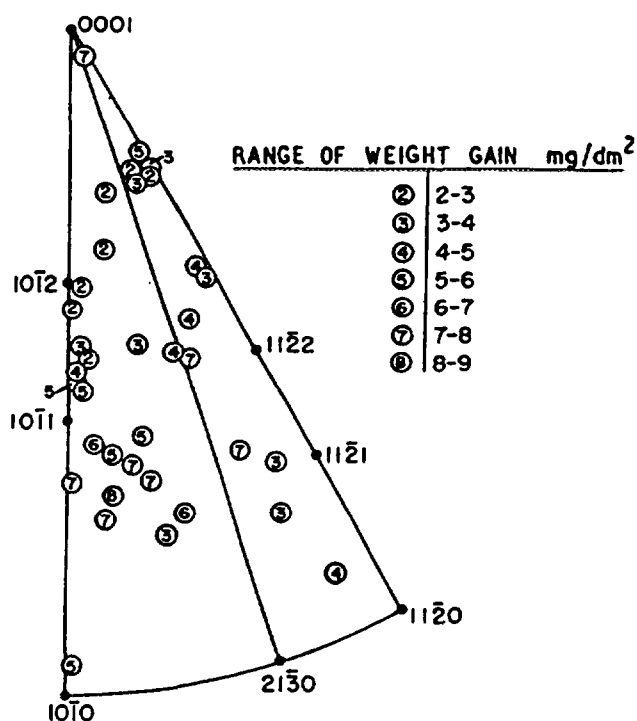
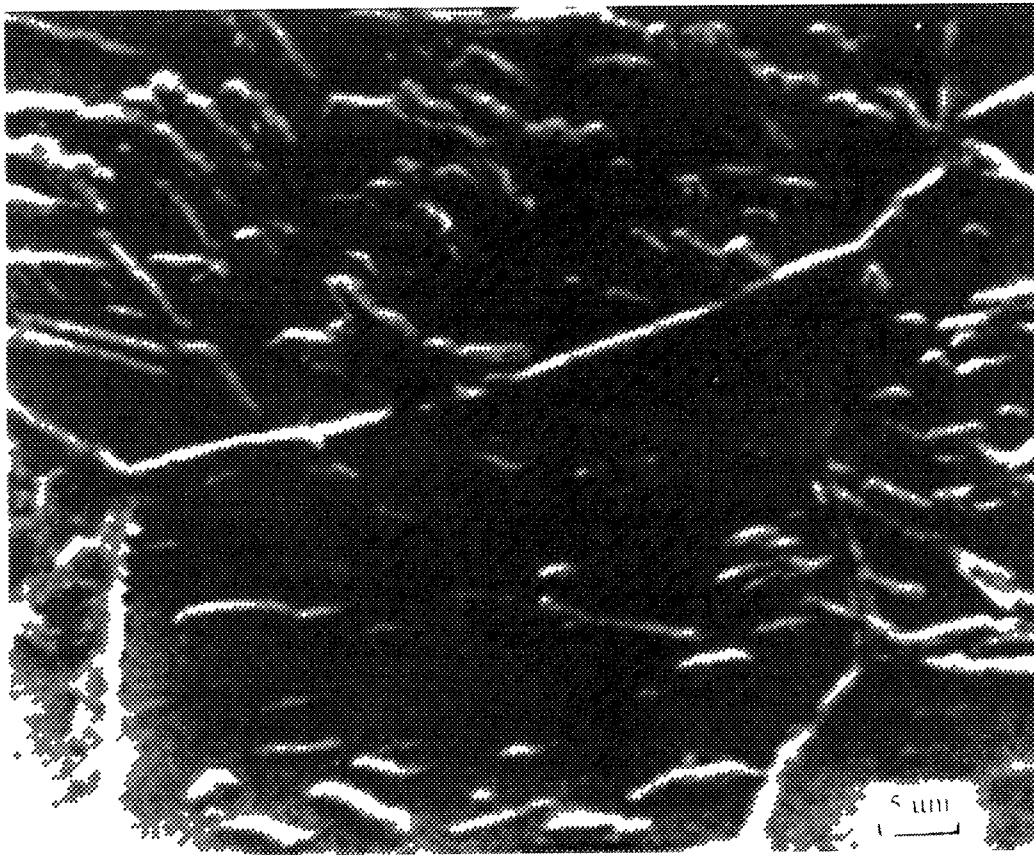
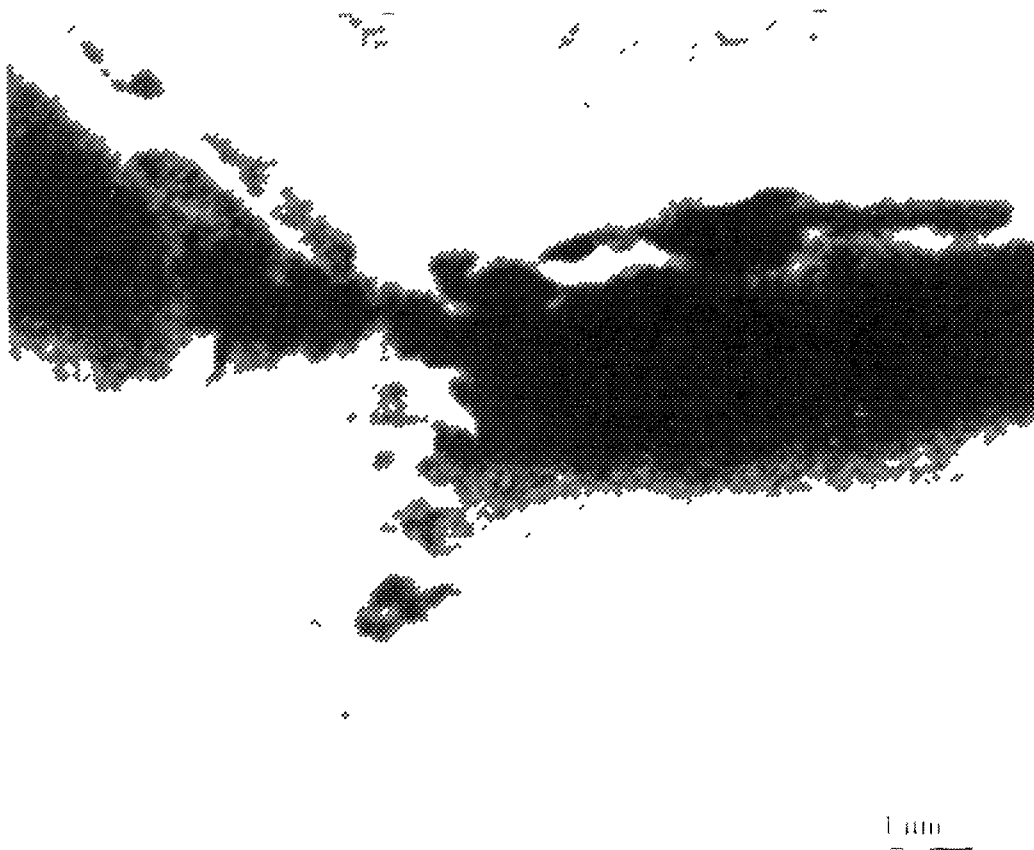


FIG. 4.6. Relation between weight gain on single crystals of van Arkel zirconium (after 1 min. in steam at 500°C, 1 atmosphere) and surface orientation [49].

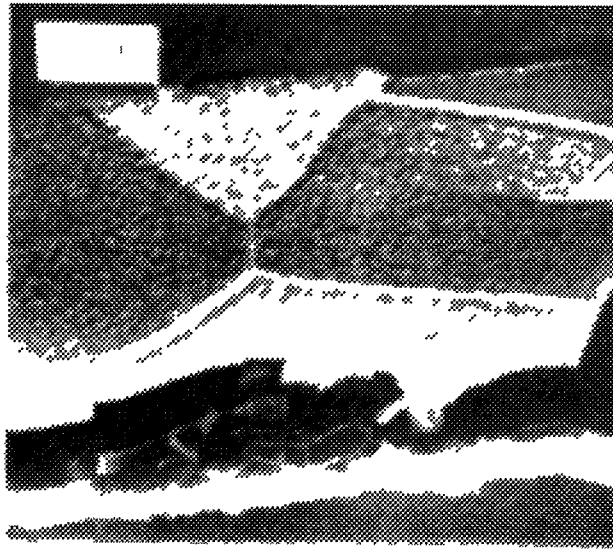


(a)

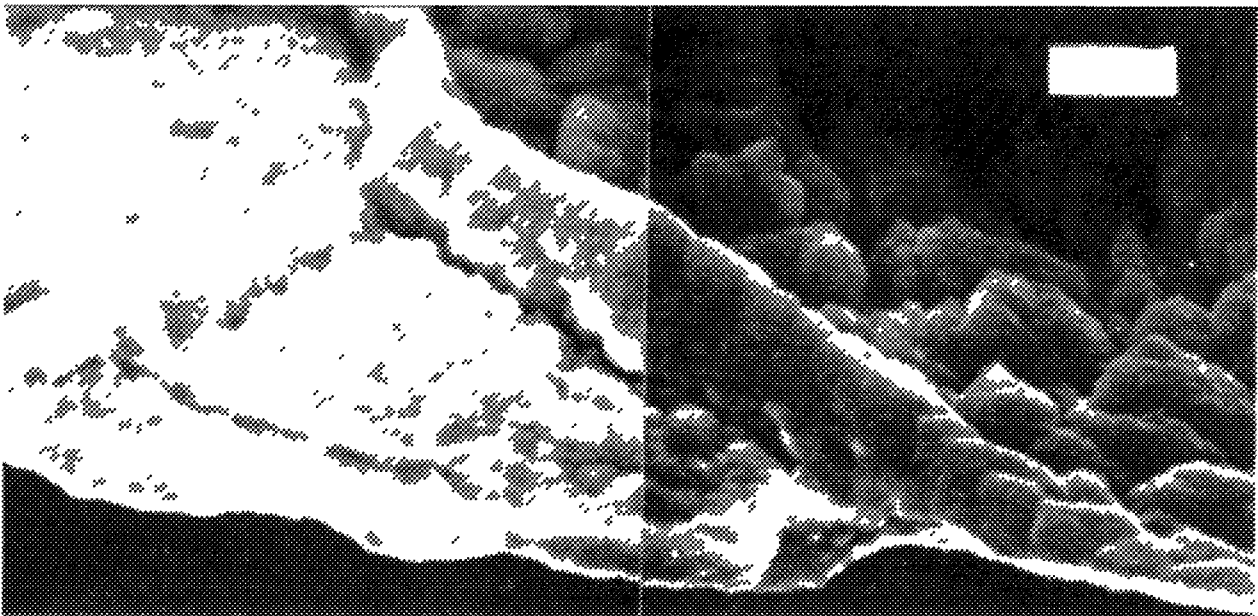


(b)

FIG 4 7 (a, b) Oxide ridges formed at metal grain during the oxidation of van Arkel zirconium in steam outside surface



(c)



(d)

*FIG 4 7 (c, d) Oxide ridges formed at metal grain during the oxidation of van Arkel zirconium in steam oxide-metal interface topography*

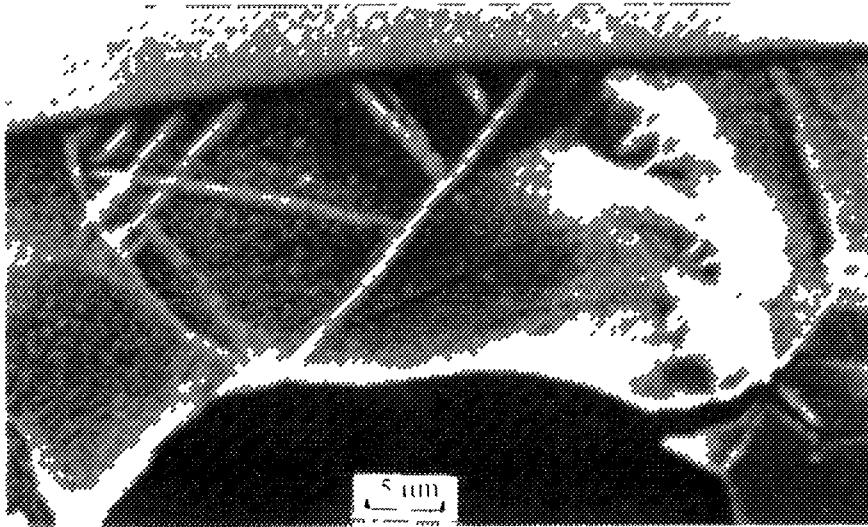


FIG. 4.8 Development of a rough oxide-metal interface. The centre of the central grain is still showing a relatively planar interface whereas roughening of the interface has spread over the rest of the interface. The straight ridges of thicker oxide are at twins and the curved ones are along grain boundaries. Mean oxide thickness  $0.4 \mu\text{m}$  ( $2000\times$ ) [50]

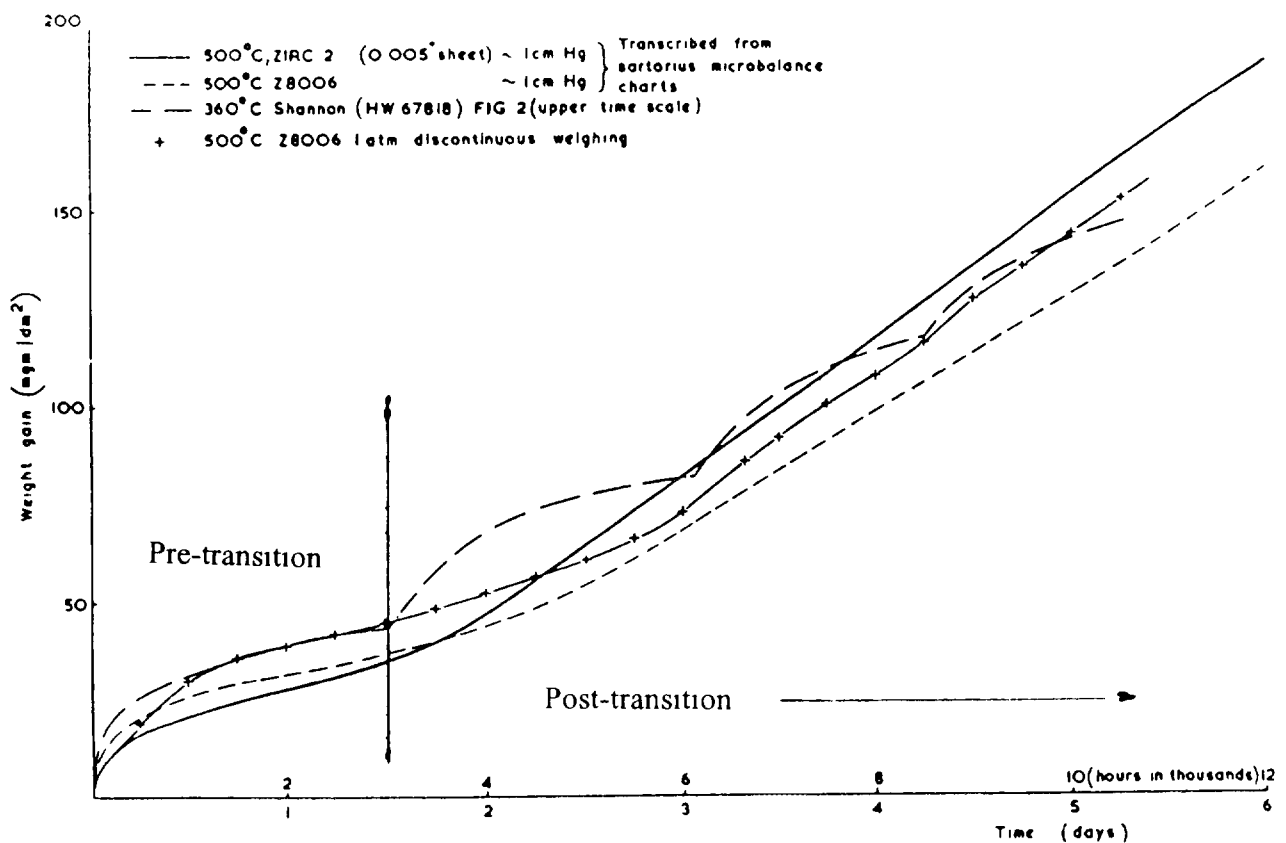
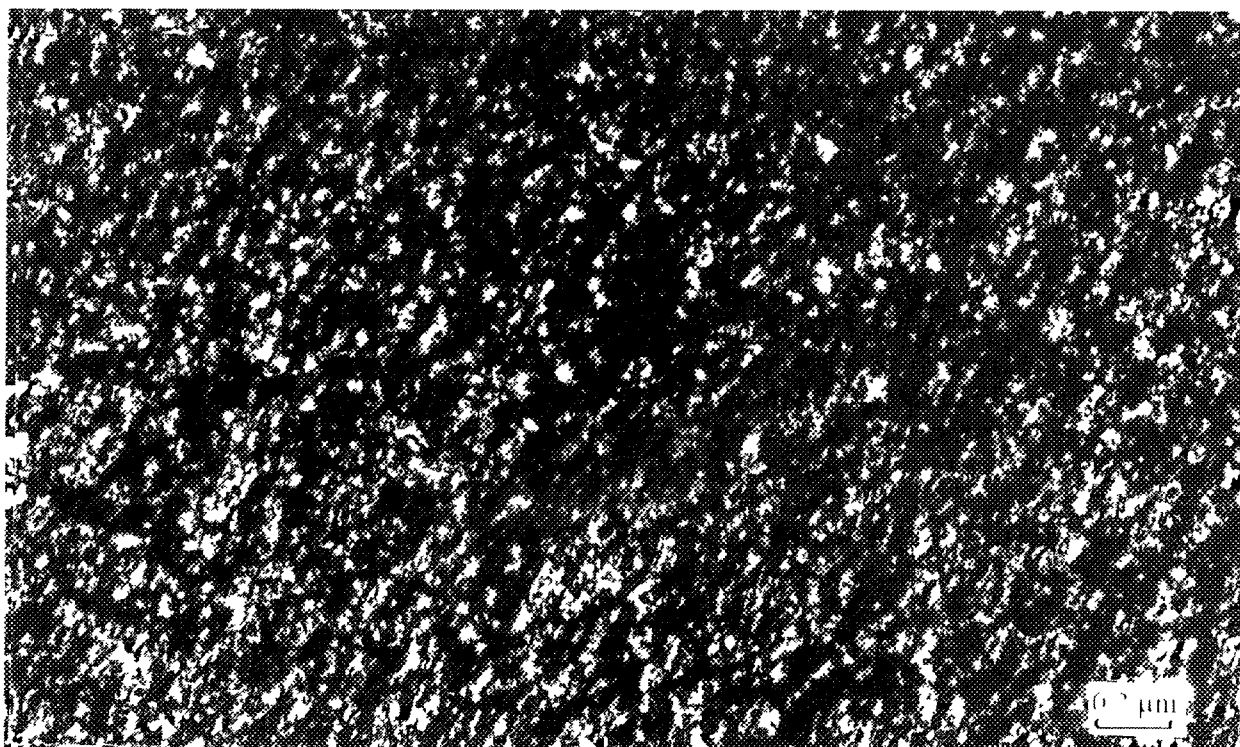
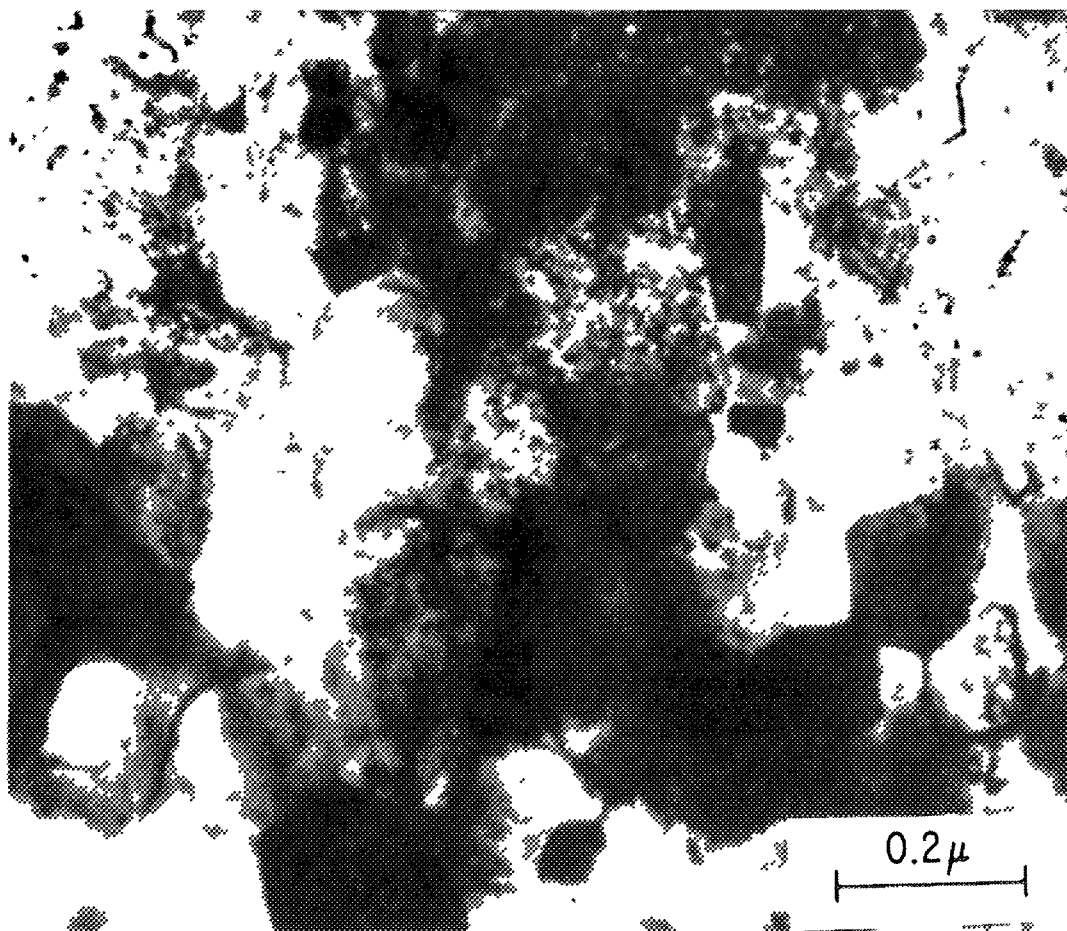


FIG. 4.9 The shape of the Zircalox 2 oxidation curve [158]





*FIG 4 10 Transmission electron microscopy of zirconium oxide films Top Bright field view of oxide adjacent to the oxide-metal interface (section parallel to the interface), Bottom Dark field view of oxide crystallite morphology in a thin oxide formed at 300°C in oxygen on zirconium*

On massive specimens this volume change must be accommodated normal to the free surface, by a combination of crystallographic and deformation processes that have yet to be explored completely. It is observed that the crystallographic and morphological texture that develops in the oxide is always perpendicular to the oxide/metal interface; that it is not dependent on metal orientation, and that those oxide orientations that develop predominantly in the texture [25] are just those orientations that are needed to minimise the compressive stresses in the plane of the surface (Figure 4.11). For instance the epitaxial relations observed [54] for very thin oxide films on the (1120) face of zirconium are a mixture of:-

$$\begin{aligned} &(100)[001]_m // (0001)[1120] \text{ and} \\ &(100)[010]_m // (0001)[1120] \end{aligned}$$

while the minimum stress in the oxide is obtained for [55]  $(101)[101]_m // (1010)[1120]$ . As the oxide thickens, reflections of the form  $\{104\}$  become the most prominent on (1120) and  $\{104\}$ ,  $\{102\}$  or  $\{101\}$  are also the strongest on other orientations of the substrate [25]. However, it is evident that no unique epitaxial relationship exists for thermal oxide films on zirconium [54]. This suggests that the increase in crystallite size and the texture that develops is driven by the compressive stresses produced by oxide growth. Early comparisons of the number of possible epitaxial orientations of monoclinic  $\text{ZrO}_2$  (m- $\text{ZrO}_2$ ) on hexagonal Zr, and those actually observed in stripped oxide films, led to the conclusion that only those m- $\text{ZrO}_2$  orientations were present which would be expected if the oxide formed initially as cubic or tetragonal  $\text{ZrO}_2$  (t- $\text{ZrO}_2$ ) and subsequently transformed to monoclinic. The recent work of Godlewski et al. [56,57] has suggested that this conclusion was correct and that a large fraction of the oxide crystallites at the oxide/metal interface form initially as t- $\text{ZrO}_2$ .

An opposing argument has been made that the compressive stresses influence the diffusion of oxygen directly through an effect on the anion vacancy volume [58]. However, this mechanism does not seem to be able to predict the development of the oxide texture, and is difficult to formulate for a system where lattice diffusion is a minor contributor to the oxygen ion flux. Such effects might represent a further contribution to the low exponents in the rate law, but are difficult to assess in a system where crystallite boundary diffusion predominates.

Although approximating to a cubic or quartic growth curve, the kinetics of pre-transition oxide growth are more complicated than suggested by the single rate law [59]. At least one well defined inflection in the thin oxide film region (0.5-0.7  $\mu\text{m}$ ) separates the pre-transition period into two distinct periods (Figure 4.12). One corollary of these perturbations to a smooth kinetic curve is that the temperature dependence of oxidation seldom gives a smooth Arrhenius plot, thus indicating that more than one rate limiting process is operating [59]. The causes of this change in kinetics and the nature of the early growth have been investigated and explanations suggested [26], but for present purposes these variations can be ignored since under irradiation in-reactor we will always be concerned with thicker oxides than this.

When the oxide reaches a thickness of about 2  $\mu\text{m}$ , the oxidation rate increases to a post-transition, approximately linear, rate [6,51,57]. This linear rate may also increase slowly [60] with increasing thickness over long periods of time (Figure 4.13), but this latter effect is not well established at present. At relatively high temperatures ( $\geq 400^\circ\text{C}$ ) and when measurements are taken continuously with a microbalance (or similar technique), and thereby at low pressure, the change in kinetics to the post-transition linear rate is smooth [61] and no sudden discontinuities are observed (Figure 4.14). At lower temperatures, high pressures, and when the weighings are done discontinuously (as in all autoclave testing), the post-transition period is initiated by a sudden increase in rate and is followed by a series of oxidation cycles [62], not unlike the initial pre-transition period in size and duration (Figure 4.15). These cycles eventually disappear and an effectively linear post-transition rate becomes evident.

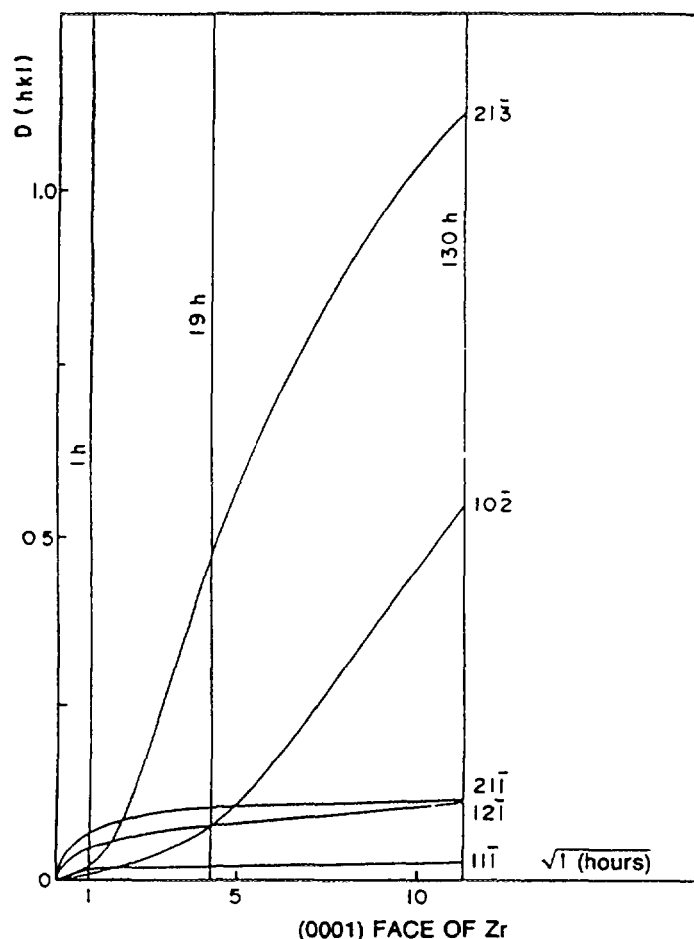


FIG. 4.11 Variation in X-ray peak intensities ( $D_{hkl}$ ) observed on the (0001) face of a zirconium single crystal during oxidation [25]

The transition process is indicative of the generation of porosity in the previously impervious oxide film. There seem to be at least two different types of flaw generated at this time, the first are cracks normal to the oxide surface that can pass most of the way through the oxide but are usually infrequent except at corners or edges. The second are fine pores (probably at crystallite boundaries) that form a network within the oxide [26,63]. The question of whether cracks also form parallel to the plane of the surface at this time, or whether these are artefacts of the metallographic technique has been argued extensively [64,65], and at present no unequivocal evidence for their presence is available. Cracks normal to the surface seem to be more prominent in circumstances that encourage cyclic post-transition kinetics and relatively absent when smooth transition curves are observed.

There are two aspects of the cyclic post-transition behaviour that require discussion at this point. The first which will be discussed now is the practical problem of whether or not the cycles are caused, or at least accentuated, by the thermal cycles necessitated by the discontinuous weighing technique, the second, which will be discussed later (section 4.2.5), is the mechanistic question of whether the cycles do, or do not, represent the growth of successive layers of pre-transition barrier layer oxide following a sudden breakdown of the original impervious oxide by some degenerative process.

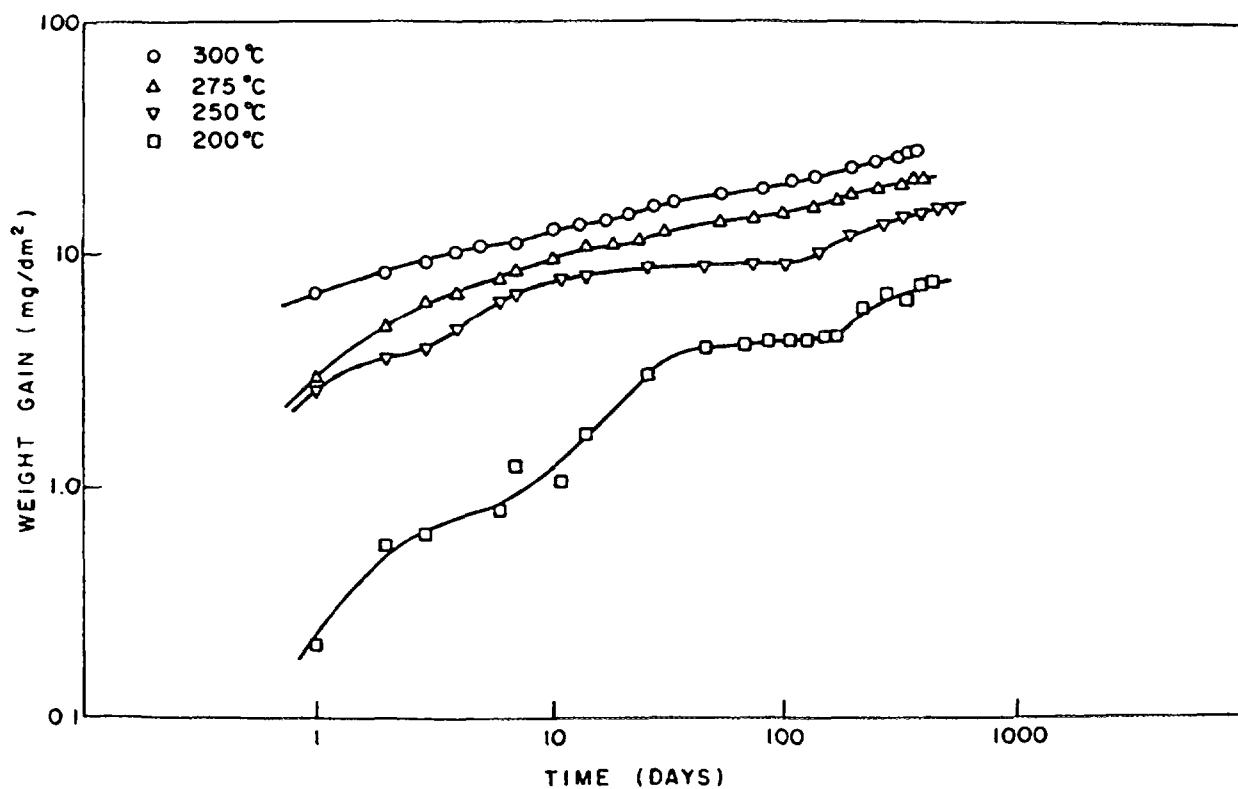


FIG. 4.12. Oxidation of Zircaloy-2 (Ac) in water at 200-300°C [59].

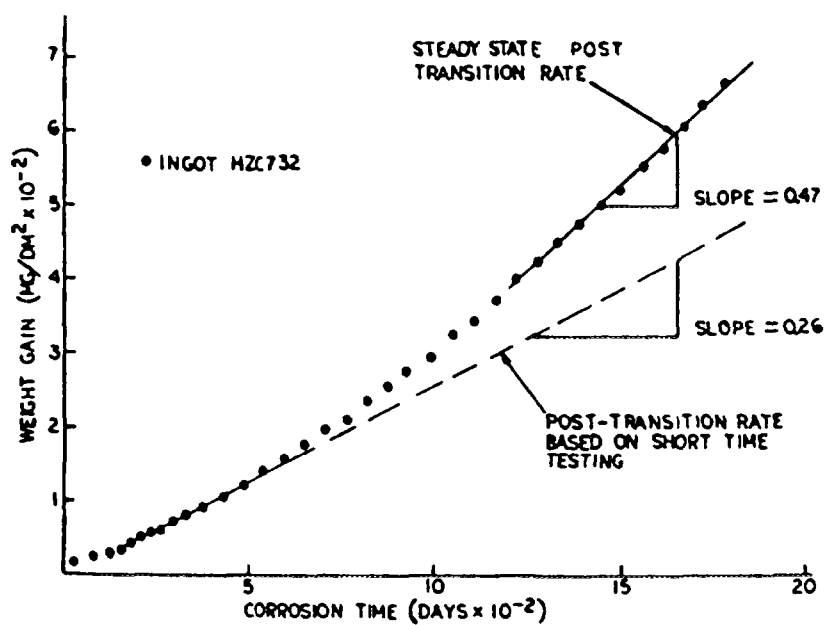


FIG. 4.13. Corrosion weight gain of Zircaloy-4 in water at 633K [60].

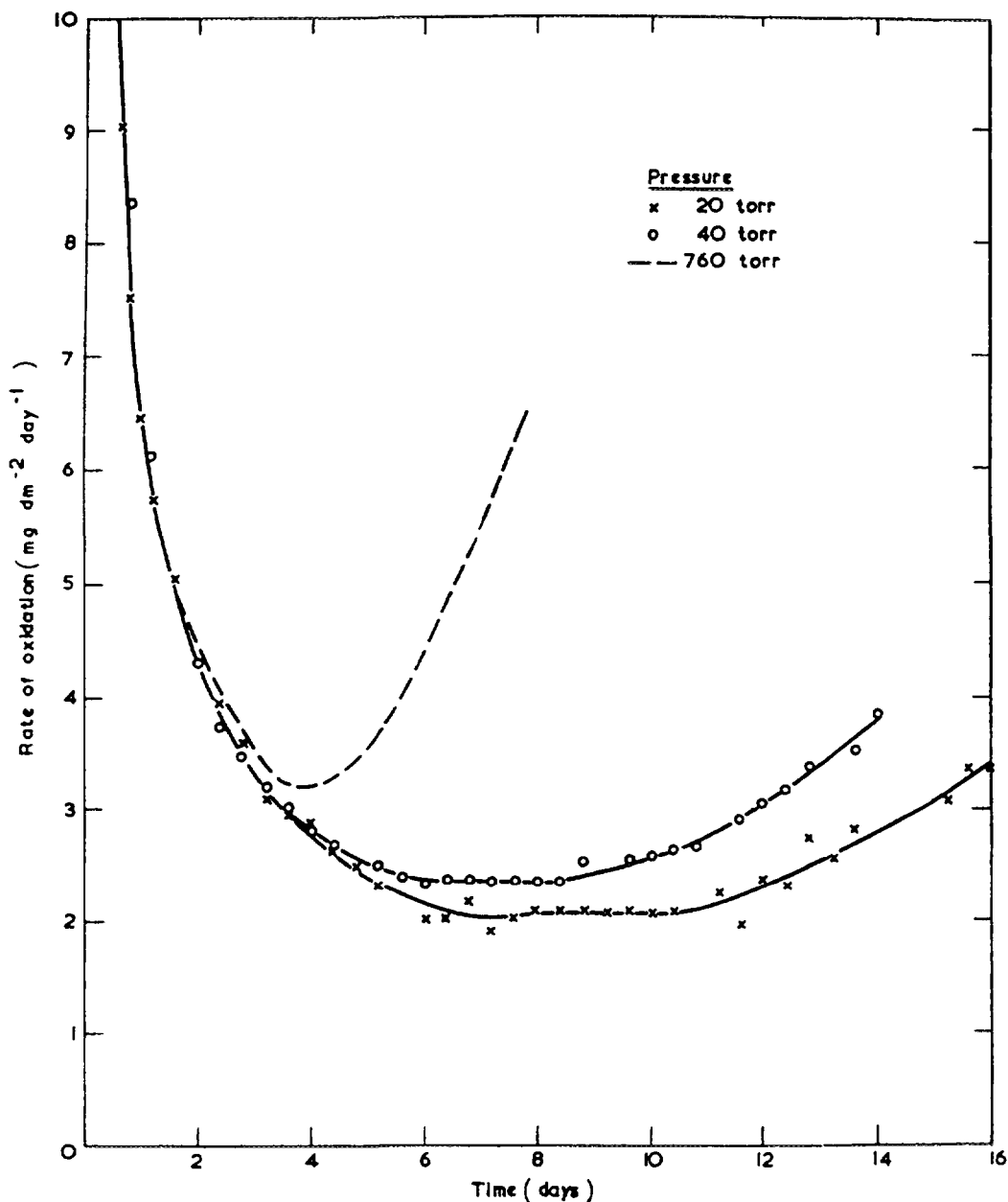


FIG 4 14 Reaction of Zircalov-2 with water vapour at 450°C Effect of pressure on the propagation of the cubic to linear transition [61]

The influence of thermal cycling on the kinetics of oxidation has never been fully investigated. Several early studies examined the effect of frequent thermal cycles during the pre-transition period [66] and found no effect at the 95% confidence level (Figure 4.16). None of these studies was extended up to the normal transition in the oxidation kinetics so that a definitive answer could be given. A recent autoclave test [67], in which the oxide impedance was measured regularly and where no thermal cycles occurred, has shown definitively that cyclic post-transition oxidation occurs in 350°C water (aqueous electrolyte) without any thermal cycling.

#### 4 2 1 2 Zr-Nb alloys

The oxidation kinetics of the Zr-Nb alloys differ somewhat from those of the Zircalloys. Often no clearly defined rate transition is evident and a steady change from cubic to linear kinetics is

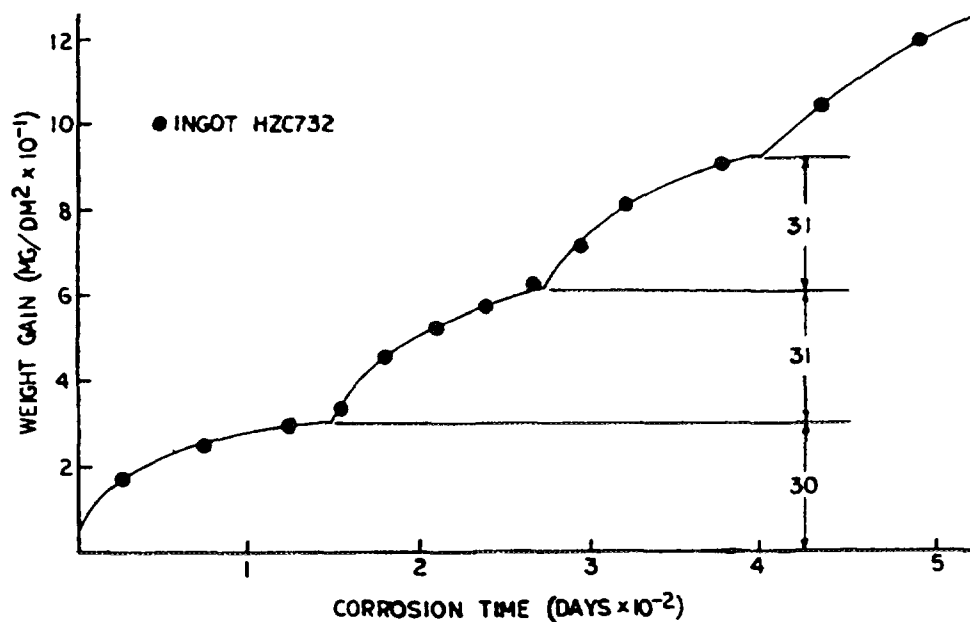


FIG. 4.15. Short-time corrosion weight gain of Zircaloy-4 in water at 633K [60].

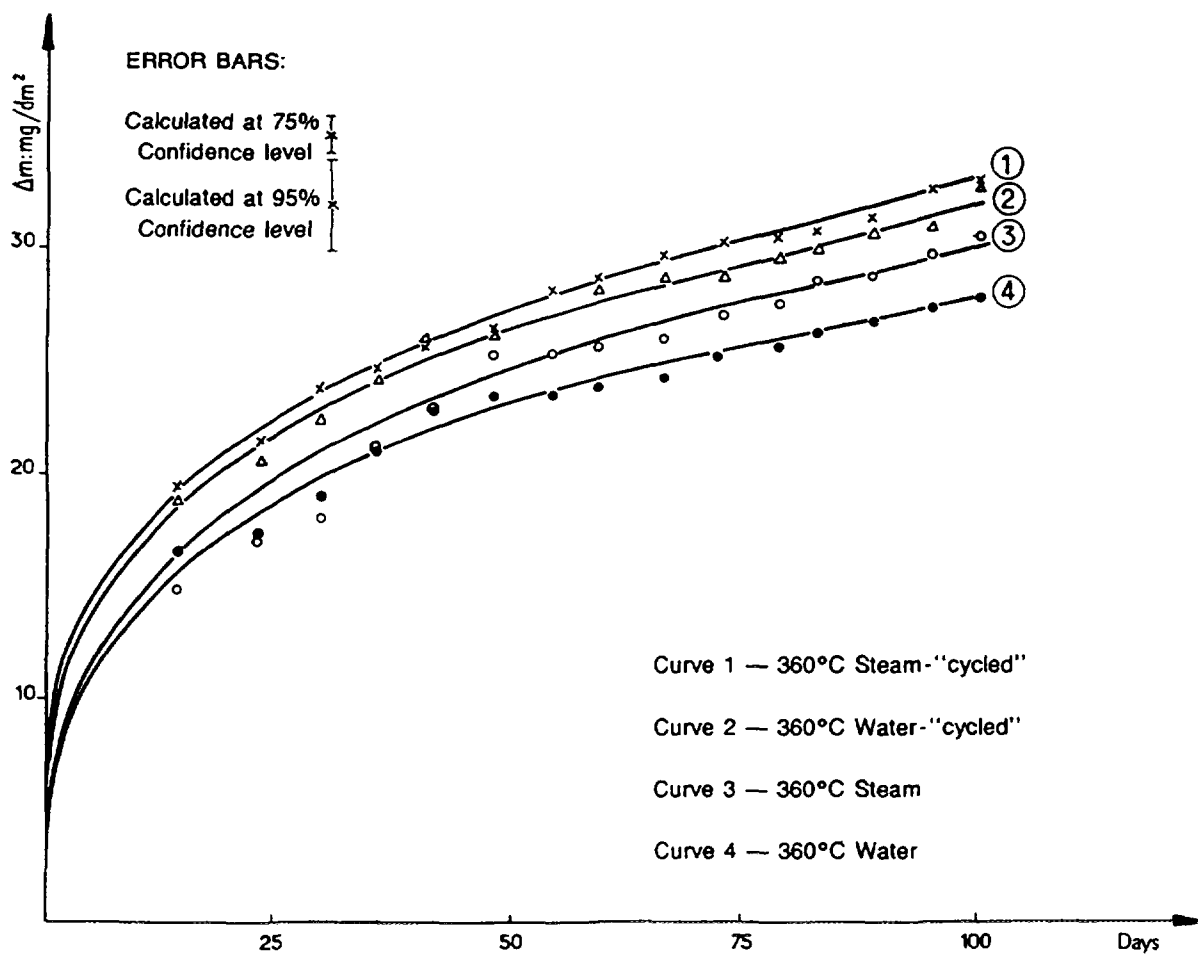


FIG. 4.16. Influence of thermal cycling on pre-transition corrosion of Zircaloy-2 [66].

observed. This is analogous to the para-linear oxidation kinetics regarded as indicative of the slow development of porosity in the oxide from the start of oxidation, with the remaining barrier oxide eventually reaching a limiting thickness. Examples of this behaviour are shown in Figure 4.17 for the Zr-2.5%Nb alloy [12,68] and in Figure 4.18 for the Zr-1%Nb alloy [68,69].

A change in the temperature of the water from 285°C to 300°C has only a weak influence on the corrosion rate of Zr-1%Nb alloy. This is the same temperature range over which relatively small increases in pre-transition corrosion were observed for the Zircalloys [59]. After 500 days of autoclave testing the oxide film thickness on Zr-1%Nb alloy specimens was not more than 2 µm, and the kinetics will show a rate decreasing with time. A further rise in water temperature to 350°C showed an increase of only a factor of 2-2.5 in weight gain after 400 days when compared with the 300°C data. After up to 1000 days of autoclave testing at 350°C the oxide films retained their dark colour, adhered firmly to the base metal, and did not exceed 5 µm thickness. The hydrogen content of the samples tested did not exceed 30 wt ppm. In 350°C laboratory water the corrosion can be described by a parabolic rate law up to 1000 days

$$\log \Delta w = 0.2 + 0.5 \log t \quad (4.1)$$

for  $\Delta w$  in mg/dm<sup>2</sup> and time (t) in hours. This parabolic dependence also persists in KOH solutions typical of WWER operation, but here the weight gains were somewhat lower than in pH 7 water [68].

The Zr-2.5%Nb alloy may also show some irregular temperature dependence at low temperatures. Early results for heat-treated Zr-2.5%Nb ( $\beta$ -quench + 500°C anneal) [70] suggested that a rate transition at long exposure times became more severe as the temperature went down so that long-term rates at  $\leq 200^\circ\text{C}$  could be higher than at 275°C (Figure 4.19). This was explained as a peculiarity of early batches of the alloy with high iron contents [71], but the possibility of it occurring for other batches at longer times than the maximum exposure in these tests (~2500 days) cannot be discounted.

Another important difference between the corrosion of the Zr-Nb alloys and the Zircalloys in laboratory tests is that the former show increased corrosion rates in the presence of traces of oxygen in the water, whereas the latter do not (Figure 4.20). One important consequence of this for the Zr-1%Nb alloy is that in oxygenated mixtures of water and steam (resulting from boiling in the loop), an increase in either steam or oxygen concentration results in larger oxide film thicknesses, and can also result in nodular corrosion of the alloy. In saturated steam at 285°C (10-36 mg/l oxygen) the corrosion rate is 4-5 times that in water (0.2-0.9 mg/l oxygen) or in a water/20-30% steam mixture (0.36 mg/l oxygen) (Figure 4.21). Similar behaviour was observed in tests at 350°C (Figure 4.22). The hydrogen content of the specimens in these tests remained low at ~20 wt.ppm [72].

In steam at 400°C, with 20-40 mg/l oxygen, the corrosion of Zr-1%Nb alloy specimens remained close to parabolic

$$\log \Delta w = 0.3 + 0.58 \log t \quad (4.2)$$

however, with further increases in temperature the protectiveness of the oxide films degraded so that at 450°C the kinetics became closer to linear

$$\log \Delta w = 0.35 + 0.71 \log t \quad (4.3)$$

and the oxide thickness reached 60 µm after 4,000 hours. After steam tests of 300 hours lamellar oxide films were formed that peeled off in large pieces when the specimens were pulled in tension. At high steam temperatures the hydrogen contents reached high values; after 3,500 hours at 500°C (for example) hydrogen contents of 1,000 wt.ppm were observed, with a heavily hydrided surface layer of 20 µm thickness.

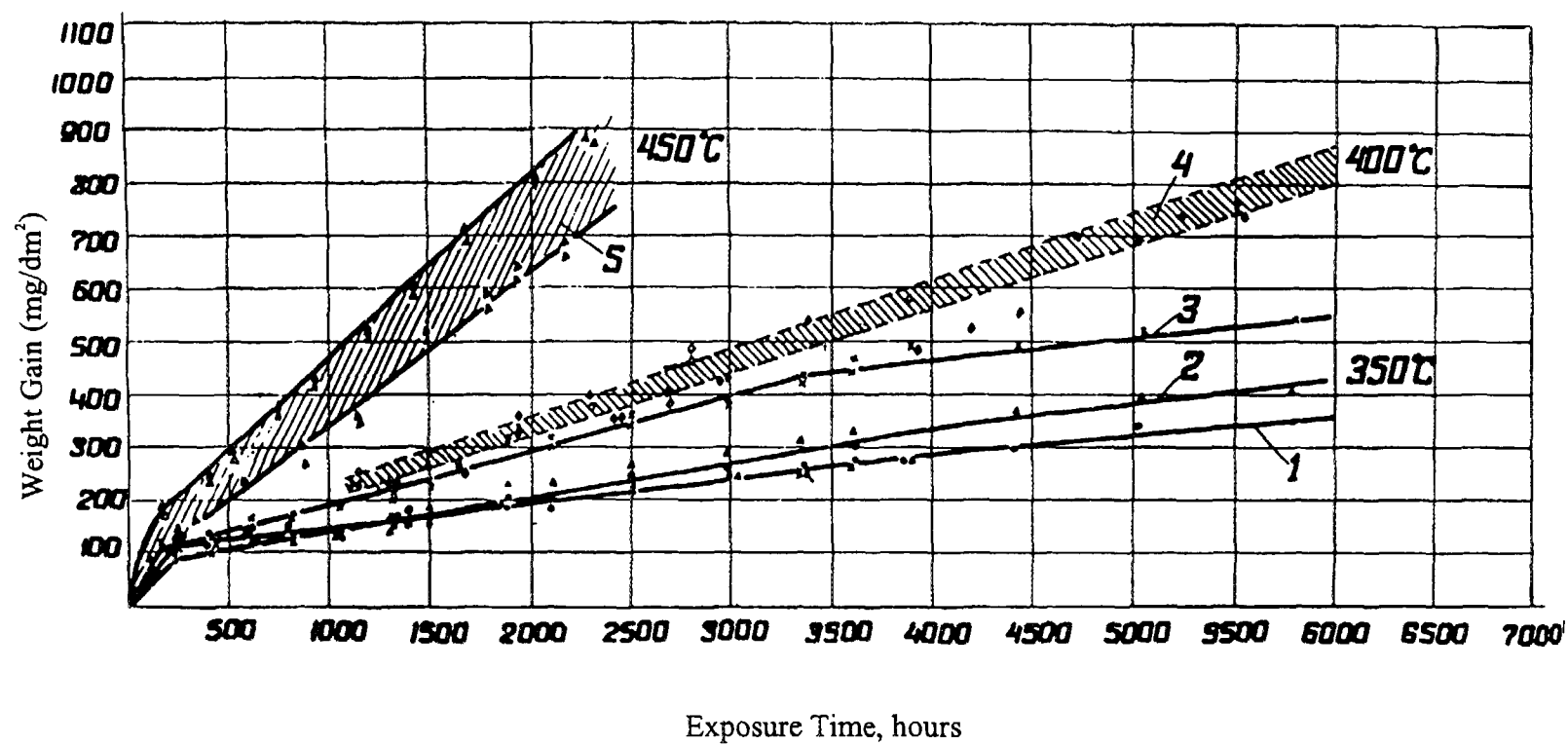


FIG. 4.17. Corrosion of alloys with 2-5% niobium in water and superheated steam at various temperatures [68]. 1. Zr-2%Nb; 2. Zr-2.5%Nb; 3. Zr-5%Nb; 4. Zr-2.5-3%Nb; 5. Zr-2.5%Nb.



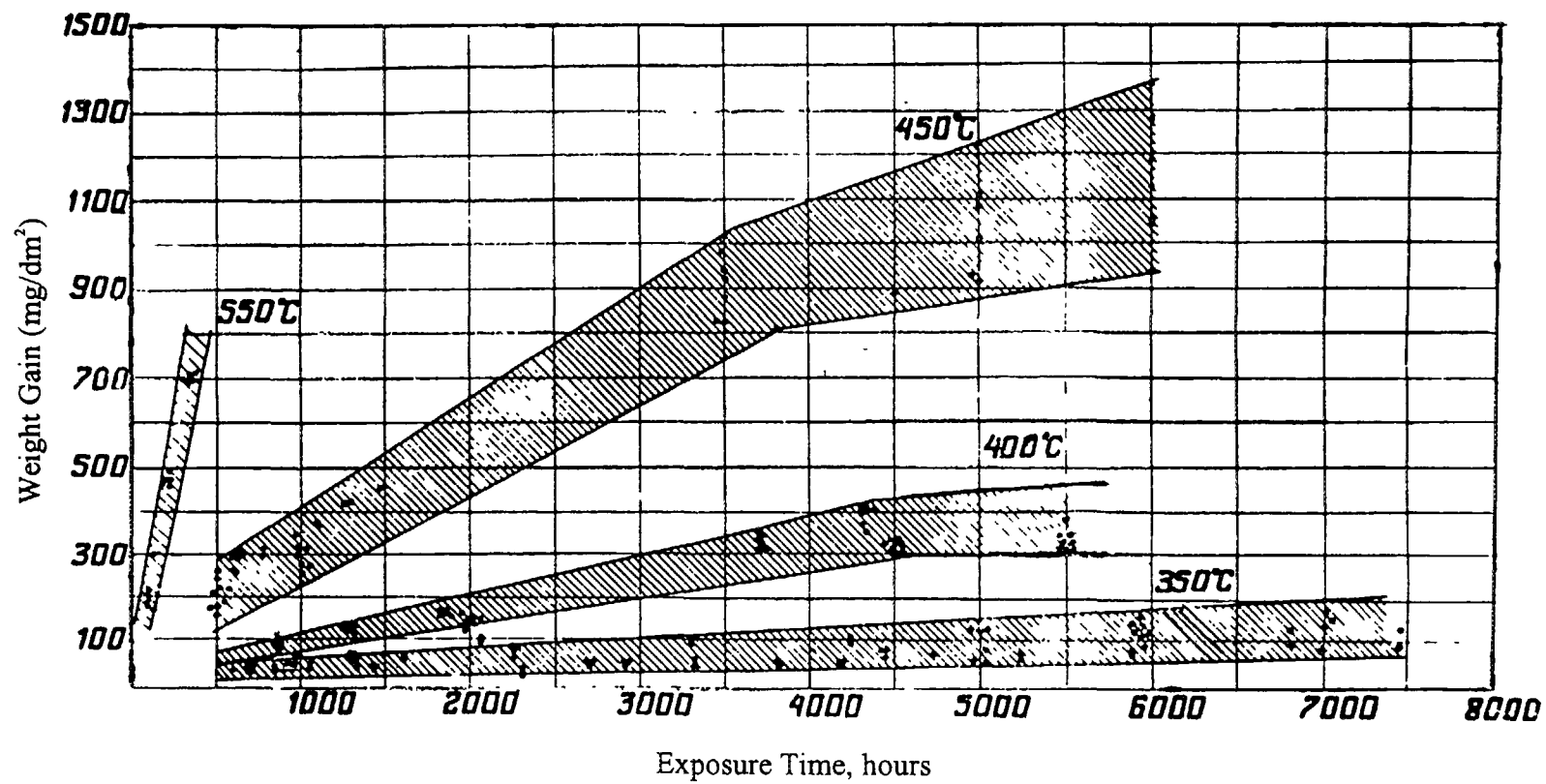


FIG. 4.18. Corrosion of zirconium alloy with 1% niobium in water and superheated steam at various temperatures [68].

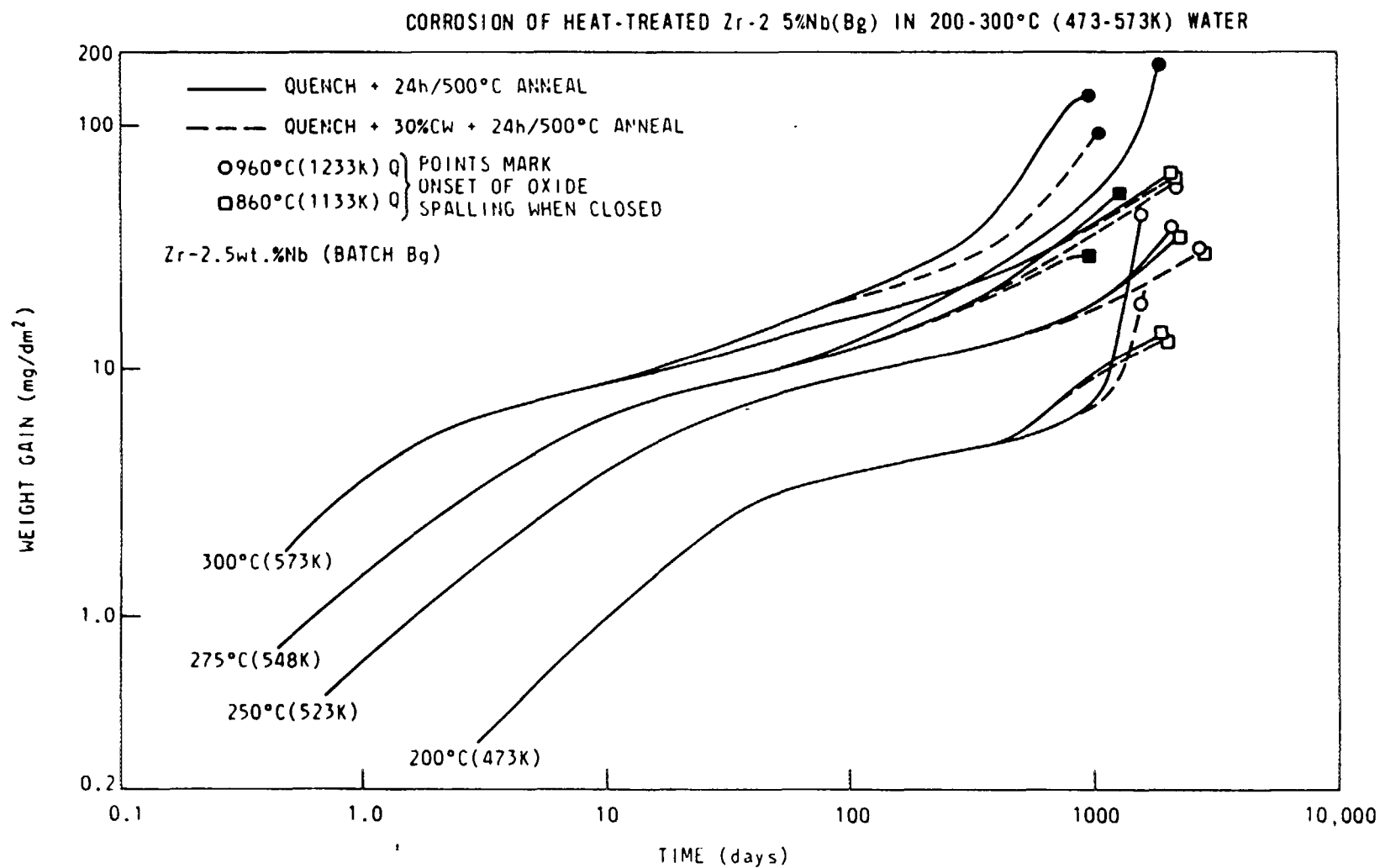


FIG. 4.19. Corrosion of heat-treated Zr-2.5%Nb (batch Bg) in 200-300°C (473-573K) water [70].

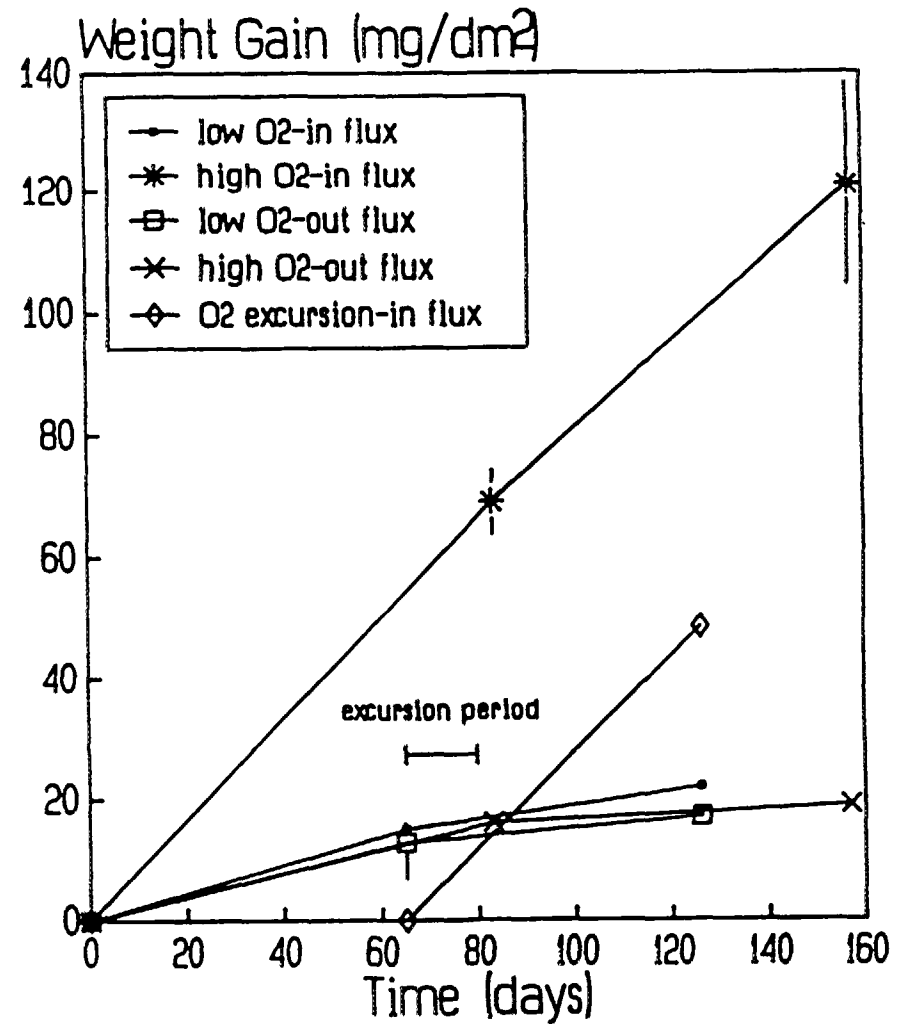
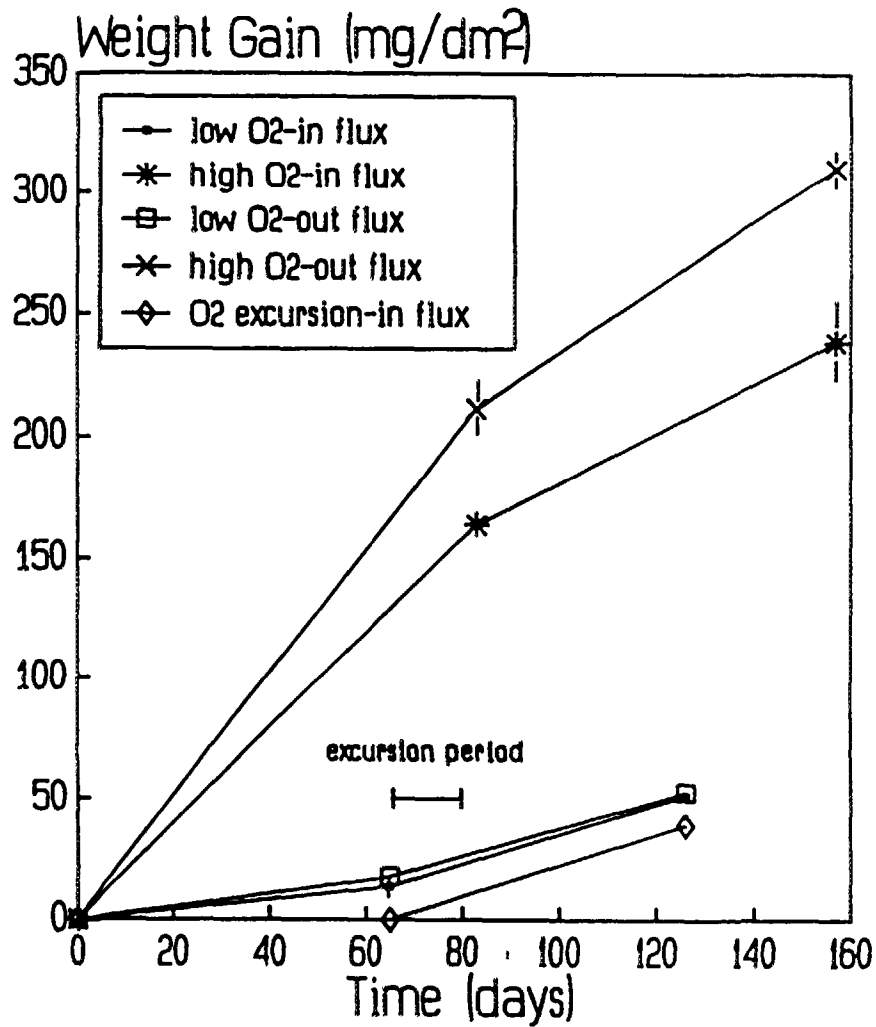


FIG. 4 20. Corrosion of bare Zr-2.5%Nb (left) and Zircaloy-2 (right) pressure tube specimens in 568K water in the U2 loop of NRU [524]

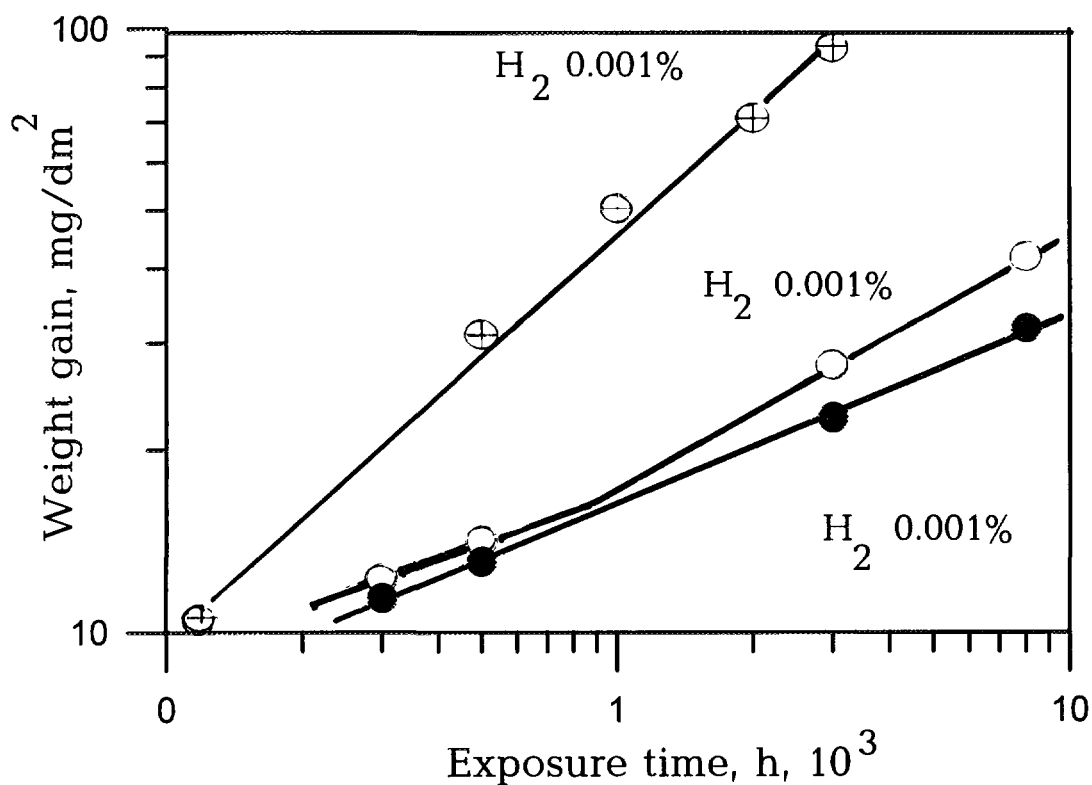


FIG. 4.21. Corrosion of Zr-1%Nb in water, water + steam and in steam at 285°C. 1. Water,  $O_2=0.2-0.9$  mg/l; 2. Water + steam,  $O_2=0.36$  mg/l, 20-30% steam; 3. Steam,  $O_2=10-36$  mg/l [72].

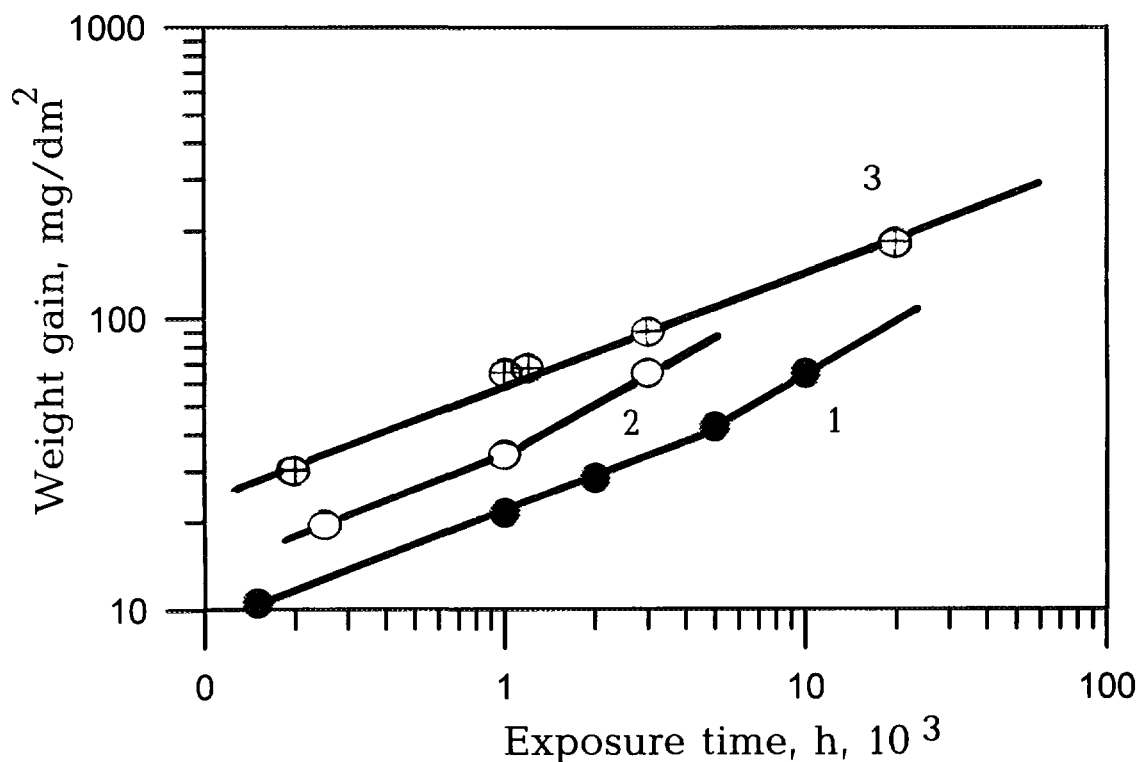


FIG. 4.22. Corrosion of Zr-1%Nb in water and in water + steam at 350°C. 1. Water,  $O_2=0.2-0.9$  mg/l; 2. Water + steam,  $O_2=0.03$  mg/l; 3. water + steam,  $O_2=20-30$  mg/l, 20-30% steam [72].

The effect of pH already noted in Chapter 1 appears to be general for all alkaline solutions. At 300°C the weight gains of all specimens were lower than in water for all the alkalis tested (KOH, NaOH,  $\text{NH}_4\text{OH}$  and LiOH) and a small reduction was also observed in  $\text{H}_2\text{SO}_4$  at pH 5 (Figure 4.23). In the light of current hypotheses about  $\text{ZrO}_2$  dissolution in such solutions [72,73] it would be interesting to know how much of the reduced weight gains may have resulted from local oxide dissolution (see Section 4. 2. 3. 2). In LiOH solutions with 70 ppm  $\text{Li}^+$ , ZIRLO (Zr-1%Nb-1%Sn-0.1%Fe alloy) seems to show lower corrosion rates than Zircaloy-4 (Figure 4.24). However, reported results [74] for binary Zr-Nb alloys indicate that both Zr-1%Nb and Zr-2.5%Nb are much more sensitive to accelerated corrosion in LiOH solutions than the Zircaloys especially following transients to higher LiOH concentrations (Figure 4.25). Effects of LiOH will be discussed in more detail later (section 4. 2. 3. 2.).

#### 4. 2. 2. Pre-transition oxidation mechanism

A comprehensive model for the growth of pre-transition oxide films requires the following information:

- a. A full description of oxide film structure and the evolution of the crystallite size, size distribution and texture; phase composition; the nature of the reasons for the restricted selection of monoclinic crystallite orientations (e.g. does that imply that at temperature the crystallites were tetragonal or cubic and stabilised by the compressive stresses); knowledge of the diffusion kinetics in the lattice and at crystallite boundaries. Figure 4.26 is a simplified attempt to represent a pre-transition oxide film [26].
- b. The nature of the electrical properties of the oxide. Since  $\text{ZrO}_2$  is intrinsically an insulator, dopants have a big effect on conductivity [75]. Localized doping, or localized regions of high conductivity for other reasons, are particularly important (Figure 4.27) [75,33]. Evidence shows that the intermetallics represent such regions in the Zircaloys and unalloyed zirconium (which usually contains  $\text{Zr}_2\text{Fe}$  or  $\text{Zr}_3\text{Fe}$  precipitates), but not in Zr-2.5%Nb which is generally free of them in the cold-worked condition if the Fe impurity concentration is low [26]. In this alloy the transition metal impurities dissolve preferentially in the  $\beta$ -Zr phase.
- c. Correlations of oxidation kinetics with oxygen diffusion in  $\text{ZrO}_2$  fit best with crystallite boundary diffusion [19,20] which is many orders of magnitude higher than that for lattice diffusion at normal reactor temperatures (Figure 4.28); but the details of this process, rather than average behaviour over large areas, are needed because of the localised thickness variations that develop at the oxide-metal interface.
- d. Electrochemical studies show that high fields persist across the oxide (Figure 4.29), and that this electronic resistivity is a significant component of the overall oxidation resistance [29]. However, a detailed understanding of local conduction effects remains absent for oxides in high temperature water, and is especially important under irradiation.
- e. In order to describe the overall oxidation process we must concentrate on the closed circuit electrochemical aspects. The electronic current flows at local sites (intermetallics) in the Zircaloys and the surface current of electrons or protons represents an electrochemical potential variation across the surface. Thus, the surface potential is expected to be very position dependent. Little or no evidence on this is available even at low temperatures.
- f. For alloys other than the Zircaloys we must make individual studies, e.g. Zr-2.5%Nb has few intermetallics, and evidence suggests that electronic conduction is relatively homogeneous. Thus, surface potential variations may be much smaller than for the Zircaloys.
- g. The evolution of the oxide structure and the incorporation of alloying elements in pre-transition oxides are not well known - Electron microscopy gives good data in the very thin film region of oxide evolution. Ion milling of thick films is possible with difficulty but at intermediate thicknesses (0.5-4  $\mu\text{m}$ ) the films are not well characterized. Similarly, the distribution and location of impurities and alloying elements across the oxide [76] are known on a macro scale for thick films from Auger Electron Spectroscopy (Figure 4.30) but evidence on pre-transition oxides is slender and not always believable, and evidence on the scale of the oxide crystallite

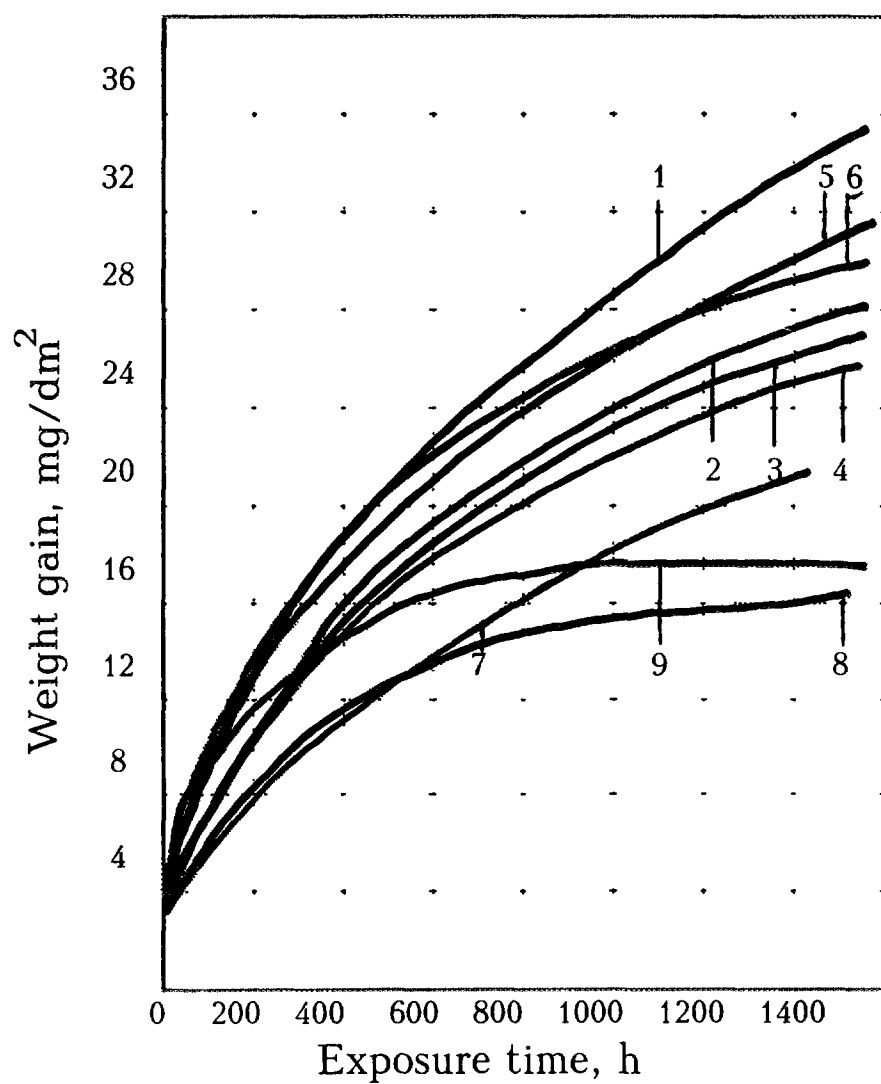


FIG 4-23 Corrosion of Zr-1%Nb in water and solutions at 310°C 1 Detonized water pH 5.8 2 NH<sub>4</sub>OH pH 7 3 NH<sub>4</sub>OH pH 9 4 NH<sub>4</sub>OH pH 11 5 H<sub>2</sub>SO<sub>4</sub> pH 5 6 NaOH pH 7 7 LiOH pH 9 8 NaOH pH 9 9 KOH pH 9 [72]

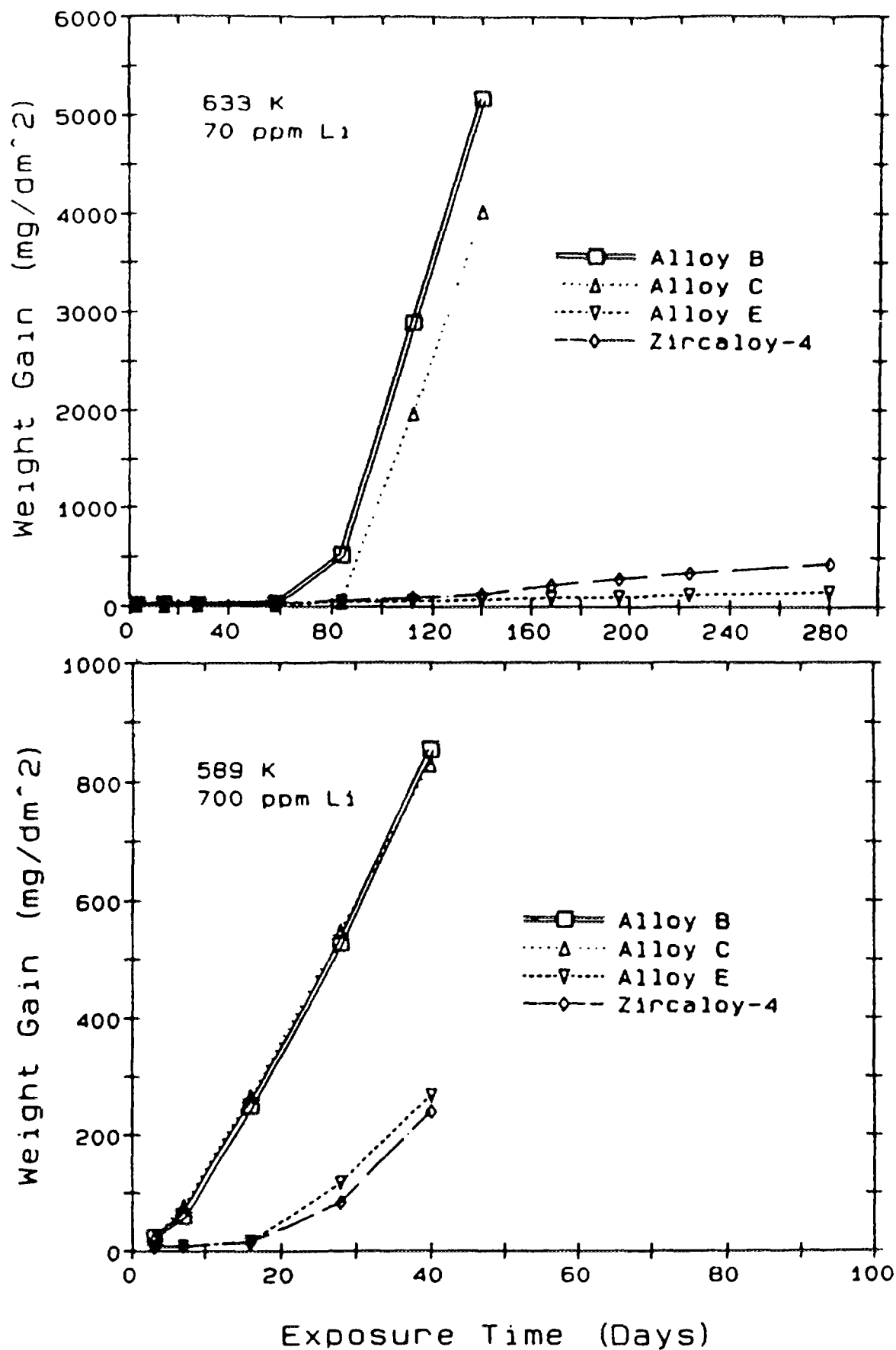


FIG. 4.24. Corrosion weight gains versus exposure time in LiOH solutions containing (top) 70 ppm lithium (0.01M) at 633K, (bottom) 700 ppm lithium (0.1M) at 589K. Alloy B is Zr-2.5%Nb; Alloy C is Zr-1%Nb; and Alloy E is ZIRLO [74].

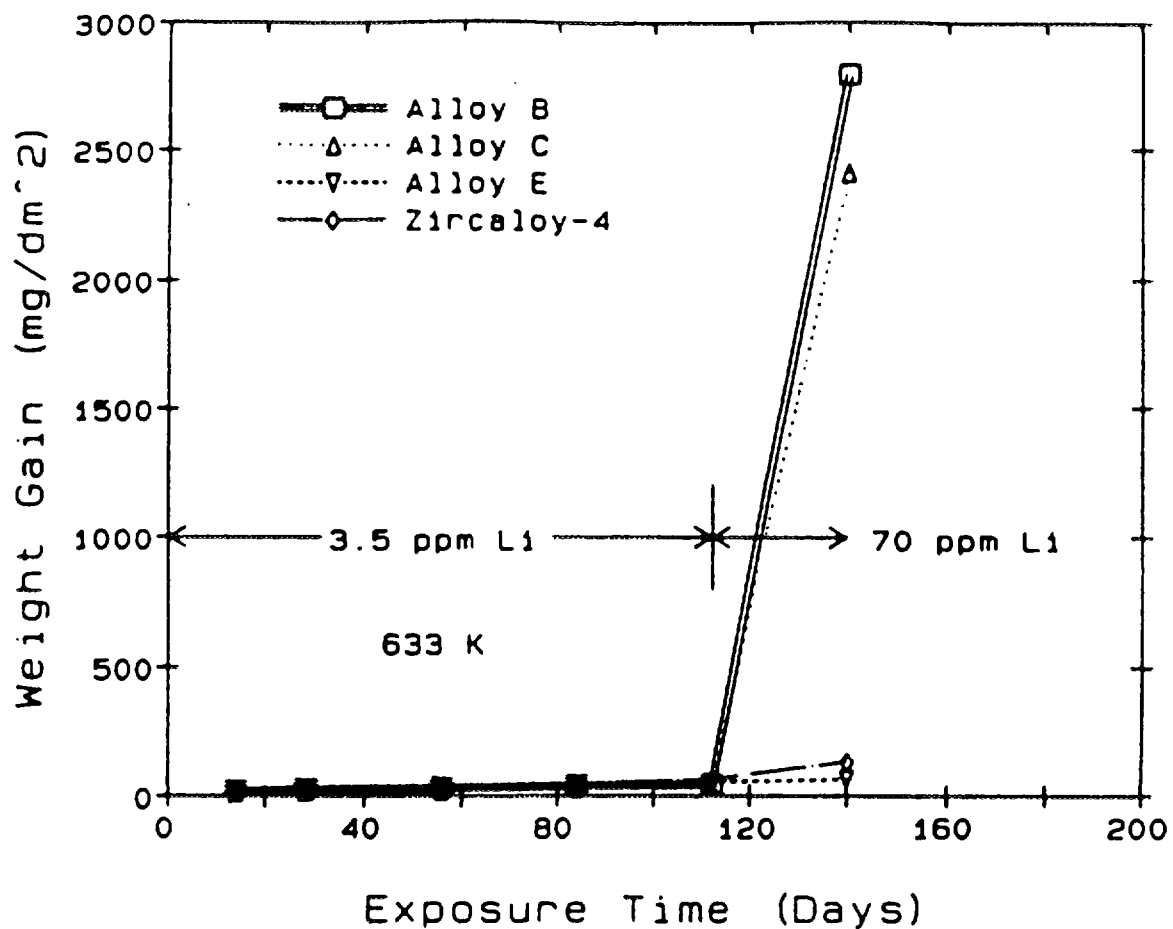


FIG. 4.25. Corrosion weight gain versus exposure time at 633K in LiOH solutions. Lithium concentration was 3.5 ppm (0.0005M) for 112 days, then 70 ppm (0.01M) for an additional 28 days (Alloys B, C and E are the same as in the previous FIG.) [74].

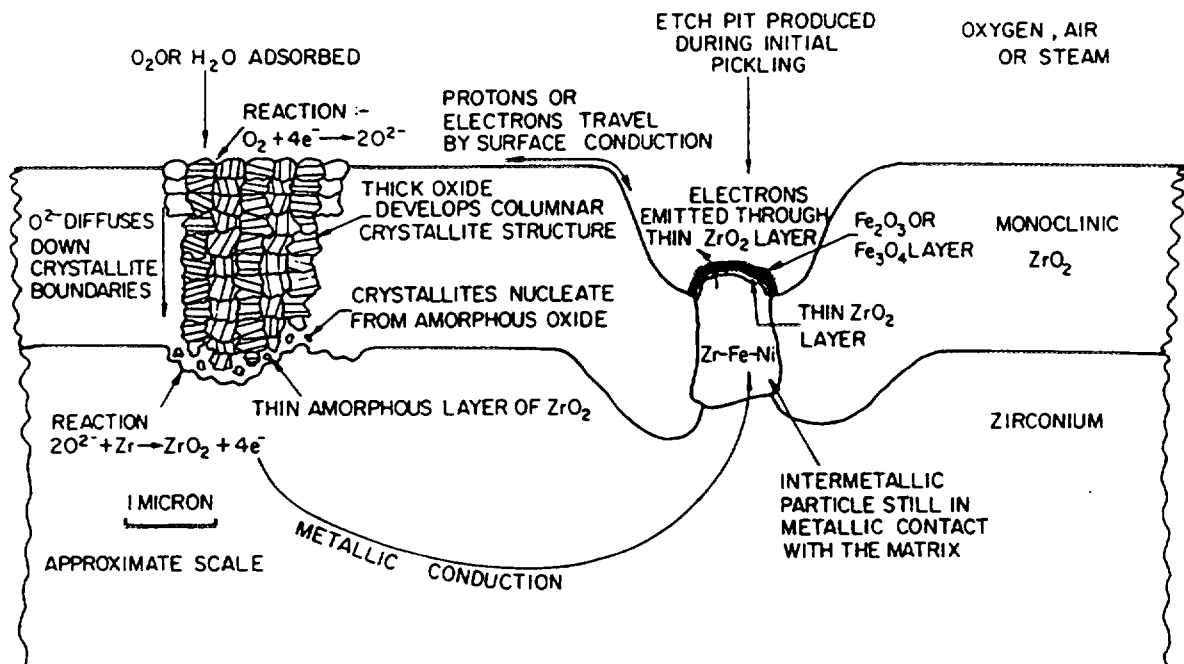


FIG. 4.26. Schematic diagram of the oxide film on Zircaloy-2 and the processes occurring in it during oxidation [26].



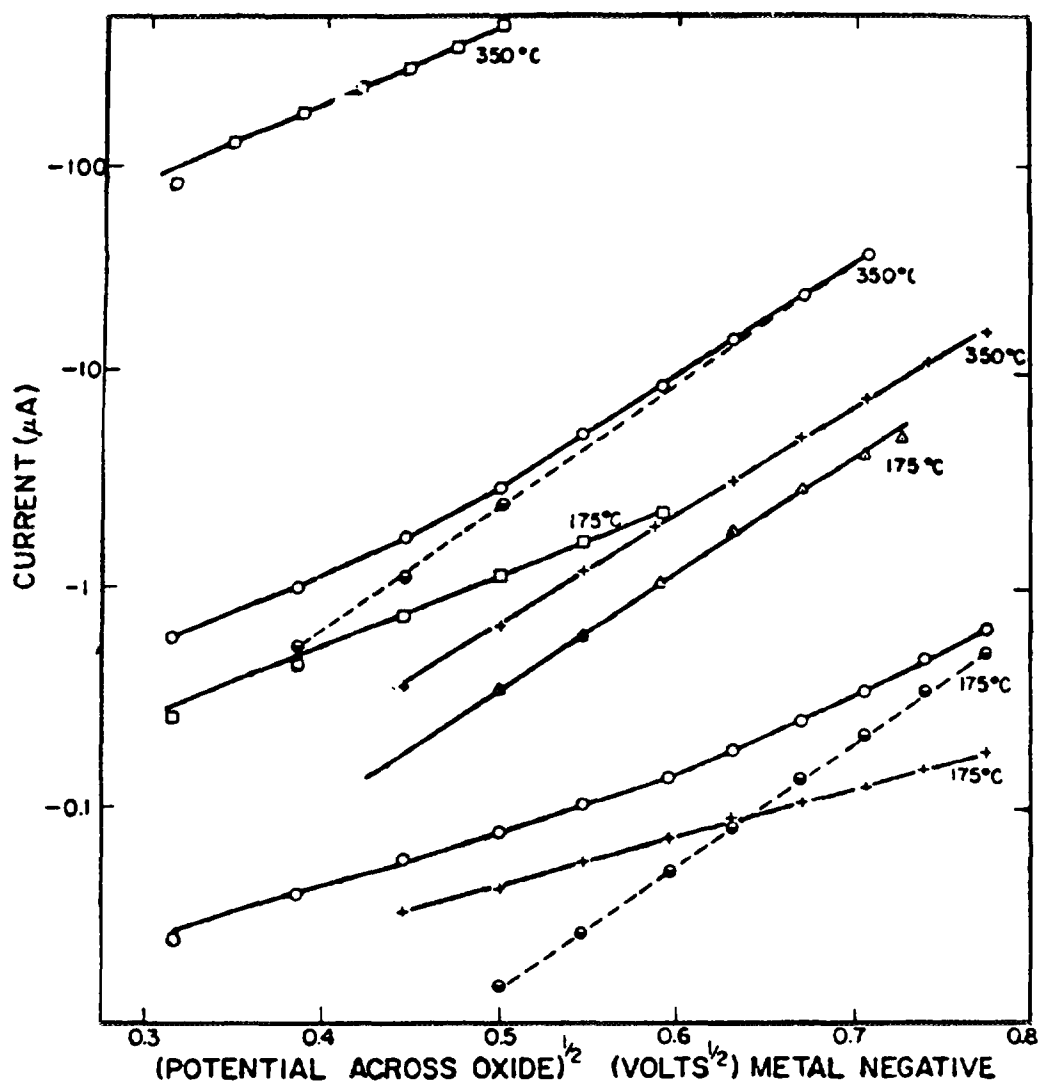


FIG. 4.27. Log  $I$  versus  $V^{1/2}$  (Schottky) plots for forward electronic (metal negative) characteristics of: + Zircaloy-2 oxidized in steam (800 psi) at 350°C to a weight-gain of 19 mg/dm<sup>2</sup>; O, Zircaloy-2 oxidized in dry air at 350°C to a weight-gain of 19 mg/dm<sup>2</sup>; O, as before but with prior subtraction of an ohmic component of  $4 \times 10^6 \Omega$  at 175°C and  $3.2 \times 10^5 \Omega$  at 350°C; + Zircaloy-2 oxidized in air at 350°C to a weight gain of 19 mg/dm<sup>2</sup> and then coated with magnetite (~10 nm) in 300°C water containing Fe(OH)<sub>3</sub>; Δ, an anodic ZrO<sub>2</sub> film (30 nm) on crystal-bar zirconium coated with Fe<sub>2</sub>O<sub>3</sub>. Specimen areas: 8.5 cm<sup>2</sup> [33].

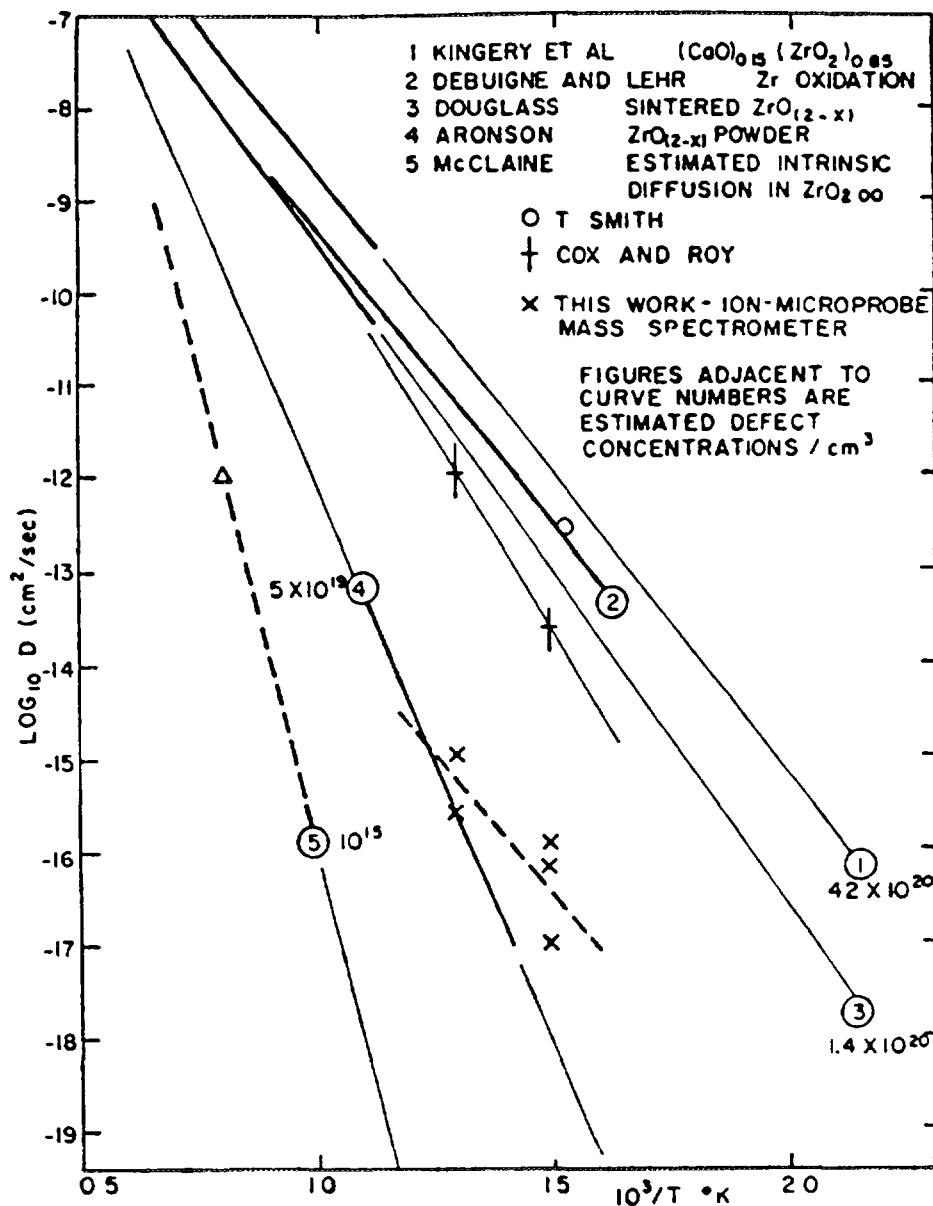


FIG 4.28 Diffusion coefficients for oxygen in zirconia (for references see original) [20]

size is still completely absent. Whether the alloying additions and impurities segregate at crystallite boundaries or occupy substitutional or interstitial positions in the oxide lattice, and their effective valence in barrier-type oxide films, is unknown for all species. A start on such measurements has been made for Fe in  $\text{ZrO}_2$  by Mossbauer Spectroscopy [77], and Scanning Transmission Electron Microscopes (STEM) capable of analyses on the scale of the oxide crystallite size are becoming available.

A start has been made on closing the gaps in our knowledge of the fate of the alloying elements in the oxide film. The alloying by minor additions of Fe, Cr and Ni to the Zircalloys and of Nb in Zr-1%Nb and Zr-2.5%Nb alloys enhances significantly the corrosion resistance of Zr metal. In every case, the major fraction of the alloying element is not soluble and precipitates as a second phase or phases. The nature and spatial distribution of these precipitates are dependent on the thermal history during processing (e.g. section 6.2 for Zircaloy). In order to understand the mechanism of this improvement in corrosion resistance, several microstructural studies have recently been undertaken by STEM of the oxide layer [42,78,79]. A schematic view of the behaviour of one type of

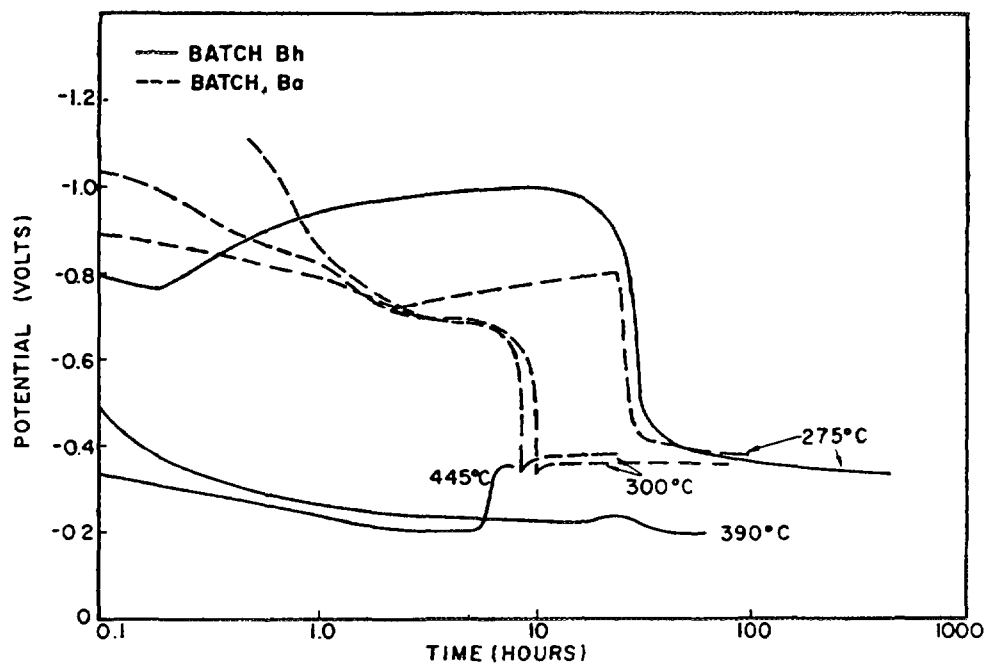


FIG. 4.29. Potential versus time curves for Zircalov-2 in fused salt (Bh and Ba refer to the designations of two batches of Zircalov-2) [29].

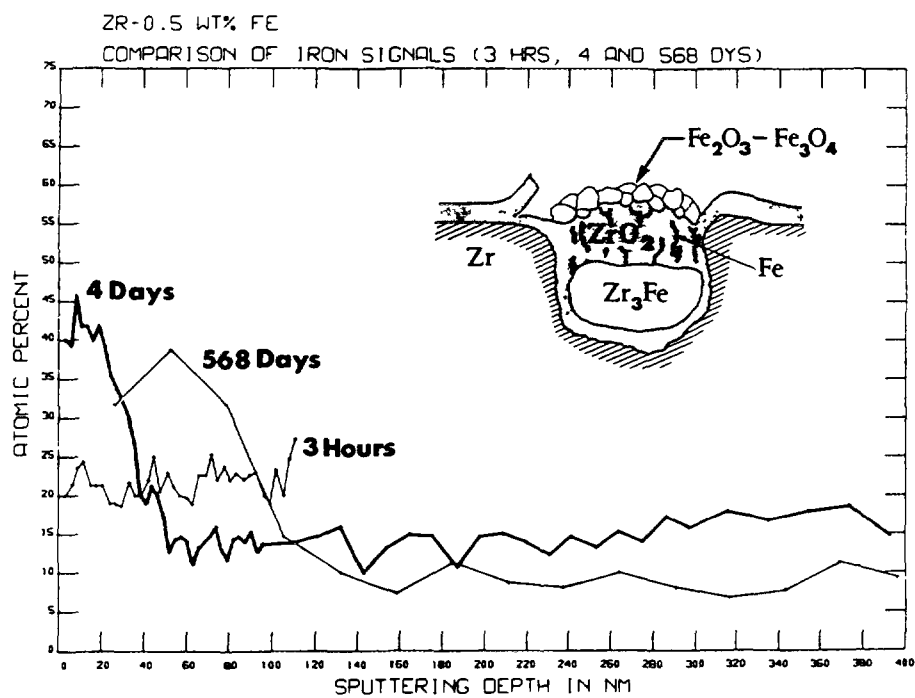
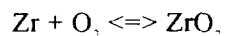


FIG. 4.30. Iron profile for three different lengths of oxidation at 573K, within the oxide film formed on a  $Zr_3Fe$  precipitate [76]

precipitate is presented in Figure 4.31. It was found that the precipitates were incorporated unoxidized in the surrounding dense oxide layer of zirconia (Figure 4.32) and then slowly transformed. The subsequent oxidation of Zr and Cr led to the release of Fe as metallic particles at the edge of the precipitates (Figure 4.33). This indicates that the oxygen potential is lower there than that corresponding to the oxidation of Fe. Indeed, it varies between the boundary conditions at both interfaces of the dense layer:

- at the metal/oxide interface, the oxygen potential corresponds to the equilibrium



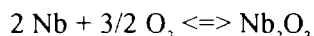
- while at the roots of the pores, i.e., where the water can reach, the oxygen potential corresponds to the reduction of water:



adjusted to allow for the incomplete absorption of hydrogen by the metal which can result in an  $\text{H}_2:\text{O}_2$  ratio in the pores that is much larger than 2.

In some cases, the precipitates were found to transform to an intermediate amorphous state in the dense oxide layer. This amorphous transformation is not due to irradiation (as discussed in section 8. 1. 3. 3.) but may be attributed to the doping of the intermetallic by hydrogen, or to a departure of the particle stoichiometry from  $\text{AB}_2$ , as the nearest neighbour distance between atoms is different from that obtained after an irradiation induced amorphous transformation [79]. In all cases, the final oxidation of the precipitates occurs when the growth of the oxide layer leaves them surrounded by the porous oxide. Then the oxygen potential is high enough to allow iron to oxidise. When oxidised, these precipitates mainly form tetragonal zirconia, while the surrounding matrix is monoclinic. The stability of this allotropic form could be enhanced by Fe or by the very fine grain size observed.

For Nb bearing alloys, the Nb-rich precipitates are considered to oxidise at the same time as the surrounding matrix, since the oxygen potential of the reaction:



is similar to the potential for the oxidation of zirconium.

The process by which the unoxidized precipitates are embedded in the zirconia layer could help to explain the improvement induced by the addition of the insoluble alloying elements, i.e., they act as a source of Fe within the zirconia itself, contributing to a chemical stabilisation of the tetragonal phase [43]. The diffusion of Fe from the unoxidized precipitates into the surrounding matrix is very different in autoclaved samples compared with irradiated samples. It is very limited in an autoclave experiment, but more significant under irradiation. The impact of this difference will be discussed in section 8. 1. 3. 3. 2. [80].

Examination of thin oxide films on cold-worked Zr-2.5%Nb alloy has shown some interesting differences from the above. Although much of the oxide consists of columnar  $\text{ZrO}_2$  grains, as is the case for Zircaloy oxidation, the  $\beta$ -Zr phase at the  $\alpha$ -Zr grain boundaries oxidises more rapidly than the  $\alpha$ -Zr matrix, and there seems to be more evidence for the presence of amorphous  $\text{ZrO}_2$ , both at the oxide/metal interface and at columnar crystallite boundaries (Figure 4.34) than is observed for oxide films on Zircalloys [81-83]. The Zr-1%Nb alloy is an alloy with a primarily  $\alpha$ -Zr structure which may have small precipitates ( $<0.1 \mu\text{m}$ ) of either  $\beta$ -Zr or  $\beta$ -Nb depending upon the heat treatment although most commercial heat treatments will not result in  $\beta$ -Zr precipitates in the final product. No detailed studies of the oxide structure have been reported.

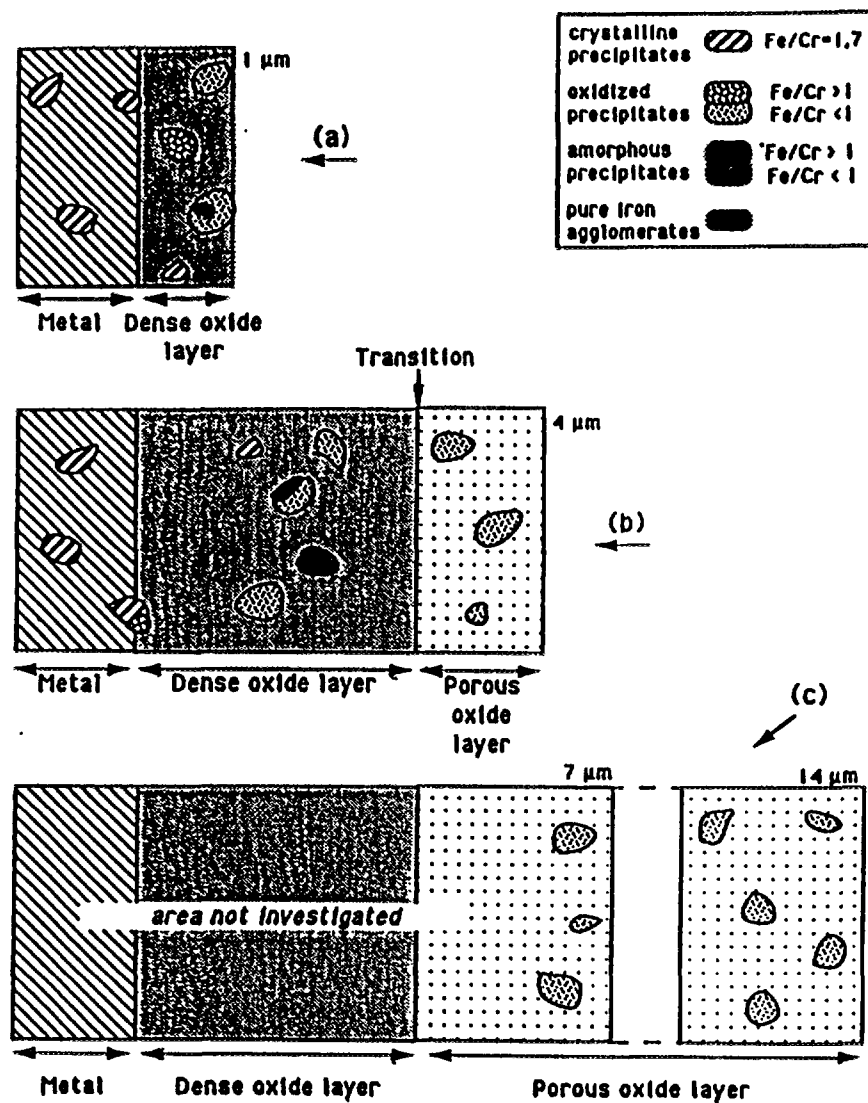


FIG 4.31. Schematic view of the various oxidation states of the intermetallics in  $\text{ZrO}_2$ . (a) After 3 days oxidation (1  $\mu\text{m}$ ). (b) After 40 days oxidation (4  $\mu\text{m}$ ). (c) After 420 days oxidation (14  $\mu\text{m}$ ) [42].

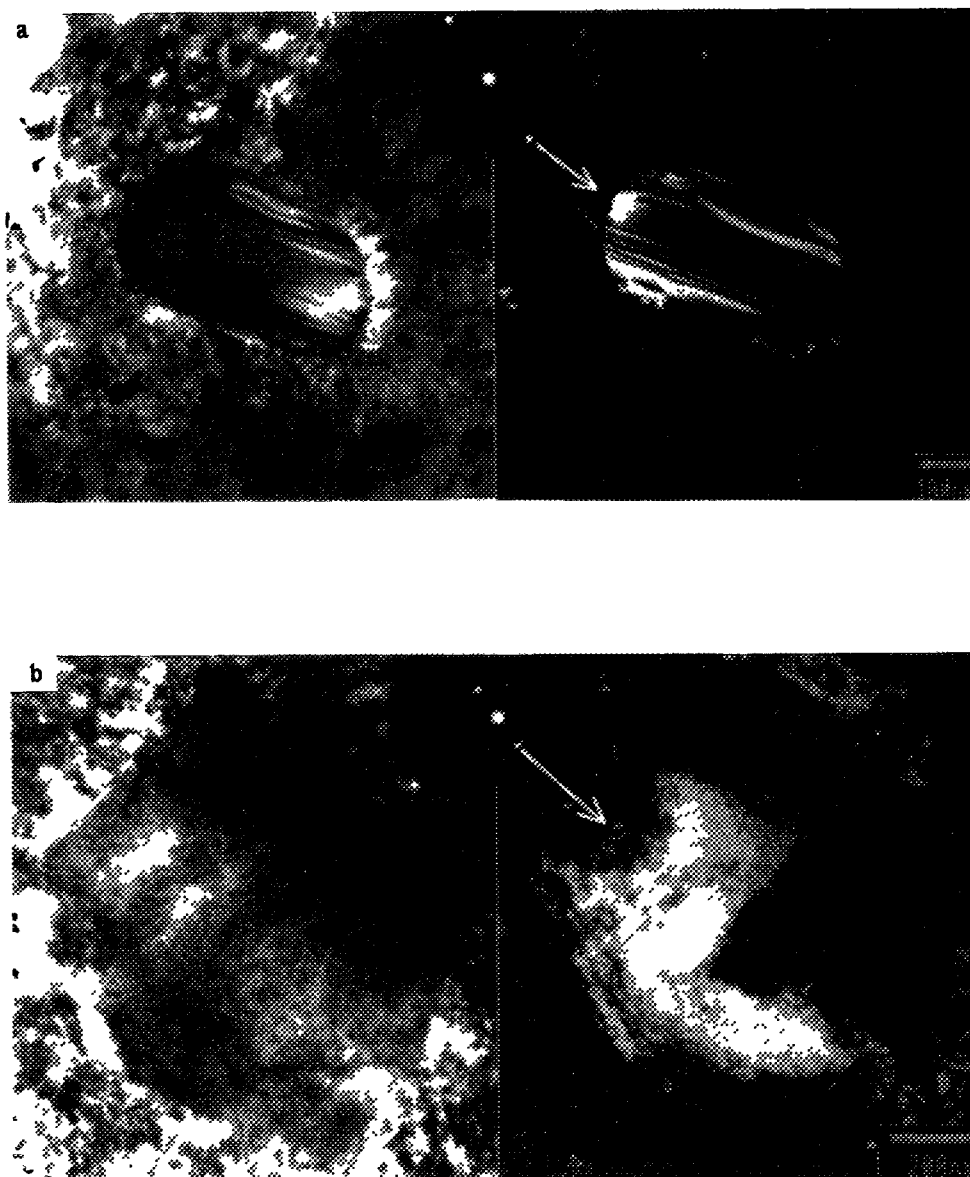
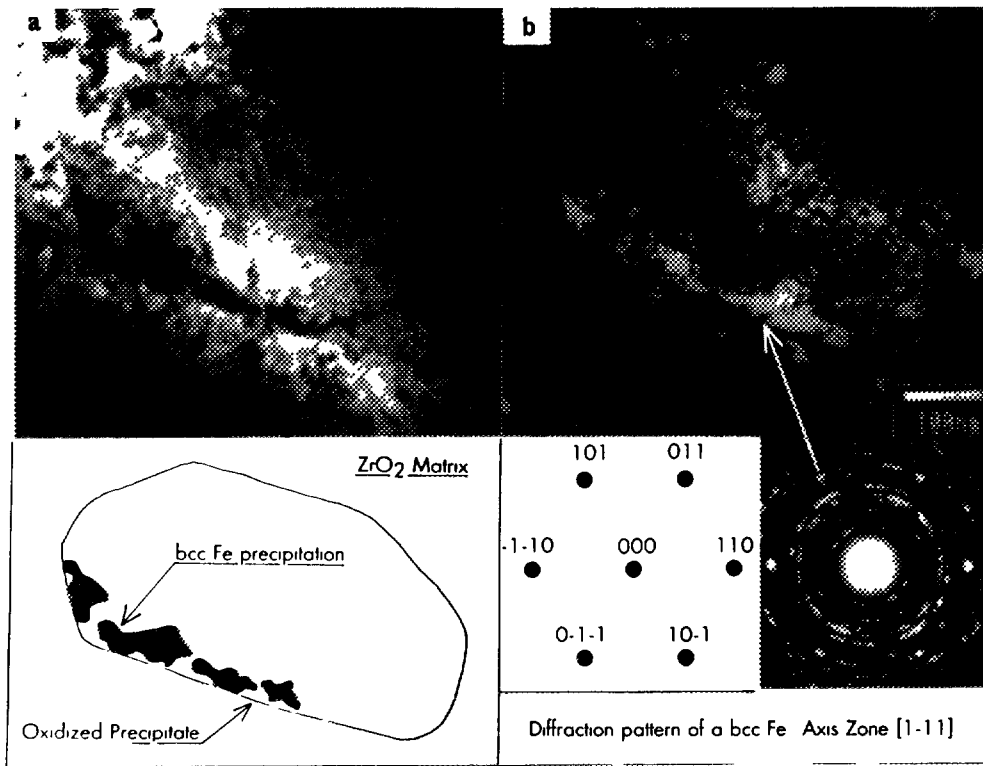


FIG 4.32. Various states of the precipitates located in the bulk of a 4  $\mu\text{m}$  thick oxide layer (at about 1  $\mu\text{m}$  from the metallic interface). (a) Unoxidized precipitate Dark-field from a  $\langle 1013 \rangle_{\text{hcp}}$  Zr(Fe, Cr), reflection (b) Microcrystalline oxidized precipitate Dark-field from a tetragonal  $\text{ZrO}_2$  spot (c) Amorphous precipitate. The first ring of the amorphous diffraction pattern corresponds to a first neighbour distance of 0.28 nm [42]



**FIG 4.33.** Rejection of iron during precipitate oxidation. (a) Microcrystalline oxidized precipitate located at the water-oxide interface of a 1  $\mu\text{m}$  thick oxide layer. (b) Dark-field of a  $\langle 110 \rangle$  bcc iron agglomeration reflection and some of the adjacent tetragonal spot [42].

#### 4 2 3. Mechanism of oxide breakdown on the Zircalloys

##### 4 2. 3 1. In water and gases

The fact that there is an acceleration in the oxidation rate at the transition point in Zircalloys implies an effective reduction of the protective fraction of the total oxide film. The processes causing this thinning are the source of some contention. Early work showed that cracking of the oxide occurred, as crack networks were seen in post-transition oxide films by electron-microscope replica techniques (Figure 4 35). However, recent studies of thick oxide films formed at 340-360°C on current Zircaloy-4 cladding batches have not found any evidence for such large cracks [84]. Only fine porosity was seen, similar to that first identified during oxidation at higher temperatures (~500°C) and low pressure (1 atm.) where few large cracks were seen after the rate transition. This led to the suggestion that networks of fine pores were involved in the transition process (Figure 4.36 [26,85]). The onset of these breakdown processes occurs by a process of local nucleation followed by spreading across the surface. Edges, support holes, punched-in identification numbers and a "random" distribution of other surface sites provide the initiation points [86]. During transition a spotty appearance, that is superficially similar to nodular corrosion, often appears. However, during the normal rate transition there is little difference in oxide thickness between white spots and the surrounding black oxide [86].

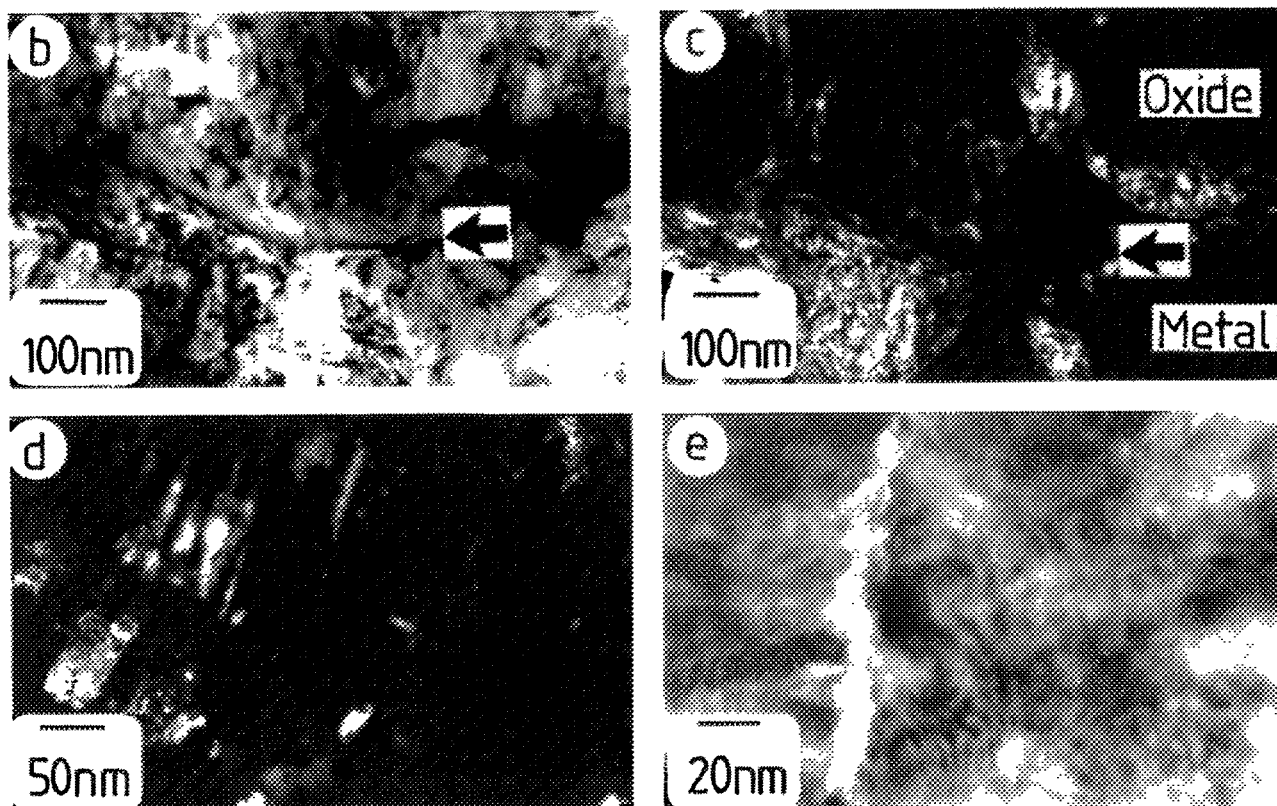
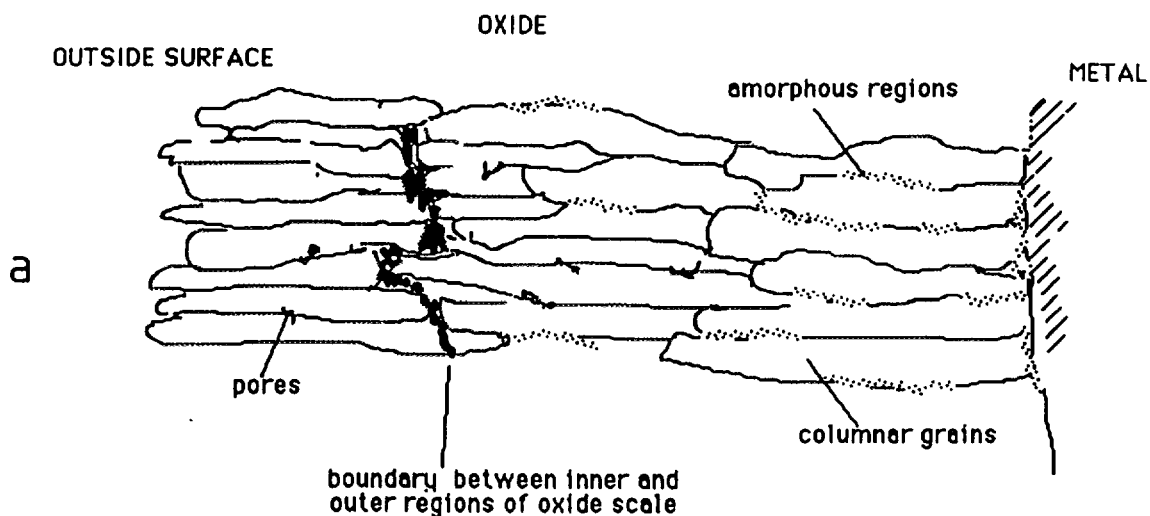


FIG. 4.34. Oxide film formed on Zr-2.5%Nb alloy. (a) Schematic diagram of scale features; (b) bright-field and (c) dark-field images of metal/oxide interface region; (d) dark-field image for amorphous contrast above interface; (e) bright-field image from near to the top of the scale showing amorphous region disrupting columnar oxide structure [83].



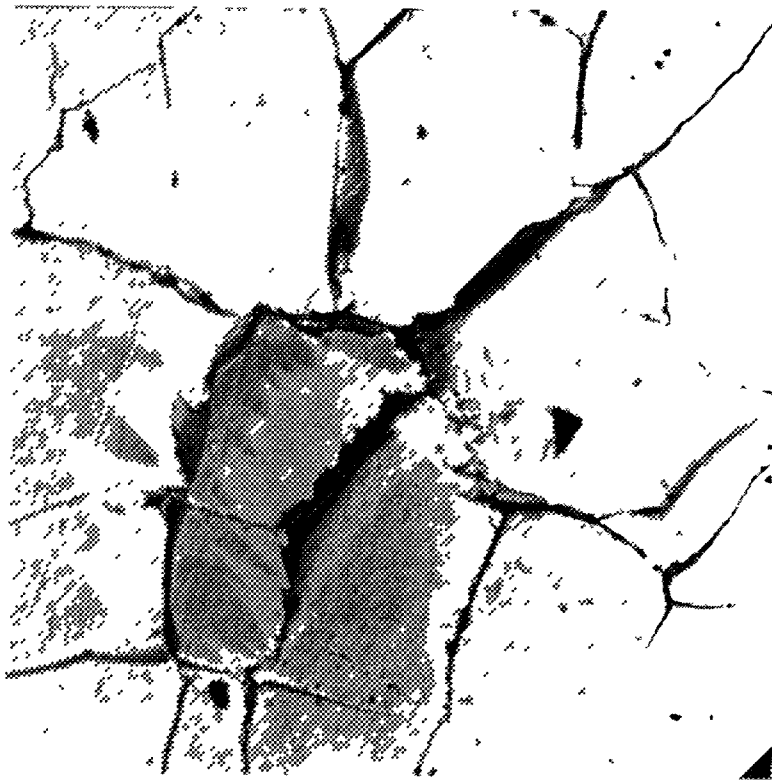


FIG 4.35 Zircaloy-2 surface after oxidation in steam at 350°C (billet Z8006, 192 days at 350°C, weight gain 40 mg/dm<sup>2</sup>). Specimen surface was uniformly covered with cracks at about this frequency (6000×) [26]

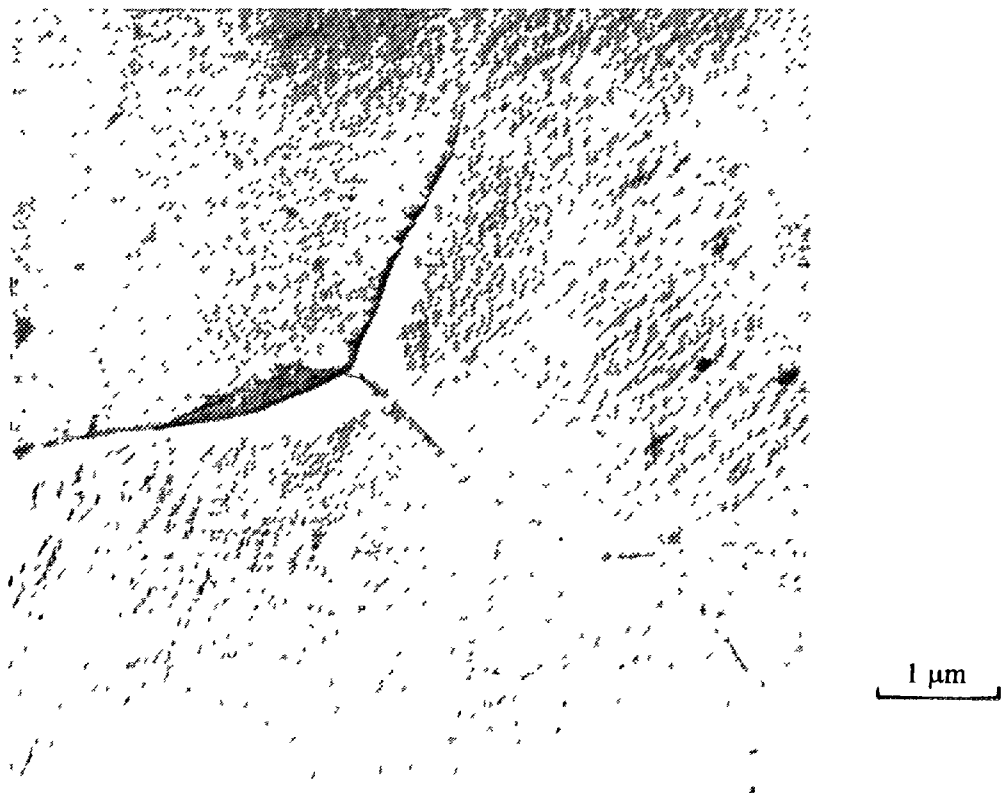


FIG. 4.36. Zircaloy-2 surface after oxidation in steam at 500°C (billet Z105, 12 days at 500°C, 1 atm, weight gain 360 mg/dm<sup>2</sup>). Only a few small cracks like this were seen on the whole surface (16000×) [26]

Porosimetry with mercury filling the pores (Figure 4.37) under pressure, was able to measure both the effective diameter of the pores and their depth of penetration, since the mercury filling the pores short-circuits that fraction of the total oxide thickness. Thus, the ratio of the final to the initial resistance of the oxide gives an approximate value for the non-porous fraction of the oxide. AC impedance measurements with metallic and electrolyte contacts can also give an indication of the depth of penetration of the pores as the electrolyte will soak into the porous layer. These results have suggested that the pores approached close to, if not right up to, the metal/oxide interface, leaving no thickness of barrier oxide that is significantly thicker on average than the normal air-formed oxide (2-5 nm) [63,85]. Results indicated that, on average, pores were smaller in oxides on Zr-2.5%Nb than on Zircaloy-2, and were already evident at weight gains much less than the transition weight gain for the Zircaloys, in accordance with a para-linear oxidation mechanism where porosity should start to develop from the beginning of oxidation (Figure 4.38). Although early studies of post-transition

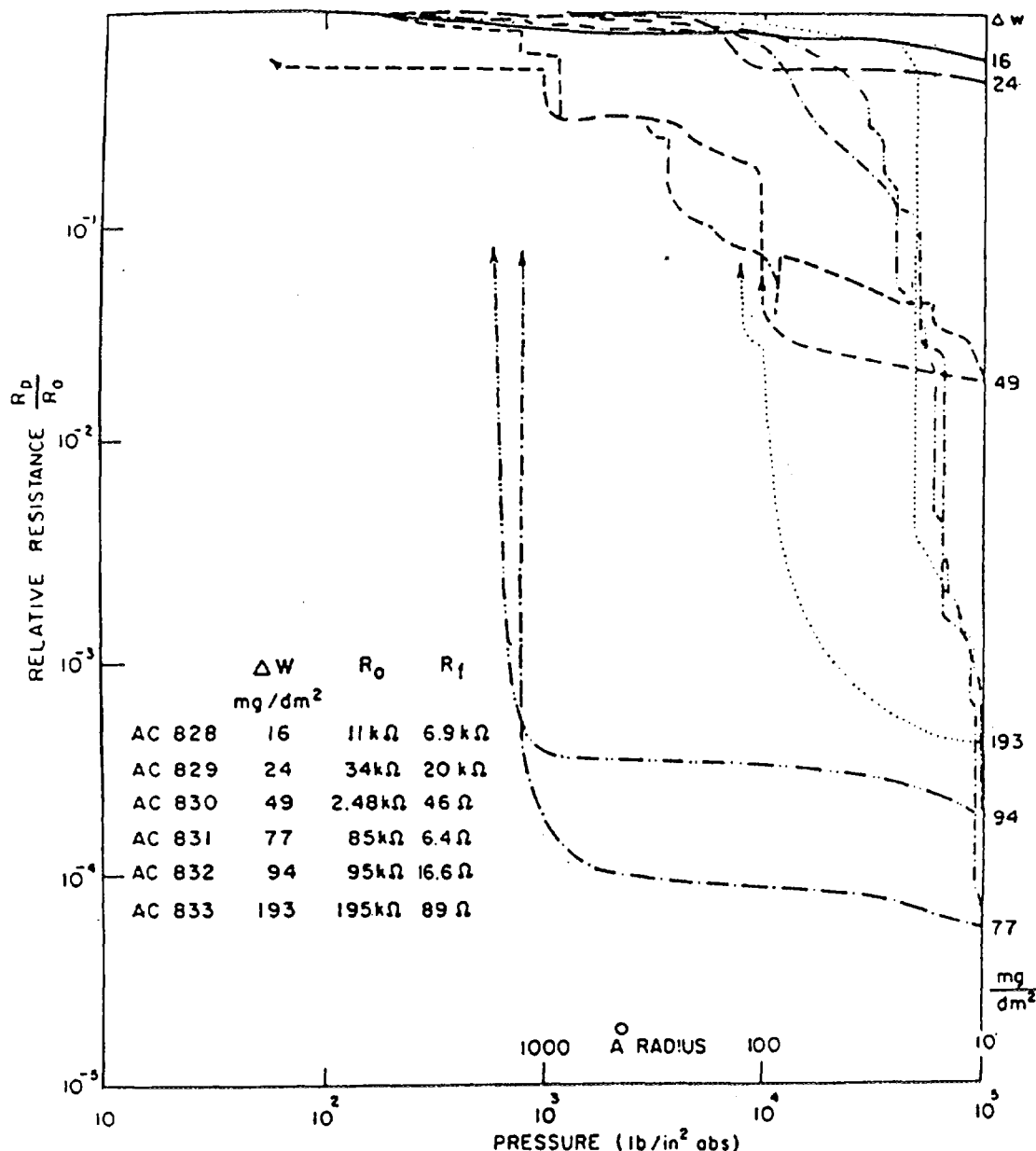


FIG. 4.37. Development of porosity in oxide films formed on Zircaloy-2 in 400°C steam. Note appearance of porosity prior to normally accepted weight gain at transition (~30 mg/dm<sup>2</sup>).  $R_0$  is initial resistance,  $R_p$  is resistance at any pressure ( $p$ );  $R_f$  is final resistance at max. pressure [63].

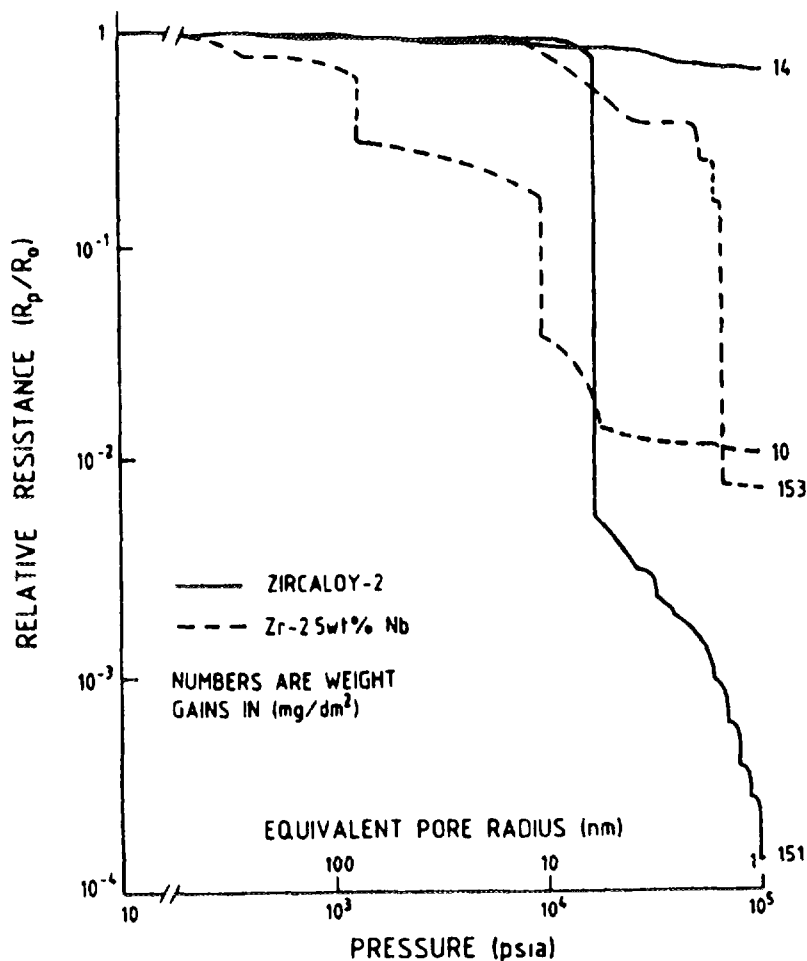


FIG 4 38 Comparison of porosimeter results on oxidized films on Zircaloy-2 and Zr-2 5%Nb [98]

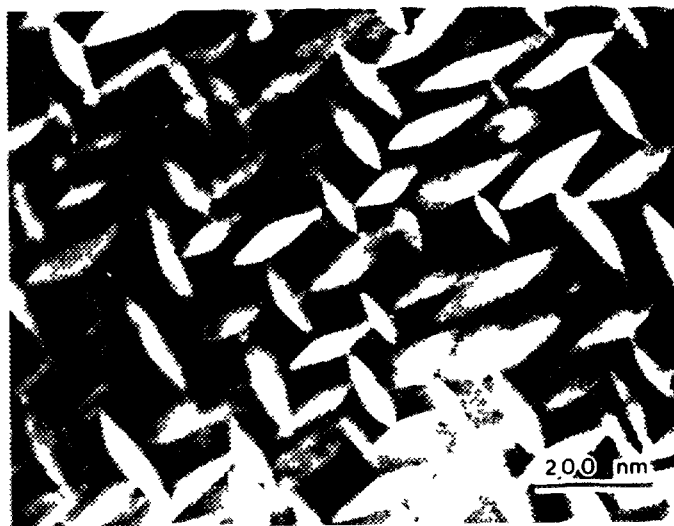
oxides showed networks of cracks in oxides formed in water in the range 300-360°C, these observations have not been confirmed by examination of current cladding batches [84]. Thus, the discontinuous cyclic post-transition oxidation kinetics that are well established for the Zircaloys do not appear to be explicable simply by the generation of networks of gross cracks at the start of each cycle. The fine porosity is always found in post-transition oxides, and the current view is that in high purity water or steam, this porosity may be generated by the martensitic transformation of tetragonal to monoclinic  $ZrO_2$  [56,57,87]. Porosimetry also suggested that there was no post-breakdown reformation of thick barrier oxides in steam and water, as suggested by Kass [88]. It appears, however, that in the thick oxides the porosity may branch as it progresses inwards producing the most pores at or near the oxide/metal interface and the least at the oxide/environment interface [84]. Hence, the cyclic nature of the kinetics may still result from the cyclic propagation of the pore network by the martensitic transformation.

The argument that these pores or cracks only progress a fraction of the way through the oxide has been made both on mechanical grounds, and on the basis of impedance measurements in aqueous solution. The high compressive stresses in the oxide film at the oxide-metal interface were concluded to decline monotonically towards the surface of the oxide [89]. This was based on the assumption that fresh oxide layers formed by inward migration of oxygen alone. Thus, if the first oxide layer is formed at its compressive yield stress, each successive oxide layer that forms (at its compressive yield) will add an increment of tensile stress to the adjacent layers of both oxide and metal to balance the stresses. There still remain some doubts about this interpretation of the evolution of the oxide

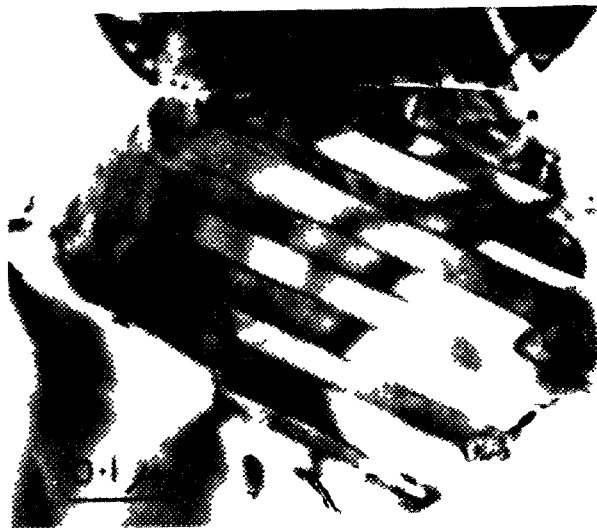
stresses. A crack or pore initiating at the surface (because this region has gone into tension) should penetrate only to the level where the net stress in the oxide is zero after redistribution of the stresses in the oxide. The mechanical argument cannot explain the deep penetration of the porosity revealed by the mercury porosimetry and the effects of step changes in oxygen and steam pressure during post-transition oxidation [90,91]. Impedance measurements in aqueous electrolytes give good indications of the presence of porosity but not of its closeness of approach to the metal/oxide interface because of the interposition of the double layer impedance between the electrolyte and the barrier oxide. Interpretation of the nature of the double layer inside very small pores is imperfect and the use of the whole specimen area, rather than the area of the pores, to interpret the impedance due to the porosity is probably incorrect. Much work is being done currently by impedance spectroscopy to try to improve the interpretation of impedances resulting from the pore structure [92-96].

The mechanisms by which the various defects form in the oxide are still generally unclear. The stress gradient through the oxide, that results from its formation exclusively by oxygen migration, should result in the surface layer eventually going into tension. On such an hypothesis, the outer layer would crack once it went into tension and the cracks would propagate to the position of zero stress in the oxide, but should not propagate to the oxide/metal interface (even after the stresses in the oxide are redistributed). The measured stresses on the oxide are considerably greater than the yield stress of the metal matrix so that stresses in the metal should not change this pattern significantly. Another hypothesis for generating small microcracks in the oxide derives from the observation that those monoclinic  $\text{ZrO}_2$  crystallites forming on the surface are just the restricted range of orientations that could be expected if the oxide were formed initially as cubic or tetragonal  $\text{ZrO}_2$  and transformed subsequently to monoclinic  $\text{ZrO}_2$  [53,97]. On this hypothesis the oxide film would be a form of partially stabilised zirconia (PSZ), with a significant percentage of tetragonal  $\text{ZrO}_2$  maintained by the high compressive stresses. As any given tetragonal crystallite moves out in the oxide (by formation of fresh oxide below it) this stress would decrease, and would eventually become too small to stabilize tetragonal  $\text{ZrO}_2$ . The crystallite would then undergo a martensitic transformation that can lead to a twinned structure and generate microcracks in commercial ceramics (Figure 4.39) [87]. Such cracks could then interlink to form the fine pores, or act as nuclei for grosser cracks. In this instance, although such microcracking should initiate at or near the oxide/environment interface it should progress to the point in the oxide where the compressive stress in the oxide equalled that necessary for the stability of tetragonal  $\text{ZrO}_2$ . This would predict much deeper cracking than the simple mechanical hypothesis, and would result in a barrier layer thickness dependent on the matrix strength (since the maximum stress achievable in the oxide is influenced by the creep strength of the substrate). If the stress decreases approximately linearly with distance through the oxide from the oxide/metal interface to the oxide/environment interface then, for a high strength alloy such as Zr-2.5%Nb, the position at which the tetragonal/monoclinic transformation of the  $\text{ZrO}_2$  occurred would be further from the oxide/metal interface in this instance than for an alloy with a weaker matrix. This could explain the thicker barrier layer in oxides on Zr-2.5%Nb than on the Zircalloys [98].

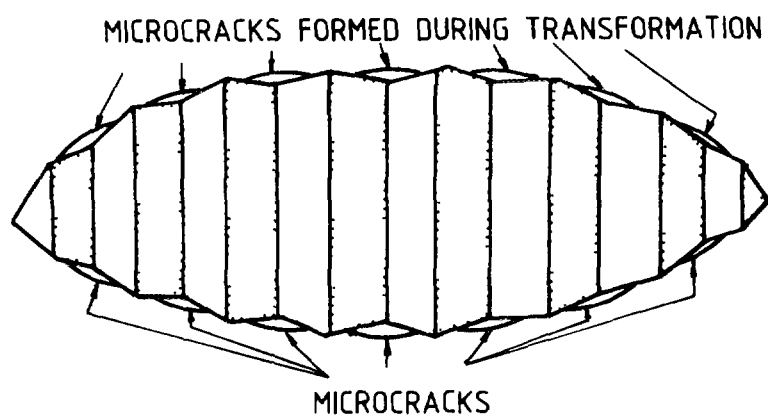
Recent work has been carried out to elucidate the stabilisation of tetragonal zirconia. Using Raman spectroscopy on tapered sections of the oxide layer, it was possible to analyse the content of the tetragonal phase in the oxide for different oxide thicknesses [57]. It was claimed that close to the metal oxide interface, the tetragonal content was high (in the range of 30-40%), and decreased sharply just at the transition. Using X-ray diffraction, lattice parameter measurements led to the conclusion that this transition is associated with a simultaneous relaxation of the compressive stresses in the zirconia. The proposed explanation for the transition is the fact that, as the oxide builds up, the matrix balances the compressive stresses induced by the oxide with tensile stresses in the metal up to a level where it relaxes by plastic deformation. This leads to a lower stress level in the oxide and thus helps the tetragonal phase to transform into monoclinic. The associated development of a fine porosity induced by the martensitic transformation leads to a change in boundary conditions. The external boundary is now defined by the locations of the roots of the pores. Other explanations could invoke the recrystallization of the zirconia induced during its thermal history. Indeed, in hot water, stabilised tetragonal zirconia transforms into the monoclinic form [99].



(a)



(b)



(c)

FIG. 4 39 Partially stabilized zirconia containing  $t$ -ZrO<sub>2</sub> particles, (b) Transformed ZrO<sub>2</sub> particle in Al<sub>2</sub>O<sub>3</sub>, (c) Mechanism of microcrack formation during twinning on transformation [87].

The degradation of the corrosion resistance of zirconium alloys in LiOH solutions is a special case of oxide breakdown where the mechanism is known to be different from the above. The accelerating effects of concentrated LiOH on the corrosion of the Zircalloys (Figure 4 40) have been known for many years [100-104]. It results in thick porous oxide films from an early period of corrosion. At very high lithium hydroxide concentrations, for example 0.5 molar (3,000 ppm Li) the pre-transition kinetic period disappears, and linear oxidation with the formation of porous oxides proceeds from the start of the experiment. At somewhat lower lithium hydroxide concentrations, approximately cubic pre-transition kinetics are exhibited with little evidence of an enhanced corrosion rate but with reduced times to transition (Figure 4 41). Below approximately 400 ppm Li for Zircaloy-4 and below 60 ppm for Zr-2.5%Nb, no effect on corrosion kinetics in the pre-transition region has been observed [104-106]. X-ray diffraction studies have sometimes indicated the presence of lithium zirconate in the oxide, but this is not universally accepted. Recent work [107] suggests that much of the Li<sup>+</sup> in the oxide is leachable, and that it is mainly contained within the interconnected porosity. TEM studies of the morphology of thick porous oxide films formed in LiOH have been reported [96,108] and show that they are much more porous than the normal post-transition oxides. Mechanisms that have been proposed to explain the lithium hydroxide enhancement effects are [73]

- 1 Incorporation of Li<sup>+</sup> in the lattice in place of a Zr<sup>4+</sup> ion (as in lithium zirconate) thus creating additional anion vacancies which increase the rate of oxygen diffusion
- 2 The lithium influences the recrystallization process leading to a higher grain boundary area and greater nucleation of pores and cracks in the oxide
- 3 Lithium increases the number of pores which penetrate the barrier layer by the preferential dissolution of inter-linked tetragonal or cubic sites in the lattice. The additional porosity then increases the corrosion rate by allowing the rapid transport of oxygen to the oxide/metal interface

Early ideas about the mechanism concentrated on incorporation of Li<sup>+</sup> in the oxide and its effect on diffusion controlled oxidation. However, this hypothesis is clearly wrong as effects on the pre-transition growth rate are minimal. Despite the absence of any apparent differences between corrosion weight gains in pH 7 and pH 10-12 (measured at room temperature) solutions at 300°C, studies of the polarisation curves (measured in fused salt at 300°C) of specimens oxidised in these LiOH solutions show differences (Figure 4 42). These results show that (at a point where the specimen weight gains were all essentially equal), the oxides formed in LiOH containing solutions were all much more electronically conducting than oxides formed in neutral water. Thus, lithium hydroxide can apparently affect the electrical properties of thin oxide films under conditions where no changes in the pre-transition corrosion kinetics were observed.

Most of the recent studies have concentrated on the mechanism for generating porosity and accelerating the post-transition corrosion. In one hypothesis [109] the dissolution of the ZrO<sub>2</sub> to form pores by the formation of Li<sub>2</sub>O from Zr-OLi groups was thought to be occurring, with reprecipitation of any zirconium oxide that was dissolved. In practice, an even simpler explanation seems to be the correct one, that t-ZrO<sub>2</sub> is preferentially soluble in concentrated high temperature LiOH solutions [73,110]. This process is capable of generating pores in otherwise pore-free oxides, and hence of rapidly initiating the transition to linear kinetics. At lower concentrations of LiOH ( $\leq 10^{-2}$  molar) only superficial pores can be formed by this dissolution, and an accelerating corrosion rate probably only ensues when deeper pores, that allow LiOH concentration, are formed by another process. As a result the pre-transition kinetics remain largely unaffected as long as the pores remain superficial, and effects are seen when the normal kinetic transition point is approached [110,111].

The nature of the redeposited oxide remains uncertain. It was initially thought that it might be largely amorphous if it formed by a precipitation process, however, an alternative possibility is that it might hydrothermally recrystallize on pre-existing crystallites [112]. In this situation, the "redeposited" ZrO<sub>2</sub> may form larger than normal crystallites. Such crystallites have been observed in

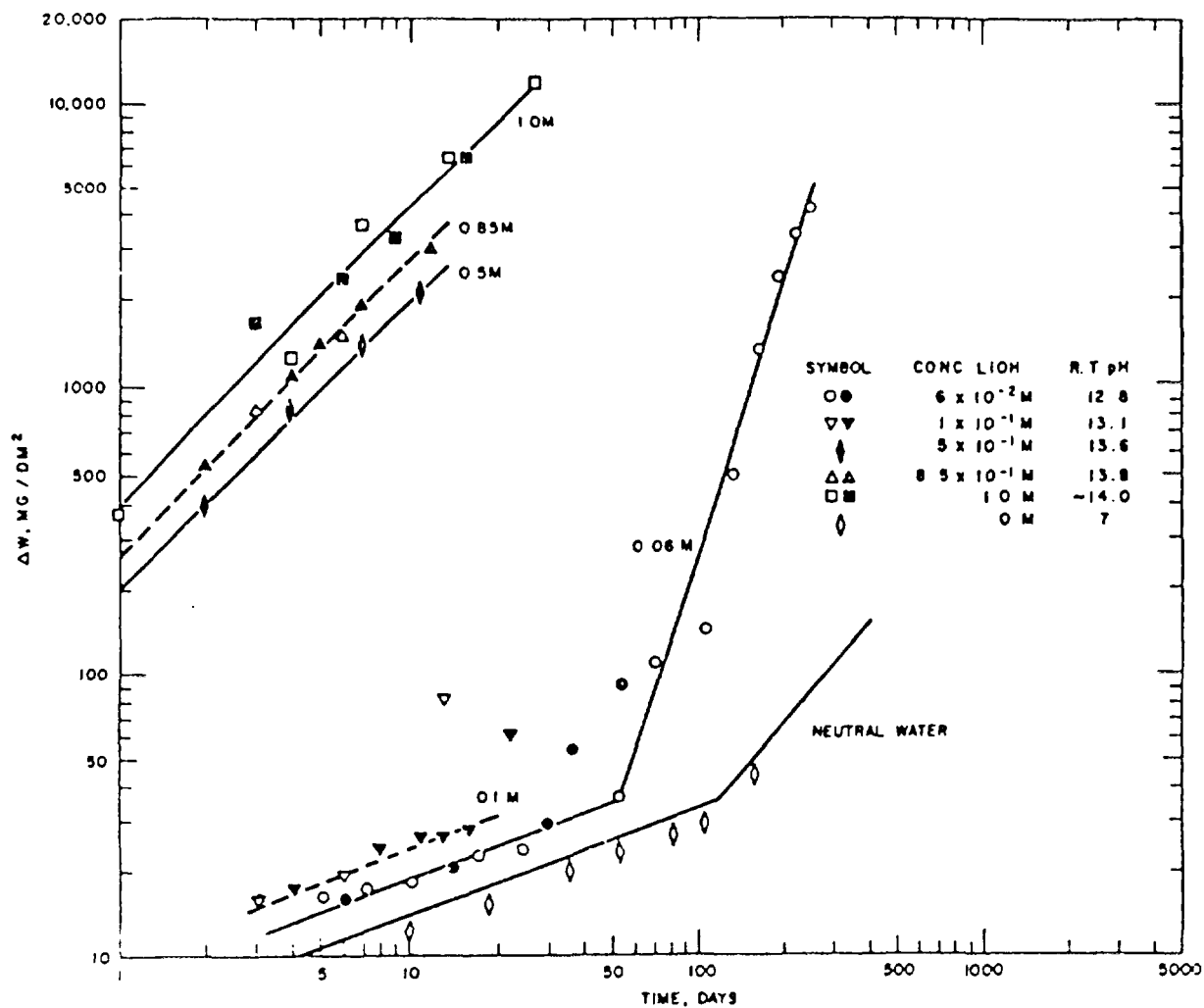


FIG. 4.40. Zircaloy weight gain in concentrated lithium hydroxide solutions (360°C in static autoclaves) [102].

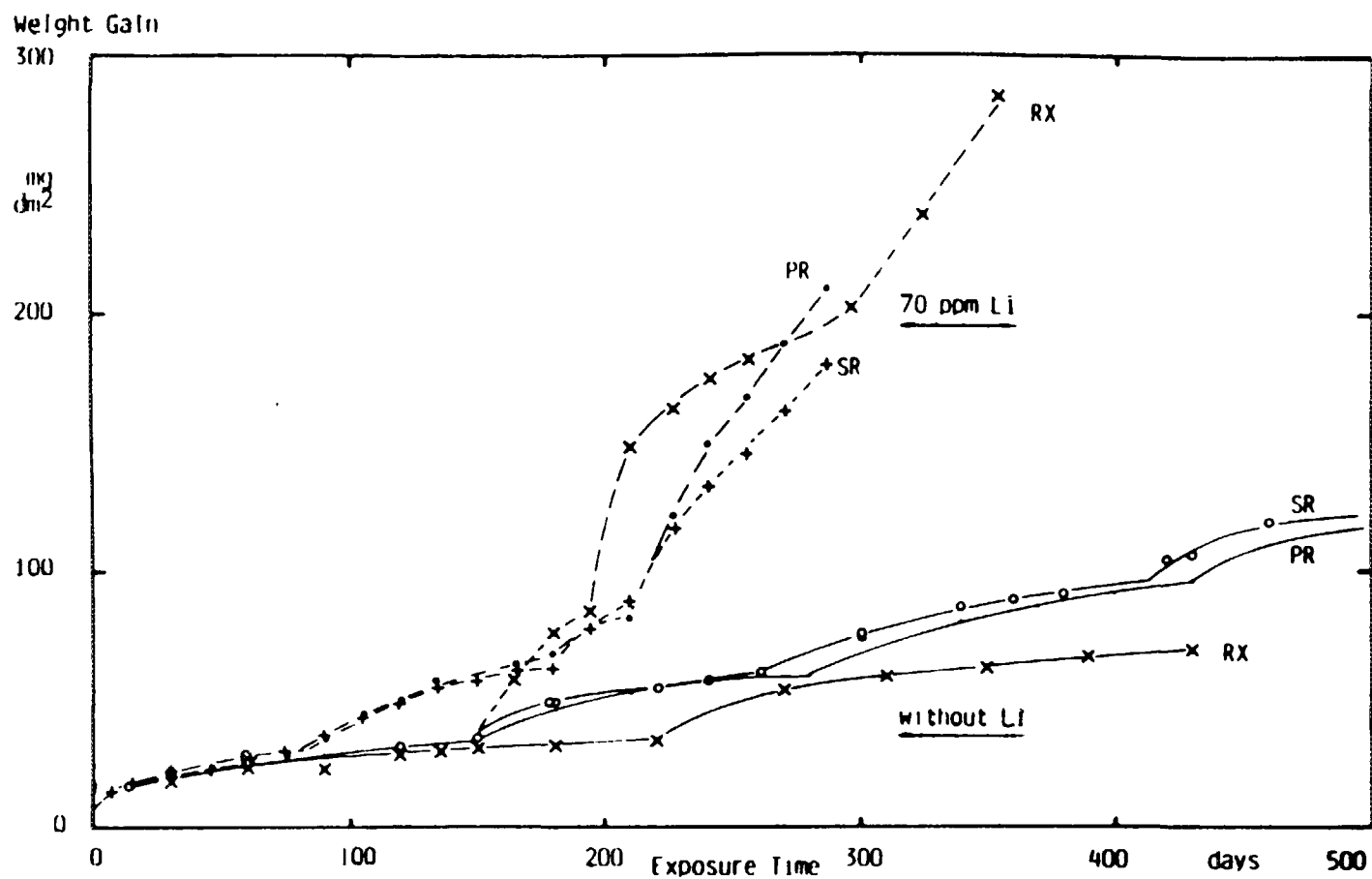


FIG. 4.41. Influence of LiOH on corrosion of Zircaloy in pressurised water at 350°C [125].



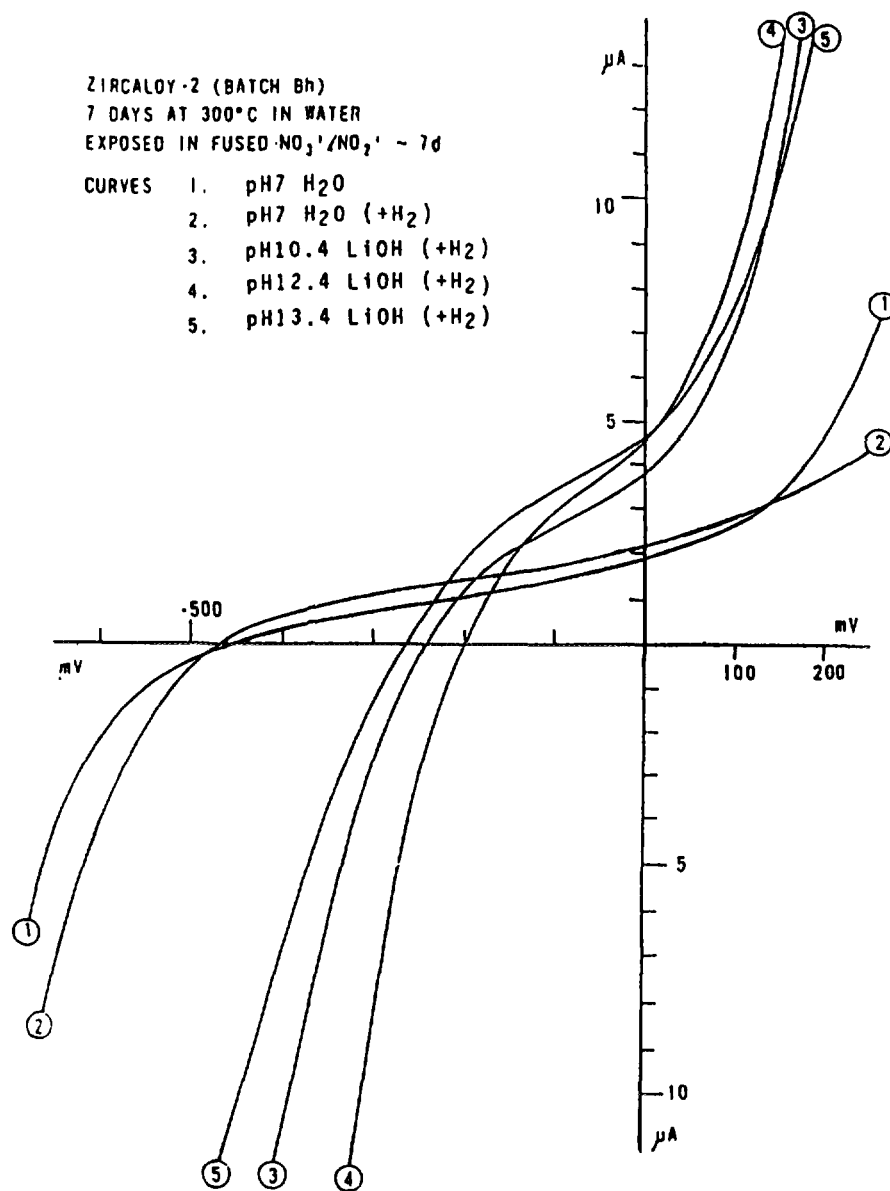


FIG. 4.42. Polarisation curves in fused salt at 300°C measured on oxide films formed in water or  $\text{LiOH}$  [505].

oxides formed in both out-reactor loops and in reactors operating with LiOH chemistry [113]. Studies have also shown that the beneficial effects of boric acid in mitigating effects of LiOH in concentrated solutions [114,115] arise from enhanced reprecipitation blocking porosity, rather than from any effect on the ZrO<sub>2</sub> dissolution process itself [110,111]. This dissolution and redeposition hypothesis raises questions about whether, under irradiation, disordered primary knock-on tracks in the oxide might be sites for easy dissolution even at low bulk LiOH concentrations [116-118].

A summary of some other recent publications in this area shows

- (i) Direct evidence supporting postulate 3 above has recently been produced, the creation of pores in pretransition oxides formed in water being observed after exposure to solutions containing high lithium hydroxide concentrations [73].
- (ii) Ding and Northwood [119] investigated the corrosion of Zr-2.5%Nb material in high lithium hydroxide concentrations. Preferential grain boundary attack by the lithium hydroxide was observed above a LiOH concentration of 1.2-4.8 g·litre<sup>-1</sup> (310-1,250 ppm Li). The authors talk about "destruction" of the barrier oxide film and formation of cracks and pores, but offer no explanation of how this happens.
- (iii) Ramasubramanian et al. [105,107] proposed postulate 2 as a result of observations of LiOH effects on the corrosion of Zr-2.5%Nb. Undissociated LiOH molecules were postulated to form Zr-OLi groups attached to the surface and these were thought to retard the normal recrystallization processes, thus maintaining a high grain boundary area through which oxygen diffuses or causing the generation of porosity.
- (iv) Recent work by Jeong, Ruhmann and Garzaroli [120] has also shown that the degree of corrosion enhancement is approximately inversely proportional to the ionic radius of alkali metal ions (Li, Na, K, Rb, Cs) although this appears to favour a solid state diffusion mechanism such as postulate 1, this is also the order of ZrO<sub>2</sub> solubility observed in hydrothermal exposures to LiOH, NaOH and KOH [112].
- (v) There is no evidence for Li<sup>+</sup> mobility in ZrO<sub>2</sub>, or that Li<sup>+</sup> is present in the oxide before effects of LiOH are seen when the LiOH concentration is changed [74].

#### 4.2.4 Mechanism of oxide breakdown in Zr-Nb alloys

In the case of the Zr-Nb alloys the kinetics of the rate transition do not necessarily follow the form observed for the Zircalloys. For instance, the Zr-2.5%Nb alloy often shows a traditional parabolic form of kinetics where no well defined increase in oxidation rate occurs (Figure 4.43) [121]. This is generally explained as the development of porosity from the start of oxidation, that ultimately reaches an equilibrium (linear rate) when the rate of development of porosity and of new barrier oxide become equal. This view is confirmed by porosimetry and impedance measurements that show similar (but perhaps a bit smaller) pore sizes than in the Zircalloys, with much thicker barrier oxide layers for Zr-2.5%Nb (Figure 4.38) [121]. The mechanisms for the formation of this porosity have not been elucidated in detail, but are thought to be basically similar to those described for the Zircalloys.

#### 4.2.5 Post-transition growth

Once the post-transition oxide film develops an equilibrium pore and crack structure, the oxidation rate becomes effectively linear. As has been pointed out, the cyclic nature of the kinetics after transition may represent cycles of formation of grosser cracks in the oxide. Since recent studies (unlike studies of early batches of Zircaloy) do not show evidence for such gross cracks at the oxide surface, it must be concluded that these cycles are initiated by some internal cracking process, such as that which leads to the presence of layering in the oxide. There is no unequivocal evidence to support a reformation of a thick barrier layer at any time during these cycles [63,85,88].

In-reactor, where a further increment of irradiation-induced creep and growth may be present [116], an additional factor may be present whereby creep of the substrate might induce cracking at or

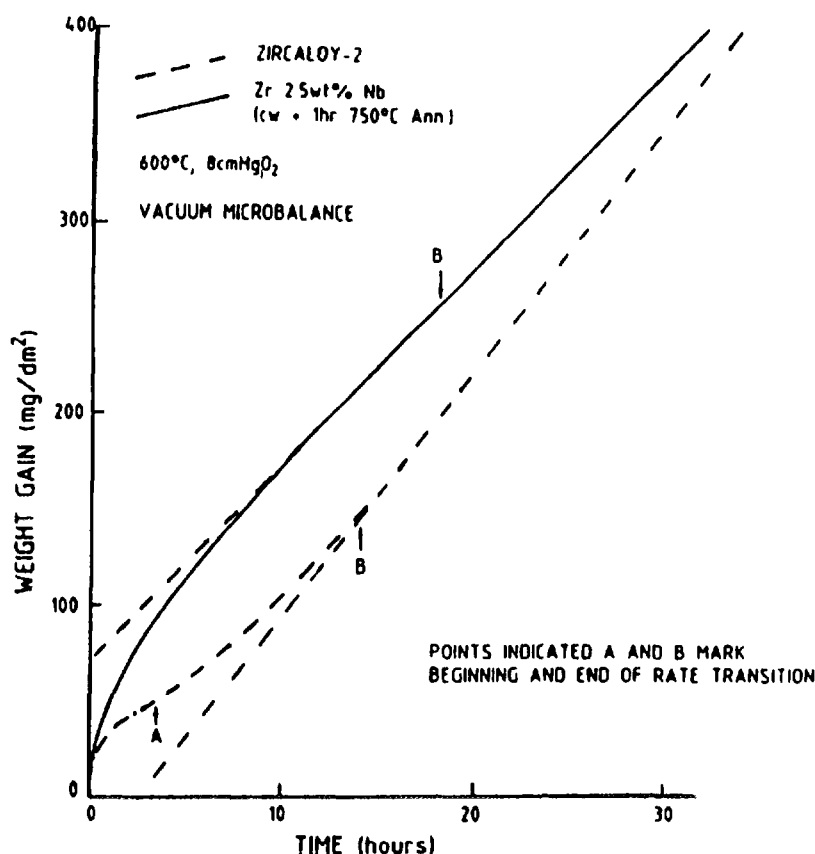


FIG. 4.43 Out-reactor corrosion of Zr-2.5%Nb (quenched from 880°C cold-worked and aged 6 hours at 500°C) and Zircaloy-2 in 360°C water [12]

near the oxide/metal interface. Such cracks would then propagate outwards until they reached the surface. Localised creep of the substrate may also occur at the oxide-metal interface during out-reactor corrosion as part of the processes that accommodate the volume change during oxide formation. If so, then a similar crack nucleation process could occur. However, tests performed under creep conditions in steam, at a relatively high temperature (400-500°C), suggested that the growing oxide could accommodate some deformation of the substrate (Figure 4.44) unless a critical creep rate was exceeded [122].

A distinction between these various hypotheses may be possible with a careful combination of electron microscopy and impedance techniques, although the relaxation of stresses during the preparation of TEM foils may induce cracks that were not there to begin with. In thick oxides cracks penetrating only to the approximate position of the neutral axis can often be seen metallographically, but are normally too few to explain the overall oxidation behaviour, although they do seem to cause regions of locally thick oxide. If small pores are developing from the interlinking of microcracks produced by either of the other two hypotheses, then a distinction might be made if we could establish whether pores start to develop at the oxide/environment interface or the oxide/metal interface. Impedance spectroscopy techniques using a variety of contacts on the outer surface (including immersion techniques) and analysis of the frequency spectrum may be able to resolve this, even if the pores cannot be seen in electron microscope replicas, however, the present

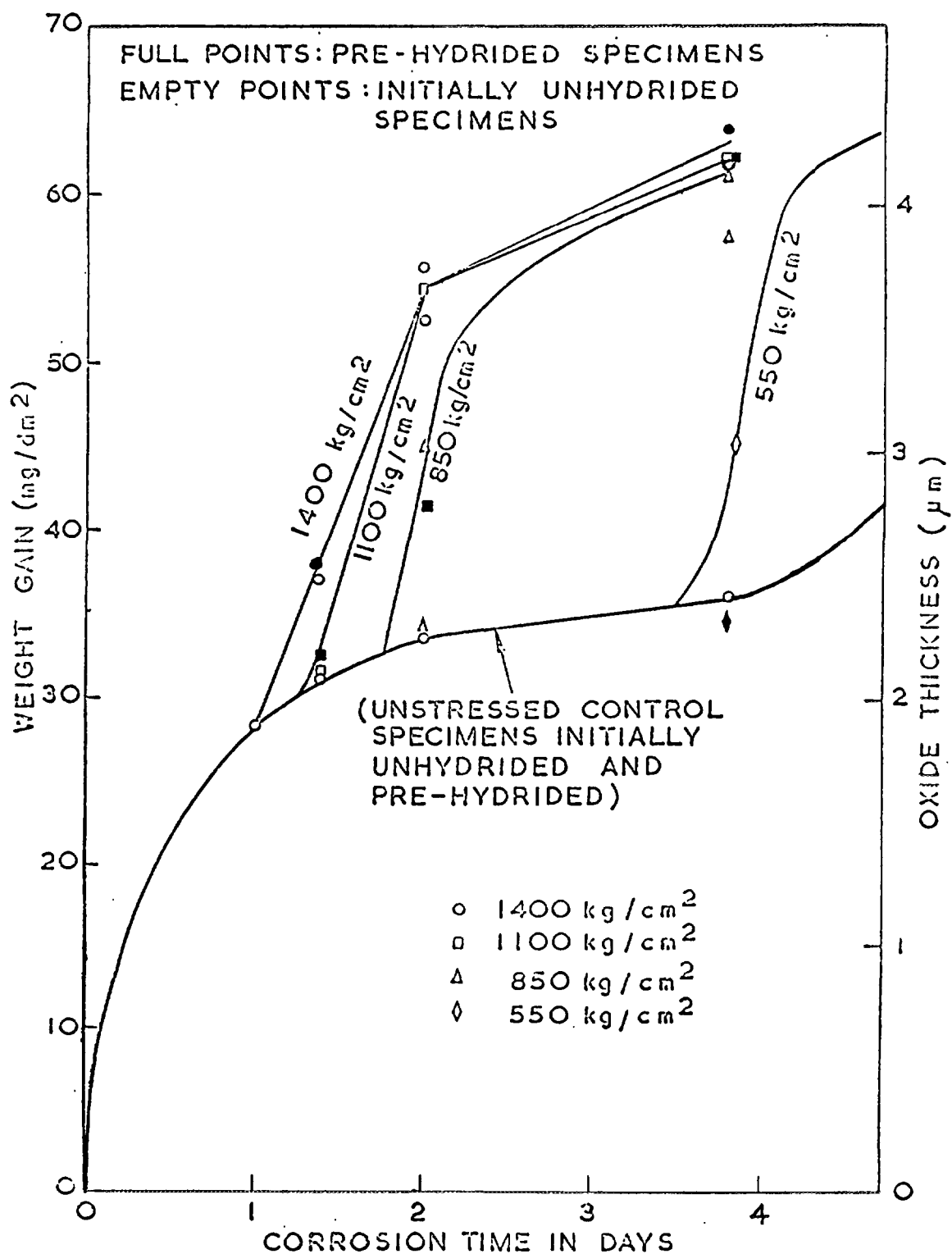


FIG. 4.44. Effect of applied stress on the extent of corrosion of Zircaloy-2 in atmospheric pressure steam at 475°C [122].

state of development of the interpretation of such data does not yet allow firm conclusions to be reached. Such measurements in bulk PSZ claim to be able to distinguish bulk from grain boundary diffusion (for example) [123]. In high temperature water the potential for dissolution processes to enlarge these pores, or to cause them in the first place (as seems to occur in concentrated LiOH solutions) must also be considered [107], especially as under heat flux conditions the elevation of the boiling point by LiOH will ensure the presence of more concentrated solutions within porous oxide films than the concentration within the water [63].

Concentrated LiOH solutions affect corrosion rates in the post-transition region more than in the pre-transition region. For example, Figure 4.45 shows enhancement of Zircaloy corrosion above approximately 30 ppm Li [124]. Several authors [e.g. 104,124] conclude that the increase in corrosion appears to be associated with a non-leachable lithium content in the oxide when this exceeds approximately 100 ppm. However, whether this is a cause of the phenomenon, or an effect of redeposition from concentrated LiOH solutions remains to be established.

More recently, autoclave experiments have shown dramatic effects in ameliorating, or inhibiting, the lithium hydroxide enhancement when boric acid is present at a boron concentration of greater than 50-200 ppm [114,115,125-127]. For example, the data in Figure 4.46 for exposures to 220 ppm lithium solutions yield an enhancement in the post-transition corrosion rate by a factor of approximately 18 in the absence of boric acid but by only a factor of approximately 1.2 in the presence of boric acid ( $B > 50$  ppm) [114,115]. It was also found that the inhibition by boric acid of lithium-enhanced corrosion was associated with a reduced concentration of lithium incorporated in the oxide. One theory postulated to explain the inhibiting effect is the removal of surface  $-OLi$  groups by reaction with non-ionised boric acid molecules [105]. The above discussion was restricted to autoclave measurements. Further information on lithium hydroxide effects in non-isothermal laboratory loops is given in section 6.4 and some assessments of lithium hydroxide effects on fuel cladding corrosion are briefly reviewed in section 7.3.

Mechanistic studies have been carried out to establish how the local dissolution of  $ZrO_2$  in LiOH is modified in the presence of  $H_3BO_3$  and have led to some unexpected results [110]. It was found that the addition of  $H_3BO_3$  (1,000 ppm B) to 0.1 molar LiOH solutions had no apparent effect on the local dissolution of oxide films preformed in 300°C water. The pores grew with an apparently identical frequency and depth to those observed in boric acid free 0.1M LiOH [110]. Similarly, no effect of boric acid additions was seen during the regrowth of the barrier oxide film after a transient exposure to 1.0 molar LiOH. Only when boric acid was present in high concentrations (8,000 ppm B) during a transient exposure to 1.0 molar LiOH did it inhibit the development of through-thickness pores in the oxide film. Under these conditions the oxidation transient that would have ensued was eliminated (Figure 4.47). Thus boric acid seems to be incapable of influencing the dissolution of  $ZrO_2$  to form pores in oxide films, but will apparently enhance reprecipitation to plug deep pores and thus prevent the approach of porosity up to the oxide/metal interface. At present, the evidence is insufficient to distinguish between a mechanism whereby the boric acid addition changes the chemistry at the bottom of a pore so that the solubility of the  $ZrO_2$  is reduced, from a mechanism whereby the  $ZrO_2$  still dissolved at the bottom of the pore but is reprecipitated immediately in the presence of boric acid to form a precipitate which effectively plugs the pore tightly enough to prevent easy diffusion of oxidising species. These two mechanisms should be distinguishable by careful TEM studies of such oxide films. Since the dissolution of  $ZrO_2$  films appears to occur even in low LiOH solutions ( $10^{-4}$  molar PHWR chemistry) under irradiation [128], a new model for in-reactor oxidation of zirconium alloys has been proposed that is based on the dissolution of primary knock-on damage spikes in all high temperature water conditions [117,118]. The only effect of changes in LiOH concentration would then be in the rate of dissolution of the damage spikes in the oxide.

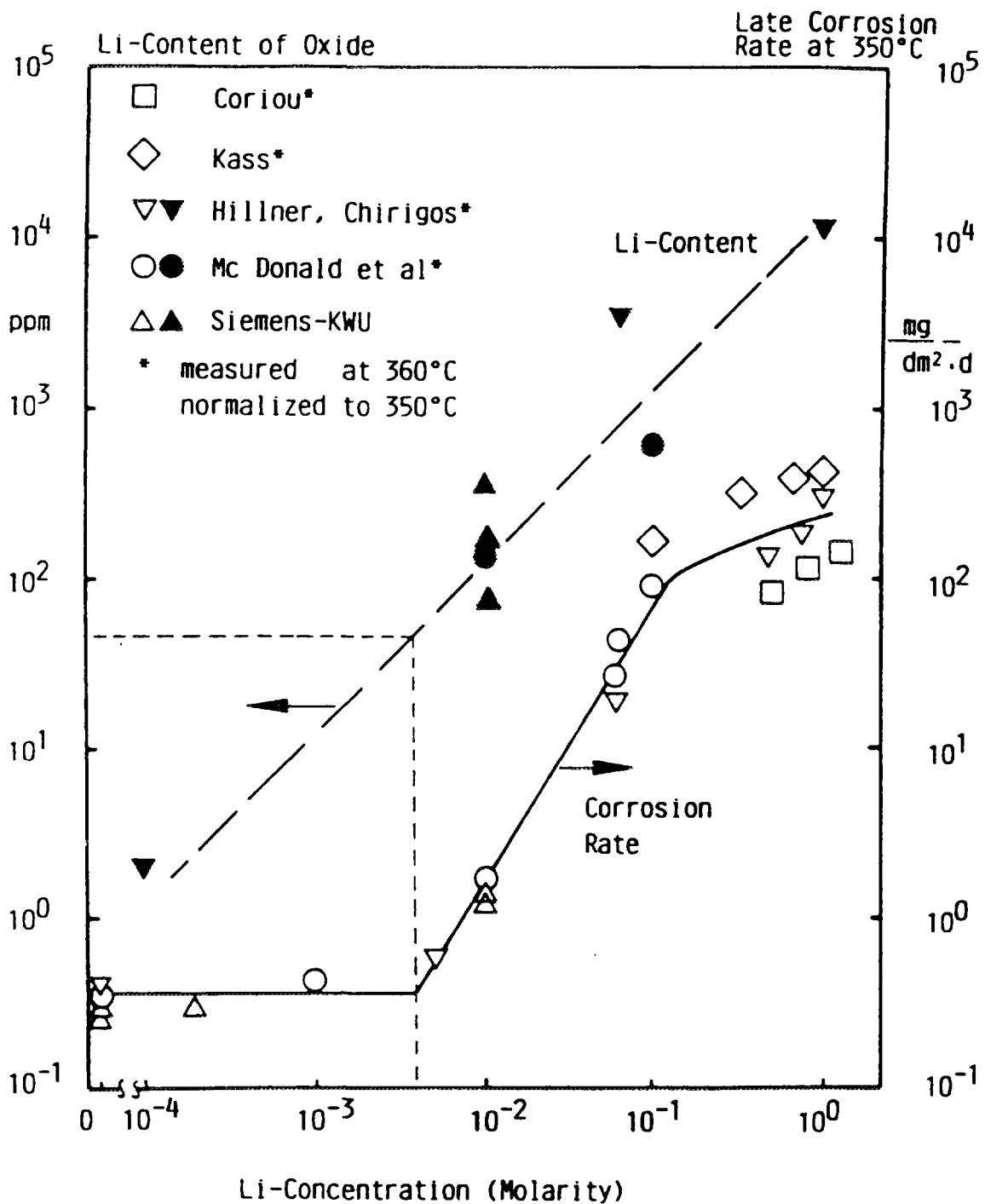


FIG. 4.45. Effect of LiOH on corrosion of Zircaloy at 350°C, and the Li content in the grown oxide layer [125]. References in this are given in the original paper [125].

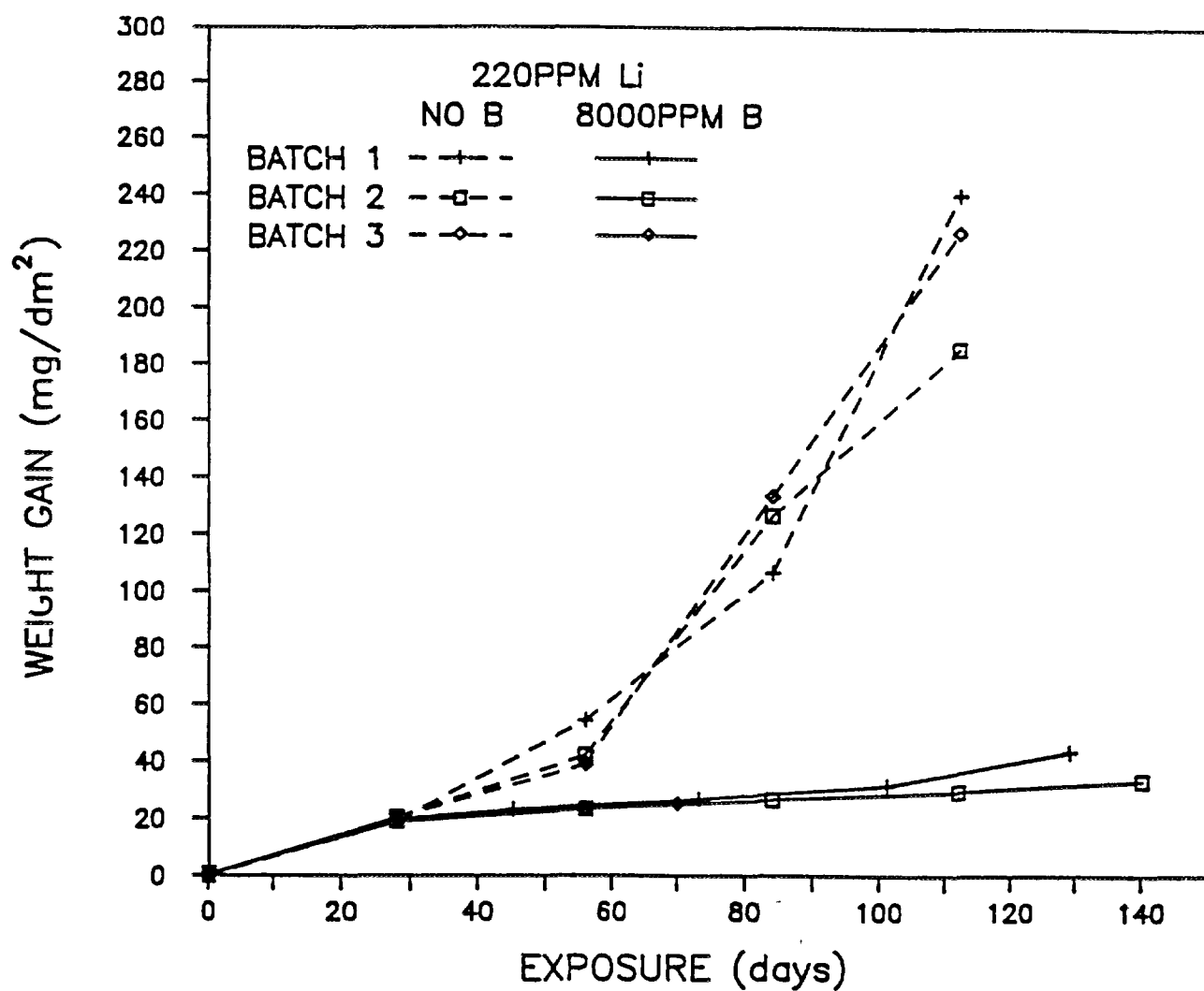


FIG. 4.46. Effect of boron on corrosion of Zircaloy-4 in a concentrated LiOH solution [114].

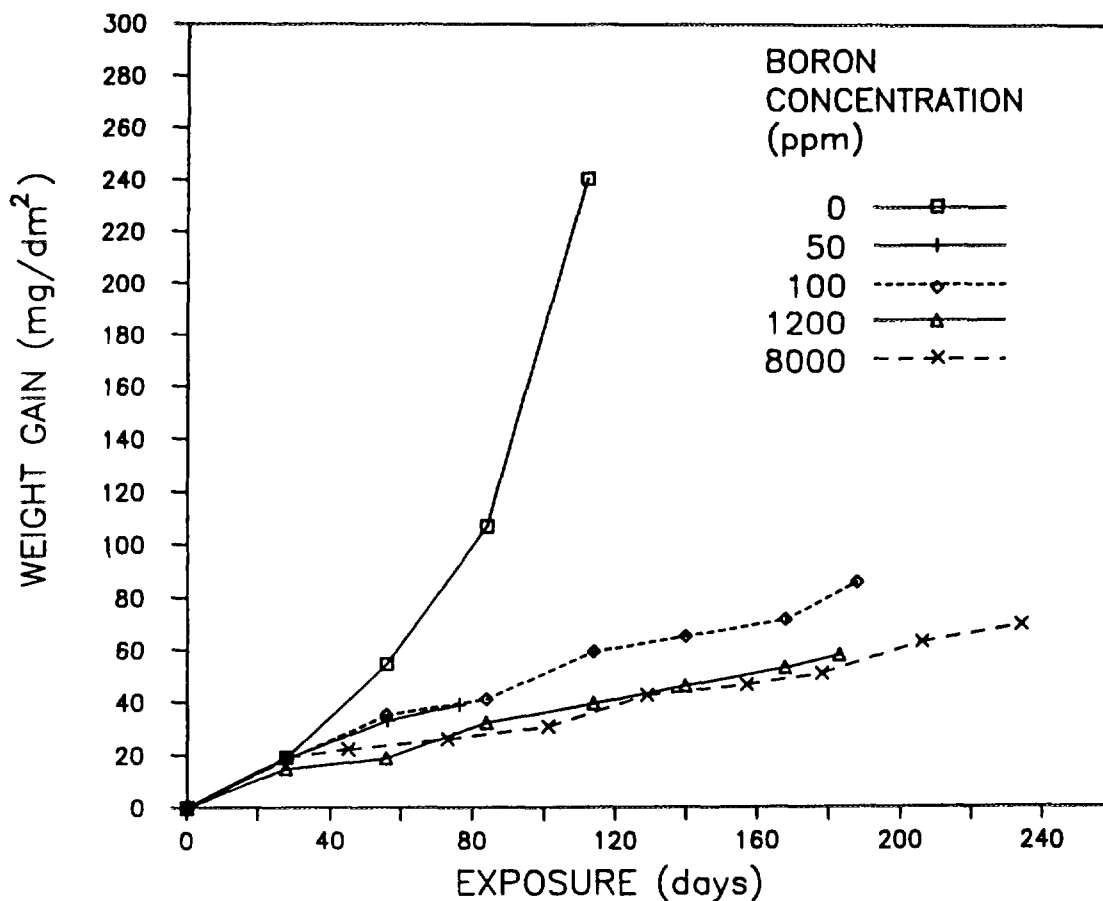


FIG 4 47 Behaviour of Batch 1 clad in simulated hideout environments containing 220 ppm of lithium and boron additions in the range 0 to 8,000 ppm [114]

#### 4 3 NON-UNIFORM (NODULAR) OXIDE FORMATION

This phenomenon is particularly relevant to nodular corrosion under BWR water chemistry conditions. Unfortunately no out-reactor simulation of this has yet been achieved in high temperature water in the laboratory, although many causes of white-oxide-spot formation have been investigated in the past [86]. These can be summarized as

- Formation at carbide particles;
- Formation at large intermetallics,
- Formation at gas-void stringers,
- Formation with impurities (e.g. F, Cu, etc.) in the water,
- Formation at hydrides

None of these seems to be capable of explaining the BWR observations. However, nodule formation in 500°C high pressure steam seems capable of giving good correlations with observed material lot variability in-reactor [129]. Variations on the 500°C steam test in the form of either a dual temperature test (simulating preoxidation) [130] or a higher temperature 520°C test (claimed to give better discrimination of batches) [131] are now being recommended. Whatever the precise test conditions used,  $\beta$ - or ( $\alpha + \beta$ )-quenched material gives the best resistance in the high temperature test, and also in-reactor (see section 6 2)



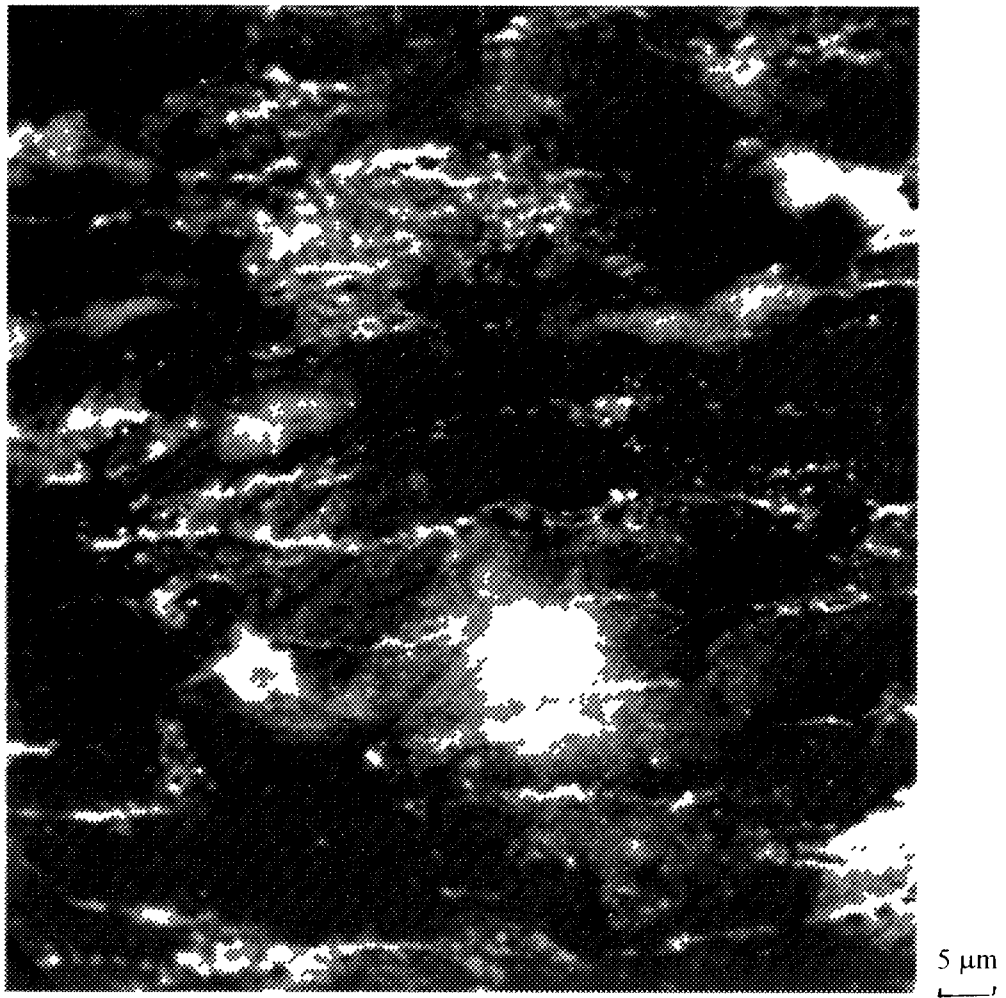
Despite this there are clearly aspects of the in-reactor behaviour that are not normally present in the steam test (e.g. electrochemical and galvanic effects), so one is left wondering how close is the scientific comparability of the two phenomena. The experiments of Urquhart and Vermilyea in 500°C steam with applied potentials [30] suggest the importance of such effects but do not necessarily cause the same phenomenon since the currents were not limited in these tests. Thus, local ohmic heating (such as causes the breakdown of anodic oxide films) cannot be eliminated as a possible cause of their observations.

#### 4. 3. 1. Nodular oxide formation

There is not much definite knowledge of the mechanism of nodular oxide formation in 500°C steam. The work that has been done suffers from a number of limitations. Thus, virtually all of the experimentation that purports to demonstrate that nodules initiate in precipitate free areas of surface has been performed on samples heat treated to generate very large grains, and to displace virtually all the intermetallics to the grain boundaries [132-134]. Such material would, of course, not have passed the standard 400°C steam test, and would have shown white oxide spots (nodules) after prolonged corrosion in 400°C steam. The rest of the work has been done on non-Zircaloy materials (e.g. unalloyed zirconium) that are relatively intermetallic free, and that are also traditionally expected to fail a 400°C steam test and develop white oxide "spots". An example of such effects can be seen in the laser glazing studies of Sabol et al. [135], where depletion of the alloying elements in the surface degraded the corrosion resistance. Thus, use of this evidence requires us to accept that all nodules will form away from intermetallics because it has long been known that some poorly heat treated materials nucleate nodules at such locations. In support of this the work of Demars, Givord and Armand is often quoted [136]. However, only one of their heat treatments (an  $\alpha + \beta$  treatment with no further  $\alpha$  anneal) gave nodules that formed within the grains. After even short low temperature anneals the white spots were located at the sites of the heavily segregated intermetallics. Figure 4.48 gives an example of such nucleation of white spots at an early stage of growth. These would develop with prolonged exposure in 400°C steam (or 300°C water) but would not give a highly regular nodule outline even after long exposures.

Similarly, the work that claims to show hydride precipitation at the metal-oxide interface as the cause of nodule nucleation suffers from severe problems [137]. At the experimental temperature none of the specimens appears to contain enough hydrogen for the solubility to have been exceeded. Thus, the evidence for clusters of local hydride precipitates after quenching such specimens from 500°C appears more probably to be a result of the local rapid ingress of hydrogen following nodule nucleation, rather than a cause of it. In support of this, evidence that a critical hydrogen ingress rate must be exceeded locally before solid hydride layers can be formed near the oxide/metal interface can be found in the literature (Figure 4.49). The generally more severe nodular corrosion of Zircaloy-4 compared with Zircaloy-2, despite the lower hydrogen uptake rates of Zircaloy-4 directly contradicts such a mechanism. A further difficulty that confronts the hypothesis that nodules nucleate at interfacial hydrides is the observation that, during high temperature oxidation ( $\geq 500^\circ$ ) in the Zircaloys, hydrogen and hydrides are effectively excluded from a thin layer at the oxide/metal interface where high concentrations of dissolved oxygen result from diffusion of this species into the metal (Figure 4.50) [138,139].

Another hypothesis [140] explains nodular corrosion as a result of subsurface intermetallics that become embedded in the pre-transition oxide. There, it is argued they represent cathodic sites that can lead to the formation of gaseous hydrogen within the barrier oxide, thus disrupting the oxide and initiating the formation of a nodule. It is not clear that the arguments for why such an hypothesis should be dependent on oxygen in the water are valid, and thus the results should not be a function of the reactor water chemistry. Nevertheless, the implication of hydrogen in the process cannot be dismissed, as nodular oxidation does not occur in high pressure oxygen at 500°C. It may be that hydrogen liberated within the oxide at buried intermetallic particles is the critical factor as suggested by several authors [141,142]. However, we should be careful not to fall into the same errors that have



*FIG 4 48 Local white-oxide formation along intermetallic stringers in Zircaloy-2 after 14 days, 400°C steam test (2000×)*

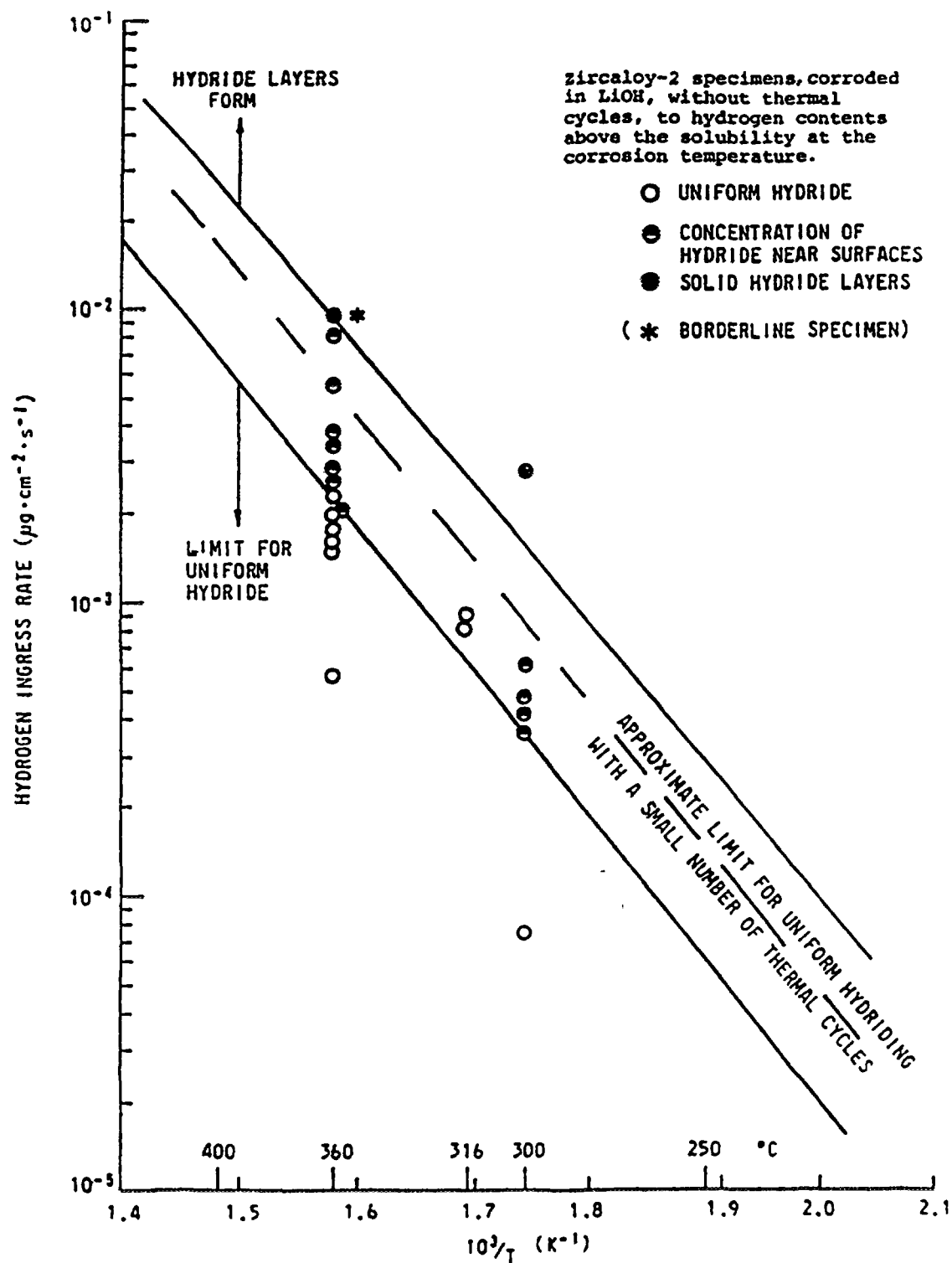


FIG. 4.49. Critical hydrogen fluxes for surface hydride layer formation [227].



*FIG 4 50 Redistribution of tritium at the oxide-metal interface (portion of the oxidized sample annealed in argon at 800°C for 2 hours, air cooled) Note the absence of tritium in the metal zone adjacent to the oxide due to the high dissolved oxygen level there and tritium enrichment in the next metal zone with a low oxygen content [139]*

beset mechanistic studies of effects of LiOH (i.e. arguing about whether the effect was a result of  $[Li]$  or  $[OH]$  when it is a property of LiOH aq.) In this instance, we should avoid blaming the effect on hydrogen when it may be the result of some property of the high temperature high-pressure steam itself

#### 4 3 2 Mechanism of nodule formation

The studies in 500°C steam have concentrated on the variables associated with the metallurgical structure of the cladding. However, although this variability between cladding batches is one of the obvious features of the in-reactor phenomenon, as is shown by the dependence of nodular corrosion on second phase precipitate size and distribution [143], there are clearly other factors that control the incidence of nodule formation. The same batches of cladding can behave quite differently in different reactors. The other factors that may be important in BWRs are as follows

##### 4 3 2 1 Galvanic effects

These result from contact with or proximity to stainless steels or nickel alloys. This effect was shown most clearly in SGHWR with the mixed-grid experiment in which alternate grids at the bottom of a fuel bundle were either Zircaloy or stainless steel [144]. Nodular corrosion occurred predominantly at the stainless steel grids, and was distributed symmetrically about them, whereas the small numbers of nodules seen at Zircaloy grids were generally downstream of the grids. The effect is also evident in examples of control blade handle "shadows" appearing on the adjacent fuel channel [145], and the common observation of spots of thick oxide around points of contact of the cladding with Inconel springs in an otherwise Zircaloy grid. A further manifestation of this phenomenon is the evidence for ridges of thick oxide on the SGHWR Zircaloy-2 pressure tubes adjacent to the stainless steel grids on the fuel bundles [146], and the like observation on the Zr-2 5%Nb pressure tubes in RBMK reactors [147]. Lemaignan and others have blamed all these "shadow" effects on proximity to elements giving

high  $\beta^-$  ray emissions in-reactor (see section 8. 2. 4.). These effects may still mechanistically be electrochemical, however, if the  $\beta^-$  irradiation serves to enhance the local water and  $\text{ZrO}_2$  conductivities and hence increase electrochemical currents that can flow locally. The protection of a precipitate free Zr-1.5%Sn alloy from accelerated corrosion in 350°C water by welding a single large piece of  $\text{Zr(Fe/Cr)}_2$  intermetallic to one end of the sample is probably a further example of electrochemistry at work in the oxidation of zirconium alloys [148].

#### 4. 3. 2. 2. Effects of impurities

Effects of impurities such as copper in the reactor water are shown by the evidence that copper in the water is one of the primary factors leading to CILC failures (Crud Induced Localised Corrosion, an advanced form of nodular corrosion) [149,150], and by the general reduction in the frequency of nodules on otherwise similar batches of cladding when the copper alloy condenser tubes in a reactor are replaced by titanium tubes. In the grosser forms of nodular attack (CILC failures) it is evident that other factors are important as well. The Ca, Mg and Si content of the water may be critical in forming the hard impervious crud layers that are thought to participate in CILC failures. This aspect of the problem was certainly thought to be critical in the early life CILC failures in SGHWR [149]. The presence of a hard, free-standing crud layer that can support a steam-filled crack between it and the oxide; or the formation of such steam-filled cracks within the oxide are essential to the final failure stages. Measurements of the thermal conductivity of high Cu crud [149] showed that it was higher than that of  $\text{ZrO}_2$ , and so, unless such layers are excessively thick, the temperature rise across them (in the absence of a steam-filled crack in the system) will be insufficient to cause the high temperatures at the  $\text{Zr/ZrO}_2$  interface that are needed to get the high corrosion rates and hydrogen migration that are observed.

#### 4. 3. 2. 3. Effects of radiolytic species

Effects of radiolytic species in the water are clearly important since the phenomenon of nodular corrosion is not evident in reactors without the presence of dissolved oxygen in the water [151], and has not been reproduced in the laboratory in highly conducting electrolytes by any form of electrochemical polarisation attempted so far [31]. This may arise from oxygen added with the feedwater or more usually from radiolytic production. The presence of boiling in the system is important only to the extent that it causes partitioning of the radiolytic species (e.g. oxygen and hydrogen) into the steam phase, and thus changes the concentrations in the water phase. The direct reaction of radiolytic species with the metal surface is unable to account for the oxidation rates observed unless unreasonably long diffusion distances, and hence long lifetimes for the species are assumed. Thus, the actual quantities of radiolytic species produced are thought to be less important than shifts in the equivalent redox potential of the irradiated water, and hence in the surface electrochemical potential of the Zircaloy that results during irradiation. However, the computation of radiolytic species concentration in porous media has still to be performed.

#### 4. 3. 2. 4. The local power and flux spectrum

The local power and flux spectrum appear also to be important, as the differences reported between Gd-rods and  $\text{UO}_2$ -rods [150] cannot be understood on the basis of local power or flux, since the Gd-rods are operating at lower power than the  $\text{UO}_2$ -rods in the critical early irradiation period when nodules are initiating. It has been argued, however, that  $\beta^-$  emissions by the Gd rods resulting from electron/positron pair production by capture gammas are the cause of these differences. There are also other differences in the radiation spectrum seen by the cladding on Gd-rods compared with  $\text{UO}_2$ -rods. This may be an important aspect of the difference, since a fuel pin can be likened to a large self-powered flux detector, and the net flux of charged particles from the zirconium oxide into the water will represent a polarisation current that can change the local surface potential of the cladding. Calculations of the magnitudes of these currents (see Chapter 6 and reference [456]), however, suggest that they are too small to be the cause of these effects. This makes it difficult to explain the

differences seen between nodular corrosion over plena (e.g. those in the high flux regions of segmented rods) and the lower nodular coverage seen on adjacent fuelled regions [150]. The absence of a direct correlation with either local power or heat flux is illustrated further by the common observation that nodular corrosion is often more severe on the unfuelled Zircaloy-4 channels than on the fuel cladding contained in them, although in this instance material differences must be regarded as a significant part of the overall effect.

#### 4. 3. 3. **Simulating nodular corrosion in high temperature water**

In-reactor the important factors in the extent of nodular corrosion for a given metallurgical condition of the alloy include the following:

- Fast neutron irradiation;
- The radiolysis of the water and stripping of  $H_2$  and  $O_2$  into the steam phase during boiling to leave an excess of  $O_2$  that originates primarily in the feedwater. Radiation effects in the downcomer introduce important differences from plant to plant [151];
- The presence of specific impurities in the water (e.g. Cu);
- The influence of galvanic contacts, local  $\beta^-$  irradiation effects or electrochemical currents arising from proximity to stainless steel or Inconel;
- Modifications of the redox potential of the system, such as results from adding  $H_2$  to the water;
- Increased conductivity of oxide and water resulting from local  $\beta^-$  fluxes.

While not all of these factors could be effectively simulated in the laboratory (e.g. fast neutrons), many could be. No attempt is known of autoclave testing in which the  $H_2/O_2$  ratio in the water, the polarization of the specimen, and the presence of reducible species such as  $Cu^{+}$  were used as independent variables. It is interesting to note that for Zr-1%Nb alloy cladding it appears possible to obtain apparently nodular corrosion in an out-reactor loop in the presence of added oxygen. The sensitivity of Zr-Nb alloys to the presence of  $O_2$  in the water is well known.

At present we seem to be no nearer to an understanding of the precise micromechanisms leading to nodular corrosion. Metallurgical processing of the cladding to give careful control of the intermetallic precipitate size has done much to mitigate if not to completely eliminate the phenomenon, and as a result funding for further mechanistic studies has declined. Nevertheless, a recent paper suggesting that Si in the precipitates may be important in nodule nucleation, indicates that it may not be so much the actual precipitate size, but what else is in it other than Zr, Fe, Cr or Ni that may be the critical factor [152].

## 5. HYDROGEN ABSORPTION

Zirconium alloys absorb hydrogen as a consequence of the corrosion reaction with water, as well as by other mechanisms which may be observed in defected fuel and where contact with dissimilar metals occurs. Hydrogen has very limited solubility in zirconium alloys, this being less than 1 ppm(wt) at room temperature, about 80 ppm at 300°C and about 200 ppm at 400°C. Whenever the solubility is exceeded a zirconium hydride phase will be precipitated, and as this phase is brittle it can have an impact on the mechanical properties of the alloy. The extent to which this embrittlement of the alloy occurs depends on the volume fraction of hydride present, its orientation within the alloy (and with respect to the principal stress direction) and the degree of interconnectedness of the hydride platelets. Hydrogen redistributes easily at elevated temperatures migrating down a temperature or concentration gradient and up a stress gradient (again provided the solubility is exceeded). The concern about hydrogen uptake is related to concern about the potential embrittlement of the zirconium alloy component and the ability to predict when this might occur. The worst embrittlement occurs at low temperatures when hydrides are oriented normal to the principal stress (usually a hoop stress in tubing). The next most serious situation arises when the terminal solid solubility TSS is exceeded in a component such as a pressure tube that is highly stressed for long periods of time potentially leading to delayed hydride cracking (DHC) failures. Fuel cladding, because it operates under heat flux, can tolerate high average hydrogen contents (600-1,000 ppm or more) without significant embrittlement at operating temperature because the temperature gradient concentrates the hydrides in the outer layers of the cladding, leaving most of the wall thickness free of precipitated hydrides at the operating temperature. Without precipitated hydrides there can be no embrittlement.

There are still many unknown factors in the mechanisms of hydrogen absorption by zirconium alloys. Not least of these is the shortage of good values for the diffusion of hydrogen either in the ZrO<sub>2</sub> lattice or in crystallite boundaries. Since early experiments purporting to measure these usually turned out to be studies of the breakdown of the oxide, one might expect our knowledge of this breakdown process to be more complete. However, because the fact that oxide breakdown was occurring was ignored, and because of the difficulties in characterising these breakdowns, we actually know no more about breakdown processes than we do about diffusion in coherent oxide films.

Zirconium alloys are normally protected against hydrogen ingress by the surface oxide film, which presents a good barrier both to hydrogen ingress, and to the egress of hydrogen already in the metal. However, laboratory work has shown that, at room temperature under conditions of straining at a notch, this oxide film offers little protection, and zirconium alloys are susceptible to rapid cracking (up to 10<sup>-5</sup> m/s) in gaseous hydrogen [153,154]. These experiments revealed only small differences in the crack velocities of the same alloys which show surprisingly large differences in crack velocity under DHC conditions, where the cracking results only from internal hydrogen [155]. Thus, the protective status of the surface oxide film, and presence or absence of cracks or pores passing through it to the metal/oxide interface are key factors in determining the extent of hydrogen uptake.

### 5.1 HYDROGEN ABSORPTION MECHANISM

There are four essentially different mechanisms by which the hydrogen content of an already fabricated zirconium alloy component can be increased. These are -

- (i) Absorption during the normal corrosion processes that occur in high temperature aqueous solutions. Hydrogen pickup fraction is defined as the ratio of hydrogen entering the metal to that released by the corrosion reaction during the same period.
- (ii) By direct reaction of a clean (no species other than zirconium) surface with gaseous hydrogen.
- (iii) By diffusion of hydrogen through a metallic bond with a dissimilar metal in which hydrogen has a higher activity.
- (iv) By cathodic polarisation of zirconium in an electrolyte.

All four of these mechanisms have been observed in appropriate circumstances in nuclear reactors. The first is always with us whenever zirconium alloys are exposed in high temperature water, and attempts to reduce the hydrogen ingress rate by this mechanism were one of the driving forces during the development of the Zircalloys [51]. Absorption of gaseous deuterium from the annulus gas of a CANDU reactor into the outside of the pressure tubes was a contributing factor in the failure of the Pickering-2-G16 pressure tube [156]. Diffusion of deuterium from the end-fitting steel, through the metallic contacts at the rolled joints, into CANDU pressure tubes was first noticed during the investigations of the early DHC cracking of Zr-Nb pressure tubes in Pickering-3 and 4 [157], and the accumulation and migration of this hydride have been monitored ever since. Although observed experimentally at elevated temperatures, cathodic hydriding of zirconium alloys in water has only been observed in low temperature reactors [128].

#### 5. 1. 1. Hydrogen uptake during corrosion

Direct reaction of gaseous hydrogen with the zirconium at the bottoms of pores is not a possible route for hydrogen ingress during pre-transition oxidation because there will always be at least a thin barrier layer of oxide at the oxide/metal interface. When oxide films become porous, in the post-transition region of oxidation kinetics, the pores which develop may penetrate momentarily up to the oxide/metal interface, as is indicated by the effects of instantaneous pressure changes on the instantaneous oxidation rate in both oxygen and steam [90,91]. However, there will always be enough oxidant available to produce at least a thin barrier layer at the bottom of the pore very quickly and, in general, it is thought that ingress of hydrogen during any brief periods when bare metal is accessible at the bottom of a pore or crack will be negligible. Even when the protective oxide is thin, however, hydrogen uptake can reach 100% of that released from the corrosion reaction (Figure 5.1) for Zircaloy-2 [158]. This is thought to be an effect of the  $Zr_2(Fe, Ni)$  intermetallics, and would not be applicable to the post-transition oxidation case, since the development of pores around intermetallics may be inhibited by stabilisation of  $t-ZrO_2$  (see section 8. 4. 1).

Oxidation studies using  $T_2/H_2O$  mixtures [159] have shown that, during normal oxidation, no  $T_2$  enters the metal (Table 5.1) until the thermally-induced exchange reaction has progressed to the point where a measurable fraction of HTO has been formed. Thus, the hydrogen isotopes which enter the metal do so as an integral part of the reaction of the zirconium with water molecules, and not by reaction with any dissolved hydrogen in the water. Studies have shown that this situation persists (Figure 5.2) until hydrogen over-pressures in the system of tens of MPa are present [160]. An increasing percentage uptake of corrosion hydrogen is observed for Zircaloy-2 (but not for Zircaloy-4) with increasing hydrogen over-pressure, but this does not reach or exceed 100% until the highest pressures employed in Figure 5.2.

During the reaction of zirconium alloys with water the hydrogen is liberated, initially, as an adsorbed hydrogen atom on the oxide surface, when a proton is discharged by an electron emerging through the oxide film. The site at which this occurs depends on the morphology of the oxide film (see Figure 4.26). Thus, for alloys of the Zircaloy type, which contain additions of Fe, Cr and Ni (to a total of ~0.3 wt%) in the form of a distribution of second-phase particles, the electron current flows primarily at sites where intermetallics partially, or completely, short-circuit the oxide [161]. In alloys containing no, or few, such intermetallic particles of the transition metals (e.g. Zr-2.5%Nb) the electron current flows homogeneously through the bulk of the oxide [161]. Russian workers [162] have examined a range of Zr-Nb alloys from 0-1.5%Nb and find that the hydrogen uptake percentage decreases steadily over this range (Figure 5.3). Although the oxidation rate increases with increasing niobium content over this range the reduction in the percentage uptake of hydrogen results in a roughly constant quantity of hydrogen being absorbed by the different alloys. Data on hydrogen uptake by Zr-1%Nb alloy over a range of temperatures is given in Figure 5.4.



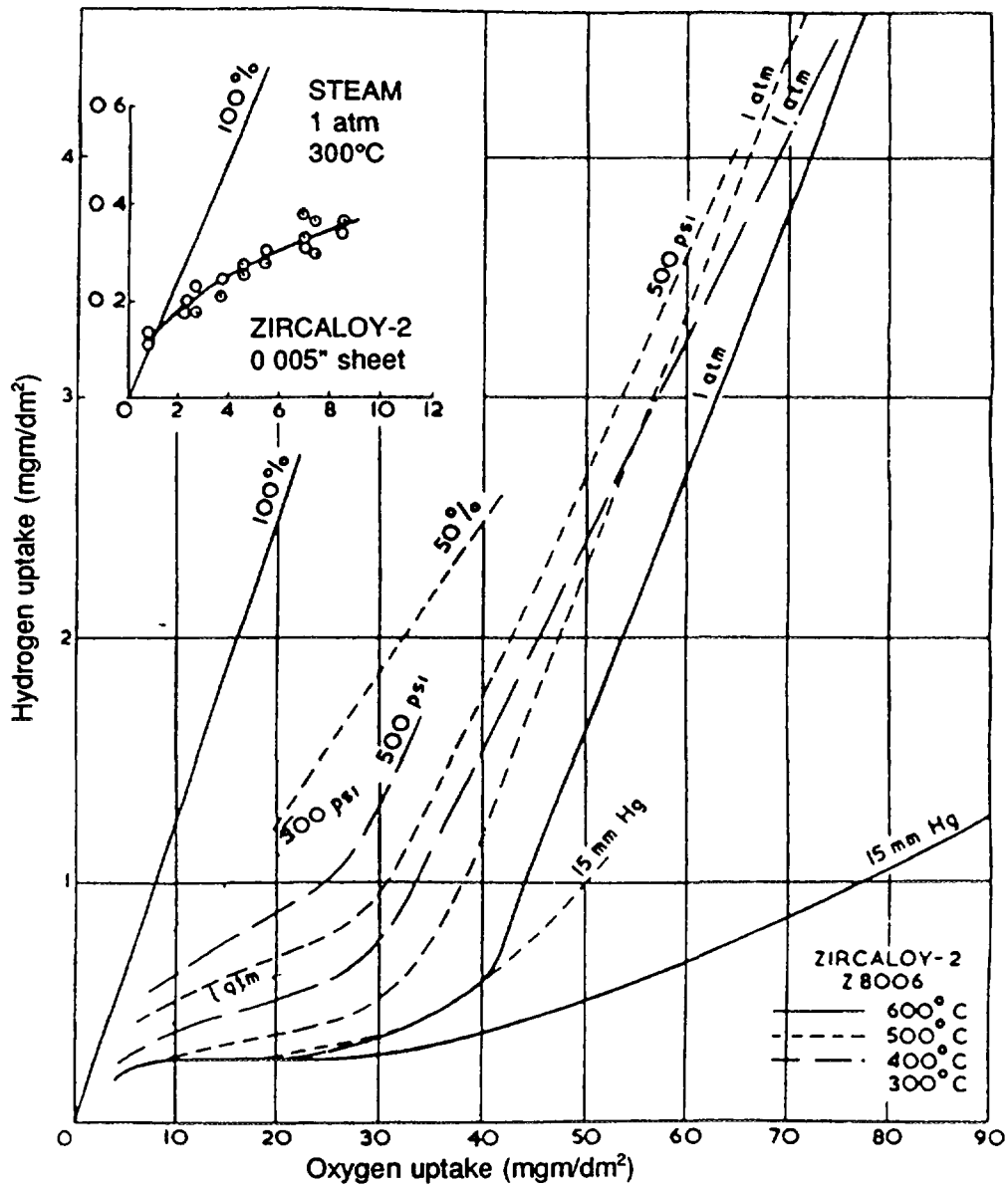


FIG 5.1 Change in hydrogen uptake rate with oxide film thickness for Zircaloy-2 [158]

Table 5.1. Oxidation in  $T_2/H_2O$  mixtures

Sample	Temp. (°C)	Time (h)	Wt. Gain (mg/dm <sup>2</sup> )	Hydrogen Absorption			Observations
				ppm	% Theor.		
GR40 Zr-2.5 wt% Nb (1)	400	66.0	15.5	14	21.2		No significant tritium uptake.
GR41 Zr-2.5 wt% Nb (2)	400	113.0	14.5	13	23.4		Small amount of tritium in oxide and metal.
GR42 Zircaloy-2 (3)	500	24.5	24.5	39	23.0		No tritium detected in oxide or metal.

(1) Heated at 1000°C in vac. for 1 h and quenched.

(2) Heated at 880°C in vac. for 72 h and quenched, reheated at 500°C for 6 h. The large amount of isothermal  $\alpha$ -phase present in this sample probably results from oxygen absorption during the long anneal at 880°C.

(3) Preoxidized in  $O_2$  at 500°C for 24 h;  $\Delta w = 28.2 \text{ mg/dm}^2$ .

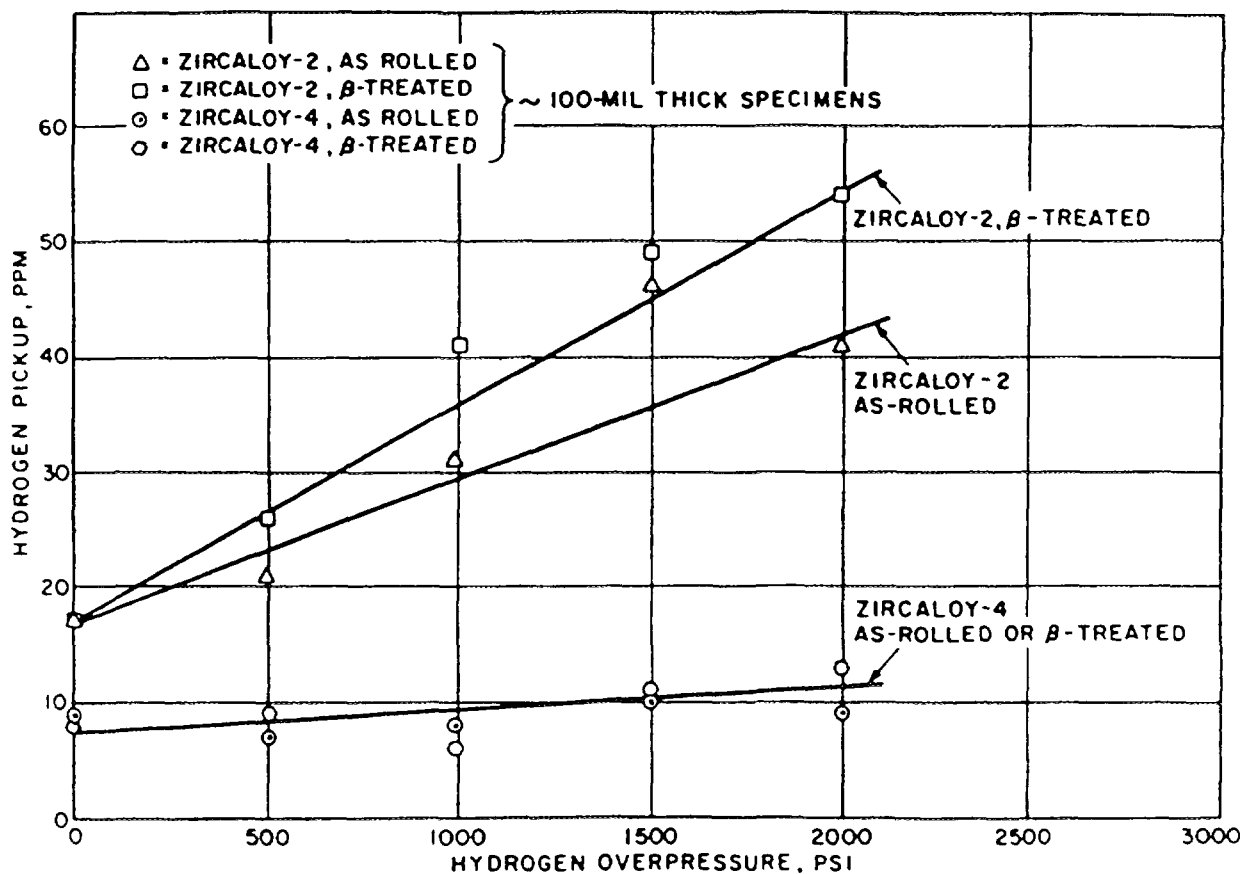


FIG. 5. 2. Hydrogen pickup by Zircaloy-2 and Zircaloy-4 as a function of hydrogen over-pressure after 14 days exposure in 343°C water. 100% uptake is not exceeded for these specimens and conditions until 40-50 ppm hydrogen has been absorbed [160].

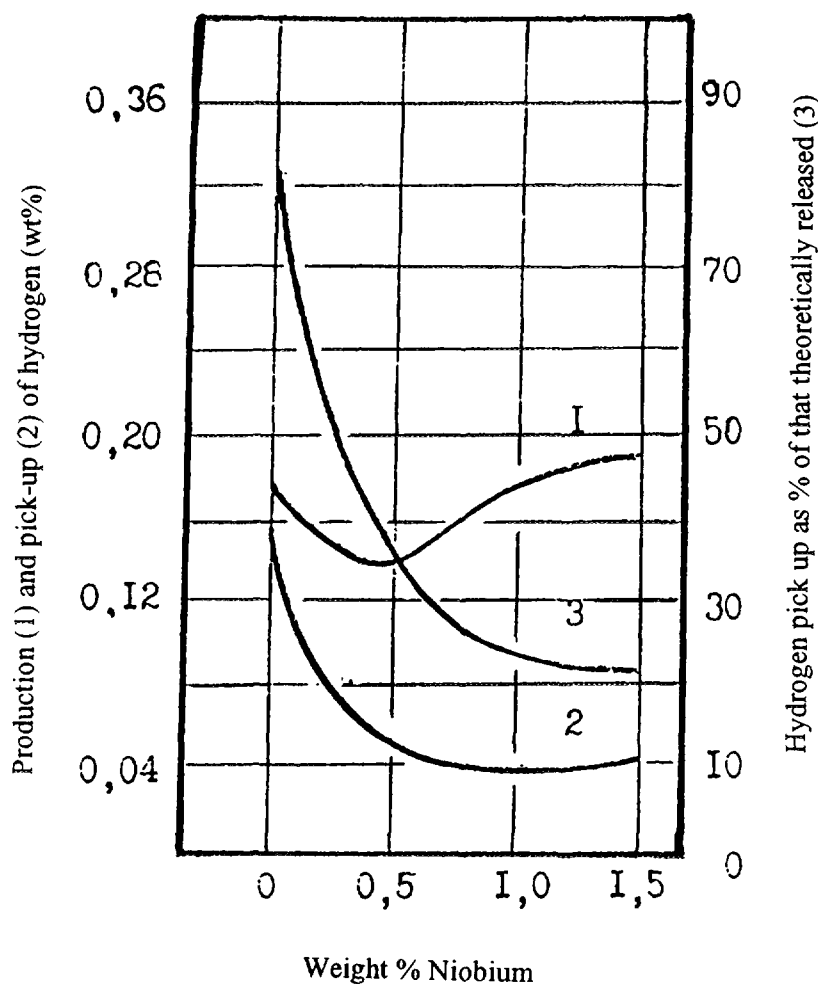


FIG. 5. 3. Effect of niobium in zirconium alloys on the absorption of hydrogen in water for 18000 hours at 350°C [72].

The hydrogen atoms released by the discharge of the protons (either locally at intermetallics, or uniformly over the surface) then either recombine, and are evolved as hydrogen gas, or diffuse into the metal. In order to get into the metal they must diffuse through whatever barrier layer of  $ZrO_2$  is present at, or near, the site of proton discharge or through the intermetallic particles themselves (or their oxidation products) if these proved to be easy diffusion paths for hydrogen, and hence could act as "windows" for its ingress through an otherwise protective oxide.

There is little direct knowledge of the precise hydrogen species that can diffuse in  $ZrO_2$ . The possibilities are  $OH^-$  diffusion,  $H^+$  hopping from anion to anion, diffusion of interstitial hydrogen atoms or hydride ions, and probably other processes. It is the competition between the rates of the recombination/evolution and the diffusion processes which determines the proportion of the corrosion-hydrogen which enters the metal. Any local situation which affects the relative probabilities of recombination or ingress into the metal will, therefore, affect the hydrogen uptake percentage. Despite the importance of this step in the reaction, no measurements of hydrogen recombination rates on either pure or doped zirconia surfaces are known.

The presence of alloying additions, such as nickel, which are thought to decrease the rate of the recombination reaction, or even, under some conditions, to directly dissociate molecular hydrogen

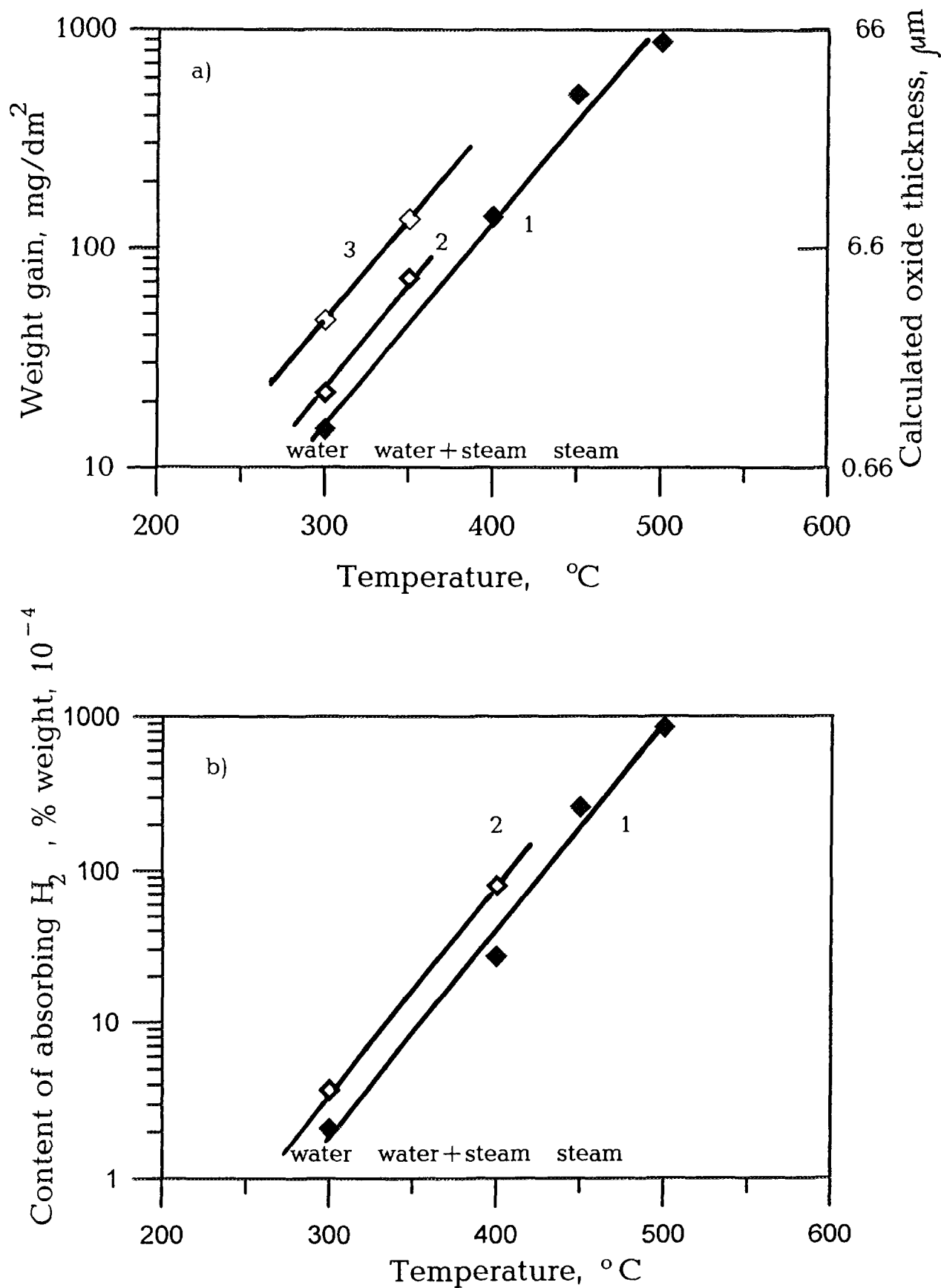


FIG. 5. 4. Effect of temperature on the oxidation (a) and hydriding (b) of Zr-1% Nb in steam, water and water + steam [72]: a) 1 -  $\text{O}_2$ , 20 - 40  $\text{mg}/\text{l}$ , 3,000 h; 2 -  $\text{O}_2$ , 0.2 - 0.9  $\text{mg}/\text{l}$ , 10,000 h; 3 -  $\text{O}_2$ , 10 - 40  $\text{mg}/\text{l}$ , 10,000 h and b) 1 - 3,000 h; 2 - 10,000 h.

dissolved in the water [160], could then lead to high percentage uptakes for the corrosion hydrogen by allowing a greater opportunity for the hydrogen atoms to diffuse into the metal. It was for this reason that nickel was eliminated from the alloy in the development of Zircaloy-4 from Zircaloy-2 [163]. It is also notable that the hydrogen uptake percentage shown by Zircaloy-4 in water is virtually independent of the hydrogen over-pressure (Figure 5.2), unlike that of Zircaloy-2 [160], thus adding further weight to the argument that the presence of nickel can lead to the direct dissociation and ingress of hydrogen dissolved in the water, when this is present in excess.

The presence of dissolved oxygen, or other oxidising species (e.g. nitric acid), is able to speed up the removal of the discharged protons from the  $\text{ZrO}_2$  surface and hence reduce the percentage hydrogen uptake (Figure 5.5). The precise mechanism by which this is achieved, whether by direct reaction of oxygen dissolved in the water with hydrogen atoms on the surface, or by the substitution of the reduction of oxygen by the electrons for the reduction of protons (as the cathodic reaction), has not been identified. The presence of dissolved hydrogen in the water, as we have seen above, has virtually no effect on alloys without nickel containing precipitates, and only a small effect on Zircaloy-2, until very large concentrations are present. Once the oxide film becomes porous, in the post-transition oxidation region, the hydrogen apparently finds it more difficult to evolve at the oxide surface, for there is a general tendency for percentage uptakes to increase [158]. This effect is thought to be a combination of the reduced diffusion distance through the thin barrier layer of  $\text{ZrO}_2$  in the porous oxide, coupled with the increased difficulty involved in diffusing out of the porous oxide when recombination no longer occurs on the oxide surface. These effects are smaller at temperatures typical of reactor operation than at higher temperatures (Figure 5.1).

The strong correlation (Figure 5.6) of hydrogen uptake percentages with the nature of the elements in the intermetallic precipitates [26], coupled with the observations of localised electron conduction at these sites, leads to the inference that the hydrogen entering the metal does so via some specific property of the oxide formed over these intermetallics. The nature of these oxide films [164] is only now being elucidated so the understanding of this aspect of the uptake mechanism may change rapidly in the near future. However, preliminary results suggest that elements like Fe and Ni may remain in the zero oxidation state in the oxide on an intermetallic and possibly also within the bulk oxide if they migrate away from the intermetallics either thermally or under irradiation (see section 8.4.1). The state of agglomeration of these atoms has not yet been established, but the possibility of continuous filaments of metal (stringers) within these oxides cannot yet be ruled out. Such stringers could account for both the high local electrical conductivity [165] and the easy ingress of hydrogen at these sites.

Although it is thought that, in alloys containing large numbers of intermetallic particles large enough to partially, or completely, short-circuit the oxide, the hydrogen from the corrosion reaction enters the metal at these sites, it was thought from tritium autoradiography that the uniform oxide between the intermetallics contained a significant (Figure 5.7), but unknown, concentration of hydrogen [139]. However, the inability to distinguish tritium in the oxide, separately from tritium in a suboxide hydrogen peak that is often observed just below the oxide film in the metal (see later) may be a confounding factor where autoradiographs of oxides  $<1\ \mu\text{m}$  (the approximate depth limit of the technique based on the range of tritium betas) are involved. That the quantity of tritium in such oxides appeared to be roughly proportional to oxide thickness (Figure 5.8), for interference-coloured oxides (when interference colour, oxide thickness and darkening of the autoradiograph were compared), suggests a relatively constant concentration of tritium in these oxides, with little concentration gradient through them. Attempts to measure this concentration using only infra-red spectroscopy techniques [166] were unsuccessful, but indicated that the concentration of OH in  $\text{ZrO}_2$  films was probably  $<5\%$ . SIMS measurements indicate high concentrations of hydrogen to be present distributed in a profile reminiscent of a diffusion profile. Diffusion coefficients have been calculated from these profiles [81,82], but the profiles do not change in the expected way with increasing time, remaining essentially fixed after quite short diffusion times (Figure 5.9). Nevertheless, H can be exchanged for D rapidly and quantitatively in these profiles (Figure 5.10) without a change in the

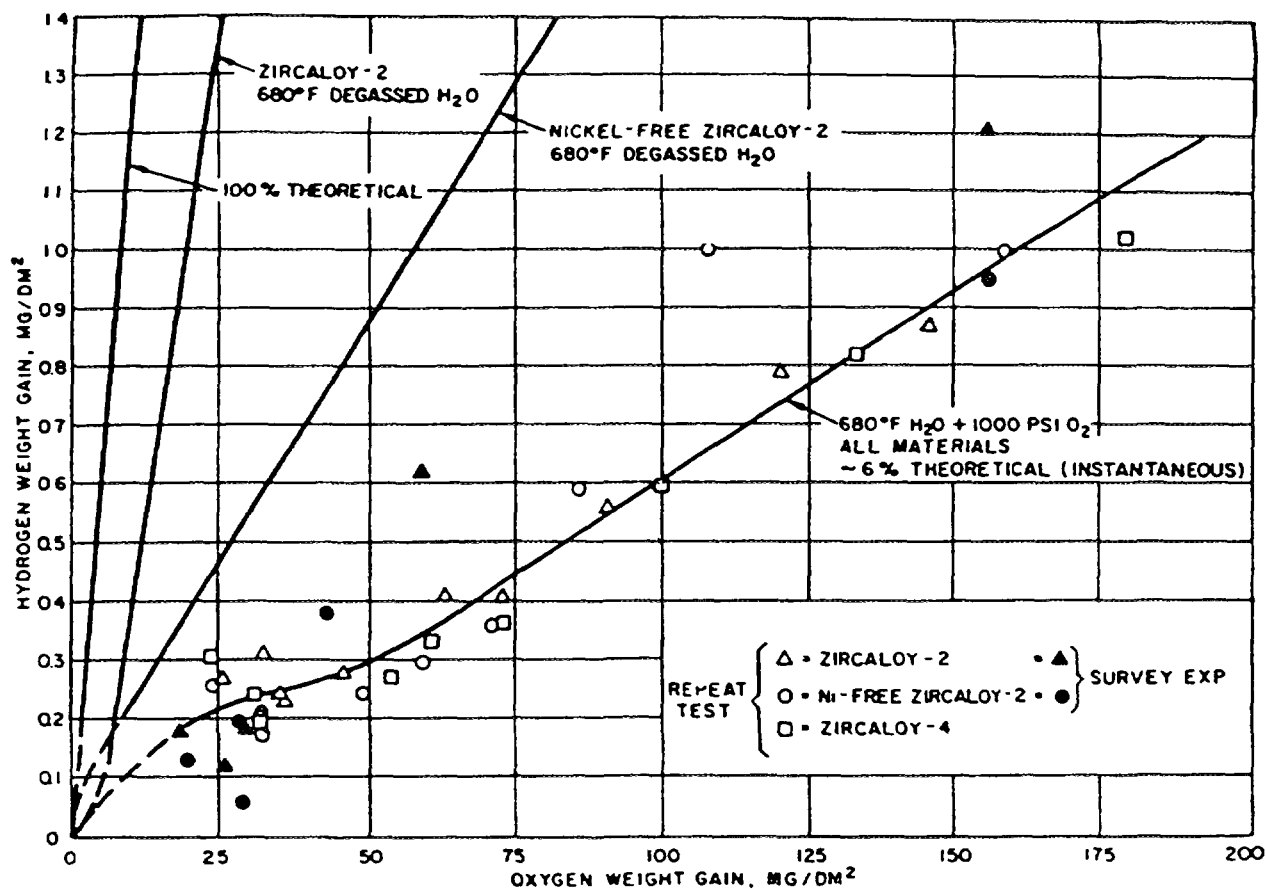


FIG. 5.5. Effect of the oxygen content of the water on hydrogen uptake by Zircaloys in 360°C water [160].

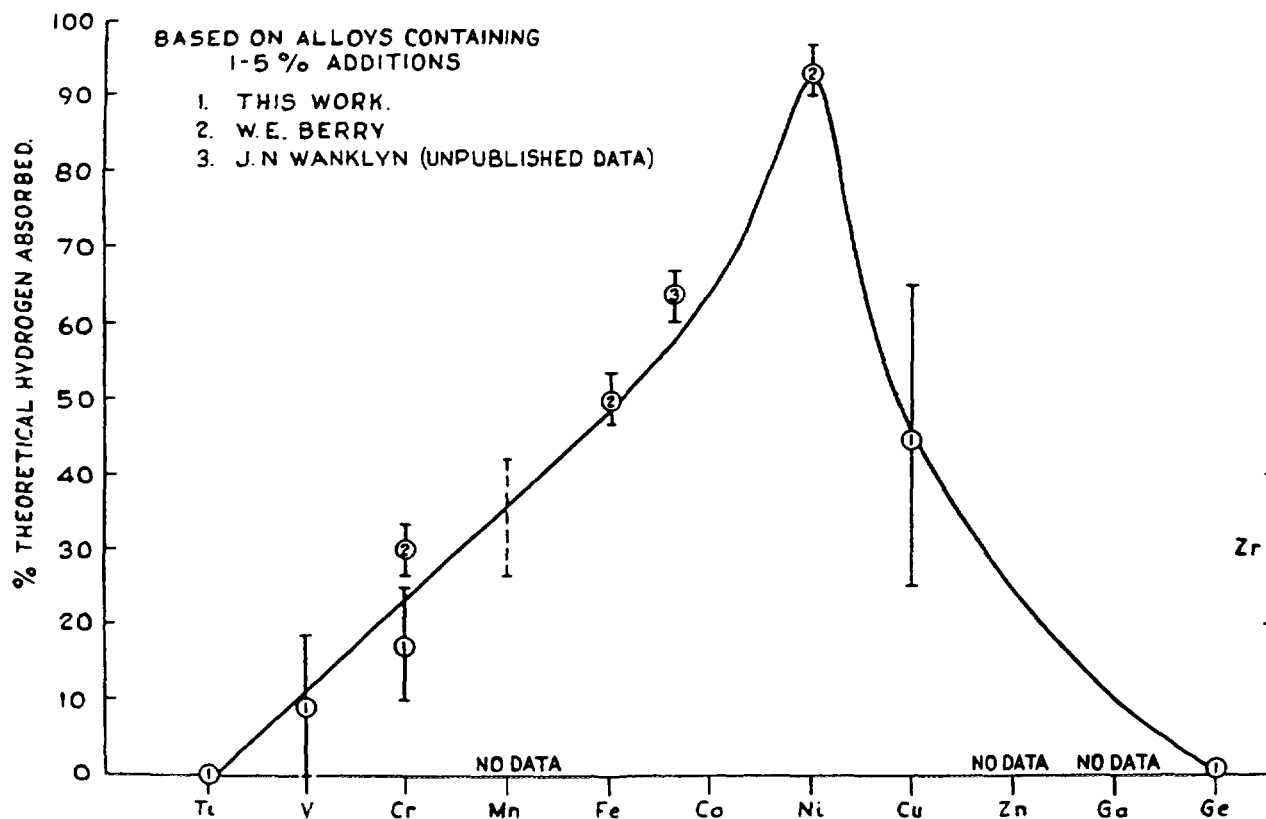


FIG. 5.6. Effect of some alloying elements in intermetallic form on hydrogen uptake percentage [26].

FIG. 5. 7. Autoradiograph showing a uniform tritium content in a thin zirconia film formed in  $T_2O$  for long enough to saturate the oxide (oxidized in  $O_2$  at  $400^\circ C$  for 66.5 hours to weight gains of  $12.7 \text{ mg/dm}^2$ ; oxidation continued in  $T_2O$  at  $400^\circ C$  for 48 hours to total weight gain of  $14.4 \text{ mg/dm}^2$ ). Compare with non-uniform tritium distribution in FIG. 5.17 [139].

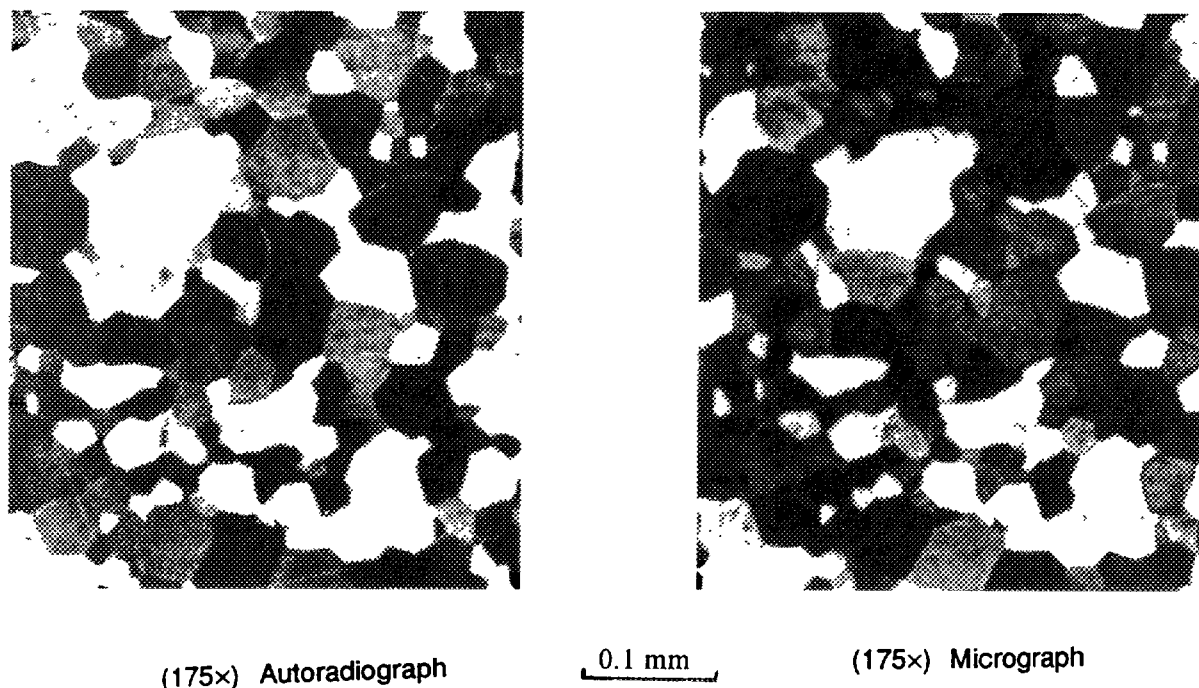


FIG. 5. 8. Surface autoradiograph showing tritium content proportional to oxide thickness. Note that in a black and white print the "darkness" of the interference coloured oxide is *not* proportional to the thickness of the oxide, the correlation must be done using a colour print. Oxidized in  $T_2O$  at  $400^\circ C$  to a weight gain of  $1.9 \text{ mg/dm}^2$  [139].

profile shape [167]. At present, the precise nature of these profiles is uncertain. They are thought to represent structural features of the oxide (e.g.  $OH^-$  groups in the crystallite boundaries or on the walls of very small pores) that are essentially immobile but where the H/D exchange reaction can take place easily.

Despite the known presence of hydrogen in the uniform oxide film there is still little knowledge of its mobility. The long-term stability of autoradiographic specimens against exchange of the tritium with laboratory water vapour suggests that the mobility is low, but does not permit the calculation of other than an upper bound for the mobility. If, as observed, the tritium content of an  $0.5 \mu\text{m}$  oxide film remains apparently unchanged after one year at room temperature, the permeability of tritium through these films must have been much less than  $\sim 10^{-19} \text{ mole} \cdot \text{m}^{-2} \cdot \text{s}^{-1}$  at room temperature. This is very much lower than the value extrapolated from the elevated temperature tests [168,169], which we have already argued represents surface diffusion down pores (Figure 5.11).

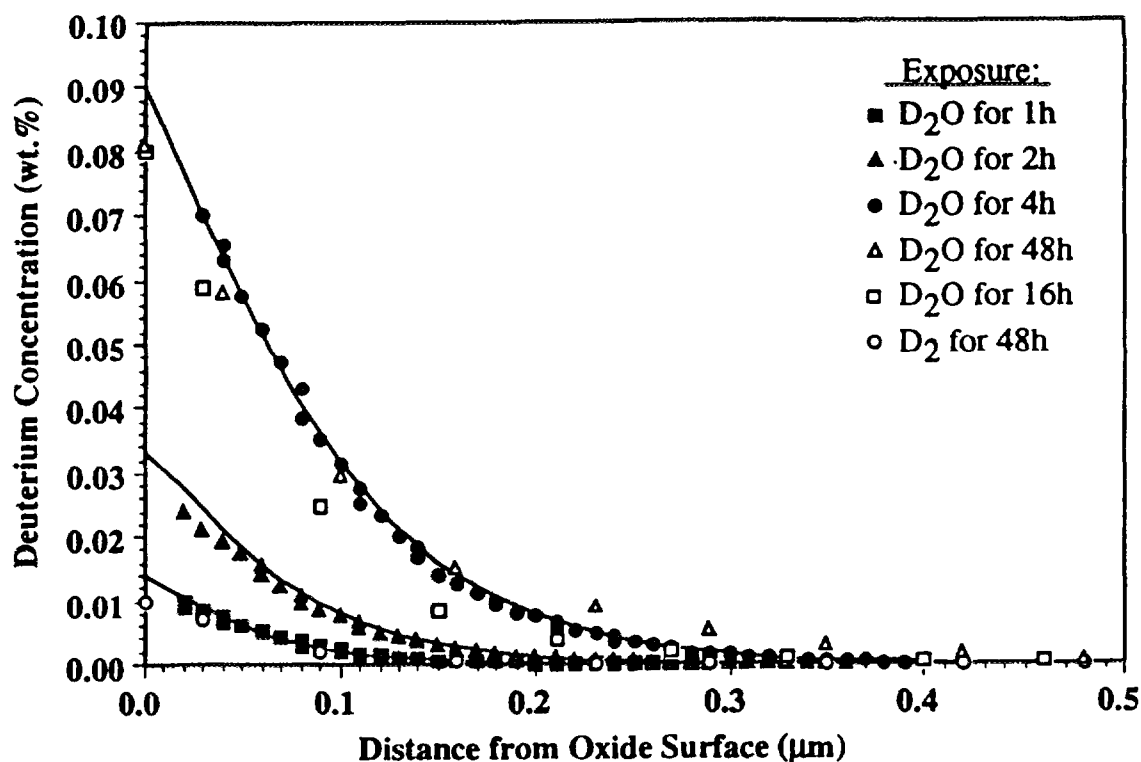


FIG. 5. 9. Deuterium through-oxide-thickness depth profiles following exposures to  $D_2O$  and  $D_2$  at  $300^\circ C$ . The solid lines represent a Fickian diffusion model fitted to the 1, 2 and 4 hour profiles for Zr-2.5%Nb oxide films. The inferred apparent diffusion coefficient is approximately  $1 \times 10^{-18} m^2 \cdot s^{-1}$  [167].

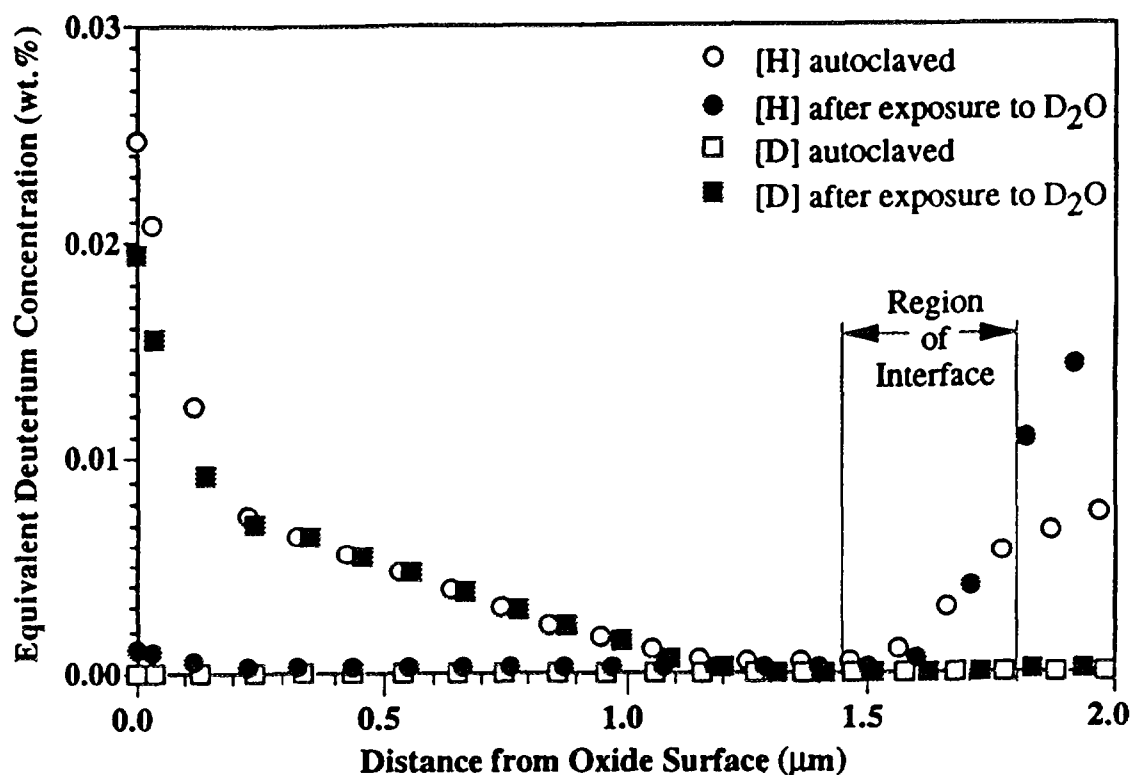


FIG. 5. 10. Deuterium and hydrogen through-oxide-thickness profiles (after exposure at  $300^\circ C$  for 168 hours) to a stream of argon bubbled through  $D_2O$ . The samples were pre-filmed by steam autoclaving at  $400^\circ C$  for 48 hours. Note that hydrogen and deuterium in the oxide on the Zr-2.5%Nb alloy specimen can be exchanged quantitatively by this treatment without any change in the profile [167].



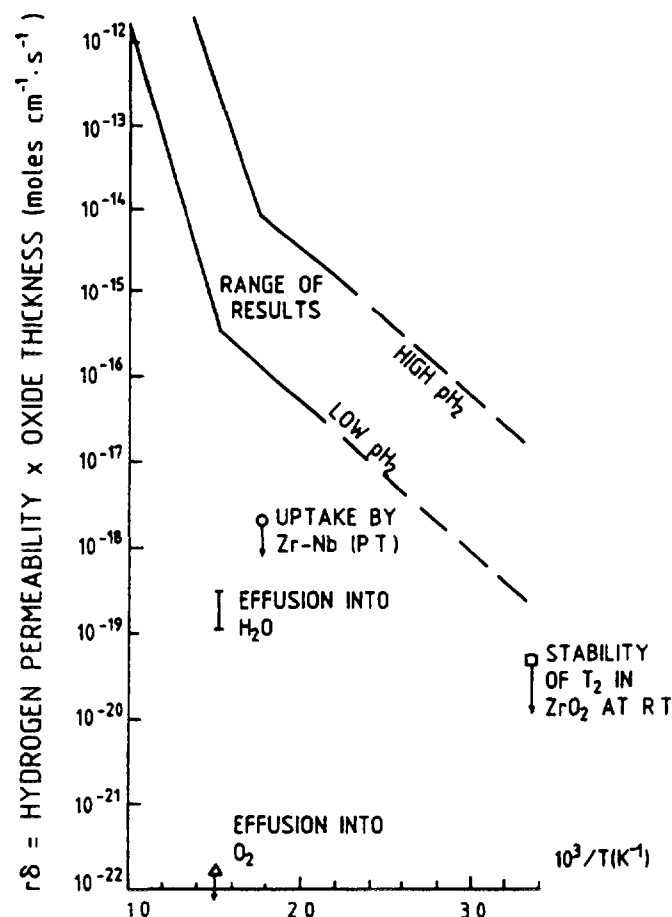


FIG 5 11 Comparison of the permeability data of T. Smith with other estimates of the apparent hydrogen diffusion of hydrogen in  $\text{ZrO}_2$  films [189]

Recent work by nuclear reaction techniques [170] on  $\text{ZrO}_2$  films formed in  $400^\circ\text{C}$  air, shows that the hydrogen in the  $\text{ZrO}_2$  is tightly bonded and relatively immobile. Values for the diffusivity from these experiments are in good agreement with the above, being in the region of  $10^{-20} \text{ m}^2 \cdot \text{s}^{-1}$ . However, in these experiments also the implanted hydrogen peaks fail to behave as expected. Instances of large losses during implantation, of apparently extensive irradiation damage during implantation, and of peaks decreasing in area without increasing in width, suggest the presence of microporosity either initially or created in many oxides [170-172]. If hydrogen in the oxide lattice is relatively immobile then possibly these micropores or the oxide crystallite boundaries may be the ingress route through protective oxides.

Thus, we arrive at a picture whereby hydrogen uptake in alloys containing intermetallics of Fe, Cr and Ni is controlled by release of the hydrogen atoms at the sites of these particles, and migration of them perhaps via the same intermetallics, perhaps by way of stringers of metallic Fe or Ni in the oxide, into the metal. In such a case the hydrogen uptake rates may be determined by processes very different from those controlling the oxidation rate. Thus, the two processes may show different dependencies on metallurgical factors. The oxidation process then is merely supplying the source term for the hydrogen uptake processes. This appears to be the case as the tin content of Zircaloy-4 is reduced. The corrosion rates of such alloys decrease with decreasing tin content in-reactor, whereas the final hydrogen contents change little, resulting in an increase in the calculated uptake percentage [173].

In alloys containing few such particles (e.g. Zr-2.5%Nb) the hydrogen must migrate more uniformly through the oxide, which has a low diffusivity for hydrogen. This difference in mechanism can account for the large differences in the observed deuterium uptake rates in Zircaloy-2 and Zr-2.5%Nb alloy pressure tubes [121]. If we assume that the very low rates of uptake by Zr-2.5%Nb are entirely controlled by diffusion through the oxide film, then we can use these rates to calculate an upper bound for the permeability of  $\text{ZrO}_2$ . This gives us a value of  $\sim 10^{-18}$  mole  $\text{m}^{-1} \text{s}^{-1}$  for the permeability at  $290^\circ\text{C}$ . This is in the same range as the results from effusion into steam [159], especially if the actual barrier layer oxide thickness is quite thin (i.e. if the oxide is post-transition). Without a knowledge of the hydrogen concentrations in these oxides, it is not possible to estimate a true diffusion coefficient, but the permeabilities estimated above are consistent with the very low diffusion coefficients in the surface layer measured by the workers at North Carolina State University [174,175], University of Toronto [170,171], and Ontario Hydro [82].

The present situation with regard to hydrogen uptake mechanisms during corrosion is very fluid and can be summarised as follows:

- The hydrogen absorbed by the zirconium during corrosion in water comes from the water molecules dissociated during the corrosion process and not usually from other sources such as gaseous hydrogen dissolved in the water. Thus, the use of a "hydrogen uptake percentage" that relates the amount of hydrogen absorbed to the amount of hydrogen liberated by the corrosion reaction is a convenient method of expressing the behaviour of a particular batch of alloy under particular environmental conditions. It is not a unique property of an alloy but depends on the alloy chemistry, fabrication and exposure conditions.
- The instantaneous fraction of the hydrogen released by the corrosion reaction which is absorbed (by a given alloy) varies as the oxide film thickens. For some alloys (e.g. Zircaloy-2) it is high initially and decreases during growth of the pre-transition oxide film, only to increase again when the oxide becomes porous [158] after transition (Figure 5.1). For other alloys (e.g., van Arkel Zr-Zr-Fe binaries and Zircaloy-4) it appears to be relatively constant throughout the growth of the protective oxide, apart from the very thin film region (Figure 5.12) [176]. The initial apparently zero uptake in this figure requires an error of only 1-2 ppm H in the knowledge of the initial hydrogen content of the metal to explain it. This difference between the initial pre-transition hydrogen uptake curves for Zircaloy-2 and Zircaloy-4 probably reflects an effect of the absence of nickel containing intermetallics in Zircaloys. In water at  $\sim 300^\circ\text{C}$  the scatter in the available data is such that the use of a constant percentage uptake is acceptable for practical purposes, but has no specific mechanistic significance.
- The percentage uptake can vary enormously with alloy composition, from 0-100% [177]. However, only a few alloys (e.g. alloys containing high nickel contents) apparently have the ability to dissociate water or hydrogen molecules and absorb hydrogen from these sources, leading to uptakes  $>100\%$  of that equivalent to the oxygen reacting [178,179]. It cannot be established easily whether this excess hydrogen came from hydrogen dissolved in the water rather than from dissociation of additional water molecules.
- Other conditions being equal, oxygen additions to the water will reduce the hydrogen uptake and hydrogen additions will increase it. The size of these effects differs significantly between Zircaloy-2 and Zircaloy-4 [51], and in this instance is also ascribed to an effect of nickel in the Zircaloy-2 (Figure 5.2).
- Virtually nothing is known about the form of the hydrogen in  $\text{ZrO}_2$  or how it migrates through it. OH(OD) stretching frequencies measured by infra-red appear to be less than would be necessary to account for the amount of H(D) measured by SIMS. Even the question of whether hydrogen migrates uniformly through the oxide or locally via defects or (oxidised?) intermetallics is unresolved. Diffusion rates of H(D) implanted in  $\text{ZrO}_2$  films are very low [170,171], and SIMS profiles can be interpreted to give very similar diffusion rates [81,82,167,180]. However, no correlation of such profiles with actual amounts of H(D) absorbed have yet been made, and the hydrogen isotopes do not seem to migrate as expected from the laws of diffusion.

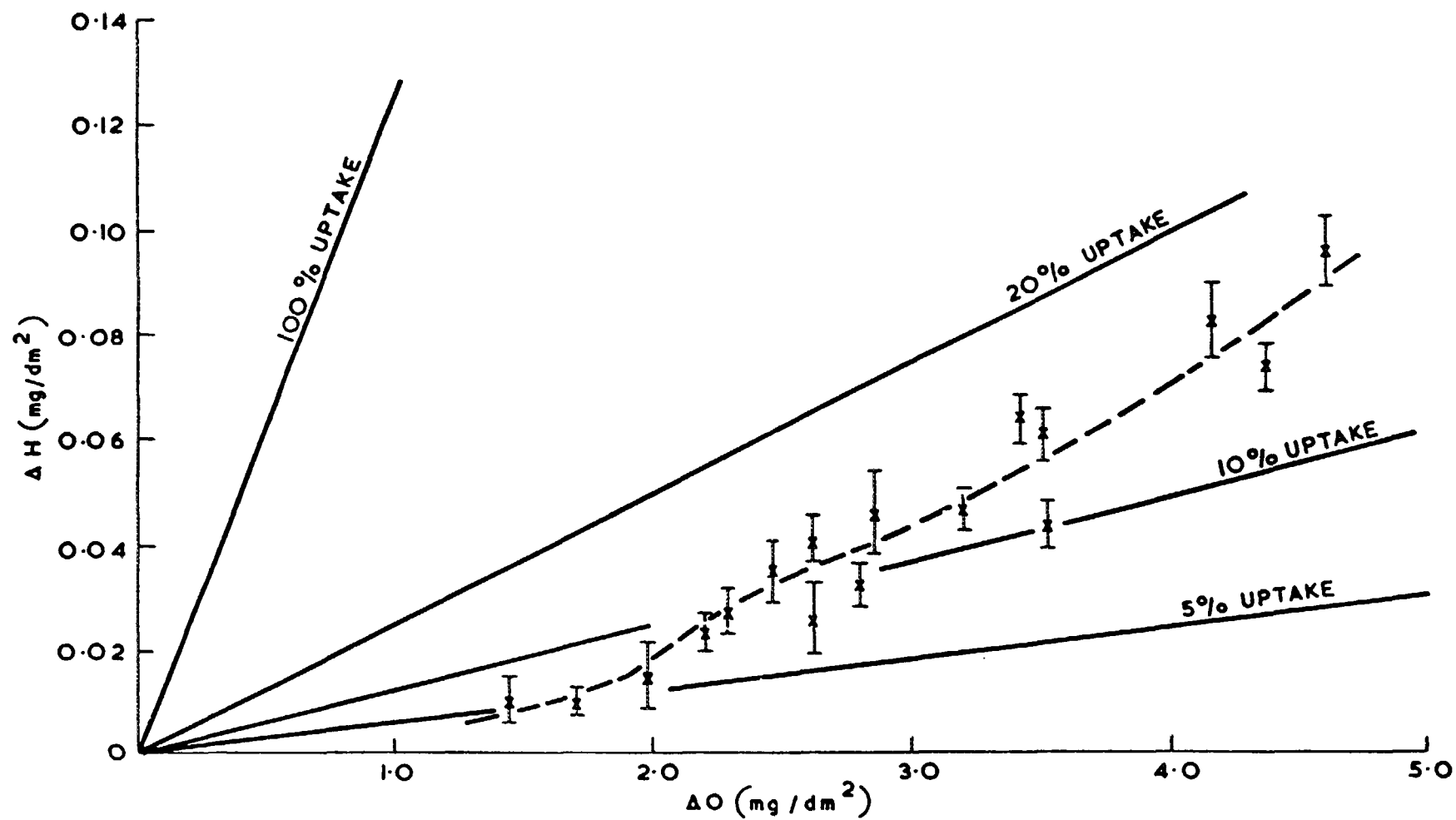


FIG. 5. 12. Hydrogen uptake of Zr-1%Fe in steam at 500°C, 1 atm (up to 5 mg/dm<sup>2</sup>). Note that a small error in the knowledge of the initial hydrogen content of the alloy could account for the apparently zero initial uptake [176].

- With all the other uncertainties in our knowledge of the hydrogen uptake mechanisms in zirconium alloys it is impossible to say whether or not irradiation has any direct effect on hydrogen absorption during corrosion. It may be that the effects of irradiation influence only the corrosion process, and that hydrogen absorption processes are changed only to the extent that oxide morphology may be different under irradiation, if the oxide growth mechanism is different.

### 5.1.2 Absorption of hydrogen gas

Even thin  $\text{ZrO}_2$  films represent a very effective barrier to hydrogen uptake when specimens are exposed to hydrogen gas [181-183]. However, after a variable incubation time the oxide films break down and rapid absorption of hydrogen occurs (Figure 5.13). The arguments have always been over precisely what changes are occurring in the oxide during this incubation time, and how the hydrogen migrates through the oxide. Oxide films on zirconium are unstable thermodynamically with respect to oxygen in solution in metal [44]. Whenever an oxidised zirconium alloy sample is held in an atmosphere containing insufficient oxygen to maintain oxide film growth in competition with the oxygen dissolution process, some breakdown of the film will occur. It was established early [184], that enough oxygen to maintain the normal oxidation rate was necessary to prevent rapid hydriding in  $\text{H}_2/\text{H}_2\text{O}$  mixtures (Figure 5.14).

These observations led to the postulate that, for any conditions of temperature, pressure and oxidant, there should be a critical hydrogen/oxidant ratio below which the oxide film would remain protective, and gross reaction with hydrogen would be prevented [185]. There could still be a slow absorption of hydrogen by reaction with the oxidant if this were a hydrogen containing molecule. Several investigators [185,186] have established these critical ratios, for a limited range of environments, and they are generally observed to be in the range  $10^{-2}$ - $10^{-6}$  (Table 5.2). The results were quite variable, and may show a change with temperature. In the range of 300-400°C the tendency is for the ratio to decrease. Thus, very small concentrations of oxidising species in hydrogen gas are sufficient to prevent direct surface reaction with hydrogen at reactor operating temperatures. This effect was borne out in experiments on cracking in hydrogen gas where small oxygen additions were sufficient to inhibit crack growth [154]. However, it is notable (by comparing the total pressure and the critical ratio in Table 5.2) that more oxygen appeared to be necessary to ensure passivation of strained metal at the crack tip, than appears to be the case for the reaction on a smooth surface.

If insufficient oxidising species are present to prevent the oxide film from slowly dissolving in the zirconium matrix, then, after an incubation time required for dissolution in the metal to lead to "breakdown" of the surface oxide [181-183,186], a rapid direct reaction with hydrogen gas ensues (Figure 5.13). The progress of the oxide "breakdown" process was monitored by Shannon, during the incubation period, by measuring the electrical resistivity (Figure 5.15) of the oxide film [184]. The resistivity of the oxide declines rapidly with time, as a result of the increasing hypostoichiometry of the oxide, and hydriding commences once the resistivity declines below a critical level. The hypostoichiometry changes because the rate of dissolution of oxygen atoms from the oxide into the metal now exceeds the rate at which replacement oxygen atoms can be acquired from the environment. In addition to the increasing electronic conductivity associated with this process, an increase in the number of anion vacancies will result.

As a result of these observations, investigators studying the rate of reaction of hydrogen with oxidised zirconium surfaces have been tempted to postulate that hydrogen is migrating via these anion vacancies as interstitial hydrogen [168,169]. From their experiments they have then calculated diffusivities for hydrogen in the  $\text{ZrO}_2$  lattice. However, there is no unambiguous evidence from these experiments to support an argument that hydrogen is migrating via the  $\text{ZrO}_2$  lattice at all. The diffusivities which they calculate are very high for such a lattice diffusion process, and lie in a range more typical of surface diffusivities. Experiments of this type give permeation rates  $10^7$  (or more) times those measured by effusion experiments using tritium [159,174,175]. From these, a diffusion coefficient for tritium in the surface layer (arbitrarily defined as the first 5  $\mu\text{m}$ ) of  $10^{-9} \text{ m}^2/\text{s}$  at 300°C

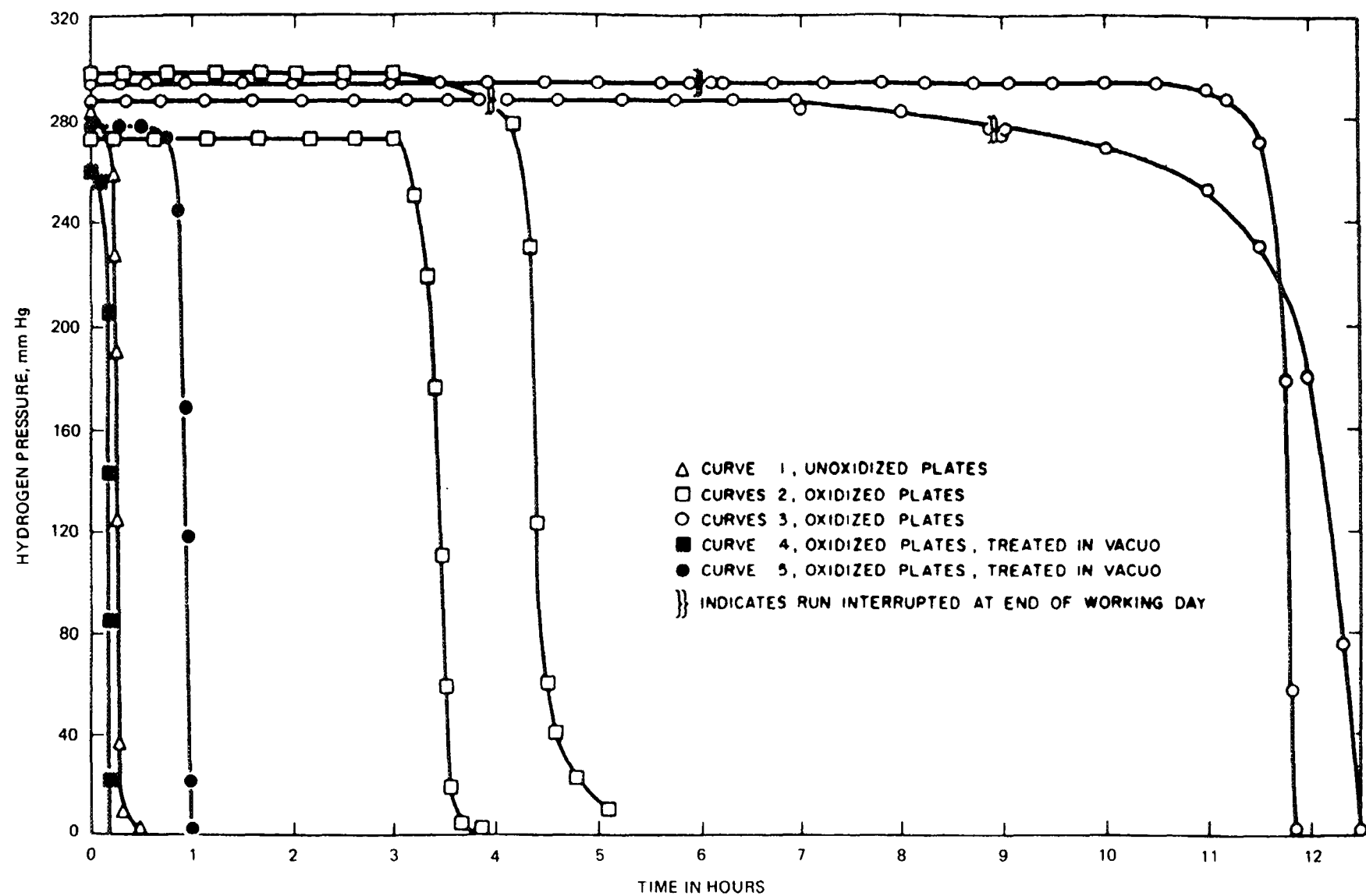


FIG. 5.13. Incubation times for absorption of hydrogen gas at 400°C by zirconium with various initial oxidation treatments [181].

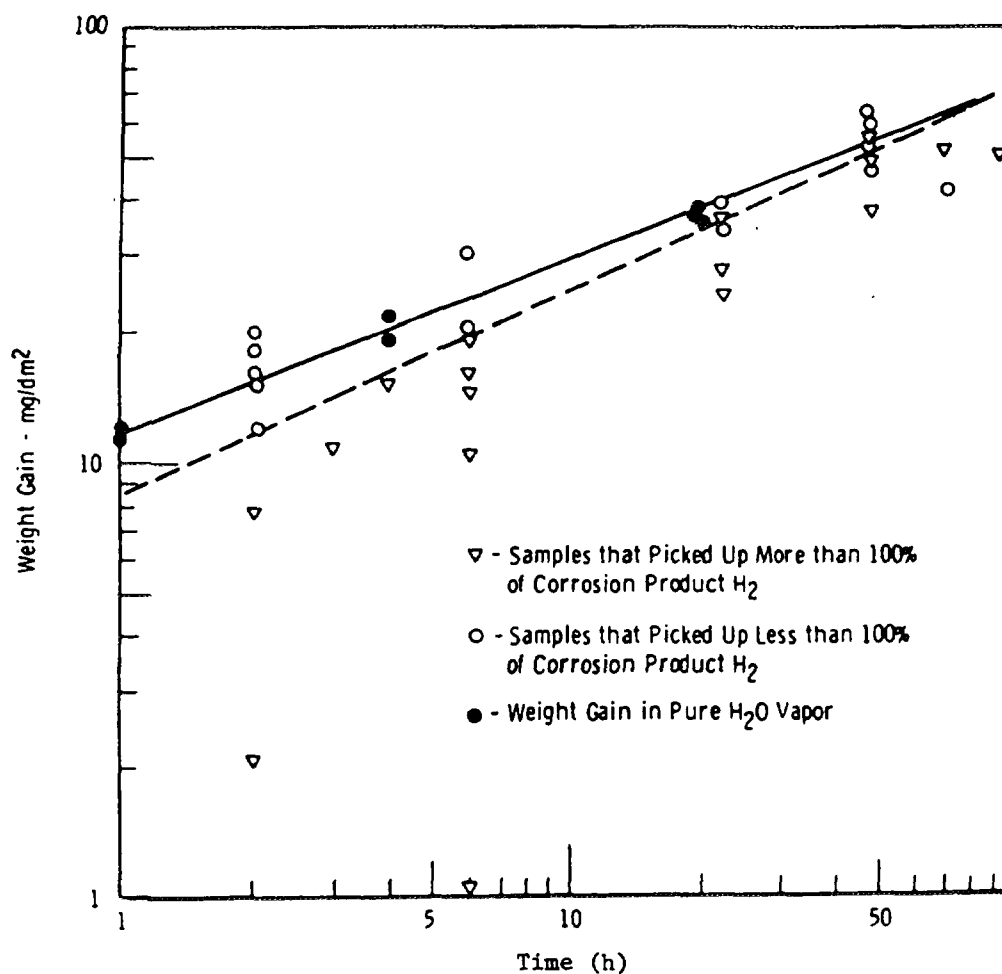


FIG. 5. 14. Plot showing the influence of the oxidation rate during exposure to H<sub>2</sub>/H<sub>2</sub>O mixtures at 400°C on hydrogen uptake [184].

Table 5.2. Critical H<sub>2</sub>/oxidant ratios for direct heating  
(References refer to the original table in Ref. [189])

Material	Temperature (°C)	H <sub>2</sub> Pressure (atm)	Critical Ratio	Author	Ref.
Zircaloy-2	343	6.5 x 10 <sup>-2</sup> -1.0	10 <sup>6</sup> -10 <sup>8</sup>	Boyle & Kisiel	9
"	400	1.3 x 10 <sup>-2</sup>	10 <sup>2</sup>	Shannon	7
"	320	1.0	10 <sup>5</sup>	Gibby	BNWL-150 (1965)
"	300	1.0	10 <sup>5</sup>	Une	10
"	400	1.0	10 <sup>2</sup>		
"	25	0.1	10 <sup>2</sup> -10 <sup>3</sup>	Coleman & Cox	5
Zr-2.5% Nb	25	0.1	10 <sup>2</sup> -10 <sup>3</sup>		

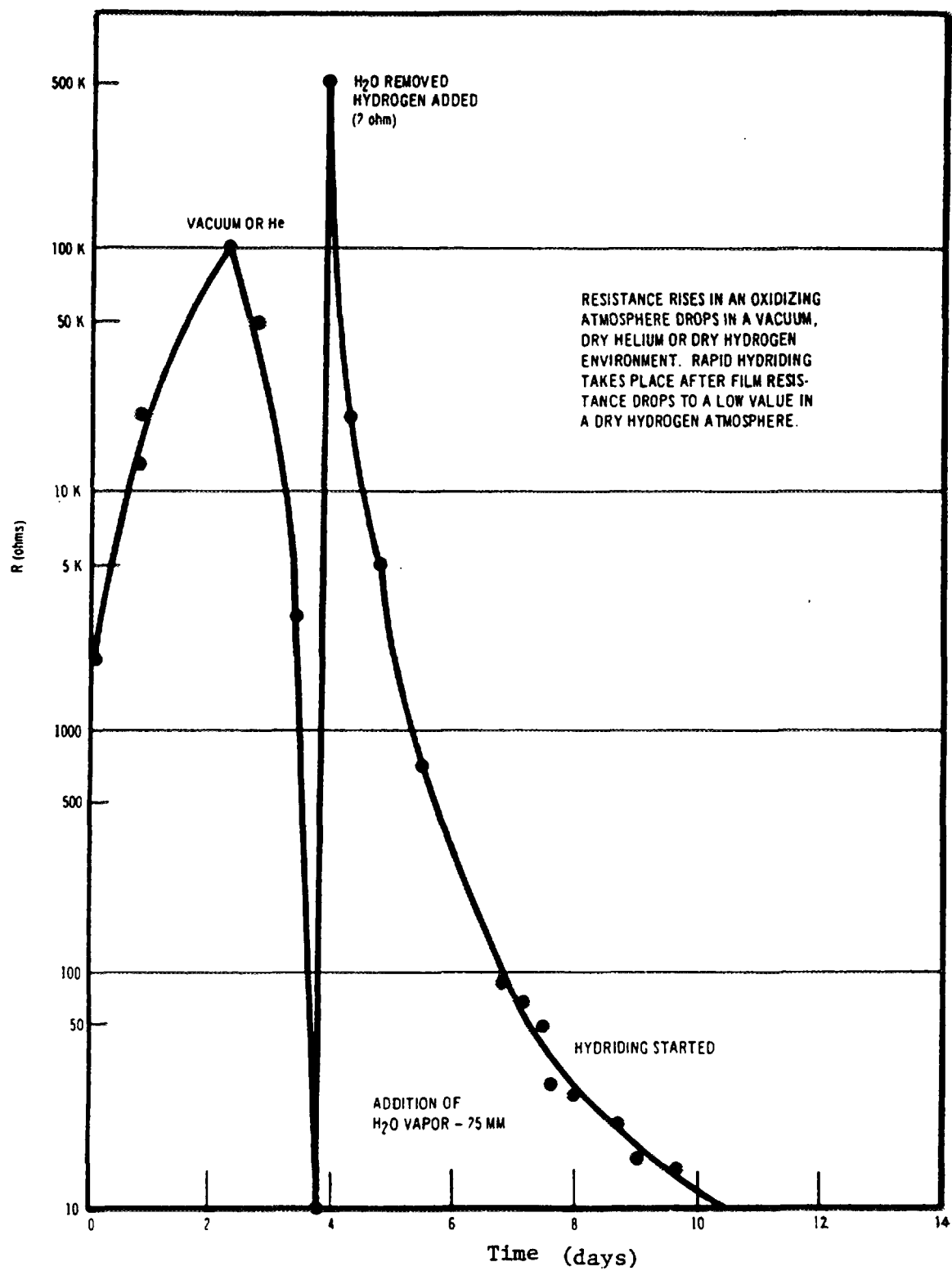


FIG. 5. 15. Plot of the electrical resistance for Zircaloy-2 exposed to gaseous environments at 450°C [184].

was estimated [174] At the start of such an experiment the  $T_2$  concentration in the alloy is known, and is assumed to be zero at the oxide/environment interface The diffusion of tritium in any suboxide zone of metal is assumed to be fast compared with that in the oxide, so that the calculated numbers are relevant to diffusion in the oxide This is in good agreement with values which have been obtained from other techniques (see section 5.1.1)

There is some circumstantial evidence that hydrogen entering the metal under these conditions does not pass through the oxide lattice Tritium autoradiography [139] has shown that, when a specimen pre-oxidised in  $O_2$  or air was exposed to  $T_2$  gas, tritium appeared in the metal core but the oxide film remained essentially free of tritium (Figure 5.16) Other experiments showed that tritium, built into the oxide film during reaction with  $T_2O$ , remained fixed once the specimen was cooled and did not migrate into the metal, or exchange with the hydrogen in the environment, over periods of years [159] This again suggests that the diffusivity in the oxide is orders of magnitude less than that calculated from the reaction rate experiments [168,169] Conversely, tritium absorbed in porous oxide films, by exposure to  $T_2O$ , exchanged rapidly with hydrogen in the environment and vanished in periods of, at most, a few days [159] Thus, at the very most, any tritium which was present in the oxide on the specimens heated in  $T_2$  gas had exchanged with the laboratory environment, and vanished, by the time the autoradiograph was exposed This indicates strongly that the  $T_2$ , which entered the metal in these experiments, did so via pores or cracks in the oxide and not by diffusion through the bulk of the oxide lattice Autoradiographs of similar specimens pre-oxidised in oxygen and then exposed to  $T_2O$  showed tritium both in the metal and in the oxide (Figure 5.17) This shows the fundamental difference between reaction with  $T_2$  and  $T_2O$

The experiments of Shannon [184] and Smith [168,169,187] gave no direct clues to the microscopic nature of the "breakdown process" in the oxide film, other than for the accompanying changes in conductivity and stoichiometry The implicit assumption that these would be homogeneous changes is carried by the deductions subsequently made It became clear that complete dissolution of the oxide film was too slow a process (Figure 5.18) to account for the durations of the observed incubation times prior to the onset of rapid hydrogen absorption [188] Studies showing that the electrical resistivity of the oxide fell to very low values (Figure 5.15) prior to rapid hydriding [184] led to arguments that hydrogen was migrating via the point defects that had been generated However, the tritium autoradiography studies showed that, when oxidised specimens were exposed to gaseous hydrogen, entry was gained at the end of the incubation time by migration through physical flaws (holes) generated in the oxide, without passing through the oxide lattice [139] Thus, the hydrogen was probably reacting directly with bare zirconium surface exposed at the bottom of these flaws The diffusion coefficients for hydrogen in zirconia deduced from experiments in which oxidised zirconium specimens were exposed in hydrogen gas [168,169,187] did not, therefore, represent an actual diffusion of hydrogen through the  $ZrO_2$  lattice

The question of what the nature of the defects were that were generated by exposure to low  $pO_2$  environments remained to be answered One possible such defect was identified in experiments in which pre-oxidised van Arkel zirconium specimens were annealed in vacuum [189] Electron microscope studies [190,191] of the oxide films formed on zirconium, of similar purity to that used in the hydrogen diffusivity studies, showed that the oxide films formed in a far from uniform and parallel-sided manner Ridges of thick oxide form preferentially along many grain boundaries and big variations in the oxide thickness occur from grain to grain (see Figure 4.7a) Many of these features have also been recognised from optical microscopy [192] However, the lines of cracks (see Figure 4.7b) which form in the oxide along these ridges, and along grain boundaries separating grains which grow thick and thin oxide films [190-193], are less easily seen in the optical microscope These cracks are encouraged by the curvature in the oxide/environment interface introduced by the local variation in oxide thickness and the high Pilling-Bedworth ratio of  $\sim 1.56$  These factors cause the outer surface of the oxide to go into tension, whereas oxide films formed as a planar layer on a smooth surface remain in compression at the same point in time



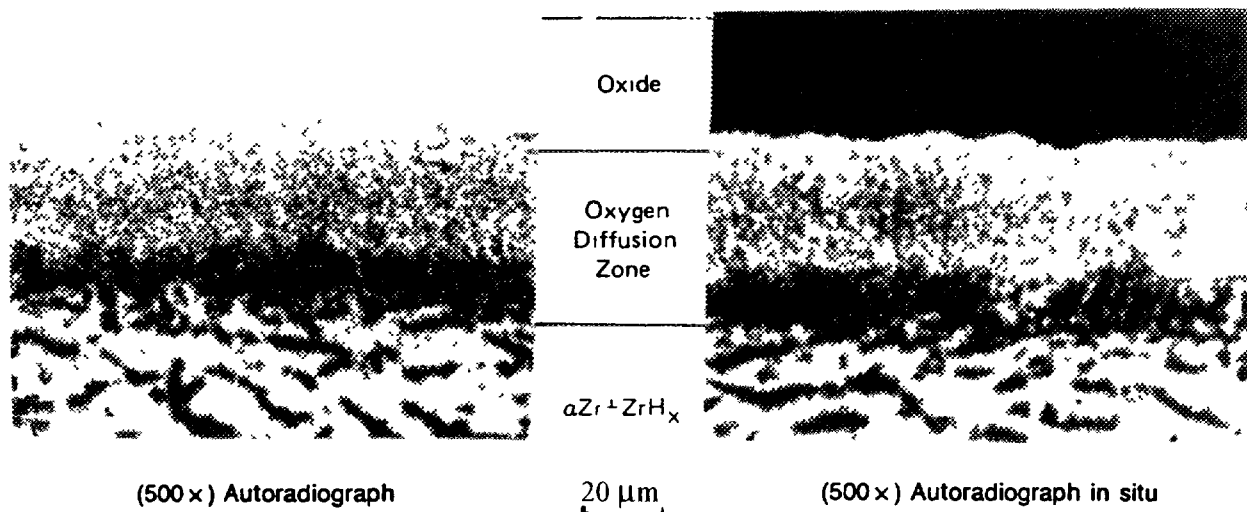


FIG 5 16 Autoradiograph showing lack of tritium absorption by a thick oxide film formed in O when subsequently exposed to T. Oxidized in O<sub>2</sub> at 600°C for 66.5 hours to a weight gain of 684 mg/dm<sup>2</sup>, exposed to T<sub>2</sub> gas at 800°C for 16.5 hours [139]

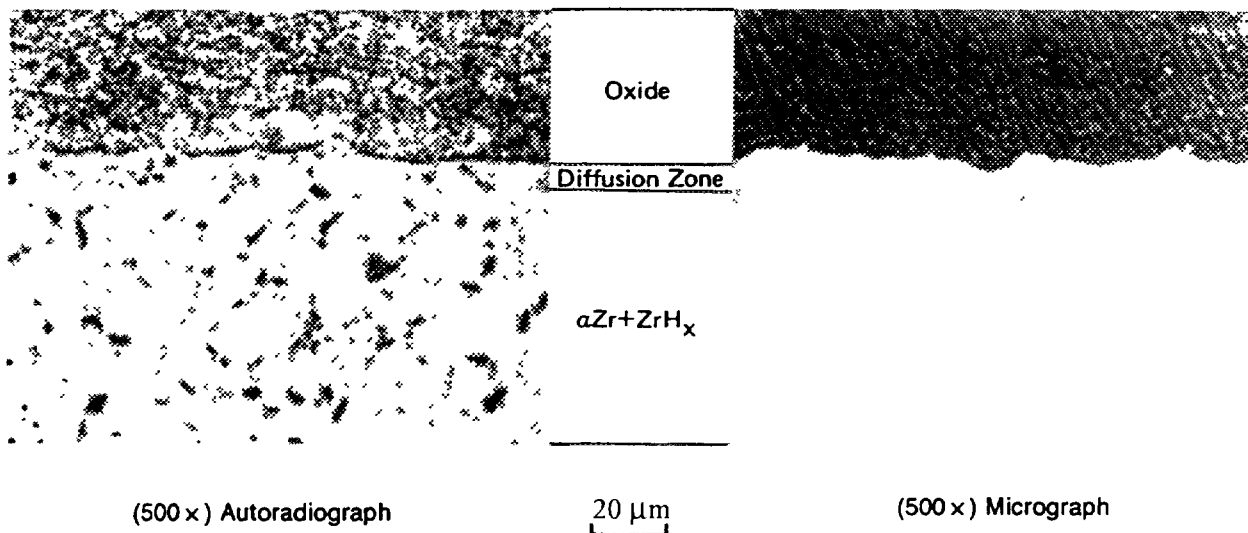


FIG 5 17 Autoradiograph showing tritium incorporated locally in a thick oxide film formed in O when subsequently exposed to T<sub>2</sub>O. Oxidized in O<sub>2</sub> at 600°C for 66.5 hours to a weight gain of 727 mg/dm<sup>2</sup>, exposed to T<sub>2</sub>O vapour at 400°C for 72 hours, additional weight gain 5 mg/dm<sup>2</sup> [139]

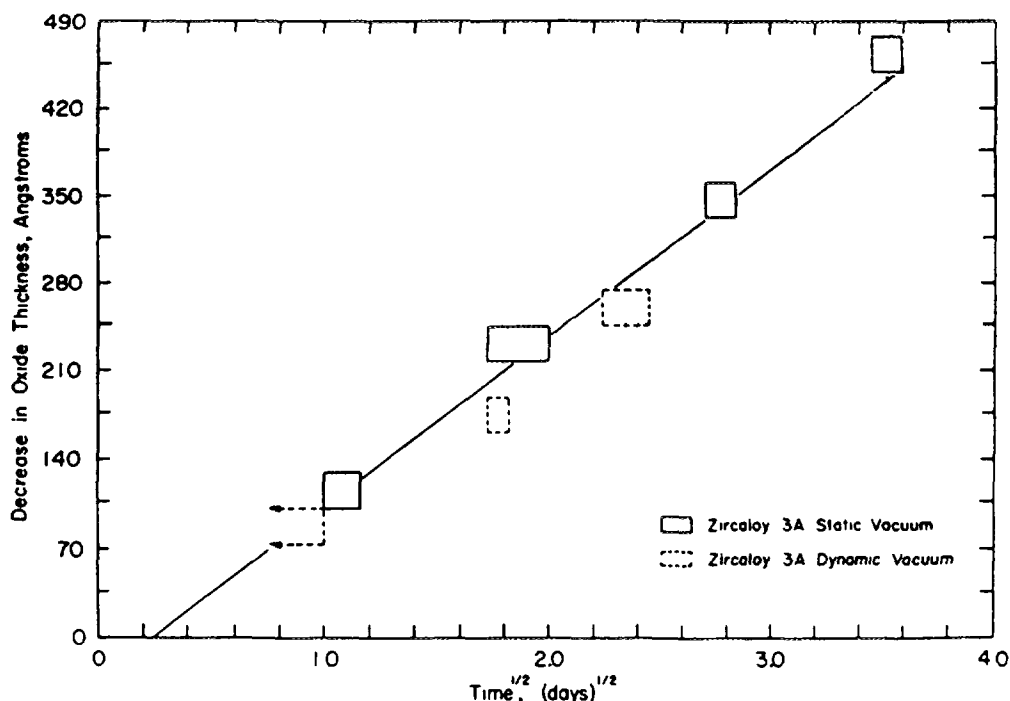


FIG 5 18 Decrease in thickness of interference-coloured oxide films as a function of annealing time in vacuo at 400°C [188]

However, even in regions where cracks form in the outer part of the oxide, the inner layers of the oxide will remain in compression because the new layers of oxide form at the oxide-metal interface by inward diffusion of oxygen. Thus, there will probably always be a thin layer of protective oxide at the bottom of these cracks. This argument is supported by the observation that cracks are visible in the oxide surface formed during oxidation, and yet these oxide films continue to present excellent barriers to the ingress of hydrogen. Hence, such cracks are not the routes by which hydrogen enters the metal, although they may help to initiate, or become part of such a route during the "breakdown" process. That these cracks do not penetrate to the oxide/metal interface is shown in SEM studies of stripped oxide films. Examination of the oxide/metal interfaces [50,189] clearly showed the ridges of thick oxide along grain boundaries (see Figure 4 7d), and the variations in oxide thickness from grain to grain (see Figure 4 7c), but did not reveal any signs of cracks penetrating through to the interface at these locations. In instances when the stripping process induced cracking of the oxide, these cracks generally cut across oxide ridges at grain boundaries (Figure 5 19), suggesting that these sites were not even regions of weakness in the oxide. Only occasionally have cracks running parallel to, and within, the oxide ridges been seen at the oxide-metal interface. Some other route which allows direct access of hydrogen to the oxide/metal interface, must develop during the incubation period, therefore.

When a specimen, with an oxide film such as those above, is heated in an environment (vacuum or  $H_2$ ) containing insufficient oxidant to maintain the normal growth of the oxide, the rate of oxygen dissolution in the metal will exceed the rate of formation of new oxide. Under these conditions, the oxide film will slowly dissolve in the metal. This process has been observed (Figure 5 18) by following the thinning of interference-coloured oxide films in the optical microscope [188,194]. On the scale of resolution of this instrument the dissolution process appears to be uniform provided that the metal core has not become saturated in oxygen [48,194]. However, autoradiography of  $^{18}F$  reveals the oxygen distribution by way of the  $^{18}O(p,n)^{18}F$  reaction [48] and shows that preferential diffusion of oxygen along zirconium grain boundaries occurs.

When the dissolution of oxide films is studied by electron microscopy, examination of the oxide/metal interfaces shows that the thinning of the oxide is not uniform. Because of the preferential diffusion of oxygen along the grain boundaries in zirconium, the dissolution of the oxide ridges at these sites occurs preferentially and inhomogeneously (Figure 5.20). This irregular dissolution of the grain boundary ridges leads to the formation of large pores in the oxide. These pores are thought to pass right through the oxide film because similar rows of pores have been seen when oxide films on specimens exposed to low oxygen partial pressure environments were viewed from the outside by a replica technique (Figure 5.21). These pores also occur in the oxide away from the prior metal grain boundaries, perhaps because of enhanced local oxygen diffusion at incoherent twins, or dislocation pile-ups.

The uniform dissolution of the bulk of the oxide, seen in the interference colour studies [188,194], is probably the process which leads to the observed drop in oxide resistivity [184,186]. However, the preferential dissolution of the oxide at grain boundaries, and other sites, which leads to the formation of arrays of pores at these locations, is probably the process which terminates the incubation period, and leads to the rapid direct reaction of hydrogen with the metal. Since these pores appear to pass right through the oxide, there will be no oxygen diffusion barrier to prevent such a reaction at these sites. Thus, none of the investigations which purported to measure the diffusivity of hydrogen in  $\text{ZrO}_2$  by exposing pre-oxidised specimens in hydrogen gas will have measured such a quantity, and alternative techniques for measuring the hydrogen diffusion coefficient in  $\text{ZrO}_2$  must be applied.

It cannot be concluded that similar flaws will be generated in oxide films on other alloys during exposure to low  $p(\text{O}_2)$  environments. However, similar pores have been observed to develop in thin ( $\sim 1 \mu\text{m}$ ) oxide films on Zr-2.5%Nb alloy specimens after heating at  $380^\circ\text{C}$  in a low pressure hydrogen environment [202], although no correlation with metal grain boundaries could be made in this instance. The general features of localised oxygen dissolution into the metal interacting with local variations in oxide properties will probably be common to all instances. However, if the original oxide is thick and already relatively porous, the stresses set up by the oxygen dissolution process in the oxide near to the interface may lead to local cracking of any residual protective barrier oxide, rather than the generation of the regular pores observed above. Individual examination of specimens by high resolution techniques would be needed to characterise any actual instance.

### 5. 1. 3. Hydrogen absorption via metallic contacts

Although hydrogen absorption through a metallic contact may be the most trivial of the four mechanisms mechanistically, it nevertheless has important practical aspects as it may be one route for ingress of excess deuterium into the ends of pressure tubes (Figure 5.22) from the 403 SS end fitting [157]. The zirconium alloy pressure tube is in good metallic contact with the end-fitting steel in the three grooves of the rolled joint. The factors which control ingress by such a route should, therefore, be considered.

When a galvanic couple between a zirconium alloy and a nickel or iron alloy is exposed to high temperature water the zirconium alloy becomes anodic and the transition metal alloy cathodic. The cathodic part of the corrosion process then occurs on the transition metal surface and protons are discharged there and may be absorbed by the transition metal. The effective surface areas of the two parts of the couple will be determined by the conductivity of the water, and in high purity water only small areas adjacent to the point of contact should be effective, although under irradiation this limitation may be relaxed by the effect of irradiation on the conductivity of the electrolyte [195,196]. The distance from the points of closest approach of the two metals in the water and the point of metallurgical contact will be important for the hydrogen migration, but not for the oxidation. This is

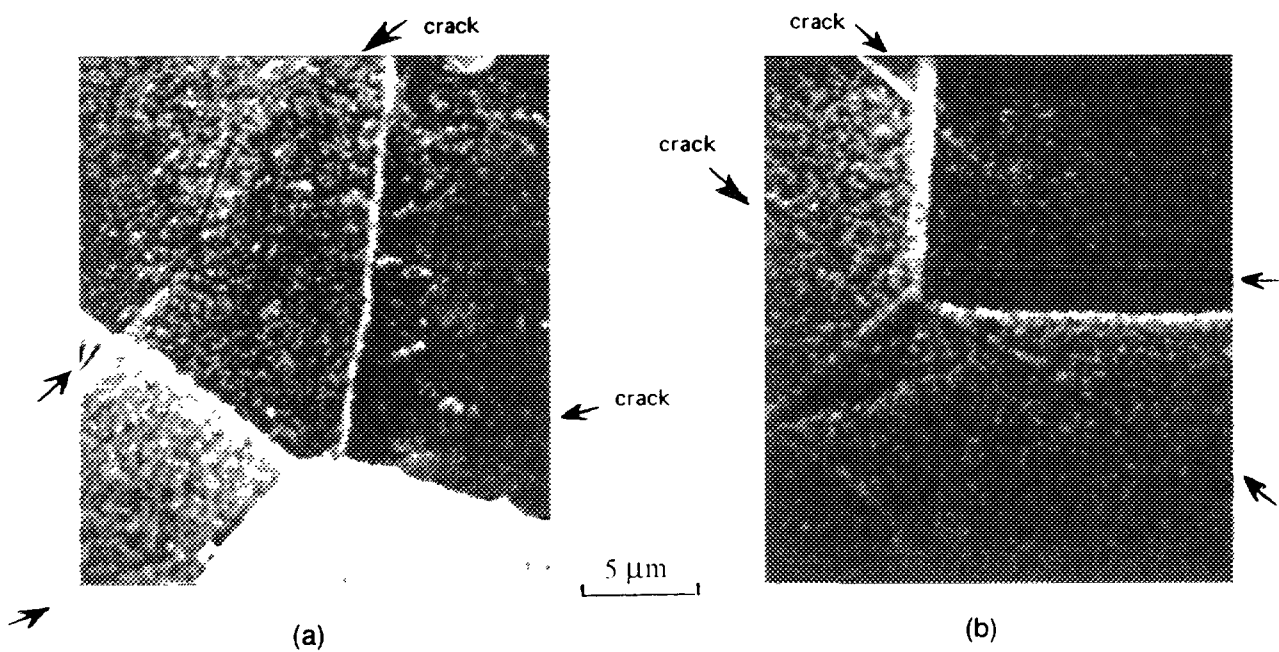


FIG. 5. 19. Oxide-metal interface of stripped oxide films showing cracks induced by the stripping process (3,000 $\times$ ). Note that these cracks do not follow the oxide ridges observed in these thin films [189].

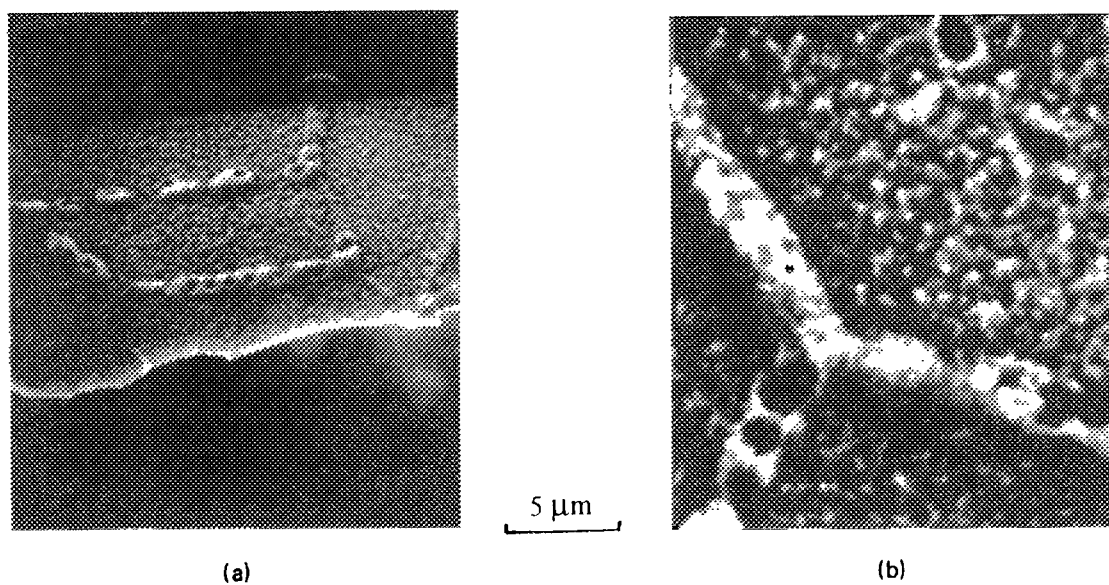


FIG. 5. 20. Oxide-metal interface of a specimen after oxidation and subsequent vacuum annealing at 500°C. Note the break-up of the oxide ridges and the formation of pores along the prior metal grain boundaries. (a) 1,000 $\times$ , (b) 3,000 $\times$  [189].

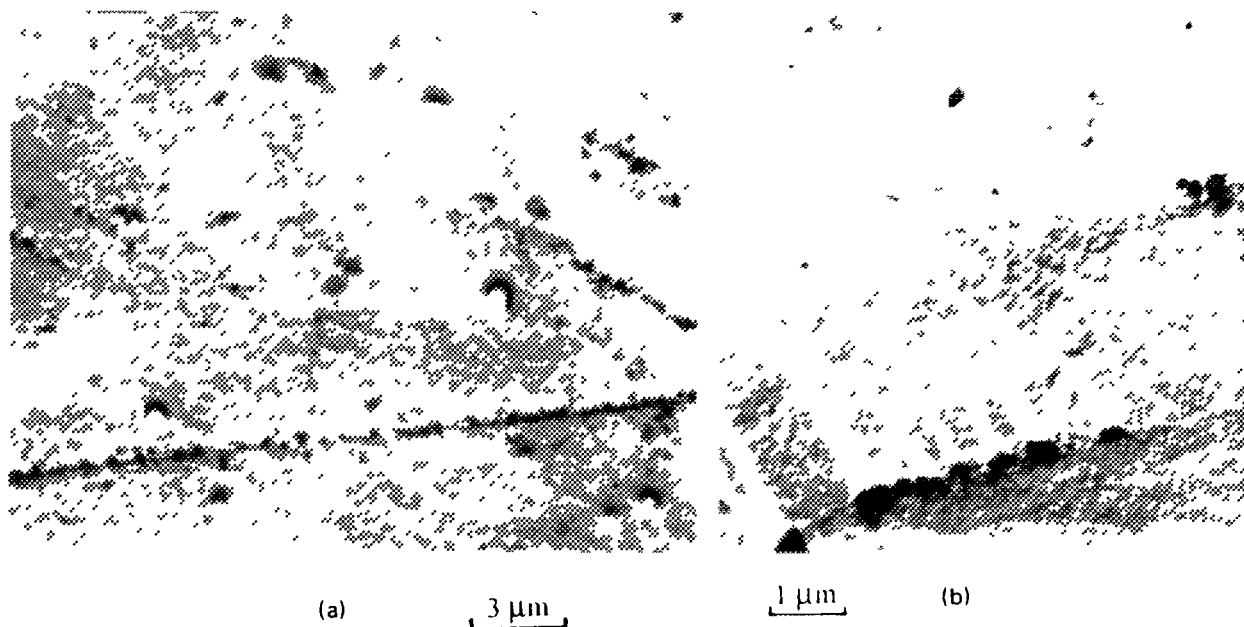


FIG 5.21 Replica of the zirconium oxide surface of a specimen heated in a low oxygen partial pressure environment (He). A similar array of pores is observed to those seen in the previous FIG. Note that the diameter of the pores at the surface appears to be smaller than that observed at the oxide-metal interface. (a)  $4\,000\times$  (b)  $10\,000\times$  [189]

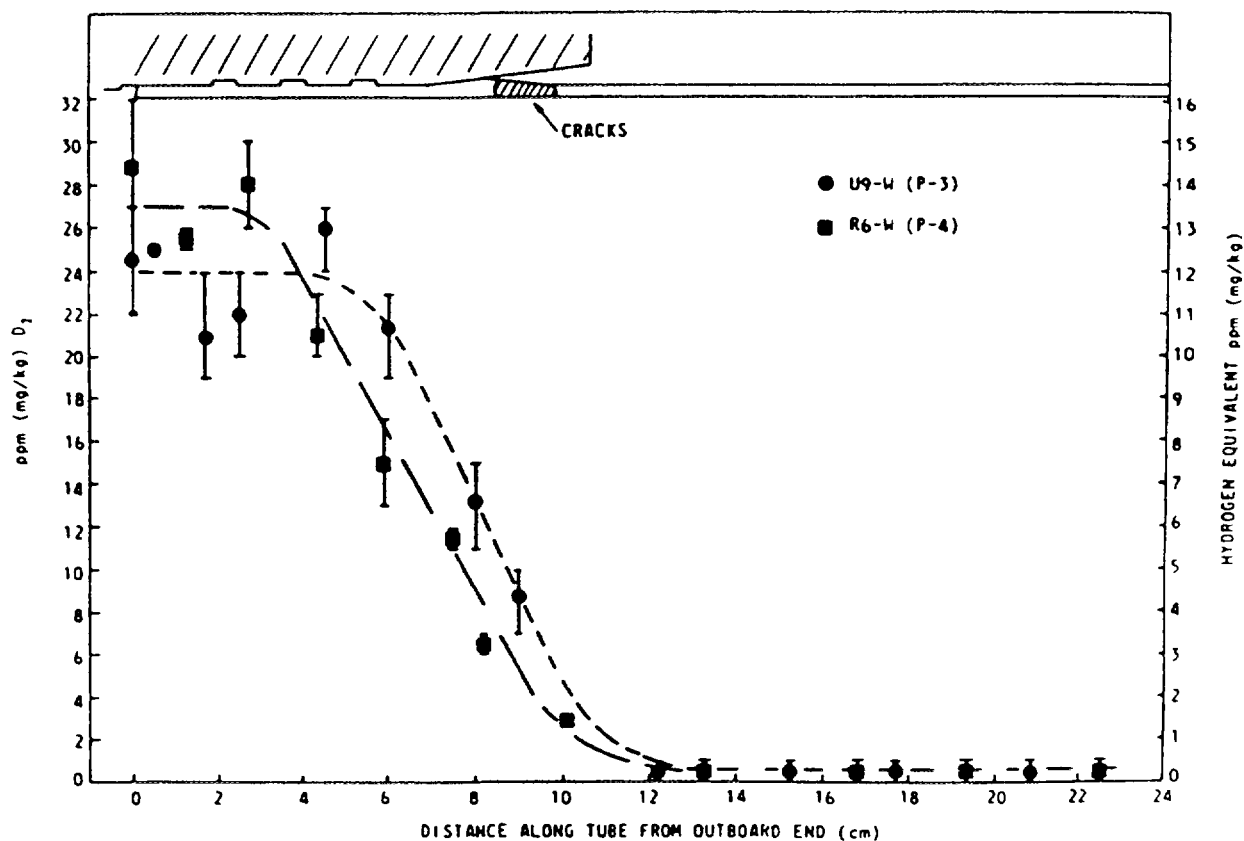


FIG 5.22 Increase in the deuterium concentration at the inlet ends of two Zr-2.5%Nb alloy pressure tubes in the Pickering reactors as a result of diffusion from the end-fitting steel [157]

evident in the instance of localised oxidation opposite a platinum implant [195,196], where the electrical contact was distant from the point of closest approach of the platinum implant and the facing zirconium surface. In this instance, accelerated oxidation but no excess hydriding occurred, whereas adjacent to the platinum implant both accelerated oxidation and enhanced hydrogen contents were observed.

In the case of the Inconel to Zircaloy bonds [195,197], where the interface between the Inconel and the Zircaloy-2 was exposed to the water, and diffusion distances for both hydrogen and electrons were short, both excess oxidation and excess hydriding were observed adjacent to the bond. No enhanced hydrogen uptake was observed in Zircaloy/Zircaloy crevices [196,197], but enhanced oxidation was seen, perhaps from enhanced radiolysis or from LiOH concentration [530]. Although it might be expected that the diffusivity of hydrogen in the transition metal would affect the rate of migration into the zirconium alloy via the metallurgical bond, there is no evidence for a comparison (say) between Inconel and stainless steel. However, where high temperature water is in contact with zirconium alloy/transition metal bonds close to, or at, the interface between them, the rate of the cathodic reaction on the transition metal may be more important than the hydrogen diffusivity in it. In these circumstances, the higher nickel content of Inconel than of stainless steel and the specific effects of nickel with regard to the hydrogen recombination reaction may mean higher excess hydrogen absorption for zirconium alloy/Inconel bonds than for zirconium alloy/stainless steel bonds. This seems to be borne out by the results of Urbanic's [198] experiments on Zr-2.5%Nb tubes with plugs of various metals inserted in them. If these results are compared with some properties of the various metals (Table 5.3) it would appear that the exchange current density for the hydrogen evolution reaction is more important than the hydrogen permeability in determining the uptake by zirconium alloys. However, there is insufficient evidence at present to reach a firm conclusion about the important factors determining the rate of excess hydrogen uptake in zirconium alloys metallurgically bonded to transition metals; the indications are that we should look at the efficiency of the coupled metal as a cathode, rather than its diffusion properties. However, if a crevice is also involved at the point of contact, then possible changes in both corrosion and hydrogen uptake rates within the crevice may be involved in the overall phenomenon.

#### 5.1.4 Hydrogen uptake during cathodic polarisation

Cathodic polarisation of zirconium alloys in an electrolyte, such as sulphuric acid, at room temperature will produce a solid surface hydride layer on zirconium alloys at current efficiencies typically <1% [199]. This technique has been used for charging specimens at low temperature so that the structure is not disturbed by the use of elevated temperatures. Several similar techniques for cathodic charging at elevated temperatures have also been reported using fused caustic soda or aqueous solutions at temperatures of 300-350°C [200,201]. Current efficiencies again are very low and tend to be very variable. As a result such methods have not gained acceptance because of the difficulties in metering in known quantities of hydrogen - the usual aim of such techniques. An analogous cathodic uptake process can also occur in chemical polishing solutions (e.g.,  $\text{NH}_4\text{HF}$ ) that do not contain nitric acid. The pitting process that often results from localised anodic dissolution under poor pickling conditions can also give hydriding at the corresponding cathodic sites where the hydrogen evolution reaction occurs.

In practical situations the cathodic polarisation can be achieved by a galvanic couple between the zirconium alloy and a sacrificial anode (usually an aluminium alloy). In the laboratory it is difficult to get any significant hydrogen uptake by this process in typical reactor water. This results from a combination of the low conductivity electrolyte and the relatively high resistivities of the oxide films normally present on both zirconium and aluminium surfaces. However, a number of observations of significant hydriding in low temperature reactors, such as Hanford Production Reactors and Research Reactors (e.g. ATR), have been reported [128,201-207]. In these situations some of the restraints that made it difficult to achieve significant hydriding in attempted laboratory simulations seem to be relaxed. In particular, it is thought that irradiation enhances the conductivity of both the oxide films on the two metals and of the reactor water to the point where significant galvanic currents can be passed during irradiation that would not be possible in its absence.

Table 5.3. Comparison of hydrogen uptake by zirconium alloy/metal couples with physical properties of the coupled metal.  
(References refer to the original table in Ref. [189])

Metal	Exchange current density for H <sub>2</sub> (1) (log i <sub>0</sub> )	Diffusion coeff. of H <sub>2</sub> at 400°C (cm <sup>2</sup> .s <sup>-1</sup> )	Enthalpy of solution of H <sub>2</sub> (kcal/mol)	Permeability to <sup>3</sup> H at 400°C (cm <sup>3</sup> (STP)mm.h <sup>-1</sup> .cm <sup>-2</sup> atm <sup>-1/2</sup> )	Hydrogen uptake	
					Ref. [197] (2)	Ref. [198] (3)
Cu	-6.70	9.0 x 10 <sup>-6</sup> (4)	+0.47 (4)	3.6 x 10 <sup>-4</sup> (5)	-	13
Fe	-5.93	1.5 x 10 <sup>-4</sup> (4)	+0.28 (4)	1.5 x 10 <sup>-1</sup> (6)	-	-
Inconel	-5.46	8.0 x 10 <sup>-7</sup> (7)	-	5.4 x 10 <sup>-3</sup> (7)	152	-
304 S/S	-5.37	3.0 x 10 <sup>-7</sup> (8)	-	3.5 x 10 <sup>-3</sup> (6)	-	380
403 S/S	-	5.8 x 10 <sup>-5</sup> (9)	-	4.6 x 10 <sup>-2</sup> (9)	-	1380
Ni	-5.17	5.0 x 10 <sup>-6</sup> (4)	+0.16 (4)	3.0 x 10 <sup>-2</sup> (6)	-	3780
Pt	-3.73	5.1 x 10 <sup>-3</sup> (4)	+0.75 (4)	1.1 x 10 <sup>-3</sup> (6)	354	>10000(9)

- (1) Comprehensive Treatise of Electrochemistry, Vol.2, Eds. Bockris, Conway, Yeager & White, Plenum, NY, 1981.
- (2) mg/kg H<sub>2</sub> in Zircaloy-2 after 60 d coupled to metal in 300°C water under irradiation.
- (3) Peak H<sub>2</sub> concentration at centre of Zr-2.5 wt% Nb tube after 10 days in pH10 LiOH with 1.1 MPa H<sub>2</sub> overpressure.
- (4) J. Völkl and G. Alefeld, Chapter 5, Diffusion in Solids, Recent Developments, Eds. Nowick and Burton, Ac. Press, New York, 1975.
- (5) G.R. Caskey et al., Corrosion, 1976, 32 (9).
- (6) R.W. Webb, Permeation of H through Metals, NAA-SR-10462 (1965).
- (7) W.M. Robertson, Met. Trans. A, 1977, 8A.
- (8) M.R. Louthan and R.G. Derrick, Corr. Sci., 1975, 15.
- (9) V.F. Urbanic [198].

In high temperature reactors or reactor loops, there is no well established instance where cathodic hydrogen uptake has been demonstrated. Since aluminium alloys, the only likely sacrificial anodes, are not usually present under these conditions, it is probably this factor rather than any other that results in the absence of such in-reactor observations. In a recent experiment, where samples were cathodically polarised in a dilute  $\text{Na}_2\text{SO}_4 + \text{CuSO}_4$  solution at  $300^\circ\text{C}$  [31], extensive hydriding occurred, so the presence of any stray polarising currents in-reactor could be just as effective as galvanic contacts if they were present.

## 5.2 EFFECTS OF HYDROGEN CONTENT ON OXIDATION

Provided the hydrogen content of the alloy is maintained in solid solution there seems to be no reason to expect any effect on the oxidation process. Suggestions that the oxidation rate of bulk zirconium hydride, however, is faster than that of unhydrided zirconium remain anecdotal [208]. Thus, once the terminal solid solubility (TSS) of hydrogen at the oxidation temperature is exceeded an effect of hydride on the oxidation rate may be dependent upon whether or not hydride particles are present at the oxide-metal interface (i.e. whether oxygen ions diffusing through the barrier oxide layer at the interface find a  $\text{ZrH}_x$  layer or an  $\alpha\text{-Zr}$  layer to react with). However, such effects have been explained as a result of surface damage (cold work) caused by hydride precipitation rather than from the presence of the hydride particles. The distribution of hydrides at, or near, the oxide/metal interface is determined by local variations in the effective TSS, interaction of hydrogen and oxygen in solution in zirconium to affect the hydrogen activity [209,210], the temperature gradient and the local stress gradient at the oxide metal interface.

If the hydrogen solubility (TSS) were a unique quantity at every point in the zirconium alloy, then once the solubility was exceeded, any hydrogen subsequently absorbed should precipitate as a layer of solid hydride at the surface. This surface would be the surface through which the hydrogen was gaining entry, for an isothermal component, or the coldest surface of the component in the presence of temperature gradients [211]. However, there are preferred sites for hydride precipitation in zirconium alloys (i.e. the solubility is not a fixed quantity at every point), so that hydrides precipitate relatively uniformly throughout isothermal specimens, and as a broad diffuse band near the outer (colder) surface of fuel cladding [211,212]. These local variations in solubility permit the solubility to be progressively exceeded within isothermal specimens as small concentration gradients can continue to exist even in the two phase ( $\alpha\text{-Zr} + \delta\text{-ZrH}_2$ ) region. These effects are accentuated when the specimens are thermally cycled as a result of the additional effect of the hysteresis between the heating and cooling curves for hydrogen solubility [213,214]. In combination these effects lead to the "supercharging" phenomenon, whereby, during hydrogen absorption, concentrations well above TSS can be achieved throughout isothermal specimens [215-220].

The diffusion of hydrogen in zirconium metal is very rapid [221-223], so that the hydrogen diffusivity away from regions of hydrogen ingress is generally greater than that of most hydrogen uptake processes occurring during corrosion. It is uncommon, therefore, to observe layers of solid hydride at the surface of specimens corroded in high temperature aqueous solutions under isothermal conditions. This can be achieved if the hydrogen ingress rate is high enough to exceed the rate of hydrogen transport into the bulk of the metal. In practice this can be achieved during isothermal corrosion in concentrated  $\text{LiOH}$  solutions [102,103,219,224-226] and during reaction with gaseous hydrogen. Data from such experiments have been used to estimate the critical hydrogen fluxes that must be achieved before solid hydride is observed at specimen surfaces [227] during isothermal experiments.

A further calculation of the critical flux of hydrogen needed to maintain solid hydride at the hot inside surface of fuel cladding has been made by Markowitz [228], who predicts that an ingress rate of  $0.181 \text{ mg cm}^{-2} \text{ s}^{-1}$  at  $\sim 300^\circ\text{C}$  must be achieved. This is much higher than the critical rates necessary during isothermal experiments ( $\sim 2 \times 10^{-3} \text{ mg cm}^{-2} \text{ s}^{-1}$  at  $300^\circ\text{C}$ ) and which can be achieved in concentrated  $\text{LiOH}$  (see Figure 4.49). Rates such as that predicted by Markowitz can only be achieved by the direct reaction of a gaseous hydrogen atmosphere with a bare metal surface. Initial



rates for this reaction, which is dependent upon  $[p(H_2)]^{1/2}$ , can be estimated from the work of Gulbransen and Andrew [182,229]. If it can be assumed that the  $[p(H_2)]^{1/2}$  dependence of these rates extends to reactor operating pressure then an initial ingress rate of  $2.5 \text{ mg cm}^{-2} \text{ s}^{-1}$  is achievable at  $300^\circ\text{C}$  and 15 MPa inside a defected fuel pin once all the oxygen from the water has reacted. These rates decrease parabolically with time as they become controlled by diffusion through the thickening layer of solid hydride that forms. A corollary of this is that a much lower rate of hydrogen ingress is capable of maintaining a solid hydride layer on the cold outer surface of fuel cladding when the hydrogen ingress process is occurring at this surface.

Another factor which influences the distribution of hydrides is the interaction between interstitial hydrogen and oxygen in  $\alpha$ -zirconium [209,210]. This only becomes significant at high oxygen concentrations in solid solution. Typically, these are only found in the oxygen diffusion zone that develops beneath the oxide film during oxidation at high temperatures ( $\geq 500^\circ\text{C}$ ). However, the presence of stresses induced by the oxide growth process in this region may also affect the hydrogen distribution. It is these effects that are responsible for the hydride (tritium) free layers observed on the zirconium side of the oxide/metal interface (see Figure 4.50) in tritium autoradiography experiments [139] and for the subsurface hydrogen peaks observed in specimens examined by NRA techniques [170,171,230,231]. These are probably also the reasons why an increase in the oxidation rate of Zircaloy-2 specimens in  $500^\circ\text{C}/1 \text{ atm}$  steam was not observed when the hydrogen TSS was exceeded [158] even though a reduction in hydrogen uptake rate was observed after this occurred. An increase in oxidation rate was found in these experiments [232,233] at high hydrogen contents (Figure 5.23). However, examination of the oxide surfaces showed that gross cracking had taken place, and the increased oxidation rate could not be unequivocally ascribed directly to the hydrogen content.

Surface damage by hydrogen ingress had previously been reported by Schwartz and Vaughan [208]. They argued that the process of pre-hydriding specimens produced the equivalent of a cold worked surface that caused increased corrosion. This effect was seen whether the hydrogen was extracted (to less than 100 ppm) or not before corrosion. Both sets of specimens were given the same thermal treatment and no subsequent re-preparation of their surfaces. This explanation did not seem to be borne out when specimens pre-hydrided to a maximum of 3,000 ppm H by gaseous hydriding at  $400^\circ\text{C}$  showed no accelerated oxidation and gave oxidation rates within (but at the top of) the scatter band for all as-received specimens of the same Zircaloy batch in  $500^\circ\text{C}$ , 1 atm steam [158]. Even pre-hydrided specimens that did not have their surfaces carefully re-prepared (by grinding and attack polishing) showed only slightly higher oxidation rates (Figure 5.24). In addition a pre-hydrided specimen (1,850 ppm H) held in a temperature gradient ( $300\text{--}350^\circ\text{C}$ ) showed no accelerated oxidation on its cold surface after more than 50 days exposure (weight gains still in the pre-transition range) in 1 atm steam.

It was concluded from this work that in order to see an effect the hydrogen had to be absorbed during corrosion, and that the mechanism might be degradation of the oxide as a result of the volume change in the metal near the oxide/metal interface resulting from the hydride precipitation. This conclusion seems to be supported by results obtained by Wanklyn [28] for specimens cathodically polarised for 48 hrs in  $325^\circ\text{C}$  water (+ electrolyte), where cathodically polarised specimens had less protective oxide films. However, this degradation was observed irrespective of the amount of hydrogen absorbed (i.e. the current efficiency of the cathode reaction Table 5.4) suggesting that it might be the passage of the current itself that was degrading the oxide films [28]. Nevertheless several more recent studies [234-236] have claimed to see accelerated oxidation rates for pre-hydrided specimens. Garde used specimens of fuel cladding pre-hydrided in long 633K autoclave tests in water and by gaseous hydriding in  $400^\circ\text{C}$  (673K) hydrogen. Garde's specimens had their outer surfaces only re-prepared by grinding on SiC paper. Kido's surfaces were not re-prepared after hydriding, and these surfaces were not compared with specimens where the hydrogen was subsequently removed as in the experiments of Schwartz and Vaughan [208]. Re-preparing specimens after hydriding by pickling the surface may still leave the surfaces heavily pitted. An effect of the pitting at hydrides (during re-preparation by pickling) on the ensuing oxidation rate was the only effect observed when

Table 5 4 Hydrogen uptake and film properties of polarized and unpolarized specimens  
(Duration of experiments, 48 hours at 325° C Current density, 0.15mA/cm<sup>2</sup>)

Alloy	Specimen Number	Unpolarized				Polarized					
		Hydrogen uptake ppm	Weight Gain, W, mg/cm <sup>2</sup>	Capacity C, $\mu$ F/cm <sup>2</sup>	1/CW <sup>*</sup>	Hydrogen uptake ppm	Hydrogen uptake mg/cm <sup>2</sup>	Hydrogen uptake %	Weight Gain, W, mg/cm <sup>2</sup>	Capacity, C, $\mu$ F/cm <sup>2</sup>	1/CW <sup>*</sup>
Unalloyed	(10/1) 9	Not detected	0.076	0.181	73	44	0.006	2.1	0.15	0.89	7.3
	(8/2) 24	16	0.075	0.158	84	55	0.006	2.3	0.22	0.50	9.1
	(10/1) 33	-	-	-	-	68	0.009	3.3	0.19	0.40	13
Ni-0.1wt%	10	28	0.11	0.092	99	730	0.084	26	0.36	0.27	10
	32	24	0.08	0.55	220	950	0.120	35	0.30	0.26	13
	20	-	-	-	-	950	0.122	36	0.38	0.29	9.2
Ni-0.5wt%	8	73	0.10	0.073	137	950	0.103	39	0.38	0.11	25
	11	56	0.09	0.069	161	1800	0.214	70	0.31	0.25	13
	17	98	0.09	0.053	210	-	-	-	-	-	-
	19	-	-	-	-	980	0.126	51	0.31	0.14	24
Fe-0.1wt%	12	Not detected	0.054	0.077	240	39	0.004	1.4	0.11	0.18	49
	16	Not detected	0.079	0.086	147	55	0.006	1.8	0.11	0.23	40
	21	-	-	-	-	170	0.016	6.1	0.11	0.20	46
	22	-	-	-	-	180	0.020	6.2	0.14	0.19	40
Sn-0.7wt%	23	34	0.12	0.156	53	230	0.023	7.8	0.40	0.40	6.2
	25	22	0.21	0.146	33	100	0.013	4.7	0.36	0.46	6.1
	26	-	-	-	-	-	-	-	-	-	-
Pt-0.5wt%	13	75	0.13	0.066	117	510	0.061	19	0.16	0.12	52
	14	50	-	-	-	870	0.099	43	0.17	0.12	49
	18	83	0.11	0.049	185	910	0.087	27	0.17	0.12	51
Zircaloy-2	1	10	0.14	0.055	129	220	0.030	9.9	0.10	0.12	84
	2	Not detected	0.11	0.041	224	210	0.032	14	0.09	0.15	73
	3	2.5	-	-	-	200	0.029	13	0.10	0.11	98

\* A perfect ZrO<sub>2</sub> film should give a 1/CW value in the range 260-280. Lower values than this indicate a variety of defects in the film. The lower the 1/CW value the more defective is the oxide film.

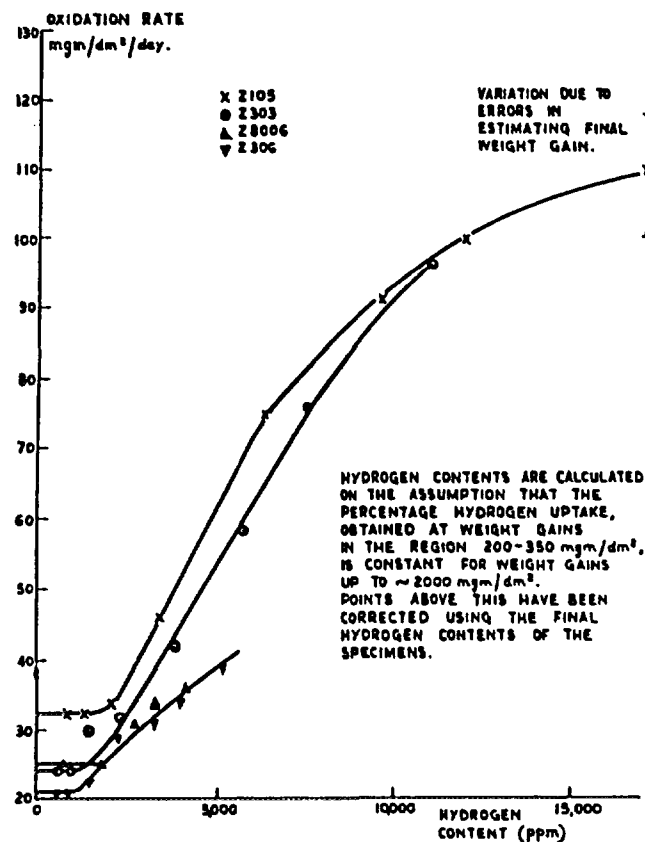


FIG. 5. 23. Post-transition oxidation rates versus estimated hydrogen content for long oxidations of Zircaloy-2 in 500°C atmospheric pressure steam. Note that severe cracking of the specimens occurred (with a corresponding increase in available surface area) for weight gains above about 1000 mg/dm<sup>2</sup> [233].

the hydrogen subsequently went into solution during oxidation [237]. The post-hydriding weight gain data in either 633K (360°C) water or 673K (400°C) steam must therefore be treated with caution, as should any argument that explains differences in the final oxidation rate, or the time to transition, on the hydrogen content in the initial long-term corrosion tests because of the small data base. This totalled 6 specimens including 4 different cladding batches with two different (pickled, belt ground) initial surface treatments (on some specimens, inside and outside surface preparations differed) and no control specimens where the wall thickness was varied in order to vary the time at which TSS was reached. It is uncertain, therefore, whether any clearly demonstrable effect of hydride content can be based on this work.

The work of Kido [235,236] apparently shows evidence (Figure 5.25) of a hydrogen content effect that is less equivocal. The specimen surfaces were not re-prepared, so that arguments about the effect of hydriding damaging the surface cannot be answered. If the oxygen partial pressure at the start of gaseous hydriding was low, then little incorporation of oxygen in the surface would have occurred and effects from this source would be absent. Clearly, increased corrosion curves in 360°C (633K) water were observed, as was deeper penetration of the oxide metal interface along heavily hydrided regions in the banded hydride structure on the cut ends of the fuel cladding specimens. Thus, there may be less doubt that an effect of hydrogen content was seen in this instance than in some other studies. However, the regions of thicker oxide were much broader than the hydride

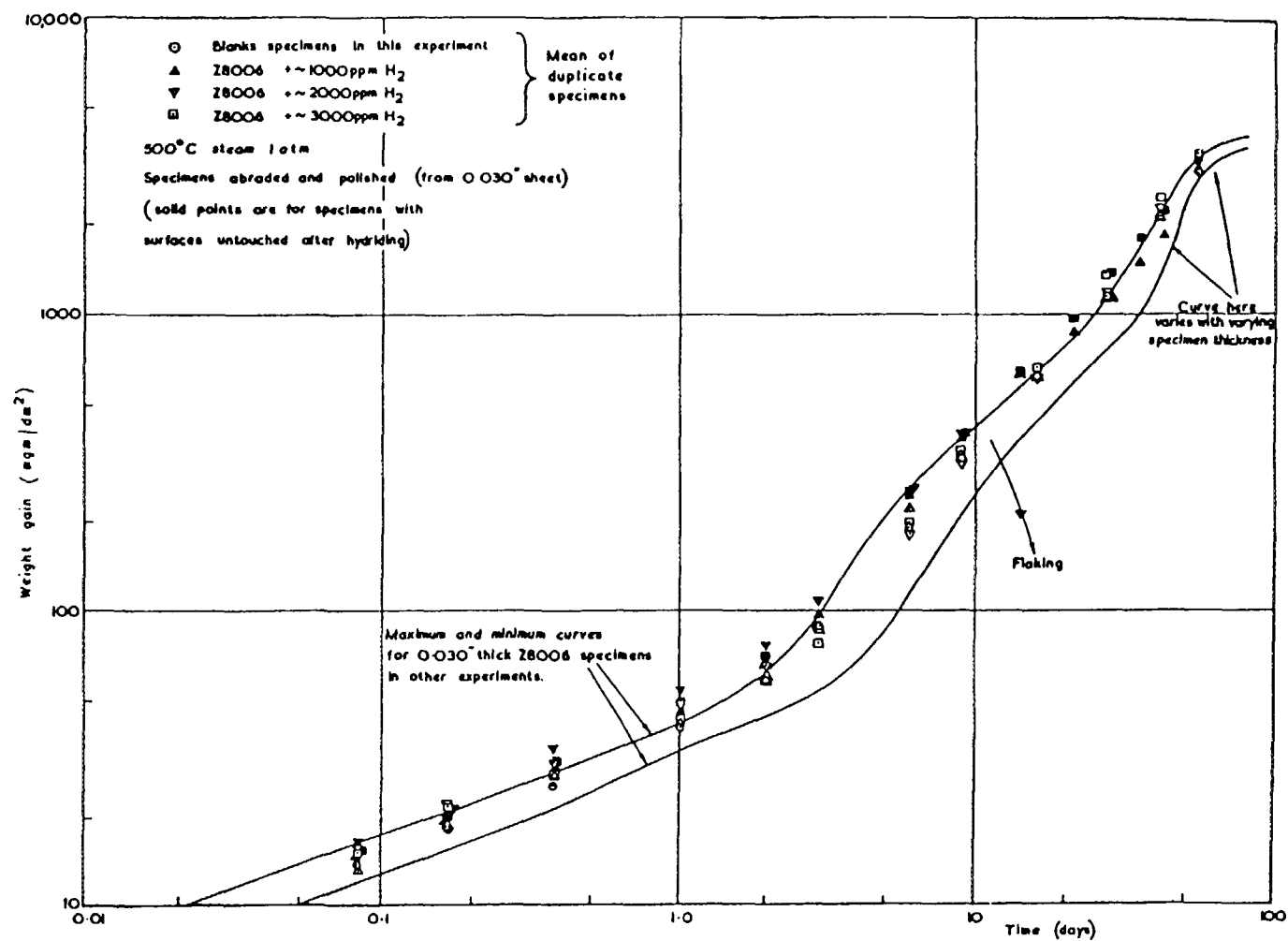
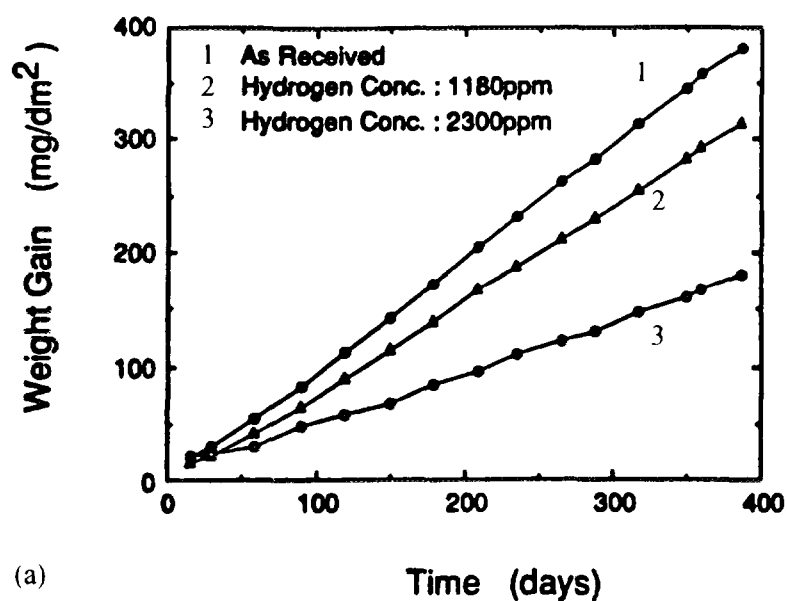
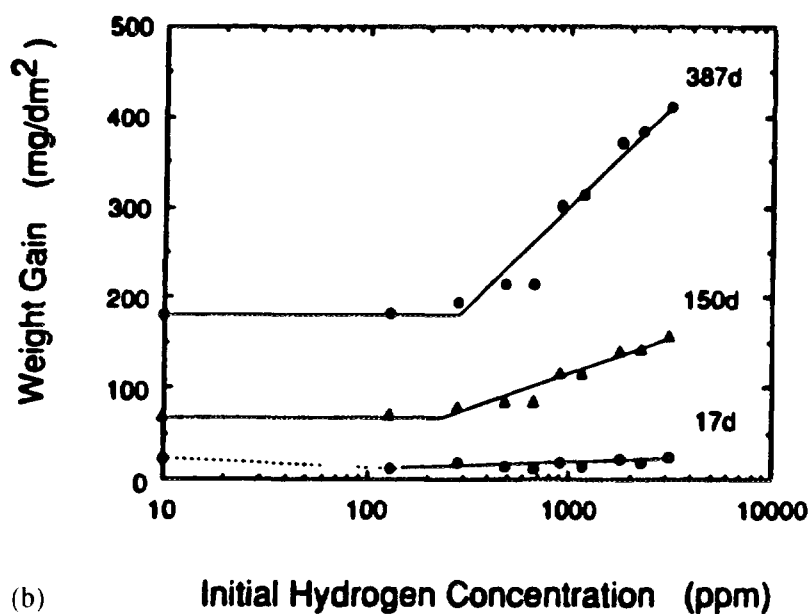


FIG. 5. 24. The effect of the initial hydrogen content on the oxidation of Zircaloy-2. Specimens were pre-hydrated in hydrogen gas at 400°C; half of them had their surfaces re-prepared by abrading and attack polishing (to produce a smooth surface without the gross pitting that occurs if pre-hydrated specimens are pickled); all were oxidized in 500°C atmospheric pressure steam in the same furnace [158].



(a)



(b)

FIG. 5.25 Effect of hydrogen content of pre-hydrated specimens on corrosion of Zircaloy-4 in 360°C (633K) water (a) Comparison of 633K corrosion weight gains for three samples with different initial hydrogen concentrations (b) 633K corrosion weight gains for all specimens at 17, 150 and 387 days as a function of initial hydrogen concentration [236]

platelets and the increased local oxide thickness was much smaller than the size of the effect predicted from the weight gains. Thus, an alternative explanation of these results may still be possible.

Finally, in recent tests in which fuel cladding samples were cathodically polarised in dilute  $\text{CuSO}_4$  solution at  $300^\circ\text{C}$  [31] for much longer times ( $\sim 120$  days) than Wanklyn's specimens [28], increases in corrosion rate of a factor of 2-3 were seen. Specimens were heavily hydrided, and because of the relatively low temperatures the hydrides were concentrated close to the oxide-metal interface. In some regions the concentration at the interface was near to being a solid hydride layer (Figure 5.26). If a rough estimate of the local hydrogen contents at the oxide/metal interface is made from the metallographs then these data can be plotted on a normalised plot of oxidation rates, along with the other positive results (Figure 5.27). The tests cannot eliminate an explanation that the effect was the result of damage to the oxide, rather than the presence of hydride, however.

We have still not resolved the question of whether prehydriding specimens gives different results from hydriding during the corrosion reaction, because of the uncontrolled effects of surface condition in the former situation and the hypothesis that the passage of hydrogen through the oxide film damages it [28,208]. However, it is becoming apparent that there may be a positive effect of hydrogen concentration on the oxidation rate of the Zircaloys, and that factor should be recognised in modelling the behaviour of high burnup fuel cladding. It appears that such effects are most likely to be observed when local conditions are such as to produce local layers of solid hydride at the metal oxide interface [31,235,236]. Knowing just when such hydride layers are present in fuel cladding is not easy as local temperature gradients both through wall and longitudinally at pellet/pellet interfaces are important factors. Inclusion in models of an effect of hydride on fuel cladding oxidation cannot, therefore, on present evidence, be based merely on average hydrogen contents [238].



FIG. 5. 26. An almost continuous band of solid hydride adjacent to the oxide/metal interface in a specimen of Zircaloy-4 fuel cladding cathodically polarised in  $300^\circ\text{C}$   $\text{Na}_2\text{SO}_4$  for 120 days [31].

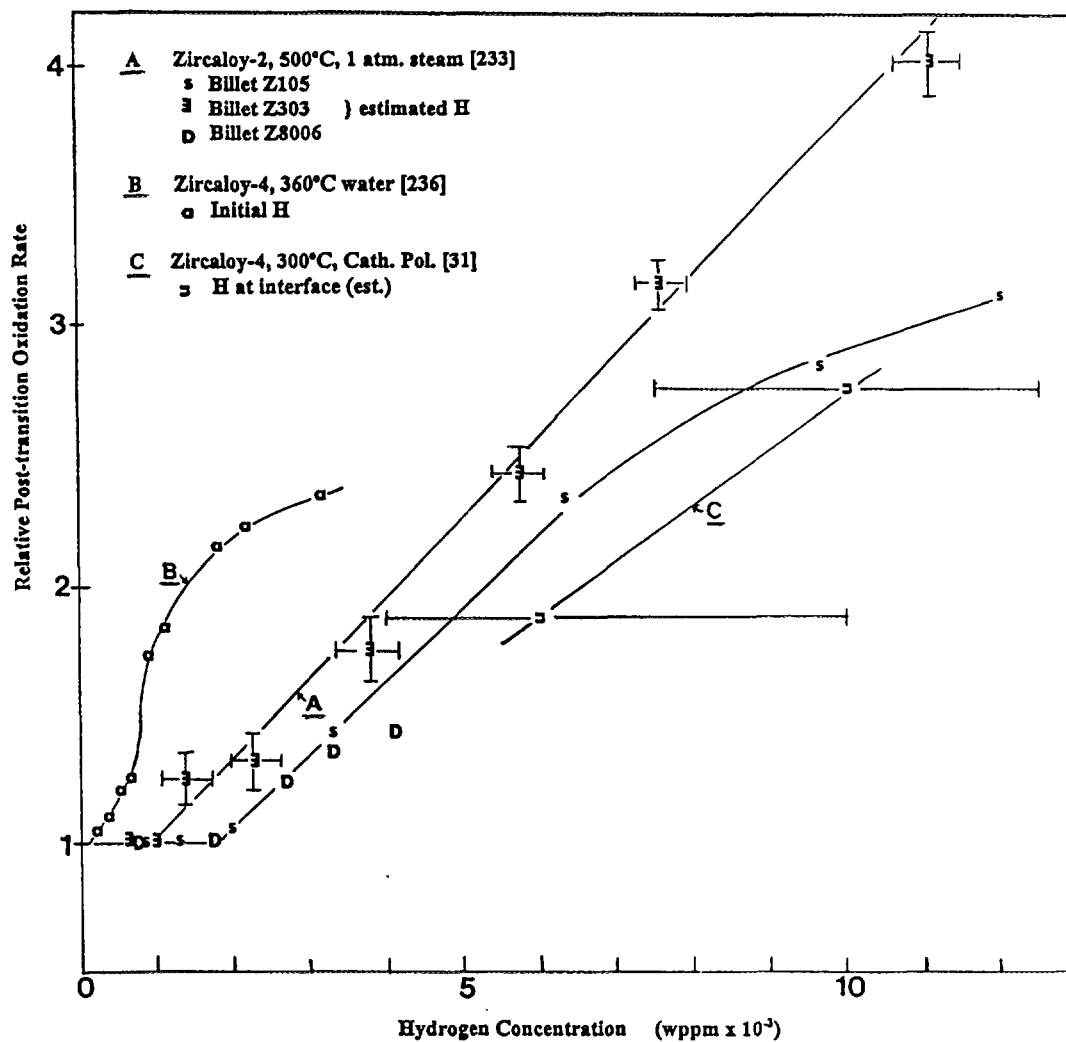


FIG. 5. 27. A comparison of various experiments showing an increase in oxidation rate with hydrogen content where different hydrogen ingress methods were applied. (a) Normal H increase during 500°C oxidation [233]. (b) Prehydrogenating in  $H_2$  gas at 400°C [236]. (c) Cathodic polarisation during 300°C aqueous corrosion [31].

## 6. FACTORS AFFECTING THE CORROSION OF ZIRCONIUM ALLOYS IN REACTORS

The first three Chapters dealt with the fundamentals of zirconium alloy corrosion and metallurgy. This was followed, in Chapters 4 and 5, by detailed discussions of corrosion and hydriding, in which relevant laboratory data and observations were reviewed in an attempt to reach an understanding of the mechanisms involved. The present Chapter, together with Chapters 7 and 8, is oriented more specifically to reviewing, and where possible quantifying, all the factors which are believed to influence the corrosion of zirconium alloys in reactor environments.

The required performance of zirconium alloys in reactors, defined as performance criteria for corrosion, hydriding and mechanical properties, depends on a complex interaction of many parameters. This is summarised [239] in an interaction matrix presented in Figure 6.1. Even considering corrosion alone, it is clear from the interaction matrix that a large number of factors needs to be considered. Thus, it is impossible to optimise the corrosion properties of zirconium alloys by altering only one parameter, for example, the chemical composition. Unfortunately, alteration of one parameter to improve one performance criterion (e.g. corrosion) may lead to a worsening of performance in another (e.g. mechanical properties). Thus, the optimisation procedure is, of necessity, a complicated process of finding the best compromise between often divergent parameter values.

Factors which influence zirconium alloy oxidation in reactors include:

- Alloy composition;
- Metallurgical conditions during fabrication;
- Surface condition;
- Chemistry of reactor coolants;
- Temperature of reactor coolants;
- Heat flux through the cladding;
- Irradiation (radiation type, intensity and fluence);
- Crud deposition.

The above factors are reviewed in the present Chapter, with the exception of the last two factors on irradiation and crud deposition, which are treated in Chapter 8. Some of these effects may be synergistic, for example coolant chemistry (lithium hydroxide) together with heat flux, and crud deposition together with heat flux.

### 6. 1. ALLOY COMPOSITIONS FOR NUCLEAR APPLICATIONS

#### 6. 1. 1. Alloy types

Pure zirconium cannot be used in reactor systems due to its mechanical softness and low corrosion resistance in water environments. Present day commercial alloys in general are based on binary, ternary or quaternary alloy systems. As shown in Chapter 2 very different elements with very different solubilities are alloyed with zirconium. Table 6.1 gives examples of alloys from the three alloy systems which are commonly used commercially. Table 6.2 gives the compositions of a number of alloys which have been used experimentally or commercially.

Up to the mid-to-late eighties, to a large extent, only four alloys (listed in the last column of Table 6.2) were used commercially in nuclear systems. Two of these, Zircaloy-2 and Zircaloy-4, were established by a military programme, circa 1950 (Naval Nuclear Propulsion Program). The compositions of these standard Zircaloys, and of two Zr-2.5%Nb alloys, are defined by the American Society for the Testing and Materials (ASTM) for nuclear application as shown in Table 6.3. These compositions have remained unchanged for nearly 30 years. The first two alloys are used for cladding, and for structural materials such as guide tubes, in fuel assemblies and spacers. The last alloy, R 60904, is used exclusively in CANDU reactors. For cladding tubes, only Zircaloy-2 and Zircaloy-4 are specified by the ASTM. Other alloys outside the ranges defined by the ASTM standard





have been developed and are under irradiation in nuclear power plants. In Russian PWRs (WWERs) Zr-1%Nb alloys are used.

Table 6.1 General types of zirconium alloys

Type	Components	Examples
Binary Alloys	Zr Nb Zr (Fe, Cr) Zr (Fe, V)	Zr-2.5%Nb, Zr-1%Nb Valloy (Zr-0.2%Fe-1.2%Cr) Zr-0.25%Fe-0.2%V
Tertiary Alloys	Zr Sn (Fe, Cr) Zr Nb (Fe, Cr)	Zr-4 (Zr-1.4%Sn-0.2%Fe-0.1%Cr) Zr-3 (Zr-0.25%Sn-0.25%Fe)
Quaternary Alloys	Zr Sn Nb (Fe, Cr)	ZIRLO (Zr-1%Sn-1%Nb-0.1%Fe) Ozhennite - (Zr-0.2%Sn-0.1%Nb-0.1%Fe) E635 (Zr-1.2%Sn-1%Nb-0.4%Fe)

#### 6.1.2 Alloy development programmes

A systematic determination of the dependence of corrosion performance on the concentrations of alloying elements can only be performed by varying one element at a time, keeping the matrix as constant as possible. Such experiments are the basis for every alloy optimisation. The tests are performed in the laboratory, but much more reliable information can be obtained from in-pile experimentation. As an example, the effect of tin variation in a Zr, Fe, Cr matrix on the out-of-pile corrosion behaviour is shown in Figure 6.2 [240]. A steep decrease of corrosion with decreasing Sn content in the range below 1% Sn is observed in the 350°C corrosion test. This beneficial effect on corrosion resistance of optimising the Sn content is very dependent on the matrix as seen from Figure 6.3 [241]. In this test the variation of Sn in a pure zirconium matrix does not really have an effect on the corrosion behaviour. This example demonstrates the difficulty of classifying the influence of special elements on the corrosion behaviour without carefully considering the matrix in which the element concentration is investigated and under the experimental conditions in which the tests are performed. If the results from out-of-pile experiments are used to predict the corrosion behaviour in the reactor, a number of further restrictions and influences have to be considered. In some cases depending on the reactor exposure conditions, even contradictory results are observed. As an example the effect of tin content will again be taken. The in-pile corrosion performance varies as a function of tin content in a similar manner to out-of-pile tests in PWRs, giving a beneficial effect with decreasing Sn concentration. However, the reverse effect is observed if the alloys are irradiated in a BWR (Figure 6.4) [242].

These examples show the difficulty in formulating generalised classifications of element dependencies with respect to their effects on corrosion.

Stimulated by the general trend to higher fuel burnup, longer residence times, increased cycle lengths with the need for higher coolant lithium levels, alloy development programmes for materials with improved corrosion resistance were carried out by nearly all manufacturers of materials for nuclear applications.

For instance, a large development programme for improving the corrosion resistance of Zircalloys, and to qualify new alternative zirconium based alloys, has been carried out by Siemens KWU [243]. Many samples of small ingots with large variations in chemistry and different fabrication routes were tested both in and out of pile. The out-of-pile corrosion tests were performed in pure water and steam over a range of temperatures (300-420°C) and in lithiated water at 350-360°C. Corrosion coupons were exposed in a high temperature PWR by positioning them in segmented water rods. The coupons

Weight gain (mg/dm<sup>2</sup>)

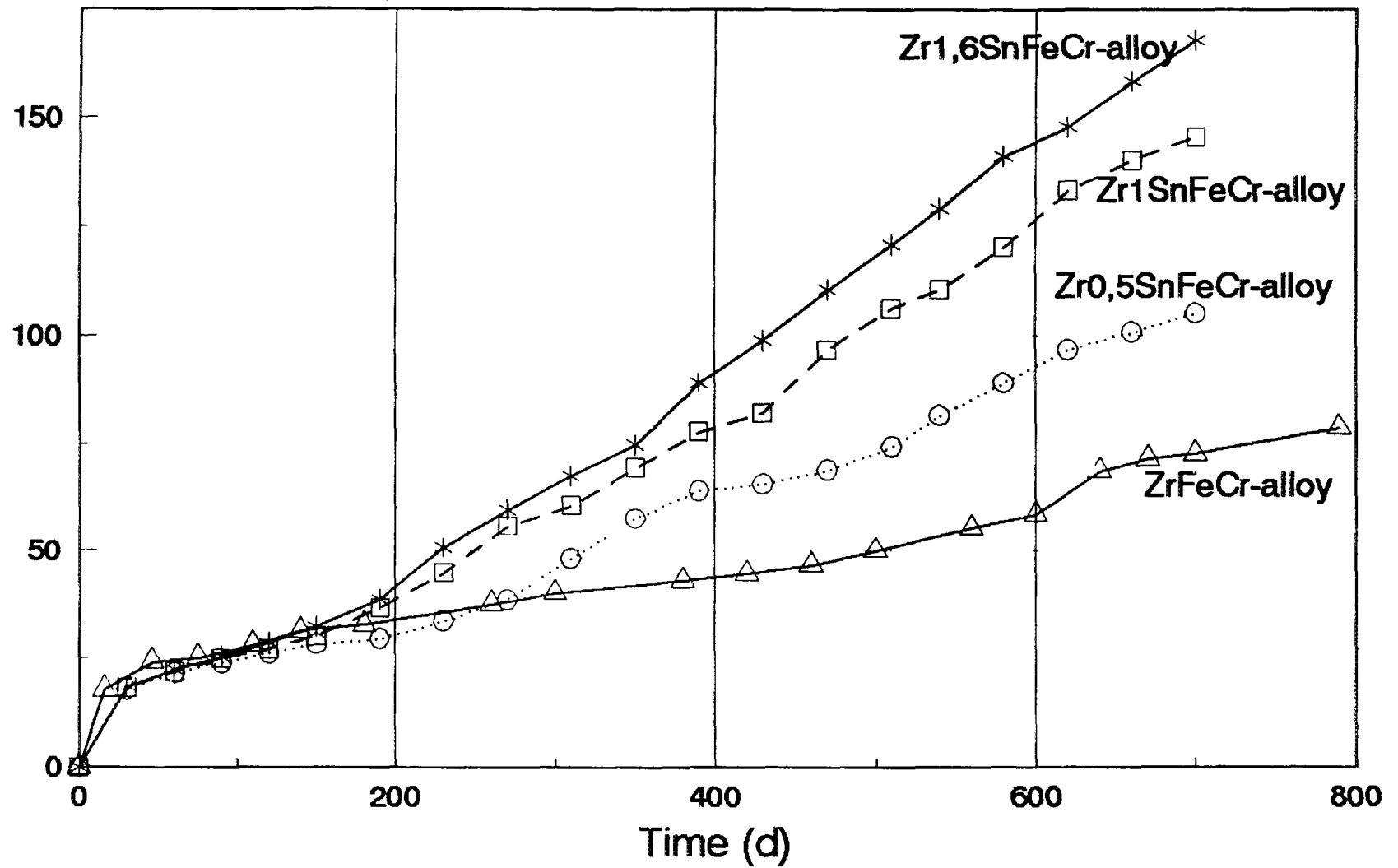


Figure 6.2. Effect of tin on out-of-pile corrosion of zirconium-based alloys with Fe and Cr in hydrogenated water at 350°C [240].

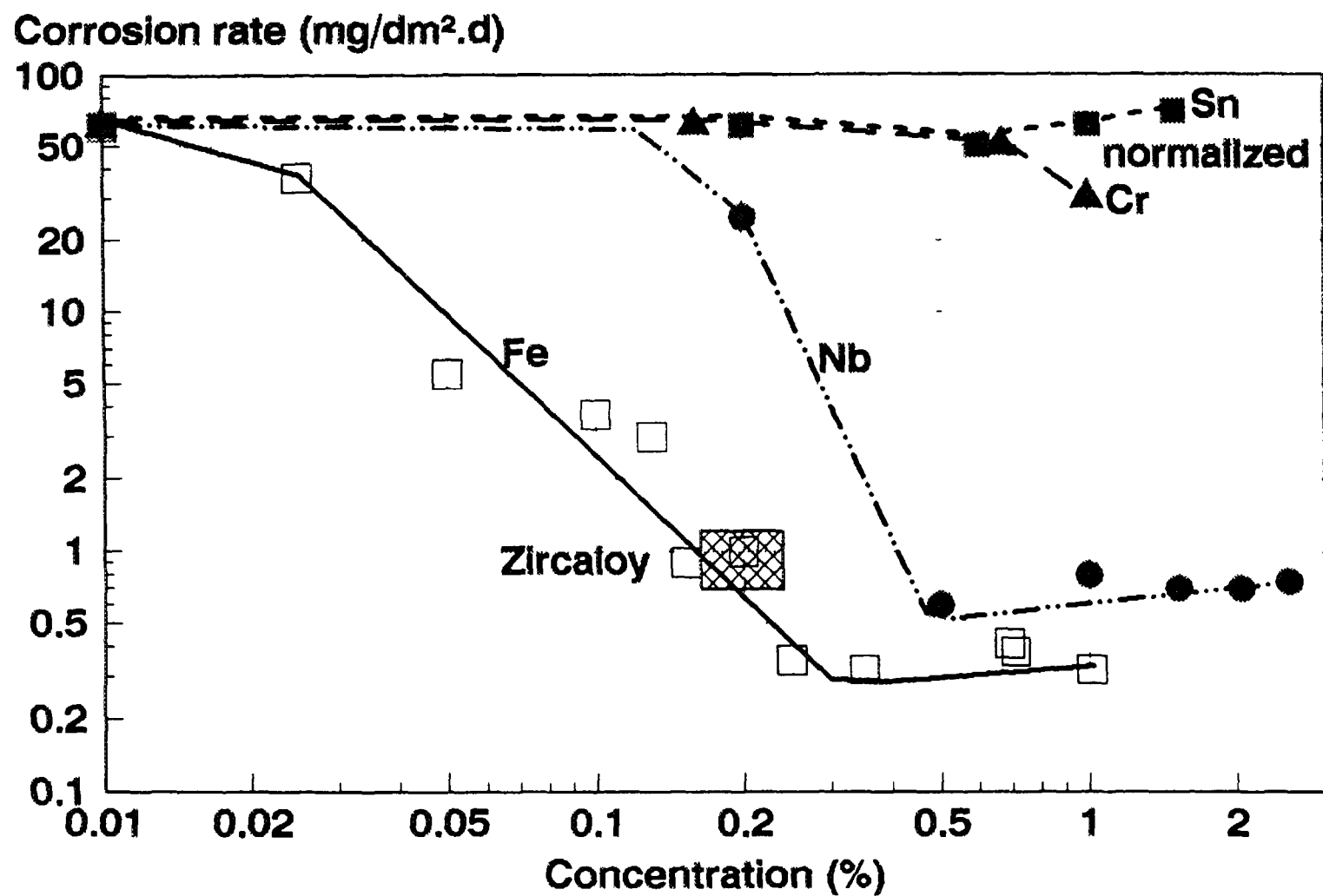


Figure 6.3. Effect of various alloy constituents on corrosion in 400°C, 105 bar steam [241]

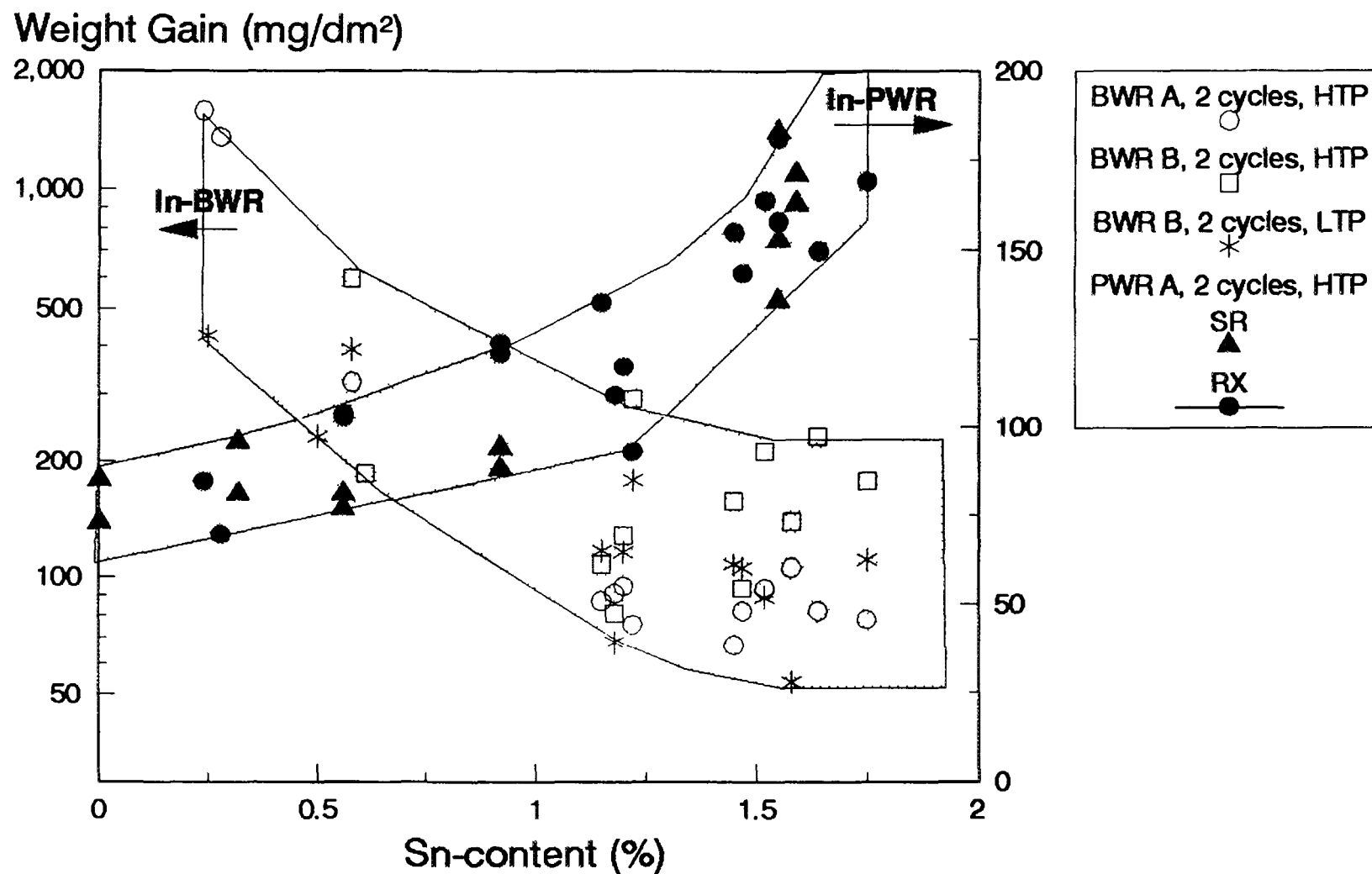


Figure 6.4 Influence of tin on in-reactor corrosion of zirconium Alloys processed at high temperatures (HTP) or low temperatures (LTP) [242]

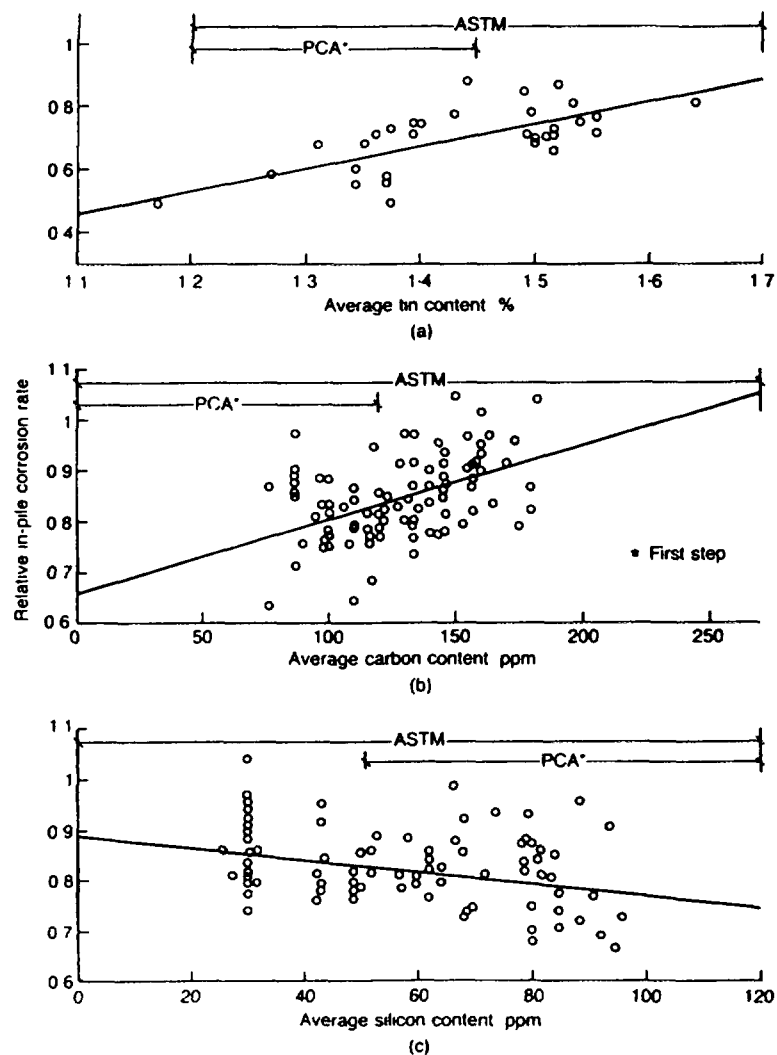


Figure 6.5. Effects of tin, carbon and silicon on corrosion in PWR [243]. PCA denotes low tin alloy.

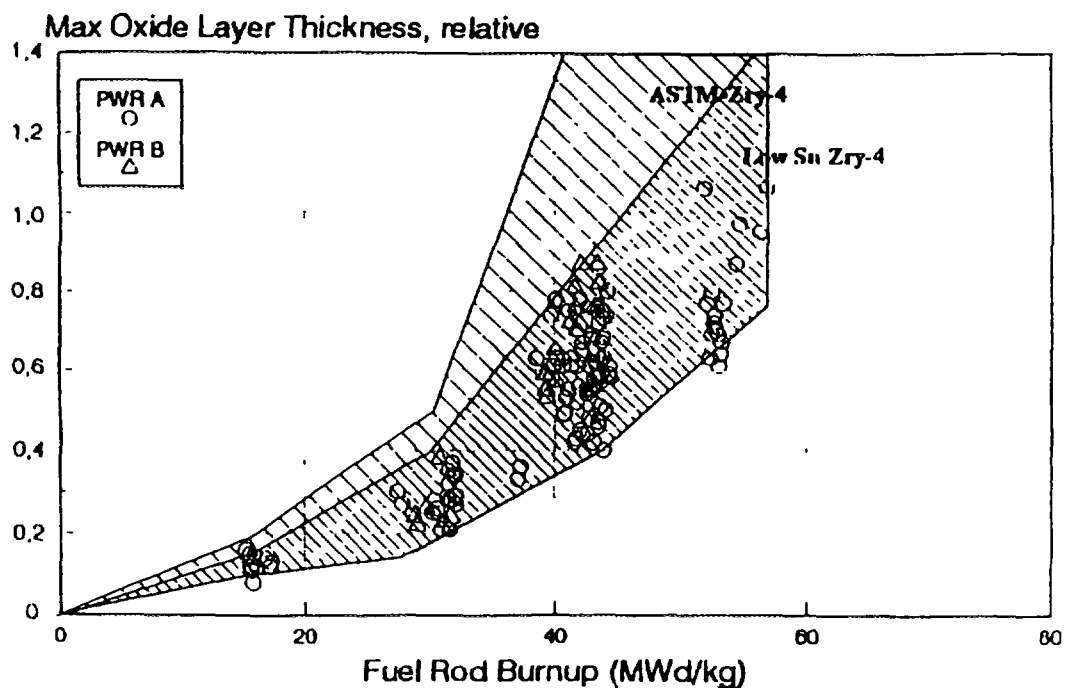


Figure 6.6. Corrosion experience with low tin Zircaloy-4 cladding [246].

were irradiated for up to six yearly cycles (approximately 2,000 days). Pathfinder (experimental) fuel rod irradiation programmes were performed to evaluate the effects of fabrication parameters and alloy chemistry. An extensive development programme by Westinghouse has led to the specification for ZIRLO, and other fuel vendors have carried out their own development programmes.

Table 6.2. Experimental and commercial alloys for nuclear applications

Alloy	Typical Weight %							Commercial Application
	Sn	Nb	Fe	Cr	Ni	O	Mo	
Zry-1	2.5							
Zry-2	1.5		0.13	0.10	0.05	0.11		BWR Clad & Structures
Zry-3A	0.25		0.25					
Zry-3B	0.5		0.4					
Zry-3C	0.5		0.2		0.2			
Zry-4	1.5		0.21	0.10		0.13		PWR Clad & Structures
ELS 0.8	0.8		0.3	0.2				PWR duplex cladding
ZIRLO	1.0	1.0	0.1					
NSF 0.5	1.0	1.0	0.5			0.10		
NSF 0.2	1.0	1.0	0.20			0.10		
Valloy			0.15	1.2				
Ozhennite- 0.5	0.2	0.1	0.1		0.1			
Scanuk	0.06	0.6	0.04	0.32			0.22	
Excel	3.5	0.8					0.8	
E110 (Zr-1%Nb)		1				0.06		WWER and RBMK Clad
Zr-2.5%Nb		2.5				0.12		CANDU P/T*
E635	1.2	1	0.4			0.06		
E125		2.5				0.06		RBMK P/T*

\* Pressure Tubes

#### 6. 1. 2. 1. Standard PWR materials

A significant improvement in standard Zircaloy-4 cladding performance was obtained by a reduction in the tin concentration and limitations on C and Si content, within the ASTM specified ranges. This development was initiated by a statistical evaluation of the corrosion behaviour of standard Zircaloy-4 in different PWRs which revealed that both variations in the alloy chemistry and variations in fabrication routines were responsible for the observed scatter. It was found that the alloying element Sn and the impurities C and Si influenced the corrosion behaviour (Figure 6.5) [243]. Similar results have been reported by others [244,245]. Low tin Zircaloy-4 with Sn levels typically between 1.2% and 1.4% was irradiated to more than 50 MW·d/kgU burn-up in a high temperature PWR plant (Figure 6.6) [246]. Each data point represents the maximum measured oxide

thickness on a single fuel rod. As expected, the corrosion rate of low Sn Zircaloy-4 is near the lower range of the band observed for ASTM specified Zircaloy-4. A significant reduction of scatter in corrosion behaviour has been achieved by chemistry modification and as a result of a improved fabrication process control. The performance in a PWR of typical BWR-materials, such as Zircaloy-2, with Sn contents of 1.3% or 1.5% was reported as excellent by ABB workers [247].

Table 6.3 Compositional ranges of standard alloys

ASTM Ref	R 60802	R 60804	R 60901	R 60904
Name	Zircaloy-2	Zircaloy-4	Zr-Nb	Zr Nb
Alloying elements (mass %)				
Sn	1.2-1.7	1.2-1.7		
Fe	0.07-0.2	0.18-0.24		
Cr	0.05-0.15	0.0700-0.13		
Ni	0.03-0.08			
Nb			2.4-2.8	2.5-2.8
O	usually 0.1-0.14	usually 0.1-0.14	0.09-0.13	To be specified
Impurities (ppm)				
Al	75	75	75	75
B	0.5	0.5	0.5	0.5
Cd	0.5	0.5	0.5	0.5
C	270	270	270	150
Cl	Alloy el	Alloy el	200	100
Co	20	20	20	20
Cu	50	50	50	50
HI	100	100	100	50
H	25	25	25	25
Ie	Alloy el	Alloy el	1500	650
Mg	20	20	20	20
Mn	50	50	50	50
Mo	50	50	50	50
Ni	Alloy el	70	70	35
N	80	80	80	65
Pb		-		50
Si	120	120	120	120
Sn	Alloy el	Alloy el	50	100
Ta	-	-	-	100
Ti	50	50	50	50
U	3.5	3.5	3.5	3.5
V	-	-	-	50
W	100	100	100	100



## 6 1 2 2 Alternative alloys for PWRs

Siemens conducted an initial exploratory program in which some 120 different alloys were fabricated into strip samples and/or cladding tubes. Different fabrication routines were used for many of the alloys in order to obtain different microstructures and to test the effects of processing variations on the corrosion and mechanical behaviour of the materials. The tubing was fabricated as through-wall cladding or in the form of DUPLEX cladding. DUPLEX cladding consists of Zircaloy-4 tubing with an integral metallurgically bonded thin (75-200  $\mu\text{m}$ ) outer layer of a different zirconium-based alloy.

The different compositions investigated can be conveniently grouped into the following four alloy systems:

- 1 Zr, 0.2 - 1.1%Sn, Fe-Cr (V, Mo, Ni, Ge, Te, Pt)
- 2 Zr, 0.2 - 2.6%Nb
- 3 Zr, 0.2 - 2.5%Nb, Fe, Cr (V, Cu)
- 4 Zr, 0.2 - 1%Sn, 0.1 - 1%Nb, Fe (Cr, V, Ge, Pt)

All the materials were evaluated under different test conditions. Over two thirds of the strip materials were tested inside water rods in a BWR for up to six years. The tubular materials were used in a high efficiency (hot) PWR. Fuel rods with alternative zirconium alloy cladding were irradiated for up to seven cycles up to a rod average burn up of 80 MW d/kgU. Many of the materials tested were found to have better corrosion behaviour than low tin Zircaloy-4 when evaluated in the autoclave tests and much better performance than Zircaloy-4 in reactor tests.

However, many of the alloys showing very good corrosion resistance when tested in pure steam or water showed poor corrosion resistance when tested in water containing LiOH. Corrosion behaviour in lithiated water is considered to be important since in the future fuel is expected to operate with significant void fractions and relatively high local lithium hydroxide concentrations may develop in-reactor due to this type of operation.

The final selection of alternative zirconium alloy cladding was based on a statistically broad range of information including mechanical behaviour under normal operating conditions and during transients (LOCA). These considerations led to the selection of an Extra Low Sn (ELS) Zr-Sn-Fe-Cr alloy with a further reduced Sn content and higher Fe and Cr levels compared with Zircaloy-4. The improved corrosion performance, relative to Zircaloy-4, up to a high burn-up is indicated in Figure 6.7 [246] and superior performance compared with Zircaloy-4 when tested in lithiated water is indicated in Figure 6.8 [246]. This alloy is used as DUPLEX cladding which combines the good mechanical properties of the Zircaloy base material to the high corrosion resistance of the new alloy.

Results from a development program performed by FRAMATOME have been reported [245], which also show the beneficial effect in-pile of reducing the tin content. The best alloy in this investigation programme was a 1% niobium alloy (Figure 6.9) [245].

Westinghouse has developed the quaternary alloy, ZIRLO (Tables 6.1 and 6.2) which has completed three 18-month cycles of irradiation in the North Anna PWR [248]. It was found to have peak corrosion rates, on average, approximately 77% lower than standard Zircaloy-4, exposed simultaneously, after a burn-up of 46.4 MW d/kgU. Additional tests were carried out in the BR-3 reactor to a burn-up of 68 MW d/kgU and high resistance to lithium attack was demonstrated.

## 6 1 2 3 BWR materials

A large out-of-pile data base exists world-wide today from tests in 500-520°C high pressure steam on the effects of material condition and chemical composition. However, the validity of these results

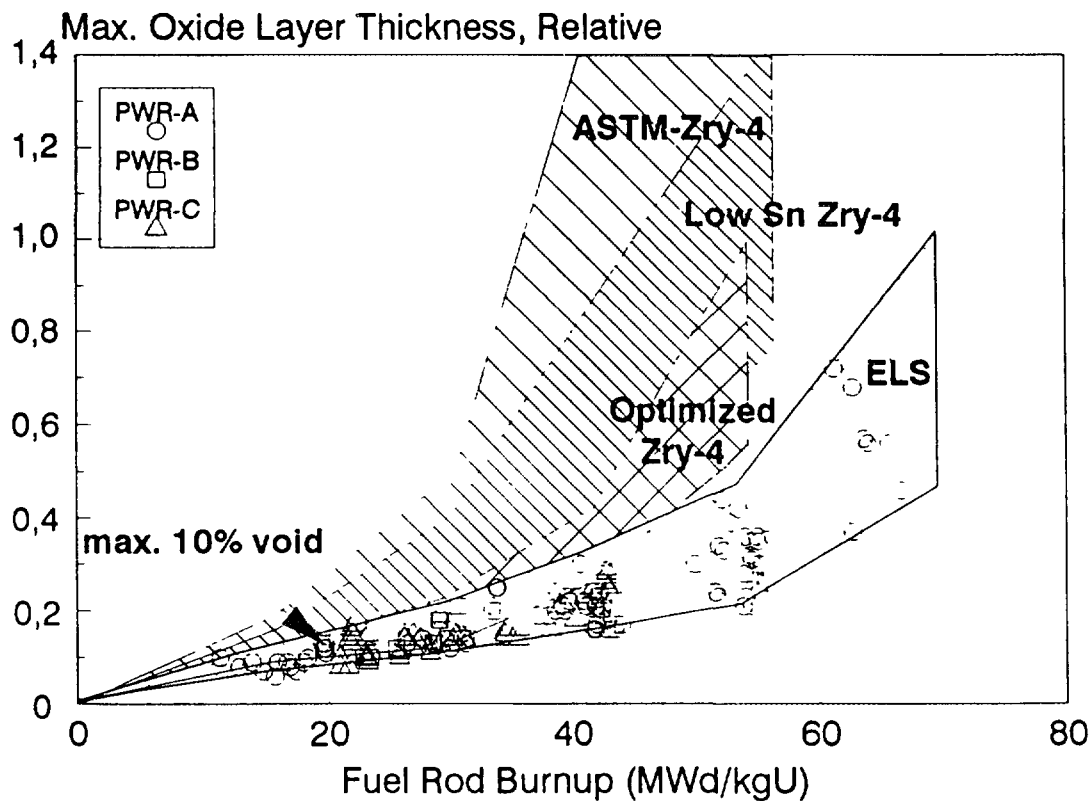


Figure 6.7. Corrosion experience with ELS cladding [246].

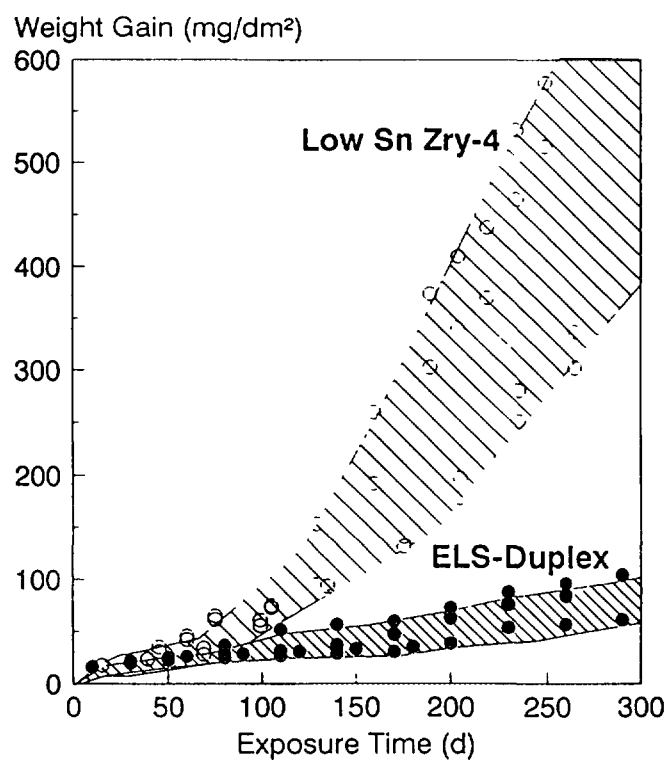
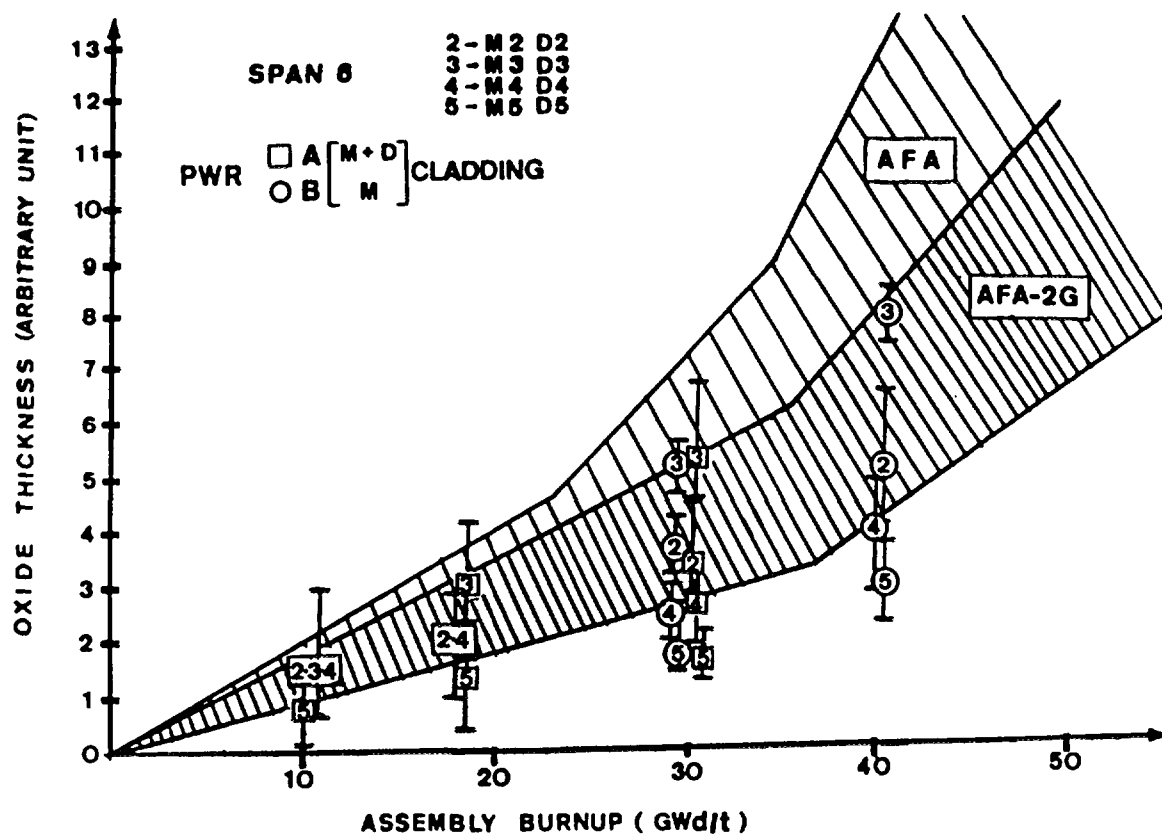


Figure 6.8. Corrosion of ELS-DX in 10 mmol LiOH at 350°C [246].



Key to nominal chemical compositions in Figure 6.9 above

Alloy Reference	Tube		Alloying elements (% weight)					
	Solid-wall	Coextruded	Sn	Fe	Cr	O	Nb	V
Zircaloy-4	AFA  AFA-2G	Substrate						
		AFA	1.2/1.7	0.18	0.07	0.09		
		OR AFA-2G	1.2/1.5	0.24	0.13	0.16		
2	M2	D2	0.50	0.20	0.10	0.20		
3	M3	D3	0.50	0.25		0.12	0.50	
4	M4	D4	0.50	0.60		0.12		0.30
5	M5	D5				0.12	1.0	

Figure 6.9. Corrosion of experimental alloys for fuel cladding in a pressurised water reactor environment [245].

for the behaviour in BWRs has to be considered carefully. Both the large difference in temperature and the effect of neutron flux may change the influence of some material parameters. Different temperature dependencies for certain material parameters can even invert the ranking with respect to nodular corrosion (Figure 6.10) [249]. In out-of-pile corrosion tests in water at 300°C nodular corrosion occurred after extended exposure times in Zircaloy alloys containing only transition metal elements (Fe, Cr, V) but no tin. On the other hand, these kinds of alloys behaved extremely well in 500-520°C steam tests. Several studies on the effect of chemical composition in a high temperature, high pressure steam, environment [143,250] showed that the tin content should be as low as possible to minimise nodular corrosion. Data from BWR irradiation experiments do not confirm this conclusion, probably due to the much lower operating temperature. Therefore, the basis for material optimisation of Zircaloy alloys for BWR application has mainly been based on experience from in-pile experimentation. Highly reliable data can be derived from experimental fuel elements (pathfinder fuel elements) where the cladding composition of different fuel rods was varied with respect to material condition and chemical composition. Another data set was generated from test coupons irradiated in a BWR within segmented water test rods (WTR) which were inserted in water rod positions in the fuel assembly. In the following, the most significant results related to alloy composition effects are reported.

A pronounced effect of the tin content on corrosion in BWRs is obvious from Figure 6.11 [249]. Here the weight gains (measured on test coupons exposed for 4 cycles in a BWR at the same axial position in the test rod) are plotted versus the tin concentration in the alloy. The figure indicates that nodular corrosion increases significantly with decreasing tin content below the ASTM range for Zircaloy-2 but is less pronounced within this range. These findings are in contradiction to out-of-pile results from high temperature steam test, but are in accordance with the behaviour of the same alloys in 350°C water tests. A variation in corrosion rate with silicon content is also shown for Zircaloy-4 (Figure 6.12) [249]. The lowest weight gains were measured for the highest Si content. A beneficial effect of Si on corrosion could be also confirmed by out-of-pile 400°C steam tests. A variation of the chromium content in the test coupons has a beneficial effect on corrosion in BWRs (Figure 6.13) [249]. There are some indications that iron may also have a beneficial effect, but probably less pronounced than in the case of chromium. Out-of-pile water tests indicate a beneficial effect of iron and less pronounced effects for chromium and nickel.

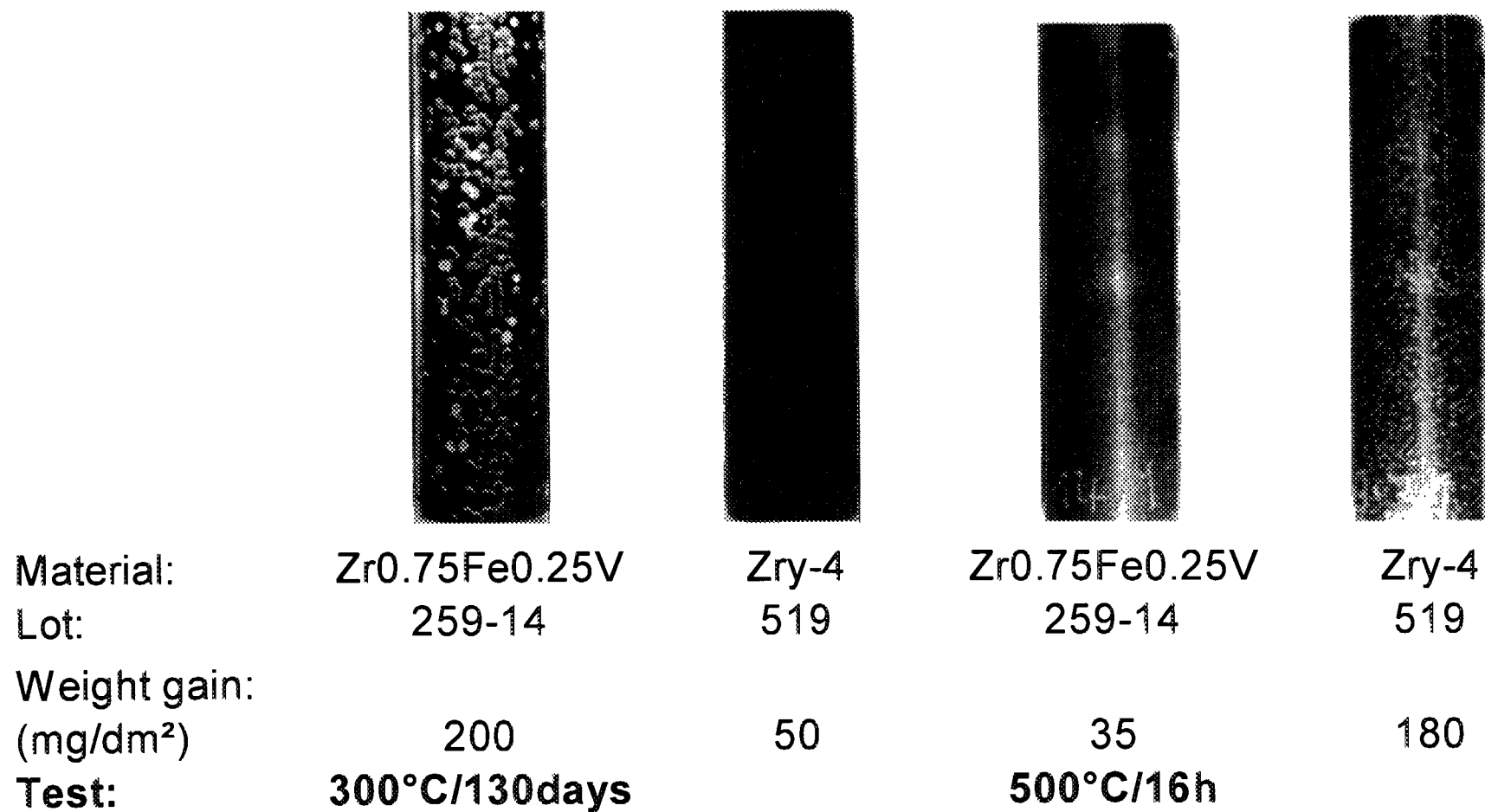
On the basis of published and unpublished results BWR materials for high burn-up should have a tin content in the middle or upper range of the ASTM band for the Zircaloys. Chromium levels, and probably also iron levels, should be high, preferably somewhat above the ASTM range defined for Zircaloy. Silicon should be added as an alloying element in the material. However, there is some contrary evidence on the last point [152].

Other manufacturers have also studied compositional effects on the corrosion under BWR and PWR conditions. For example Japanese workers [244] studied the influence of tin, iron, chromium, niobium, molybdenum and vanadium on zirconium corrosion in out-of-pile tests. They report a beneficial effect of low tin and niobium on corrosion. Surprisingly they found no dependence on Fe and Cr contents.

## 6. 2. METALLURGICAL VARIABLES

### 6. 2. 1. Precipitate Size

The primary metallurgical factors that have been found to correlate with the corrosion resistance of the Zircaloys are the size and distribution of the second phase particles, and the amount of residual strain in the  $\alpha$ -Zr lattice [143,250,260]. The alloying elements in these particles (Fe, Cr, Ni) have solubilities in  $\alpha$ -Zr that are less than, or comparable to, the common impurity levels (especially for Fe) found in unalloyed zirconium. Therefore, the major fractions of these alloying elements are always present, at operational temperature, in the form of precipitates. In the  $\beta$ -region above 950°C



*Figure 6.10. Effect of test temperature on ranking for nodular corrosion [249].*

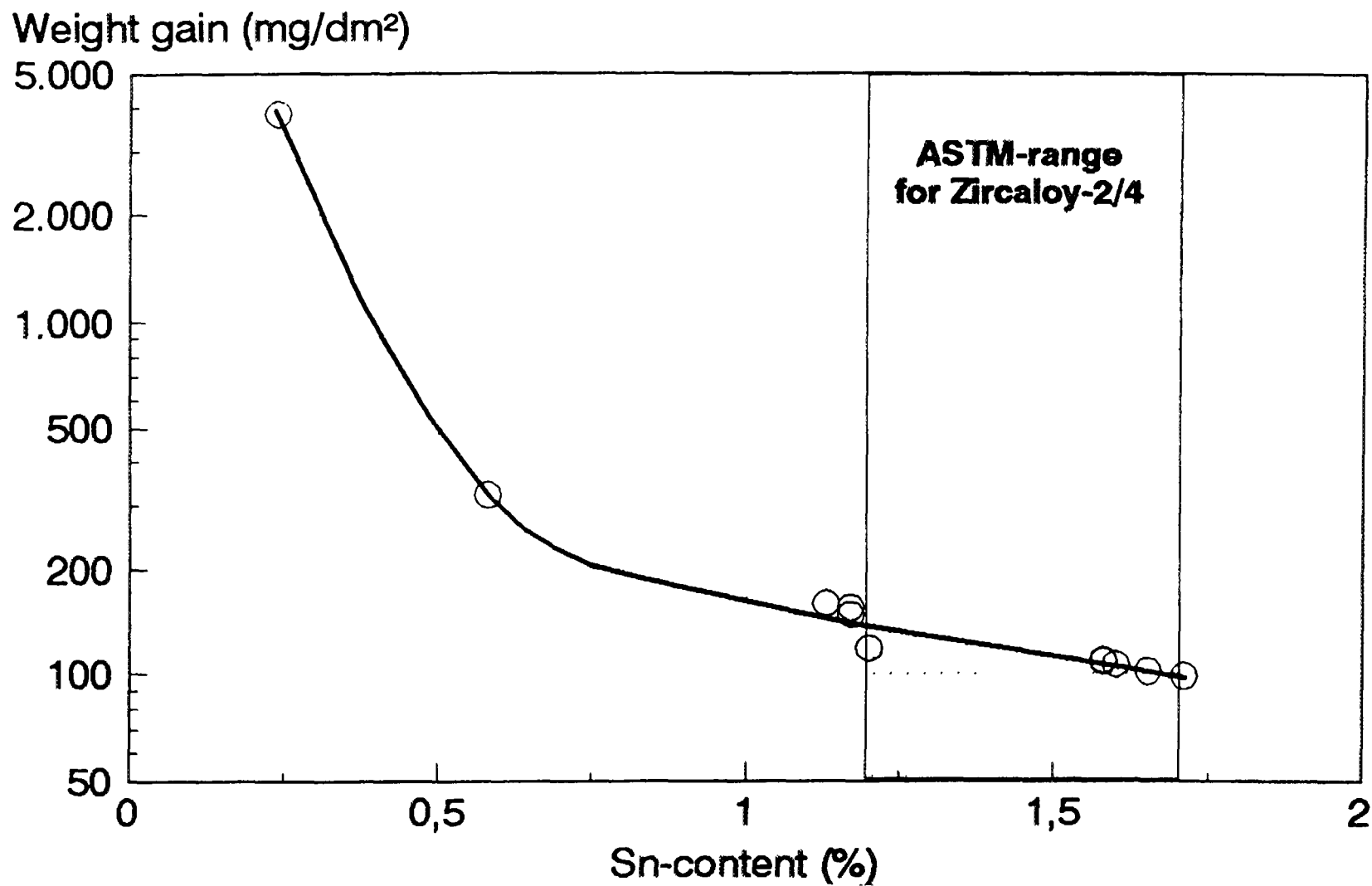


Figure 6.11. Effect of tin on the corrosion of Zr-Sn-Fe-Cr-alloys in BWRs after 4 cycles of exposure (WTR coupons) [249].

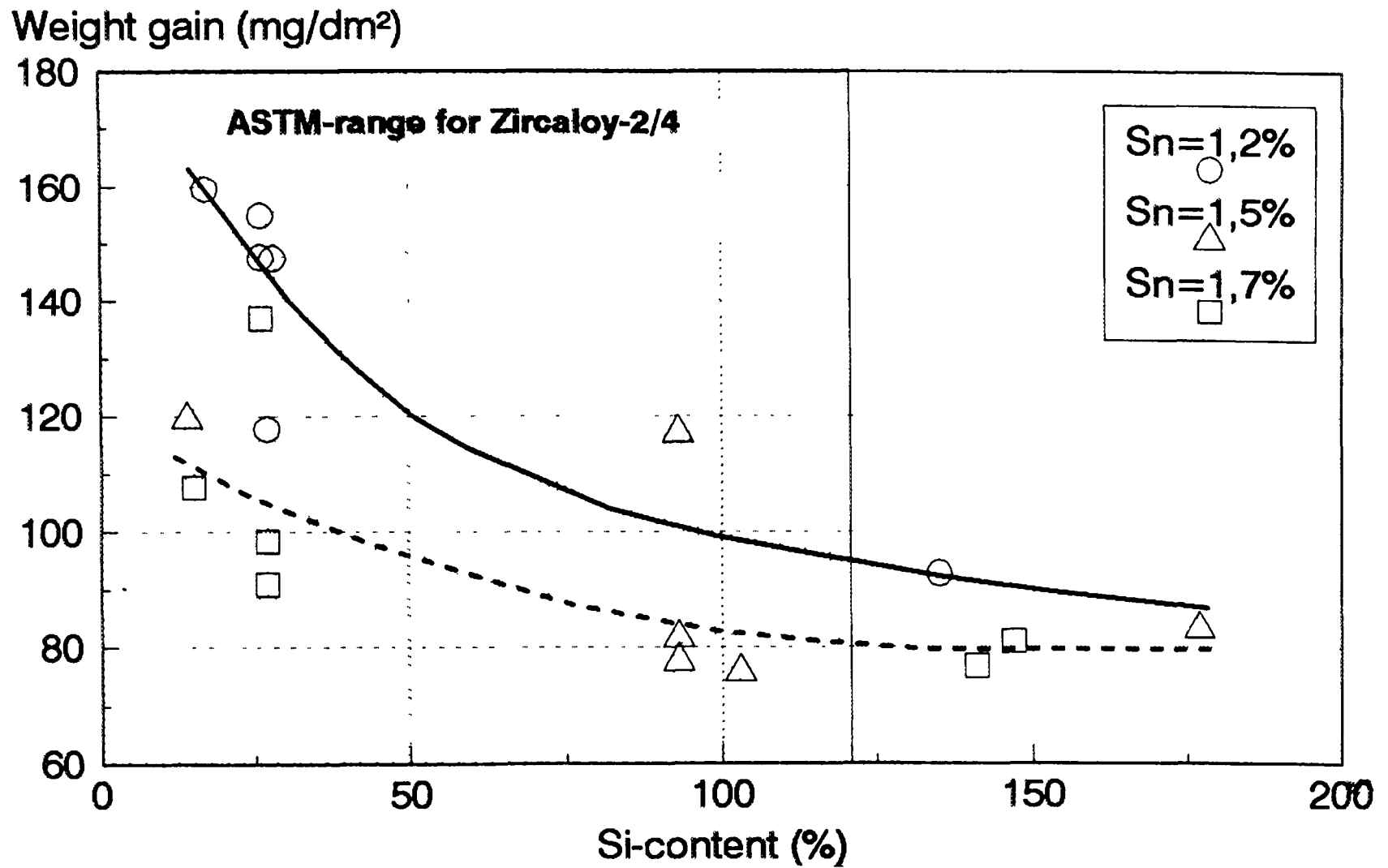


Figure 6.12. Effect of Si and Sn on the corrosion of Zircaloy-4 in BWRs after 4 cycles of exposure (WTR Coupons) [249].

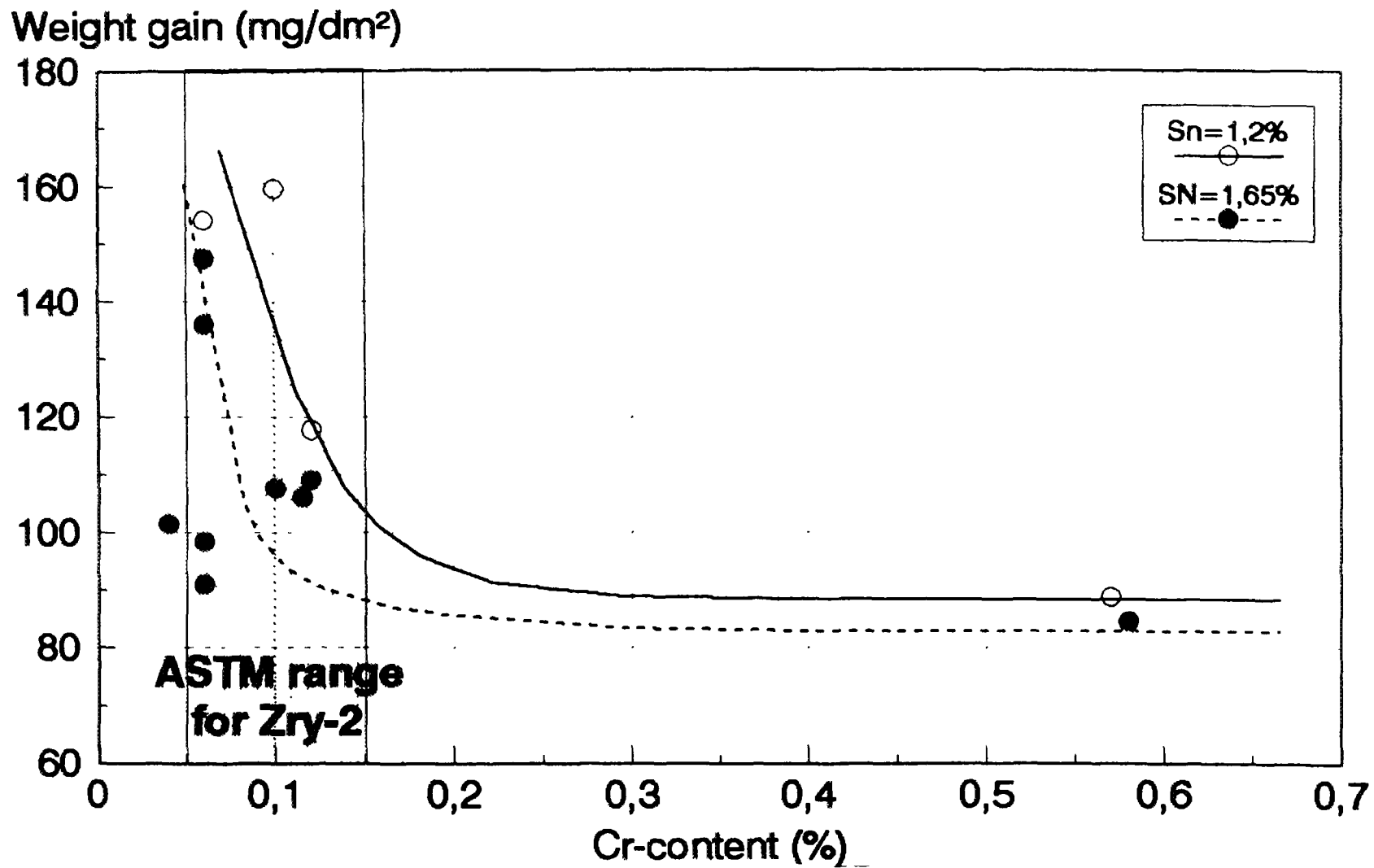


Figure 6.13. Effect of Cr and Sn on the corrosion of Zircalov-4 in BWRs after 4 cycles of exposure (WTR Coupons) [249].



(see section 2.3) the transition elements Fe, Cr, Ni are in solution [251]. The possibility of maintaining them in super-saturated solid solution by quenching, as opposed to forming submicroscopic precipitate nuclei, requires quenching rates of the order of  $1,500 \text{ K}\cdot\text{s}^{-1}$  (i.e. much higher than in any commercial process with quenching rates of typically about  $50 \text{ K}\cdot\text{s}^{-1}$ ).

Modern fabrication routes include a fast quenching step in the fabrication sequence in which the initial size distribution of the precipitates is established. Starting from this second phase particle (SPP) distribution all further thermo-mechanical treatments increase the mean precipitate size in the materials. The regulation and adjustment of the fabrication parameters which determine the size distribution of the precipitates is very important.

All annealing steps are defined by the temperature at which the annealing is performed and a period of time over which this temperature is applied. The combination of these two variables proved to be important in manufacturing a high quality material for cladding tubes and fuel assembly components with reproducible properties. Originally this factor was introduced in 1984 by Steinberg et al. [252] as an accumulated annealing parameter which sums up all applied heat treatments in the alpha phase region of zirconium during fabrication. They used a “growing function” of sigmoidal shape having the general formula:

$$\ln k' = \ln[(a-y)/(y-b)] = kx \quad (6.1)$$

to describe the sigmoidal shape of experimental curves of yield strength,  $R_{p_{0.2}}$ , versus temperature and time in the form

$$\ln k' = \ln[(R_{p_{0.2}}^{\max} - R_{p_{0.2}})/(R_{p_{0.2}} - R_{p_{0.2}}^{\min})] = kA \quad (6.2)$$

where,  $A = t \exp(-Q/RT)$ . The activation temperature,  $Q/R$ , was determined to be 40,000 K from an Arrhenius plot of  $\ln k'$  versus  $1/T$ .

If more than one annealing step was involved, the final yield strength was described by summation over each of the time/temperature steps,  $i$ , as follows:

$$A = \Sigma(A_i) = \Sigma(t_i \exp(-Q/RT_i)) \quad (6.3)$$

where  $t_i$  is the effective time of annealing step,  $i$ , at temperature,  $T_i$ . This parameter is termed the “A-Parameter” (also termed the “ $\Sigma A$ -Parameter”).

This concept was successfully applied to describe the dependence of the mechanical or metallographic properties of Zircaloy cladding [252] (yield strength, degree of recrystallization) but it should be recognised that the accumulated annealing parameter does not intrinsically describe directly a physical process such as precipitate growth or corrosion. Nowadays the annealing parameter is well accepted and applied by fabricators and researchers in the zirconium community [253-257]. The benefit of the concept is mainly as an engineering tool for the continuous fabrication of quality materials. But it should be kept in mind that, without modification, it cannot be applied to different alloy compositions nor used to describe the variation of other material parameters than mechanical properties.

Nevertheless, in-laboratory and in-pile measurements of oxide thickness and corrosion rates could be reasonably well correlated with the A-Parameter (Figure 6.14) [258,259]. The physical metallurgical property responsible was identified as the growth of the collective of intermetallic phases present in the alloy as precipitates [259]. In this way the earlier observed dependence of corrosion rate on the average precipitate diameter [260] was understood (Figure 6.15). These investigations also showed clearly the different behaviour in different types of power reactors of identical materials with identical annealing parameters. Low mean precipitate sizes achieved by  $\beta$ -

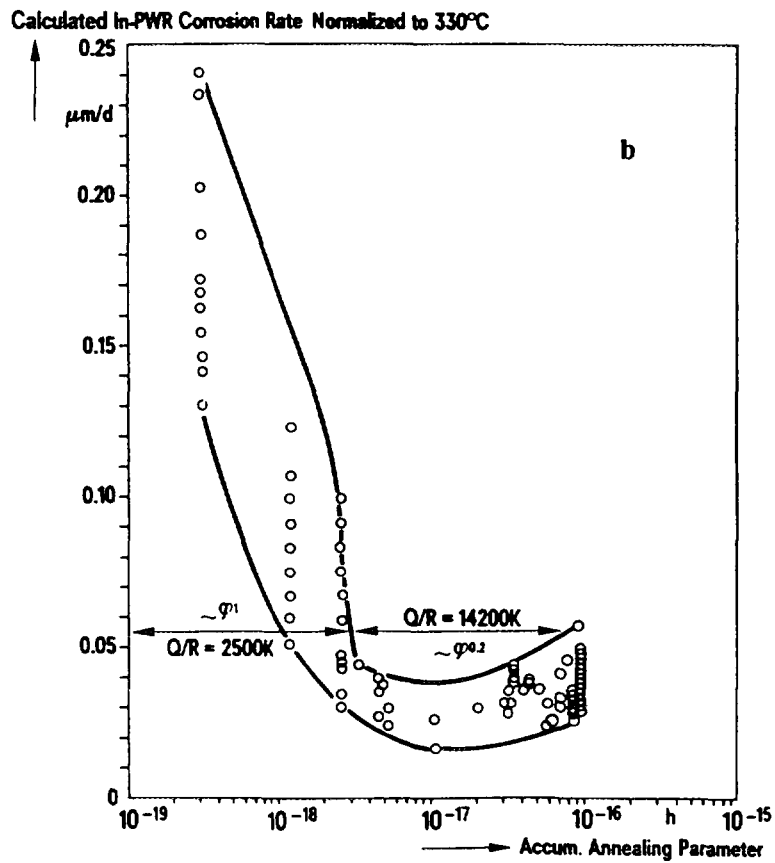
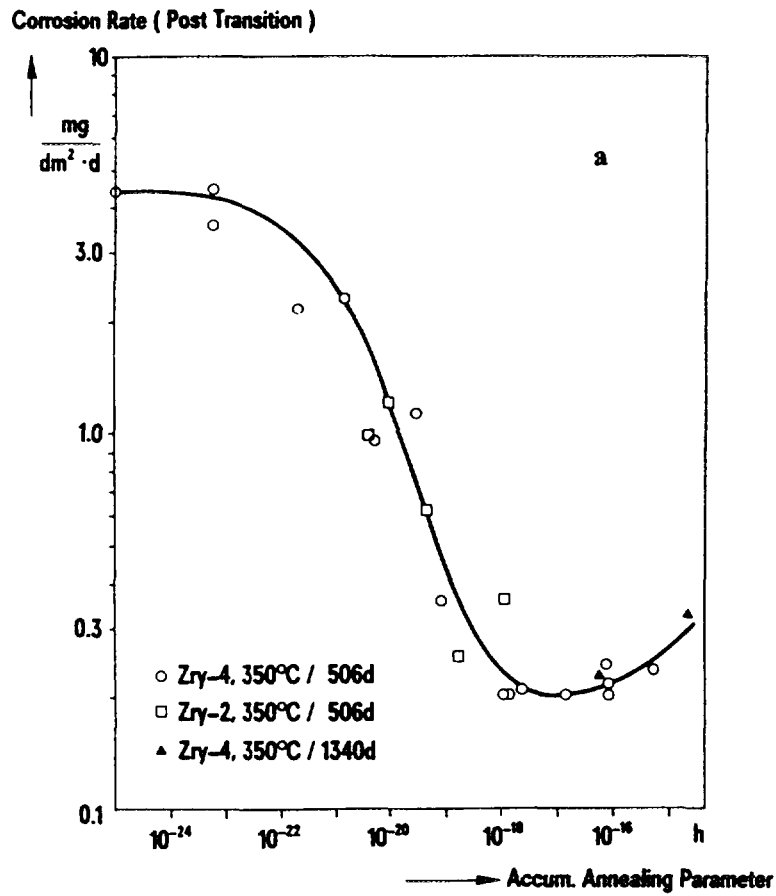


Figure 6.14. Influence on corrosion of the A-Parameter from in-pile and out-of-pile measurements [259]. a Out-reactor corrosion at 350°C, b Corrosion of Zircaloy-4 in PWR.

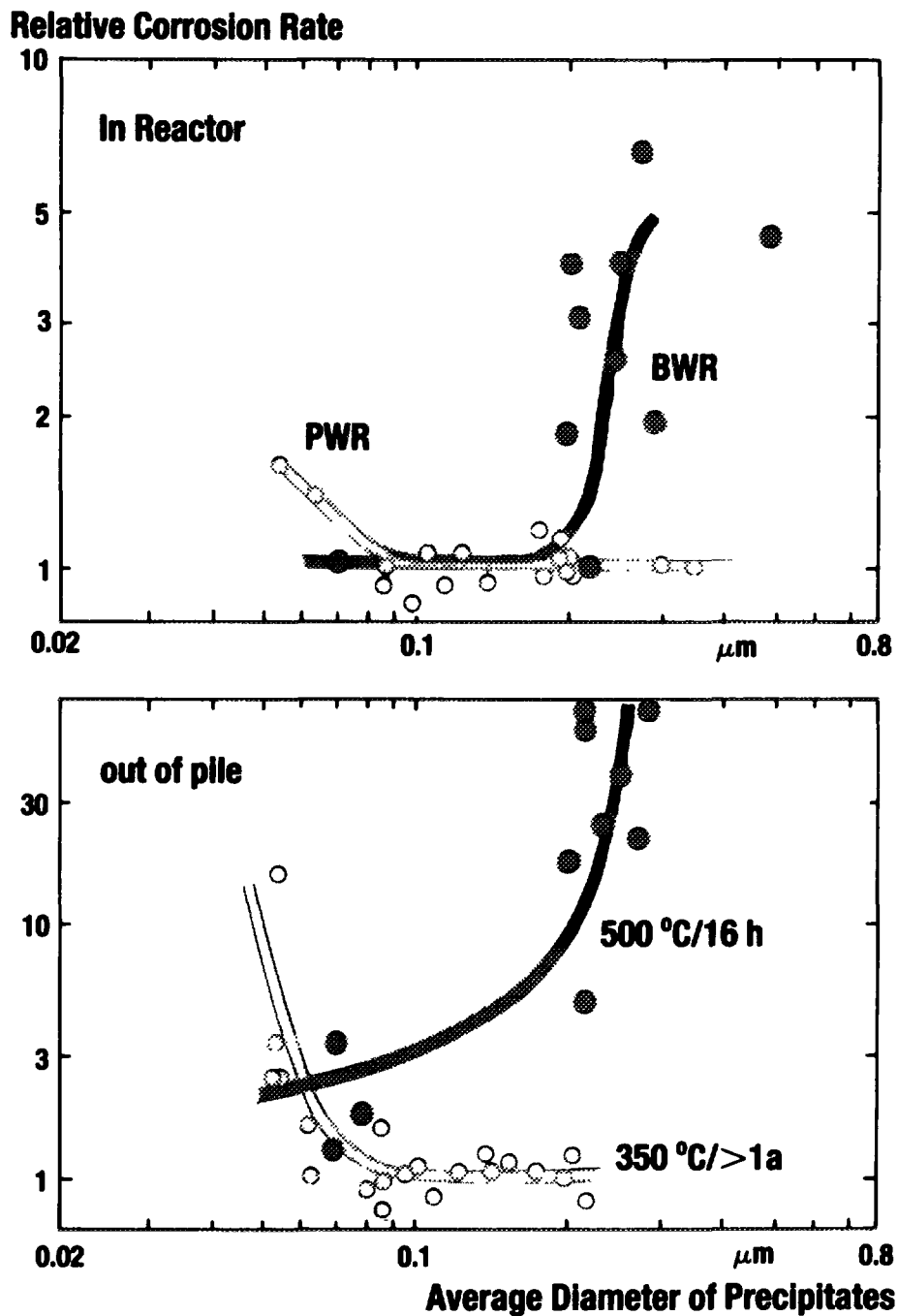


Figure 6.15. Correlation of corrosion to the mean diameter of second phase particles in Zircaloy. Comparison of in-pile and out-of-pile results [260].

annealing are beneficial in BWR systems where they can eliminate nodular corrosion but detrimental in PWR systems. However, it has to be kept in mind that precipitate size is not the only factor which influences the corrosion behaviour of zirconium alloy cladding in pressurised water environments (fabrication-induced parameters such as texture, degree of cold work, Q-ratio and condition of the cladding are influencing factors with different degrees of effectiveness Figure 6.1)

Detailed investigations of the growth of precipitates in Zircalloys with different heat treatments revealed that a modification of the annealing parameter is advisable, especially if short-term heat treatments are involved and a higher accuracy is demanded. The improved parameter is termed the "Particle Growth Parameter" (PGP) mathematically defined in Table 6.4. This parameter allows a direct correlation of the heat treatment versus the final mean size of precipitates in Zircaloy materials [261] after a set of heat treatment steps.

Table 6.4 compiles the different annealing parameters with their mathematical definitions commonly used in literature, their field of application and values for the implied constants. Different Q/R values of either 31,818 K, 40,000 K, 32,000 K and 18,700 K are used for different parameters. For practical purposes these differences in the numerical values of Q/R are significant, as shown by the example in Table 6.4 for a 750°C, 2h anneal. The comparison also shows that the PGP and the ABB A-Parameter exhibit comparable values for the same annealing step.

Table 6.4 Annealing parameters

	A-Parameter		PGP, Particle Growth Parameter	SOCAP Second Order Cumulative Annealing Parameter
	ABB	Siemens KWU		
Formula	$A \cdot \Sigma \exp(-Q/RT)$	$A \cdot \Sigma \exp(-Q/RT)$	$PGP \cdot \Sigma \exp(-Q/RT) \cdot 10^{14} \text{ h}$	$D^3 - D_0^3 \cdot (kt/T^2) \exp(-Q/RT) \cdot k = 1.1 \times 10^{-11} \text{ m}^3 \text{ s}^{-1} \text{ K}$ $D = \text{precip. diam. (m)}$
Actn temp	Q/R = 31,818 K	Q/R = 40,000 K	Q/R = 32,000 K	Q/R = 18,700 K
Relevance	Corrosion	Mechanical Properties Recrystallization	Corrosion, Precipitate Growth	Precipitate Growth
Stage of Application	after $\beta$ Quench	originally after cold work, now after $\beta$ Quench	after $\beta$ Quench initial particle size specified	at any annealing step
Example 750°C, 2h Anneal	$6.2 \times 10^{-14} \text{ h}$	$2.1 \times 10^{-1} \text{ h}$	5.25	-
Typical Values	[263]			[268]
PWR	$10^{-1} \text{ h}$	$40 \times 10^{-18} \text{ h}$	8	$2 \times 10^{-1} \text{ m}$
BWR	$10^{-11} \text{ h}$	$1 \times 10^{-18} \text{ h}$	1	$4 \times 10^{-1} \text{ m}$

\* This formula is for a single annealing stage and can be used successively where the starting diameter  $D_0$  is the final diameter from the preceding stage.

The PGP parameter differs from the old A-Parameter in a modification of the activation temperature (Q/R=32,000 K) which takes into account the different physico-chemical mechanism involved. The PGP is also an empirical parameter fitted to experimental data. It describes the growth kinetics of a population of precipitate particles, using a mathematical growth function, rather than being derived from basic physical laws. The advantage of the PGP is its much higher accuracy in

application to BWR materials where short-term and fast continuous annealing are applied during manufacture. A similar annealing parameter for describing corrosion behaviour was used by ABB using an activation energy of 63 kcal/mol ( $Q/R=31,818$  K) [262,263].

A more basic physical concept to describe the growth of precipitates is the concept of diffusion controlled growth of precipitates under equilibrium conditions (Ostwald ripening) applied to solid phase zirconium alloys [264,265]. This concept was successfully applied by Gros and Wadier for Zircaloy, following the LWS-theory modified by Kahlweit [266], and led to the evaluation of the Second Order Cumulative Annealing Parameter (SOCAP), defined in Table 6.4 [267]. When the second order kinetics of the growth process is fulfilled the size distribution of the precipitates can be directly calculated and compared with measured values. The model requires knowledge of a kinetic constant  $k$  and the activation energy ( $Q/R=18,700$  K) of the growth process, both determined by the authors from experimental data.

A comparison between the A-Parameter and SOCAP is presented in Figure 6.16 [267]. Three different annealing parameters (Siemens A-Parameter, ABB A-Parameter and SOCAP) for irradiated cladding with different fabrication sequences are compared in Figure 6.17 [268]. Each parameter is correlated to a corrosion parameter  $E'$  [268]. Despite the fact, mentioned above, that the A-Parameter (with activation temperature of 40,000 K) is not suitable for describing corrosion behaviour, the general applicability of all three parameters is obvious from Figure 6.17. This figure indicates that the corrosion behaviour of Zircaloy-4 cladding in PWRs is improved by longer and/or higher temperature anneals in the alpha range after the material has been beta quenched. The authors stated that the best correlation with corrosion susceptibility is provided by the Second-Order Cumulative Annealing Parameter.

#### 6.2.2 Influence of quenching conditions

The size of the second phase precipitates has a large influence on corrosion as discussed above. The size of the precipitates in the material depends on the quenching rate from the  $\beta$ -temperature range and on the subsequent process and annealing temperatures in the alpha-range. The dependency of the quenching rate was reported from out-of-pile experiments [143], and recently from an in-reactor investigation programme [242]. Several tube sections from a Zircaloy-4 lot were quenched under controlled conditions at varying rates. Some of these quenched sections were then annealed for 8 h at 750°C ( $A = 8.4 \times 10^{-17}$  h) to obtain a large precipitate size. Fig. 6.18 from [242] shows a large effect of the quenching rate if tested without any annealing in BWR-A and in a 500°C steam test. Here the quench rate dependency probably reflects mostly the precipitate size, which is small only in the case of a fast quenching rate. Those coupons which were quenched with the highest rates showed consistently low corrosion after two cycles of irradiation in a BWR. After 4 cycles, uniform corrosion increased again at the highest quenching rates. The high sensitivity of Zircaloy with very fine intermetallics to increased corrosion at long exposure times has been discussed in detail [249]. For the annealed samples, where only the distribution of the precipitates is expected to vary with the quenching rate, Figure 6.18 reveals a small influence on corrosion in PWRs and in out-of-pile water and a moderate influence in BWRs. In cladding tubes where quite large hot and cold deformations are applied after the  $\beta$ -quenching the precipitate distribution becomes more uniform and less dependent on the  $\beta$ -quenching rate. Therefore, the  $\beta$ -quenching rate is not considered to have a large influence on corrosion if a certain precipitate size (required for good corrosion resistance) is achieved by the subsequent annealing treatment, as is usual for PWR cladding. However, a high quenching rate is certainly advisable for a controlled adjustment of medium precipitate size, as is necessary for optimised BWR cladding.

#### 6.2.3 Influence of final annealing

The final annealing ("condition") of cladding determines the degree of recrystallization established by the final heat treatment. In out-of-pile testing (Figure 6.19) [269] the effect of the final

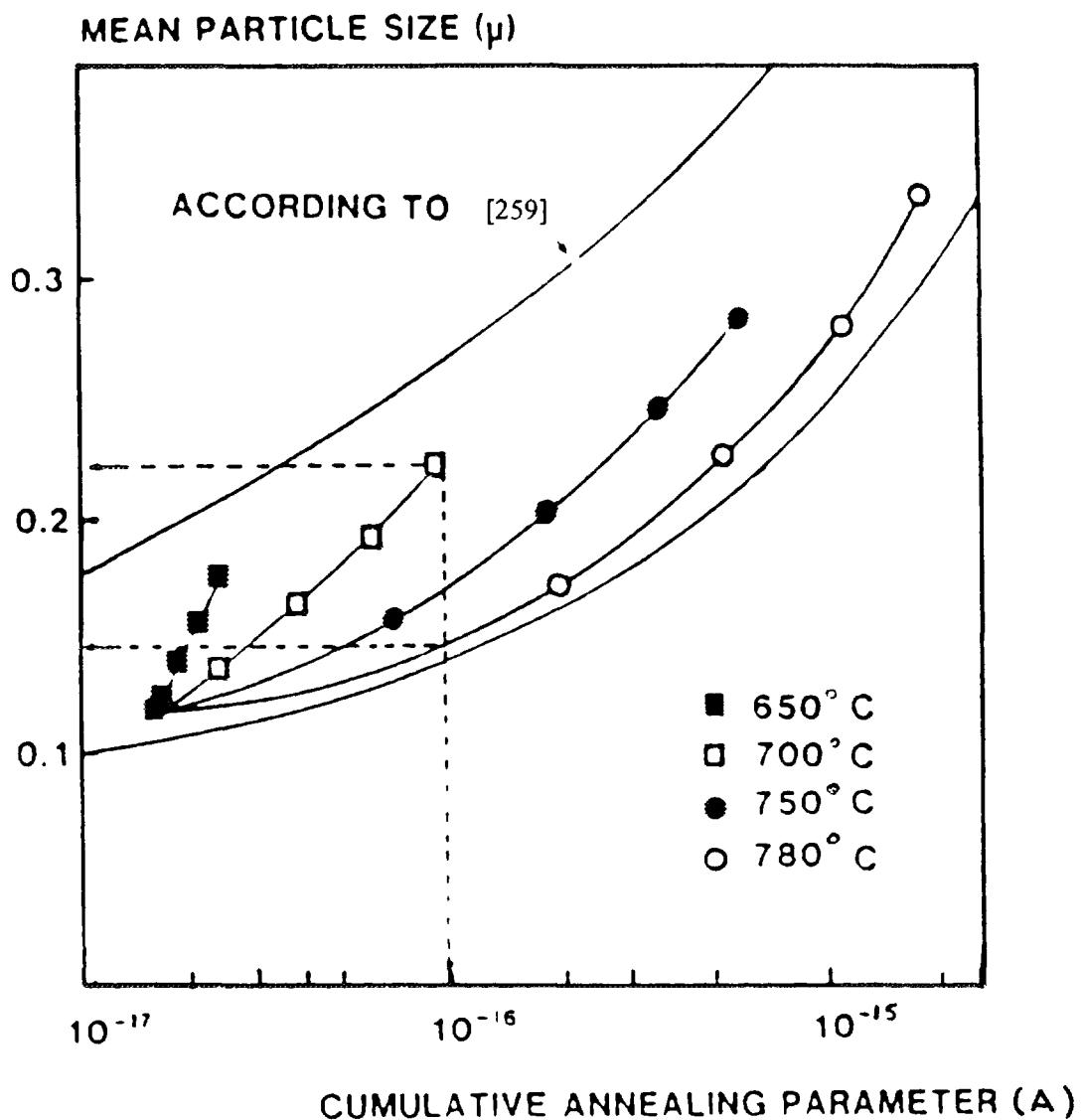


Figure 6.16. Comparison of precipitate diameters calculated with the SOCAP and the A-Parameter [267]. The points are calculated from the SOCAP relationship (Table 6.4); the band enclosed by the two solid lines is from a correlation between the A-Parameter and precipitate size.

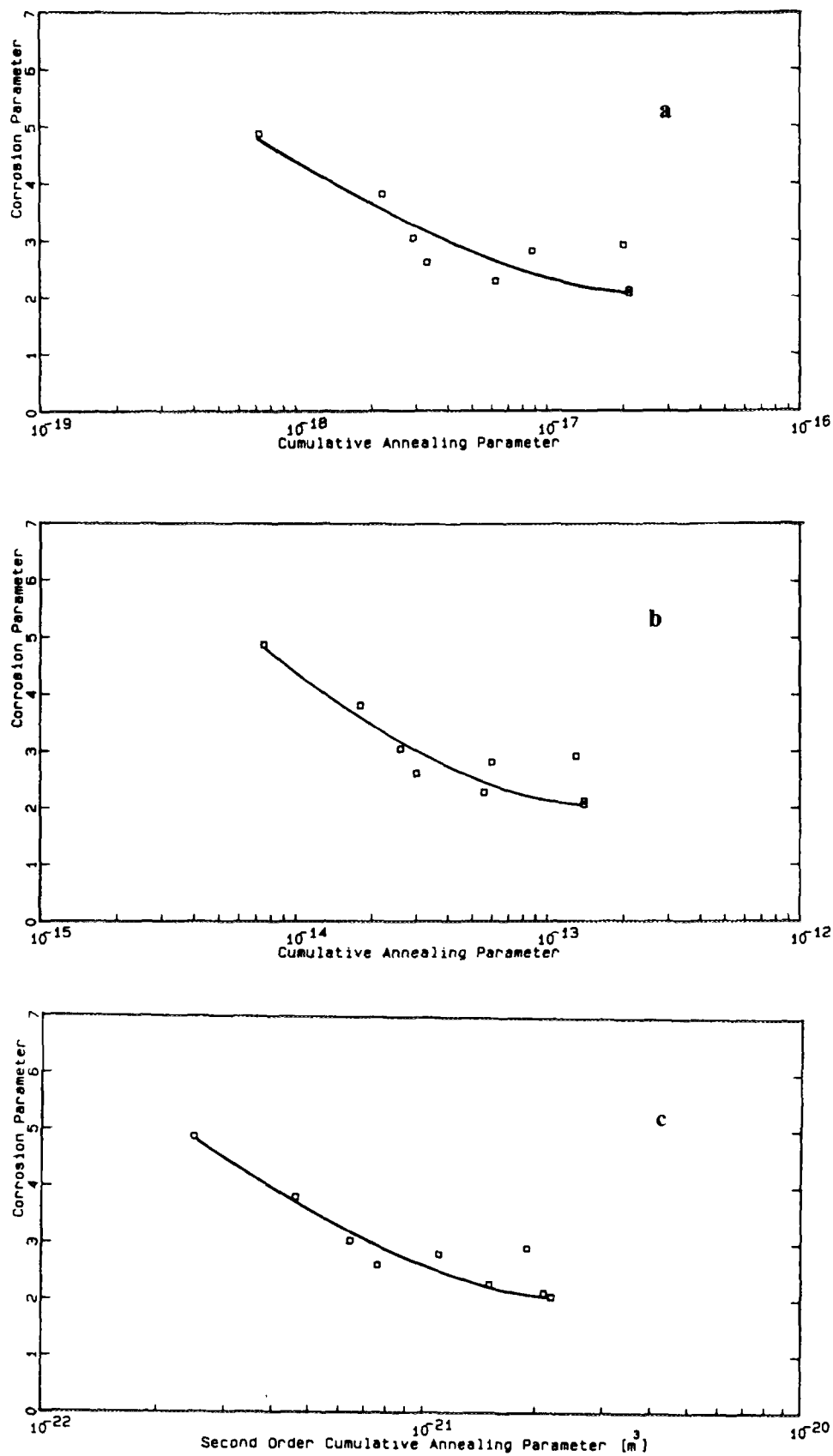


Figure 6.17. Comparison of corrosion parameter  $E'$  for different annealing parameters for in-pile corrosion [268]. **a** As a function of cumulative annealing parameter ( $Q/R = 40,000K$ ), **b** As a function of cumulative annealing parameter ( $Q/R = 31,500K$ ), **c** As a function of second-order annealing parameter (SOCAP).

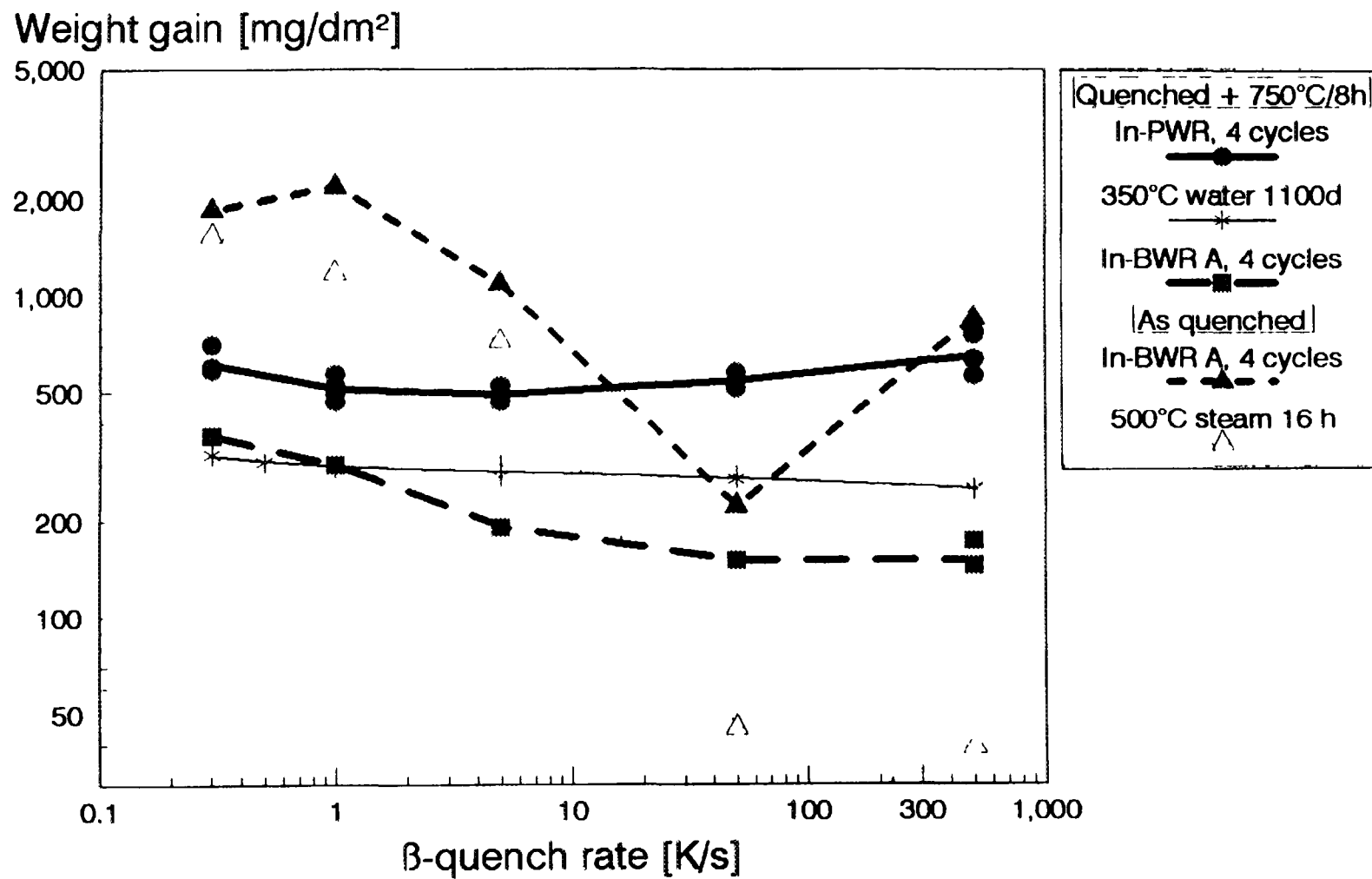


Figure 6.18 Effect of  $\beta$ -quench rate on corrosion of Zircalov-4 in PWRs, BWRs and out-of-pile experiments [242]



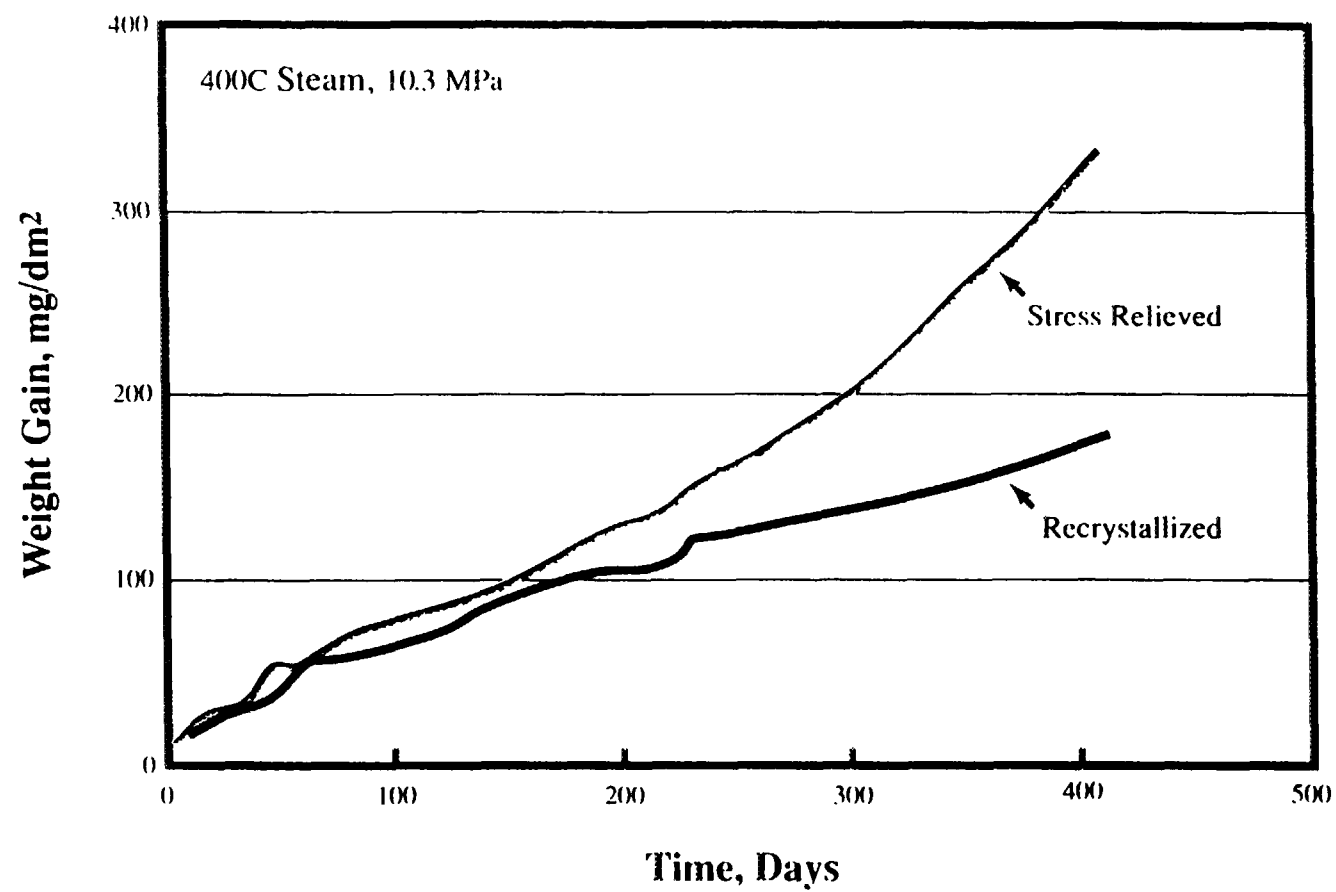


Figure 6.19. Comparison of stress relieved and recrystallized Zircaloy-4 tubing tested in 400°C Steam [269].

heat treatment on the corrosion of Zircaloy-4 tubing in 400°C steam is quite marked, even though the difference in cumulative annealing parameter is negligible. Recrystallized tubing has consistently lower weight gains than stress relieved cladding. An explanation of this behaviour has been given by Charquet et al. in an experimental study which showed a significant difference in the corrosion behaviour for different crystal planes [270]. However, it is remarkable that this effect could not be verified for in-reactor corrosion behaviour. No clear difference in corrosion was found for stress relieved (SRA) and recrystallized (RXA) cladding (Figure 6.4) [242].

#### 6.2.4 Influence of cold work and deformation sequence

The possibility that other factors than heat treatments may influence corrosion resistance was confirmed by an experimental cladding fabrication program [271]. For some of the fabrication sequences investigated the effects of cold deformation and texture overcompensated the expected detrimental effect of the annealing parameters lying outside of an optimal range, as concluded from 500°C steam corrosion test results. However, as for the case of recrystallization (section 6.2.3), it is necessary to consider whether or not this behaviour is also representative of in-pile behaviour especially for BWR materials.

#### 6.2.5 Initiation of nodular corrosion in BWR materials

The question of whether nodular corrosion in BWRs nucleates at intermetallic particles, between intermetallic particles, or as a collective property of a group of grains, has yet to be resolved [132,133]. The resolution of this question will have a considerable effect on our understanding of the response to changing metallurgical variables of the corrosion resistance of the Zircaloys. Final annealing can change factors such as lattice strain without significantly changing the particle size and distribution. Thus, a knowledge of the initiation mechanism for nodular corrosion is essential if changes in fabrication routes are to be made on a rational basis.

#### 6.2.6 Effect of metallurgical conditions on the corrosion of Zr-Nb alloys

##### 6.2.6.1 Zr-1%Nb alloy

Corrosion properties of Zr-1%Nb are significantly dependent on its structure, and that is governed by hot working and heat treatment. Table 6.5 gives weight gains of alloy samples as tested in water and steam after anneals at 580, 700 and 800°C [72]. The advantage of annealing at 580°C can be explained by the Zr-Nb phase diagram (see Figure 2.4).

Table 6.5 Corrosion of Zr-1% Nb alloy samples during testing (mg/dm<sup>2</sup>)

Sample condition	Water, 350°C, 7500 h	Steam, 400°C, 3000 h
Anneal at 580°C, 5 h	50	45
Anneal at 700°C, 1.5 h	80	100
Anneal at 800°C, 1.5 h	Oxide film spalling	130

An anneal above the monotectoid temperature can lead to the retention of a  $\beta$ -Zr phase which degrades the corrosion resistance of the alloy (Figure 6.20) [273]. A very careful approach is needed when choosing schedules and conditions of hot working to avoid metastable phases in the Zr-Nb alloy structures and to produce states closest to equilibrium. This is most important for welded joints.

Water and steam corrosion of the alloy, as annealed at 580°C and 700°C, proceeds by the parabolic law to form surface oxide films firmly adhering to the base metal (Figure 6.21). In 8,000-20,000 h tests the hydrogen pick-up fraction was less than 10% for materials in which anneals were at 580°C and 700°C.

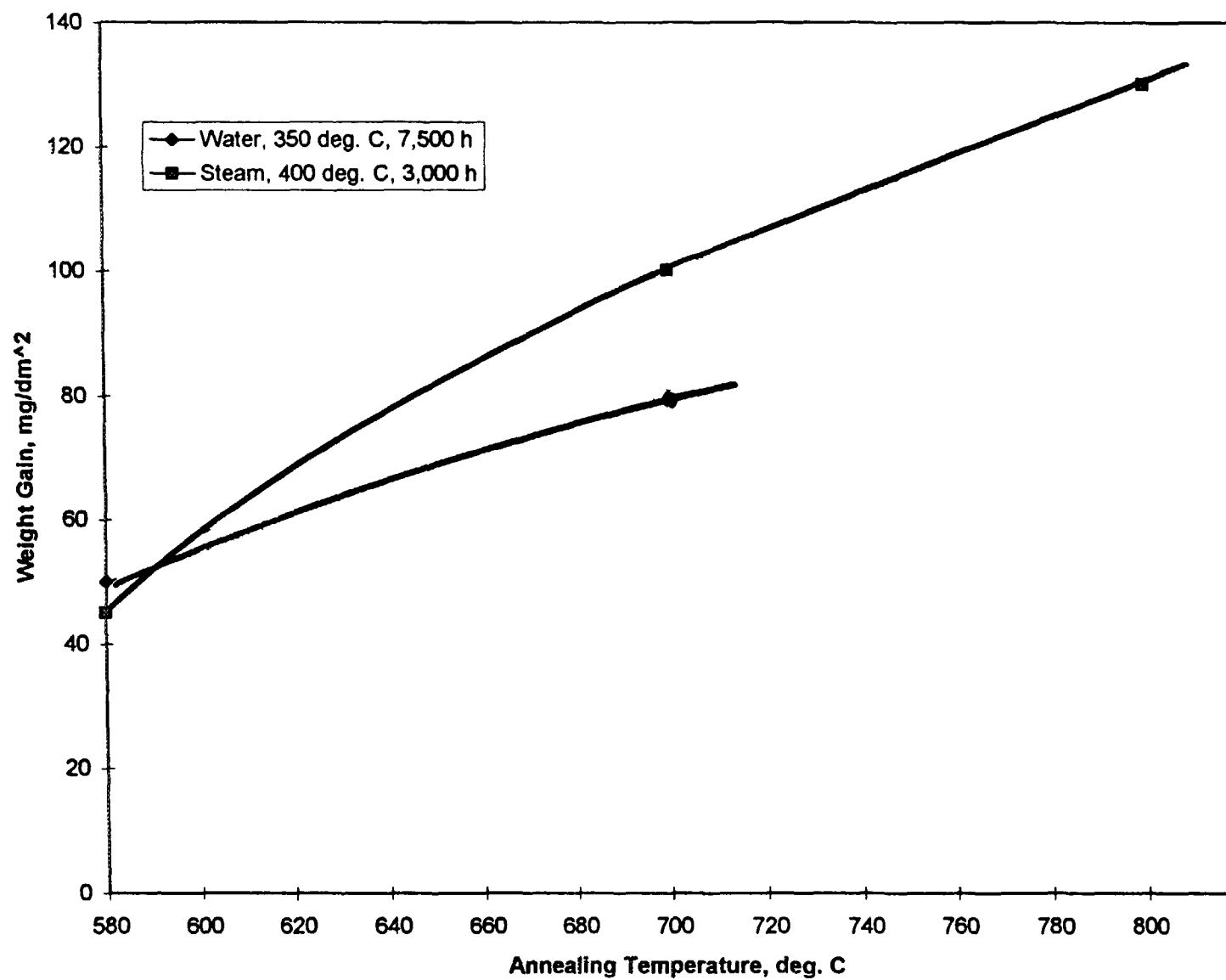


Figure 6.20. Degradation of the corrosion resistance of Zr-1%Nb following annealing at above the monotectoid temperature

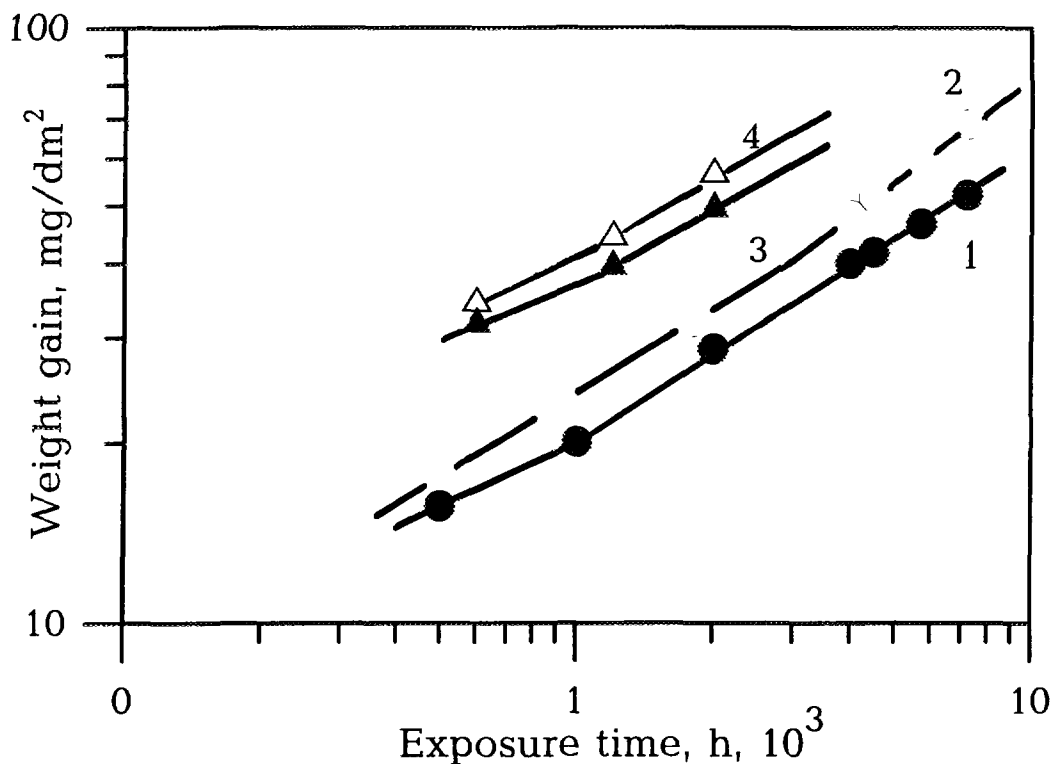


Figure 6.21. Oxidation of Zr-1%Nb in water at 350°C (1,2) and steam at 400°C (3,4). (1,3) annealing at 580°C and (2,4) annealing at 700°C.

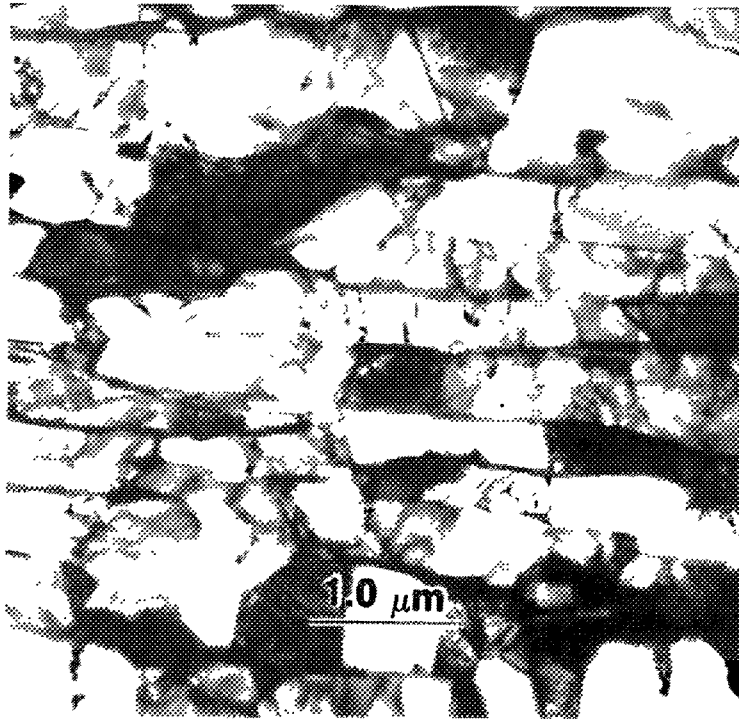
The shining dark-coloured oxide films that formed during corrosion on samples annealed at 580°C duplicate the crystallographic orientation of grains of the metal-substrate, i.e. rolling texture. Grey oxide films formed on samples annealed at 700°C and contained fine light intergranular oxide crystals of random orientation, i.e. there was a recrystallization of the compact black coloured oxide.

#### 6. 2. 6. 2. Zr-2.5%Nb Alloy

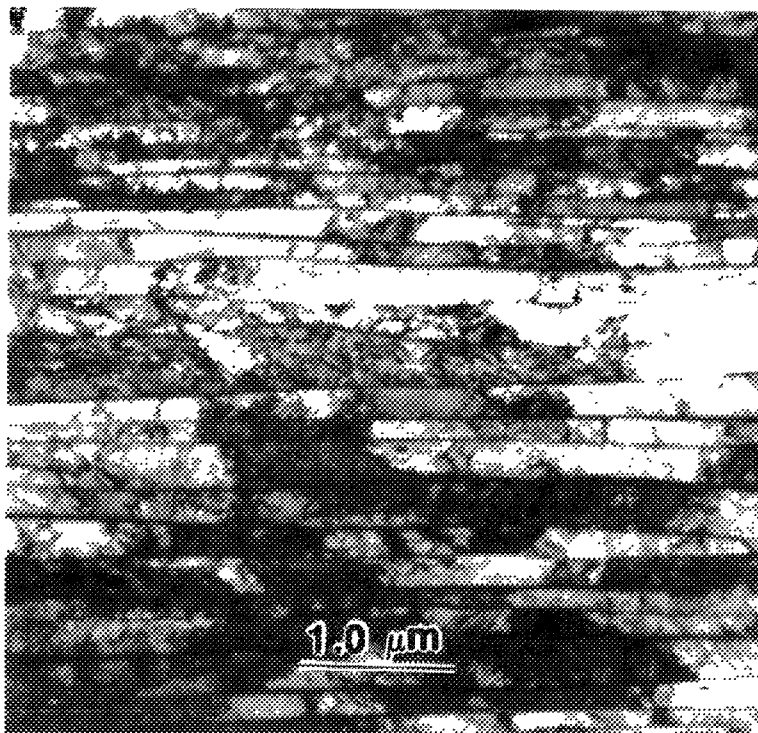
In the case of Zr-2.5%Nb pressure tubes the fabrication variables affect primarily the size, distribution and phase composition of the residual  $\beta$ -Zr phase [274]. For the cold-worked (C.W.) condition the corrosion and hydrogen uptake properties in CANDU water chemistry appear to be better than for the heat-treated (H.T.) condition (usually an  $(\alpha+\beta)$  quench, followed by cold-reduction and a final age at  $\sim 500^\circ\text{C}$ ) [121]. The reason for this appears to be the continuous film of  $\beta$ -Zr(Nb), left along  $\alpha$ -Zr grain boundaries following extrusion, that is not decomposed by the C.W. treatment followed by the usual 400°C stress relief (Figure 6.22). This structure should be compared with the discrete  $\beta$ -Nb precipitates produced in the H.T. alloy. Ageing in reactor results firstly in the break-up of this continuous  $\beta$ -Zr phase, and ultimately its decomposition to  $\beta$ -Nb [275]. This ageing process reduces the short-term corrosion rate. No effect on the long-term corrosion properties has yet become evident [275]. Re-exposure of irradiated samples has confirmed that both thermal and irradiation ageing have equivalent effects on the corrosion process.

#### 6. 3. SURFACE CONDITIONS

Chemical polishing (in mixed nitric/hydrofluoric acids) of zirconium alloy surfaces was introduced early in the development of these alloys as a means of obtaining reproducibly good corrosion behaviour during corrosion testing in autoclaves. However, consistent care with



(a) as extruded the elongated  $\alpha$  grains contain few dislocation networks.



(b) extruded and cold worked 25%. The elongated  $\alpha$  grains with a high dislocation density.

*Figure 6.22. Typical microstructures of Zr-2.5%Nb pressure tubes showing the  $\alpha$  grains elongated in the axial direction.*

neutralising (stop bath) and washing after pickling are needed to prevent enhanced oxidation from "pickle staining" if residual fluoride were left on the surface. There has, therefore, been a desire to avoid this costly and risky operation.

Over the years, a change has progressively been made, by many fuel vendors, from the standard chemically polished and autoclaved (400°C steam) initial surface for fuel cladding, firstly by eliminating the autoclaving treatment, and subsequently by substituting belt-ground surfaces for chemically polished ones. Although tests in high pH solutions in the laboratory suggest that such changes might lead to significant changes in the corrosion of the surfaces, no significant differences have been reported in pH 10 (measured at room temperature) solutions in laboratory autoclave tests. The assumption has been made therefore, that such changes in surface preparation cause no deleterious effect on the long-term corrosion of the cladding. Other effects such as variability between batches of cladding may have obscured any effects that are present, but it cannot be assumed on present evidence that such effects will be absent. Surprisingly variable results for belt-ground surfaces in laboratory autoclave tests have been reported [276], and lead to the suspicion that perhaps these surfaces are more susceptible to contamination during preparation than pickled surfaces.

Investigation of the effect of surface preparation on the results of 500°C high pressure steam tests [277] has shown little difference between ground and pickled surfaces. Pre-oxidation by autoclaving at 300–400°C or by anodic oxidation delayed nodular attack significantly, but did not prevent it. The delay in nodule nucleation was dependent on the oxide thickness rather than the mode of formation.

Cladding and structural materials for in-pile use are fabricated with reproducible surface conditions. In the early days this reproducible clean surface finish was performed by pickling in mixtures of hydrofluoric and nitric acid. This treatment leaves traces of zirconium oxyfluorides on the surface which cannot be removed by rinsing in water. The bad influence of fluoride contamination on corrosion is well known [278]. In order to detect residuals from pickling, fabricators used autoclaving of the cladding (mainly for BWR application). High local fluoride concentrations were revealed by high local corrosion and the affected material could be discarded. Later on autoclaving was suspected of inducing increased corrosion rates in reactors. This observation initiated an experimental programme performed in the Halden BHW (279) which included pickled, autoclaved and anodically oxidised surfaces. The investigation concluded that corrosion is not affected by autoclaving or the anodising pre-treatment. Autoclaving was beneficial, but only for pickled surfaces. Some beneficial effect was observed for anodically oxidised material.

The autoclaving of surfaces has lost its attractiveness today and thus the surface treatment of materials exposed to the coolant of light water reactor is belt grinding for both BWR and PWR application. Some years ago Siemens cladding was electropolished. This treatment produced a surface as smooth as pickling, but avoided fluoride contamination. Later on a fine belt polishing surface treatment was developed to replace the hazardous electropolishing procedure. It was shown by in-pile investigations in a high efficiency PWR that there was no significant difference in corrosion between flash electropolished and belt ground surfaces [280].

## 6.4 COOLANT CHEMISTRY

Water coolants are highly controlled and include deliberate chemical additives which may influence zirconium alloy corrosion. Lithium hydroxide is particularly important, since it can markedly influence oxidation if conditions facilitate the concentration (hideout) of lithium in the oxide. Boric acid is added in PWRs for reactivity control. The coolant chemistry also influences the solubilities of coolant-borne metallic impurities (e.g. iron, nickel, copper, etc. arising from corrosion release from circuit surfaces) which may deposit as crud (metal oxides) on fuel rod surfaces and which have, in some cases, appeared to contribute to accelerated oxidation of both BWR and PWR cladding. Crud-induced acceleration is discussed in section 8.3. In addition, small concentrations of impurities (F, Cl, etc.) may be found in reactor coolants and it is important to understand the

potential effects of such impurities and the levels below which effects on corrosion are negligible or tolerable. The possible influence of dissolved oxygen also needs to be considered. This will be present in "oxidising" coolants (e.g. some BWR coolants) but in any case it will be produced by radiolysis whenever this is present as discussed in section 8.2.

#### 6.4.1 PWR chemistry

##### 6.4.1.1 Chemistry recommendations

The EPRI PWR Primary Water Chemistry Guidelines [281] make recommendations on certain chemistry parameters. Important parameters are termed control parameters, three levels of operator action (culminating in plant shutdown) being recommended when parameter values fall outside each Action Level. Other parameters are termed diagnostic parameters, guidance being given for investigating anomalous values. Table 6.6 lists values for the primary coolant during power operation.

##### 6.4.1.2 Boric acid

PWRs contain boric acid for reactivity control, the concentration is reduced with time during a fuel cycle, usually being near zero at end of cycle. For a twelve month cycle, the initial boron concentration is typically 1,200 ppm but is reduced rapidly over the first few days of the cycle to approximately 900 ppm whilst the xenon and samarium poisons (neutron absorbers) build up to equilibrium levels in the fuel. Thereafter the boron concentration is reduced approximately linearly at  $\sim 3 \text{ ppm d}^{-1}$ . For an 18 month cycle the initial boron concentration is typically 1,800 ppm dropping to  $\sim 1,400$  ppm after a few days.

##### 6.4.1.3 Lithium hydroxide

Lithium hydroxide is added to render the coolant slightly alkaline in order to inhibit deposition of corrosion products on the fuel cladding and to reduce the corrosion rates of structural materials (stainless steels and Inconels) to low levels. As well as avoiding any possibility of physical degradation, addition of LiOH also reduces the quantity of radioactive corrosion products ( $^{60}\text{Co}$ ,  $^{58}\text{Co}$  etc.) which give rise to most of the radiation dose to station personnel. Minimising crud deposition avoids the possibility of crud induced corrosion acceleration (section 8.3). However, as discussed in section 4.2.5, above certain concentration levels, lithium hydroxide increases zirconium alloy corrosion rates and it may also increase stress corrosion cracking, especially of Inconel 600, present in many reactors as steam generator tubing and control rod drive mechanism penetrations. Thus, the optimum level of lithium hydroxide in the coolant has been a research issue for many years.

Table 6.6 EPRI PWR primary coolant chemistry specification for power operation [281]

<u>Parameter</u>	<u>Action Level</u>		
	1	2	3
<u>Control Parameters</u>			
Chloride, ppb	>50	>150	>1500
Fluoride, ppb	>50	>150	>1500
Sulphate, ppb	>50	>150	>1500
Hydrogen, $\text{cm}^3 \text{ STP kg}^{-1}$	<25, >50	<15	<5
ppm	<2.2, >4.5	<1.3	<0.44
Oxygen ppb	>5	>100	>1000
Lithium	Consistent with Station Lithium Program		

Diagnostic Parameters	Typical Value
Conductivity, mS cm <sup>-1</sup> at 25°C	Consistent with Li/B concentrations
pH at 25°C	Consistent with Li/B concentrations
B	As required for reactivity control
Suspended Solids, ppb	<10
Silica	<1000

As discussed in section 4.2.5, in single phase coolants and in short term laboratory experiments, lithium hydroxide appears to significantly affect Zircaloy corrosion, only above a concentration of approximately 30 ppm Li in coolants free of boric acid. Boric acid ameliorates (reduces) the detrimental effect of lithium hydroxide above a boron concentration of approximately 100 ppm. However, in two phase coolants, the local concentration of lithium hydroxide increases due to hide-out. In the presence of a heat flux, voidage may occur either on the surface of the fuel cladding or inside pores in the oxide layer. However, concentration of lithium hydroxide as a result of boiling elevates the boiling point and may suppress the boiling after a certain period (section 9.2.1). Under two-phase heat transfer, heat flux and lithium hydroxide enrichment constitute a potential accelerating mechanism. Loop experiments illustrating this effect are shown as curve (4) versus curve (2) in Figure 6.23. Above approximately 15% voidage, the lithium hydroxide effect rapidly increases as shown in the circumferential variations in Figure 6.24. In addition, Zircaloy cladding, subjected at the beginning of life to boiling conditions, undergoes shorter transition times, as well as subsequent faster post-transition corrosion rates. The absence of a pre-transition state, with an oxide film of higher porosity, may occur at high void fractions ( $\alpha \approx 30\%$ ) with 10 ppm lithium in the bulk water as illustrated in Figure 6.25. This figure also shows that the oxide layer, formed at normal PWR lithium levels of 2.2 ppm, significantly protects the cladding from boiling-induced acceleration of corrosion kinetics. After transition, the increase in porosity, extending up to the metal/oxide interface, either (i) causes increased incorporation of LiOH (and then accelerated corrosion) or (ii) is caused by increased preferential dissolution of zirconium oxide by LiOH [118], the increase in porosity itself leading to accelerated corrosion.

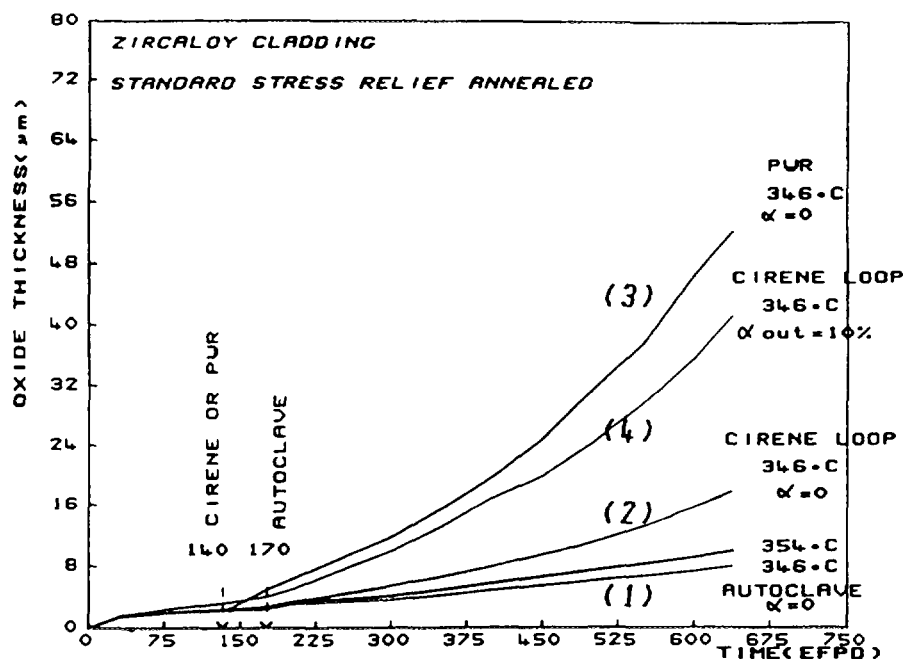


Figure 6.23 Corrosion kinetics - effect of void fraction on corrosion in lithiated solutions



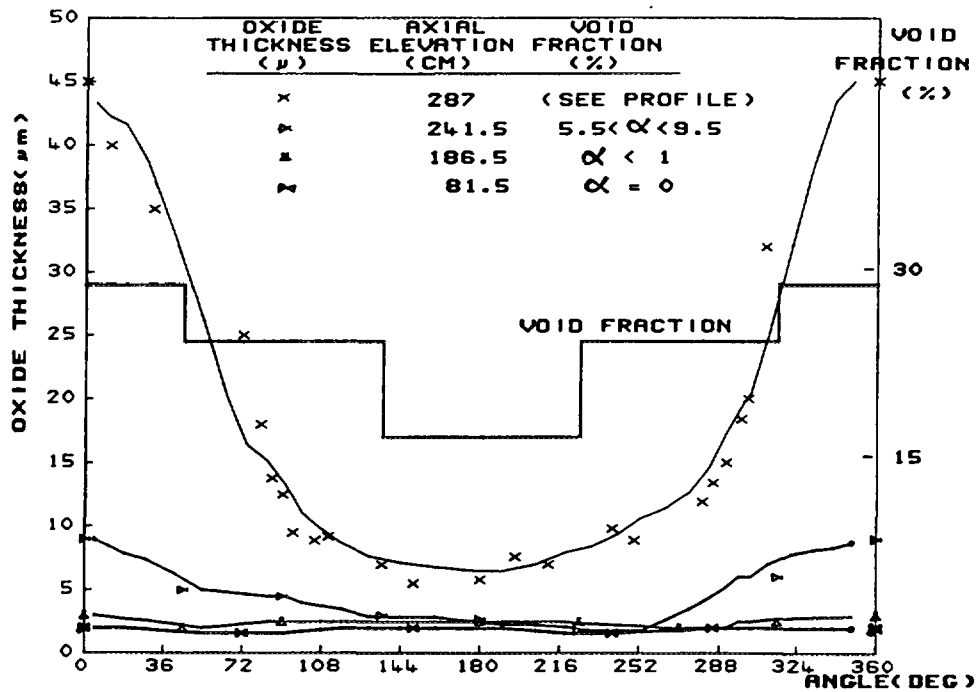


Figure 6.24. Azimuthal corrosion in the Cirene loop.

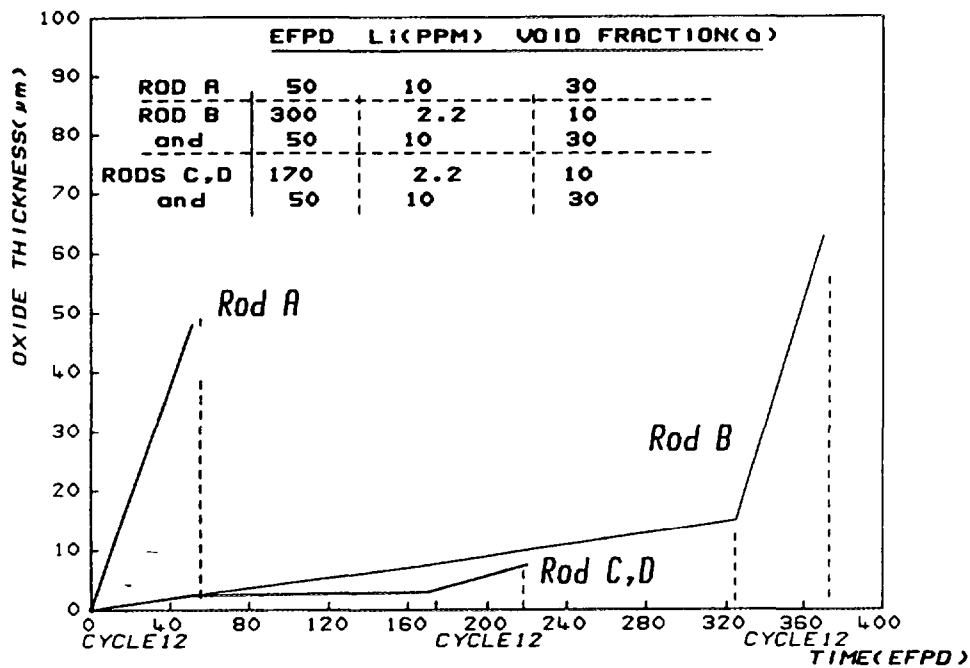


Figure 6.25. Corrosion kinetics - effects of LiOH and void fraction.

Normally, high voidage levels do not occur in PWR coolants and, thus, any lithium hydroxide enhancement by this mechanism may be less severe. In-pile loop experiments at Halden, in Norway, in a borated coolant containing 4-4.5 ppm Li and 1,000 ppm B appeared to show little detectable lithium enhancement in thick oxides, as discussed in section 7. 3. 2. 2. Oxide thicknesses on several PWRs operating elevated lithium chemistry regimes have been examined for lithium enhancement. Exposure for one or two extended (18 month) cycles of elevated lithium at Millstone-3 PWR led to no detectable effect, although there was considerable variability in the data (see section 7. 3. 2. 5.). Elevated lithium chemistry was concluded to have increased oxide thicknesses by approximately 10-15% at the St Lucie-1 PWR (see section 7. 3. 2. 1.). Operation of elevated lithium chemistry in the Ringhals-2, -3 and -4 units over approximately a five year period was said to have no negative effect on oxidation [282,283]. No detailed analyses have been performed on Oconee-2 oxide thicknesses after one cycle of elevated lithium operation, although comparisons have been made with earlier operation at lower lithium levels in which some allowance was made for crud deposition [284].

Lithium hydroxide attacks certain Zr-Nb alloys more than Zircaloy-4, but some Zr-Nb-Sn alloys, for example ZIRLO and E635, are reported to be more resistant than Zircaloy-4 to lithium hydroxide attack [74,285,286] (See Figures 4.24 and 4.25).

#### 6. 4. 1. 4. Coolant chemistry regimes

One of the most complex issues is the choice of lithium-boron (pH) chemistry regime. The EPRI recommendations are complicated somewhat by the new recommendation [281] to calculate pH values at the average coolant temperature,  $T_{ave}$ , (mean of the core inlet and outlet temperatures) rather than at a fixed temperature such as 300°C. Ignoring this complication, Figure 6.26 presents recommendations for pH values calculated at 300°C. Operation below pH 6.9 is not recommended in order to avoid excessive crud deposition on fuel cladding and increased radiation fields. As is seen from Figure 6.26, at the beginning of 18 month and 24 month cycles (boron  $\geq 1,800$  ppm) the required lithium concentration exceeds 3.5 ppm. In order to avoid these higher lithium concentrations for planned future operation of 24 month cycles, German workers are currently considering alternative strategies, including substitution of KOH for LiOH and the use of boric acid enriched in  $^{10}\text{B}$  [287]. During the 1980s most plants operated the “co-ordinated pH 6.9 regime” (Figure 6.27) and some plants still do. The advantages of reduced dose rates led some plants to operate the “elevated lithium regime” in the mid- to late 1980s, notably Ringhals-2, -3 and -4. With this regime the lithium is held at approximately  $3.35 \pm 0.15$  ppm until a pH of 7.4 is attained and, thereafter, this pH is maintained until the end of the cycle. Elevated lithium operation offers an opportunity for investigating any lithium hydroxide induced acceleration of corrosion (see sections 6. 4. 1. 3. and 7. 3.). However, it is believed that, at the time of writing, no plant is operating in this regime and many plants currently operate in the intermediate regime, known as the “modified lithium regime”, either in the form illustrated in Figure 6.27 or modifications of it.

#### 6. 4. 1. 5. Hydrogen and oxygen

Dissolved hydrogen is maintained in the coolant in order to recombine rapidly with oxygen radicals formed by radiolysis (section 8. 2.), for the purpose of inhibiting the stress corrosion cracking and general corrosion of circuit components [281]. The recommended hydrogen concentration is currently 2.2-4.5 ppm (Table 6.6). This is sufficient to reduce the oxygen concentration to an undetectable level. Garzarolli et al. [125] found that an extremely high concentration of hydrogen peroxide (6%) increased Zircaloy-4 corrosion rates by only about 15% and that a normal concentration of hydrogen (3 ppm) apparently decreased corrosion rates by about 15%. Early Westinghouse tests [288] showed a factor three increase in the corrosion rate of Zircaloy-2 at very high hydrogen concentrations (300 ppm). Recently, French tests have indicated that hydrogen at much lower concentrations than 2.2 ppm can still suppress radiolysis [289] and, thus, operation of PWRs at less than the recommended hydrogen concentration may be contemplated. At the Obrigheim PWR, nodular oxide thicknesses of 80  $\mu\text{m}$  were attained on fuel cladding after operating for 512 days at an oxygen concentration of 300 ppb in the absence of a hydrogen over-pressure [289].

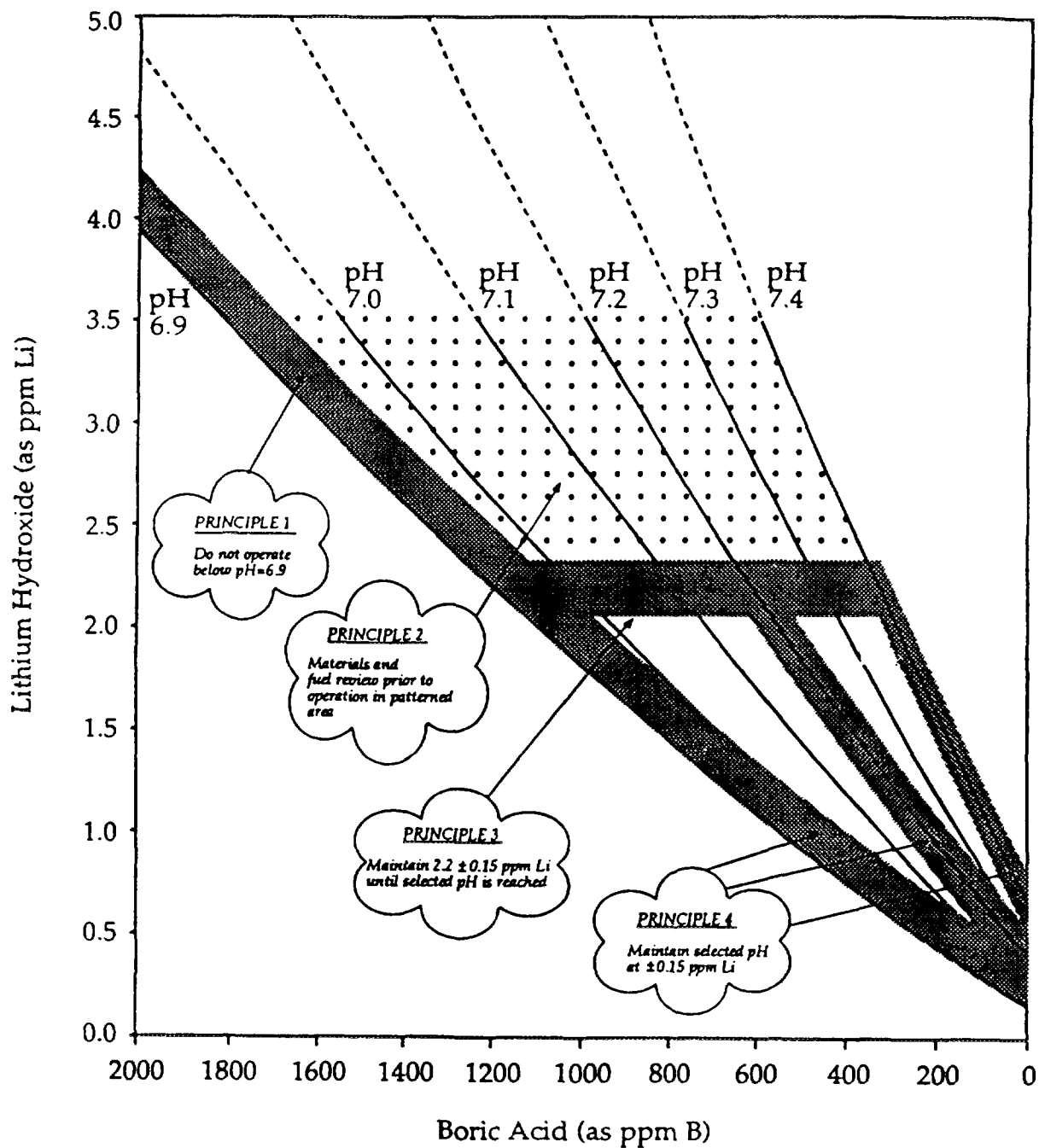


Figure 6.26. EPRI recommendations on PWR primary coolant chemistry regimes: pH values calculated at 300° [281].

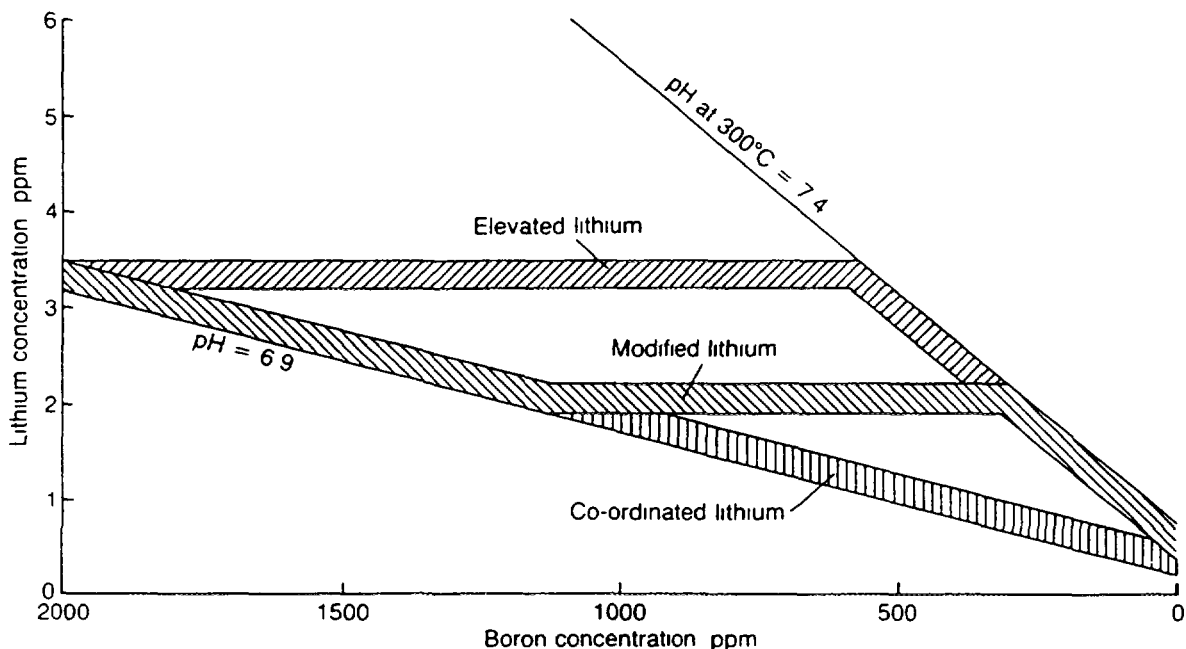


Figure 6.27 Various lithium-boron modes of operation in PWRs (from WOOD) (Approaching consensus in the optimum pH for PWRs, (Nucl Eng Int August 1990 p28)

Hydrogen dissolved in the coolant does not enter zirconium alloys, since the oxide layer presents a barrier to transport (see section 5.1) and, therefore contributes little or nothing to hydriding. However, it was reported [290] that some Ringhals-2 fuel assembly guide tubes had >100% hydrogen pick-up, due to direct absorption from the coolant through a (non-standard) sensitised grit blasted surface.

#### 6.4.1.6 Impurities

Chloride, fluoride and sulphate are controlled in order to inhibit stress corrosion cracking of austenitic stainless steels, although fluoride control is also required to inhibit zirconium alloy corrosion [281].

Laboratory data on the effect of impurities on Zircaloy-4 corrosion has been reviewed in [124-125]. Significantly increased corrosion was found at relatively high fluoride concentrations (10 ppm). It has been stated [288,291] that fluoride begins to accelerate Zircaloy-4 corrosion between  $10^{-3}$  and  $10^{-2}$  molal (19-190 ppm) at 360°C and that corrosion resistance is unaffected by chloride and iodide at  $10^{-2}$  molal. The specification for fluoride is usually set much lower than these high levels to protect against concentration effects during boiling (see Table 6.6). Fluoride is produced in reactor water by neutron capture in  $^{18}\text{O}$  to form  $^{19}\text{F}$ .

Garzarolli et al. [125] reported that a moderate increase in corrosion was caused by high concentrations of chloride, chromate and cation resin. Nitrides, sulphates, anion resin, hydrazine and  $\text{Fe}_2\text{O}_3$  had no noticeable effect. High concentrations of  $\text{Cr}_2\text{O}_3$ ,  $\text{NiO}$ ,  $\text{NiFe}_2\text{O}_4$  and  $\text{SiO}_2$  caused a reduction in the time to transition but had no effect on the post-transition corrosion rate.

#### 6.4.1.7 Zinc addition

Following experience in BWRs (section 6.4.2.3), the deliberate addition of 10-40 ppb zinc to PWR primary coolants is currently under investigation in several countries (e.g. [292]) and by EPRI.

and Westinghouse [293], with a view to both inhibiting stress corrosion cracking of certain Inconel 600 components and to lowering PWR radiation fields. One of the issues is deposition onto, and compatibility with, fuel cladding surfaces. A plant demonstration in the USA is proceeding at the time of writing. With evidence accumulating that boric acid may be protecting the cladding from enhanced corrosion by LiOH, caution should be exercised with additions that might interfere with the precipitation of complex borates in the porous oxide film [111,113,114] (see section 4.2.5).

#### 6.4.2 BWR chemistry

In the past, recommendations for optimising BWR water chemistry were aimed at high purity, characterised mainly by conductivity. Now several additives are in use, hydrogen to prevent intergranular stress corrosion cracking, iron to retain  $^{60}\text{Co}$  on the fuel rods, and zinc injection to reduce  $^{60}\text{Co}$  absorption on out-of-core circuit surfaces. BWR water chemistry is reviewed, for example, in [294,295]. EPRI issued Normal Water Chemistry Guidelines and Hydrogen Water Chemistry Guidelines in 1988. These have been revised and collated into a single document [296].

##### 6.4.2.1 Hydrogen water chemistry

In the absence of dissolved hydrogen, the oxygen in the feedwater is typically 200-400 ppb and this is sufficient to cause concern over stress corrosion cracking in sensitised steels under tensile stress. This concern is removed by injecting 0.2-2 ppm hydrogen. However, this may cause other concerns, including hydrogen pick-up by the fuel cladding, which has caused some plants, in particular in Sweden, to discontinue hydrogen water chemistry [294]. There were also indications in some plants of increased radiation fields, thought to be due to corrosion product release as the oxide on out-of-core stainless steels changed from a haematite to a magnetite structure [297]. Nevertheless, many plants still regard hydrogen water chemistry as the best option and in [298] it was stated that at that time 16 US plants utilised Hydrogen Water Chemistry compared with 18 that operated Normal Water Chemistry.

##### 6.4.2.2 Iron injection and Ni/Fe control

$^{60}\text{Co}$  and  $^{58}\text{Co}$  activities, in the coolant and deposited on surfaces, can be minimised if the crud deposited on the fuel cladding is in an insoluble form and, therefore, should not be dissolved appreciably during irradiation. Nickel-(cobalt)-iron-spinel, of a simplified chemical formula  $\text{NiFe}_2\text{O}_4$ , is such a sparingly soluble compound. This can be formed by injecting iron in ionic form into the feedwater in order to keep the Ni/Fe ratio theoretically at 0.5, but in practice it was found that a ratio of  $<0.2$  was required [294,299]. This technique has been adopted particularly in Japanese and Swedish BWRs. Control of the Ni/Fe concentration ratio in Japanese plants successfully limited radiation fields in newly commissioned plants but was causing concern after prolonged operation [300]. In some Japanese plants, a new heat treatment has been adopted for fuel cladding and this seems to affect the interaction between the clad and the corrosion products in the coolant, influencing radioactive corrosion product transport and, hence, radiation fields [300].

In contrast to injecting soluble iron to control Ni/Fe ratios, removal by filtration of particulate iron is reported to be increasingly important in controlling radiation fields and deposits on fuel cladding [298].

##### 6.4.2.3 Zinc injection

In early BWRs it was noticed that those with brass condenser tubing had lower radiation fields (most BWRs no longer have brass condensers). Arising from this discovery zinc is now deliberately injected into the coolant of a number of BWRs (13 out of 34 US plants listed in [298]). The zinc is incorporated into oxide films on out-of-core surfaces and modifies the nature of the oxide, reducing the film thickness. This, in turn, reduces both the production of  $^{60}\text{Co}$  and  $^{58}\text{Co}$  and their rates of incorporation into oxide films on out-of-core surfaces. Unfortunately zinc is activated to  $^{65}\text{Zn}$  and this

gives rise to a significant radiation dose. Thus, in some plants zinc depleted in  $^{64}\text{Zn}$  is injected at significant cost. At the Millstone-1 BWR the optimum natural zinc concentration adopted for Cycle 13 was 3-5 ppb, taking into account the detriment from radioactive  $^{64}\text{Zn}$  production [301] although values of 4-15 ppb were utilised in the previous cycle. At these low concentrations there appears to be little or no concern about the possibility of zinc deposition on fuel cladding leading to increased Zircaloy corrosion.

#### 6. 4. 2. 4. Effect of impurities

The Japanese BWR Hamaoka 1 experienced fuel failures during 1990 caused by a combination of anomalous water quality and cladding susceptibility to corrosion [302]. The poor water quality was considered to be due to high conductivity spikes. These were thought to be caused at start-up by sulphate and nitrate (organic decomposition products), during normal operation by sodium (from demineraliser resins) and at shutdown by sodium sulphate dissolving from deposits on fuel cladding.

Tests have been carried out in the Halden in-pile BWR test loop on the effect of  $\text{Cu}(\text{NO}_3)_2$ ,  $\text{Zn}(\text{NO}_3)_2$  and high  $\text{O}_2$  on Zircaloy-2 and on several new cladding alloys [303]. Nodular corrosion was produced in the reference chemistry (without additives) and in high oxygen. Copper sulphate and copper nitrate suppressed nodular corrosion.

Reference should be made to section 8. 3. 3. for the effect of impurities (in particular copper) in producing Crud Induced Localised Corrosion (CILC) failures. A computer code has been described which simulates the hide-out of various chemical species in the fuel cladding crud [304]. This attempts to relate the micro-environment in the crud layer to the bulk coolant and is potentially relevant to cladding integrity, crud deposition and activity transport.

#### 6. 4. 3. **WWER chemistry**

The coolant specifications for WWERs at the time of writing are given in Table 6.7. However, consideration is currently being given in the Czech Republic to changing to an Action Level system based on the EPRI PWR Guidelines (Table 6.6). Alkalinity is achieved by adding KOH rather than LiOH. Li is present at a low concentration, produced from  $^{10}\text{B}$ , but is restricted in concentration by removal in one of the demineralisers. Figure 6.28 gives the Czech (NRI) and Russian (VNIIAES) primary chemistry regimes for WWER-440 and WWER-1000 units [305,306]. The specifications are for the equivalent potassium concentration defined by:

$$[\text{K}^+]_{\text{eq}} = [\text{K}^+] + 40[\text{Li}^+]/7 + 40[\text{Na}^+]/23$$

The concentration of ammonium hydroxide does not appear in this formula, but contributes somewhat to the alkalinity. Ammonium hydroxide is added in place of hydrogen in order to produce a chemically reducing coolant, much of the ammonia decomposing to produce hydrogen under radiolysis.

At some plants, as well as adding ammonium hydroxide, hydrazine has been continuously injected. It has been claimed that this reduces the electrochemical potential, thereby reducing corrosion rates of stainless steel, leading to lower corrosion product activities. However, laboratory work does not support this and any benefit in-reactor is likely to be a result of increased ammonium hydroxide concentrations in the coolant caused by the presence of hydrazine [307]. In the Czech Republic it is proposed to change from ammonium hydroxide to hydrogen addition and to change from Zr-1%Nb to Zircaloy-4 cladding, as in Western PWRs.

For Zr-1%Nb alloy, very few fuel failures have occurred in Slovak and Czech Republic PWRs and oxides on fuel cladding have been thin [308]. Coolant chemistry values in the primary coolant of a number of Russian PWRs have been tabulated and reviewed [309]: in some fuel rods, large carbonaceous deposits had caused severe nodular corrosion and fuel failures.

Table 6.7. WWER primary water chemistry specifications for normal operation at power [286,305]  
(some variation for different countries)

Parameter	Unit	WWER-440	WWER-1000
Ammonia	ppm	>5	>5
Hydrogen	cm <sup>3</sup> ·(STP)·kg <sup>-1</sup>	30-60	30-60
	ppm	2.6-5.3	2.6-5.3
Chlorides + Fluorides	ppb	<100	<100
Oxygen	ppb	<10	<5 or <10
Iron	ppb	<20 or <200	<20 or <200
Copper	ppb	<20	<20
Boric acid*	g/kg	0-9	0-13.5
KOH	ppm	depends on boric acid conc.	
Coolant temperature			
Inlet	°C	268	290
Outlet	°C	290	320
Coolant pressure	MPa	12.5	16.0

\* 5.59 ppm boric acid = 1 ppm boron.

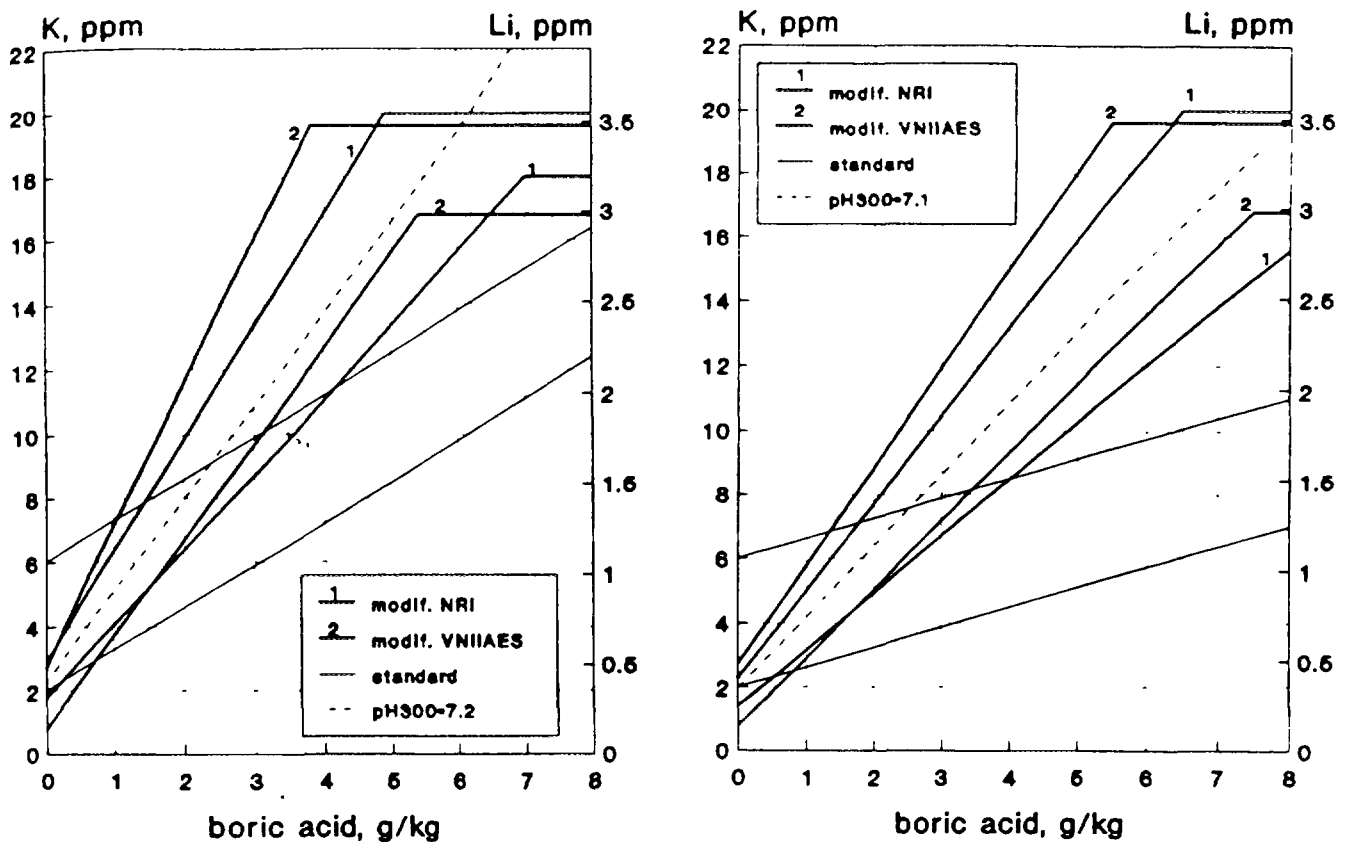


Figure 6.28. WWER recommended primary coolant chemistry regimes for Czech (NRI) and Russian (VNIIAES) Plants: WWER-440 Units (left), WWER-1000 Units (right) [305].

#### 6. 4. 4. PHWR (CANDU) chemistry

PHWR coolant (as opposed to the separate moderator) does not contain boric acid and deuterium is added in place of hydrogen in order to reduce neutron absorption, necessitated by the use of natural uranium fuel. Coolant chemistry specifications for several PHWRs are given in Table 6.8 [310-312]. Although PHWRs have somewhat lower coolant lithium concentrations than PWRs, this does not necessarily mean that lithium hydroxide effects are of less interest, since there is no boric acid amelioration effect, due to the absence of boric acid in the coolant. Research is proceeding currently in Canada on the benefits of zinc injection for reducing radiation fields.

Oxygen excursions have led to Zr-2.5%Nb and Zircaloy 2 pressure tubing corrosion being exceptionally high at high oxygen concentrations of 600 ppb [313]. It was shown [82] that the thin black oxide on pre-oxidised Zr-2.5%Nb pressure tubing acted as an excellent barrier to hydrogen ingress.

Table 6.8. Primary coolant specification for PHWRs

	Pressure Vessel	Pressure Vessel- Atucha 1	Pressure Tube- Embalse	Pressure Tube- Indian PHWR
Reference	[310]	[311]	[311]	[312]
Lithium (ppm)	1-2	1-2	0.7-2	-
Deuterium (cm <sup>3</sup> /kg)	6	6	0.5-4 ppm	3-20
Oxygen (ppm)	0.05	0.05	0.1	0.01
Chloride (ppm)	0.2	0.2	0.2	0.3
Fluoride (ppm)	-	-	-	0.05
Ammonia (ppm)	-	-	-	0.5
pD(25°C)	10.5-10.9	10.5-10.9	10.3-10.8	10.0-10.5
Conductivity (μS/cm)	30	30	20-60	30
Silica (ppm)	>4	4	-	-
Crud (ppm)	1	1	-	0.1
Dissolved Fe (ppm)	0.5	-	-	-

Note: For Atucha plants the lithium, deuterium, oxygen and chloride are described as "limiting values", the other parameters as "recommended values".

#### 6. 5. EFFECT OF TEMPERATURE

In PWRs at normal temperatures, corrosion in the post-transition region is linear with an activation energy assessed to be in the range of approximately  $Q/R=15,000-17,000$  for Zircaloy alloys (see section 7. 3.). The operating temperatures of PWRs are, in general, higher than those of BWRs and WWER-440s and, thus, clad corrosion during normal operation is of greater interest in PWRs since it can limit the allowable fuel burn-up.

It is important to consider oxidation at higher temperatures in order to assess the consequences of potential accidents, in particular Loss-of-Coolant Accidents (LOCAs). A number of studies have been made of high temperature oxidation, only a selection of which can be mentioned here.



### 6. 5. 1. High temperature oxidation of Zircaloy alloys

At temperatures below the  $\alpha/\alpha+\beta$  transition (approximately 810°C for Zircaloy-4) a zirconia film is produced with significant oxygen diffusing into the underlying  $\alpha$  metal. It has been observed [314] that the kinetics change from cubic to approximately linear with time in the range 600-800°C (as at lower temperatures) the value of the weight gain at transition increasing with temperature (Figure 6.29). Beyond the cubic/linear transition, the oxide exhibited extensive cracking.

At higher temperatures, the  $\alpha$ -Zircaloy transforms to the  $\beta$ -phase containing some diffused oxygen. However, an outer rim remains in the  $\alpha$ -phase, stabilised by a larger concentration of oxygen. Overlying this is the zirconia film. These changes lead to embrittlement of the cladding [315] and at temperatures close to the phase transition temperature the kinetics of oxidation are complex. At temperatures above the phase transition, in a study of Zircaloy-4 between 900-1500°C [316], the weight gains in the oxide layer and in the stabilised  $\alpha$ -Zr[O] became parabolic at temperatures greater than approximately 1,000°C [315] with activation energies of  $Q/R=18,060$  and  $24,230$ , respectively. In a study of Zircaloy-2 and Zircaloy-4 in the range 1,150-1,850°C [317], parabolic kinetics were observed throughout, there being a sharp increase in the parabolic rate constant at approximately 1,580°C with little change in the activation energy. No transition occurs even up to a very high oxide thickness.

Recent studies have generally found the Baker-Just correlations, produced in 1962 and adopted many years ago for safety calculations, to be conservative. Many studies of high temperature oxidation have been performed in unpressurised steam, however, it is important to realise that oxidation increases at higher pressures [318].

### 6. 5. 2. High temperature oxidation of Zr-1%Nb alloys

Results of tests between 300-1,400°C are given in [69]. At normal temperatures (300-350°C) long term (30,000 h) tests have shown the kinetics to be parabolic over the whole time period (Figure 6.30). This contrasts with the Russian model given in [272] and in section 7. 4. 2. 1 which assumes linear kinetics above approximately 3  $\mu\text{m}$ . Between 350°C and 600°C the kinetics change with time from cubic to parabolic to almost linear ( $t^{0.84}$ ). At 500-600°C a significant increase in corrosion with increase in pressure was observed. Pre-oxidation was found to be effective in limiting corrosion rates during high temperature excursions. At higher temperatures, in the  $\alpha+\beta$  and  $\beta$  regions, parabolic correlations were proposed for the oxide thickness and the width of the  $\alpha$ -Zr[O] layer. Parabolic kinetics were found [319] over the temperature range 700-1,100°C and Zr-1%Nb was found [69] to exhibit similar (though slightly lower) corrosion rates to Zircaloy-4, despite there being significant differences in the structure of the oxide and the  $\alpha$ -Zr[O] layer, between these two alloys over this temperature range.

## 6. 6. EFFECT OF HEAT FLUX

Because of the strong temperature dependence of corrosion, accurate predictions are required of the temperature of the oxide/metal interface [320,321], (see also section 7. 2. 1.). The heat fluxes in power reactors are high enough to generate a significant temperature rise across the oxide thickness, given by the following relationship:

$$T = T_w + \phi S / \kappa$$

where

- $T$  is the temperature of the oxide/metal interface (K);
- $T_w$  is the temperature of the outer oxide surface (K);
- $\phi$  = heat flux ( $\text{W}\cdot\text{m}^{-2}$ );
- $\kappa$  is the oxide thermal conductivity ( $\text{W}\cdot\text{m}^{-1}\cdot\text{K}^{-1}$ );
- $S$  is oxide thickness (m).

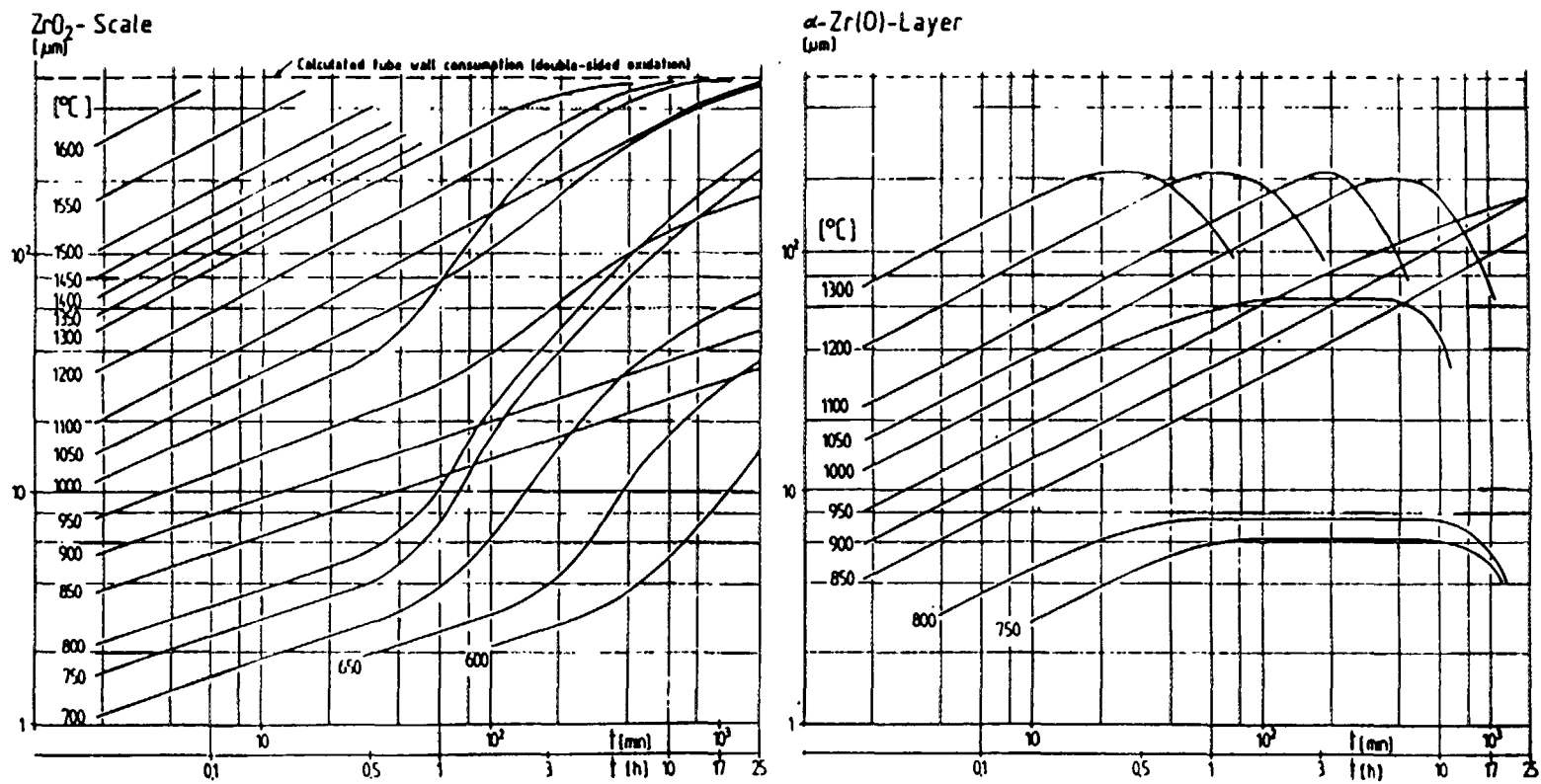


Figure 6.29. Thicknesses of oxide layer and  $\alpha$ -Zr(O) layer on Zircaloy-4 cladding from high temperature steam oxidation [314].

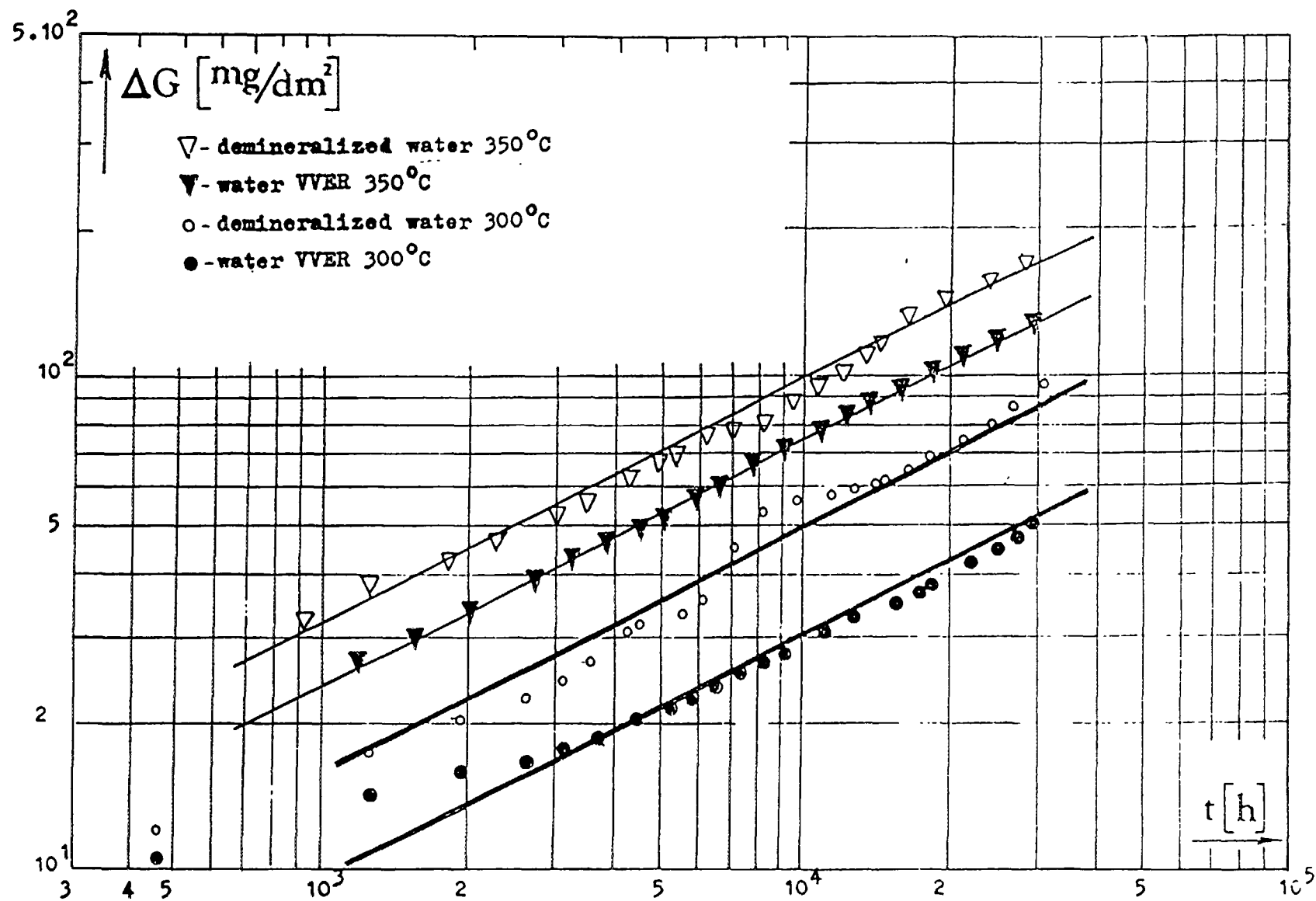


Figure 6.30. Long term oxide weight gain on Zr-1%Nb cladding at 300-350°C [69].

Table 6 9 shows various measurements of thermal conductivity. The range of values is extremely high, though in PWRs a much more restricted range is utilised in corrosion modelling (section 7 2 3). An additional thermo-hydraulic effect occurs during nucleate boiling in that the temperature,  $T_w$ , at the outer surface of the oxide increases weakly with increase in heat flux (see section 7 2 2).

French workers have concluded that there is an additional effect of heat flux independent of thermo-hydraulic effects, after comparing oxide thicknesses obtained in the presence of a heat flux in the CIRENE loop with those in the absence of a heat flux obtained in autoclave experiments [321]. This is illustrated in Figure 6 23 which shows significantly higher corrosion rates in the presence of a heat flux than in its absence, at a temperature of 346°C and with zero voidage (curves (1) and (2) in Figure 6 23). In the same manner, in an out-of-pile loop, the corrosion rate inside the heat flux region (Zone B in Figure 6 31) was higher than that in the plenum region at the same temperature (Zone A). The lithium concentration was 5 ppm in the loop coolant.

Table 6 9 Measurements of thermal conductivity

Manner of Oxide Formation	Oxide Thickness ( $\mu\text{m}$ )	Thermal Conductivity ( $\text{W m}^{-1} \text{K}^{-1}$ )		Experimental Method
		25-120°C	260-400°C	
ZrO stabilised with CaO 35.5-87.7% T.D.		1.67	1.76	
Oxidised in 360°C water	1-2	1.4, Error bars 4.3-0.3		Calorimetry
Zr-2 oxidised in 400°C steam	1.7-11.6	2.1, Error bars 3.8-0.8		
Oxidised in 360°C water, 1.25 mol/kg LiOH soln	19	0.76		Calorimetry
Oxidised in 450°C steam	54 19	0.88 0.70	6.3 5.45	
Oxidised in 450°C air	53 19	1.07 1.20	6.27 4.00	
In steam at high temperature	135 20 22	1.3 1.3	0.9 0.15 0.93	Diffusivity
Stabilised with 5% CaO (5.2 g cm <sup>-3</sup> )			2.7	
ZrO sprayed onto tungsten	<700		0.6	Calorimetry
ZrO (5.35 g cm <sup>-3</sup> )			1.9	

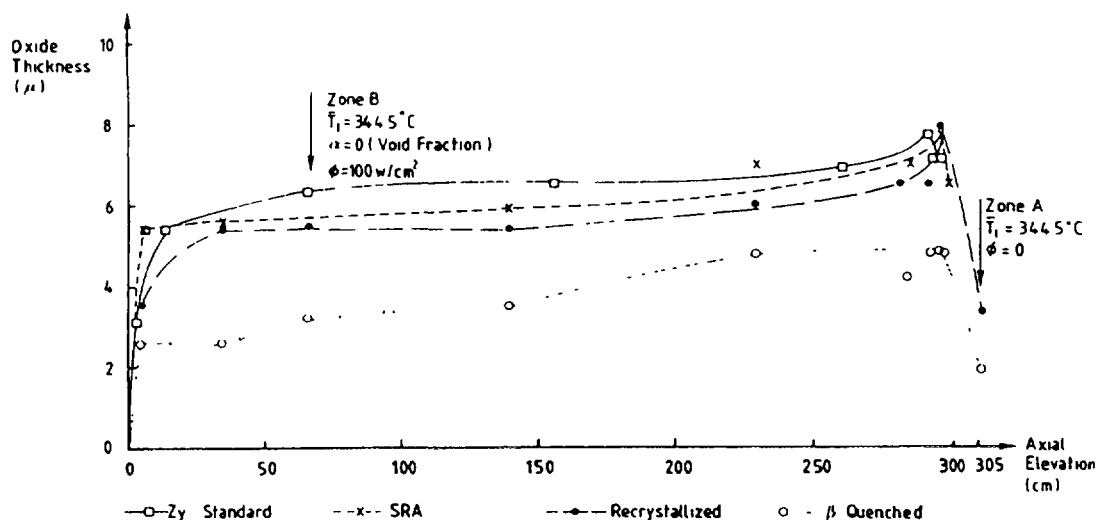


Figure 6.31. Corrosion profile in an out-of-pile loop.

French workers have produced a model for this additional heat flux effect, based on an increase in the vacancy flux set up by the heat flux which, in turn, increases the rate of transport of oxygen [321]. Since the effect appears to be predominantly in the presence of high lithium hydroxide concentrations, it is possible that there may be a synergistic effect between heat flux and lithium hydroxide. However, it may then be difficult to differentiate between this effect and the lithium hydroxide hideout effect (induced by boiling inside oxide pores or at the oxide surface) which also increases corrosion rates. The lithium hydroxide hideout effect accelerates corrosion to a degree which increases with increase in heat flux, but this is generally regarded as being due to a local increase in the lithium hydroxide concentration, rather than to a mechanism based on an increase in anion vacancy flux, which anyway could not be significant if the oxide is porous.

Plans for tests in a Thermal Gradient Test Facility in the USA have been described [322]. This was to be used for determining oxide thermal conductivities, but the presence of an additional heat flux effect proposed by the French, as described above, could be sought. However, it was also proposed to use high concentrations of lithium hydroxide in the loop to speed up corrosion, but this might cause difficulties in interpreting any effect as a lithium hydroxide effect, a heat flux effect or a synergistic heat flux and lithium hydroxide effect.

With respect to BWRs, there is some evidence that an increase in heat flux, above certain levels, in a boiling coolant decreases the oxidation rate, possibly due to a decrease in the concentration of dissolved oxygen in the coolant as a result of oxygen stripping [323].

## 7. MODELLING OF IN-REACTOR CORROSION OF ZIRCONIUM ALLOY FUEL CLADDING

### 7. 1. INTRODUCTION

Corrosion models might usefully be classified as mechanistic models, semi-empirical models, and models which appear to be almost entirely empirical. As is clear from the discussions in the present document, corrosion of zirconium alloys is complex and further work is required to obtain universal agreement on kinetic mechanisms, in order to determine which parameters have a significant effect on corrosion and to quantify these parametrical effects. Thus, the development of fully mechanistic models is at an early stage.

A necessary pre-requisite, for predicting numerical values of oxide thicknesses on fuel rods, is the calculation of axial temperature profiles at relevant positions in core, as discussed in section 7. 2. For Zircaloy alloys, the relevant temperature is the oxide-metal interface temperature, since new oxide is formed here. Firstly, coolant-oxide interface temperatures (wall temperatures),  $T_w$ , are predicted and then the increase in temperature through the oxide layer must be calculated from a knowledge of oxide thermal conductivity. The calculation of oxide thickness is, therefore, an iterative process, since an increment in oxide thickness causes an increase in the oxide-metal interface temperature which, in turn, increases the corrosion rate ("temperature feedback mechanism").

A number of semi-empirical numerical models have been developed for predicting in-core corrosion of fuel cladding, and those applicable to Zircaloy alloys in PWRs are described in section 7. 3. Such models are necessary for predicting whether, or not, unacceptable oxide thicknesses may develop on any fuel rods before final discharge from the core. Oxide thicknesses greater than approximately 100  $\mu\text{m}$  are usually regarded as unacceptable. Models also have a role for investigating special effects caused by particular exposure conditions (e.g. high lithium hydroxide levels). For this application, plant data obtained under the normal and the special exposure conditions, are compared with model predictions, in order to factor out, as far as possible, the dependencies of corrosion on temperature, heat flux and exposure time, thus enabling any other effect on corrosion rates to be revealed.

There are considerable uncertainties in model predictions, for a number of reasons including the following:

- Most models are empirical, or semi-empirical, in nature and may contain assumptions which are not scientifically well founded, thus making extrapolation hazardous outside the conditions to which the models have been fitted [117,118].
- There is considerable batch-to-batch variability in corrosion performance, due to variability in alloy composition (between batches and versus axial position within a given batch) and variability in heat treatment (e.g. due to temperature differences within the furnace during annealing). Most models do not take these considerations into account and, therefore, models should be fitted to a wide data base in order for predictions to be representative of typical average behaviour.
- Models are currently unable reliably to include all relevant variables, due to uncertainties in mechanisms, especially in relation to possible thick film and radiation fluence effects which may be exhibited in some cases, for example amorphization of intermetallic precipitates (e.g. [324]). There are probably insufficient experimental data at present for reliably quantifying a number of effects, for example hydride precipitation at the metal-oxide interface (e.g. [234]).
- There may be significant uncertainties in calculated values of oxide-metal interface temperatures and of local power histories.
- There are uncertainties in measured oxide thickness values to which models are fitted, due to accuracy limitations of eddy current measuring devices, to crud deposition and (on thick oxides) spalling or oxide blistering.

Section 7. 4. discusses models of a more mechanistic nature. Cox's model differs in nature from the models discussed in section 7. 3. and was derived from conclusions reached on the basic mechanisms of irradiation enhancement and lithium hydroxide enhancement. Two Russian models for corrosion of Zr-1%Nb fuel cladding are outlined, one for uniform corrosion in WWERs and the other for nodular corrosion in RBMKs. The latter describes elevation of the oxide-metal interface temperature due to crud deposition (Crud Induced Localised Corrosion, (CILC)).

## 7. 2. CALCULATION OF OXIDE-METAL INTERFACE TEMPERATURES

For full details, reference should be made to standard text books on thermalhydraulics. Only the relevant basic principles will be addressed here.

### 7. 2. 1. Single phase coolants

The temperature difference across the laminar boundary layer, between the wall and the bulk turbulent fluid, is related to heat flux by:

$$\phi = h(T_w - T_b) \quad (7.1)$$

where

$\phi$  = heat flux ( $\text{W}\cdot\text{m}^{-2}$ );  
 $T_w$  = wall temperature (K);  
 $T_b$  = temperature of bulk fluid (K);  
 $h$  = heat transfer coefficient ( $\text{W}\cdot\text{m}^{-2}\cdot\text{K}^{-1}$ ).

The heat flux,  $\phi$ , through the cladding and through the laminar boundary layer, may be obtained from the product of (i) percentage reactor power as a function of time (ii) core averaged heat flux at 100% power (iii) core relative axial power profile (iv) the relative rod power and (v) the fraction of the heat generated inside the fuel (typically 97% in Western PWRs).

The single phase heat transfer coefficient,  $h$ , is calculated from one of a number of alternative dimensionless correlations, the most well known being the Dittus-Boelter correlation:

$$\text{Nu} = 0.023 \text{ Re}^{0.8} \text{ Pr}^{0.4} \quad (7.2)$$

where

$\text{Nu} = hd/k$  is the Nusselt number;  
 $\text{Re} = \rho du/m$ , the Reynolds number;  
 $\text{Pr} = c_p \mu/k$ , the Prandtl number;  
 $h$ , the heat transfer coefficient ( $\text{W}\cdot\text{m}^{-2}\cdot\text{K}^{-1}$ );  
 $d$ , the equivalent diameter of the flow channel (m);  
 $k$ , the thermal conductivity of the fluid ( $\text{W}\cdot\text{m}^{-1}\cdot\text{K}^{-1}$ );  
 $\rho$ , the fluid density ( $\text{g}\cdot\text{m}^{-3}$ );  
 $u$ , the fluid velocity ( $\text{m}\cdot\text{s}^{-1}$ );  
 $\mu$ , the viscosity ( $\text{g}\cdot\text{m}^{-1}\cdot\text{s}^{-1}$ ) and  
 $c_p$ , the specific heat ( $\text{W}\cdot\text{s}\cdot\text{g}^{-1}\cdot\text{K}^{-1}$ ).

The example in Figure 7.1 shows that significant differences in wall temperature,  $T_w$ , can be obtained using different correlations. The variation of up to  $7^\circ\text{C}$  is sufficient to cause a variation in calculated oxide thicknesses of up to 30% for thin films and a greater variation for thick films, due to the temperature feedback effect. Thus, zirconium alloy corrosion models, fitted to benchmark reactor

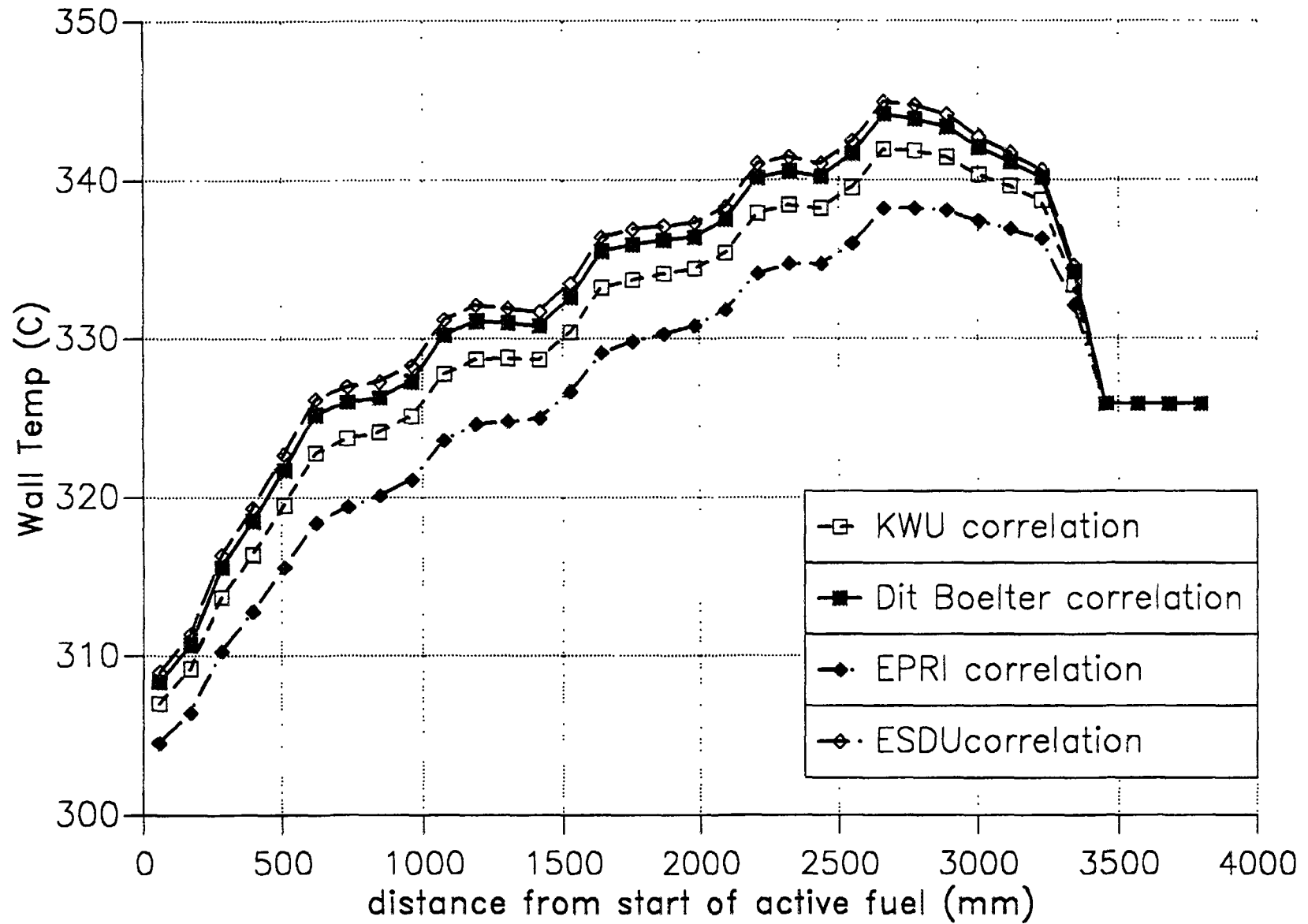


FIG. 7. 1. Example of effect of different single phase heat transfer correlations on predicted clad wall temperatures (NE predictions using VIPRE Code).



data using wall temperatures calculated in a particular manner, should not strictly be used in conjunction with wall temperatures calculated in a different manner

The core is made up of a number of inter-connected sub-channels, up which the fluid flows between the fuel rods. The equations of coolant mass, momentum and energy conservation are solved as a function of axial position. This can be performed most accurately with the aid of thermo-hydraulic codes, for example COBRA [325], VIPRE [326] and FLICA. These allow the core to be divided into a number of lumped sub-channels, each of which may encompass one, several or many sub-channels. One or more lumped sub-channels contain the rod(s) of interest and neighbouring lumped sub-channels need to be included in the thermo-hydraulic model, owing to cross-flow between sub-channels. Cross-flow may be promoted by mixing vanes in the fuel grids and effects on mass and heat transfer may be obtained from correlations devised from multi-channel hydraulic tests. Increased pressure drops also occur at the grids. The presence of control rod guide tubes within lumped sub-channels needs to be taken into account, since these do not contribute to heat flux and are different in diameter to fuel rods. The mass flux through the core is slightly lower than the total mass flux, owing to the core by-pass flow (for example, through control rod guide tubes etc.)

Oxide thickness measurements are usually carried out on the outer faces of peripheral rods on the outside of fuel assemblies. There may be a significant temperature difference between the inner and outer faces of peripheral rods, since the adjacent assembly may be of a very different power level, thus significantly lowering or raising the temperature in the gap between the two assemblies. This should be borne in mind when devising the thermo-hydraulic model for the prediction of oxide layer growth on peripheral rods. It is also possible for some fuel vendors to measure oxide thicknesses on internal rods without removing them from the assembly, using, for example, the French SABRE technique.

The fuel grids cause additional turbulence, lowering the wall temperature due to the increased heat transfer. The following equation has been given [280,320] for the increase in heat transfer coefficient downstream of fuel grids

$$h_x = h_\infty(1 + d_h/x) \quad (7.3)$$

where

- $h_x$  is the heat transfer coefficient at a distance  $x$  downstream of a grid,
- $h_\infty$  is the heat transfer coefficient at infinite distance from a grid,
- $x$  is downstream distance from a grid,
- $d_h$  is the hydraulic diameter of the sub-channel

This effect, which may not be taken into account in some thermo-hydraulic code predictions, causes a very significant lowering of oxide film thickness downstream of the fuel grids. However, at mid-span positions (midway between adjacent fuel grids) the effect on oxide thickness should be negligible.

## 7.2.2 Two phase coolants

In PWRs the majority of fuel rods are exposed to single phase coolant, but a small number of rods may be exposed to two phase flow along the upper parts of the fuelled region, particularly in plants with high inlet temperatures and high heat fluxes.

When the wall temperature exceeds the local (wall) saturation temperature,  $T_{sat}$ , the bulk coolant remaining below the saturation temperature, vapour bubbles begin to nucleate on the walls (sub-cooled nucleate boiling). When the nucleate boiling regime is first entered, the bubbles stay attached to the walls, but as the heat flux increases, bubbles become detached and collapse in the sub-cooled

bulk flow. The wall temperature exceeds the wall saturation temperature by an increment (superheat),  $\Delta T_w$

$$T_w = T_{sat} + \Delta T_w \quad (7.4)$$

For nucleate boiling  $\Delta T_w$  may be calculated using several different correlations. Two such correlations [327] are the Jens-Lottes correlation:

$$\Delta T_w = 25.0 \cdot \phi^{0.25} \exp(-P/62) \quad (7.5)$$

and the Thom correlation:

$$\Delta T_w = 22.65 \cdot \phi^{0.5} \exp(-P/67) \quad (7.6)$$

where  $\phi$  is in  $\text{MW} \cdot \text{m}^{-2}$  units and  $P$  is the pressure in bar. For typical values of  $\phi = 0.7 \text{ MW} \cdot \text{m}^{-2}$  and  $P = 150$  bar, these give a  $\Delta T_{wall}$  of  $2.0^\circ\text{C}$  and  $3.4^\circ\text{C}$ , respectively, showing a small difference in calculated values. The Thom correlation is recommended in [327]. Since values of  $\Delta T_w$  are not great, and do not vary greatly with heat flux, the wall temperature does not vary greatly with axial position along those portions of the fuel rods experiencing sub-cooled nucleate boiling. The pressure drop is higher in two phase flow than in single phase flow under the same conditions.

The value of the void coefficient,  $\alpha$ , (fraction of the flow cross-section occupied by steam) is of relevance to two phase flow, particularly in relation to lithium hydroxide hideout effects. (Lithium hydroxide effects may be relevant to single phase coolants as well). In two phase flow calculations, the vapour content is normally predicted as the water quality (mass of vapour per total mass), for which several different correlations may be used. The void fraction may then be obtained from the water quality using a relationship which assumes either that the vapour moves at the same velocity as the water, or that there is some slip between the two phases. Again, there are alternative expressions depending on the degree of slip assumed. Unfortunately, at the low values of voidage which may be encountered during normal operation (up to a few percent), large fractional differences in void fraction may be obtained using different methods (e.g. Bowring model, Levy models etc.). This can hinder comparison between two phase corrosion results obtained in different establishments. This is particularly relevant to the question of determining the void fraction at which lithium hydroxide hideout begins to cause a rapid escalation in corrosion rate.

### 7.2.3 Oxide thermal conductivity

The temperature of the oxide-metal interface may be calculated from a knowledge of oxide thermal conductivity:

$$T = T_w + \phi \cdot S / \kappa \quad (7.7)$$

where

$T$  is the temperature of the oxide/metal interface (K);  
 $T_w$  is the temperature of the oxide/water interface (K);  
 $\phi$  = heat flux ( $\text{W} \cdot \text{m}^{-2}$ );  
 $\kappa$  is the oxide thermal conductivity ( $\text{W} \cdot \text{m}^{-1} \cdot \text{K}^{-1}$ );  
 $S$  is oxide thickness (m).

As shown in Table 6.9, a very wide range of oxide thermal conductivity values have been measured.

A narrower range of values (between approximately  $0.8$  and  $2.0 \text{ W} \cdot \text{m}^{-1} \cdot \text{K}^{-1}$ ) have been assumed in Zircaloy corrosion codes. In some cases values are assumed to be independent of oxide thickness and,

in others, to decrease with increase in oxide thickness. This narrower range is still sufficient to cause considerable variability in predicted corrosion rates. For example, for a heat flux of  $0.7 \text{ MW m}^{-2}$ , the temperature drop across an  $80 \text{ }\mu\text{m}$  oxide is  $70^\circ\text{C}$  for a thermal conductivity of  $0.8 \text{ W m}^{-1} \text{ K}^{-1}$  but  $31^\circ\text{C}$  for a value of  $1.8 \text{ W m}^{-1} \text{ K}^{-1}$ . This difference is sufficient to cause roughly a four-fold increase in post-transition corrosion rate in some corrosion models, based only on the temperature coefficient of oxidation. The difference could be greater if lithium hydroxide effects were exhibited.

An example of calculated differences in oxide thicknesses versus time, using constant thermal conductivities of  $1.2$  and  $1.8 \text{ W m}^{-1} \text{ K}^{-1}$ , is given in Figure 7.2, which shows predictions using Nuclear Electric's ZIRC code (section 7.3.2.5). It is seen that the temperature feedback effect causes an escalation in corrosion rates, giving very different predicted behaviour for thermal conductivities within the range of uncertainty. Thus, it is very difficult to separate the normal consequences of the temperature feedback effect from the consequences of other effects which are postulated to increase corrosion rates. Examples of such effects are lithium hydroxide, a separate effect of heat flux on the diffusion of oxygen through the oxide (section 6.6), and the amorphization and structural transformation of intermetallic particles [324] (section 8.1.3.3).

The temperature feedback effect in Figure 7.2 causes predicted oxide thicknesses to increase to infinity after a finite time, at a rapidity which depends on all the assumed model conditions. The predictions in Figure 7.2 were for a fixed oxide thermal conductivity, but oxide thicknesses escalate even more rapidly if the thermal conductivity is assumed to decrease with increase in temperature. The precise predictions of any model should be viewed with caution, particularly for thick oxides. The predictions in Figure 7.2 were for a model with a multiplicative irradiation enhancement factor which is independent of temperature (section 7.3.2.5). If irradiation enhancement reduces with increase in temperature [328], this may reduce the rate at which oxide thicknesses escalate at long exposure times. A further cause for caution in viewing predictions for thick oxides is the possible effect of spalling and blistering on the measurements.

### 7.3 SEMI-EMPIRICAL MODELS FOR ZIRCALOY CORROSION IN PWRs

Semi-empirical models are usually based on:

- 1) Fits to laboratory autoclave data obtained in the absence of a heat flux and in the absence of radiation
- 2) Fits to laboratory loop data in the presence of a heat flux but in the absence of radiation
- 3) Re-normalisation to plant data in order to accommodate irradiation enhancement, and other possible in-plant effects

With regard to 3), the models should be best fits to oxide thicknesses in both the axial direction (as a function of height along the fuel rod, see Figure 7.3) and in the radial direction (for different rods with different exposure histories).

There is considerable variation in the data available and, hence, considerable variation in the models which have been developed. Most models for Zircalloys were developed for standard cladding, prior to the production of 'optimised' or 'improved' cladding with tighter controls on composition (Sn, C and Si) and on heat treatment. Such models are expected to over-predict corrosion of optimised/improved cladding, since few models currently appear to incorporate alloy composition or heat treatment as variables. More new models for optimised/improved cladding are likely to become available shortly.

Some models incorporate effects such as coolant lithium hydroxide and hydride formation (section 7.3.3), either from a particular set of laboratory data or from a statistical analysis of reactor data. However, no consensus presently exists on the presence, or absence, of lithium hydroxide effects at normal in-reactor concentrations of lithium hydroxide in primary coolants (sections 4.2.5 and 9.2.1.1). There is little evidence of a consistent and significant effect either from Halden in-

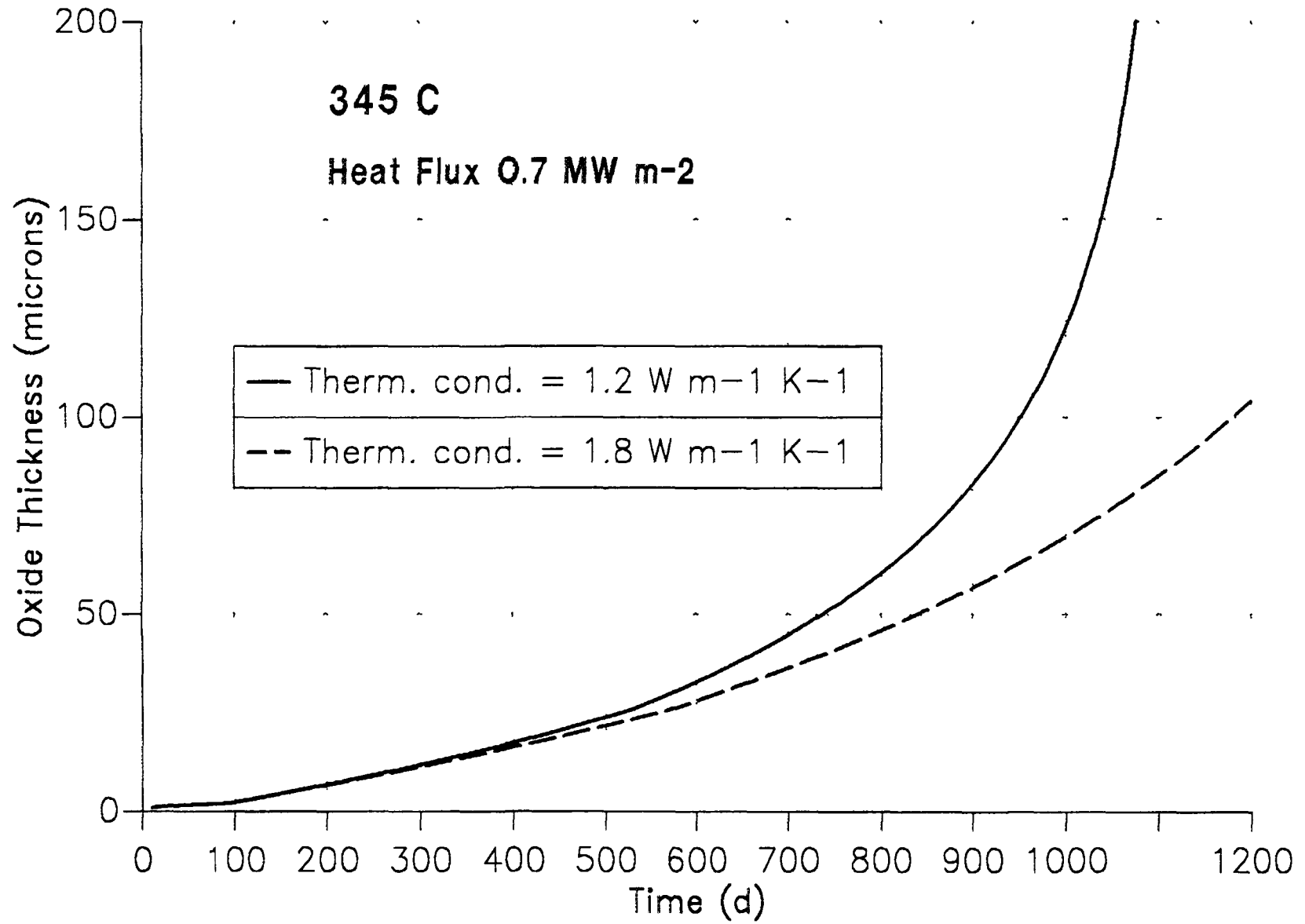


FIG 7 2 Example of effect of different oxide thermal conductivity values on predicted oxide thicknesses (NI-ZIRC Code predictions)

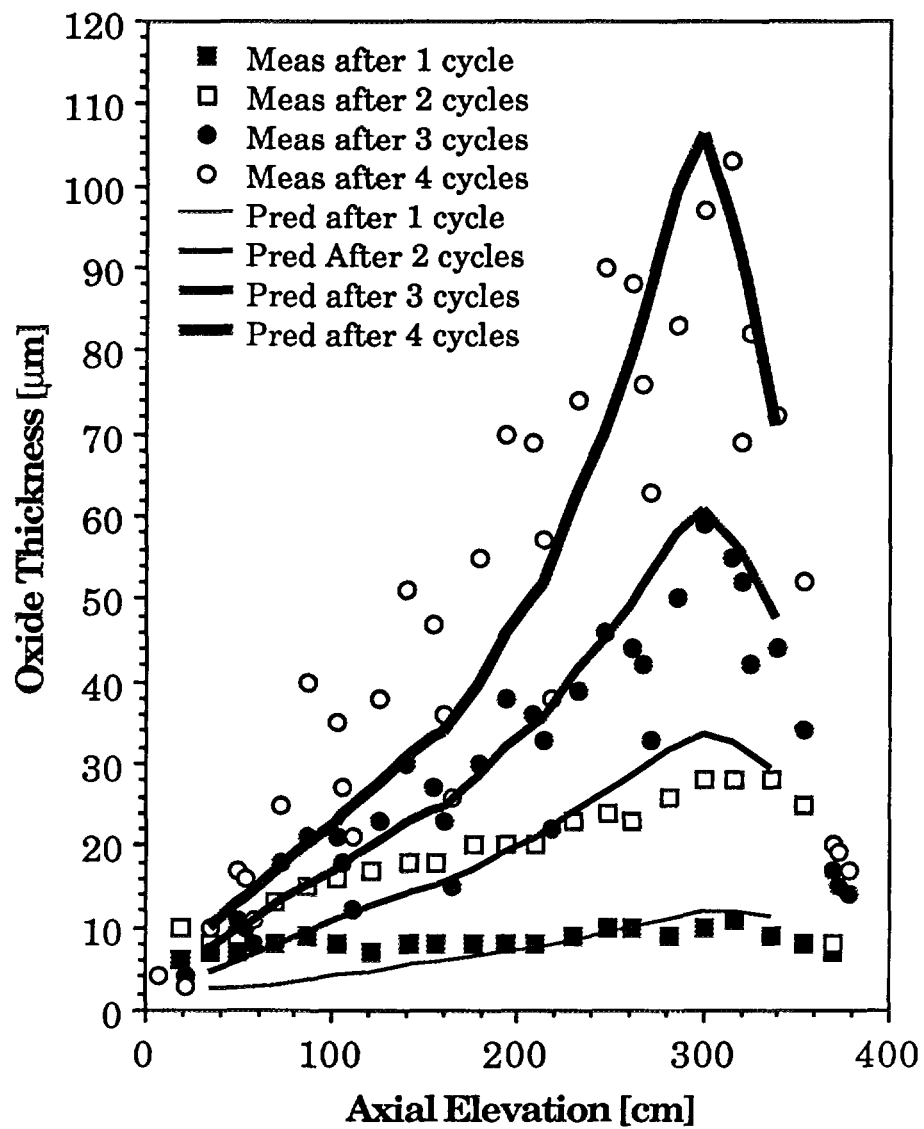


FIG. 7. 3. Comparison between predictions and measurements as a function of axial elevation, new ABB Atom Model [336].

pile loop data in a coolant containing 4 ppm lithium and 1,000 ppm boron (section 7 3 2 2 ) or from elevated lithium operation in PWRs (section 7 3 2 5 ) Accurate quantification of the accelerating effects of hydride formation (section 5 2 ) is difficult with the limited data presently available Present uncertainties in the 'true' values of primary factors (activation energies, thermal conductivities, etc ) enable similar predictions to be made, with and without, incorporating additional effects (lithium hydroxide, hydrides etc )

### 7 3 1 Generic formulation for semi-empirical models

Most models assume cubic kinetics in the pre-transition region i e

$$S^3 = C_1 \exp(-Q_1/RT) t \quad (7.8)$$

where

$S$  is the weight gain or oxide thickness,  
 $t$  is the time,  
 $Q_1$  is the pre-transition activation energy,  
 $C_1$  is the frequency factor and  
 $R$  is the Universal Gas Constant

[329] gives the following relationship between oxide thickness and weight gain

$$1 \mu\text{m} \sim 14.7 \text{ mg dm}^{-2}$$

For numerical calculation in time steps, the time differential is required

$$\Delta S/\Delta t = C_1 \exp(-Q_1/RT)/3S^2 = [C_1 \exp(-Q_1/RT)]^{1/3} / 3(t')^{1/3} \quad (7.9)$$

where time,  $t'$ , lies somewhere within the  $n^{\text{th}}$  time step Owing to the cubic nature of the kinetics, assuming  $t'$  to be in the middle of the time step can lead to inaccuracies unless small time steps are chosen The most accurate position of  $t'$  within each time, as a function of time step number, can be determined by calculation

After reaching a certain transition weight gain or oxide thickness,  $S_t$ , (of the order  $2 \mu\text{m}$ ), linear kinetics are assumed

$$\Delta S/\Delta t = C_2 \exp(-Q_2/RT) \quad (7.10)$$

where

$C_2$  is the post-transition frequency factor and  
 $Q_2$  is the post-transition activation energy

$S_t$  is assumed to be constant in some models, but dependent on temperature in others Some models do not model the cubic pre-transition region since, for reactor applications, only relatively thick oxides are of interest This implies that, on a graph of oxide thickness versus time, back-extrapolation passes through the origin Most data show this to be a not unreasonable approximation The frequency factors and activation energies may be assumed constant or dependent on temperature or on other variables In some models, the post-transition corrosion rate is assumed to increase above a certain critical weight gain In-core exposure is assumed to increase the corrosion rate by a multiplicative fitting factor,  $f$ , often referred to as the 'irradiation enhancement factor' This is assumed either to be a constant or to depend on temperature or neutron flux In some models, an irradiation enhancement factor is applied in the pre-transition region, either to equation (7.8) or (7.9),

in other models no irradiation enhancement is assumed in this region. All the models reviewed here (section 7. 3. 2.) assume that there is irradiation enhancement in the post-transition region.

Most published model descriptions specify values of oxide thermal conductivity but in many cases, few details are given of clad wall temperature calculation, which is an important consideration (sections 7. 2. 1. and 7. 2. 2.).

### 7. 3. 2. Individual models of simple generic form

Published details of several models are given below. Details of several other models do not appear to have been published in the open literature.

#### 7. 3. 2. 1. MATPRO model [268,330]

This is one of the older models, having the following parameter values:

Pre-T Frequency Factor	$C_1 = 4.976 \times 10^9 \mu\text{m}^3 \cdot \text{d}^{-1}$
Pre-T Activation Energy	$Q_1/R = 15,660 \text{ K}^{-1}$
Post-T Frequency Factor	$C_2 = 8.288 \times 10^7 \mu\text{m} \cdot \text{d}^{-1}$
Post-T Activation Energy	$Q_2/R = 14,080 \text{ K}^{-1}$
Trans. Oxide Thickness	$S_t = 7.749 \exp(-790/T) \mu\text{m}$
Irradiation Enhancement	$f_i = 120.3 \exp(-0.007118 \times T_w)$

Note that the irradiation enhancement factor is dependent on the oxide-coolant interface temperature, rather than on the oxide-metal interface temperature.  $f_i$  is applied to equation (7.8) in the pre-transition region, as well as to equation (7.10) in the post-transition region, thus enhancing the corrosion rate in the pre-transition region by the cube root of the enhancement factor. MATPRO was used by Van Swam and Shann [268] for analyzing oxide thicknesses on a range of Zircaloy-4 rods of different cladding types (compositions and heat treatments). It was found that a further dimensionless parameter, E, was needed to account for irradiation enhancement, i.e.,

$$\text{Irradiation enhancement factor} = E \cdot f_i$$

where, E, was a constant ranging between 2.07 and 4.87 for the nine cladding types investigated, with a mean value of 2.95.

The thermal conductivity was:

$$\kappa = 1.73 \text{ W} \cdot \text{m}^{-1} \cdot \text{K}^{-1}$$

and the COBRA thermalhydraulics code was used to predict clad wall temperatures.

The same type of analysis was applied to investigating the possible effect of elevated lithium operation on Zircaloy-4 corrosion in the St. Lucie-1 PWR [331]. The corrosion parameter, E, required for fuel exposed to elevated lithium operation was found to be 10%-15% higher than for rods exposed to normal chemistry (<2.2 ppm Li). This difference in corrosion rate was said to be statistically significant. However, the difference is small compared with the effect of cladding type (heat treatment and composition) as shown above, although the effect of cladding type was apparently taken into account in the analysis.

#### 7. 3. 2. 2. EPRI/KWU/C-E model [320]

The form of the model was derived from fits to literature data, from data obtained in German tests and from appraisals of relationships proposed previously. The model parameters are:

Pre-T Frequency Factor	$C_1 = 1.89 \times 10^{10} \mu\text{m}^3 \cdot \text{d}^{-1}$
Pre-T Activation Energy	$Q_1/R = 16,250 \text{ K}^{-1}$
Post-T Frequency Factor	$C_2 = 8.04 \times 10^7 \mu\text{m} \cdot \text{d}^{-1}$
Post-T Activation Energy	$Q_2/R = 13,766 \text{ K}^{-1}$
Trans Oxide Thickness	$S_1 = 2.14 \times 10^7 \exp(-5417/T - 0.0117T) \mu\text{m}$
Irradiation Enhancement	$f_1 = 1 + 3.22(M\phi)^{0.24}$
Thermal conductivity	$\kappa = 1.5-2.0 \text{ W} \cdot \text{m}^{-1} \cdot \text{K}^{-1}$

The constant in the equation for the irradiation enhancement factor,  $f_1$ , is:

$$M = 7.46 \times 10^{-19} \text{ m}^2 \cdot \text{s} \cdot \text{neutron}^{-1}$$

for a fast neutron flux,  $\phi$ , (greater than 0.8-1 MeV) in units of neutrons $\cdot\text{m}^{-2}\cdot\text{s}^{-1}$ .  $f_1$  was applied to the post-transition region but not to the pre-transition region.  $f_1$  values are in the range 3 to 4 for typical core neutron fluxes

Model predictions were compared with data from four KWU plants. Good fits were obtained to data from the two lower temperature plants (observed/predicted = 0.98 and 0.94) which provided the bulk of the data, but the model significantly over-predicted values for the two higher temperature plants (observed/predicted = 0.5 and 0.74).

The heat transfer correlation for predicting wall temperatures was:

$$\text{Nu} = 0.023 \cdot \text{Re}^{0.8} \cdot \text{Pr}^{0.43} \quad (7.11)$$

This is designated the KWU correlation in Figure 7.1: out of five correlations, this gave the best agreement with sample data obtained from a KWU tube bundle. The thermal hydraulic model was a simplified model given in Appendix B of [329].

The EPRI/KWU/C-E model was used recently to analyse data from high lithium (4 to 4.5 ppm lithium, 1,000 ppm boron) exposure of Zircaloy-4 fuel rods in the Halden PWR test facility [332]. There was generally reasonable agreement between measurements and predictions. In one of the upper (hot) rods, measurements were higher than predictions at the top (hottest) part, whereas in the other upper rod the reverse was the case. Thus, there was little evidence for a consistent and significant lithium hydroxide effect. Interestingly, these particular results showed little sign of corrosion acceleration for thick oxides (40 to 90  $\mu\text{m}$ ), even in the presence of temperature feedback across the thick oxide layer (section 7.2.3) and of a high lithium hydroxide concentration in the coolant.

Sheppard et al. [333] fitted the EPRI/KWU/C-E model to four plants of three designs (Combustion Engineering, Babcock and Wilcox and Westinghouse) for oxides of intermediate thickness (up to 40  $\mu\text{m}$ ). The agreement was described as good, the mean error in the peak oxide thickness ranging from -18.8% to +6.5% in the four fits. The thermal conductivity used was  $\kappa = 1.5 \text{ W} \cdot \text{m}^{-1} \cdot \text{K}^{-1}$  and the irradiation enhancement factor,  $f_1$ , was applied to oxides of thickness  $> 5 \mu\text{m}$ , rather than to the whole of the pre-transition region. The heat transfer correlation was that given in equation (7.11), clad wall temperatures being calculated using a single channel thermo-hydraulic model. This included fuel grid effects and the influence of neighbouring rods, albeit only from the eight nearest neighbours.

### 7.3.2.3 French COCHISE model

The parameters for the version of this model which was developed in the late 1980's by the CEA, are as follows [321,334]



Pre-T Frequency Factor	$C_1 = 11.4 \times 10^{10} \mu\text{m}^3 \cdot \text{d}^{-1}$
Pre-T Activation Energy	$Q_1/R = 17,171 \text{ K}^{-1}$
Post-T Frequency Factor	$C_2 = 4.0 \times 10^{11} \mu\text{m} \cdot \text{d}^{-1}$
Post-T Activation Energy	$Q_2/R = 18,391 \text{ K}^{-1}$
Time to Transition	$t_t = 8\,857 \times 10^{10} \exp(921/T - 0.035T) \text{ d}$
Irradiation Enhancement	$f_i$ included in the value of $C_2$
Thermal conductivity	$\kappa = 1.6 \text{ W} \cdot \text{m}^{-1} \cdot \text{K}^{-1}$

Note that the transition is specified as a particular time, rather than a particular oxide thickness. The activation energy in the post transition region is much higher than in the MATPRO and EPRI/KWU/C-E models. Both the post-transition activation energy and the time to transition were obtained from comparisons of oxide thicknesses on rods at different axial positions [321].

The clad wall temperatures were predicted with a CEA multi-channel model which treats cross-flow and utilises a different correlation for the heat transfer coefficient than those in Figure 7.1

The COCHISE model predictions, together with those from the EPRI/KWU/C-E and ABB Atom models, were compared with Zircaloy-4 data from seven plants [334]. It was concluded that irradiation enhancement was independent of fast neutron flux ( $>10^{17} \text{ neutrons} \cdot \text{m}^{-2} \cdot \text{s}^{-1}$ ), contrary to assumptions in the EPRI/KWU/C-E and ABB Atom models, and operated from the transition thickness, rather than from some critical thickness greater than at transition, as assumed in [333] and in the ABB Atom model (section 7.3.2.4.). Although the irradiation enhancement factor,  $f_i$ , was not given explicitly, [334] states that comparisons with data from loops and reactors gave a value of 2.5-3

Subsequently a more complex version of the COCHISE model was developed, incorporating lithium hydroxide and heat flux effects, as described in section 7.3.3.2

#### 7.3.2.4 Swedish ABB Atom model

The original model was described in [335], but numerical details of the irradiation enhancement factor were not given. Recently, the model has been revised [336], resulting in alterations to some of the parameters, which are now as follows for Stress Relief Annealed (SRA) Zircaloy-4 cladding

Pre-T Frequency Factor	$C_1 = 7.05 \times 10^{10} \mu\text{m}^3 \cdot \text{d}^{-1}$ for 1.5 w/o Sn $C_1 = 4.95 \times 10^{10} \mu\text{m}^3 \cdot \text{d}^{-1}$ for 1.3 w/o Sn
Pre-T Activation Energy	$Q_1/R = 16,250 \text{ K}^{-1}$
Post-T Frequency Factor	$C_2 = 2.0 \times 10^8 \mu\text{m} \cdot \text{d}^{-1}$ for 1.5 w/o Sn $C_2 = 1.6 \times 10^8 \mu\text{m} \cdot \text{d}^{-1}$ for 1.3 w/o Sn
Post-T Activation Energy	$Q_2/R = 13,766 \text{ K}^{-1}$
Time to Transition	$t_t = 7.98 \times 10^{-8} \exp(13,150/T) \text{ d}$
Irradiation Enhancement	$f_i = 1 + 1.7 \times 10^{-20} \times (S - 6) \times \phi$ where $\phi$ is in $\text{neutrons} \cdot \text{m}^{-2} \cdot \text{s}^{-1}$ , $S$ in $\mu\text{m}$ $f_i^{\text{max}} = 2.42$
Thermal conductivity	$\kappa = 2.0 \text{ W} \cdot \text{m}^{-1} \cdot \text{K}^{-1}$

It is seen that some account is taken of the tin content in the alloy, based apparently on a comparison between two rods only. The irradiation enhancement factor,  $f_i$ , is linearly dependent on both fast neutron flux ( $> 1 \text{ MeV}$ ) and on oxide thickness above  $6 \mu\text{m}$ , thus causing a continuous acceleration in corrosion. However, relative to some models, this acceleration is offset by use of a higher value for the oxide thermal conductivity ( $2.0 \text{ W} \cdot \text{m}^{-1} \cdot \text{K}^{-1}$ ). Below  $6 \mu\text{m}$ ,  $f_i$  is unity,  $f_i$  is capped

at a value of  $f_i^{\max} = 2.42$  at high oxide thicknesses. The linear dependencies of  $f_i$  on oxide thickness and neutron flux are very different from most other models. The activation energies,  $C_1$  and  $C_2$ , are the same as in the EPRI/KWU/C-E model.

The model has been fitted to a range of PWR data (e.g. Figure 7.3). The clad wall temperature is calculated with either a closed subchannel model or, more accurately, with a multi-channel model consisting of a 3x3 matrix of rods with the rod of interest in the middle. The single phase heat transfer correlation is a modification of the Dittus-Boelter equation:

$$Nu = [0.042(Y/d) - 0.024]Re^{0.8}Pr^{0.4} \quad (7.12)$$

where

$Y$  is the rod-to-rod pitch and  
 $d$  is the rod diameter.

This correlation gives higher heat transfer coefficients than the standard Dittus-Boelter correlation, equation (7.2), at least for some assembly designs. The Thom relationship, equation (7.6), is used for two phase heat transfer.

#### 7. 3. 2. 5. Nuclear Electric (UK) ZIRC model

The model parameters for this model are [337]:

Pre-T Frequency Factor	$C_1 = 1.6 \times 10^{10} \mu\text{m}^3 \cdot \text{d}^{-1}$
Pre-T Activation Energy	$Q_1/R = 16,250 \text{ K}^{-1}$
Post-T Frequency Factor	$C_2 = 1.50 \times 10^8 \mu\text{m} \cdot \text{d}^{-1}$ , $S < 25.9 \mu\text{m}$ , $C_2 = 1.94 \times 10^8 \mu\text{m} \cdot \text{d}^{-1}$ , $S > 25.9 \mu\text{m}$
Post-T Activation Energy	$Q_2/R = 14,172 \text{ K}^{-1}$
Trans. Oxide thickness	$S_t = 1.98 \mu\text{m}$
Irradiation Enhancement	$f_i = 1.1 \times \text{Pre-trans.}$ , equation (7.9) $f_i = 2.5 \times \text{Post-trans.}$
Thermal conductivity	$\kappa = 1.5 \text{ W} \cdot \text{m}^{-1} \cdot \text{K}^{-1}$

The VIPRE thermalhydraulics code was employed to predict clad wall temperatures, utilising the Dittus-Boelter heat transfer correlation, equation (7.2).

The above parameter list is the revised formulation after fitting to data for Zircaloy-4 cladding from the North Anna 1 and Millstone-3 PWRs [337]. Autoclave tests showed an increase in corrosion rate above  $26 \mu\text{m}$ , hence the 29% increase in the frequency factor,  $C_2$ , above this oxide thickness. Fits to test data from a European reactor were obtained using irradiation enhancement factors  $f_i$  of 2.5 in both the pre- and post-transition regions, and using thermal conductivity values which declined linearly from  $1.5$ – $0.8 \text{ W} \cdot \text{m}^{-1} \cdot \text{K}^{-1}$  over the range  $48$ – $65 \mu\text{m}$ . However, these parameter values were subsequently found to over-predict oxide thicknesses in the Ringhals-3, Millstone-3 and North Anna-1 PWRs and a pre-transition factor of 1.1 and a fixed thermal conductivity of  $1.5 \text{ W} \cdot \text{m}^{-1} \cdot \text{K}^{-1}$  were found to give an optimum fit.

The code incorporates a correlation for the effects of recrystallization of the Zircaloy on corrosion rate. However, normally the fractional recrystallization is not quoted, and is usually assumed to be zero for SRA material utilised for most commercial Zircaloy cladding.

When ZIRC was used to analyse data for exposure to two cycles of elevated lithium chemistry at Millstone 3, oxide thicknesses were found to be generally lower than those for exposure to coordinated pH<sub>T</sub> 6.9 chemistry [337-339] and this was concluded to be due to batch-to-batch differences in the cladding. An example of one comparison is given in Figure 7.4. Therefore, it was concluded that elevated lithium had not significantly increased corrosion.

### 7.3.2.6 Earlier models

In 1985 Cox reviewed four earlier models by Asher, Dalgaard, Hillner and Dickinson, together with the EPRI/KWU/C-E and MATPRO models [340]. Figure 7.5 shows a comparison between predicted post-transition rates for the various models reviewed.

### 7.3.2.7 Summary of simple semi-empirical models

Clearly, there is some diversity in the form of the various models and there is considerable diversity in parameter values. This is partially reflected in the comparison of predicted post-transition corrosion rates shown in Figure 7.6, which differ by up to a factor of three. The curves designated 'MATPRO Min' and 'MATPRO Max' are for the extremes of the material-dependent irradiation multiplier,  $E$ , in Van Swam and Shann's work (section 7.3.2.1). The MATPRO values are for thin oxides, since the wall temperature has been taken as the temperature of the oxide/metal interface. For the EPRI/KWU/C-E and ABB Atom models, the fast neutron flux was taken as  $6 \times 10^{17} \text{ n m}^{-2} \text{ s}^{-1}$ . The NE-ZIRC values designated 'thin' and 'thick' were for values less than, and greater than 25.9  $\mu\text{m}$ , respectively. The ABB Atom values designated 'Max' and 'Min' were for irradiation enhancement factors of 2.42 and 1.0, respectively, and for material with tin contents of 1.5 w/o and 1.3 w/o respectively.

Figure 7.6 should not be taken as a definitive comparison of the models, owing to differences in the methods by which oxide-metal interface temperatures are calculated and to differences in the materials on which the codes were benchmarked. Table 7.1 presents a comparison of transition thicknesses and times to transition, again showing very significant differences in the predicted values. Figure 7.7 presents a comparison of oxide thickness predictions versus exposure time for the models described in section 7.3.2. The MATPRO predictions were for an  $E$  parameter value (multiplier for the irradiation enhancement factor) of 2.95, the mean of the values quoted in [268] (section 7.3.2.1). ABB Atom values were for a tin content of 1.4%, from the mean of parameter values for 1.5 and 1.3 % tin contents (section 7.3.2.4). For the ABB Atom and EPRI/KWU/C-E models, the predictions were for a fast neutron flux ( $> 1 \text{ MeV}$ ) of  $6 \times 10^{17} \text{ neutrons m}^{-2} \text{ s}^{-1}$ . The implementation of the EPRI/KWU/C-E model was the same as that by Sheppard et al. (section 7.3.2.2 [333]). Thus, these comparisons are only examples for particular choices of those parameters values which are variables in some of the models but not in others. In addition, as stated above, the comparisons are not definitive due to differences between the various models in the methods used for calculating clad wall temperatures.

With respect to the use of code predictions as an aid in investigating elevated lithium effects, the conclusions on corrosion in Millstone-3 and St. Lucie-1 (sections 7.3.2.5 and 7.3.2.1) were based on cross-comparisons of measurements with and without high lithium hydroxide concentrations in the coolants. The measurements were normalised to code predictions (measured/predicted ratios) in order to factor out, as far as currently possible, the dependencies of corrosion on temperature, heat flux and time. The conclusions were not, therefore, based on absolute comparisons between measurements and predictions, which is a less reliable method for investigating special effects such as those due to coolant lithium hydroxide.

In most models, the relationship for the transition oxide thickness (or transition time) is a function of temperature. There may be problems in specifying an appropriate temperature in these relationships, when analysing plant data in which the temperature varied with time. Such variations

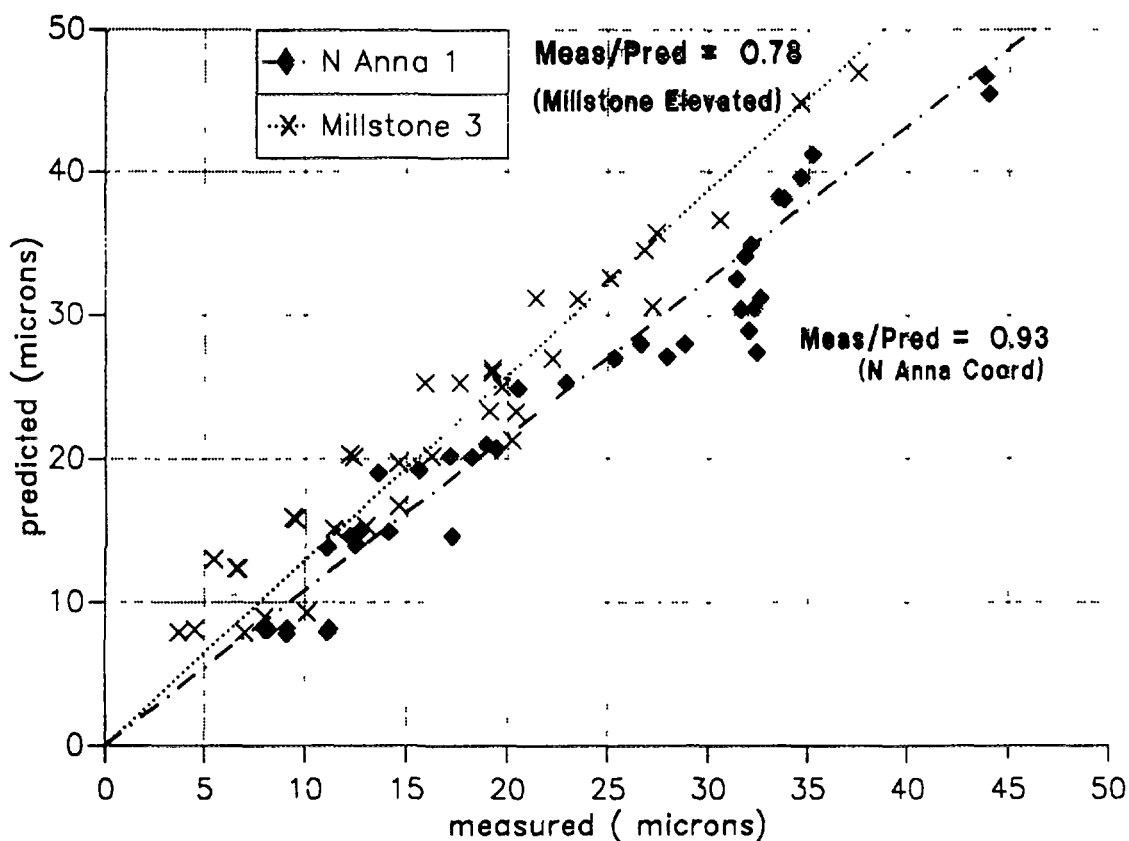


FIG 7 4. An example of comparisons between oxide thicknesses for exposures to normal lithium chemistry in North Anna-1 PWR and elevated lithium chemistry in Millstone-3 PWR. Measured values scaled to NE ZIRC Code predictions

are common during the first fuel cycle, when many plants operate at variable power levels considerably less than 100% for significant periods.

TABLE 7.1. Comparison of oxide thicknesses at transition and times to transition

Model	Transition Thickness ( $\mu\text{m}$ )		Time to Transition (d)	
	300°C	350°C	300°C	350°C
MATPRO	1.95	2.18	562	125
EPRI/KWU/C-E	2.06	2.44	953	165
COCHISE	2.12	2.64	862	150
ABB Atom				
1.3% Sn	1.80	2.09	739	117
1.5% Sn	2.03	2.35	739	117
NE-ZIRC	1.98	1.98	755	78

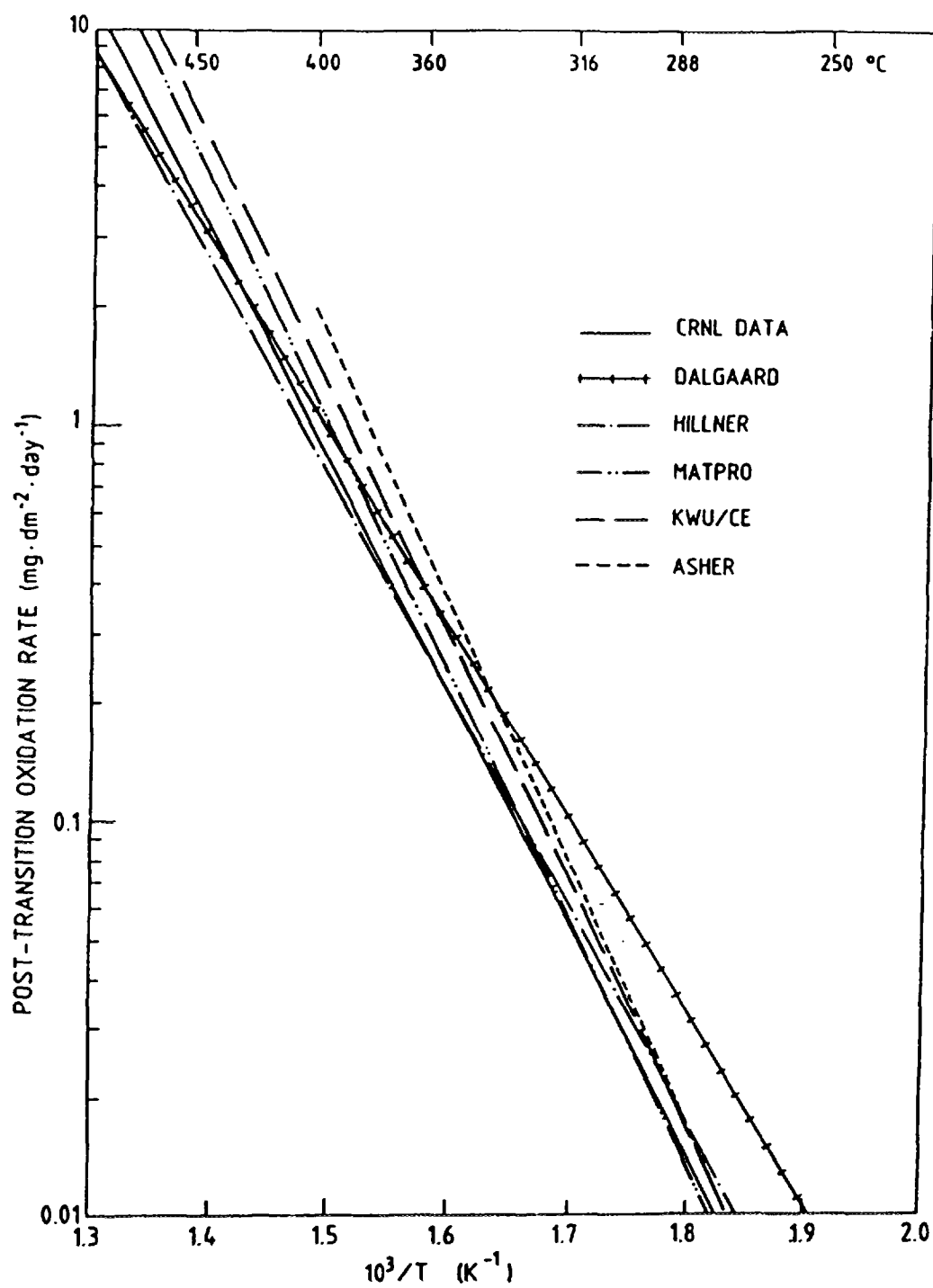


FIG. 7.5. Comparison between post-transition oxidation rate for early models [340].

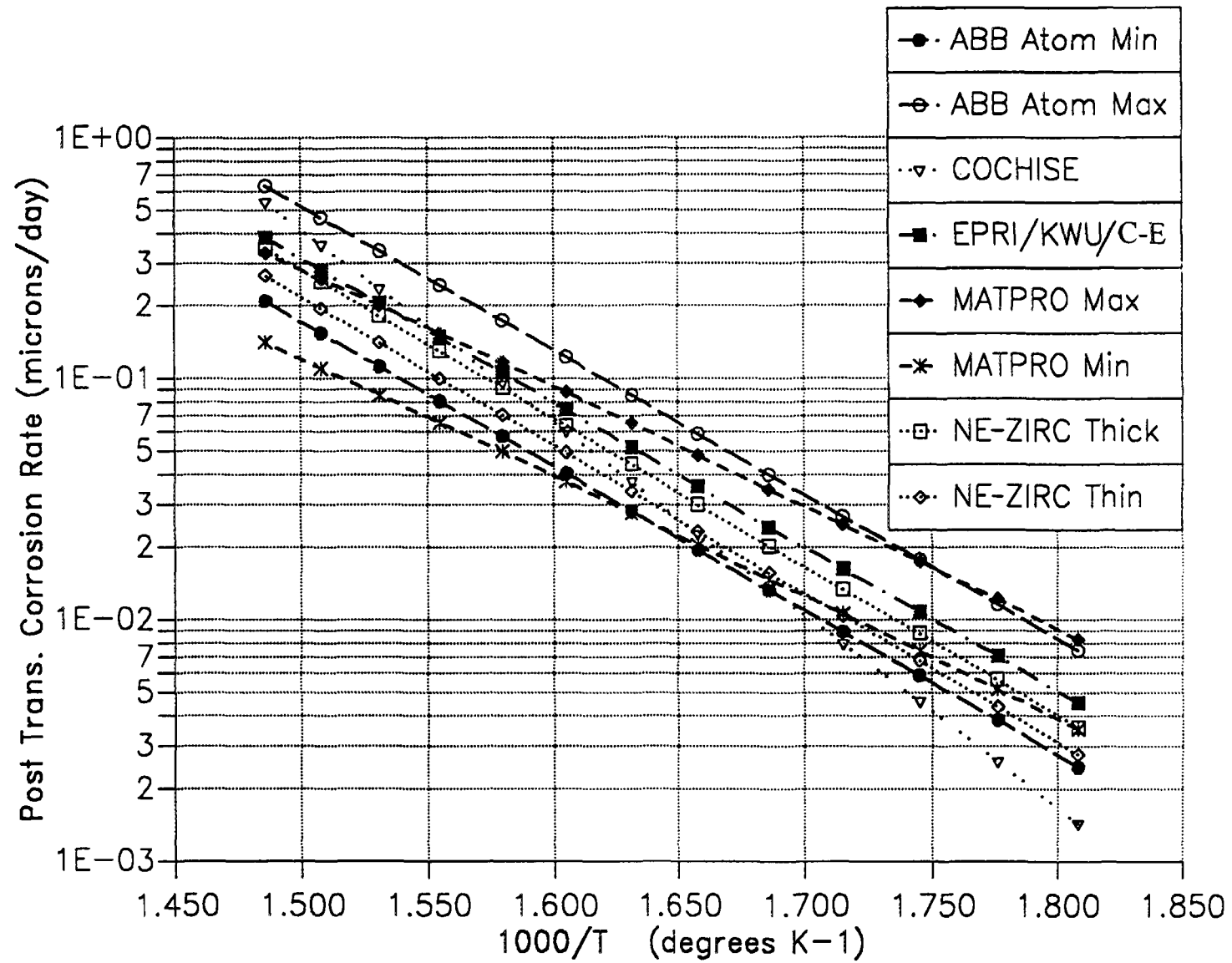


FIG. 7.6. Comparison between post-transition oxidation rates for models reviewed in section 7. 3. 2.

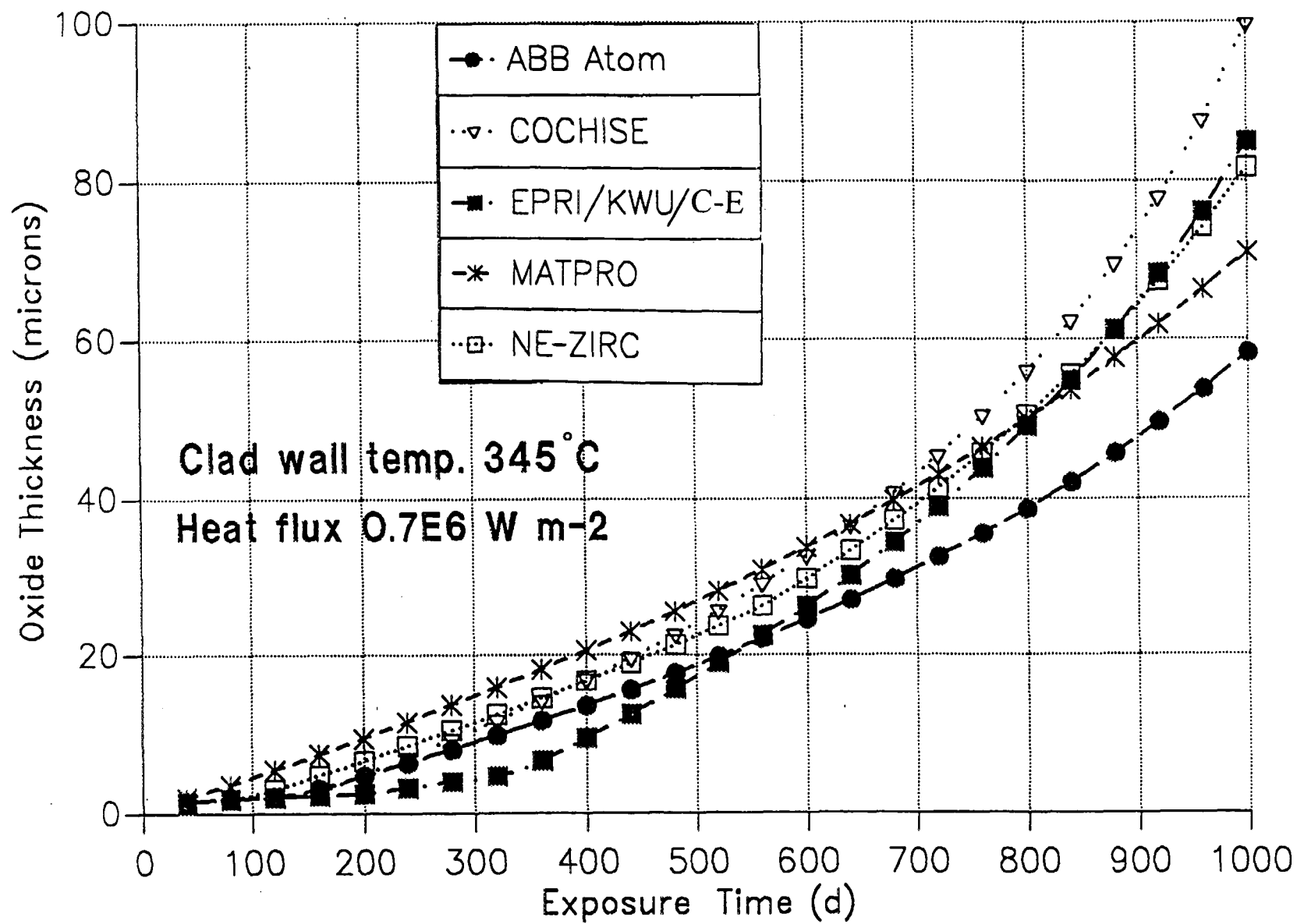


FIG. 7.7. Comparison between predicted oxide thicknesses for the models reviewed in section 7. 3. 2.

### 7 3 3 Individual models incorporating additional effects

#### 7 3 3 1 Westinghouse model

A brief description of a model incorporating lithium hydroxide effects was published by Westinghouse in 1994 [248]. A standard equation for the post-transition corrosion rate, equation (7 10), obtained from laboratory data was modified by factors for lithium and fast neutron flux in-reactor enhancement as follows.

$$\Delta S/\Delta t = [\Delta S/\Delta t]_{ab}[A + L] \quad (7 13)$$

where

$$\begin{array}{lll} \text{for } S < 10.2 \mu\text{m} & A = 1, & L = 0 \\ \text{for } S > 10.2 \mu\text{m} & A = b\phi^p, & L = d \times S \times [Li] \\ \text{with} & & \\ & b, p, d \text{ constants} & \\ & [Li] = \text{lithium concentration} & \end{array}$$

This model was derived from statistical fitting to a large body of Westinghouse plant data. The lithium dependence was derived partly from an analysis of elevated lithium chemistry in the Millstone-3 PWR. However, as stated in section 7. 3 2 5 an independent analysis of elevated lithium chemistry in the Millstone-3 plant concluded that it was not possible to demonstrate a lithium hydroxide effect [248,337,338].

#### 7 3 3 2 A new COCHISE model

A revised version of the French CEA COCHISE model, incorporating the effects of lithium hydroxide, boron and heat flux, has been presented [341-343]. Suggested behaviour in the pre-transition and post-transition regions was of the following form:

$$dS'/dt \text{ (pre) or } dS/dt \text{ (post)} = \exp(a + b[Li]) \{ 1 + C[Li]S\phi/\kappa RT^2 \} F_{\text{boron}} \exp\{-(c + d[Li])/RT\} \quad (7.14)$$

where

[Li] is coolant lithium concentration,  
 $\phi$  is heat flux,  
 $\kappa$  is oxide thermal conductivity;  
 $F_{\text{boron}}$  is a factorial reduction from the presence of boron in the coolant;  
 $a, b, c, d$  and  $C$  are constants (different for the pre- and post-transition regions).

The heat flux dependence was derived from a theoretical treatment predicting an increase in vacancy flux in the presence of a heat flux [334] (section 6. 6 ). The lithium and boron dependencies were derived from static autoclave experiments. The boron dependence appears as independent of the lithium dependence.

#### 7 3 3 3 A new EPRI model

The elements of a new EPRI model have been presented in [344]. This takes into account the tin ( $F_{\text{Sn}}$ ) and the iron contents ( $F_{\text{Fe}}$ ) of the alloy, heat flux ( $F_{\text{QA}}$ ), the effects of lithium ( $F_{\text{Li}}$ ), fast neutron flux ( $F_{\text{f}}$ ) and hydriding ( $F_{\text{H}_2}$ ) in the post-transition region:

$$ds/dt = C_2 F_{\text{Li}} F_{\text{Sn}} F_{\text{QA}} (1 + F_{\text{H}_2} + F_{\text{Fe}} + F_{\text{f}}) \exp(-Q_2/RT) \quad (7 15)$$



The dependencies of the various parameters were based on a literature survey, although there appeared to be little justification advanced in the particular case of a lithium hydroxide effect. The activation energy,  $Q_2$ , was calculated from plant axial oxide thickness profiles, rather than from laboratory data.

## 7.4 MECHANISTIC MODELS

A number of workers have produced mathematical expressions for proposed mechanisms in order to explain certain aspects of corrosion behaviour. Some of these are presented in section 7.3.3 above. For example, French workers have addressed the influence of stress and heat flux on the diffusion of oxygen through oxide films [334]. French workers have also investigated a new rationale for irradiation enhancement, proposing that this is due, at least in part, to lithium recoiling into the oxide after production in the coolant by the  $^{10}\text{B}(n,\alpha)^7\text{Li}$  reaction [342]. Other examples are given elsewhere in this document. It appears, however, that a complete understanding of all aspects of corrosion has not yet been attained.

### 7.4.1 Cox's model

The elements of a new type of model, potentially applicable to both PWR and BWR water chemistry, have been elucidated by Cox, based on a re-evaluation of the mechanisms by which corrosion is enhanced by irradiation and by high concentrations of lithium hydroxide [118].

Irradiation enhancement is attributed to the generation of additional oxide porosity by dissolution of damage spikes in the oxide caused by primary knock-on atoms after fast neutron collisions (Figure 7.8). New oxide then grows at the base of the pore at the oxide-metal interface. The effect of lithium hydroxide is also attributed to the generation of additional porosity, via preferred dissolution of inter-linked tetragonal or cubic  $\text{ZrO}_2$  sites in the lattice, with recrystallization of monoclinic oxide on the surface.

The resulting relationship for the post-transition corrosion rate is

$$1/S' = K_1/(K_2\phi + S'_x + S'_{Li}) + K_3/S'_y \quad (7.16)$$

where

$S'$  is the in-reactor corrosion rate,  $dS/dt$ ,

$S'_y$  is the rate of oxide regrowth at the pore base,

$S'_{Li}$  is the rate of oxide growth from pores created by dissolution in lithium hydroxide,

$K_1$ ,  $K_2$ ,  $K_3$  are constants and

$S'_x$  is the corrosion rate for metals with the appropriate irradiation induced structure, given by the out-reactor rate multiplied by a constant to account for the effects of irradiation on the structure

$$S'_x = \text{Constant} \times C \cdot \exp(-Q/RT) \quad (7.17)$$

It was suggested that  $S'_{Li}$  should be linearly proportional to lithium hydroxide concentration.

The model thus contains additive terms for the effects of irradiation and lithium hydroxide, rather than multiplicative terms used in semi-empirical models discussed in section 7.3.

At the time of writing, values for the constants in the equations had not yet been derived.

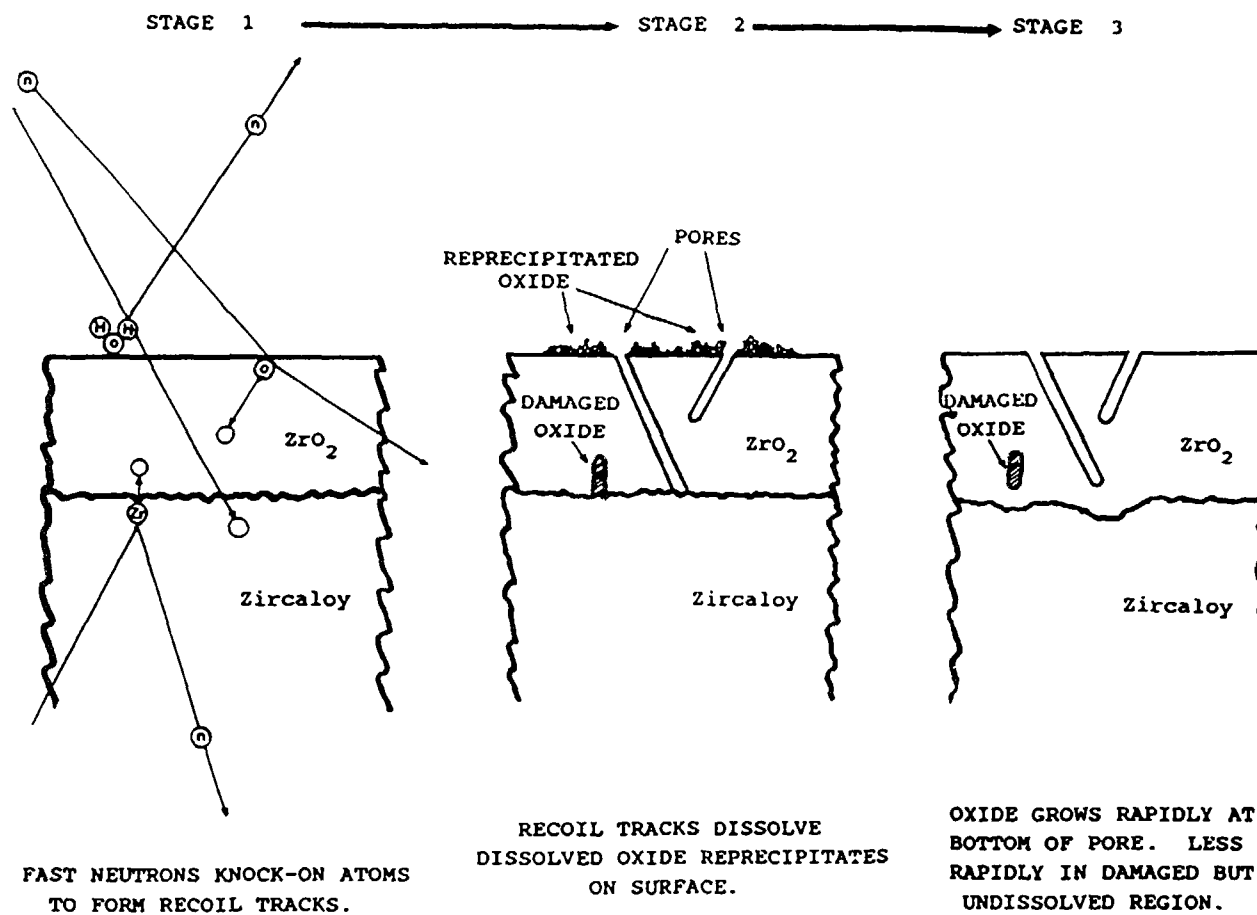


FIG. 7. 8. Schematic diagram of irradiation corrosion mechanism assumed in Cox's new mechanistic model [118].

## 7 4 2 Russian models for Zr-1%Nb cladding [345,272]

### 7 4 2 1 Model for post-transition uniform corrosion

The initial oxidation stage obeys parabolic kinetics producing a protective dense black film. At approximately 3  $\mu\text{m}$  a transition to linear kinetics occurs (Figure 7 9), characterised by the growth of a porous white film on top of the black pre-transition oxide. Following Johnson [197], two components of corrosion growth, are assumed

$$dS/dt = dS_T/dt + dS_\phi/dt = k_T + k_\phi \quad (7 18)$$

where the first term is the thermal component and the second term is the component due to radiation

The thermal component is of the same general form as equation (7 10)

$$k_T = k_0 \exp(Q_2/RT) \quad (7 19)$$

Mechanistically, the Russian model for post-transition growth is based on an oxide dissolution mechanism in which dissolved zirconia is transported along fine pores in the dense thin oxide film next to the oxide-metal interface. The transported zirconia is re-precipitated at the pore exit, increasing the width of the outer porous oxide layer. Dissolution of the dense layer is balanced by formation of new dense oxide at the oxide/metal interface and, hence, the width of the dense layer remains approximately constant and corrosion is approximately linear. At equilibrium, the thermal component can be described by Fick's First Law for diffusion of dissolved zirconia down the pores

$$k_T \propto D(\Delta m/l)(S_q/V) \quad (7 20)$$

where

$D$  is the diffusion coefficient of the dissolved zirconium solubility products in water ( $\text{m}^2 \text{s}^{-1}$ ),  
 $\Delta m$  is the concentration difference in the dissolved species over the pore length (mole  $\text{kg}^{-1}$ ),  
 $l$  is the pore length, (m),  
 $V$  specific volume of oxide ( $\text{m}^3 \text{kg}^{-1}$ ),  
 $S_q$  unit surface area ( $\text{m}^2$ )

The diffusion coefficients of the various species are not known and are approximated to the self diffusion coefficient of water,  $D_w$ . The maximum possible value of  $\Delta m$  is equal to the solubility,  $m$ . Substituting these approximations in equation (7 20) and summing over the various dissolved zirconium ions (in particular  $\text{Zr}(\text{OH})_3^+$ ,  $\text{Zr}(\text{OH})_4$ ) and taking logarithms yields

$$\ln(k_T) = \ln(\Sigma m_i) + \ln(D_w) + \ln(\text{Constant}) \quad (7 21)$$

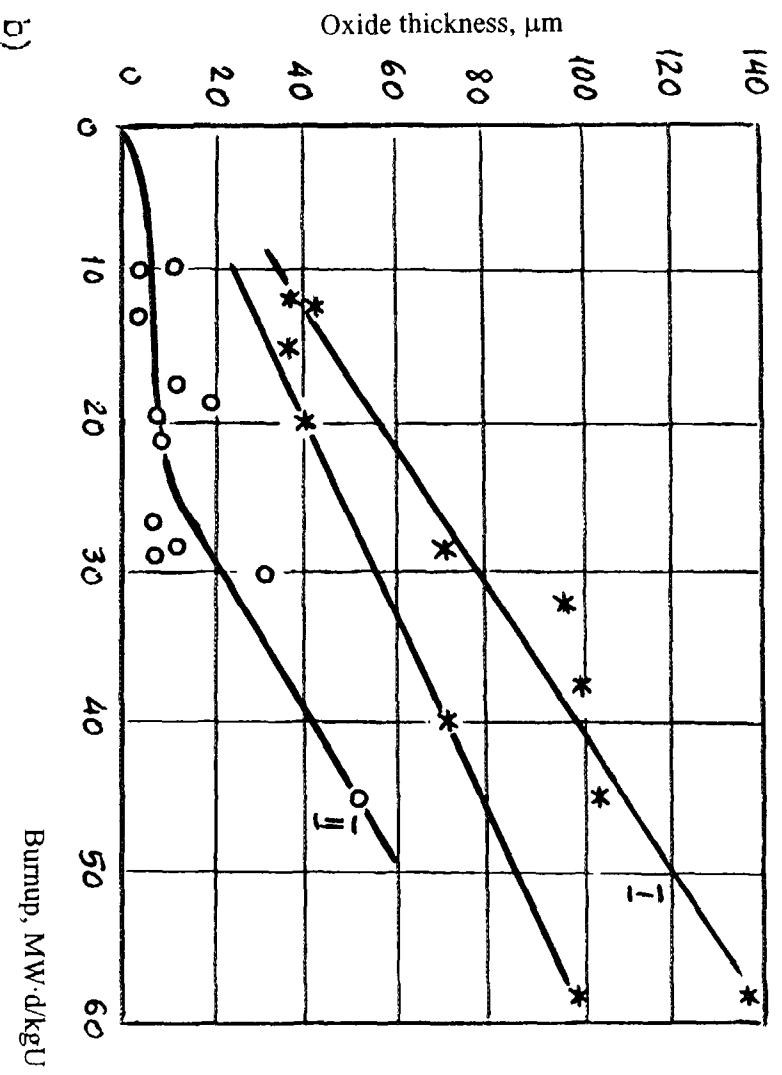
Some support for the model is given in Fig 7.10 which shows that the corrosion rate behaves in a similar manner to the solubility as the pH is varied. Similar models have also been presented in Russia for corrosion of iron- and copper-based alloys

The activation energy for the radiation component is expected to be low i.e.  $Q_\phi \sim 0$ . It is assumed that the radiation component is dominated by the dissolving effect of  $\text{H}_2\text{O}_2$  formed by radiolysis

$$k_\phi = f[\text{H}_2\text{O}_2]_{st} \quad (7 22)$$

where  $[\text{H}_2\text{O}_2]_{st}$  is the stationary concentration of  $\text{H}_2\text{O}_2$  inside the pores

a.)



b.)

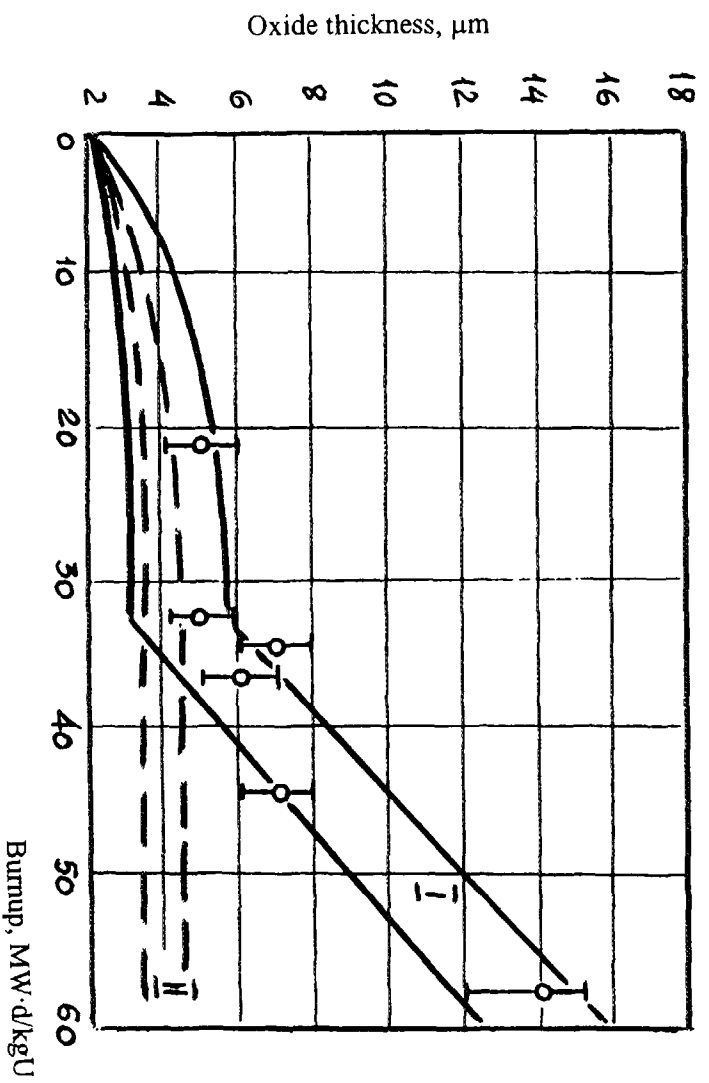
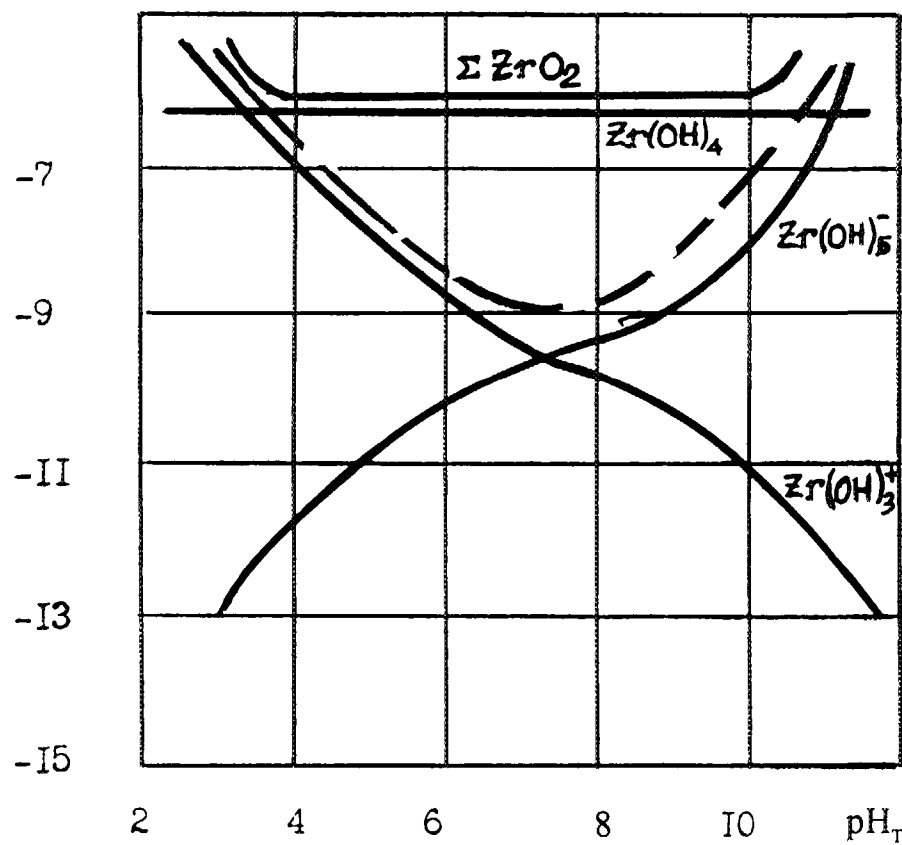


FIG. 7. 9. Oxide thickness versus fuel burn-up for: a) RBMK; I - nodular corrosion; II - uniform corrosion; b) I - WWER-1000; II - WWER-440.

$\log (m_{Zr})$



$\log (k_{Zr})$

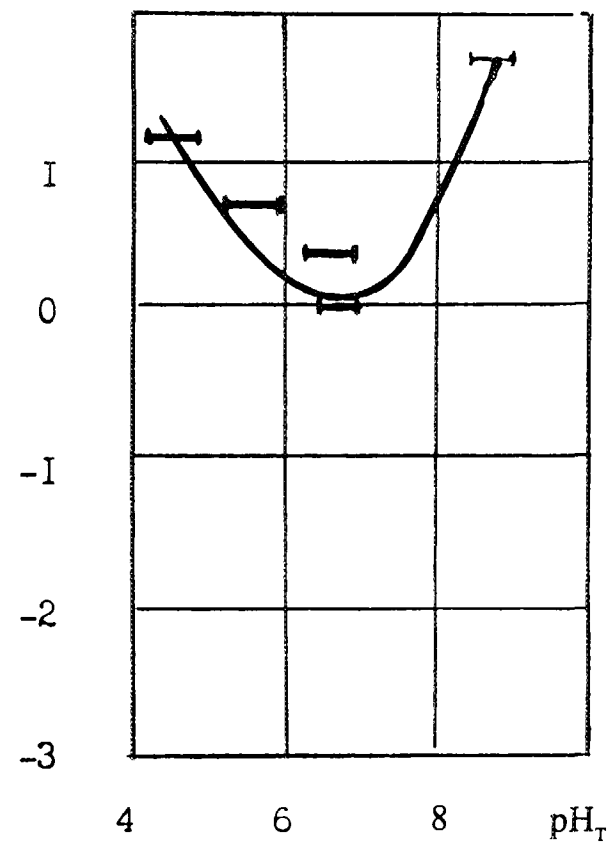


FIG. 7.10. Comparison between dependence on pH of (a) calculated solubilities of zirconium corrosion products and (b) measured values of corrosion rate.

For two phase conditions in RBMK reactors, solving the material balance equation for the simplified radiolysis scheme and simplifying the resultant expression yields [272]

$$k_{\phi} \propto [H_2O_2]_{st} \propto \phi^n (K^{H_2}/p) \alpha \quad (7.23)$$

where

- $\phi$  is fast neutron flux,  $n = 0.5 - 1$ ,
- $K^{H_2}$  is Henry's Law Constant for  $H_2$  dissolved in the coolant,
- $p$  is the partial pressure of hydrogen,
- $\alpha$  is the void fraction

For single phase flow in WWERs the radiation component,  $k_{\phi}$ , is presumed to be zero since the  $H_2O_2$  concentration is suppressed by reaction with the hydrogen dissolved in the coolant

#### 7.4.2.2 Model for nodular corrosion in WWERs and RBMKs

Nodular corrosion in RBMKs occurs as result of localised deposition of iron-based corrosion products on the cladding at locations in the upper parts of fuel assemblies where the heat flux, neutron flux and rate of steam generation are most intense. By analogy with equation (7.18) the local corrosion rate in the linear region is assumed to be composed of a thermal component,  $k_T^{loc}$ , and a radiation component,  $k_{\phi}^{loc}$ . The thermal component is given by an expression similar to equation (7.19) but with the temperature increased due to the temperature rise across the deposit. It is assumed that this temperature rise is proportional to the mean concentration of iron-based corrosion products in the coolant,  $C_{ave}$ . The radiation component is assumed to be given by equation (7.23) but with the local void fraction increased by the presence of the localised deposit. From these assumptions the following equation for the localised increase in corrosion rate can be derived [272]

$$dS^{loc}/dt = k_T^{loc} + k_{\phi}^{loc} = k_0 \exp\{-Q/R[T + q_{ave} KC_{ave}/\kappa_c]\} + N\phi^n (K^{H_2}/p) \alpha_{ave} (1 + MC_{ave}^{1.2}) \quad (7.24)$$

where

$k_0$  and  $N$  are constants,

- $T$  the mean temperature at the oxide/metal interface,
- $q_{ave}$  the mean heat flux through the cladding,
- $K$  the distribution coefficient for the deposition of corrosion products on to the cladding at the location,
- $\kappa_c$  the thermal conductivity of the corrosion product deposit,

and where

$$M = (1/\pi d)(a\kappa K/\kappa_c)^{1/2} \quad (7.25)$$

where

- $a$  is the cladding thickness,
- $\kappa$  is the thermal conductivity of the zirconium alloy oxide,
- $d$  is the cladding diameter

In connection with the void fraction dependence in equation (7.24), Figure 7.11 shows comparisons between corrosion rate and void fraction in various environments

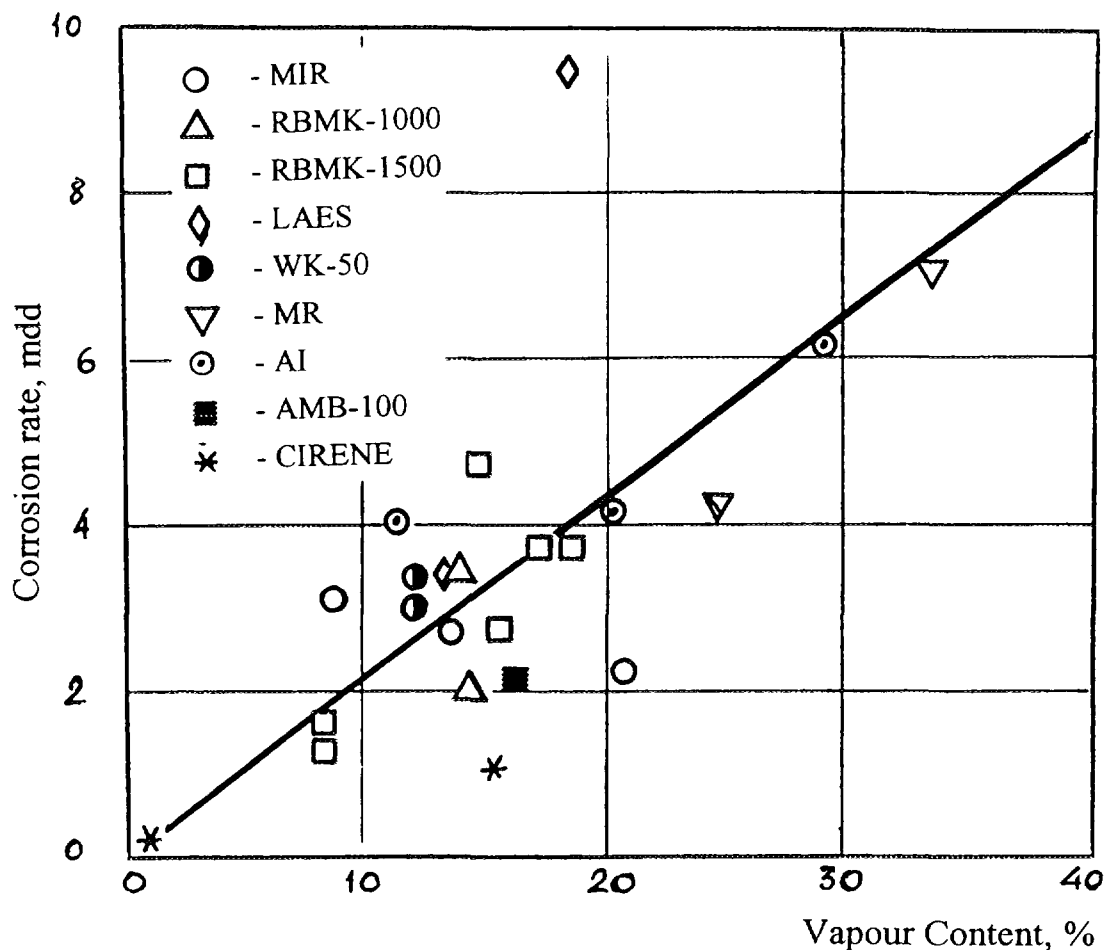


FIG 7.11 The vapour content influence on linear corrosion rates in various environments (mdd  $\text{mg dm}^{-2} \cdot \text{d}^{-1}$ )

For WWERs  $k_{\phi}^{\text{loc}}$  is assumed to be zero since the dissolved hydrogen in the coolant suppresses the hydrogen peroxide produced by radiolysis. Thus, for WWERs the second term in equation (7.24) is put equal to zero. For examples of this phenomenon in WWERs see section 6.4.3. and Figures 8.24 and 8.26

The predictions of these models of nodular corrosion have been compared with plant measurements of oxide thickness (Figures 7.12 and 7.13)

## 7.5 SUMMARY OF PWR CORROSION MODELLING

As stated in section 7.3.2.7., a large number of simple models of generic form have been produced. These vary in parametrical values. More recently, the number of available models has further increased due to the appearance of mechanistic and semi-mechanistic models which have very little in common with each other. Many models have been fitted to plant data and, therefore, should give reasonable overall predictions for past operating conditions. However, different models are likely to predict significantly different parametrical dependencies and may give significantly different predictions when extrapolated to new conditions (e.g. high burn-up). This is not surprising in view of the lack of a consensus in the mechanistic understanding of corrosion processes and in view of variations in experimental data and the manner in which the data have been interpreted by different modellers.

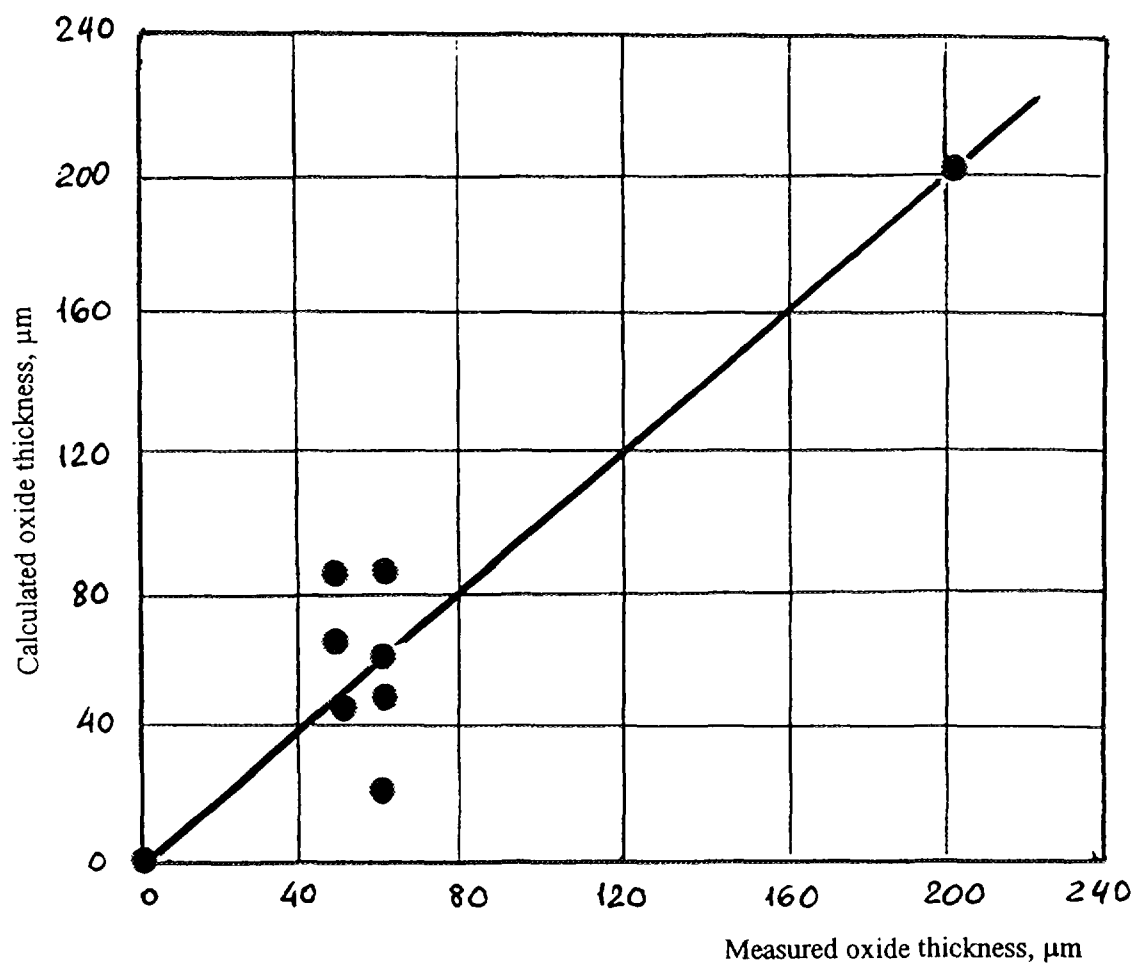


FIG. 7. 12. Correlation between calculated and measured nodular corrosion thicknesses for WWER coolant chemistry.



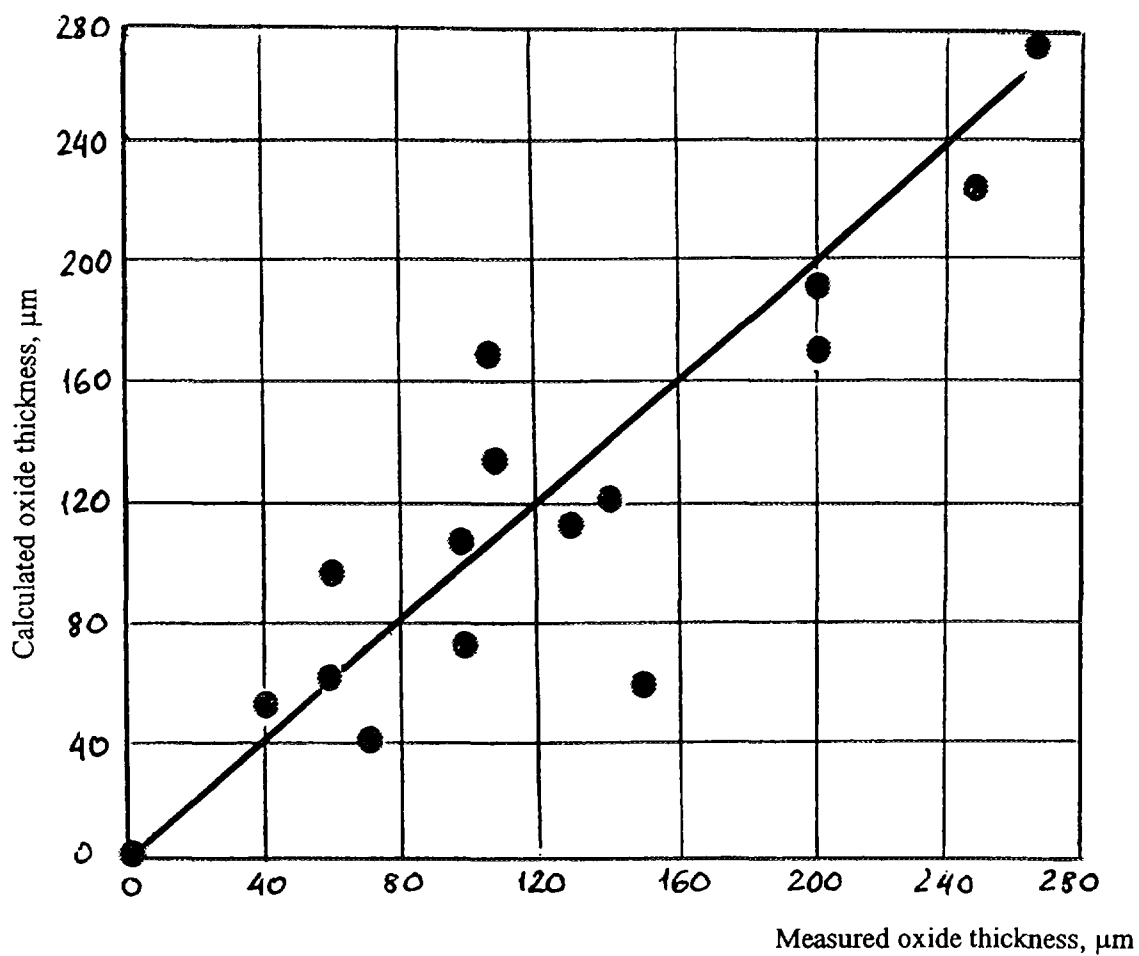


FIG. 7. 13. Correlation between calculated and measured nodular corrosion thicknesses for RBMK coolant chemistry.

## 8. IRRADIATION EFFECTS ON CORROSION

### 8.1 IRRADIATION DAMAGE

The term "irradiation damage" is a common description of very different phenomena. Any process that could induce a change in the crystallographic and chemical structure of any material under irradiation could be considered as inducing irradiation damage. Usually the damage taken into consideration is only that which remains after normal thermal recovery. Under classical irradiation conditions, some of the damage is indeed recovered on a very fast time scale: an electron ejected from an atomic cloud induced by an energetic photon is recovered in a few picoseconds in metals due to the delocalized nature of the electrons. The same process in largely ionic material, like zirconia, may not recover at ambient temperature until after a few hours, leaving a localised charge defect around a given atom [346].

For irradiation by massive particles like neutrons, the energy transfer from the particle to the target atom may be sufficient to allow the particle to move away from its site, giving birth to a pair of defects (vacancy plus interstitial). In addition, this primary knock-on atom may have enough energy itself to induce another displacement. This is the so-called "collision cascade".

#### 8.1.1 Fast neutron damage in the metals

In reactors, fast particles include neutrons, primary recoil atoms and Compton electrons created by gamma rays. Indeed, above 700 keV, Compton electrons will transfer up to 40 eV to a metallic atom, enough to induce its displacement, but an order of magnitude analysis gives them a negligible contribution to the total irradiation damage by atom displacement. In a similar way, the recoil energy in either of the  $\alpha$  or the  $\beta$  emission processes may be high enough to induce displacement of the recoiling atom, however the contribution of those processes to the total damage is also negligible, except in very specific cases.

In the case of metals, most of the structural damage induced during neutron irradiation in power plants is due to elastic interactions with fast neutrons. Usually the experiments reported on the effect of irradiation on microstructure are scaled with the total fluence received by the material. In order to compare material irradiated under various conditions (i.e. various neutron spectra) a common procedure is to compute the damage in terms of displacements per atom (dpa).

The number of scattered zirconium atoms (per target atom) for a given fast neutron flux is expressed by

$$N = \sigma \phi$$

where

$\sigma$  is the elastic scattering cross section and  
 $\phi$  the fast neutron flux

The incoming neutron transfers part of its kinetic energy to the target Zr atom by elastic interaction. This latter will receive, for a 1 MeV incident neutron, a maximum recoil energy of

$$(E_r)_{\max} = 40 \text{ keV}$$

and a mean value of

$$(E_r)_{\text{mean}} = 20 \text{ keV}$$

These energies are much higher than that necessary for the atom to escape from its site and the displaced atom itself will displace other atoms, inducing a collision cascade. This process induces

a high density of elastic interactions, in the so-called nuclear stopping regime (i.e. a regime where the loss of energy of the ion in the matter is due to Coulombic interactions with the nuclei of the target). This region of energy loss is mainly controlled by screened Rutherford scattering [347]. Secondary ions will then interact with target atoms until the energy transferred is below a critical value needed for displacement: the displacement energy,  $E_d$ . In the case of Zr, the value of this energy threshold has been measured to be slightly dependent on orientation [348,349]:

$$E_d = 25 \text{ to } 27 \text{ eV.}$$

The number of secondary ions induced by the primary atom can be deduced from hard sphere collision cascade analysis [350]:

$$\langle n \rangle = kE_p/(2E_d)$$

The value of  $k$ , an efficiency parameter, is usually taken to be close to 0.8.

Immediately following this cascade displacement event, most of the interstitial atoms will anneal with vacancies in the surroundings, by elastic recombination. The diameter of the volume in which this recombination occurs is of the order of a few atom diameters. After this athermal annealing, a typical value of  $\langle n \rangle = 300$  displaced atoms is found in a typical collision cascade [351]. Figure 8.1 gives a typical example of such a displacement cascade for a 20 keV Zr recoil atom in zirconium using the TRIM computer code [352]. The net result is the creation of many pairs of interstitials and vacancies. The vacancies are mostly located at the centre of the cascade, while the interstitials are ejected at the periphery. After the elastic spontaneous recombination, thermal motion will induce diffusion and the possibility of recombination of the point defects. Thus a time dependent evolution of the concentration of the point defects will occur. The fraction of the number of displaced atoms to the number of atoms per volume, leads to the quantity used to measure the irradiation damage, the displacements per atom (dpa). A recent review of these mechanisms has been written by Robinson [353]. The availability of powerful computers has led to a better knowledge of the cascade history and of the relation between primary recoil energy and surviving defect number. For typical metals, the number of surviving defects is roughly 1/10 for a 10 keV primary recoil, as computed by molecular dynamics [354]. As the neutron elastic interaction cross section is neutron energy dependent, the relationship between neutron flux and damage rate is a function of the neutron flux spectrum. Very few complete computations are available on the correspondence between fluence and damage for different types of reactors [355,356]. Typical values of correspondence between fluence ( $E > 1 \text{ MeV}$ ) and dpa are:

$$d = b\phi t$$

where

$d$  is damage (dpa);  
 $\phi$  is fast neutron flux ( $\text{n}\cdot\text{m}^{-2}\cdot\text{s}^{-1}$ );  
 $b$  is  $2\times 10^{-25}$  for most power plants, and  
 $t$  is time (s).

giving a value of a few dpa per cycle in typical light water nuclear power plants (PWR or BWR).

## 8. 1. 2. Displacement damage in other structures

### 8. 1. 2. 1. Damage in intermetallic precipitates

This computation of neutron damage for Zr atoms in a Zr matrix has to be extended to other atoms or other structures, in particular for the intermetallic precipitates and the  $\text{ZrO}_2$  oxide layer. This is in principle possible, if scattering cross sections and displacement energies are available. For the metals, neutron scattering cross sections are available and are independent of the chemical state of the

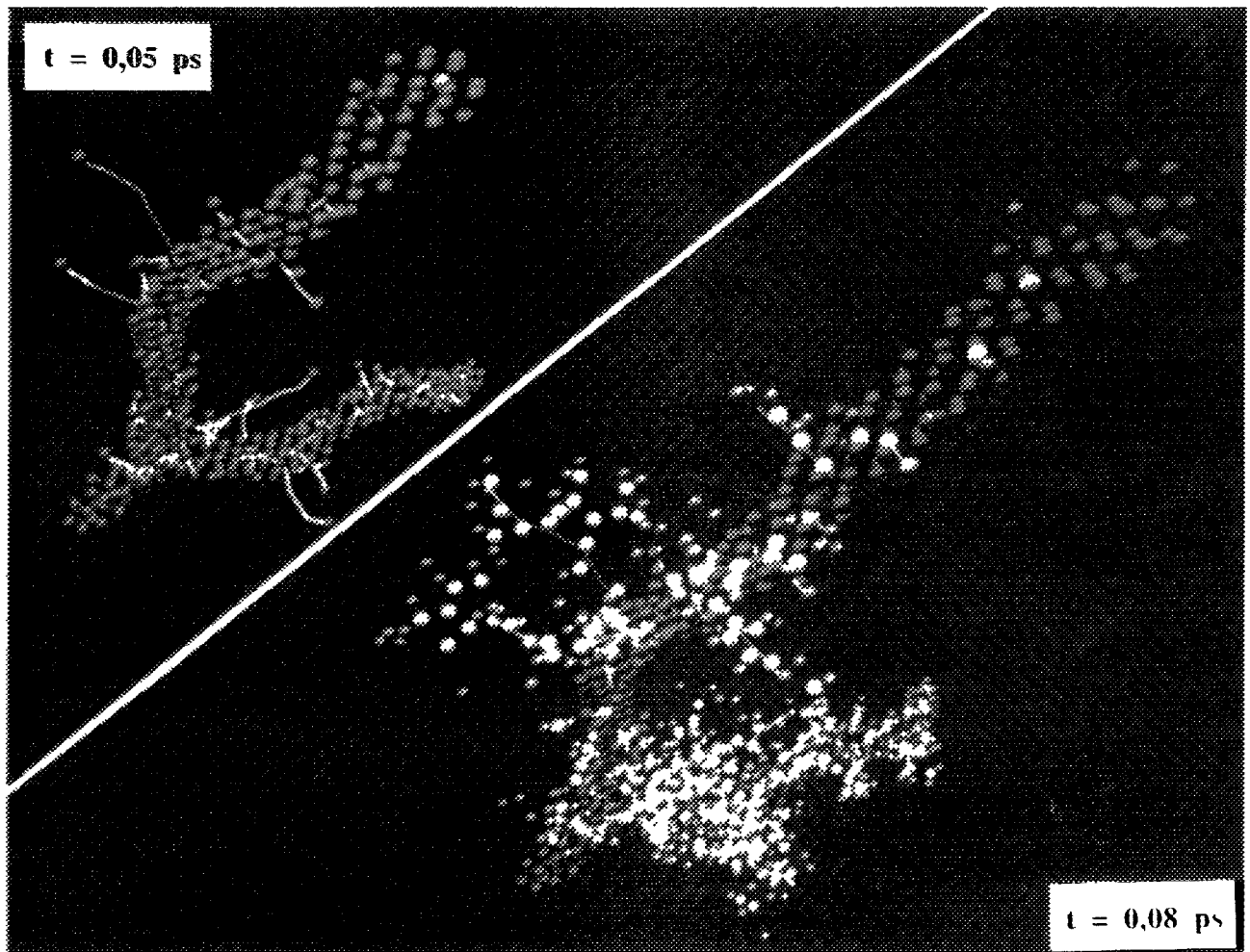


FIG 8 1 Displacement cascade formation in an intermetallic compound The blue atoms are slightly displaced from their normal lattice sites, the yellow atoms are knocked out, forming vacancies, and the red are the resulting interstitial atoms

target atom [357] Thus the transferred energy is a quantity easy to compute In order to know the damage, displacement energies  $E_d$  have to be known precisely In the case of intermetallics, measurements or molecular dynamics (MD) computations have been made in a few cases As reviewed in [358], various results can be obtained Using MD computations, it has been found that, for the CuTi compound, the displacement energies differ by a factor of 1.6 for Cu and Ti, while, in the VS<sub>1</sub> phase, they are the same for S<sub>1</sub> and V In addition,  $E_d$  for Cu has been found to be the same whatever might be the phase in the series Cu, CuAu and CuAu<sub>2</sub> In addition, in the case of the intermetallic compound Zr<sub>2</sub>Al, no significant changes of the displacement energies have been reported when compared with the pure metal [359] In the absence of any measurements for the intermetallics in the current Zr alloys, a value of 25 eV would be a fair estimate for all the chemical species (Fe, Ni, Cr and Zr) in the Zr<sub>2</sub>(Ni, Fe) and Zr(Fe, Cr)<sub>2</sub> phases

Therefore, the extent of the damage can be considered to be the same for any Zr atom, regardless of its original location in the metallic alloy A specific consideration should be given to the case of intermetallics for these ordered alloys, the annihilation of an interstitial on a vacant site will not always lead to the disappearance of a defect Indeed in some cases the atom will move to the site

of a similar atom (displacement), but in a large number of cases (depending on the stoichiometry), the interstitial will return to the normal location of another species (replacement). This leads to an "anti-site defect". A sketch of the different types of irradiation defects in intermetallics is found in Figure 8.2 [358].

#### 8.1.2.2 Damage in the oxide

In the oxide, the values of the displacement energies have to be measured for both atoms O and Zr. In addition, due to the largely ionic nature of the bonding, the defects are charged and of higher energy than in metals. In the case of magnesium oxide (MgO), the values obtained for  $E_d$  for the metal ion are more than twice as large in the oxide as in the metallic phase [360]. Therefore, the relationship between neutron flux and damage will be quite different in the oxide phase compared to that in the metal. In the case of  $\text{UO}_2$ , displacement energies have been measured using high voltage electron microscopy. A large difference was found for the two types of atoms: 40 eV for U atoms and 20 eV for O atoms. This leads to similar contrasts in the number of displaced atoms if U or O atoms are taken into account [361]. As another example, for alumina, the oxygen displacement requires more than twice the energy needed for the aluminium atom (79 and 24 eV, respectively) [346]. For zirconia, neither of the two displacement energies are known, but a similar contrast should be expected.

In the case of an oxide, as reviewed recently [346,362], the mechanism of radiation damage generation is more complex than in metals. In such materials atomic displacements can be produced either by nuclear interactions, as in metals, or as a consequence of the electronic interactions, induced by charged secondary ions.

In non-metals, electronic damage can be more efficient per unit of energy deposited than are knock-on displacements. The electronic losses along fast charged-particle trajectories far outweigh the energy transferred by mechanical collisions. Therefore, most of the incident particle energy is eventually available to generate radiolytic displacements. Moreover, during the electronic stopping process of the secondary knock-on ions, some damage may occur in this ionically bonded material. Indeed, although in this regime the electronic perturbation is relaxed in a very short time in the metal, due to the nature of the free electrons, this will not be the case for ceramics, since the electrons are localised. Recent experiments on superconducting ceramics, irradiated with high energy ions, showed structural damage during the electronic stopping regime, while nothing was observed in metals [363]. Similarly, the very high sputtering yields of oxides irradiated with energetic ions in the electronic stopping regime can only be explained by the assumption of severe damage induced by this process [364]. In general a much higher damage rate should be expected in the zirconia than in the matrix nearby.

During the recombination step after displacement, defect mobility may be appreciably enhanced under irradiation as a consequence, not only of the mechanisms operating in the metal (irradiation enhanced diffusion), but also due to the alteration of the electronic states of the defects and to the different mobilities of the defects created, such as F or H centres. Figure 8.3 gives an example of these charged defects in ionic crystals. Long range electrostatic interactions of the defects will influence their aggregation and recombination properties [346]. In the case of ionic materials, direct ionisation due to photons has to be considered. For an irradiation by gamma-rays at an intensity of  $10^5 \text{ G h}^{-1}$ , the displacement production rate is of the order of  $2 \times 10^5 \text{ dpa h}^{-1}$  [365]. This value, although small compared to the damage induced by neutron or primary recoils, has to be considered when analysing the corrosion behaviour after irradiation during intermediate storage.

In the case of ionic insulators, such as zirconia, a specific phenomenon, which could be relevant to corrosion under irradiation, has to be considered: the radiation induced conductivity (RIC). Any source of irradiation with a high energy deposition rate will induce in a ceramic insulator a temporary electron conduction. The energy transferred to some electrons can be high enough that they will move from the valence band to the conduction band. Most of them will recombine with the

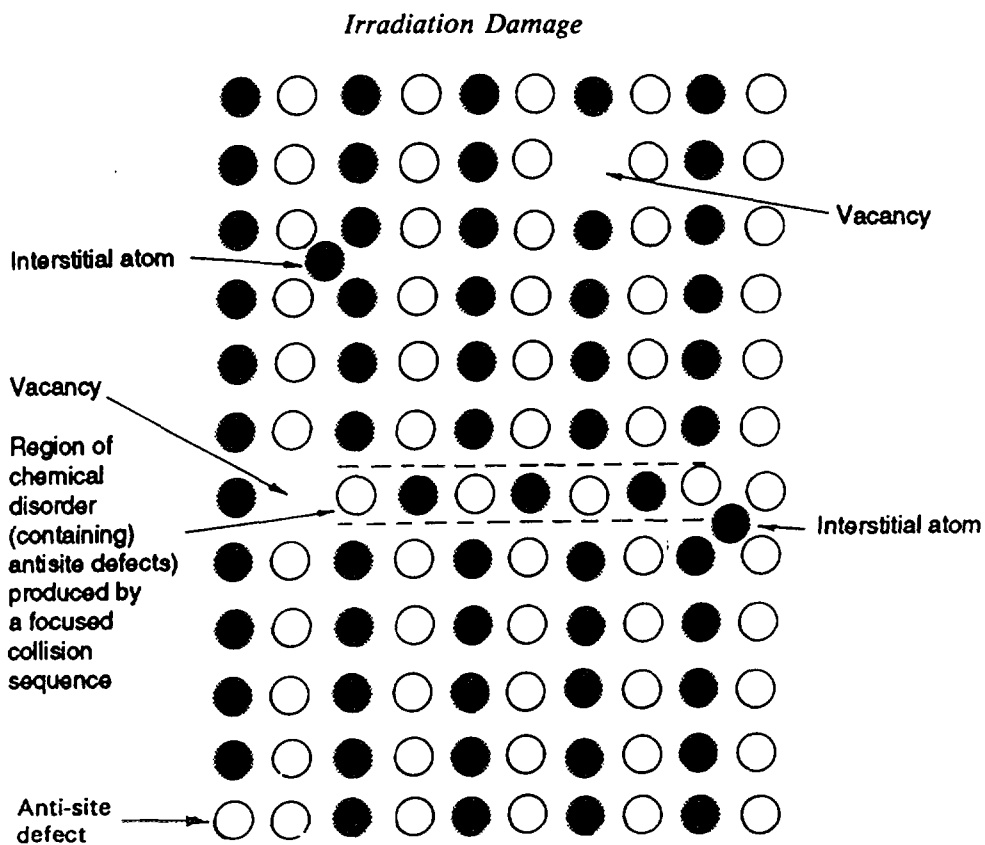


FIG. 8.2. The different types of irradiation point defects in an intermetallic compound.

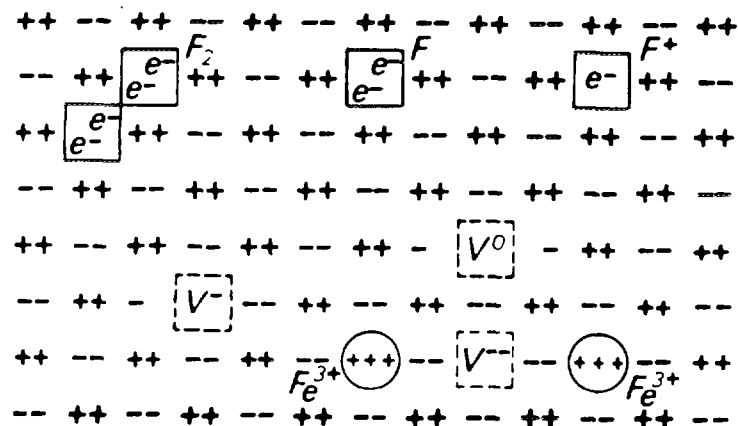


FIG. 8.3. Point defects in an ionic compound.

associated hole within a few  $10^{-11}$  s. However, some will escape the recombination process and diffuse under the applied electrical field. No specific studies of RIC have been performed in zirconia, but for alumina, the electrical conductivity has been found to increase linearly with energy deposition rate, between  $0.1$  and  $10^7$  Gy·s<sup>-1</sup> at 350°C [366]. For the other ceramics measured, the conductivity was also found to be roughly proportional to the energy deposition rate and for typical power reactors would give, for a pure zirconia, an electrical conductivity in the range of  $0.1$  to  $10$  mS·m<sup>-1</sup> [346].

In addition to the RIC, a radiation induced electrical degradation (RIED) has been observed in several cases of ceramics irradiations [346]. In these cases, the displacement damage induced by irradiation leads to a permanent loss of electrical insulation behaviour. When the process was observed, it occurred for doses lower than  $10^{-2}$  dpa. In reactor the doses are larger (a few dpa) and if this phenomenon exists in ZrO<sub>2</sub>, it could enhance the electron conduction of the zirconia, having thus an effect on the oxidation rate under irradiation, if electronic conduction is rate limiting. However, some controversy exists on the exact nature of the phenomenon [346].

### 8. 1. 3. Effect of irradiation on microstructures

#### 8. 1. 3. 1. Zirconia microstructure

Few observations are reported on the effect of irradiation upon the structure of bulk zirconia. Y<sub>2</sub>O<sub>3</sub>-stabilised zirconia has been irradiated at different temperatures (up to 1,025 K) to a fluence of  $4.4 \times 10^{25}$  n·m<sup>-2</sup> and a small swelling was observed (about 1.5%) at intermediate temperatures ( $\sim 1/3$  T<sub>m</sub>) that could be attributed to dislocation loops observed by TEM [367]. An irradiation-induced monoclinic to cubic phase transformation of zirconia was obtained at 370 K and a fluence of  $10^{24}$  n·m<sup>-2</sup>. The irradiation permitted the observation of a phase transformation from the low temperature stable monoclinic to the high temperature cubic phase. A proposed explanation was based upon the internal stresses developed around the point defects that could stabilise the cubic phase. This irradiation induced cubic phase transformation remained stable up to 1,070 K [368]. Subsequent work attributed this phase transformation to fission spikes associated with traces of fissile material contaminating the samples [369].

Recent STEM observations have been performed on irradiated oxide layers. It was found that the microstructure of the zirconia had a tendency for a higher grain size when grown in reactor, and that in that case no strong epitaxial relationship could be found between the base metal and the oxide. In addition, the oxide layer grown in reactor was much less stable and had a higher tendency to recrystallise during moderate heating by the electron beam [370]. There are no new reported microstructural observations of bulk zirconia irradiated in reactor and observed afterwards.

Close to the precipitates, the zirconia grown in reactor can have various forms, depending of the state of the precipitates after irradiation [80]:

- In the case of an oxide layer grown on a metal where the precipitates were not fully amorphous, (i.e. early in life or, at least, before the end of the second irradiation cycle), then when trapped in the zirconia layer, the precipitates were rich in Fe and the surrounding zirconia was doped afterwards with Fe (up to 4-6 %). This high Fe content of the zirconia can be explained by a fast neutron-induced ballistic diffusion that will lead to Fe concentrations in ZrO<sub>2</sub> above the solubility limit, since such a local effect is not observed during autoclave testing. The effect of this doping is a chemical stabilisation of the tetragonal phase of the zirconia surrounding the former precipitate.
- For an oxide grown later in the in-reactor lifetime, the precipitates have lost all their Fe due to the amorphous transformation and, when trapped in the zirconia layer, they will not be able to contribute to any Fe doping of the zirconia. No tetragonal phase can then be found surrounding these precipitates. This effect of irradiation on the phase transformation is not directly due to the flux, but seems to be controlled by the presence of the precipitates and their delayed oxidation.

Figure 8 4 describes the different morphologies obtained for those precipitates incorporated in the zirconia layer for increasing irradiation times in a power reactor [80]

Anodic dissolution of the oxide, and reprecipitation on the free surface, has been observed in specially designed experiments (high UV photon flux), leading to a porous oxide with a high corrosion rate at low temperature [128] These conditions, when transposed to power reactors, could give an explanation for local dissolution of the zirconia enhanced by the high electrical field due to an irradiation photocurrent

In the case of corrosion-grown oxide layers, experiments using replicas or thin foils of irradiated or unirradiated Zr alloys, showed that the layer is porous with cylindrical pores of radius in the range of 3-5 nm [98] and that the grain size of the zirconia is very small, of the order of 20-40 nm, with small holes at triple grain boundaries [81]

#### 8 1 3 2 Zr matrix microstructure

Unless noble gases are intentionally added to zirconium alloys, no bubble formation under irradiation by neutrons is reported [371,372] This difference in behaviour, compared with the stainless steels in fast reactors, is attributed to a reduced efficiency of edge dislocations to trap the interstitial atoms Other reasons are given, such as anisotropic diffusion in the hcp lattice or internal residual stresses, following thermo-mechanical processing, due to the anisotropy in the expansion coefficient and Young's modulus

As recently reviewed by Griffiths [372,373], various investigations have been performed on the nature of irradiation defects induced in Zr alloys [374,375] It is usually reported that after an irradiation to a fluence of 2 to  $3 \times 10^{23}$  n m<sup>-2</sup>, interstitial and vacancy loops are observed They are of  $a/3 \langle 1120 \rangle$  type in planes close to (1010) (prismatic planes) The ratio between interstitial and vacancy loops is irradiation temperature dependent Higher irradiation temperatures increase the number of interstitial loops [376,377] The simultaneous occurrence of the two types of dislocation loops (interstitial and vacancy) is in contradiction with the standard theory of point defect diffusion and recombination The residual stresses induced by the anisotropy in the thermal expansion coefficients of Zr following thermo-mechanical processing, or the anisotropic differences in point defect diffusion behaviour, could be the reasons for this discrepancy This phenomenon remains an open question

Several recent observations have reported recrystallization and grain growth in the matrix at high fluences and moderate temperatures this was the case for Alloy E - 635 irradiated to  $4 \times 10^{25}$  n m<sup>-2</sup> at 310-320°C [286] or Zircaloy 2 after  $8 \times 10^{25}$  n m<sup>-2</sup> at 288°C [378] At high temperature (above the temperature used in power reactors) full recovery occurs during irradiation

For very high fluences in the range of 3 to  $8 \times 10^{25}$  n m<sup>-2</sup>,  $\langle c \rangle$  component dislocation loops are observed [379,380] These  $\langle c \rangle$  type loops are only of vacancy type and their growth seems to be induced by a 2-D precipitation of the Fe released from the amorphous precipitates in a way similar to stacking faults [381] Indeed these large  $\langle c \rangle$  loops are found at a higher density close to those precipitates [382] A strong correlation between the formation of these loops and a significant increase of irradiation growth rate (breakaway) was noticed Growth is defined as the fuel rod, or pressure tube, elongation under irradiation caused by the anisotropic formation of interstitial loops on specific crystallographic planes The strong texture of the cladding tubes, or of the pressure tubes, then leads to an increase in axial length Detailed mechanisms are still under discussion [383,384]

The growth may have an effect upon corrosion kinetics The consequence of growth has to be considered on two different scales



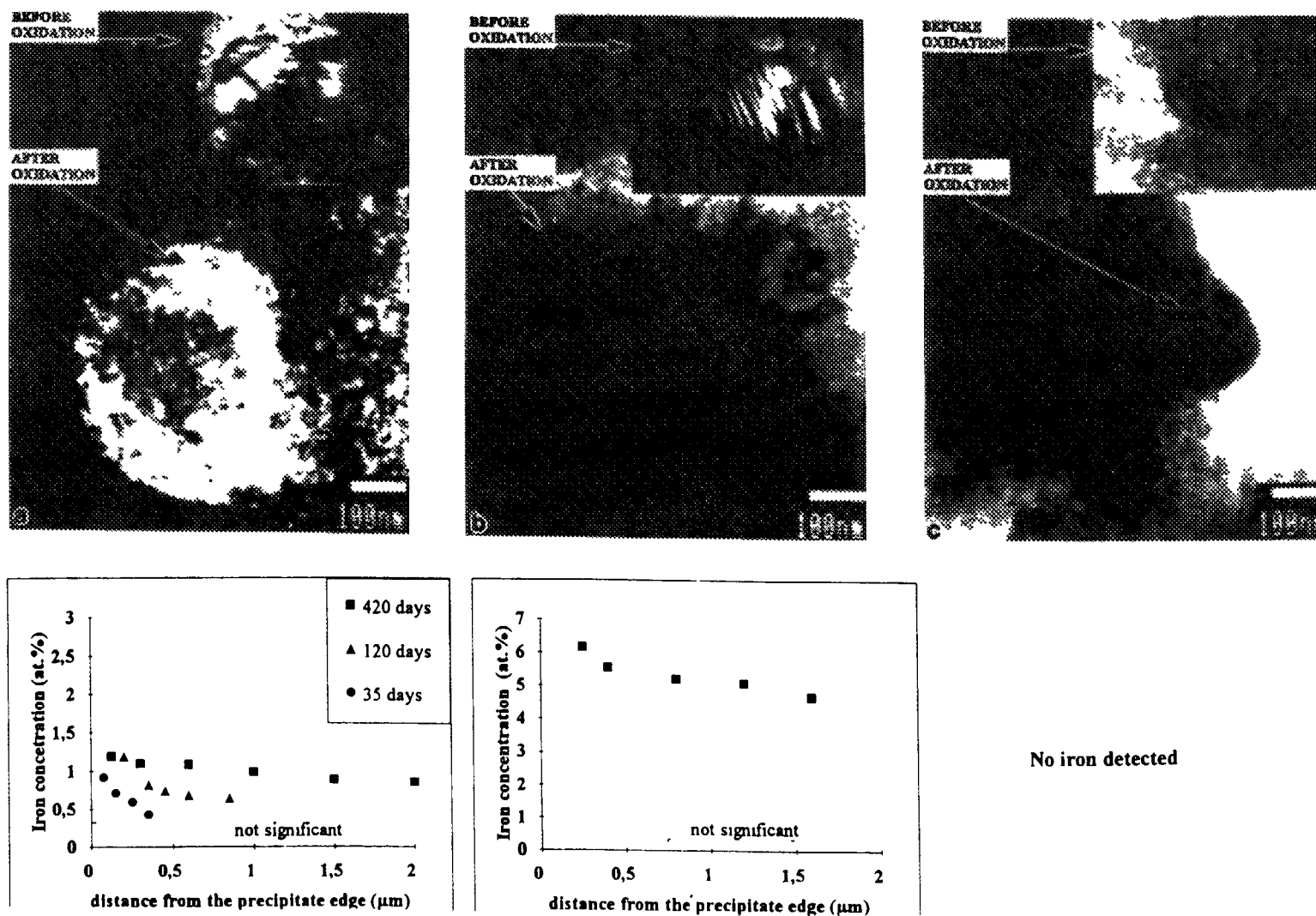


FIG 8.4. Incorporation of intermetallic precipitates in the zirconia layer for 1, 2 and 3 PWR cycles

- The corroded cladding may be considered as a composite material for which any dimensional change in the metallic part (cladding growth) will induce tensile stresses in the outer oxide layer.
- On a microscopic scale, as the growth of Zr alloys is the result of individual grain geometry changes (shrinkage in  $\langle c \rangle$  direction), grain to grain strain incompatibilities will induce high tensile stresses in some specifically oriented grains. According to the various models of growth kinetics, stresses have been computed up to values of 25 MPa [385].

The effect of tensile stresses upon corrosion kinetics has been studied in a limited number of cases [386] and no effect was reported. In the case of a very high Li content of the coolant, it was found that the corrosion rates were increased at 350°C under hoop stresses of 66 MPa, but this did not occur in steam and it was concluded that the higher corrosion rate was due to the high H pick-up and to the high concentration of hydrides near the metal-oxide interface in Li rich water [387]. Changes in irradiation conditions may lead to a renewed interest in this area, since enhanced corrosion kinetics could be expected from these effects.

### 8. 1. 3. 3. Second phase precipitate microstructure

#### 8. 1. 3. 3. 1. Types of Precipitates

The types of precipitates usually present in Zr cladding are described in detail in section 2. 2. and are briefly summarised below:

Due to the very fine scale of Zr-alloy microstructures, the second phase particles have been analysed in detail only recently [388-391]. A general review of second phase particles was performed by Charquet [9]. Table 8.1, taken from this review, gives a list of these secondary phases. For Zircaloy-4, after a standard heat treatment (stress relieved or recrystallised) the most common precipitate is the Laves phase  $\text{ZrCr}_2$  in which some Fe is substituted for Cr. The Fe/Cr ratio is dependent upon the temperature of the final heat treatment and is usually found to be close to 2. These precipitates usually have a hexagonal crystal structure but an fcc structure has been reported after fast cooling rates. A typical appearance of such a precipitate in recrystallised Zircaloy-4 is shown in Figure 2.3. The orthorhombic  $\text{Zr}_3\text{Fe}$  phase can be observed at the inter-plate boundaries of the original beta structure, for high Fe/Cr ratios after a beta quench heat treatment [392] or at equilibrium for very low Sn alloys of high Fe content [378].

In Zircaloy-2, the main types of precipitates are variations around the tetragonal  $\text{Zr}_2\text{Ni}$  and hexagonal  $\text{ZrCr}_2$  phases. In these alloys the Fe/Cr ratio is usually below 1. All these precipitates for Zircaloy-2 and -4 have been listed in detail in a review in connection with the corrosion behaviour [393]. Other impurity-induced precipitates include  $\text{ZrC}$ ,  $\text{Zr}_3\text{Si}$ ,  $\text{ZrSi}_2$ ,  $\text{ZrP}$  and  $\text{Zr}_3\text{P}$  [9]. There are also reported observations of mixed precipitates containing Si and Fe/Ni.

In the case of the alloy E635 (Zr-1%Sn-1%Nb-0.4%Fe) developed in Russia, the precipitates have been analyzed in detail using extraction replicas [286]. It has been found that, after an anneal at 580-590°C, the second phase particles are mainly hexagonal  $\text{Zr}(\text{Nb}, \text{Fe})_2$  with a lower density of orthorhombic  $(\text{Zr}, \text{Nb})_3\text{Fe}$  or tetragonal  $\text{Zr}(\text{Nb}, \text{Fe})_2$ . Thus the chemical behaviour of Nb is rather variable as it can substitute for either Zr or Fe.

For zirconium-niobium alloys, the solubility limit of Nb in Zr is about 0.6 wt% at 500°C but high temperatures lead to the complete dissolution of Nb in the stabilised beta phase and, depending on the thermal treatment, either "single phase" or "two phase" alloys can be obtained for a Nb content >1.5 wt%. Thermal treatments in the  $\alpha+\beta$  region will lead to a more complex structure, since the Nb rich  $\beta$ -Zr phase may decompose into  $\alpha'+\omega$  during the cooling process.

Table 8.1. Precipitates found in industrial Zr alloys. References refer to the original Table in Reference [9]

(A) PRECIPITATES IN ZIRCALOY-2 BASED ON ALLOYING ELEMENTS  
Sn 1.2-1.7%, Fe 0.07-0.20%, Cr 0.05-0.15%, Ni 0.03-0.08%

Methods	Heat Treatments	Precipitates		References
		Lattice	Composition	
EM	Alpha Anneal		Fe 5 - 9 % Cr 0 - 2 % Ni 4 - 9 % Sn 1 - 5 % Zr	(1) OSTBERG
TEM (TF) EDXA	600° C - 4 h	bct a = 0.65 nm c = 0.55 nm	Zr, Ni, Fe	(2) VITIKAINEN
TEM (T.F.)	800° C - 2 h	hex ZrCr <sub>2</sub> lattice: a = 0.501 nm c = 0.822 nm fcc ZrCr <sub>2</sub> lattice: a = 0.719 nm		(3) KRASEVEC
TEM STEM (T.F. and E)	700° C - 2 h	hex ZrCr <sub>2</sub> lattice: a = 0.51 nm c = 0.81 nm tetragonal Zr <sub>2</sub> Ni a = 0.659 nm c = 0.55 nm	Zr Cr 1,1 Fe 0,9 Zr <sub>2</sub> Ni <sub>0.4</sub> Fe <sub>0.6</sub>	(4) CHEMELLE
TEM (E) EDXA	Beta quench + 750° C - 7 h	hex	Zr Cr <sub>1,3</sub> Fe 0.7	(5) VERSACI
SEM-TEM EDXA	580° C - 2.5 h	hex ZrCr <sub>2</sub> lattice: a = 0.508 nm c = 0.828 nm (Sn Ni) compounds	Zr Cr <sub>1</sub> Fe <sub>1</sub>	(6) KUVAE
	Beta Quench	fcc Zr Cr <sub>2</sub> lattice: a = 0.721 nm orthorhombic a = 0.745 b = 0.582 c = 0.516 hex a = 0.846 nm c = 0.578 nm	Zr Cr <sub>1</sub> Fe <sub>1</sub> Zr Sn Zr <sub>5</sub> Sn <sub>3</sub> Sn <sub>3</sub> Al <sub>2</sub> Al	

(B) PRECIPITATES IN ZIRCALOY-4 BASED ON ALLOYING ELEMENTS  
Sn 1.2-1.7%, Fe 0.18-0.24%, Cr 0.07-0.13%

Methods	Heat Treatments	Precipitates		References
		Lattice	Composition	
TEM (TF) EDXA	800° C - 3 h	Hex ZrCr <sub>2</sub> lattice: a = 0.5079 nm c = 0.8279 nm	Zr Cr 0.6 Fe 1.4	(7) VANDERSANDE
TEM (TF)	Beta quench + 700° C - 6 h	Polytype Structure: hex ZrCr <sub>2</sub> structure fcc ZrCr <sub>2</sub> structure		(8) VERSACI
EM - SEM	800° C - 2.5 h 850° C 50 days		ZrCr <sub>0.7</sub> Fe <sub>1.1</sub> ZrCr 0.8 Fe 1.2	(9) MEMONI
SEM-EDXA (E and TF)	Many structures		(FeZr)-(FeCrSnZr) (FeSnZr)-FeCrZr	(10) CORTE
TEM (TF)	Slow cooling from beta	Zr (Cr Fe) <sub>2</sub> hex Zr (Cr Fe) <sub>2</sub> fcc		(11) MIQUET
TEM (TF)	Quench from 850° + α anneal		Zr <sub>3</sub> Fe	(12) GRANGE
TEM (S) EDXA	700° C - 6 h	Hex	Zr Cr 0.7 Fe 1.3	(5) VERSACI
SEM-EDXA TEM (TF and E)	600° C 2 h α + β quench	Hex Tetragonal fcc Zr Cr <sub>2</sub> phase tetragonal	Zr Cr 0.6 Fe 1.1 Sn metal	(6) KUVAE

(C) PRECIPITATES IN ZIRCALOYS BASED ON IMPURITIES ELEMENTS  
Usual specifications are C < 270 ppm, Si < 120 ppm, P < 20 ppm

Phases	ppm content	Lattice	References
ZrC	c > 140 - 160	fcc a = 0.47 nm	(13)(14)(15)
Zr <sub>3</sub> Si Zr <sub>2</sub> Si Si Metal	Si = 85 Si 26 - 265	Tetragonal a = 1.1 nm c = 0.55 nm a = 0.543 nm	(16) (15)
Zr <sub>3</sub> P Zr PO <sub>3</sub> -1	P < 50 to 151 P = 160	fcc a = 0.525 - 0.522 orthorhombic a = 1.67	(15)(17) (18)
Zr <sub>3</sub> P	P = 160	b = 2.78 c = 0.16 Tetragonal a = 1.08 c = 0.55	(18)

Although the role played by the precipitates in the behaviour of the fuel cladding is recognised (e.g. in the case of stress corrosion cracking [394] or corrosion behaviour [395]), it is clear that the effect of irradiation on the precipitates themselves has not been analysed in detail until recently. The first reports [396,397] showed that after irradiation an amorphous transformation can be observed in the second phase precipitates of Zircaloy-2 and -4. Depending on the irradiation temperature, the relative stability of the amorphous transformation can be expressed as follows. At low temperatures ( $<80^{\circ}\text{C}$ ) both  $\text{Zr}_2\text{Ni}$  and  $\text{ZrCr}_2$  types of precipitates become amorphous at low fluences (below  $5 \times 10^{24} \text{ n}\cdot\text{m}^{-2}$ ). At intermediate temperatures ( $250^{\circ}\text{C}$ ) a progressive amorphous transformation is observed in  $\text{ZrCr}_2$  precipitates (the transformation starts from the matrix - precipitate interface), while  $\text{Zr}_2\text{Ni}$  precipitates remain stable in their crystalline form [398]. Figure 8.5 shows the appearance of this amorphous transformation in a recrystallised Zircaloy-4 cladding tube irradiated up to 8 dpa in a power plant. It was found that this amorphous layer was growing from the precipitate-matrix interface at a constant rate, proportional to the neutron flux [355]. At the same time the amorphous zone was found to be depleted in Fe. The mechanism of this transformation, where linear time kinetics are found, can be explained by the contribution of ballistic mixing induced by the neutron flux [537]. The released iron is found in various places in the matrix, some of this Fe is trapped on the  $\langle\text{c}\rangle$  loops. The formation of very fine precipitates is a common observation after (or without) heat treatment in this irradiated structure [397]. The  $\text{Zr}_3\text{Fe}$  precipitates obtained in low Sn alloys with a very high Fe/Cr ratio were shown to remain very stable under irradiation [399].

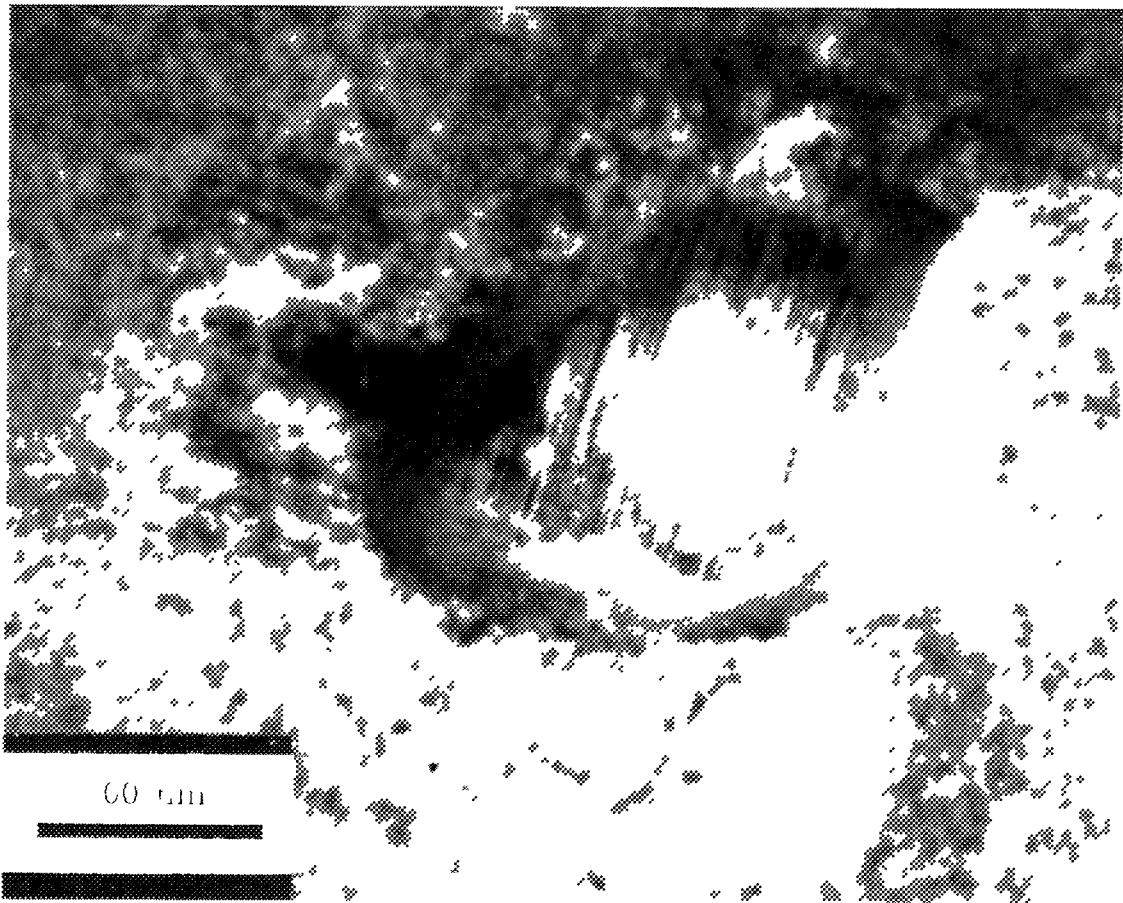
At high temperatures ( $T > 400^{\circ}\text{C}$ ) no amorphous transformation has been reported in any precipitates under the conditions of neutron irradiation, but release of Fe from the precipitates usually occurs, for the standard type of precipitates present before irradiation.

In the quaternary E635 alloy, the Zr, Nb, Fe - bearing precipitates dissolve and release Fe in the Zr matrix [286].

One corollary of the impact of temperature on the amorphous transformation of the precipitates under irradiation, is that during the history of the fuel rod, the build up of oxide causes an increase in cladding temperature. Thus, there are points in the cladding where the temperature will change significantly during irradiation: it may vary from low enough for amorphization at the beginning of irradiation to high enough to induce recrystallization at the end of irradiation. Indeed, as the oxide builds up and, as a consequence, the temperature increases, the limit for amorphous transformation is surpassed and the precipitates return to their initial crystalline form and recall the dissolved Fe back into them [400], if it has not precipitated.

Following these observations, detailed analyses of the evolution of precipitate microstructures under irradiation were performed following two main directions:

- Detailed analysis of the amorphous transformation with chemical analysis using a STEM equipped with EDAX [401,402]
  - Experimental work under simulated irradiation
- 1) In the first case, the observations lead to the conclusion that the amorphous transformation and precipitate re-resolution are, in many instances, not directly linked. The amorphous transformation is induced by the irradiation only, while the Fe, Cr and Ni re-resolution in the matrix is due to irradiation-enhanced diffusion and thermal activation which can be observed in the absence of the amorphous transformation. In the case of Fe, the fast diffusion behaviour of this species should be noted. It has been observed that the release of Fe from the amorphous precipitates occurs early in the amorphous transformation and is usually linked with the occurrence of  $\langle\text{c}\rangle$  type dislocation loops. Both phenomena are connected to a sharp increase in irradiation growth rate. A link between these observations has been proposed [401]: the loops should be vacancy type loops, with a Burgers' vector  $1/6\langle 2023 \rangle$ , located in the basal plane. The nucleation and growth of these



*FIG 8 5 Amorphous transformation of a  $Zr(Fe, Cr)_2$  precipitate after irradiation in a power reactor to 8 dpa*

loops are connected to high concentrations of interstitial impurities such as C, O, Fe or Cr. Therefore, the re-solution of the alloying elements of the precipitates under irradiation increases the development of  $\langle c \rangle$  type dislocation loops and the collateral accelerated growth. A recent experiment has been performed with recrystallised Zircaloy-4 doped, by ion implantation, with Fe to a supersaturated solid solution. Subsequent high voltage electron irradiation has been performed to induce irradiation damage. It has been shown that the excess of free Fe promotes the formation of  $\langle c \rangle$  loops and that the Fe segregates at the stacking faults corresponding to those loops, by a kind of Suzuki effect [381].

- ii) For a better understanding of the mechanisms involved, simulated irradiations have been performed using high voltage electron microscopes or heavy ion accelerators [398,403,404]. It has been shown that amorphous precipitates can be obtained (at much higher irradiation damage rates) in Zircaloy-2 and -4 without any composition change. These observations have led to the conclusion that the amorphous transformation is not induced by the composition change due to a possible irradiation-induced diffusion of alloying elements, but to the high density of point defects induced by neutron damage. This stored energy gives the driving force for a phase transformation from crystalline to amorphous. The chemical potentials of the alloying elements in the amorphous precipitates are then no longer equal to those in the matrix and re-solution is necessary for a return to chemical equilibrium [405]. The final situation may be a complete re-solution of the alloying elements of the initial precipitates in the matrix [402].

In the case of zirconium-niobium alloys, recent work [12] shows that both the  $\alpha$  and the  $\beta$ -Zr phases appear to be unstable. Some precipitation of  $\beta$ -Nb is observed in the  $\alpha$  phase and also a decomposition of the  $\beta$ -Zr filaments is reported. However, the Zr-Nb alloys seem to have a microstructure more stable under irradiation than the Zircalloys, as the irradiation induced transformation is observed at a much higher fluence.

In the zirconia layer the effect of irradiation would be very difficult to analyse. Recent observations on the microstructure of the oxide layer after corrosion testing without irradiation lead to the conclusion that, during corrosion, the chromium tends to leave the precipitates and also that the precipitates may transform to an amorphous structure once the oxide layer has grown thick enough [406].

The oxide grown in reactor has been investigated only in the last few years using STEM in hot laboratories and, up to now, very limited understanding is available. It is found that in general the grain size of the zirconia grown under irradiation is smaller and that there is a much lower tendency to develop epitaxy on the former metallic Zr grains [407]. In addition, the oxide layer formed in reactor is less stable and minor thermal treatments lead to its recrystallization. The tendency for increased stability due to Fe doping described above may be due to the irradiation only indirectly. The fast neutron flux induces this doping, but when oxidation occurs later, no Fe remains available in the precipitates and it was found that the surrounding zirconia had no tendency to transform to the tetragonal phase under irradiation [370].

#### 8.1.3.3.3 Impact upon corrosion kinetics

The crystalline-to-amorphous transformation of these precipitates, and any changes in microstructure under irradiation, have important impacts upon the mechanisms of zirconium alloy corrosion by the coolant. The exact mechanism of precipitate incorporation by the growing oxidation layer under irradiation is currently being studied in detail and the exact location and chemical state of Fe, Cr, Ni or Nb in the ZrO<sub>2</sub> is subject to ongoing investigations. A change in the detail of these mechanisms is expected due to the change from crystalline to amorphous or other irradiation-induced changes in microstructure.

During the amorphous transformation a strain field develops around the precipitates due to their change in density. The role played by the induced stress field remains to be analysed, but due to the mismatch in the lattices between Zr and ZrO<sub>2</sub> and the related stress state of the Zr-ZrO<sub>2</sub> interface, a significant effect is expected. If a change in the size and composition of the precipitates alters the corrosion kinetics, as is observed for unirradiated materials, it is expected that the changes induced by irradiation on the microstructure may have a similar effect. In the same way, changes in the matrix composition due to re-solution or irradiation-induced precipitation may also be of importance. In addition, interaction of the zirconia with the coolant leads to a change in structure and a transition from tetragonal to monoclinic is obtained after several days in a static autoclave [99]. Attempts to obtain a basic understanding of all these effects are strongly recommended.

#### 8.1.3.3.4 Oxidation without irradiation of irradiated material

If prolonged irradiation causes dissolution of small precipitates and loss of Fe preferentially over Cr from larger precipitates (with amorphization of the residual precipitates [355,372,408,409]), then highly irradiated cladding may have a different intrinsic corrosion resistance to that of as-received cladding. Since in-reactor corrosion rates are always compared with laboratory results on as-received material, any differences observed cannot be ascribed to a direct instantaneous effect of irradiation, but may incorporate effects resulting from the redistribution of the alloying elements by irradiation. This concern has yet to be addressed by post-irradiation laboratory testing of highly irradiated material. Early results showing no post-irradiation effect on the corrosion of irradiated, but unoxidized, Zircaloy specimens were based on lightly irradiated material, not irradiated highly enough to cause precipitate amorphization and dissolution [410], nor was the corrosion testing

performed on oxide layers thick enough to see a strong effect. Post-irradiation corrosion of samples from irradiated LWR cladding [320] showed an increasing duration for the memory-effect with increasing oxide thickness formed under irradiation (Figure 8.6). Only the highest irradiated sample did not return to the expected out-reactor rate after long post-irradiation exposures, and the remaining increment over the expected rate for an unirradiated specimen may be the result of changes to the precipitate structure in the matrix.

In early experiments, tests were performed on material irradiated with heavy ions to induce the amorphous transformation of the precipitates [43,411]. It was found that increasing corrosion rates were obtained if the corrosion tests were performed for a time long enough to pass the transition. A twofold increase was easily found.

In addition, the effect of microstructural changes, induced by irradiation, on the corrosion behaviour is clearly illustrated by the tests performed on material irradiated in power reactors (cladding or coupons) from which the oxide was removed by machining or etching and tested in autoclaves without irradiation. Several experiments have been performed with that aim [370,392,411]. For short corrosion tests, i.e. before the transition, no major changes between irradiated and unirradiated materials are reported. But a very noticeable change is seen for long corrosion tests. It is found that indeed an irradiated Zr alloy has a much higher corrosion rate than the same unirradiated material. The increase in uniform corrosion rates was found to be roughly proportional to the fluence, reaching a maximum value of almost three for an irradiation dose of 10

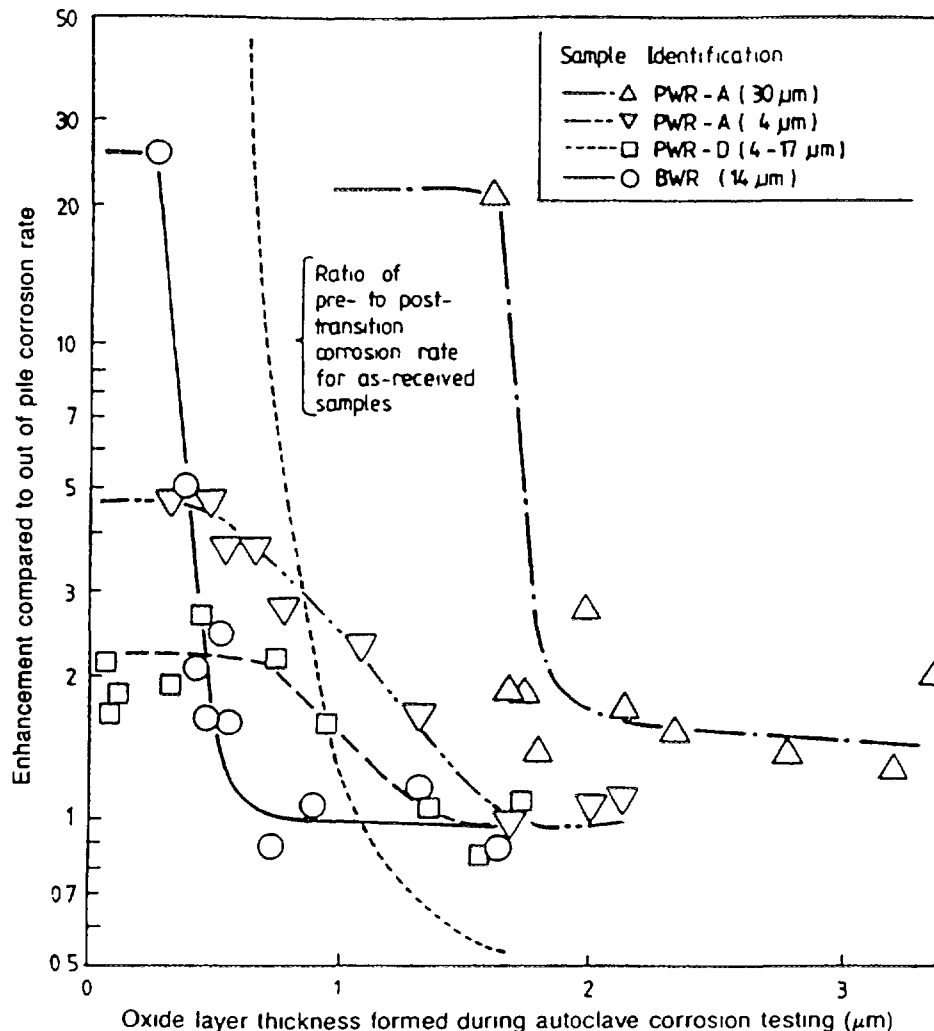


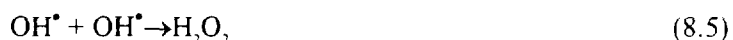
FIG 8.6 Corrosion enhancement during post-irradiation autoclave testing [320]

$\text{n}\cdot\text{m}^{-2}$ . This enhanced corrosion rate after irradiation is presented in Figure 8.7. However, in the case of nodular corrosion, the tendency for nodule formation was drastically reduced in tests performed in steam at 793 K. However the exact reason is far from being understood and may not only be the irradiation damage: some effects of the former oxidation may remain and, for instance, the hydrogen content may, in part, be responsible for this high corrosion rate. Indeed the dissolved hydrogen cannot be removed by machining as is the case for the oxide.

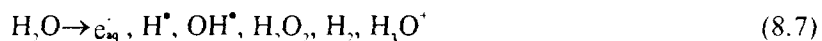
## 8. 2. RADIATION CHEMISTRY

### 8. 2. 1. Radiolysis in the bulk water

When water molecules are irradiated with ionising radiation, the ionising particle interacts intermittently with the molecules along its pathway and produces ionised and excited water molecules. The electron ejected in the ionisation process loses its energy by further ionisation and excitation processes of the water molecules, becoming thermalized and yielding a hydrated electron if it escapes the geminate recombination process. On the other hand, excited water molecules may dissociate to yield radicals, though there has been no explicit evidence to show that the excited water molecules play an important role. Overall, this leads to the formation of small spherical domains called "spurs" along the pathway of ionising species where radicals and ionic species are distributed in locally high concentrations. This situation is illustrated in Figure 8.8. The size of the spurs is inferred to be mostly 1-2 nm. The active species diffuse and partly react with each other to give some molecular and radical products as shown below.



Thus, the initial process of water radiolysis is expressed for  $\gamma$ -rays or high energy electrons by:



as a result of the intra-spur reactions. The G-value, which is usually used in the field of radiation chemistry to give the yield of a radiolysis product, is defined as the number of species produced or consumed per 100 eV of radiation energy absorbed by the medium. In the case of water radiolysis the yields of the primary species shown in equation (8.7) are normally given as primary G-values, defined as the G-values at the time when the intra-spur reactions are completed. The primary G-values for water radiolysis at ambient temperatures by  $\gamma$ -rays or high energy electrons have been measured by many workers and are well established on the basis of the large data base [412].

On the other hand, when water molecules are irradiated with neutrons in nuclear reactors, the neutrons lose their energy mainly by their elastic scattering on hydrogen atoms to yield recoiled protons. The recoiled protons lose their energy again by ionisation and excitation of the water molecules. However, the ranges of the recoiled protons are very short in water (compared with either high energy electrons or  $\gamma$ -rays) because of their larger cross-section for interaction. For instance, a 2



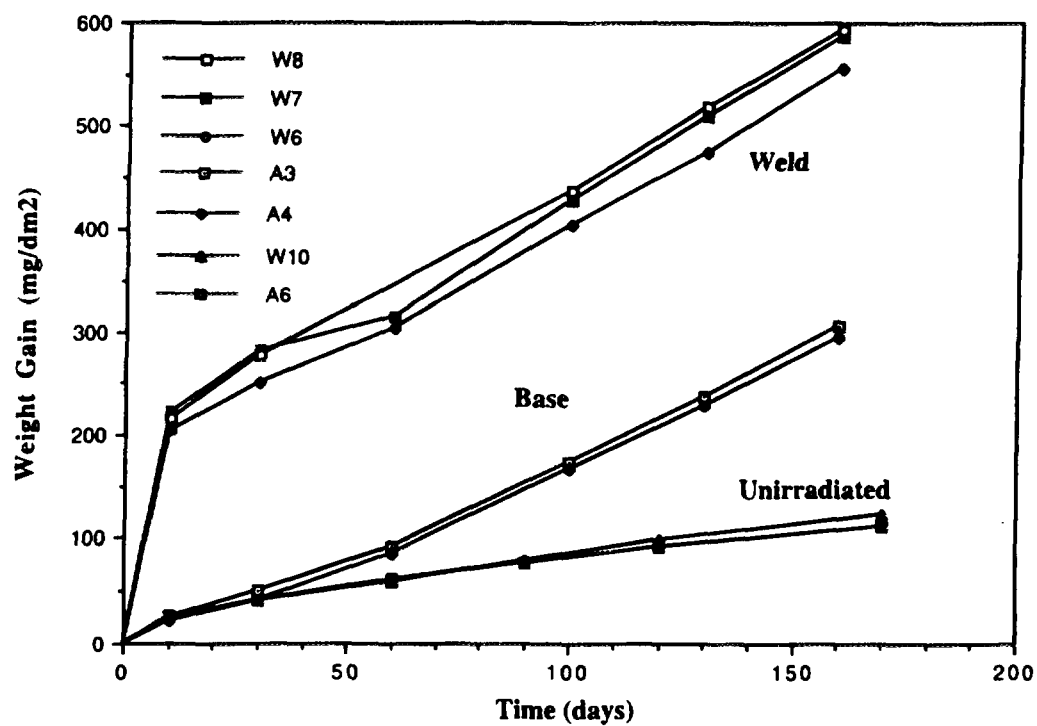


FIG. 8. 7. Accelerated corrosion of Zr alloys after irradiation in a power reactor and machining for removal of the oxide grown during irradiation [392].

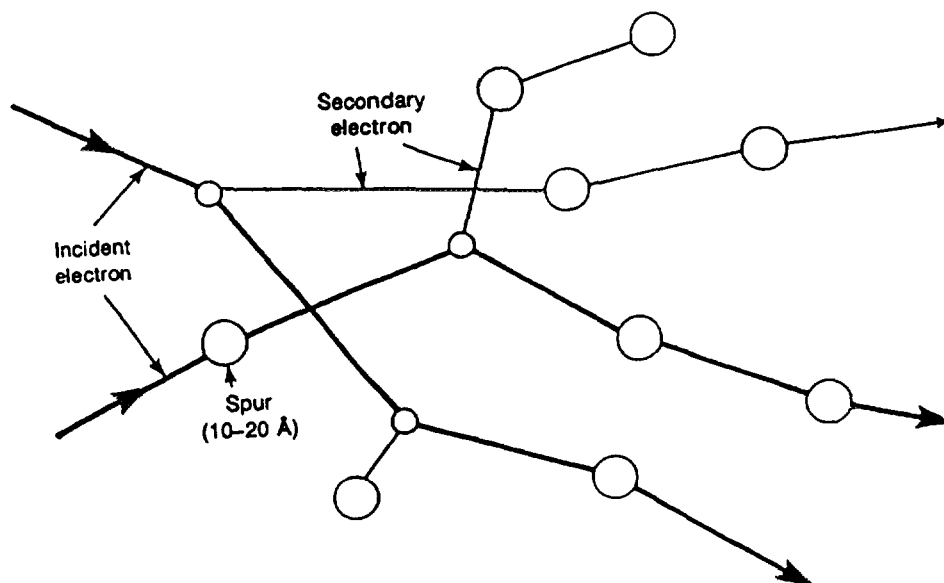


FIG. 8.8. Spur formation by high energy electrons.

MeV proton has a range of only 70  $\mu\text{m}$  in water when compared with the 1 cm range of a 2 MeV electron. In addition fast neutron G-values are not the same for light and heavy water since the energy of a fast neutron transferred to a hydrogen or a deuterium atom differs by a factor of two and since the secondary damages are also different.

High energy heavy particles are usually called "high LET (linear energy transfer) radiation", since they have larger deposition rates of energy along their tracks. It is known that the G-values of the primary products are greatly affected by the LET of the radiation, and this phenomenon is called the "LET effect".

In the case of high LET particle irradiation, the spurs produced are formed very near to each other, leading to the formation of cylindrical spurs or tracks. Consequently, the contribution of the intra-spur reactions is larger for high LET radiation. Therefore, the yields of the radical species such as  $e_{aq}^-$ ,  $H^\bullet$  and  $OH^\bullet$  are relatively higher for low LET radiation, while the yields of the molecular products increase for high LET radiation. The primary G-value data available for fast neutrons are not so abundant at present, and, hence, the reliability of the data is lower than that for  $\gamma$ -rays.

In Table 8.2 are shown the G-values of the primary water radiolysis products by  $\gamma$ -rays at ambient temperatures in comparison with those for radiolysis by fast neutrons from nuclear fissions.

Table 8.2  $\beta$ ,  $\gamma$  and neutron G-values at ambient temperature

Radiation Type	G values						
	$e_{aq}^-$	$H_2O^\bullet$	$H_2O_2$	OH	$HO_2$	H	$H_2$
$\beta$ , $\gamma$	2.7	2.7	0.72	2.7	0	0.55	0.45
fast neutrons	0.93	0.93	0.99	1.09	0.04	0.50	0.88

in reactors. It is to be noted that the G-values for fast neutrons depend, in principle, on the energy spectrum of the fast neutrons.

A material balance consideration gives the following relation for low LET radiation,

$$G(-H_2O) = 2G(H_2) + G(H^\bullet) + G(e_{aq}^-) \rightarrow 2G(H_2O) + G(OH^\bullet) \quad (8.8)$$

which gives  $G(-H_2O) = 4.2$  at ambient temperatures on the basis of the values in Table 8.2.

There has been some controversy over the temperature dependence of these primary G-values for water radiolysis. W. G. Burns et al. [413,414] reported a marked difference between the G-values at ambient temperatures and at high temperatures of 300 to 400°C, indicating decreased yields for  $e_{aq}^-$  and  $H_2O$ ,  $G(e_{aq}^-) = 0.4$  and  $G(H_2O) = 0$ , and increased yields for  $OH^\bullet$  and  $H_2$ ,  $G(OH^\bullet) = 4.7$  and  $G(H_2) = 2.0$ . Extensive work has been carried out to measure the G-values of the primary products in the high temperature radiolysis of water, and the results obtained are summarised in Table 8.3. The values reported by Burns, especially the low yield for  $e_{aq}^-$ , were inconsistent with the data reported by other workers [408,409,415-419]. Due to the lack of a consistent set of G-values available for the

primary species at high temperature, careful analytical work has been undertaken using pulse radiolysis in a pressurised vessel. The early experimental results obtained indicate a significant increase in  $G(e_{aq}^-)$  and  $G(OH^\bullet)$  with increasing temperature, but some uncertainty still remains with  $G(H^\bullet)$  and  $G(H_2O_2)$  [420]. This tendency was further confirmed and the G-values obtained are consistent and confirm the increase of  $G(OH^\bullet)$  and  $G(e_{aq}^-)$  with temperature. These value are plotted in Figure 8 9 for  $OH^\bullet$ ,  $e_{aq}^-$ ,  $H_2$ ,  $H^\bullet$  and  $H_2O_2$  in the temperature range of 20 to 300°C [421]

Table 8.3 Summary of the primary G-values measured at temperature.

Systems	pH	Observed values at 200°C	References	Observed values at 300°C [421]
(1) Pulse Radiolysis				
pure water	neutral	$G_{e_{aq}^-} \approx 3.5$	[415]	$G_{e_{aq}^-} \approx 3.2$
$Cd^{2+}$	nearly neutral	$G_{e_{aq}^-} \approx 3.5$	[415]	
benzonitrile (EtOH)	neutral	$G_{e_{aq}^-} \approx 3.4$	[416]	
methylviologen (t-BuOH)	nearly neutral	$G_{e_{aq}^-} \approx 3.4$	[419]	
H	12	$G_{e_{aq}^-} \approx 3.5$	[409]	
$HCO_2^\bullet$ ( $O_2$ -saturated)	4.4-9.2	$G_{e_{aq}^-} \approx G_{H_2} \approx 3.4$	[418]	
$HCO_2^\bullet$ ( $O_2$ -saturated)	2	$G_{e_{aq}^-} \approx G_{H_2} \approx 2.7$	[418]	
(2) Scavengers				
Fricke	strongly acidic	$G_{e_{aq}^-} + G_{H_2} \approx 3.9$	[417]	
Fricke	strongly acidic	$G_{H_2} + G_{e_{aq}^-} \approx 4.95$	[536]	
KBr	neutral	$G_{H_2} \approx 0.44$	[536]	$G_{H_2} \approx 0.3$
KNO	nearly neutral	$G_{H_2} \approx 0.46$	[420]	$G_{H_2} \approx 0.61$

W. G. Burns et al. also reported [412] that the LET effect in water radiolysis disappears at high temperature and the primary yields by fast neutrons are the same as those by  $\gamma$ -rays at high temperature. A high temperature experiment of fast neutron irradiation in acidic solutions [422], however, seems to show that a LET effect still exists at 200 to 250°C. More data are required in relation to the high temperature G-values of the primary products, especially for neutron irradiation.

The primary products shown in equation (8.7) react with each other in the bulk of the water when the water contains no solutes which are reactive with those products. There are many possible reactions involved, as shown in Table 8.4. The rate constants of all these reactions at ambient temperatures are well established, based on the abundant data from pulsed radiolysis experiments. The situation, however, is very similar to the case of the high temperature G-values, and there have been very limited data available for the rate constants at high temperatures. The consequences are important for the ability to control the effect of the radiolytic species on the corrosion of the cladding and on the wall of the pressure vessel. As discussed in [423], one has to consider the effect of temperature on both the G-values and the rate constants for the recombinations. Hence, an empirical evaluation is usually made by estimating the high temperature rate constants of the reactions in the absence of experimental data [151,424]. These experimental and evaluated values are compared in Table 8.4. Recent work [425] has been done with the purpose of analysing the effect of temperature on these rate constants. It has been shown that the rate constants cannot be simply described by an

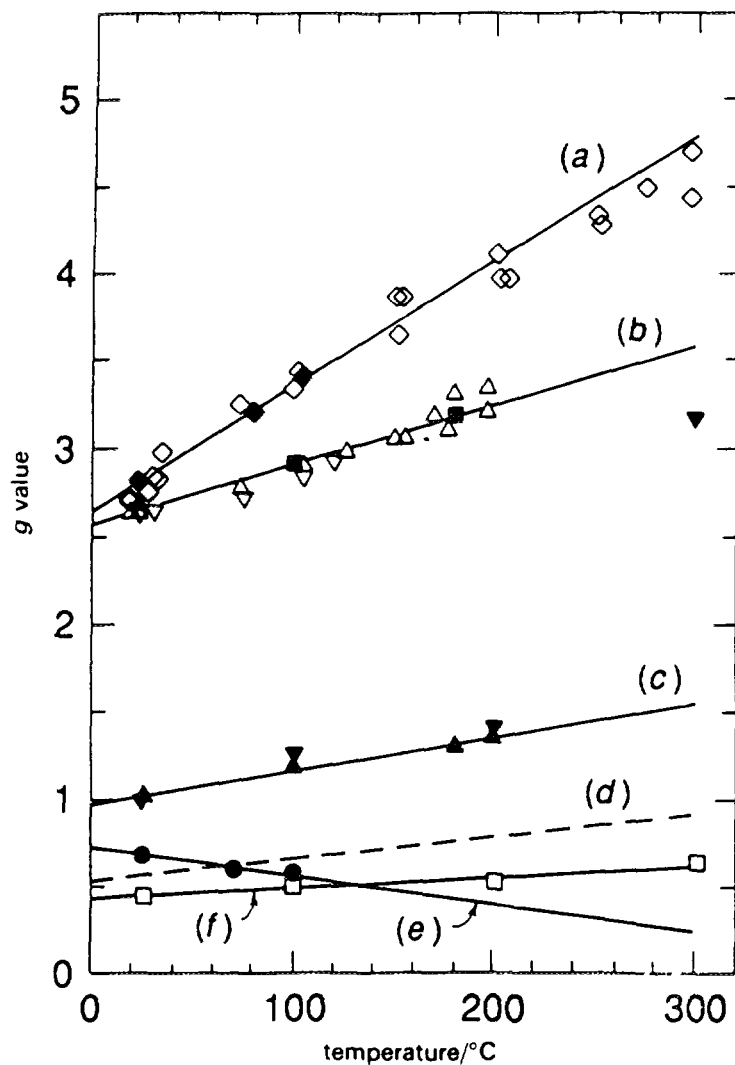


FIG 8.9 G-values for primary species as a function of temperature (a)= $g(\text{OH})$ , (b)= $g(e_{aq})$ , (c)= $g(\text{H}_2) + g(\text{H})$ , (e)= $g(\text{H}_2\text{O}_2)$ , (f)= $g(\text{H}_2)$ , (d)=calculated  $g(\text{H})$ , after Elliot [421]

Arrhenius equation, but correspond to the contribution of two independent processes, one linked with the diffusion of the reacting species and the second to the reaction rate constant. The net balance is a Noyes type equation:

$$1/k_{\text{obs}} = 1/k_{\text{diff}} + 1/k_{\text{react}}$$

The diffusion controlled term being described by a Smoluchowski equation

$$k_{\text{diff}} = 4\pi(r_A + r_B)(D_A + D_B)$$

where

$r_A$ ,  $r_B$  are the radii of the reactant species;  
 $D_A$ ,  $D_B$  are their diffusion coefficients;  
 and the rate term has a classical Arrhenius form

$$k_{\text{react}} = A \exp(-E_{\text{act}}/RT)$$

The new values are given in the last column of Table 8.4. The changes are in most cases within an order of magnitude but induce significant differences in the computation of the radiolytic species concentrations.

As inferred from Table 8.4, the radiolysis process in bulk pure water (remote from surfaces) is rather complicated, with many competing reactions. Therefore, computer simulations [151,426-428] based on the G-values of the primary products and the rate constants have been used to analyse the process by solving a set of differential rate equations involving the chemical species shown in Table 8.4. The result of a typical calculation is shown for the radiolysis of pure water by  $\gamma$ -rays at high temperature in Figure 8.10. As seen from the figure, continuous irradiation brings the system to a steady state where all the species reach constant concentrations which are determined by the kinetic equilibria and depend on the dose rate.

In Figure 8.11 a calculated result is given showing the effect of a hydrogen addition to a radiolytic system. It is seen that the addition of hydrogen reduces markedly the steady state levels of oxidising species such as  $O_2$ ,  $OH^\bullet$ ,  $HO_2$ , and  $O_2^-$ . A higher concentration of hydrogen would be necessary to reduce the level of hydrogen peroxide significantly. The reduction of  $O_2$  and the other oxidising radicals is what is expected for hydrogen additions to the primary system of a PWR, and also for hydrogen water chemistry in a BWR. The situation, however, is rather complicated for radiolysis in nuclear reactors. One factor contributing to the complexity is the boiling of water in the reactor core, which is more vigorous in BWRs. The boiling of water in the core region forces the transfer of hydrogen and oxygen into the steam phase, and consequently, makes the hydrogen additions less effective for reducing radiolysis in the aqueous phase.

Another important factor is the effect of any impurities which are very reactive with the primary products of water radiolysis and affect the overall scheme of the reactions. In the case of the reactor coolants of LWRs which do not contain reactive additives, impurities at a very low level may cause a significant effect. One such impurity in relevant systems is considered to be copper or nickel ions released to the coolant by corrosion processes.

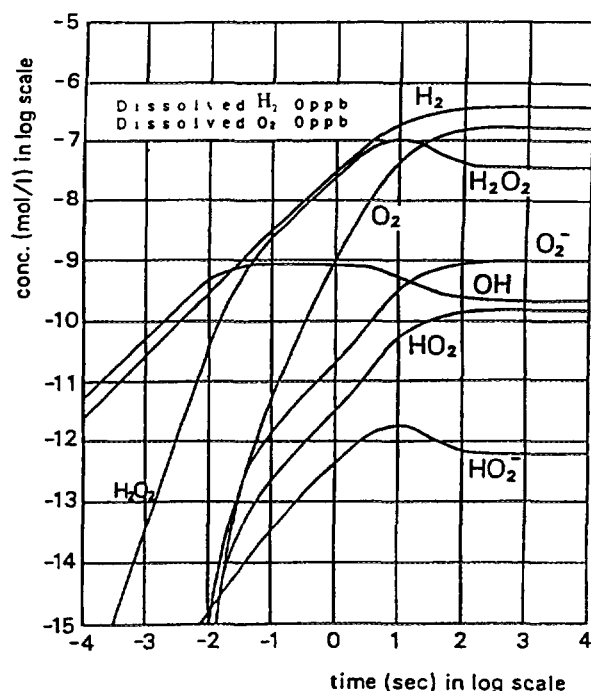


FIG 8.10 Typical result of a computer simulation for radiolysis of pure water at 250°C (G-values from Burns' data and dose rate  $4.5 \times 10^4$  R h<sup>-1</sup>)

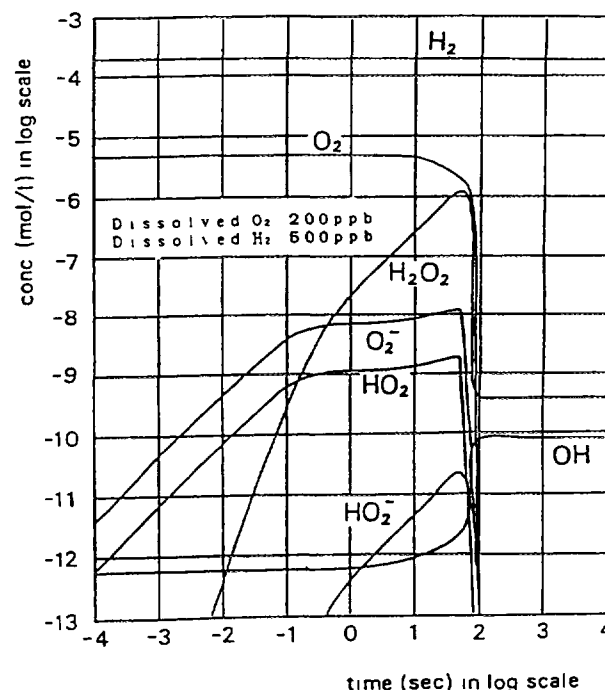


FIG 8 11 A computer simulation showing the effect of H addition for water radiolysis at 250°C. Same G-values and dose rate as for Fig 8 10

In addition, in PWRs, the control of the reactivity of the core by boric acid in solution in the primary water adds other sources of radiolysis the  $\alpha$  and L1 recoils from the  $^{10}\text{B}(n,\alpha)$  L1 reaction. For a typical PWR, the contribution is a maximum at the beginning of cycle, when the B concentration is between 1,000 and 2,000 ppm. Under those conditions, a 40% increase in radiolytic species concentration can be obtained [429].

### 8 2 2 Radiolysis near metal surfaces or in the pores surrounded by metal oxides

Water radiolysis near metal surfaces, or in small pores surrounded by metal oxides such as  $\text{ZrO}_2$ , may be different from that in the bulk water described in the previous section, being affected by the materials in contact with the water. The radiation energy absorbed by water inside the pores surrounded by metal oxides is larger than that absorbed by bulk water, because the flux of the back-scattered electrons (arising from substances with high atomic number) increases and contributes to the absorbed dose [430-432]. This effect will be more important in small pores than at metal-water interfaces, since the surface to volume (S/V) ratio is larger in the former. The extent of the increase in the absorbed dose depends on the geometry of the pores, the materials surrounding the pores, and the direction of the incident radiation. From early work, it may be inferred that an increase of up to 250% or more, relative to the absorbed dose in the bulk water, occurs when this surface effect is taken into account [430]. Thus, the local concentrations of the chemical species produced by radiation may be significantly higher in the pores than in the bulk.

Recent detailed computations have been performed on the local energy deposition rate at the water-zirconia interface. It was shown that, due to the large difference in electron density between those two media and to the contribution of photo-electrons from the dense medium, the energy deposition rate in water, in the vicinity of the interface, increased by a factor (a function of the energy of the photon) that could reach a value of 50, compared to the EDR induced by the same photon flux in the bulk of the water [433]. For a typical PWR gamma spectrum, the average value is only an increase in EDR by a factor of 2-4.

Table 8.4. Rate constants of reactions involved in water

Reaction	Rate constant at 25 °C dm <sup>3</sup> .mol <sup>-1</sup> .sec <sup>-1</sup>	Rate constant at 280 °C dm <sup>3</sup> .mol <sup>-1</sup> .sec <sup>-1</sup>
$e^- + H_2O = H^\bullet + OH^-$	1.6 E +1	1.65 E +2
$e^- + H^\bullet = H_2$	2.3 E +10	1.5 E +11
$e^- + OH^\bullet = OH^-$	3.0 E +10	4.05 E +11
$e^- + H_2O_2 = OH^\bullet + OH^-$	1.3 E +10	1.3 E +11
$2 H^\bullet = H_2$	2k = 1.0 E +10	1.6 E +11
$e^- + HO_2^\bullet = HO_2^-$	2.0 E +10	2.06 E +11
$e^- + O_2 = O_2^\bullet$	1.9 E +10	2.7 E +11
$2 H_2O + 2 e^- = H_2 + 2 OH^-$	2k = 5.0 E +9	3.0 E +7
$2 OH^\bullet = H_2O_2$	2k = 8.4 E +9	8.6 E +10
$OH^\bullet + H^\bullet = e^- + H_2O$	2.0 E +7	6.63 E +8
$H_2O + e^- + H^\bullet = H_2 + OH^-$	2.5 E +10	6.22 E +9
$H_2O + e^- + HO_2^\bullet = OH^\bullet + 2 OH^-$	3.5 E +9	8.7 E +8
$H^\bullet + OH^\bullet = H_2O$	2.0 E +10	6.0 E +11
$OH^\bullet + H_2 = H^\bullet + H_2O$	4.0 E +7	1.3 E +9
$H^\bullet + H_2O = OH^\bullet + H_2$	1.04 E -4	8.14 E +2
$H^\bullet + O_2 = HO_2^\bullet$	1.9 E +10	1.96 E +11
$H^\bullet + HO_2^\bullet = H_2O_2$	2.0 E +10	2.06 E +11
$H^\bullet + O_2 = HO_2^\bullet$	2.0 E +10	2.06 E +11
$H_2O + e^- + O_2 = HO_2^\bullet + OH^-$	1.3 E +10	1.04 E +10
$H^\bullet + H_2O_2 = OH^\bullet + H_2O$	9.0 E +7	1.2 E +9
$OH^\bullet + H_2O_2 = HO_2^\bullet + H_2O$	3.0 E +7	3.7 E +8
$OH^\bullet + HO_2^\bullet = O_2 + H_2O$	1.2 E +10	2.5 E +10
$OH^\bullet + H_2O_2 = HO_2^\bullet + H_2O$	1.8 E +8	5.97 E +9
$HO_2^\bullet + H_2O = OH^\bullet + H_2O_2$	5.7 E +5	1.89 E +7
$H^\bullet + O_2 = HO_2^\bullet$	5.0 E +10	5.16 E +11
$HO_2^\bullet = H^\bullet + O_2$	8.0 E +5	3.4 E +7
$HO_2^\bullet + O_2 = O_3 + HO_2^\bullet$	1.5 E +7	4.4 E +8
$2 H_2O + 2 O_2^\bullet = H_2O_2 + 2 OH^\bullet + O_2$	2k = 1.7 E +7	3.27 E +5
$2 HO_2^\bullet = H_2O_2 + O_2$	2k = 2.7 E +6	5.2 E +7
$H^\bullet + OH^\bullet = H_2O$	1.4 E +11	1.49 E +12
$H_2O = H^\bullet + OH^\bullet$	2.6 E -5	1.33 E -1
$OH^\bullet + O_2^\bullet = O_3 + OH^-$	1.2 E +10	7.7 E +10
$H_2O_2 = 2 OH^\bullet$ (first order, sec-1)	2.3 E -12	1.2 E -1

In this table the electrons and the protons are assumed to be solvated.

Another important factor will be the significant contributions of surface reactions to the kinetic scheme of the radiolytic reactions in the pores, or at the interface, where the S/V ratio is high. The importance of the surface reactions in systems with high S/V ratios has been pointed out by W. G. Burns et al. [434], who followed the corrosion reactions in sealed stainless steel containers, with an S/V ratio of 9.1 dm<sup>-1</sup>, under  $\gamma$ -ray irradiation by measuring the amounts of hydrogen and oxygen evolved. They observed larger radiation-induced accelerations of oxygen removal and of hydrogen formation in the presence of mild steel coupons in the containers, and interpreted these effects on the assumption that the radiolysis products, such as  $e_{aq}^-$ ,  $OH^\bullet$ ,  $HO_2^\bullet$  and  $H_2O_2$ , are removed on the surfaces at diffusionally limited rates. The detailed mechanism of the surface reactions involving the radiolysis products has not been established so far, but it may be possible that the surface reactions, rather than the bulk reactions, control the overall radiolysis process at interfaces, especially in pores with a high S/V ratio. Hence, any specific recombination capabilities of  $ZrO_2$  surfaces also needs to be considered.

Some species of radiolysis products are significantly oxidising and may be involved in the cathodic reactions which are expressed overall in equations (8.9)-(8.11).



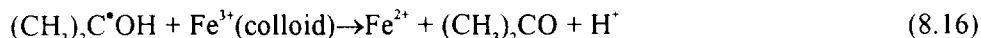
These cathodic reactions may take place under irradiation in addition to the usual ones expressed by equations (8.12) and (8.13). However, the relative importance of their contributions and the microscopic reaction mechanisms are not well known at the moment.



Henglein et al. [435] followed the interaction of  $OH^{\bullet}$  radicals with the platinum surfaces of a microelectrode by the pulsed radiolysis technique, and directly observed that  $OH^{\bullet}$  radicals react with the Pt surfaces following equation (8.14), finally yielding platinum oxide.



On the other hand,  $e_{aq}^{-}$  and  $H^{\bullet}$  are strongly reducing radicals, and are inferred to interact reductively with metal surfaces or metal oxides by analogy with other strongly reducing organic radicals. Colloidal  $Fe_2O_3$  was found by G. W. Buxton et al. [436] to be dissolved rapidly by the propan-2-ol radical, produced in aqueous solution by radiolysis through the one-electron reduction reaction shown by equation (8.16).



Henglein et al. [437,438] observed that reducing organic radicals such as the propan-2-ol radical transfer their electrons to colloidal particles of silver or gold as shown by equation (8.17).



and store electrons on them, which are finally discharged by the decomposition of water molecules, yielding hydrogen.

Hydrogen peroxide is one of the key species among the radiolysis products in nuclear reactor cores and is known to have a large effect on the corrosion of some materials. Currently, its behaviour in the coolant and in sampling systems has drawn attention, especially for BWRs in relation to hydrogen water chemistry, but is not well understood because of its instability at high temperatures. It is known that hydrogen peroxide decomposes catalytically on the surfaces of various types of materials at ambient temperatures. Various analytical studies [439-443] have shown that oxidised surfaces of stainless steels or Zircaloy catalytically enhance the decomposition of hydrogen peroxide at high temperature. It should be noted that hydrogen peroxide is not stable even in the bulk water at high temperatures and is considered to decompose homogeneously, probably yielding  $OH$  or  $O_2$  radicals.



However, production of OH<sup>\*</sup> radicals is in doubt since the reaction route for the catalytic decomposition of hydrogen peroxide on surfaces is believed [444] to be expressed by equation (8 18), giving molecular oxygen but not OH<sup>\*</sup> radicals, though no direct experimental evidence has yet been obtained



It is reported [439,440] that the catalytic hydrogen peroxide decomposition rate is proportional to the area of the surface in contact with the water, and that the surface decomposition predominates over the concomitant bulk decomposition at high temperatures in high S/V regions, such as within small diameter pipes and narrow channels or in the crevices and pores surrounded by metal oxides. This means that enhanced recombination rates of radiolytic species on ZrO<sub>2</sub> surfaces also needs to be considered and would significantly change the dynamic balance of the recombination of radio-chemical species

It is known that water adsorbed on some adsorbents, such as Zeolite or alkali halides, is effectively decomposed by radiation at ambient temperatures [445-447], and it is usually assumed that energy transfer from the adsorbents to the water molecules promotes the decomposition reactions. There are no data available on the radiolysis of water adsorbed on metal oxides at high temperatures. If the amount of water adsorbed on the surfaces is relatively much lower than the amount of the bulk water, it may not contribute significantly to the whole process

As already mentioned above, the radiolysis of water yields both oxidising and reducing species, including transient ones, and these species are considered to contribute in several ways, via the redox reactions, to the electrochemical processes related to the corrosion of the relevant materials, though the detailed mechanisms are not well understood. These processes are represented by changes in the electrochemical potentials of electrodes during irradiation. The total balance of the redox reactions determines the direction of the potential shift, and some additions, or the accumulation of specific species, may change the balance of the redox reactions. For instance, the corrosion potential of stainless steel shows a positive potential shift during  $\gamma$ -ray irradiation at high temperatures under normal water chemistry conditions in BWRs, but gives a negative one, for the same irradiation, under hydrogen water chemistry conditions as shown in Figure 8 12 [448]. This is considered to result from the fact that hydrogen additions convert the oxidising radiolysis products (including oxygen) to reducing species according to the following reactions which will be discussed in more detail later



### 8 2 3 "Thick oxide film effects"

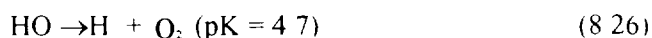
It has been realised [196,197] for more than twenty years that there exists a peculiar effect on the corrosion behaviour of Zr alloys in high temperature water under irradiation with low oxygen (PWR-like) conditions. This effect was initially explained by the "thick oxide film hypothesis" [449]. This hypothesis is based on in-reactor experiments on Zircaloy-2 specimens and may be summarised as follows. After the oxide layer on the Zircaloy surface reaches a threshold thickness, the subsequent corrosion rate of the Zircaloy is controlled by water radiolysis in oxide cracks and pores and is mainly independent of the water chemistry outside them [449]. Many, but not all, of these experiments were

performed in LiOH bearing environments without boric acid additions. There have been attempts to discount the experiments based on possible accelerating effects of LiOH. However, two of the key experiments were conducted in water dosed with  $\text{NH}_4\text{OH}$  [449, 528], with LiOH absent, so effects with LiOH cannot offer a valid explanation for the onset and propagation of the thick film phenomenon.

It has been claimed, frequently, that the radiation enhancement of Zircaloy corrosion in the aqueous phase arises from the synergistic interaction of radiation and water chemistry. It has been argued that in the early stages of Zircaloy corrosion an apparent acceleration by reactor radiation, is usually observed in oxygenated water, which is suppressed in the presence of excess hydrogen in the aqueous phase.

However, the formation of non-uniform ("nodular") oxide films in oxygenated water has made it difficult to compare true pre-transition rate constants for identical batches of Zircaloy under oxygenated and hydrogenated water conditions. Beyond a threshold oxide thickness Zircaloy specimens exposed to low-oxygen water corrode at accelerated rates under irradiation, as if they were immersed in oxygenated water. However, these early observations have not yet been reconsidered in the light of the possible effects of LiOH concentrated in the oxide film beyond a critical thickness, and the extent to which this might become trapped in thick porous oxides following a change in bulk water chemistry.

The radiolysis of water produces several types of primary species shown in equation (8.7) and described previously. Among these,  $\text{OH}^\bullet$  and  $\text{H}_2\text{O}_2$  are oxidising reagents like oxygen, one of the final products of high temperature water radiolysis, while  $e_{aq}^-$  and  $\text{H}^\bullet$  are strong reducing reagents. Approximately the same numbers of oxidising and reducing species are produced in the radiolysis of pure water. In oxygenated water  $e_{aq}^-$  and  $\text{H}^\bullet$  are converted very rapidly to  $\text{O}_2^-$  and  $\text{HO}_2^\bullet$ , respectively, which are weak oxidising reagents.



$\text{HO}^\bullet$  and  $\text{O}^\bullet$  are less reactive than  $\text{OH}^\bullet$  and have relatively longer lives.

The oxidising species produced by radiolysis may take part in the cathodic reactions in the aqueous corrosion processes of Zircaloy under irradiation, though the detailed mechanism of the cathodic reactions by transient species is not well understood and surface electrochemical reaction rates on Zircaloy surfaces are not known to be rate limiting under any conditions in water. Thus, this facilitation of the cathodic reactions might make a contribution to a synergistic interaction and acceleration by radiation in the Zircaloy corrosion under reactor conditions if there was any evidence for effects of surface reaction. There is, however, no evidence of the reversibility of the zirconium electrode with respect to these reactions to permit a conclusion on this point. Nor is there any evidence that surface electrochemical reactions are ever shown to be the rate controlling steps during the oxidation of Zr alloys to form a barrier oxide. Many observations on gaseous oxidation point to surface reactions not being rate determining. This point remains to be confirmed in the case of a dense medium like pressurised water.

On the other hand, when excess hydrogen is present the steady state concentration of the oxidising species such as  $\text{O}_2$ ,  $\text{OH}^\bullet$  or  $\text{O}^\bullet$  are markedly reduced under irradiation as already shown in Figure 8.11, while very limited changes are observed after short irradiation times, and may be higher for 10 to 100 sec (Fig 8.10). The most important reaction involved in a hydrogen-containing system

is reaction (8 19), converting the oxidising  $\text{OH}^\bullet$  to the reducing  $\text{H}^\bullet$ . In hydrogenated systems the consumption of  $\text{OH}^\bullet$ , a major reactant to  $\text{H}_2\text{O}$  and  $\text{e}_{aq}^-$ , by hydrogen makes the contribution of reactions (8 20) and (8 23) relatively more important, and reactions (8 19) through (8 23) result in back-reactions reforming water molecules reducing the final yields of the oxidising species. It has been widely accepted that the accelerating effects of radiation on Zircaloy corrosion are greatly reduced by hydrogen additions under PWR conditions, which is not the case in BWRs.

The detailed mechanism of the "thick oxide film" effect is not understood at the moment, and some possible mechanisms are discussed here. One hypothesis is that, when the thickness of the oxide layer is beyond a threshold value, the rate of supply of hydrogen into the pore through diffusion is insufficiently large to maintain the radiolytic suppression effect by hydrogen under irradiation (in the absence of corrosion hydrogen) and, therefore, that the cathodic reactions occurring at the bottom of the pore are facilitated because the radiolytic products escape reaction with hydrogen. Then, the corrosion rate of Zircaloy might be accelerated by this facilitation of the cathodic reactions, if the surface reaction were the rate controlling step. In order for this hypothetical mechanism to occur excess hydrogen in the cracks or pores has to be consumed by some mechanism. Hydrogen molecules are consumed by reaction (8 19) under irradiation to yield  $\text{H}^\bullet$  atoms if they are present in an excess amount beyond a threshold value. Therefore, only if it is assumed that most of the  $\text{H}^\bullet$  atoms produced are dissipated or consumed there (by some mechanism such as hydrogen pick-up by the metal), is it possible to show that when the oxide layers of Zircaloy have deep cracks or pores, the diffusion rates of hydrogen into the cracks or pores is not high enough to maintain a hydrogen concentration at the bottoms of the cracks or pores above the threshold value (see Appendix). However, this situation may not occur readily because the recombination reaction



of hydrogen atoms is fast enough to yield hydrogen molecules and the net consumption of hydrogen molecules is not so large.

Another possible mechanism for hydrogen consumption may be boiling of the water inside the cracks or pores. When Zircaloy has very thick oxide layers, it may restrict heat conduction and cause local boiling of water. If the boiling takes place inside the cracks or pores, this would lead to stripping of hydrogen molecules into the vapour phase and thereby reduce its concentration in the cracks or the pores [450]. Again the thick oxide layers may cause a restriction of hydrogen diffusion from the bulk water. However, this explanation cannot be applied to nodular corrosion in non-heat transfer surfaces such as channel boxes, and the only experimental evidence for a "thick film effect" was on unheated sheet specimens in an in-reactor loop.

However, it should be noted that, if the cathodic reaction (8 13) concomitantly occurs at the bottoms of the cracks or pores, then there exists excess hydrogen arising from the corrosion reactions of Zircaloy. This prevents the above sequence of reactions from occurring for long reaction times. In summary, the "thick oxide film" effect, if it has been correctly identified as such, would need to be a rather complicated phenomenon including surface reactions of chemical species produced by radiation. Such surface reactions are not otherwise known to affect Zircaloy corrosion in high temperature water.

In addition, specific consideration should be given to the fact that the computations described above assume the bulk recombination of the various radiolytic species. However, the roots of the pores of the thick oxide layer are sinks for the oxidising species and the list of chemical equations in Table 8 4 has to be extended with some surface reactions. More research work is necessary for the elucidation of the mechanism, and should take into account the fact that some key experiments were conducted with  $\text{LiOH}$  pH control while others were conducted with  $\text{NH}_4\text{OH}$  pH control. Therefore, concentration of  $\text{LiOH}$  in the oxide does not offer a defensible explanation.

#### 8 2 4 Localised corrosion and dissimilar metals

A number of phenomena with increased localised corrosion have been reported that are connected with the presence of dissimilar metals adjacent to Zr alloys. They appear mostly in boiling water conditions

- The appearance of “shadows” of the control blade handles in the nodular corrosion distribution on the adjacent fuel channels [451]
- The preferential formation of nodules on fuel cladding under the stainless steel spacer grids used in some fuel bundles. The same effect is not seen under zirconium alloy grids [144]
- The formation of ridges of thick oxide on the pressure tube adjacent to the stainless steel grids of the fuel cladding in SGHWR and RBMK reactors [452]
- The local spots of thick white oxide at points of contact with the Inconel springs in Zircaloy spacer grids [453]
- The thicker oxide on plena of segmented rods in the high flux region compared with the fuelled region of the same rod, or the higher corrosion rate of the Gd bearing fuel rods [150]
- The high corrosion rate of Zr alloys coupons under irradiation in front of platinum inserts and in the vicinity of Inconel strips [449]

Various analyses have been proposed for a general understanding of these phenomena. They are based upon either electrochemical or radiolysis phenomena. Since no definitive experiments exist to divide the two approaches, they will both be discussed

##### 8 2 4 1 Galvanic analysis

In general the extent of good electrical contact between the various components of the system is not known, since the degree of insulation provided by oxide films on the contacting surfaces is difficult to predict in the high radiation fields that are present. However, if we assume that oxide films become tolerably good conductors under these conditions, and that even high purity water has a reasonable conductivity in reactor (thought to be close to that of a pH 5 solution) then a galvanic effect becomes possible. The observations that can plausibly be ascribed to galvanic contact, combined with a short current path through the water, have already been noted in the introduction to this subsection

Taken together, these observations indicate a major effect of galvanic coupling on the corrosion rate, and sometimes on the hydrogen uptake rate alone [454], even though no actual measurements of potentials, or polarisation by stainless steel, have been made in-reactor. In BWRs where nodule nucleation may be occurring during the first one hundred days (or less) of in reactor exposure, the use of an autoclaved cladding surface may provide an initially oxidised surface that is less susceptible to local effects (e.g. of water chemistry) if the operating conditions depart significantly from the norm at the start of a reactor cycle. The abandoning of pre-autoclaving as a routine surface preparation may, therefore, leave fuel cladding more susceptible to water chemistry transients at the start of a cycle, until a normal oxide film has grown in-reactor. Oxide film resistivity measurements on oxidised Zircaloy 2 specimens [455] suggest that an average oxide thickness of  $\sim 1 \mu\text{m}$  must be reached before the intermetallics are oxidised enough to give a resistivity greater than  $10^6 \Omega \text{ cm}$ . While this thickness is close to that reached during a pre-autoclaving at  $400^\circ\text{C}$ , it would take  $>100$  days to reach the same oxide thickness on a freshly pickled surface at  $280^\circ\text{C}$  [59]. Thus susceptibility to nodular corrosion could last for a hundred days or more because of this much slower formation of the protective oxide at  $280^\circ\text{C}$  than at  $400^\circ\text{C}$  (the usual autoclaving temperature). Additional considerations, of electrochemical behaviour, are given in section 8 4 2

As described at the beginning of this section, the strong irradiation flux induces a change in water chemistry, with the presence of radiolytic oxidising species. This effect is more complex in the case of a reactive interface, like the water zirconia-interface where oxidising species can be trapped, and the energy deposition rate is increased due to the photoelectrons emitted by the metal. In the case of dissimilar metals, in addition, the irradiation flux is locally increased by an intense flux of short range  $\beta$  particles emitted by activated nuclei. A detailed analysis has been presented recently [456]. It was found that in all of the reported cases of local enhancement of corrosion rate under irradiation, it is possible to find in the vicinity an activatable species, the activation cross section and the  $\beta$  energy of which are high enough to induce a local energy deposition rate higher than the bulk EDR. For stainless steels, this process is effected through the activation of  $^{55}\text{Mn}$  leading to a  $\beta$  emission of most frequent energy 2.8 MeV. This explanation has been accepted as the major contribution for the formation of the "shadows" [451].

### 8 3 CRUD DEPOSITION AND HEAT TRANSFER EFFECTS

#### 8 3 1 PWR crud deposition

##### 8 3 1 1 Introduction

Deposits on the cladding of corrosion products (crud), mainly generated by the release of constitutive elements from all the steel surfaces of power reactors, increase the barrier to heat transfer. Consequently, extensive programs have been carried out in order to investigate the impact of crud deposition on the increase in the metal/oxide interface temperature, leading to an enhancement of the Zircaloy-4 waterside corrosion. The possible inclusion of mineral impurities (Cu, Ca, Mg, Al, Si) which decrease the thermal conductivity of the crud eventually aggravates the importance of this process, see Figure 8.13 [457,458]. In addition, crud deposition data from a large power reactor surveillance program, together with loop test data, have provided clear information concerning the appropriate chemistry control required in a PWR primary coolant (both Li/B chemistry and impurity control) to minimise crud deposition on the fuel.

A review of international practices and recommendations is available in a recent technical report from the IAEA [459] (see also section 6.4). The specifications for chemical control of the primary coolant are now limiting enough to avoid excessive deposition of crud in PWRs during normal operation. Thus, the chemical control of impurities in the primary water is nowadays no longer an operating problem, except in choosing optimum lithium levels now that many plants are moving to extended cycle operation. The potential consequences of any diminishing of attention paid to this control could lead to technical consequences of high enough concern that some details of crud deposition mechanisms and their consequences are presented in this section.

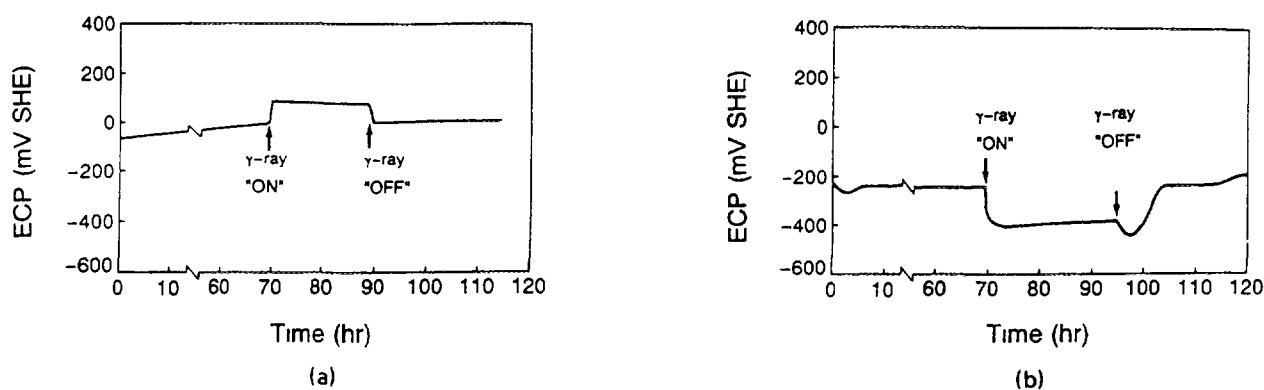


FIG. 8.12 Effect of  $\gamma$ -rays on ECP (a) under simulated normal BWR water chemistry (b) under simulated hydrogen water chemistry [448]

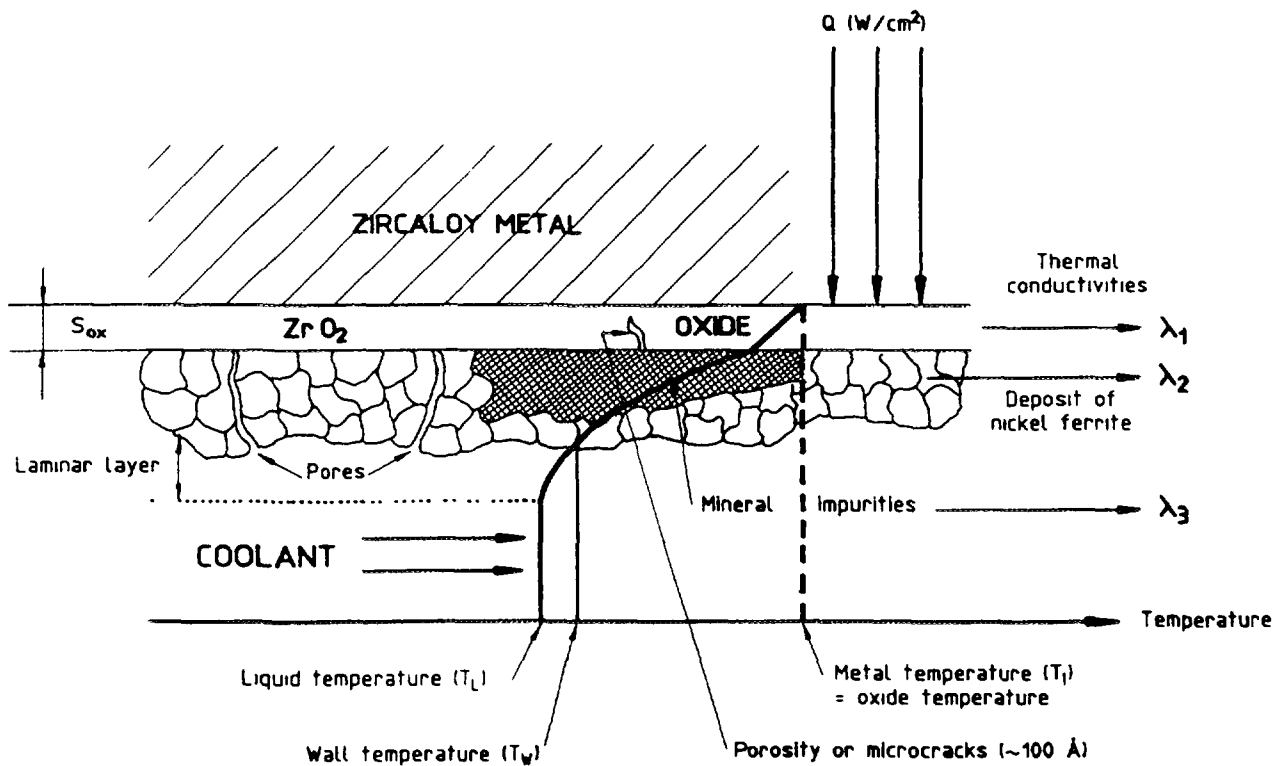


FIG 8 13 Thermal impact of crud deposition

### 8 3 1 1 1 Chemistry control during power operation

For a PWR during normal operation the nuclear reactivity control of the core is obtained by changes in boric acid concentration. An alkalisng agent (the most often used is lithium hydroxide, LiOH) is added in order to maintain a moderately high pH. Hydrogen additions mitigate the radiolytic formation of oxygen and other oxidising species. These additives, which determine the system pH and redox potential, are controlled by the chemical control unit of the plant as described in section 6 4 1.

### 8 3 1 1 2 Corrosion

The minimum concentrations of additives in the primary coolant were originally specified by the fuel vendors. Operational experience has shown that these specifications were adequate for maintaining the general corrosion rate of materials of the PWR primary circuit at a very low value. As long as lithium is greater than that required to give a pH at  $T_{ave}$  of 6.9 (Figure 6 26) [281] and hydrogen greater than 15 cm<sup>3</sup> (STP)·kg<sup>-1</sup>, the integrity of the various components is ensured for the whole life of the PWR. Upper concentration limits are also specified.

- For impurities such as chloride, fluoride and sulphate in order to prevent stress corrosion cracking (SCC) and inter-granular attack (IGA) of austenitic materials (Inconel, SS) (Table 6 6)
- For lithium hydroxide in order to minimise the corrosion of the fuel cladding. There is indeed evidence that at high lithium hydroxide concentrations the rate of Zircaloy corrosion accelerates (see sections 4 2 3 2 and 6 4 1 3). There is also some concern that increased lithium might increase the stress corrosion cracking of certain stainless steel components.

During the corrosion process, at the same time that oxidation takes place in situ, metal ions are dissolved at corroding metal surfaces and carried out through the oxide pores, the sublamellar layer and finally the bulk coolant

These ions are transported throughout the circuit. Because of the temperature gradient present in the circuit, one has to consider (when steady-state conditions are reached) that precipitation will take place at some locations, depending on chemistry and solubility laws. This precipitation leads to the formation of fine particles of oxide which coalesce and grow to a size limit imposed by the turbulence of the fluid, or precipitation occurs directly onto the cladding. Precipitation occurs on the hot fuel cladding when the temperature coefficient of solubility is negative and this occurs at a  $pH_{cr}$  value below about 7.0-7.4

When, at the location of the deposit, the fluid is saturated in the main elements, no dissolution will take place. Particles will reach the wall and the thickness of crud will then increase. The erosion forces applied to the deposited crud by the turbulent coolant will remove some of them, leaving on the cladding only the most adherent ones.

From this brief description of the main phenomena, it is understandable that the first chemistry specifications that were designed to limit the general corrosion rates in reactors might not have been sufficient for minimising crud build-up rates. In addition a reduction of deposits is strongly related to a decrease in the radioactive contamination of the circuit. Thus specific experiments were undertaken in out-of-pile loops.

Out-of-pile loops have been used extensively to study the effects of crud deposition, and of traces of mineral impurities, on cladding corrosion under single-phase and nucleate boiling heat transfer conditions [127,460]. As in an actual reactor, corrosion product release rates from the loop wall depend on the specific chemistry of each test. Furthermore, thicker crud can be obtained through the injection of crud precursors. These consist of soluble forms of Fe and Ni in deoxygenated solution percolated into an anion exchanger at the time of injection.

Typical axial variations of the thermal hydraulic parameters in those loops can lead to three successive regions with specific heat transfer characteristics (Figure 8.14)

- (1) Single phase convection,
- (2) Subnucleate boiling,
- (3) Bulk boiling

The void fraction,  $\alpha$ , is defined as the ratio of the volume of vapour to the total volume across a section. The experimental procedure includes qualitative and quantitative analyses of the crud deposit, examination of the zirconium oxide layer and examination of the clad metal. In the boiling experiments it is possible to assign to crud build-up an increasing slope in the three successive thermal-hydraulic regions as shown in Figure 8.14. A sharp increase in deposition appears in the detached boiling zone ( $\alpha \sim 1$  or 2%). The maximum crud level was approximately 30 mg/dm

Over the pH range recommended for PWR coolant operation, the influence of pH on core crud fouling was found to be negligible. This is probably because fouling under nucleate boiling conditions is more influenced by local concentration effects and increases in mass transfer than by small changes in pH.

The morphology of the crud deposit results from the nucleation and growth of vapour bubbles at preferred sites on the metal/coolant interface. These sites remain crud free, but mass transfer associated with boiling produces deposition of particles around the sites, and chimneys are formed. Thus the crud obtained under boiling is more dense, with the appearance of chimneys as

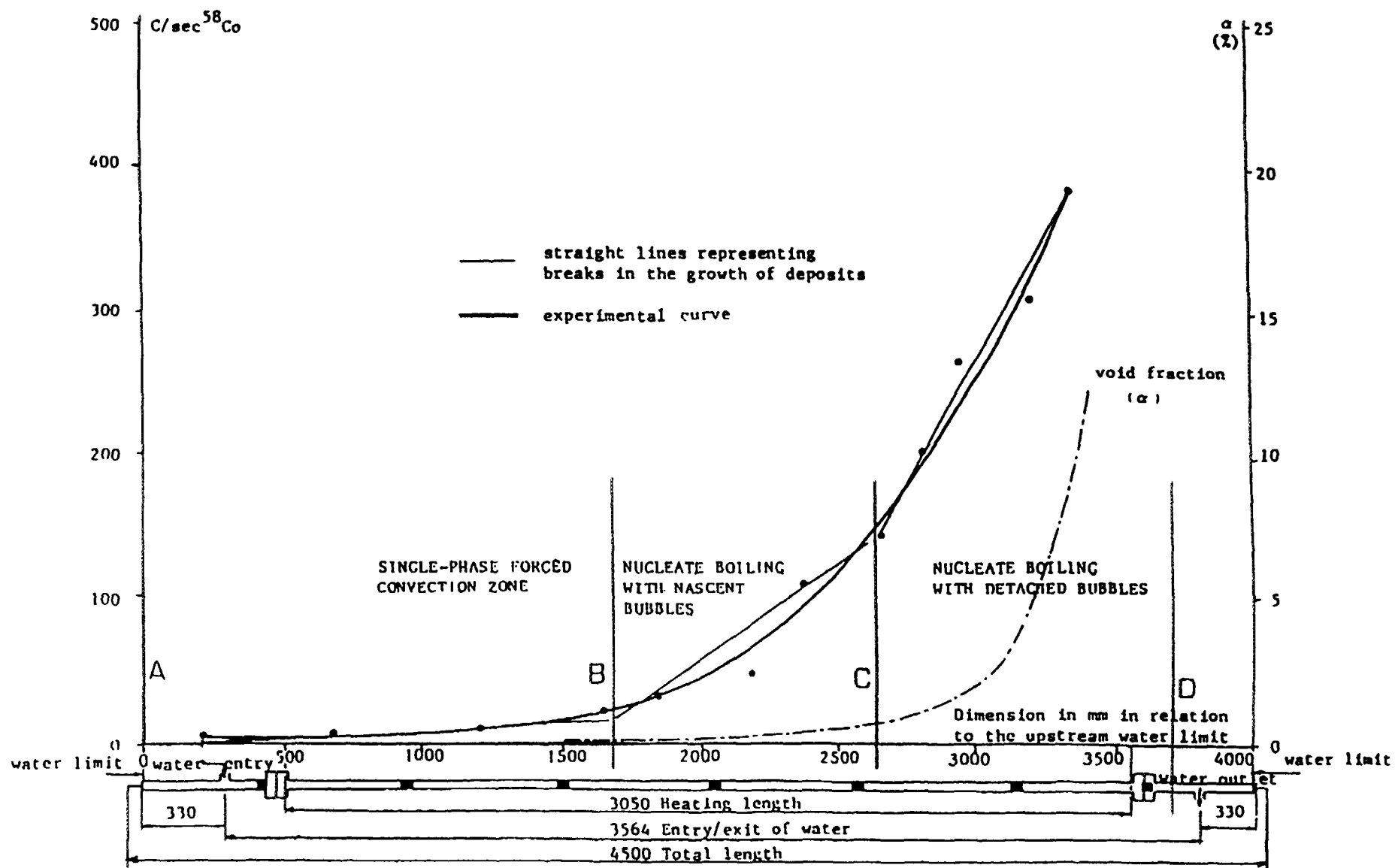


FIG. 8.14. Effect of thermal-hydraulic conditions on the deposition of corrosion products.



shown in Figure 8.15. The deposits consisted of particles  $\sim 1\text{ }\mu\text{m}$  in size; the diameters of the chimneys were about  $1\text{--}5\text{ }\mu\text{m}$ . The composition of the crud measured by X-ray dispersive analysis, is given in Figure 8.16 for samples with no chimneys (A: non-boiling zone) and samples with chimneys (B: outside a chimney and C: very close or inside a chimney). The iron to nickel ratio was constant, but a consistent enrichment in chromium was observed in the zones with chimneys. Thus, the crud deposited consisted of a  $(\text{Fe, Ni, Cr})_3\text{O}_4$  spinel, while zeolite-forming impurities with extraneous impurities (Ca, Mg, Al, Si) were negligible.

Some tests were carried out with daily replacement of 10% of the loop water (feed-and-bleed) by injection from a feed water tank and mineral impurities (calcium, magnesium, aluminium and silica) were introduced in concentrations typical of current specifications. In this case, light deposits ( $1\text{--}2\text{ }\mu\text{m}$ ) were obtained, with magnesium and calcium vs. iron ratios shown in Table 8.5 at different axial elevations. According to these data, enrichment starts in the two-phase zone at a void fraction of 1.5 to 2%.

In one case, accidental calcium contamination (up to 40 ppb measured in the loop water) formed white spots identified as a zeolite in the detached boiling zone. Dramatically increased clad-corrosion was then encountered after 120 EFPD. A photograph of this unique event is displayed in Figure 8.17.

In the case of heavy crud deposition, the appearance of a flaky texture is indicative of a strong concentration of zeolites underneath the flakes. As shown on Figure 8.18, part of the white deposit could not be separated from the zirconia film by scraping with a scalpel blade. Figure 8.19 shows an SEM view of the inner surface of such a flake turned upside-down. Crystallisation in the shape of needles is characteristic of magnesia. Chimneys running through the crud flake are also easily identified.

#### 8. 3. 1. 3. Thermal conduction effects

The cladding of rods has been subjected to oxide thickness measurements after various times of operation under nucleate boiling conditions.

In the areas under “single phase convection” and partially under “developed nucleate boiling” (void fraction less than 1-1.5 %), corrosion rates were in agreement with theoretical thermal models which take into account the heat transfer through the oxide and the crud layers. In the areas with “detached boiling” (void fraction more than 2%), there was evidence of accelerated corrosion. The axial evolution of the corrosion film is shown in Figure 8.20 for a rod after 456 EFPD. Starting at the 160 cm elevation on the rod, the water/oxide interface (wall) temperature was constant ( $343^\circ\text{C}$ ). As the sub-saturation of the bulk water decreases, a greater fraction of the energy is spent on vaporisation. In this constant wall temperature region, the zirconia thickness increased from 6 to  $16\text{ }\mu\text{m}$ .

The acceleration factor for corrosion rates in the boiling zones was approximately equal to two, compared with regions under single-phase heat transfer at the same temperature. The acceleration of clad corrosion in the boiling mode cannot be readily explained by a temperature increase at the metal/oxide interface due to the heat transfer barriers through the oxide film and the crud, or by a decrease of thermal conductivity of the zirconia or the crud. In these tests, the situation did not appear consistently worse on the rods with heavy deposits ( $\sim 10$  to  $20\text{ }\mu\text{m}$ ) than on those with light deposits. Only a slight increase in temperature at the metal/oxide interface was observed as a result of an accelerated rate of crud build-up. (The thermal conductivity of the crud was assessed to be about  $0.1\text{ W}\cdot\text{cm}^{-1}\cdot^\circ\text{C}^{-1}$ ). However, it has been demonstrated that the intrinsic corrosion properties of Zircaloy are affected under conditions where lithium is incorporated into the lattice of the oxide [461] or into micro-cracks in the post-transition film [108]. Lithium enrichment is a consequence of boiling conditions leading to a local super-concentration of lithium hydroxide at the wall of the

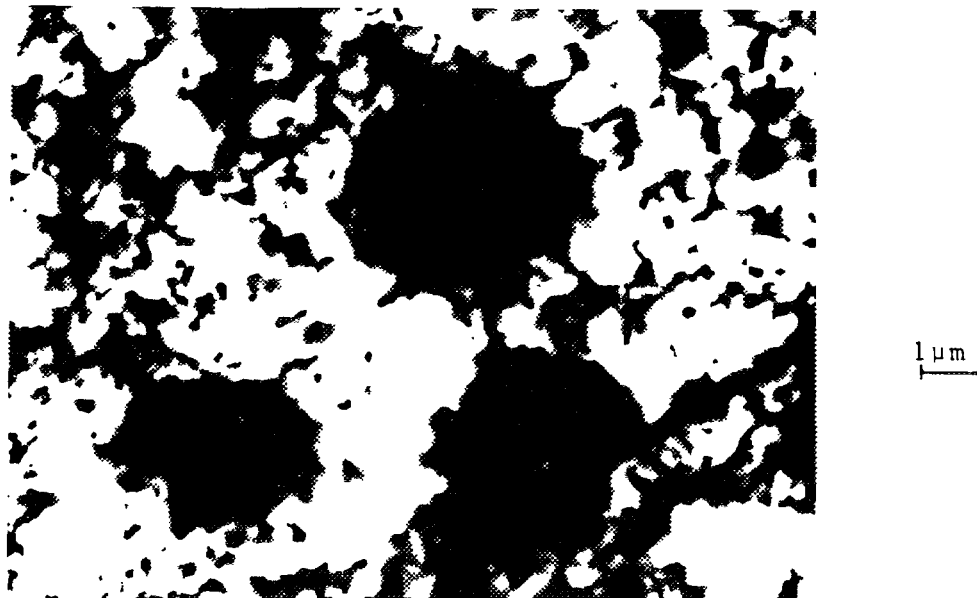
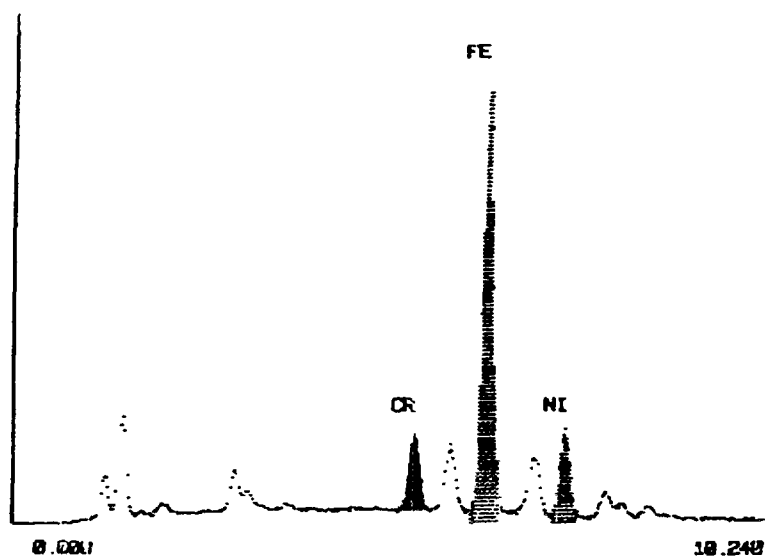


FIG. 8.15. Chimneys in crud.

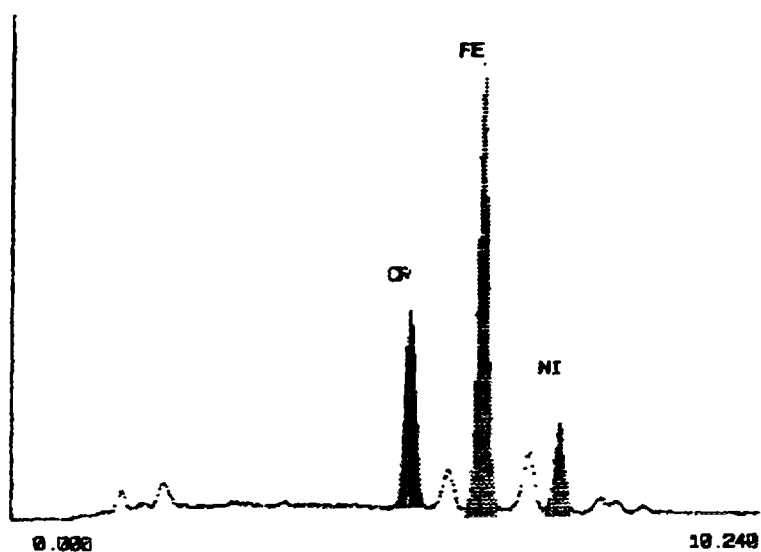
cladding and in the pores of the crud deposit and of the oxide films. This was confirmed by the detection of lithium ions incorporated into the deposits and in the zirconia layers [321]. Figure 8.21 shows a lithium profile (SIMS) across an oxide layer which has undergone an acceleration of the oxidation process. In more recent work, a good correlation has been found between the accelerated oxide growth due to LiOH and the higher retention of Li in the oxide layer [127].

Generally, crud deposition on the fuel rods of power reactors is very light or non-existent, at least under single phase heat transfer conditions. Crud scraping campaigns, visual examinations or activity build-up measurements have been performed in several reactors showing that the coordinated ( $\text{pH}_{300^\circ\text{C}} = 6.9$ ) Li/Boron chemistry seems to be efficient [462,463], but the modified Li-B chemistry regime, used more recently, is believed to be even better (section 6. 4. 1. 4.). Nevertheless, some examples of tenacious crud were found to have developed as a result of bad chemistry control of the primary coolant of reactors such as in the Saxton reactor. Coolant permeating through the crud and containing dissolved lithium hydroxide, is believed to vaporise in the chimneys of the type described above, resulting in an excessive concentration of lithium at the base of the chimney. Local coolant pH levels in excess of about 11.0 can readily develop by this mechanism (due to lithium hydroxide concentration), and cause subsequent excessive corrosion of the Zircaloy cladding. The failures observed in the Saxton reactor were believed to have been initiated by this mechanism. Direct image mass analysis (DIMA) of the heavy waterside corrosion films on the Saxton rods confirmed the presence of high levels of lithium in the oxide. As the oxide thickened, because of the high heat fluxes, the temperature at the oxide-metal interface increased rapidly causing thermal corrosion to accelerate. Thus by a mechanism of accelerated corrosion, due initially to lithium hydroxide hide out, and later due to thermally activated corrosion, failures developed rapidly under thick tenacious crud layers in the Saxton test rods.

A : Deposit in no  
Boiling Zone



B : Deposit in Boiling  
Zone : Outside a  
Chimney



C : Deposit in Boiling  
Zone : Very Close or  
Inside a Chimney

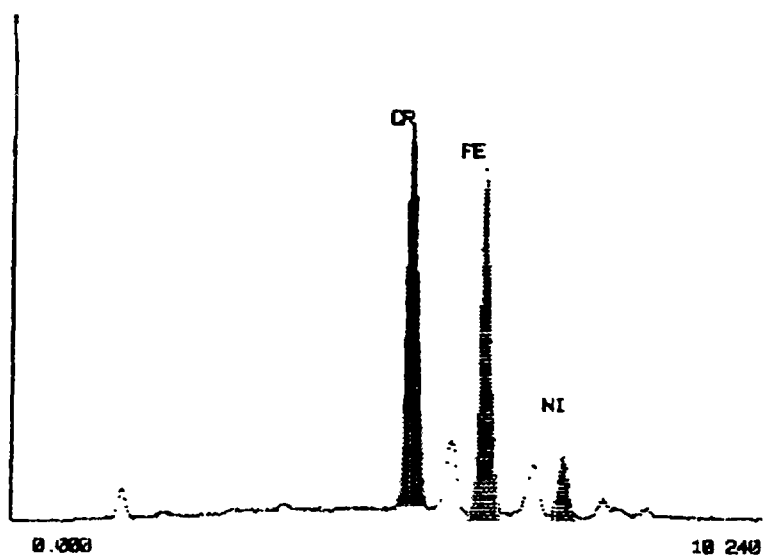


FIG 8 16. X-ray dispersive analysis of the crud composition.

Table 8.5. Nickel ferrite composition and mineral impurity enrichments in crud.

Elevation cm	Ca/Fe $\times 10^2$		Mg/Fe $\times 10^2$		Ni/Fe	
	run 1	run 2	run 1	run 2	run 1	run 2
69-73	4.6	1.3	0.9	1.5	0.18	0.12
154-158	2.2	2	0.4	1.5	0.16	0.21
194-198	5.5	4.4	1.2	3	0.47	0.20
264-268	4.1	5.3	0.9	5.7	0.35	0.30
289-293	9.5	7	2.0	8.5	0.25	0.32
343-347	124	17	8.1	15	0.32	0.34

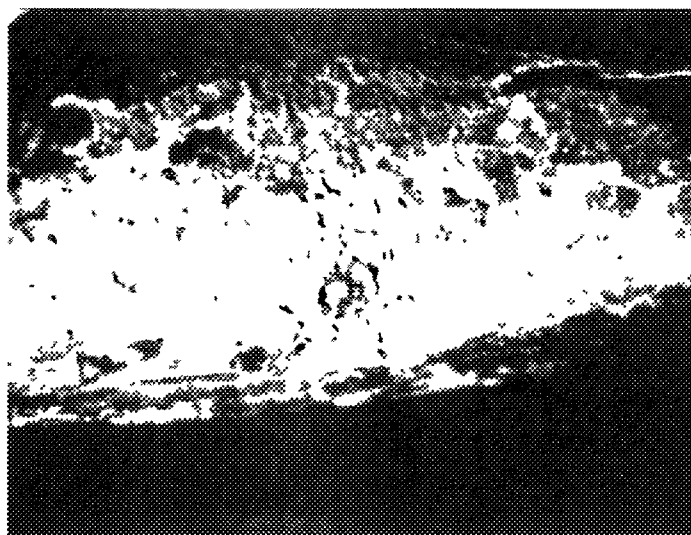
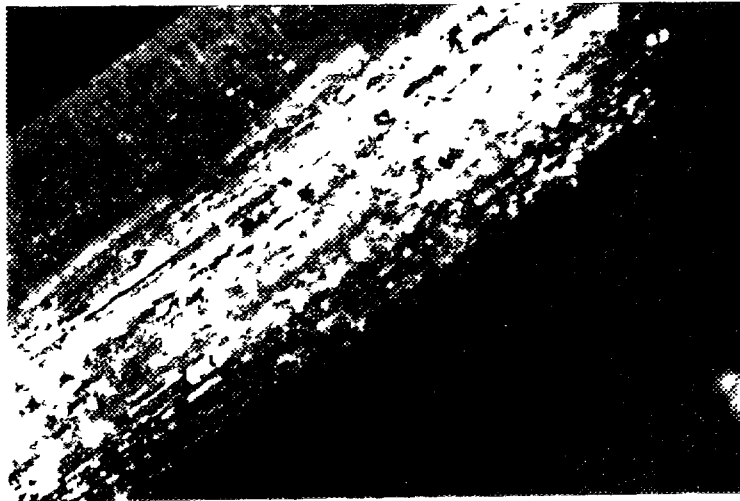
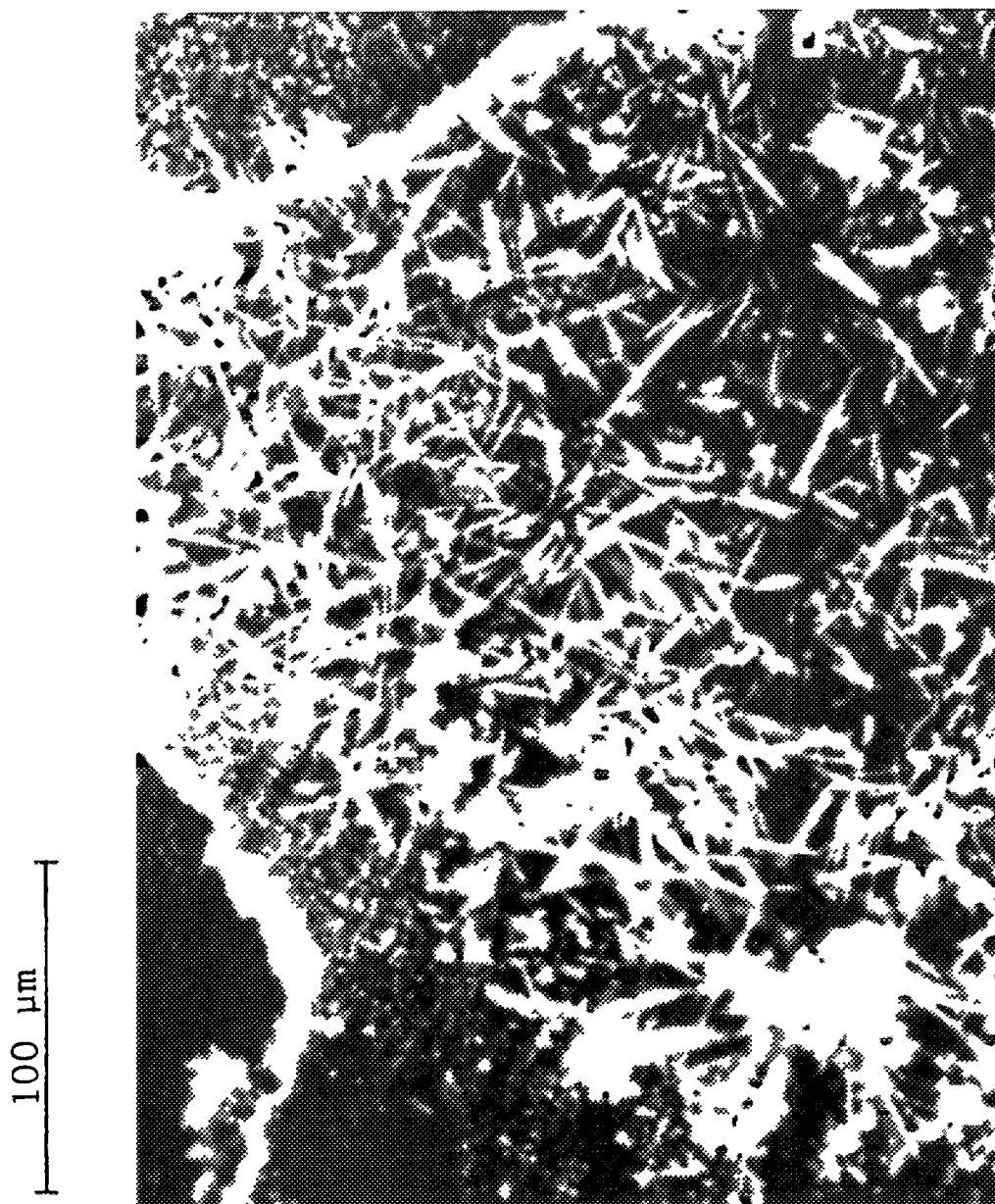


FIG. 8.17. Accidental localised corrosion for very high crud deposition.



*FIG 8 18 Loose crud obtained under heavy deposition conditions*



*FIG 8 19 SEM view of the inner side of crud removed from the cladding described in Fig 8.18*

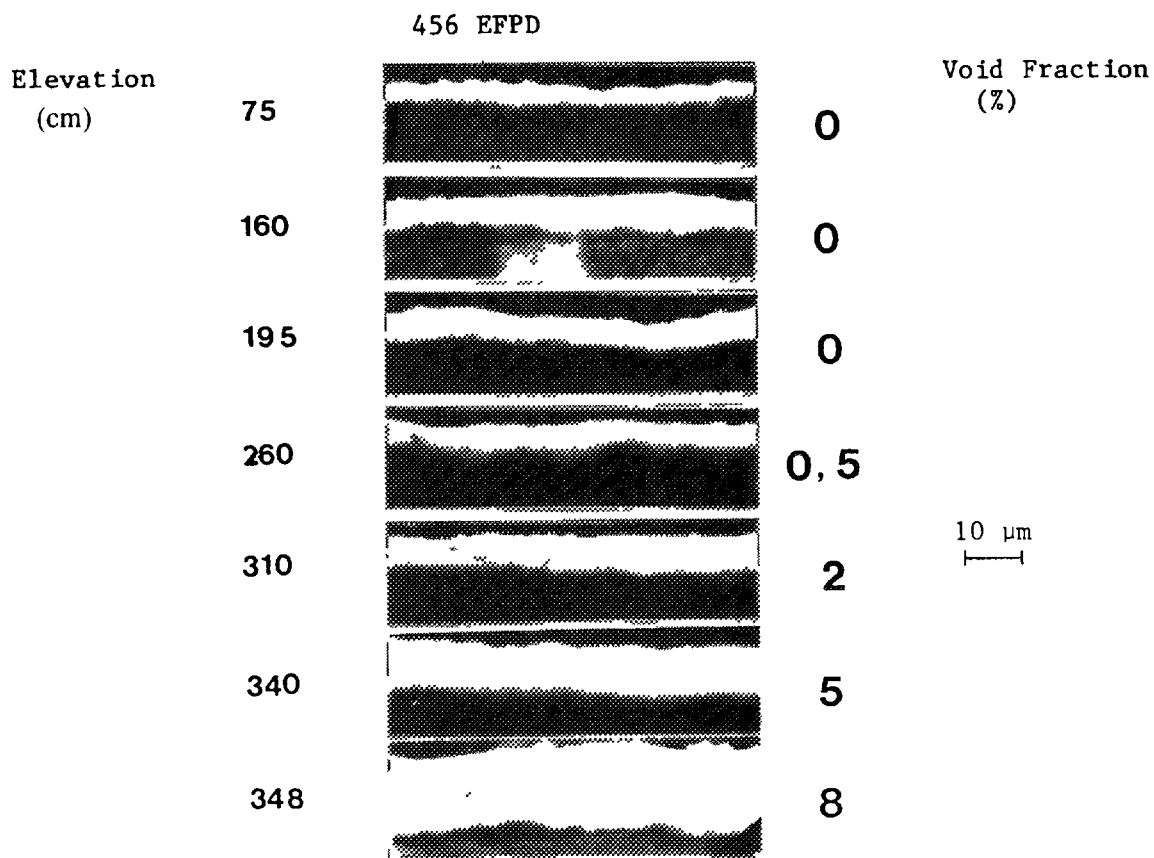


FIG 8 20 Increase in oxide thickness due to an increase of void fraction in the coolant with increasing elevation

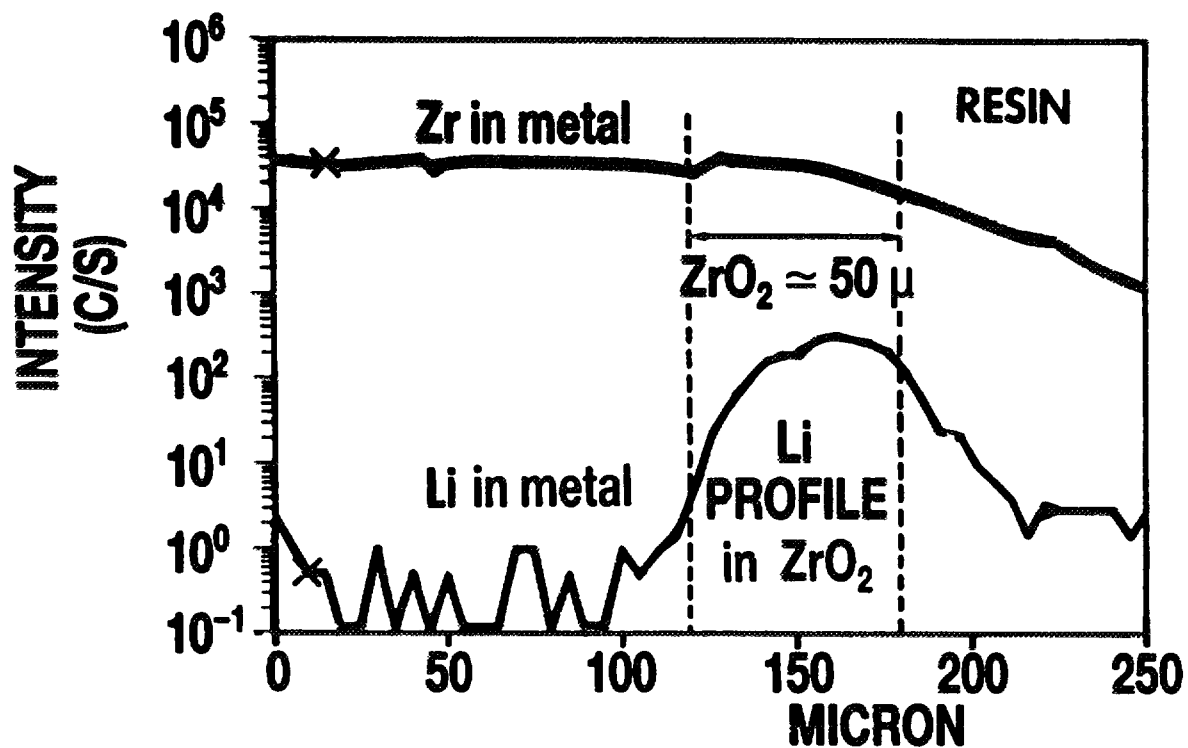


FIG 8 21 Li concentration profile (SIMS) in a zirconia layer grown in a loop simulating PWR water chemistry

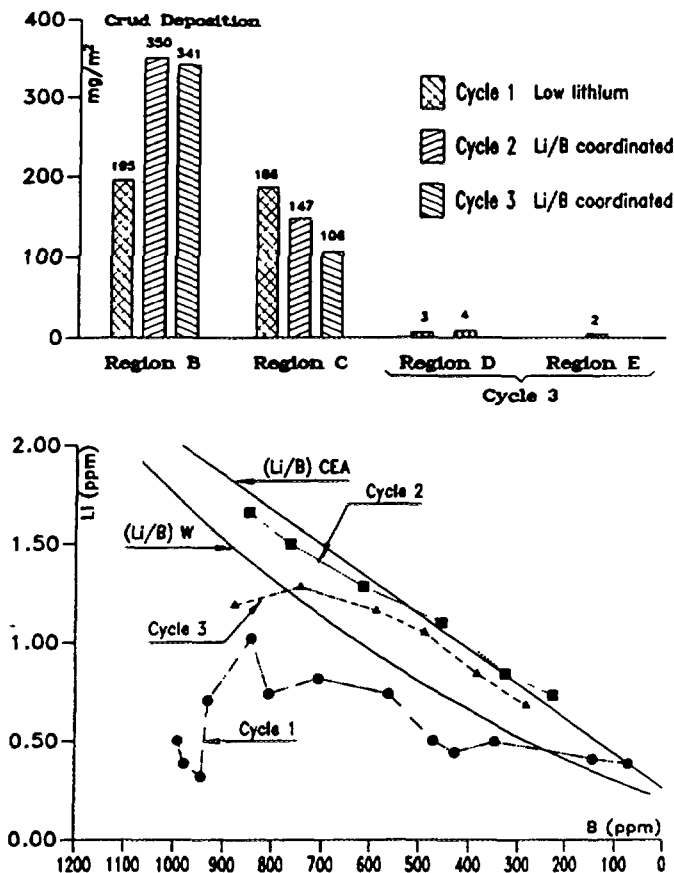


FIG 8 22 Crud build-up on Trojan fuel assemblies during the first three cycles of operation

In modern PWRs excessive crud build-up in the core is usually avoided with a carefully operated coolant chemistry control. Optimisation of the lithium hydroxide, pH, and dissolved hydrogen combine the objectives of reducing the sources of radiation fields and crud build-up. These requirements can be obtained simultaneously (since activated crud deposits in the core are the primary contributors to radiation fields) by maintaining the pH in the desired range in order to maintain a positive temperature coefficient of solubility for nickel ferrite crud in the core, and at the same time by maintaining a zeta potential at a level which prevents the attraction of colloid species to the cladding surface [464]. It was demonstrated [465-467] that a  $\text{pH}_{100}$  above 6.8-6.9 is sufficient to avoid the presence of a thick deposit in the hot part of the fuel. The effect of low pH (low lithium) operation on fuel and crud deposition was tested in the Trojan PWR during cycle 1. Heavy crud was observed, which persisted on the initial fuel throughout cycles 1, 2 and 3. Co-ordinated chemistry operation during cycles 2 and 3 gave low crud on new fuel (Figure 8 22). Experiments in the MIT in-pile loop have shown that crud deposition and the production of radioactive corrosion products are minimised at a pH of about 7.3 [468]. However, the effect of LiOH in accelerating zirconium alloy corrosion requires limiting the concentration of LiOH in water to that used in the Modified Li-B chemistry regime (Figure 6 27) [281].

In contrast, a low pH corresponding to a low lithium hydroxide is responsible for the formation of thick in-core deposits. The same effect may be observed with hydrogen concentrations below the limit required to suppress radiolysis, or more generally, with the presence of oxygen in the primary coolant [467].

### 8 3 2 WWER crud deposition

The WWER-440 and WWER-1000 reactors are provided with horizontal steam generators with straight stainless steel tubing, while most other PWRs have vertical steam generators with U-shaped tubes made of Inconel 600, Inconel 690 or Incoloy 800. The fuel element cladding of WWER-440s and WWER-1000s is made of zirconium-niobium alloy H-1 containing 1% niobium, while the fuel elements of the other PWRs are clad mainly with Zircaloy-4. The temperature and pressure, as well as the heat flux, are lower in WWER-440 reactors than in other PWRs. WWER-440 reactors use KOH and  $\text{NH}_3$  to alkalis the reactor water (see Table 6 7, section 6 4 3). The water quality specifications for WWER reactors also permit only rather small variations in reactor water pH values, through a correlation between the concentration of the alkali and the boric acid in order to maintain the specified pH. No information is available to assess WWER fuel surface crudding levels. Nevertheless, due to the low coolant and wall temperature (at least in WWER-400s with coolant temperatures of approximately 267-297°C, significantly lower than WWER-1000s of 290-325°C and modern PWRs of 290-325°C), the reduced heat flux and the appropriate applied chemistry, the thickness of the deposited crud layers is expected to be low.

### 8 3 3 BWR crud deposition

#### 8 3 3 1 BWR feed water chemistry specifications

The water chemistry of BWRs is described in section 6 4 2. Due to the continuous boiling of the coolant, crud formation is a matter of high concern and very tight control of the non-volatile species is mandatory. In addition, a specific feature of BWR water chemistry is that water radiolysis in the core is not suppressed. Unlike PWRs, water radiolysis suppression, obtained by maintaining a certain  $\text{H}_2$  concentration, is difficult because the hydrogen added is removed continuously with the steam from the core. Reactor operation at a given capacity leads to water radiolysis at a constant level. In most cases the  $\text{O}_2$  level in the recirculating coolant due to radiolysis is between 0.1 and 0.3 ppm and the  $\text{O}_2$  level in the steam produced, ranges between 15 and 30 ppm. It is known that even small amounts of oxygen in the coolant induce deleterious effects due to intergranular corrosion of the recirculation piping. It has turned out that the addition of hydrogen reduces the oxygen level in the recirculation lines through the radiolytic recombination reaction in the downcomer. Therefore hydrogen injection to the feed water system of BWRs has been proposed as a remedy piping corrosion. This water chemistry regime is called "hydrogen water chemistry" and is now operated in a number of PWR power plants [469] (see section 6 4 2 1).

In BWRs the coolant pH cannot be controlled even with the relatively non-volatile KOH or LiOH because of the danger of local increase in the concentration of these alkalis in the core. Under these circumstances, the minimisation of circuit corrosion processes in BWRs requires both the use of highly corrosion-resistant construction materials and of high-purity water throughout the cycle.

The corrosion products released from the large surface areas of the materials must be continuously removed. Condensate demineralisers, installed after the turbine condenser and before the flow re-enters the reactor vessel, are used for this purpose. However, the corrosion products released downstream of the condensate demineraliser are not removed. The oxygen concentration is very important for minimising corrosion product release to the feed water system. Therefore, the oxygen level must be controlled in the feed water. In this way fuel surface deposits are minimised and flow and radioactivation problems reduced. The reactor water is also highly demineralised, the amounts of the respective impurities being in ranges such as to guarantee the reliable operation of the fuel elements and the stainless-steel equipment and pipes as well as guaranteeing adequate purity of the steam produced. The specifications generally allow for a maximum of 100 or 200 ppb chloride, while the critical concentration is 350 ppb. The silica concentrations are specified primarily to avoid



deposits on the heat exchange surfaces in the core. A silica concentration of 1,000 ppb is sufficiently low to avoid this. However, for demineralized make-up water (specific conductivity about 0.1  $\mu\text{S}/\text{cm}$ ) the maximum silica concentration is usually between 20 and 30 ppb. Thus, silica from make-up water is rarely the source of high coolant levels of  $\text{SiO}_2$ .

### 8.3.3.2 Water reactor fuel surface crudding levels

The thickness and composition of the deposited crud layers contribute not only to the problem of radio-activation but also influence core heat transfer and pressure drop. Porous haematite deposits on simulated fuel rods do not cause large increases in cladding temperature. Laboratory tests on open-textured haematite of less than 100  $\mu\text{m}$  thickness at a heat flux of 100  $\text{W}/\text{cm}^2$  showed less than a 10°C degrees alteration of cladding temperature under BWR conditions, however, a similar deposit (but impregnated with the salts normally associated with hard water) showed a cladding temperature increase of up to 92°C degrees. The surface friction factor for a crudded rod in these tests exceeded that of a clean rod by a factor of 3.3. Both of these observations have parallels in early BWR experience when crudding levels on fuel surfaces were high. In the first year of SGHWR operation, for example, copper infilling of the  $\text{Fe}_2\text{O}_3$ -based deposit occurred leading, in some cases, to fuel cladding failures due to steam blanketing and overheating. Subsequent operation of SGHWR with considerably reduced Cu and Ni levels in feed water and lower overall crud input rates then led to no further fuel cladding failures up to final shut down, although the fuel crud thickness peaked at about 25  $\mu\text{m}$  corresponding to 1.5 to 2.0  $\text{mg}/\text{cm}^2$  of deposit. Porous deposits have been found to assist heat transfer by what has been termed "the wick boiling mechanism".

In the case of heavy crud deposition the resultant increase in temperature enhances the cladding corrosion rate, possibly leading to Crud Induced Localised Corrosion (CILC) failures. This phenomenon is promoted by the conjunction of a relatively high copper content in the coolant (due to copper bearing condensers), a power history with high end-of-cycle power (due to reactivity control by Gd bearing rods) and the use of a cladding susceptible to nodular corrosion [150]. In reported cases of CILC, the thickness of the crud was in the range of 40-60  $\mu\text{m}$ , and was mostly composed of pure  $\text{CuO}$ . The corrosion of the Zircaloy underneath was accelerated and led to a large number of cases of through wall oxidation during the early 1980s. Correction procedures included the replacement of the condensers by titanium or stainless steel tubes, installation of deep bed condensate cleanup systems, and improved water chemistry [470]. In addition the development of Zircalov processing with improved resistance to nodular corrosion has had an important contribution to the solution of this problem and no new CILC failures have been reported [471]. It should be noted that in the case of improved water chemistry and removal of Cu, the crud composition is almost entirely pure haematite, with an estimated thickness of 10-12  $\mu\text{m}$ . Since in this case, no CILC was found, the heat rating does not seem to be the only factor to be considered, since no degradation in heat transfer would have taken place. This point will be discussed in section 9.2.1.1 for the possible contribution of Cu. In a similar way, heavy crud was obtained in a WWR 1000 due to the failure of the graphite bearing of a main circulating pump. This resulted in thick graphite crud (170  $\mu\text{m}$ ) and the occurrence of localised thick oxide spots of nodular appearance [472].

In second-generation BWRs, with reduced iron levels in the feed water (<10 ppb) and with little or no use of copper alloys, few fuel defects have occurred due to crudding. Deposition levels still vary considerably depending on design, materials and operating factors, e.g., the type of feed water purification plant and its location or the addition of oxygen to the feed water. An indication of the improvement in deposition levels in the more recently commissioned BWRs is illustrated by comparing data from the SGHWR and the Swedish reactors in the summary of fuel crud deposition levels for various BWRs given below.

BWR Reactor	Typical Fuel Crud Deposition Levels, $\text{mg}/\text{cm}^2$
SGHWR	1 to 2

Swedish BWRs	0.1 to 0.5
US BWRs	<1 to 10
German BWRs	0.5 to 7.6
Japanese BWRs	0.5 to 3
RBMK	2

## 8.4 METALLURGICAL AND CHEMICAL VARIABLES

### 8.4.1 Behaviour of alloying additions

#### 8.4.1.1 Incorporation in the oxide film

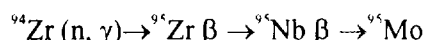
- **Solute elements** It is generally believed that both the segregation and the uniform incorporation of alloying additions that has been observed for various different species in the laboratory will persist unchanged in reactor. Virtually no work has been done to support this contention. Indeed, differences in solubility and oxidation potential should be considered for incorporation in the oxidation front as it grows. The hydrogen trapped by the metal is insoluble in ZrO<sub>2</sub> and is expected to be repelled during zirconia growth, Sn should have an intermediate behaviour, while Nb should behave as Zr. Experiments on the oxidation of RXA Zircaloy implanted with Fe have shown that the motion of the oxidation front through the implantation profile induced a broadening without displacement of the initial Fe profile, giving no clear conclusion on any transport of species like Fe, ahead of the oxidation front [113].
- **Precipitates** The precipitates are embedded unoxidized in the oxidation front due to the low oxygen potential in the dense oxide layer, as described in section 4.2.2. During irradiation, several physical phenomena have to be taken into consideration [113].
  - At the beginning of irradiation the precipitates remain in their crystalline form and are embedded in the zirconia in a similar way as in the unirradiated material. Once in the zirconia layer, the neutron flux induces a ballistic doping of the zirconia in the surroundings of the precipitates. By this process, the local Fe concentration can be much higher than the solubility limit and reach up to a few %. This doping leads to the stabilisation of the tetragonal phase of the zirconia. However, this stabilisation of the tetragonal phase only lasts up to the complete amorphous transformation in the precipitates (see section 8.1.3.1).
  - When the precipitates have lost all of their Fe by complete amorphous transformation, there is no easy way to introduce Fe into the zirconia from the Fe-free precipitates.

Thus the mechanisms of corrosion under irradiation change as the time goes on. Not only the change in microstructure affects the corrosion behaviour, as shown in section 8.1.3.1, but also the neutron flux enhances the transport mechanisms.

In the case of Zr-2.5%Nb alloy material in the commonly used cold worked condition, the  $\alpha$ -Zr matrix is supersaturated in Nb. Indeed, the equilibrium concentration is in the range of 0.2 to 0.3 % at operating temperatures, while after processing above 450°C, the matrix may have up to 0.6-0.7%Nb. This structural state is metastable, and ageing occurs during operation at temperature. This can be reproduced in the laboratory, even without irradiation, at temperatures down to ~300°C, albeit slowly at T<400°C [275]. Irradiation enhances this ageing, which also comprises some diffusion of Zr out of the  $\beta$ -Zr(Nb) phase to leave precipitates of  $\beta$ -Nb with a higher Nb content. This has been argued to be the cause of the often observed better corrosion resistance of Zr-Nb alloys in reactor than in laboratory autoclave tests [196]. Corrosion resistance is indeed observed to increase with prolonged low temperature ageing in the laboratory [473]. Testing of pre-irradiated Zr-Nb specimens in the laboratory has confirmed the validity of this hypothesis [12,474]. However, the mechanism involved seem to be an increase in corrosion resistance of the matrix with a lower solution content of Nb in the  $\alpha$ -Zr matrix.

#### 8 4 1 2 Transmutation effects

Prolonged irradiation, even of low neutron capture cross section elements, can produce significant quantities of new impurities by transmutation of the pre-existing components of the system. Irradiation of zirconium results in small quantities of niobium and molybdenum being produced, and irradiation of Zr-2.5%Nb alloy specimens produces enough molybdenum during the lifetime of a pressure tube for the alloy to become a Zr-2.4%Nb-0.2%Mo alloy. It is not known at present whether such end of life effects can have a significant impact on the corrosion resistance of the alloy, but there is sufficient concern for investigation of such effects to be in progress. Transmutation of zirconium to molybdenum by the sequence



may reach 0.2%Mo in a Zr base alloy pressure tube after 20 years ( $\sim 1.3 \times 10^{26} \text{ n m}^{-2}$ ). None of the possible transmutations of alloying additions in Zircaloy ( $^{54}\text{Cr} \rightarrow ^{54}\text{Mn}$ ,  $^{58}\text{Fe} \rightarrow ^{59}\text{Co}$ ,  $^{58}\text{Ni} \rightarrow ^{58}\text{Co}$ ,  $^{60}\text{Ni} \rightarrow ^{60}\text{Cu}$ , or  $^{100}\text{Sn} \rightarrow ^{121}\text{Sb}$ ) will produce enough product to be of concern.

#### 8 4 2 **Electrochemical effects**

The electrochemistry of zirconium alloys in high temperature water (or dilute solutions) has not been studied extensively. Thus, it is not known whether, and to what extent, polarisation affects the corrosion rate, nor do we know anything about the electrochemical surface reactions that participate in the overall oxidation process. Since they do not appear to be rate limiting, studies of these reactions are notable for their absence, although some early room temperature electrochemical studies have been performed. Polarisation experiments in fused nitrate melts in the laboratory at 300°C [29] show little effect of either anodic or cathodic polarisation on the oxidation rate, confirming the supposition that it is largely controlled by processes within the pre-transition oxide layer (Figure 8.23).

With this experience in the absence of irradiation, it has been surprising to find that repeated examples of apparently electrochemical and galvanic effects on corrosion rates in BWR conditions are appearing as previously described and referenced in section 8.2.4.

All of these phenomena can be fitted into a single mechanistic framework if these effects are related to local electrochemical (redox potential) or galvanic conditions. However, no supporting evidence or experimentation is available at present. The various effects that might be involved will be discussed separately.

##### 8 4 2 1 Redox potential of aqueous systems

The redox potential of an aqueous system in a laboratory test is determined primarily by the hydrogen to oxygen ratio derived from over-pressures of these species, in the absence of dissolved variable-valence (or easily reducible) ions. In a BWR, where these effects seem to appear primarily, the equivalent redox potential of the water is also affected by the radiolytic production of species with different oxidising or reducing properties, and by the partitioning of volatile molecular species into the steam phase. The net effect is that the equivalent redox potential of the reactor water can be expected to vary along the length of the core from inlet to outlet, and to be different again in the downcomer and external piping where recombination of radiolytic species can be expected. Thus, we might expect electrochemical effects to show as peaks in nodular corrosion that follow the calculated peaks in concentration of some of the prominent radiolytic species.

The difficulties of inserting stable electrodes into a system operating in high temperature water at 300°C, let alone into the high flux region of a reactor, has meant that few such measurements have been reported. Some measurements in the downcomer and recirculation piping of BWRs do

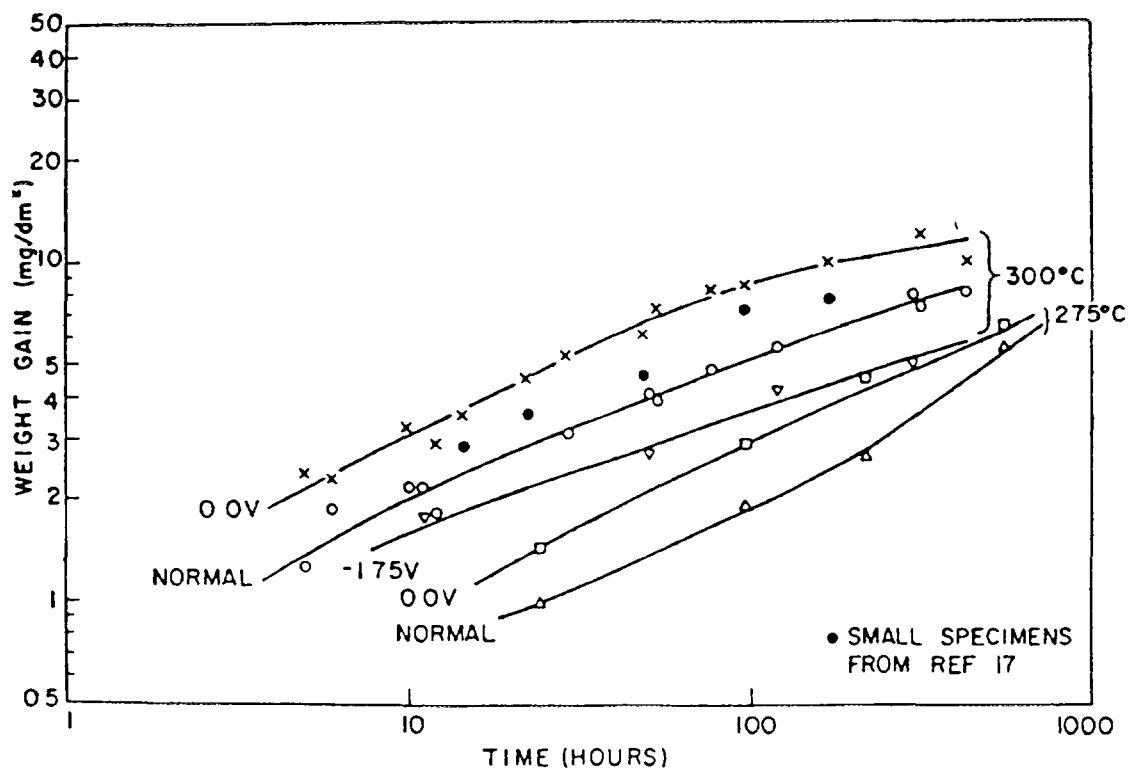


FIG 8 23 Weight gain for Zr specimens biased during oxidation in fused salts at 275 and 300°C [29]

show significant variations with location (Table 8 6) and from plant to plant, together with the expected effect of hydrogen additions (HWC). However, measurements in core show that the effectiveness of HWC may not extend throughout the core region of the reactor [475,476].

#### 8 4 2 2 Irradiation induced currents

When considering the local potential of the Zircaloy cladding and other adjacent components we should not ignore the induced currents caused by the irradiation fluxes. In many ways a reactor fuel pin is like a large self powered flux detector. The  $\text{UO}_2$  is the emitter and the cladding is the collector. However, to the extent that charged particles ( $\beta$  and primary knock-on particles) pass through the cladding, or its protective oxide film, from either side they represent an electrical current that must be factored into the overall polarisation currents experienced by the oxide film. In addition to this primary flux of charged particles induced by the fast neutron flux flowing outward from the centre of the fuel rod, there are several sources of secondary current. Recoiling protons from the water provide a significant flux through the thin oxide films (proton energies can be up to  $\sim 3$  Mev), and, although the quantity of hydrogen injected as a fraction of the total hydrogen absorbed from the corrosion reaction is negligible, the current represented by this flux cannot be immediately dismissed as negligible. A further source of polarising current is the flux of Compton electrons resulting from  $\gamma$ -ray absorption in the Zircaloy, the oxide film and the adjacent water. Because of the different densities, and absorption cross sections of the phases, these fluxes will not be equal and there will probably be a net flux of electrons out of the cladding surface which would be equivalent to an effective anodic polarising current.

Table 8.6 Electrochemical Potentials (Volts - SHE) of 304 SS in recirculation line as a function of feedwater concentrations for seven BWRs [476]

Hydrogen Concentration (ppm)	Duane Arnold	Fitzpatrick	Nuclenor	Pilgrim	Nine Mile Point 1	Peach Bottom 3	Hatch
0.0	+0.07	+0.02	+0.01	+0.10	+0.06	–	+0.13
0.5	–0.59	–0.55	–0.44	–0.07	–0.02	–	+0.02
1.0	–0.61	–0.57	–0.48	–0.40	–0.19	–0.27	–0.34
1.5	–0.64	–0.59	–0.50	–0.59	–0.51	–0.37	–0.37
2.0	–	–	–0.50	–	–0.55	–0.43	–0.37
2.5	–	–	–	–	–	–0.46	–0.37

Although we cannot accurately assess the magnitude, or even the direction, of the overall polarising current on the basis of present evidence, we can conclude in a qualitative manner that the current will vary with the local flux spectrum. Thus, changes in the balance between  $\beta$ ,  $\gamma$  and neutron fluxes, as for instance over a plenum or over Gd/ $\text{UO}_2$  pellets compared with over  $\text{UO}$  pellets, would be expected to cause small differences in the surface potential of the oxide at these locations. This offers a possible explanation for the observed differences in nodular corrosion coverage and thickness that occur at the various locations cited above (e.g. high nodular coverage of plena in high flux positions compared with the adjacent fuelled region). In order to assess the order of magnitude of these effects computations are mandatory on detailed components of the radiation induced currents including the  $\beta$  decay from neutron activated nuclei, the Compton and the photoelectrons induced by the  $\gamma$  fluxes.

#### 8.4.2.3 Effect of intermetallics

Although nucleation of nodules at a subset of the intermetallic particles present in the cladding surface has been postulated, other sites for nodule initiation have been proposed, and there is no evidence that currently distinguishes these possibilities in any unequivocal fashion. However, the absence of nodular corrosion of alloys, such as Zr-2.5%Nb, that are free from Zr<sub>2</sub>Fe precipitates (when iron impurity levels are low), and the appearance of nodular corrosion in alloys where progressively larger volume fractions of iron/chromium intermetallics were present, strongly suggested nodule nucleation at intermetallics [276]. This is only circumstantial evidence, however, and work to resolve the question is in progress. However the disappearance of the nodular corrosion observed on irradiated material (section 6.2.1), as a result of  $\beta$ -quenching treatments, supports the influence of microstructure on nodular corrosion. If this work should conclude that nodular corrosion nucleates at intermetallics, we would still need to establish a mechanism by which this might occur and would require selection rules to predict why only a small fraction of intermetallics nucleate nodules in conventional stress relief annealed (SRA) tubing, and why no intermetallics are capable of nucleating nodules in  $\beta$ -quenched tubing.

#### 8.5 CORROSION OF Zr-1%Nb CLADDING

In WWER-440 and WWER-1000 fuel rods operate under conditions of ammonia-boron-potassium-water chemistry at the maximum outer surface temperature of 320 and 350°C respectively (see Table 6.7, section 6.4.3).

The maximum life-time of the WWER-440 fuel rods investigated is five fuel cycles after an operating time of 4-5 years [477]. Under WWER-440 conditions at the average burn-up of 40 MWd kgU<sup>-1</sup>, the corrosion of the cladding is normally accompanied by the formation of a uniform 3-5  $\mu\text{m}$  thick oxide film firmly adhering to the base metal (Figure 8.24). The hydrogen content of claddings is within the range 30-60 ppm. The cladding retains a high ductility factor, i.e. uniform and total elongation at 20°C is >4% and >15%, respectively.

The in-pile corrosion of Zr-1%Nb cladding is significantly affected by oxygen available in the coolant as well as by conditions of not fully suppressed radiolysis of water in a core. In the pilot research reactor MR, fuel rods tested under conditions of strong alkaline water chemistry (no boric acid) for 12,000 h at the average fuel burn-up of 45 MWd kgU<sup>-1</sup> the oxide film thickness measured up to 400  $\mu\text{m}$  [72]. With this extensive oxidation in the presence of free oxidation radicals and oxygen in the core no significant hydrogenation of cladding took place ( $\text{H}_2 < 60$  ppm).

After 626 days of operation in Novovoronezh-1 NPP (WWER-440) at the maximum fuel burn-up of 24 MWd kgU<sup>-1</sup> under conditions of high alkaline water chemistry (pH < 9-10, ammonia,  $\text{O} = 0.015$  mg kg<sup>-1</sup>) the oxide film on the cladding reached 10-30  $\mu\text{m}$  and increased at the centre of the core. For testing times of the fuel rods prolonged up to 1,400 days, the oxide film thickness increased to 100  $\mu\text{m}$  [478,479]. The oxide film was locally damaged, i.e. it showed white oxide areas under which a higher hydride concentration was observed (Figure 8.25).

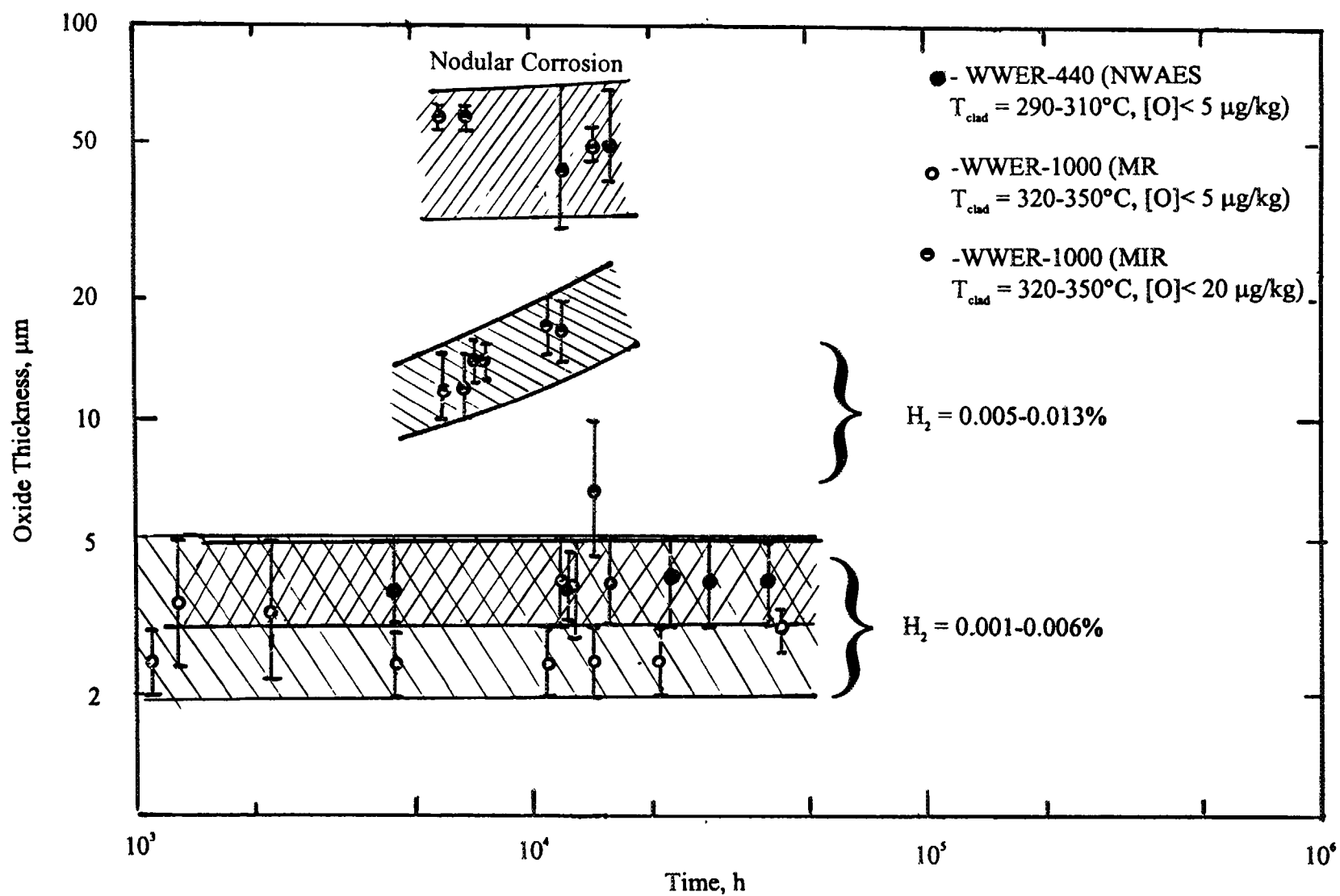


FIG. 8.24. Corrosion of Zr-1%Nb cladding.

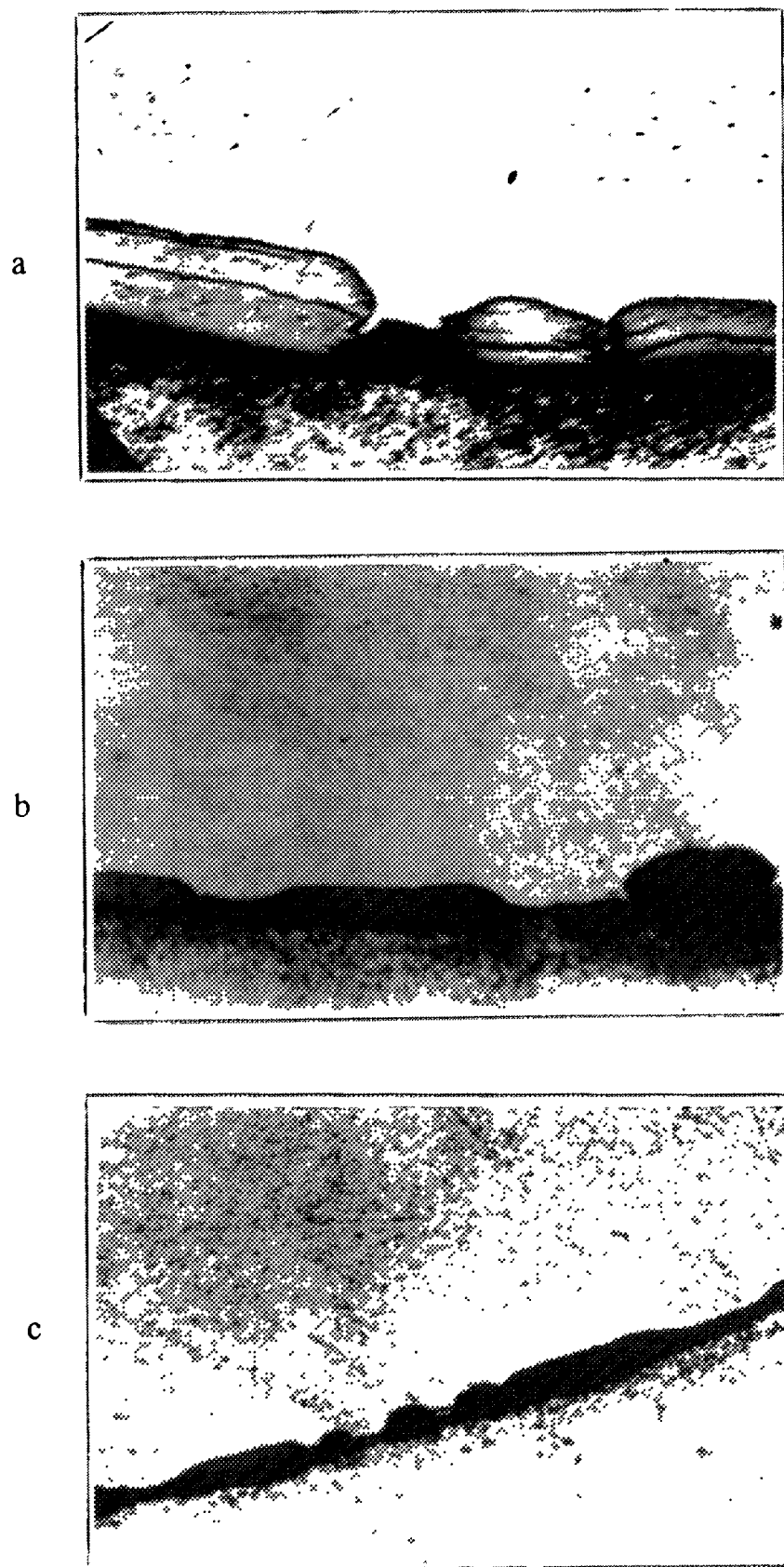


FIG. 8. 25. Kinetics of local film oxidation after irradiation during 496 (a), 745 (b) and 1370 (c) effective full power days.



Under the water-chemistry of WWER-1000s at a coolant oxygen content  $<5 \text{ mg}\cdot\text{kg}^{-1}$ , even when the maximum fuel burn-up  $90 \text{ MWd}\cdot\text{kgU}^{-1}$  is reached the cladding corrosion of test fuel rods is accompanied by the formation of a rather thin oxide film and an insignificant hydrogen uptake (Figure 8.26 and Table 8.7) [477].

Table 8.7. Conditions of experimental fuel rod testing and results of corrosion studies

Parameter	Magnitude	Cladding corrosion and hydrogenation	
		Thickness of oxide film at the outer surface, $\mu\text{m}$	Hydrogen content, ppm
Coolant pressure, MPa	16.0		
Coolant rate, $\text{m}\cdot\text{s}^{-1}$	5.5		
Coolant temperature, $^{\circ}\text{C}$			
inlet	305	3	30-60
outlet	320	(in one case a $15 \mu\text{m}$ film )	
Maximum linear heat generation rate, $\text{W}\cdot\text{cm}^{-1}$			
at the start of irradiation	490		
at the end of irradiation	200		
Fuel burn-up, $\text{MWd}\cdot\text{kgU}^{-1}$			
average	70.0		
maximum	92.9		
Time of testing at different power levels, h	40,164		

When the oxygen content of the coolant is increased to  $20 \text{ mg}\cdot\text{kg}^{-1}$  the cladding corrosion becomes more intensive and, in individual cases, nodular corrosion was observed (Fig 8.26). However, in the course of those tests cyclic power changes took place which could also influence the cladding corrosion intensity as a result of cyclic straining and, hence, damage of the oxide film.

In RBMK boiling water reactors (Table 8.8), where the water chemistry gives no control of the radiolytic gases, the corrosion of Zr-1%Nb cladding is more severe than in WWERs. After 1,048 effective days of operation in the Leningrad-1 NPP (RBMK-1000) the uniform oxide film on the cladding was  $10\text{-}30 \mu\text{m}$  thick (Table 8.9). In some areas of the cladding, nodular corrosion was observed having oxide films at nodule sites up to  $140 \mu\text{m}$  (Table 8.10). There was no nodular corrosion at the fuel-free sites of the plenum [480]. Similar corrosion of Zr-1%Nb cladding was also observed when testing pilot fuel rods in research reactors. After testing under boiling reactor conditions the hydrogen content of the cladding reached 0.02% by weight.

Table 8.8. Fuel rod operating conditions in RBMK-1000s (LNPP)

Parameter	Magnitude
Coolant temperature, $^{\circ}\text{C}$	Inlet, 270; Outlet 284
Coolant pressure, MPa	6.7
Steam content of coolant, % mass	14.5
Maximum heat flux density, $\text{kW}\cdot\text{m}^{-2}$	560
Fuel burn-up, $\text{MWd}\cdot\text{kgU}^{-1}$	Average, 18.8; Maximum 27.0
Time of testing, effective days	1,048

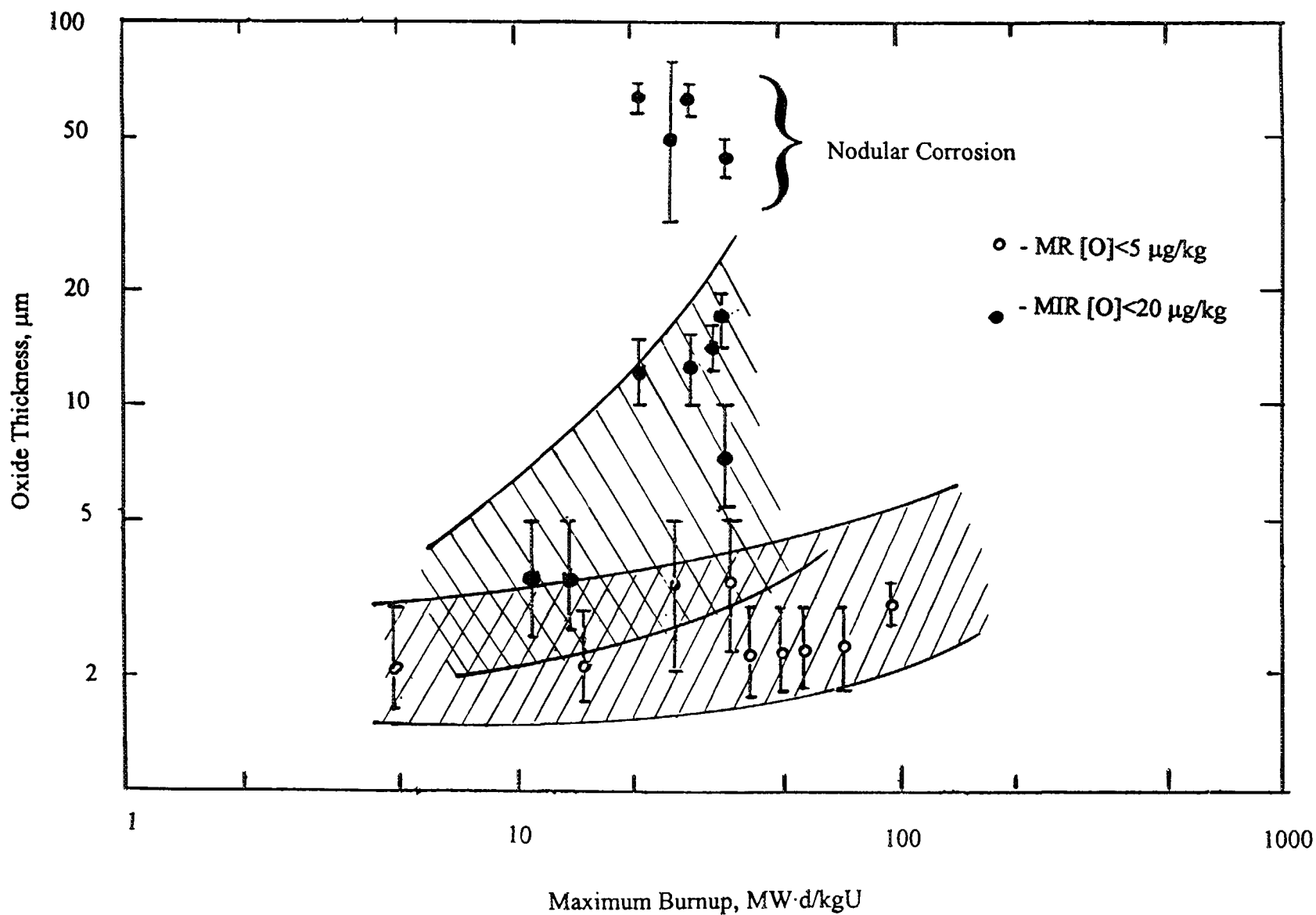


FIG. 8.26. Corrosion of Zr-1%Nb cladding (WWER-1000 conditions).

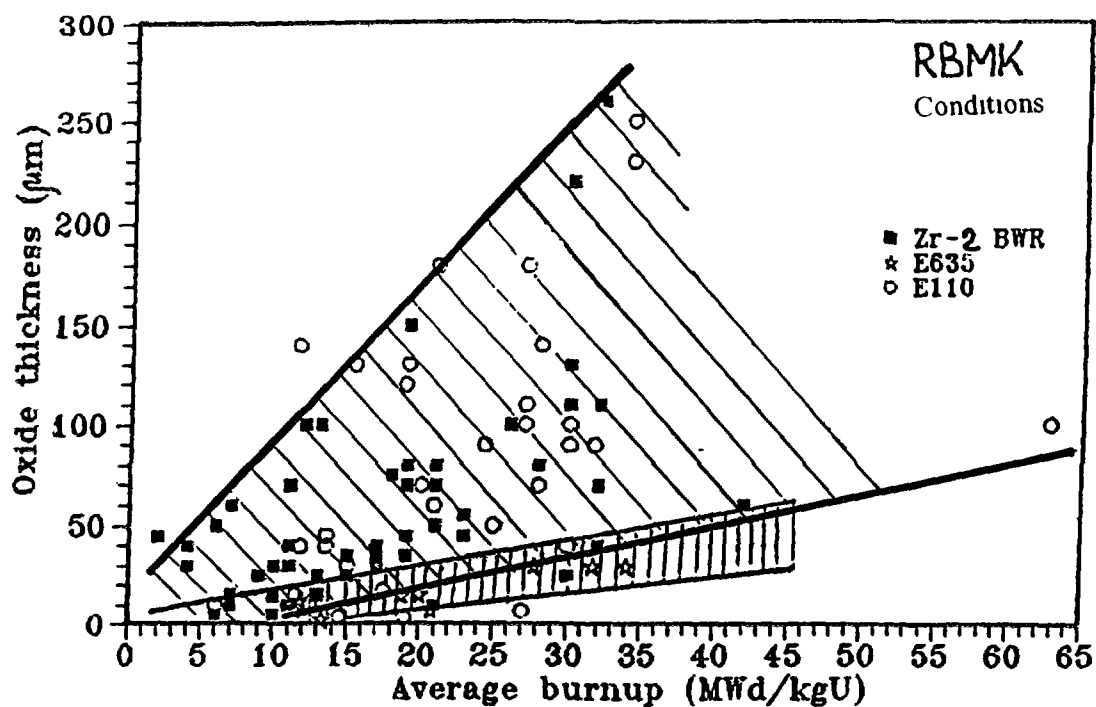
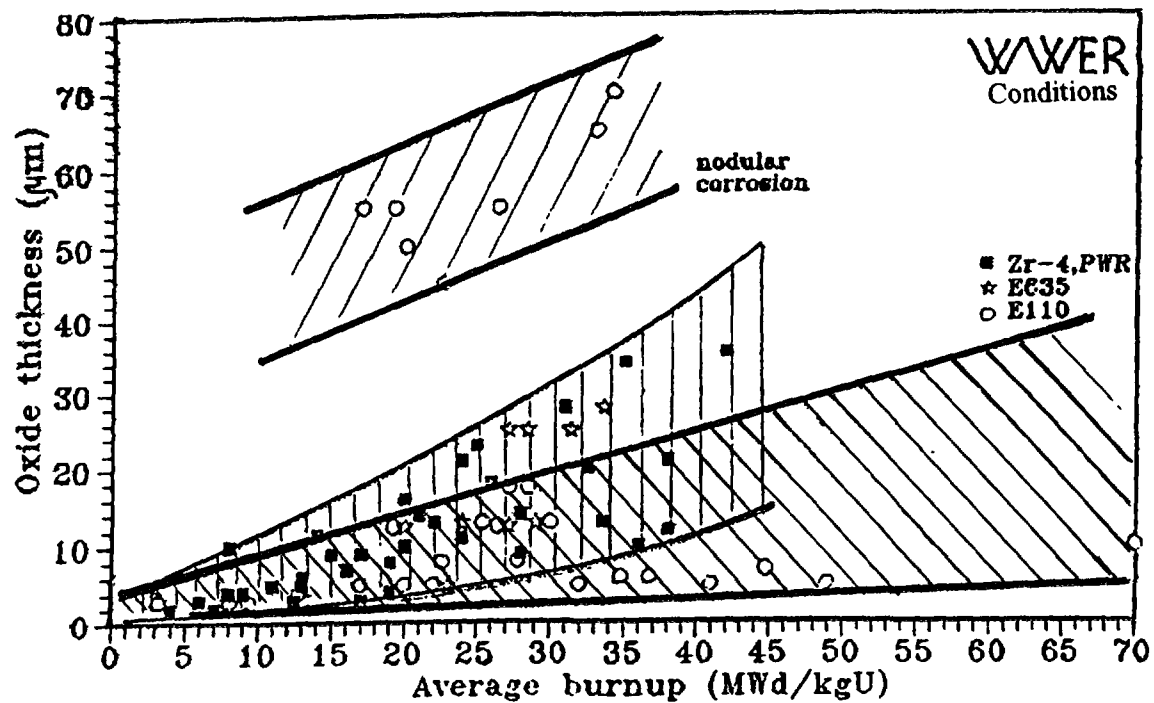


FIG. 8 27. Fuel cladding corrosion in PWRs and WWERs (top) and BWRs and RBMKs (bottom).

Higher oxidation and hydrogenation of Zr-1%Nb claddings in boiling RBMK-1000 reactors does not restrict the service life-time in operating reactors. However, increased service life and fuel operation under load following conditions can limit the life-time of Zr-1%Nb cladding because of corrosion. In Russia a group of Zr alloys have been developed that under boiling conditions have a higher corrosion resistance than those of Zr-1%Nb or Zircalloys. The most studied of this group is a multicomponent Zr alloy containing 1.0%Nb, 1.2-1.4%Sn and 0.3-0.5% Fe. Cladding made of this alloy has a high resistance to nodular corrosion (Figure 8.27) [286,480].

Table 8.9 Thickness of oxide on fuel cladding in an RBMK-1000 operated for 1,048 EFPD

Distance from bottom of FA, cm	Thickness of uniform oxide, $\mu\text{m}$	Oxide thickness in local areas, $\mu\text{m}$	
		adjacent to spacer grids	below spacer grids*
500-800	10.0	40	60
1,500-3,500	30.0	140	380

\*Stainless steel spacer grids.

## 9. PRESENT STATUS OF THE MECHANISTIC UNDERSTANDING

The extent of our understanding of behaviour under irradiation is still limited by the unknown factors that influence oxidation and hydrogen absorption in the laboratory. Before discussing the irradiation behaviour, therefore, it is appropriate to summarise the status of the mechanistic understanding of behaviour in the laboratory.

### 9.1 CURRENT UNDERSTANDING OF THE OUT-REACTOR OXIDATION MECHANISM

#### 9.1.1 Mobile species

It is generally accepted that oxygen is the most mobile species in the zirconium oxide film formed on commercial alloys [481], and that at low temperatures diffusion of oxygen along crystallite boundaries predominates over lattice diffusion [19,20]. It is usually assumed that  $O^{2-}$  is the diffusing species, and evidence for the mobility of OH is presently lacking. The evolution of the oxide microstructure, described in the next section, clearly requires that there be some mobility of the zirconium ions. However, no successful measurement of this quantity has been reported [482], and it is presumed, therefore, to be very low.

The mobility of hydrogen in the zirconia lattice is now, generally, conceded to be very low [189]. Early reports claiming high diffusion coefficients for hydrogen in zirconia films almost certainly studied migration through major flaws or cracks in the oxide that were induced by the experimental techniques. Recent work using nuclear reaction techniques [170], and implanted hydrogen, confirm the low diffusion coefficients for hydrogen in zirconia that have been deduced from hydrogen uptake rates. This low diffusivity of hydrogen in zirconia is supported further by the low jump frequencies shown in nuclear magnetic resonance studies (NMR) of oxide films formed in steam [483]. However, SIMS results show that deuterium does not migrate in the expected way, as a function of time, if the process were diffusion [167], and H and D in the oxide can be exchanged rapidly without further deepening of the overall profile. In addition, some specimens implanted with deuterium lose a significant fraction on annealing without the peak broadening [484]. There is, therefore, still much to be learned about the migration of hydrogen in oxide films, and the state of implanted hydrogen in an oxide should be established before further use of this technique is considered.

The nature of any mobile hydrogen species in zirconia remains to be established, but proton hopping between OH groups appears to be the most probable. Early arguments for H and other possible species can probably be discounted because of the basic methodological flaws in this early work [169,485]. Nevertheless, if hopping between OH groups is the mechanism then the concentration of such species identified by SIMS [167] appears to be much higher than the concentration of OH measured from OH frequencies in the infra-red spectrum [486], even when using the most recent (FTIR) Fourier transform infra-red techniques. This implies a low OH concentration in zirconia films in conflict with the high H or D concentrations that have sometimes been measured in such oxides by Secondary-ion mass spectrometry (SIMS) or nuclear reaction analysis (NRA) techniques [231,487]. The failure to continue to diffuse as a function of time suggests that hydrogen is part of some immobile complex that can nevertheless be exchanged easily. So far, no experiment has demonstrated that the hydrogen measured in the oxide is capable of diffusing into the metal, or that it is other than surface OH groups on the walls of pores or cracks in the oxide. If it were merely the latter, however, the stability of tritium (introduced by oxidation in T<sub>2</sub>O into the ZrO<sub>2</sub>) against exchange with the atmosphere is surprising [189]. There is still much scope, therefore, to improve our understanding of the form and mobility of hydrogen isotopes in zirconia films. Not the least of our areas of ignorance is whether hydrogen migrates generally through the oxide film, or locally at oxide crystallite boundaries or at intermetallic sites. The absence of intermetallic particles from CW Zr-2.5%Nb alloy material (with a low Fe impurity level) has been argued to be one reason for the very low hydrogen uptake rates observed during the aqueous corrosion of this alloy [98].

The mobility of electronic defects (electrons and holes) is also important to the oxidation process because of the high intrinsic electrical resistivity of zirconia [33,75]. The cathodic current during oxidation has been shown to flow principally at the sites of the intermetallic particles in the Zircalloys [488]. Bulk hypostoichiometric zirconia has been shown to be an n-type semiconductor [489]. However, there is a little evidence that the outer layers of the zirconia may become hyperstoichiometric in highly oxidising environments [161], resulting in a thin surface layer with p-type conductivity. Evidence for both electron and hole conduction in zirconia has been found, especially when layers of iron oxides are present on the surface [33]. A similar situation might be expected in the oxides formed over the intermetallics in the Zircalloys, which are very different from the bulk oxide film because of the high concentrations of Fe, Cr and Ni present in the intermetallics.

Since the oxide over the intermetallics is the primary conduction path for the cathodic component of the oxidation current, and since the proton discharge reaction on the surface of this oxide provides the primary source for hydrogen that ultimately finds its way into the metal, the conditions within, and at the interfaces of, these oxides on intermetallics are clearly of great importance (Figure 9.1). At present, however, we have virtually no knowledge of the precise nature of these oxides, although this area is slowly being explored (Figure 9.2) [76,491]. Oxide films on intermetallics typically show more, and larger pores in electron microscope replica studies than the oxide on the alloy matrix (Figure 9.3), only at prior metal grain boundaries are similar large pores typically seen [63]. The characteristic contrast of a pore seen by replica electron microscopy is evident in this figure, and the basis for its development is illustrated in Figure 9.4.

#### 9. 1. 2. Evolution of oxide morphology

Zirconium specimens initially carry a thin air-formed oxide film that is usually 2-5 nm thick [492,493]. The thickness obtained depends on the technique used to measure it. Electron microscopy of these air formed films initially suggested that a large fraction of this film was amorphous. However, opinion now generally [494] supports the idea that it is microcrystalline with crystallites near the resolution limit of the transmission electron microscope (i.e. about 2-3 nm diameter for the diffraction conditions in such a film). Early reports of essentially amorphous films and completely ring-type diffraction patterns were probably the result of the surface preparation techniques that were used [495].

When thermally activated oxide growth ensues, the new oxide is formed below the air-formed film by inward migration of oxygen. In the thickness range 10-100 nm the oxide appears to be almost fully crystalline when formed thermally in oxygen or steam and the average crystallite size increases with increasing oxide thickness [53]. Although the oxide crystallites are not equiaxed during this period, there is probably only a single layer of crystallites present. The question of whether this film forms by the preferential growth of some orientations of crystallite from the air formed film or whether a new layer of crystallites nucleates under the air formed film has not been completely resolved. However, the evidence favours the latter as signs of the persistence of an unmodified air formed film on top of the main oxide have been found [496].

Above about 100 nm additional layers of oxide crystallites grow as evidence of Moiré fringes becomes more common when the oxides are viewed in transmission in the TEM (Figure 9.5). With further thickening successive layers of crystallites develop even in the pre-transition oxidation period for unalloyed zirconium. However, in water and steam at 350-400°C on the Zircalloys there is a strong tendency for preferential growth of some orientations to give a generally columnar crystallite morphology [497]. Deliberate fracturing of these pre-transition films (at about the transition point) can reveal a number of these layers of oxide crystallites (Figure 9.6) [496], although it is not thought that lateral cracks were present between these layers prior to the fracturing of the film [65]. With the successive layers of crystallites formed in these films the mean crystallite size, and the degree of crystallinity appear to increase, and this may result in some highly crystallographic features within the oxide [496]. These features do not necessarily represent individual large crystallites (see later). Also present in these specimens were highly crystallographic pores that have been shown to be voids

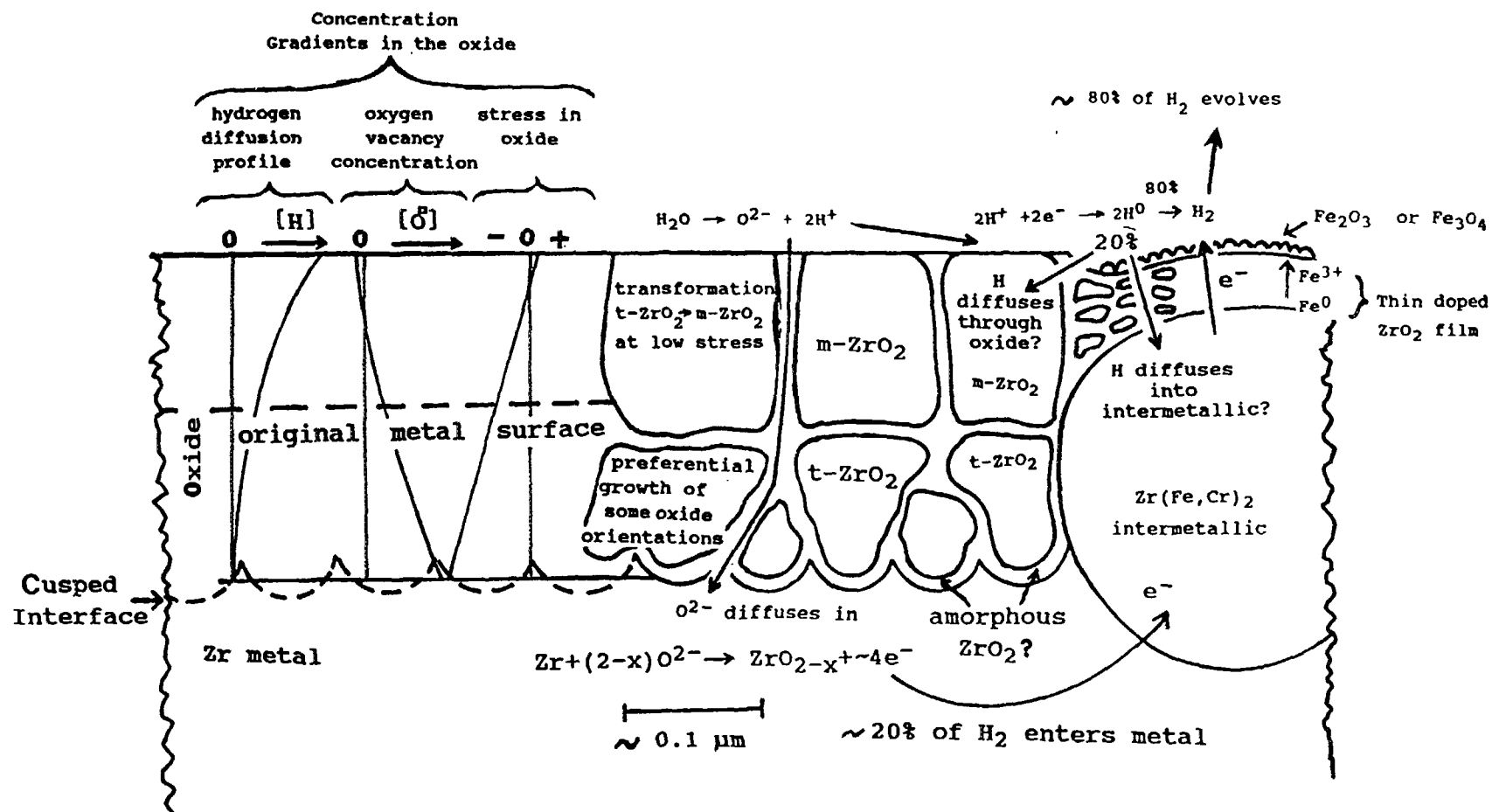


FIG. 9. 1. Simplified diagram of growth processes in thin oxide films formed on Zircaloy-4 in an aqueous environment.

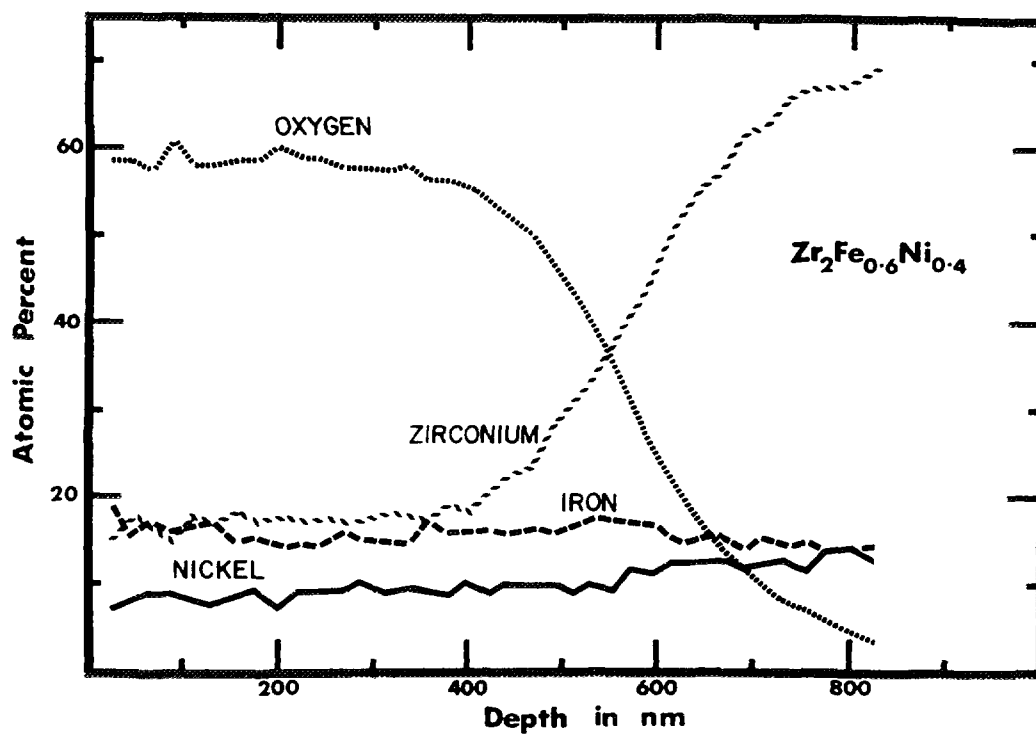


FIG 9 2 Thin oxide on amorphous  $Zr_2(Fe/Ni)$  showing that, although Fe appears to be oxidized, nickel appears to be unoxidized in the oxide [76]

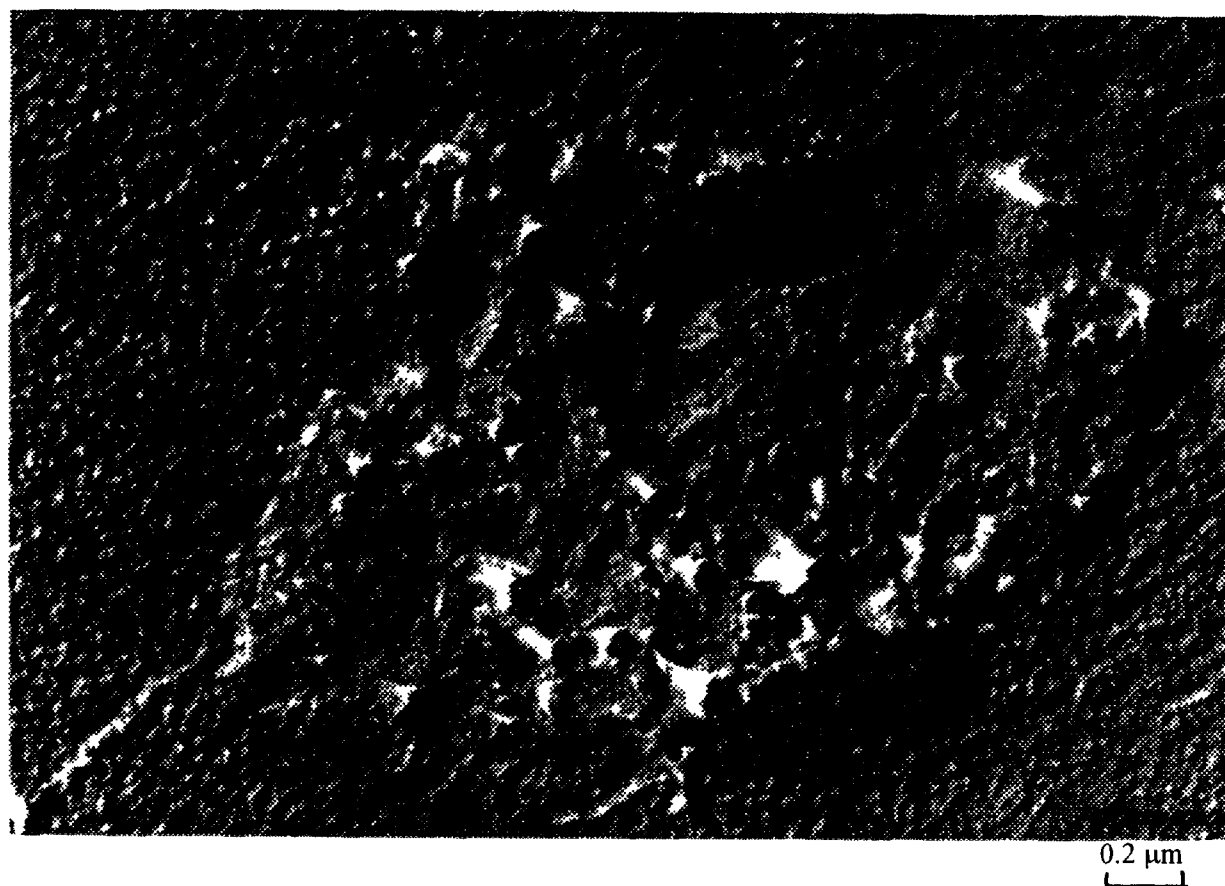


FIG 9 3 Concentration of large pores in the oxide on an intermetallic in a 10 mm oxide on Zircalov-2 (Ac-486, 360°C water,  $\Delta w$  156 mg/dm ) (50,000 $\times$ ) [63]



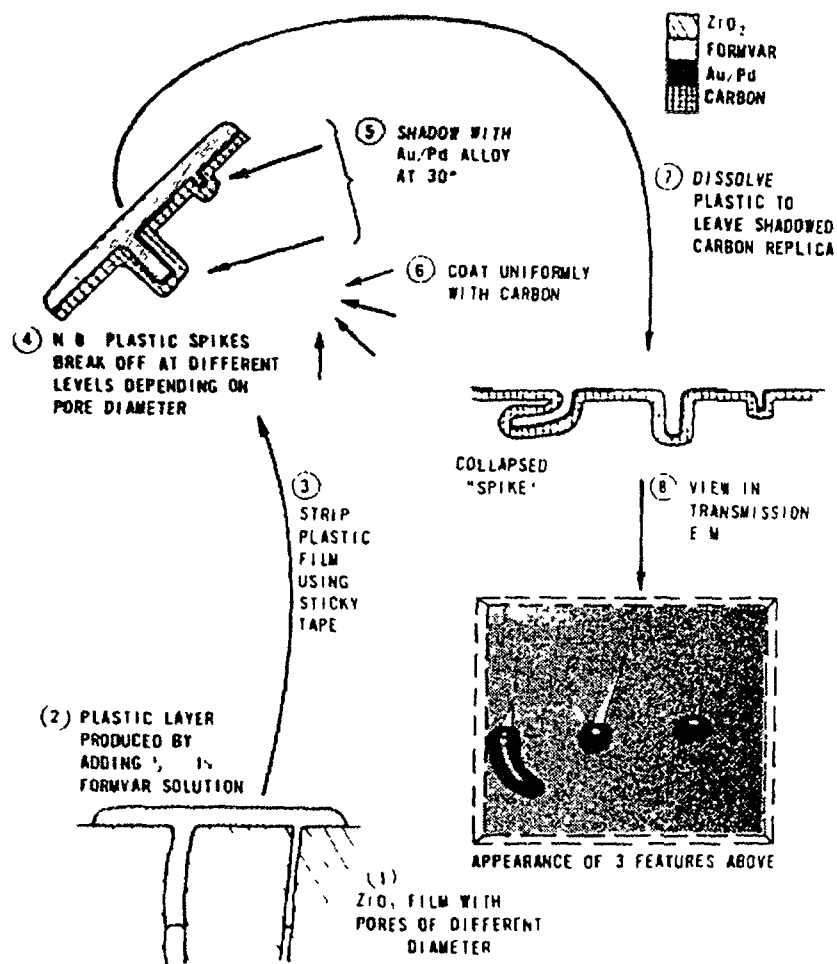


FIG 9 4. Appearance of pores in an oxide film after replication [98]

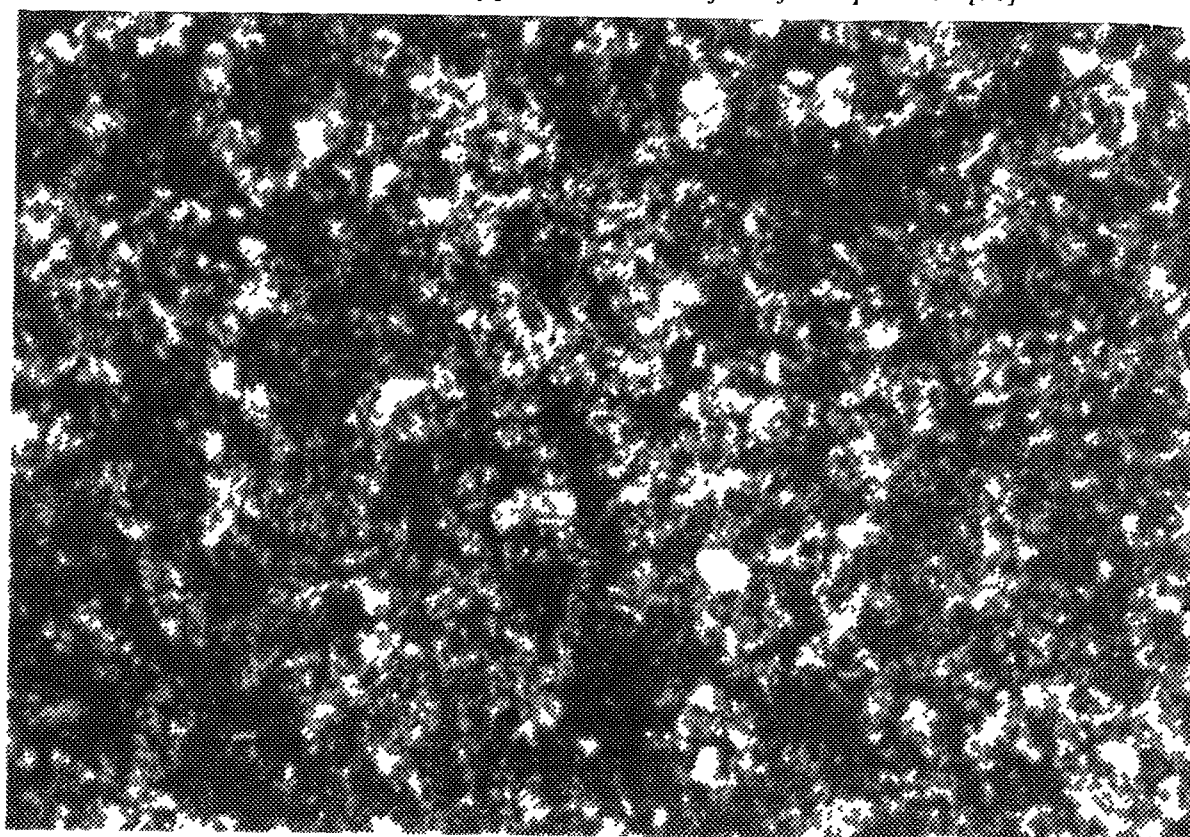


FIG 9 5 Moiré fringes in a thin oxide film formed on Zircaloy-2 (200,000×)

0.1 μm

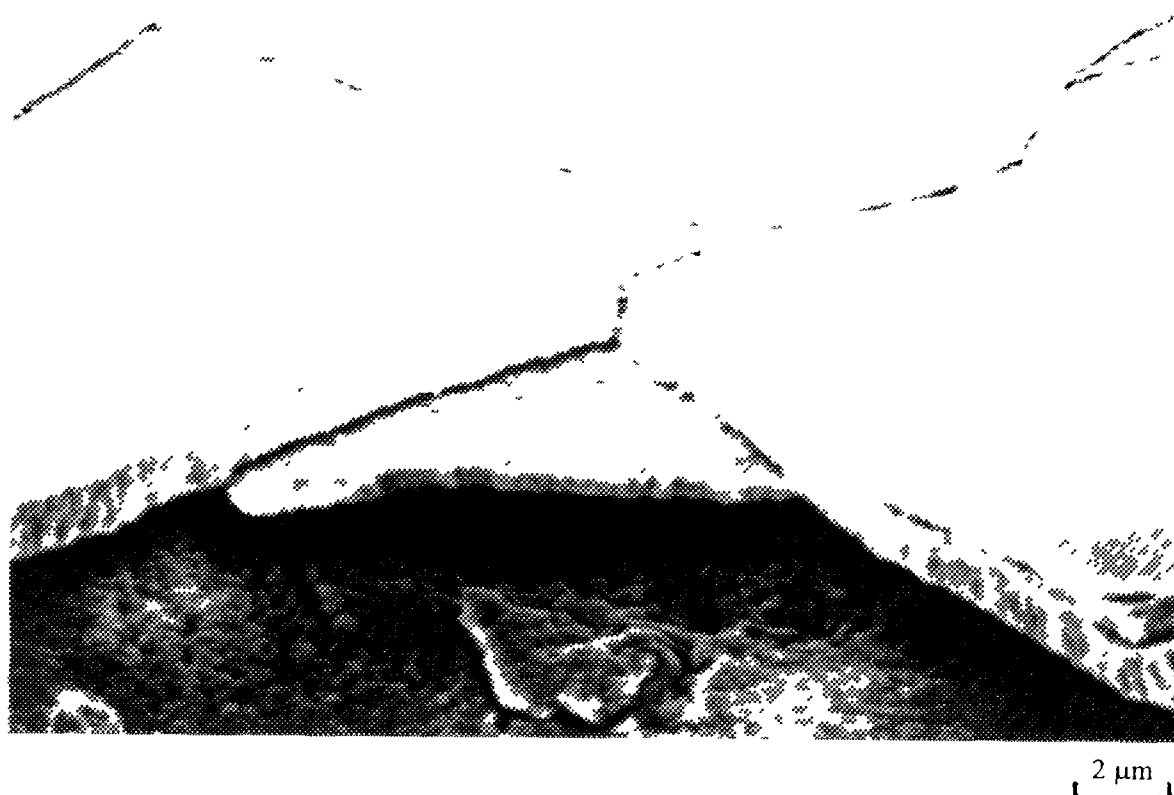
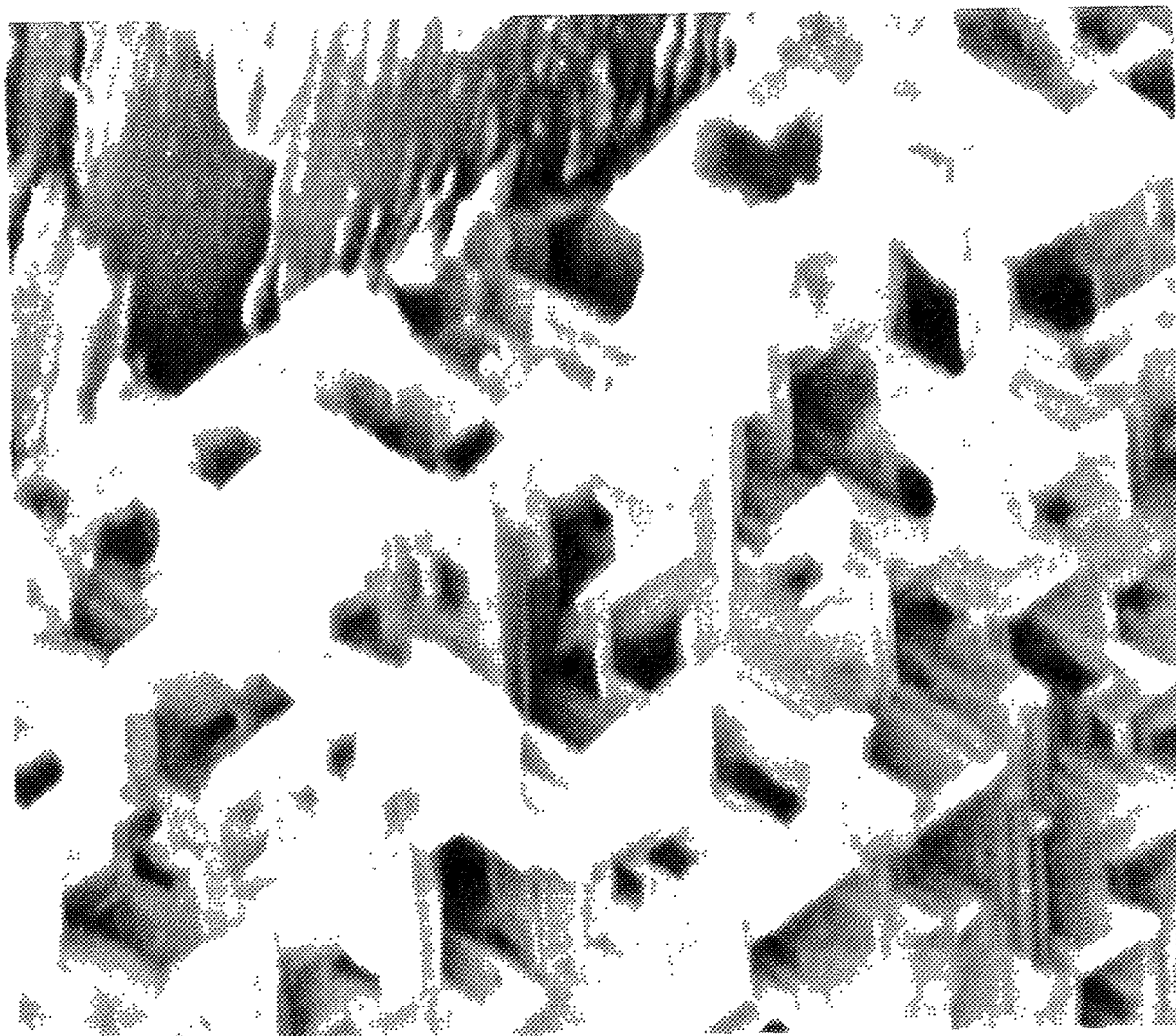


FIG 9 6 Multiple layers in a post-transition oxide on zirconium revealed by fracturing the oxide [496]

by comparing the fractography of both sides of a fractured layer of oxide (Figure 9.7). Such observations clearly have relevance to the onset of breakdown in oxide films, since these crystallographic voids appear to have been present before any surface signs of breakdown were apparent.

During the early stages of growth (up to about 200 nm) the oxide remains parallel sided and uniform over any metal grain, as shown by the uniform interference colours on any grain in recrystallised material. In stress-relieved material the local residual stresses lead to variations in interference colour over individual grains. The oxide thickness on grains of different orientation differs at any time for thermal oxides, although it does not usually for anodically formed oxides. The smoothness of the interfaces and the uniformity of thickness indicates that the electric field is important in this period of oxidation. At ~200 nm a mottling of the interference colours spreads across individual grains and eventually the whole surface. It usually starts at a grain boundary and is caused by the development of roughness at the oxide-metal interface (Figure 9.8) [50]. In mottled areas the film soon becomes grey and then black and the interference colours disappear at a much lower thickness than for anodic oxides which remain much more transparent. This effect is thought to indicate the development of the vacancy concentration gradient in the oxide, as it is the vacancies acting as colour centres that render the oxide opaque in visible light. The thinnest oxides on slow growing grains in unalloyed zirconium can remain transparent and uniform in interference colour even when most of the surface has become black [91]. A small inflection in the oxidation kinetics marks this change in oxide appearance and indicates the change from an electric field controlled growth process to vacancy diffusion control [59]. Beyond this point the cusping of the oxide/metal interface becomes more pronounced as the oxide thickens and may be related to the interfacial oxide crystallite size, although this has not been confirmed [50].



0.5  $\mu\text{m}$

FIG. 9. 7. Highly crystalline porous structure in the inner layers of a post-transition oxide on zirconium. Revealed by fracturing off the overlying layers [496].

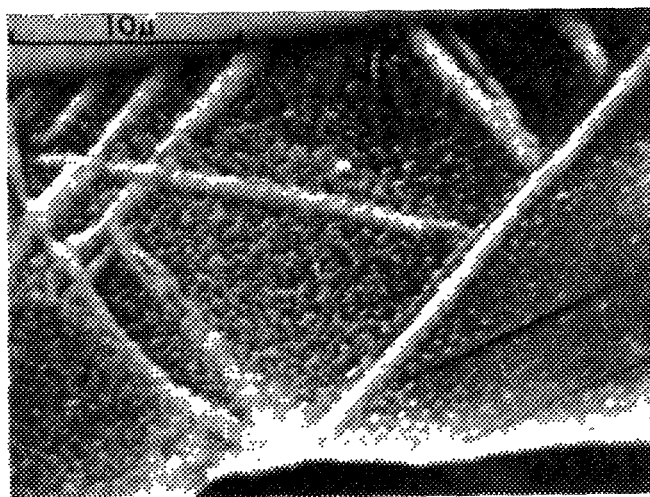


FIG. 9. 8. Inner interface of a thin oxide film ( $\sim 150$  nm) showing roughness spreading across the prior metal grain. The straight ridges of thick oxide are along twins and the curved ones are along grain boundaries. Mean oxide thickness  $\sim 0.4$   $\mu\text{m}$  [50].

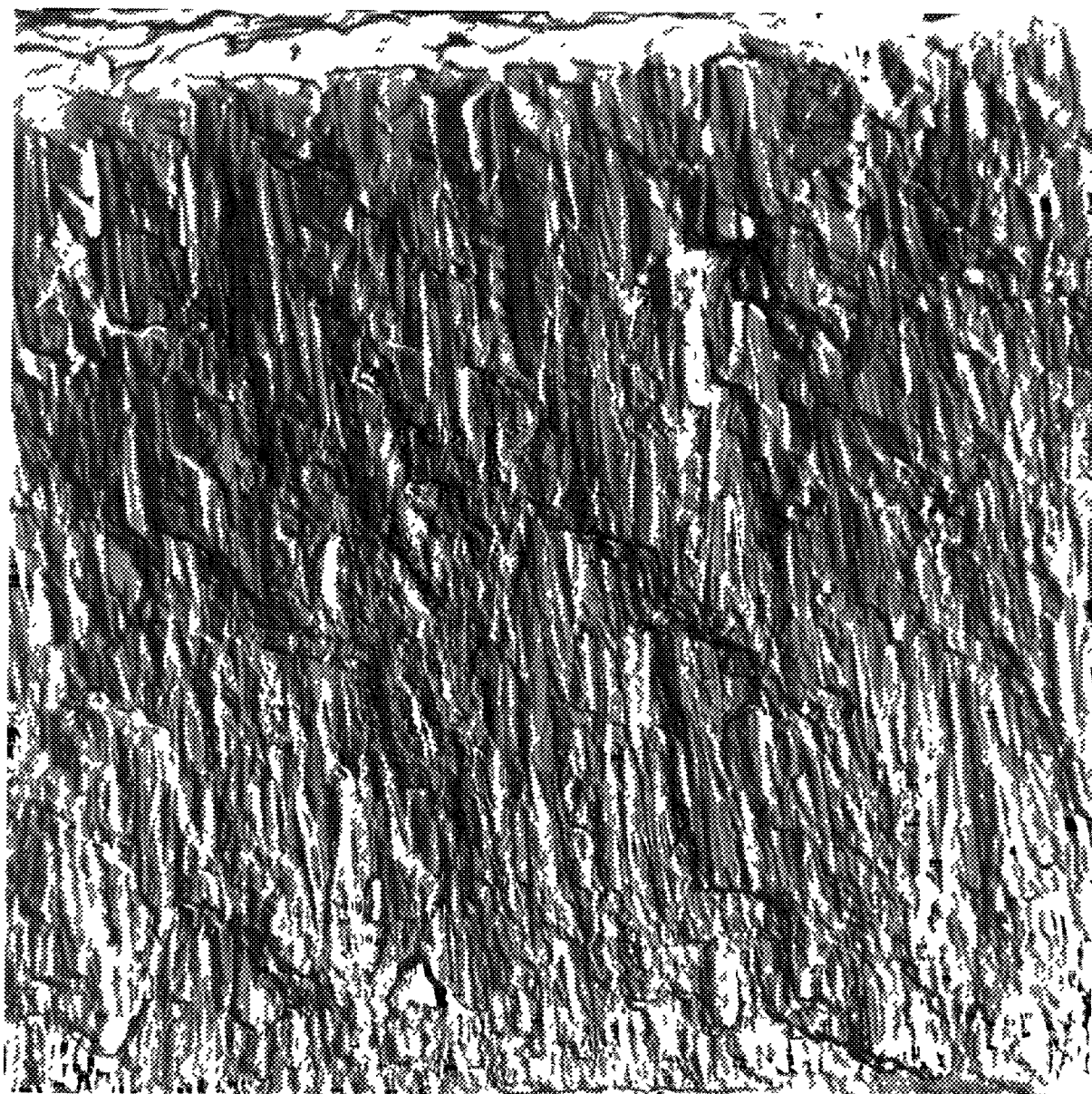
With increasing oxide thickness beyond about 2  $\mu\text{m}$  we are usually in the realm of the post-transition oxide, except during the high temperature oxidation of unalloyed zirconium in oxygen. However, whether or not the thick films are porous, both on zirconium and its alloys a strong texture develops in the oxide by the preferential growth of some oxide orientations [24,25]. This texture is a fibre texture (i.e. the preferred orientations are always perpendicular to the free surface (Figure 9.9) irrespective of the metal grain orientation) and commonly in unalloyed zirconium (and sometimes in the Zircalloys) leads to the formation of large columnar features in the oxide [23,497,498]. These columnar features appear to be single crystal, based on the similarity in size between the columnar features seen in the replicas of oxides formed on Zr at 650°C and those seen in transmission in oxide sections (Figure 9.10) from oxides formed on Zircaloy at 600°C. The large columnar crystallites can be typically >10  $\mu\text{m}$  long  $\times$  0.2  $\mu\text{m}$  diameter when formed at high temperatures such as 600°C, but are much smaller when seen in oxides formed in water at 300-360°C. Thus, the dimensions of these columns are a function of the oxidation temperature, for zirconium, increasing in size with temperature. For the Zircalloys they are evident but small at reactor temperatures, are not always seen at 600°C (compare References [23,78,96,498]), but become very evident (Figure 9.11) during oxidation at high temperatures (e.g. above the  $\alpha/\beta$  transition temperature) that are relevant to LOCA conditions [499]. At these temperatures all the intermetallic particles are in solution, which suggests that one factor limiting the formation of columnar oxides on the Zircalloys at lower temperatures may be a modification in the local oxide morphology resulting from the presence of the intermetallic particles. That the presence of iron from the intermetallics does influence the stability of t-ZrO<sub>2</sub> adjacent to them has been shown recently [43,57].

The orientations of crystallites that preferentially form the fibre texture, seem to be those that are best adapted to minimise the compressive stresses in the plane of the specimen surface [24,25]. From this it is deduced that the driving force for the development of this fibre texture is the compressive stress that has already been generated during the growth of thin films [57,78,500,501].

### 9.1.3 The development and nature of oxide porosity

At the transition in the oxidation kinetics, for the Zircalloys the oxide film becomes demonstrably porous. After this transition it is possible to observe the capillary rise of aqueous electrolytes into the previously impervious oxide [57,502-504] and to force mercury into the same features under pressure [85]. Electron microscopy reveals a variety of features on the oxide surface that can be correlated with the other forms of measurements. The porosity nucleates at a limited number of sites and spreads laterally over the surface. For Zr-2.5%Nb alloy specimens that follow a parabolic oxidation curve (without a distinct increase in oxidation rate [98] corresponding to a transition point) it is similarly possible to identify the presence of porosity from an early stage in the oxidation.

The above techniques identify two primary types of defect that appear in the oxide film. Firstly, cracks which have a high aspect ratio and show up clearly in electron microscope replicas, and secondly, pores having a nearly equiaxed cross section and a range of effective diameters that show up most clearly in the mercury porosimeter traces, but, except for the larger pores, are difficult to image clearly in electron microscope replicas. Early evidence suggested that both types were usually present, but that the relative proportions of each were dependent upon the oxidation conditions. Thus, in water or steam at  $\leq 400^\circ\text{C}$ , where the post-transition kinetic curves are highly cyclic in nature, early replica studies showed that cracks were very common, and porosimetry showed that small pores were also present in considerable numbers. Recent studies [84] on belt ground surfaces have shown that, although cyclic oxidation was observed, few cracks were observed at the outer oxide surface. Internal cracking that does not penetrate the oxide surface could explain the cyclic oxidation. In steam at high temperature and low pressure, where the kinetic transition is smooth, with no abrupt discontinuities, cracks in the oxide are few and small, whereas the porosimeter showed a wide spectrum of pore sizes [63,85]. It has been concluded, therefore, that the discontinuous cyclic post-transition curves result from repeated episodes of extensive oxide cracking.



*FIG. 9. Columnar oxide structure in thick oxide formed on zirconium in air at 650°C. Revealed by fracturing the oxide [23].*

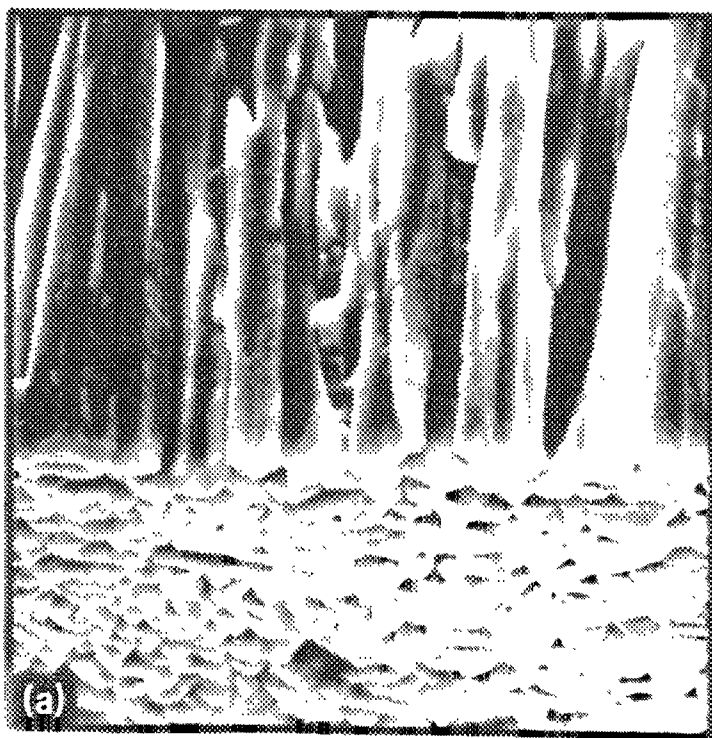
that short-circuit the more regularly developed pore structure of the post-transition oxide films but without necessarily penetrating the oxide surface. At low pressures of oxidant the pore structure develops, but without the succession of cracking episodes. There is no unequivocal evidence for reformation of a thick barrier oxide layer once the pore structure has developed in post-transition oxide films on Zircalloys. The barrier layer on Zr-2.5%Nb alloy surfaces appears to be significantly thicker than on the Zircalloys [98].

It is noteworthy that the low pressure studies often result from continuous oxidation measurements using microbalances, whereas the discontinuous curves typically arise in autoclave testing which is by nature discontinuous and involves repeated thermal cycling. This has led to the proposition that the episodes of cracking may arise from thermal stresses induced during autoclave

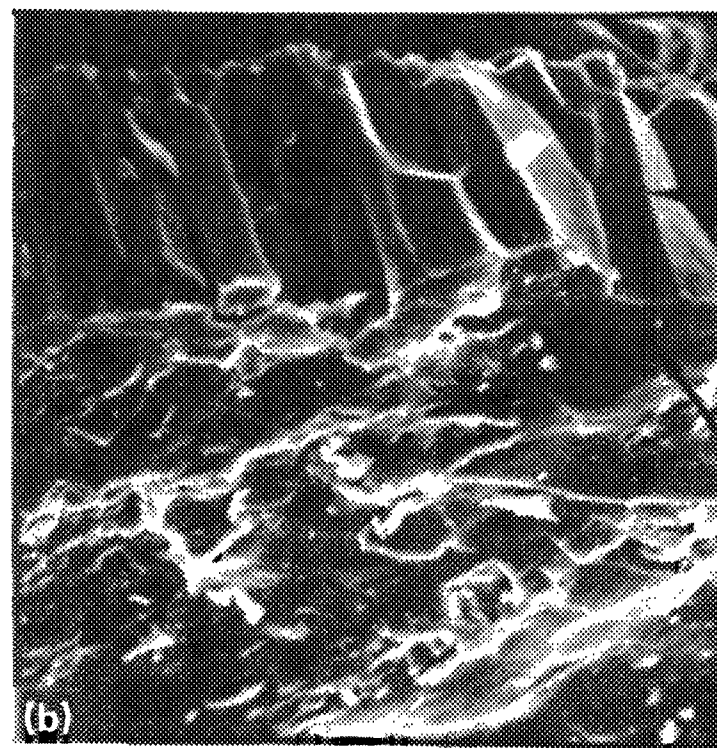


*FIG. 9 10 Thin section of columnar oxide formed on Zircaloy-2 at 600°C in air [498]*





10 μm



CROSS  
SECTION

SCALE-  
ALLOY  
SURFACE

5 μm

FIG. 9. 11. Differences in column dimensions between oxides formed (a) on Zircaloy-4 (2,000 $\times$ ), and (b) on zirconium (1,000 $\times$ ) during oxidation in the  $\beta$ -phase field (1576K) in steam [493].

shutdowns and start-ups. If this were the case then the shapes of the kinetic curves that are measured would, to some extent be artefacts of the oxidation techniques used. A recent experiment monitoring oxide growth continuously by impedance techniques has shown that cyclic oxidation occurs in the absence of thermal cycles [67].

The information obtained from porosimetry and electron microscopy does not permit us to establish the extent of interconnection of the pores that are formed. Some BET surface area measurements have permitted estimates of the extent of porosity [78,494,495] and give values 1-3% pore volume for thick oxides. However, the discrepancy between metallographic oxide thickness and that calculated from the weight gain can be >5% for thick oxides formed in 360°C water or 400°C steam. Mercury porosimetry can also measure pore volumes, but the maximum pressure of commercial porosimeters of this type is insufficient to fill the smallest pores believed to be present in zirconia films. Only by using a porosimeter that measures oxide impedance as a function of pressure can the closeness of approach of the pores to the oxide-metal interface be established [85]. Oxide impedance measurements using the capillary rise of an electrolyte, even if done in vacuo, cannot give this information because of the interfering effects of the double-layer impedances of the pore walls, and associated alternative conduction paths (Figure 9.12). In addition the use of the whole specimen area, rather than the area of the pores, to interpret the data can lead to gross overestimates of barrier oxide thicknesses. A resolution of this question is vital to an acceptance of the nature of the "barrier layer" at the oxide metal interface. The simplest definition of this barrier layer would be "that layer of impervious oxide remaining at the oxide-metal interface when the closest approach and the spacing of the crack/pore network to this interface are considered". During pressure change experiments in both oxygen [90] and steam [91] it is evident that some pores penetrate right to the oxide/metal interface, at least momentarily. Such a layer is unlikely to be uniform in thickness, but could be described either by an average thickness or by a minimum thickness. It is a dynamic phenomenon. By virtue of the inward migration of oxygen that determines the oxide growth rate, today's barrier layer is part of tomorrow's porous outer oxide.

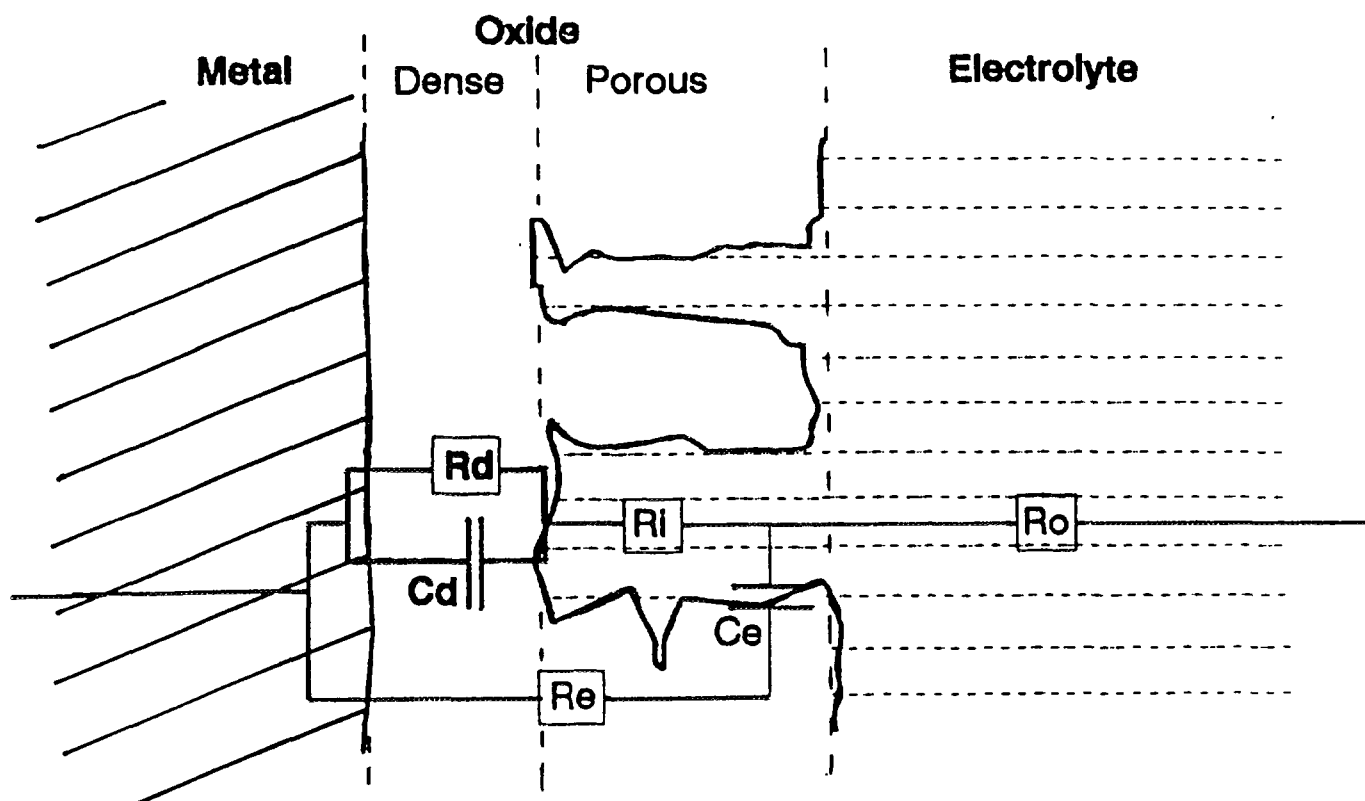


FIG. 9. 12. Equivalent electrical circuit for an oxide with a dense and porous sublayer used in analysis of impedance data [78].



Our lack of understanding of the processes creating the pores and cracks in the oxide film is reflected in the number of conflicting hypotheses that are still unresolved. These hypotheses can be grouped into three classes according to whether the cracks and pores are thought to originate from the outside, from within, or from the inside of the oxide film.

**Initiation at the outside** of the oxide is considered because the compressive stress within the oxide is a maximum at the oxide/metal interface and decreases as one moves out through the oxide, possibly becoming tensile at the outer oxide surface, especially during cooling from the oxidation temperature. This has led to two of the hypotheses below.

- 1 Rapid crack growth initiating at the outer surface as a result of tensile stresses at this location, accentuated by thermal stresses during cooling, especially on curved surfaces such as fuel cladding [89]
- 2 Slow development of small cracks at oxide triple points, once there is a tensile stress there, which propagate inwards as the stresses in the oxide readjust to the presence of surface cracks [502]
- 3 Localised dissolution and reprecipitation of  $\text{ZrO}_2$  starting at the surface (as in thick anodic alumina films) may initiate (or enlarge pre-existing) pores [128]. This has been shown to be the operating mechanism in  $\text{LiOH}$  solutions [73,110,505] and probably is also operating in-reactor where primary knock-on spikes in the oxide may provide additional sites for dissolution [117,118,128]

**Initiation within the oxide** may be demonstrated by the observation of the crystallographic voids already mentioned. There are at least two mechanisms by which this could occur.

- 4 Preferential growth of some crystallite orientations leads to the formation of crystallographic voids in the inner layers of the oxide which become interlinked and propagate to the surface [496]
- 5 The observation that the restricted set of monoclinic  $\text{ZrO}_2$  orientations present in oxide films is that which would be expected if the crystallites formed first as cubic or tetragonal  $\text{ZrO}_2$  leads to a mechanism by which cubic/tetragonal  $\text{ZrO}_2$  is stabilised by the high compressive growth stresses and transforms to monoclinic, initiating small cracks that interlink, once the crystallites have moved far enough from the oxide-metal interface that the compressive stress is no longer high enough to stabilise the high symmetry phase [57,87]

**Initiation from below the oxide** has been observed in high temperature oxidation where a deep, brittle oxygen diffusion zone is formed [506]. Thermal stresses may then initiate cracks in this layer that will run outwards through the oxide to the specimen surface. This would be hypothesis 6.

At present there is insufficient evidence to distinguish among these hypotheses. Effects of discontinuous weighing techniques and thermal cycles on the kinetics would argue for hypothesis 1 at least as the mechanism for forming the high aspect ratio cracks in the oxide. The observation of crystallographic voids in oxides on unalloyed zirconium may argue for hypothesis 4 as the mechanism for forming an interconnected pore network. The dissolution and reprecipitation hypothesis is well established in concentrated  $\text{LiOH}$ , but needs more study for application to low concentrations of  $\text{LiOH}$  and in-reactor water. Nevertheless, more work needs to be done before an understanding of oxide breakdown can be achieved. As a first step the detection (or otherwise) of porosity, within the pre-transition oxide films, that was not connected to the surface, would help to eliminate some of the possibilities.

#### 9.1.4 Oxide barrier layers

Post-transition oxidation rates on zirconium alloys are often similar to the pre-transition rate at an oxide thickness of about  $1\text{ }\mu\text{m}$ , leading to the impression that a post-transition barrier layer of about this thickness is present [91,100,507]. This argument has been justified by pointing to

impedance measurements on the post-transition oxide (by the capillary-rise technique) that seem to confirm this thickness. However, the impedance measurements need correction for the cross-sectional area of the pores and for the double layer impedance, at the surfaces of the pores, that is in series with the barrier layer impedance and this cannot easily be achieved. In addition the argument that matches post-transition rates with a selected tangent to the pre-transition curve is flawed because the fractional area of the surface accessible to the oxidant at the bottoms of the pores in the post-transition oxides is very much less than the area through which oxygen transport occurs during pre-transition oxidation. Thus, the effective barrier layer thickness must always be much less than is indicated by merely matching the slopes of the pre- and post-transition kinetic curves. We need to know how much thinner than this the barrier layer is.

Measurements with a mercury porosimeter, designed to resolve this question by measuring the impedance of the oxide during impregnation with mercury, confirmed that the minimum thicknesses of barrier layers present in post-transition oxides on the Zircalloys are in fact much thinner than the above comparison indicates [85]. The conclusion reached from these measurements was that the residual impervious oxide layer at the bottom of the pore appeared to be no thicker than the air formed oxide on a fresh surface [502]. The fact that the post-transition oxidation rate of the specimen was so much less than the initial oxidation rate of a freshly pickled specimen arises then from the small cross-sectional area of pores that approach this close to the oxide metal interface. It is of course impossible to measure the fractional area of the pores by determining the initial oxidation rate and comparing this with the post-transition rate, since the initial rate could only be determined by extrapolation of short term kinetics to the origin, and theoretical fits to such kinetics will extrapolate to infinite rate at zero time. It is possible to bring specimens up to temperature and measure an initial rate very quickly in a microbalance. Measurements of the initial oxidation rates (as performed above) (Figure 9.13), when compared with post-transition rates under the same conditions (Table 9.1) permit an estimate of the fractional area of the pores. If the minimum barrier layer thickness at the bottom of a pore is the same as the initial air-formed oxide thickness then at their points of nearest approach to the oxide/metal interface (at the lowest temperatures represented in Table 9.1) the pores represent about 2-3% of the interfacial area [158]. This is comparable to what would be expected from the 1-3% porosity that seems to be present in thick post-transition oxide films [78], and suggests that most of the pores approach the oxide-metal interface closely. The apparent increase in pore volume with increasing temperature seen in the data in Table 9.1 is thought to be more probably a result of increasing errors in measuring initial oxidation rates, as the temperature increases, than of a real increase in porosity. Other data [320,498] tend to indicate a lower porosity for specimens oxidised at high temperatures.

Table 9.1. Initial and post-transition oxidation rates for Zircaloy-2 (batch Z8006) [158]

Temperature, °C	Initial rate (from microbalance curve) mg·dm <sup>-2</sup> ·day <sup>-1</sup>	Post-transition rate (in 1 atm steam) mg·dm <sup>-2</sup> ·day <sup>-1</sup>	Ratio
450	3.03×10 <sup>2</sup>	8.01	2.7×10 <sup>-2</sup>
500	1.27×10 <sup>3</sup>	32.2	2.5×10 <sup>-2</sup>
550	2.10×10 <sup>3</sup>	115	5.5×10 <sup>-2</sup>
600	4.68×10 <sup>3</sup>	360	7.7×10 <sup>-2</sup>

The barrier layer, however, must be a residual entity of very variable thickness, and the local situation must change continually as fresh oxide forms, pores continue to grow, and occasional cracks or pores propagate right up to the interface. That a small number of cracks in the oxide do initially penetrate right to the interface (although their tips must immediately repassivate by the formation of fresh oxide) was shown at an early date by the pressure change experiments already mentioned [90,91] and by Pemsler [508], who replaced the oxidant at the end of his experiments with HCl gas (to remove zirconium as a volatile halide), and hence decorated the bottoms of any cracks which, at that moment, penetrated to the oxide-metal interface. His experiments showed that, at any point in time, only a few such cracks were present, thus confirming the dynamic nature of the situation near the oxide-metal interface. This also supports the concept that the oxide barrier-layer can only be a

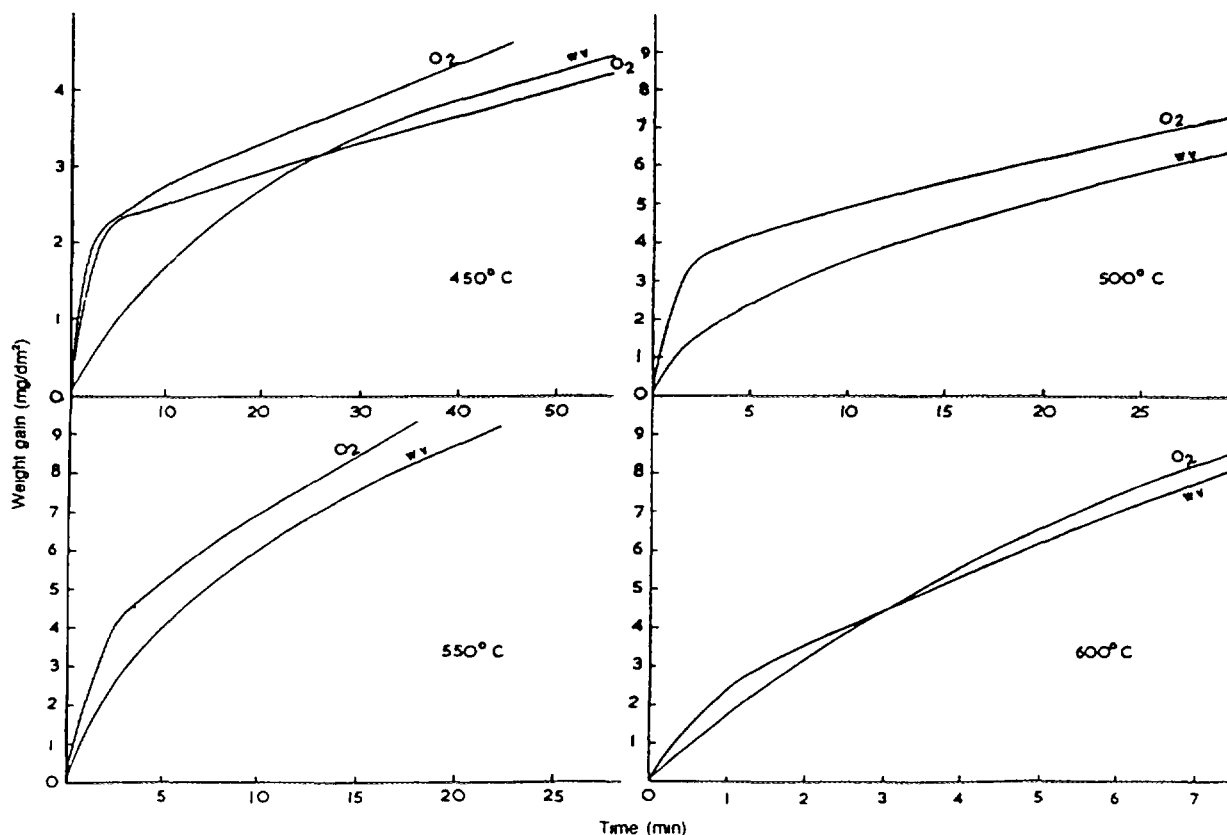


FIG 9.13 Initial Zircaloy-2 oxidation rates in oxygen and water vapour [158]

time averaged phenomenon with some bare metal possibly present at any instant in time. Any subsequent measurement of the barrier layer thickness at room temperature gives a minimum value equal to the air-formed oxide thickness (since any such bare spots would have repassivated before a measurement could be made).

Measurements of the average barrier layer oxide thicknesses on the Zircaloys and Zr-2.5%Nb alloy confirm that the latter shows a much thicker mean compact layer thickness than the former [98]. This may be understandable since the Zr-Nb alloy tends to obey para-linear kinetics (i.e. a rate law that changes continuously from parabolic or cubic to linear without any distinct increase in rate that would indicate a transition in the oxidation mechanism) which would suggest that the porosity starts to develop at the outside of these oxides, and at an early stage of oxide growth. This difference may also mean that during the oxidation of Zr-Nb specimens there is no point in time when cracks or pores approach close ( $<10$  nm) to the oxide/metal interface. This effect, coupled with the low diffusivity of hydrogen in zirconia could be the primary reason for the very low hydrogen uptake rates shown by Zr-Nb specimens.

Attempts to observe the situation at the oxide-metal interface by the examination in the TEM of slices of oxide taken through the interface have had limited success [78,96]. They suggest that even in thick films the oxide becomes crystalline close to the interface, but so far have failed to establish the distance of closest approach of pores to the interface. SEM studies that show evidence for pores emerging at the inside surface of films stripped from Zircaloy-2 specimens [84,98], confirm the closeness of approach of the pores to the interface, but cannot give an unequivocal measure of this, since it is known that a very small amount of oxide dissolves in the mixed nitric-hydrofluoric acids used to remove these oxide films [509]. Nevertheless, such observations tend to support the above argument that some pores approach very close to the oxide-metal interface at least momentarily during post-transition corrosion.

Oxide films formed on Zr-2.5%Nb alloy specimens show more complicated structures as a result of the two-phase nature of the matrix. In general the oxide films are similarly microcrystalline to those on the Zircalloys, show columnar growth, and develop porosity. Detailed studies of these oxides have been reported [81-83,167,510], however, little or no electron microscopy has been reported on oxide films on Zr-1%Nb alloy cladding.

#### 9.1.5 Effect of some variables on the oxide structure

Oxide films on zirconium alloys are typically relatively parallel sided (apart from the roughness that develops at the oxide/metal interface), and oxidation rates are generally similar in oxygen, air, water, steam, CO<sub>2</sub> and oxygen containing sodium at the same temperature [481]. Thus, the oxidation has been regarded as being controlled entirely by solid-state processes within the oxide film except in LiOH. Nevertheless, there are some situations where significant differences from this situation occur. We will consider here the more severe of these effects, namely nodular corrosion in high temperature, high pressure steam and irradiation corrosion. The case of accelerated corrosion in concentrated LiOH has already been discussed. In each instance only observations of the oxide morphology will be discussed.

##### 9.1.5.1 Nodular corrosion in high temperature steam

Above ~450°C in high-pressure steam the oxide films on the Zircalloys cease to be approximately parallel sided and develop roughly circular nodules of thick oxide with a lenticular cross-section [129]. These nodules continue to grow in diameter and thickness until they coalesce. At an early stage of their growth they can be seen to be heavily cracked, with the cracks often concentric with the nodule [141]. The nature of this cracking can be explained largely by the geometry of the nodule and the stresses generated by its growth.

The process that triggers nodule nucleation is still argued [132], the effects of this on the oxide morphology are not well characterised but it appears that nodular oxide tends to comprise equiaxed rather than columnar sub-structures [78]. Attempts to look at sections of these nodules [78], or electron or X-ray diffraction through them [137], have not produced consistent results. The question of whether the oxide is more, or less, amorphous than the uniform oxide is unresolved, as in reactor water the additional possibility of a dissolution and reprecipitation of ZrO<sub>2</sub> must be considered [117,118,128]. Such a process could lead to the precipitation of hydrous zirconia in a rapidly growing porous oxide, such as the nodules, and this might appear as amorphous zirconia when sections through nodular oxides, or X-ray or electron diffraction analyses of them were made.

##### 9.1.5.2 Accelerated corrosion in-reactor

Examinations of irradiated oxide films have been limited. Spitznagel et al. [511] could find no differences between oxide films bombarded with protons and unirradiated oxide films. X-ray evidence shows no signs of the formation of irradiation induced cubic ZrO<sub>2</sub> [26]. Garzarolli et al. [320] examined oxide films from irradiated fuel cladding in the scanning electron microscope. Although there was considerable variability in both the morphology of the oxide/metal interface and fractures of these oxides, no clear distinction between irradiated and unirradiated oxides was evident. A similar conclusion was reached by Cox [98] based on SEM examinations of the oxide/metal interface of irradiated and unirradiated oxides. Garzarolli's conclusions [320] that oxide films that had shown large in-reactor enhancements of corrosion rate were more crystalline in the oxide/metal interface region than comparable thickness unirradiated oxides (the latter often showed an apparently diffuse layer near to the oxide/metal interface) were based on judgements of the morphology seen in the SEM studies. Since this appearance at the edges of oxide samples can be affected in a major way by the imaging conditions, and in particular by local surface charging, these conclusions should be treated with caution. Recently Lemaignan has reported some TEM images of the oxide from fuel cladding irradiated in a PWR [80]. The oxide crystallites in the outer oxide were larger than those found in oxides of similar thickness grown in the laboratory, whereas close to the metal/oxide

interface the reverse was the case. This may indicate hydrothermal growth of larger crystallites by a dissolution and reprecipitation mechanism. Continuation of this work, on degraded oxide produced during rapidly accelerating corrosion, in the subsequent exposure cycle in BR-3 has confirmed such a deduction. Furthermore, it has shown that most of the oxide, formed during this rapidly accelerating oxidation, was in the form of layers of very porous, possibly hydrated, large equiaxed crystallites interspersed with layers of more normal appearing columnar oxide. Thus, it appears that the degradation processes seen here (which were ascribed to LiOH concentration) may take a repetitive cyclic form of oxide degradation followed by regrowth of a more normal oxide layer [113]. Further studies of irradiated oxide films are needed to establish confidence in the above hypothesis.

The task of studying the oxide-metal interface in the transmission electron microscope is difficult and thankless. Even on unirradiated specimens the results are very difficult to interpret [498], and limited evidence on irradiated specimens is only now becoming available. Nevertheless, evidence of this nature is vital to any understanding of the effects of irradiation on corrosion, and despite its technical difficulty investigators should be encouraged to tackle this problem. It will be important that both bright and dark field studies be undertaken and the epitaxial relationships as well as the crystallinity of the oxide at the interface be examined. Further characterisation of thick degraded oxides formed in-reactor is also needed.

## 9.2 EMPIRICAL CORRELATIONS OF EFFECTS OF IRRADIATION

Early in the study of the corrosion of zirconium alloys in aqueous reactor systems an example of grossly enhanced corrosion was observed during the development of the Homogenous Aqueous Reactor [512]. The primary cause of this rapid corrosion was the high energy deposition rate from the fissioning of the aqueous uranyl sulphate solution. The micromechanism by which this enhancement took place was not satisfactorily established, and the question of whether it resulted from enhanced solid state transport processes within the zirconium oxide, or enhanced dissolution and reprecipitation of that oxide, appeared to favour the former as clear evidence for the latter was not found at that time [513].

At much the same time evidence in PWRs suggested little or no enhancement of corrosion for the relatively short exposure times for which data were available [514], whereas early results in BWRs did show a significant increase in the corrosion rate [515] primarily in the form of nodular corrosion. In the latter instance, it was suggested that the poor metallurgical condition of the Zircaloy was an important factor, and subsequent improvements in behaviour have resulted largely from improvements in the physical metallurgy of the alloy. These have revolved around the production of material with a very small uniformly distributed second-phase precipitate population [132,133]. Mechanistic arguments supporting these fabrication changes have been based on observations made in ~500°C high pressure steam, and have been largely corroborated by the improved behaviour observed in BWRs [132,133]. However, whether the particle size is the critical factor, or is merely another useful correlation that aids in optimising cladding, may be cast into doubt by a recent experiment by Isobe et al. [148] in which a single "very large" intermetallic (welded on the end of a specimen) protected the whole specimen against poor corrosion in 360°C water. This experiment needs confirming under more controlled conditions where the electrochemical currents are measured and controlled.

In-reactor experimentation, designed to provide accurate measurements of the solid state effects of irradiation on the corrosion process were mainly carried out in CO<sub>2</sub> [516], steam [517] or fog [518] rather than in aqueous systems and confirmed that increases in the oxidation rates of zirconium alloys, although small, did occur during the growth of barrier-type (pre-transition) oxide films (Figure 9.14). Despite some argument as to whether the surface temperature of the specimens was known and well controlled in the experiments in gas atmospheres, the similarity in the sizes of the effects seen in fog (where there were no specimen cooling problems), CO<sub>2</sub> and dry steam suggests that these results are reliable. However, the actual increases in rate under irradiation (as established by weight gain measurements) were small, and no evidence for very large effects was found in such

experiments. Large effects seemed to be restricted to specific water chemistry conditions in aqueous systems. Estimates of oxidation rates in aqueous systems are often made from metallographic measurements of oxide thickness (a technique that is not very accurate for thin oxides), and such measurements in PWR water chemistry showed little or no effect in the pre-transition period, with a significant increase in in-reactor corrosion rate after transition (Figure 9.15) [519].

Comparisons of oxide thicknesses (measured after in-reactor exposure by eddy-current techniques) with those calculated from models of the corrosion process often lead to “acceleration factors” in the range 2 to 4. However, there is no justification for relating these factors to an irradiation effect, since they are basically “ignorance factors” that reflect missing components in the models. One of these components might be an irradiation effect, but has not been proved to be such. Where measurements have been made after short exposures in aqueous systems by weight gain the results have often given lower values for oxide thicknesses below about 5  $\mu\text{m}$  than expected (Figure 9.16) from the out-reactor corrosion curve [124,128,520], or from the visual appearance of the oxide. An example of the results from such a test is given in Table 9.2. Because the weights of the irradiated specimens were obtained on a different balance from that on which the initial weighing was done [520] there has been a strong temptation to dismiss these low weight gains as experimental error, and to concentrate on cases of clearly observed increased corrosion. Perhaps we have missed important clues to the material behaviour by so doing, since loss of  $\text{ZrO}_2$  in this thin film region is difficult to explain except by a dissolution process. Apparently normal pre-transition oxide thicknesses obtained by metallography (Figure 9.15) would be expected to be associated with lower than expected weight gains if dissolution and reprecipitation of the oxide were occurring in-reactor, since not all the reprecipitation might occur on the specimen surfaces in a flowing system. Further results, where both weight gains and oxide thicknesses (measured by an independent technique) were available, are necessary to resolve this situation.

## 9.2.1 Development of irradiation corrosion mechanisms

### 9.2.1.1 PWR/PHWR corrosion

The observations [121,280] of accelerating corrosion rates with increasing oxide thickness above  $\sim 10 \mu\text{m}$  on both PHWR (Figure 9.17) pressure tubes (with no heat flux), and on PWR cladding (Figure 9.18), drew attention to Johnson’s [449] earlier observations that changing the water chemistry from oxygenated to hydrogenated conditions produced no reduction in the corrosion rate of Zircaloy specimens already carrying oxide films thicker than a critical value. This “thick-film” hypothesis postulates that oxidation rates in-reactor increase above the critical thickness and continue to increase with increasing oxide thickness in PWR chemistry conditions because the chemistry inside the porous post-transition oxide progressively deviates from that in the bulk water as the oxide thickens. Chemistry conditions inside thick oxides are, thus, assumed to become more like a BWR chemistry.

While this hypothesis does not address the critical question of precisely what aspect of the BWR chemistry induces accelerated corrosion, and how this acceleration is achieved, it does qualitatively explain many of the observations of enhanced corrosion in PWR-type water chemistry. In particular it explains the similarity in the oxidation behaviour of Zircaloy-2 pressure tubes in both N-reactor [521] and Pickering [121] despite the difference in water chemistry. The N-reactor used  $\text{NH}_4\text{OH}$  for pH control while Pickering uses  $\text{LiOH}$ . However, the “thick-film” hypothesis depends upon an inability to replenish hydrogen within the porous oxide structure to permit the postulated change in water chemistry within the pores, and this is its fatal flaw. Firstly, in an initially hydrogenated aqueous system, hydrogen is not used up in suppressing water radiolysis, so that restricted diffusion down narrow pores is not an important factor. Secondly, after the development of porous post-transition films on the Zircaloys both the anodic and cathodic components of the oxidation process should be occurring at the outside of any residual barrier oxide layer and at the bottom of the pore network. Thus, provided that less than 100% of the hydrogen released by the

Table 9.2. Low weight gains observed in short in-reactor loop tests  
(second materials test bundle — U2500 phase II)

Material:	(See column headings)	Specimen Preparation:	Pickled
Specimen Size:	30 x 15 x 1 mm	Time:	25 days
Conditions:	pH 10 LiOH + H <sub>2</sub> , ~260°C	Neutron Flux (>1 MeV):	1.9 x 10 <sup>13</sup> n <sub>f</sub> v

	Zircaloy-2 (Ac)		Ni-free Zircaloy-2 (M)				Zr-2.5% Nb (T)		Zr-2.5% Nb -0.5% Cu (Am)		Zr-2.5% Nb-0.2% Fe-0.1% Cr (A)	
	$\Delta W$ (mg/dm <sup>2</sup> )	$\Delta H$ (mg/dm <sup>2</sup> )	$\Delta W$ (mg/dm <sup>2</sup> )	$\Delta H$ (mg/dm <sup>2</sup> )	$\Delta W$ (mg/dm <sup>2</sup> )	$\Delta H$ (mg/dm <sup>2</sup> )	$\Delta W$ (mg/dm <sup>2</sup> )	$\Delta H$ (mg/dm <sup>2</sup> )	$\Delta W$ (mg/dm <sup>2</sup> )	$\Delta H$ (mg/dm <sup>2</sup> )	$\Delta W$ (mg/dm <sup>2</sup> )	$\Delta H$ (mg/dm <sup>2</sup> )
In-flux specimens	-9	1.367	4	0	0.343	(2.377)	(-22)	0.606	2	1.696	0	0.946
	2	0.960	6	2	1.022	0.245	6	0.797	-9	(4.420)	2	(3.778)
	-6	0.757	-4	8	(3.475)	0.678	2	1.563	0	1.545	(25)	0.718
	9	0.511	(22)	4	0.453	(4.853)	4	(14.0)	8	1.644	4	0.629
	4	0.873	2	2	(2.840)	0.790	0	0.558	11	(9.670)	2	0.496
	4	1.276	0	4	0.480	0.671	0	0.814	0	1.923	2	0.875
	(-30)	0.696	6	3	0.415	0.279	2	0.757	9	1.756	-4	(3.076)
	2	(3.671)	(16)	2	0.645	0.698	4	0.575	7	1.878	4	(77.0)
Means	0.85	0.918	2.8		0.561		2.6	0.808	3.5	1.74	1.4	0.733
Appear- ance	Shiny black oxide		Shiny black oxide				Dark oxide show- ing pink inter- ference colours		Black oxide		Black oxide	
Est. from film thick- ness	~15 mg/dm <sup>2</sup> non-uniform		≥10 mg/dm <sup>2</sup>				6-8 mg/dm <sup>2</sup> non-uniform		≥10 mg/dm <sup>2</sup>		≥10 mg/dm <sup>2</sup>	
Lab. Auto- clave	9-11 mg/dm <sup>2</sup>		9-11 mg/dm <sup>2</sup>				10-11 mg/dm <sup>2</sup>		8-10 mg/dm <sup>2</sup>		15-17 mg/dm <sup>2</sup>	

NB: Figures in brackets have been omitted in calculating means

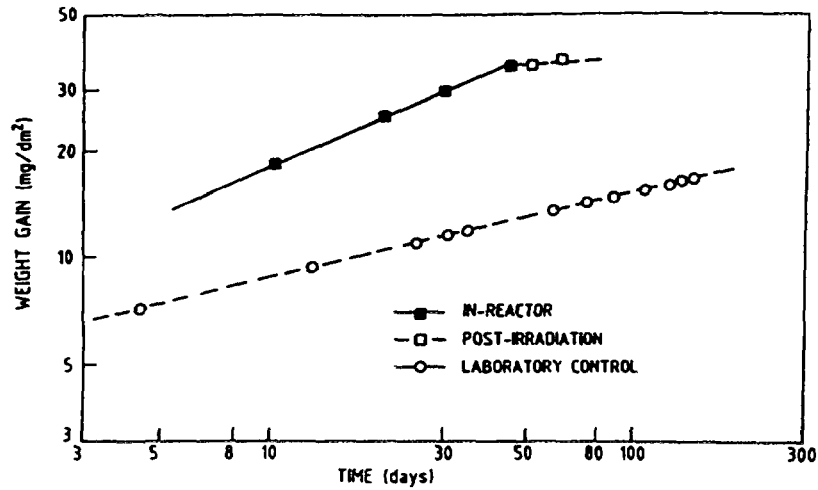


FIG. 9. 14. Effect of irradiation on pre-transition oxidation. The solid line refers to in-flux exposure, the dashed lines to out-of-flux exposure [518].

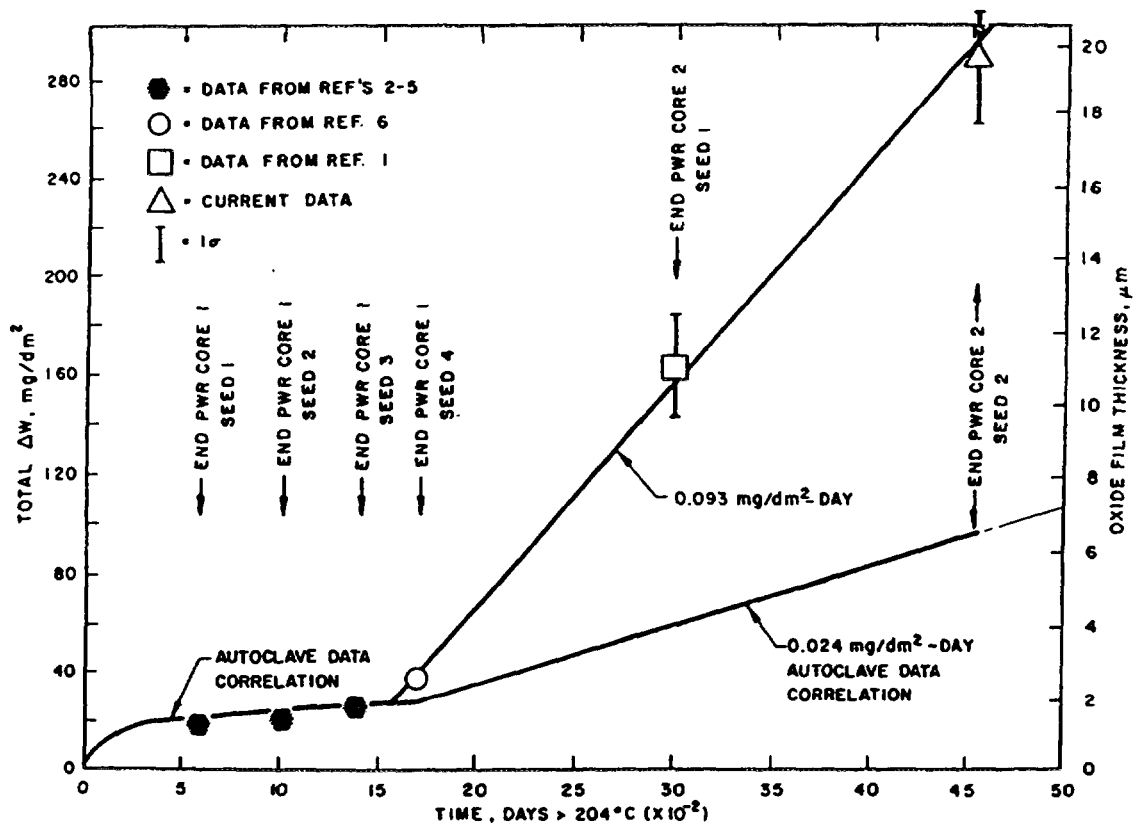


FIG. 9. 15. Total weight gain as a function of exposure time for region 2 of rod 11 from bundle 0120 (references refer to original FIG.) [519].



# Oxide Layer Thickness

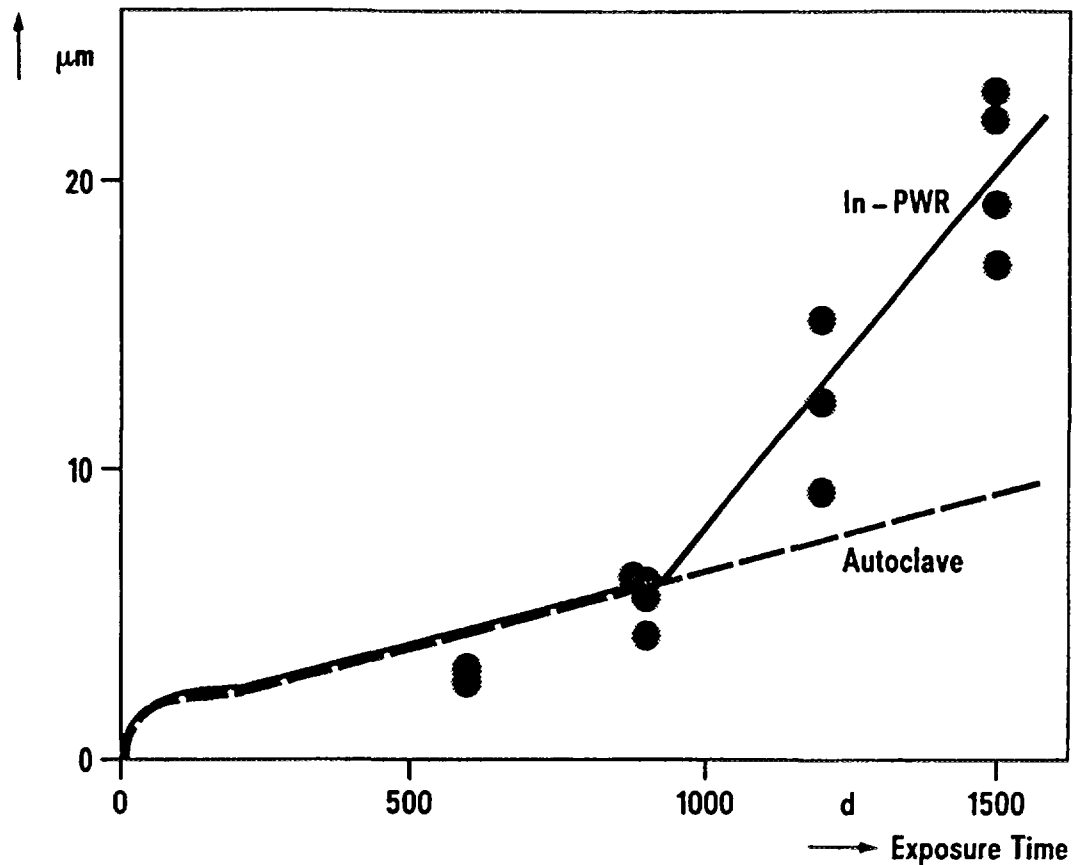


FIG. 9.16. Isothermal corrosion in a PWR at 310°C [124].

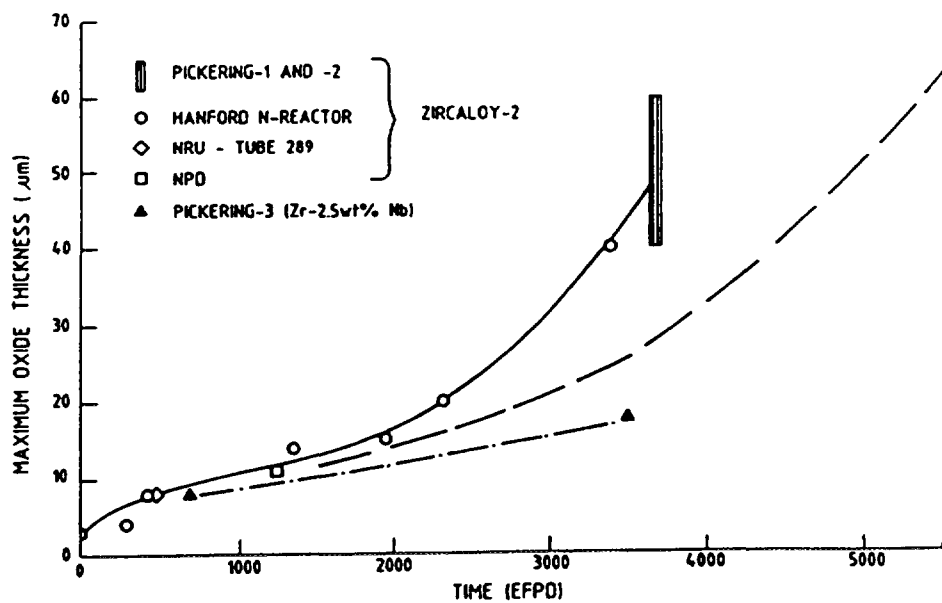


FIG. 9.17. Corrosion of zirconium alloy pressure tubes in-reactor [156].

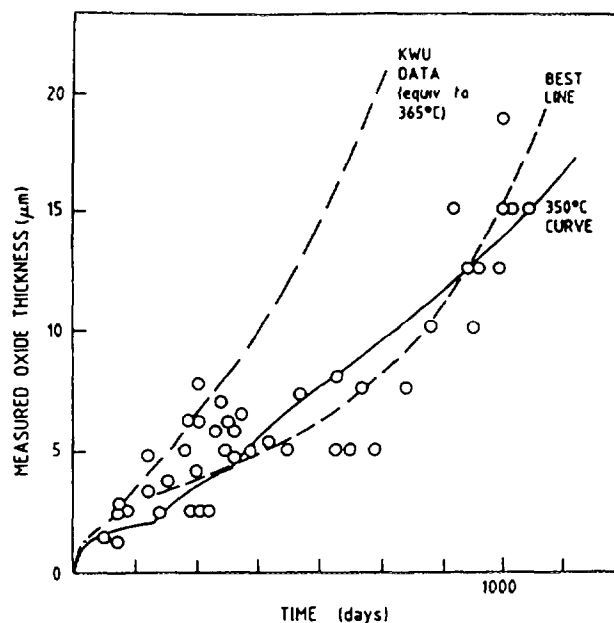


FIG 9 18 Measured and predicted oxide thicknesses in Westinghouse reactors with forced convective heat transfer, converted to an effective time scale [280]

cathodic part of the oxidation process is absorbed by the metal, enough hydrogen would be released into the pore network to provide a completely hydrogen environment if diffusion into the pores was not fast [522]

Many of the observations of the above effects have, however, been performed in LiOH water chemistry without boric acid. In the presence of LiOH, since the corrosion reaction removes the water from the solution in the pores, a progressively concentrating LiOH solution will be present, again depending upon the extent of interdiffusion between the bulk water and that in the pores. Since hydrogen pickup fractions for Zircaloy-4 are usually less than ~20%, and seldom exceed 50-60% for Zircaloy-2 under irradiation, it should be impossible to deplete the hydrogen in solution in the water in the porous oxide [522]. Under heat flux conditions an even larger concentration effect of the LiOH will arise as soon as the saturation temperature is exceeded in the oxide film because of the elevation of the boiling point of concentrated LiOH solutions. Calculations of this elevation of the boiling point show that a temperature rise across the oxide of only about 3 to 4°C above saturation is sufficient to give an equilibrium concentration of 10 molal LiOH at the bottoms of pores, again on the assumption of no rapid mixing of this solution with the bulk water. The presence of boric acid will protect against these effects of LiOH, except at the end of a fuel cycle. Thus, at present, it is difficult to say how much, if any, of the observed effects in-reactor can be firmly ascribed to irradiation effects and not to chemical effects.

Throughout this argument it has been assumed, based on the results of Coriou [101], that no similar effects will be seen in  $\text{NH}_4\text{OH}$ . Doubts have recently been engendered about the absence of effects in  $\text{NH}_4\text{OH}$  by some observations of Garzarolli [523] seen only in nickel (and not in stainless steel or Zircaloy) autoclaves. Large increases in corrosion rate were seen (Figure 9 19) in 20%  $\text{NH}_4\text{OH}$  under these conditions. If the effect of Ni arose from deposition of nickel on the  $\text{ZrO}_2$  surface from solution then a similar effect might be seen in-reactor.

A simple calculation [522], for a 10  $\mu\text{m}$  oxide film containing 10% porosity by volume (very much higher than measurements indicating ~1% porosity [78,320]), for conditions where the oxidation rate is 0.1  $\mu\text{m}/\text{day}$ , and 50% of the corrosion hydrogen is absorbed by the metal, shows that enough hydrogen to fill the pores with 100 atm hydrogen gas is released every 10 hours, and that the

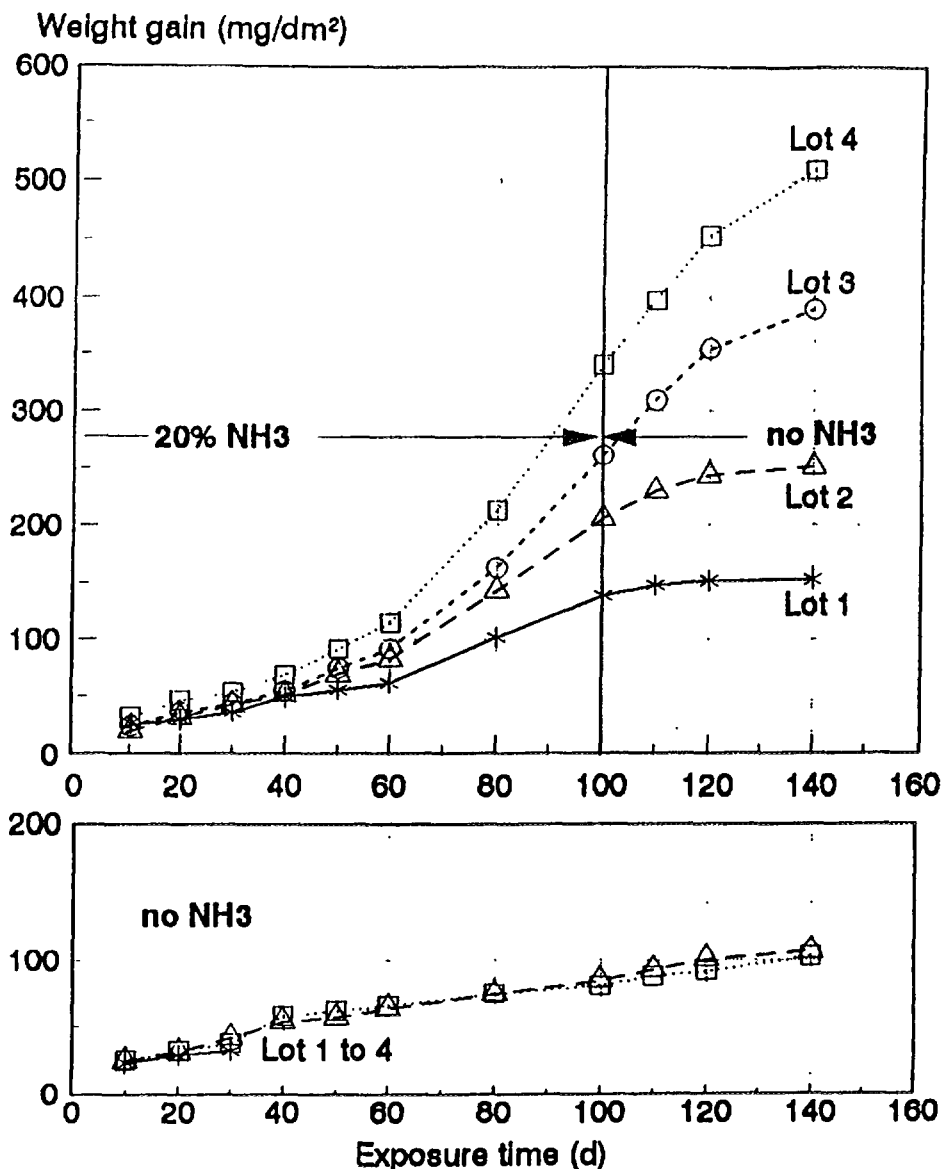


FIG. 9. 19. steam corrosion tests with and without NH<sub>3</sub>. The effect was observed only in nickel autoclaves [523].

water content of the pores is converted to new zirconium oxide and hydrogen approximately every 3 days. Thus, the precise conditions within the pore network will depend critically on pore size and interconnection and the heat flux and the effect that these will have on the degree to which the contents of the pores can mix with the bulk water. Under heat flux conditions in fuel cladding, when the saturation temperature is exceeded within the oxide, the pores should be filled with a concentrated LiOH solution, with a boiling point equal to the temperature at the bottoms of the pores in the oxide, rather than with water. Nevertheless, whatever the contents of the pores it seems unlikely that they can ever be other than highly hydrogenated and significant LiOH concentration in the pores is clearly feasible, even in the absence of a heat flux, as shown by the enhanced corrosion within crevices (both in the presence and absence of irradiation). Porous oxide films should behave in a manner similar to a collection of crevices [524].

Until we have a clear idea of just how the porosity develops in ZrO<sub>2</sub> films and how major factors such as LiOH affect it, we are in a poor position to understand in-reactor effects. TEM studies [113] show major differences between irradiated and unirradiated oxide films, and demonstrate that

oxides, on cladding showing increased corrosion in PWRs, contain larger equiaxed crystallites in the oxide than oxides formed in the laboratory, leading to a suggestion that irradiation enhances hydrothermal crystallisation of the oxide. A series of inner degraded layers of large equiaxed oxide crystallites is also seen when rapid acceleration of corrosion ensues in-reactor [113]. However, as we have no clear demonstration of just how oxide hydrothermal crystallisation processes and the development of oxide porosity by local dissolution are linked, this hypothesis requires more experimental evidence for its confirmation.

There have been prolonged arguments about the extent to which the corrosion rates of PWR cladding can be explained purely on the basis of out-reactor corrosion data and the thermal-hydraulics of the system [521], or whether an additional enhancement factor is needed [525]. Furthermore, whether such an enhancement factor is believed to be an irradiation effect [525], believed to result from a LiOH concentration effect [320], results from accumulation of hydride at the waterside oxide/metal interface [235, 326, 526] or arises from some other phenomenon, is not yet resolved. At present it appears that, since LiOH concentration can occur whether or not a heat flux is present, most observations of enhanced corrosion in LiOH solutions could be explained by such a concentration effect. However, establishing whether or not such an effect occurs in-reactor, has, so far, been beyond the abilities of current mathematical models to give a definitive answer (see section 7.3.3). One reason for this is that the cladding is only vulnerable to these LiOH concentration effects at the end of each cycle, when the boric acid concentration is depleted below the protective level. If most of the corrosion in a fuel cycle were to occur at the end of the cycle there would be no easy way to establish this, given current reactor operating modes. The differences in the behaviour of different batches of cladding could be explained by variations in the porosity of the oxide, and, hence, in the extent of mixing of the solution in the pores with bulk water. The effect of LiOH concentration is well established in the laboratory, however, testing of cladding batches at low to intermediate LiOH concentrations, and examination of the pore structure of post-transition oxide films would seem to be an area where more work is warranted.

The empirical models on which current arguments are based contain enough constants of uncertain value that it seems probable that universal agreement based on such models will be difficult to attain, especially where in-reactor thermal-hydraulic conditions are very severe (see section 7.3). However, the abilities of these largely thermal-hydraulic models to correctly estimate both the maximum intergrid oxide thickness and the minimum thickness at grid positions is still a severe test that most models fail. The micromechanistic content of them at present is small.

Although we seem to be able to qualitatively explain effects in LiOH solutions by concentrations in the porous oxide, the effects of boric acid remain a complicating factor. Tice et al. [114,115] have shown that boric acid suppressed the accelerating effects of LiOH on unirradiated specimens in high concentration mixtures of the two. The high concentrations of LiOH and boric acid were chosen based on estimates of possible concentrating effects under heat flux. However, although evidence for Li concentration has been found in oxide films, so far no evidence of B concentrations has been reported. Such evidence would be of importance to PWR operation, where suggestions to raise the Li content of the water have been made and (whether it is carried out or not) reliance is being placed on the boric acid content for protection. A potential for increased corrosion in high water temperature plants at high burnup would seem to exist at the end of the fuel cycle when boric acid concentrations are low or zero. The sensitivity to enhanced corrosion is worst at low, rather than zero, B [115] if such increases are put into practice. Furthermore, if boric acid is present in the oxide in high enough concentration to function as a mitigating factor on the effects of LiOH concentration on zirconium oxidation (in the same manner as it appears to inhibit denting on the secondary side of steam generators, namely by physically plugging pores in oxide films by depositing insoluble borates) then it may be rendered ineffective at the end of a cycle because most of the  $^{10}\text{B}$  sequestered in the pores in the oxide will be rapidly transmuted to  $\text{Li}$  and insufficient boric acid will be present in the bulk coolant to replenish the boric acid in the pores. Under such conditions it may actually serve to enhance lithium concentration in the oxide. However, the final location of such lithium is uncertain.

as recoil of  $^7\text{Li}$  during transmutation may inject some into the oxide lattice. Implantation of  $^7\text{Li}$  by such a process may not be important, however, if  $\text{ZrO}_2$  degradation by dissolution in concentrated  $\text{LiOH}$  is the operating mechanism. Because of the volatility of boric acid under boiling conditions, however, the extent to which it can concentrate in the oxide and protect against  $\text{LiOH}$  concentration effects remains unclear. Attempts to obtain circumstantial evidence for enhanced corrosion at the end of a fuel cycle have not yet borne fruit.

A further area in which  $\text{LiOH}$  concentration effects are better able to explain the observations than the thick film hypothesis is that of enhanced hydrogen uptake percentages accompanying the enhanced corrosion of PHWR pressure tubes (Figure 9 20) [121]. If the enhanced corrosion arises from a BWR-like water chemistry in the oxide film as claimed by Johnson, then the hydrogen uptake percentage should go down (Figure 9 21) [527], although increases in hydrogen uptake were observed for Johnson's own specimens with thick oxide films when hydrogen was added to the system [449], even though no reduction in oxidation rate was observed (Figure 9 22). While the uptake percentage did apparently rise to 100% following the acceleration of the oxidation of the Zircaloy-2 pressure tubes in Pickering, and would, therefore, have permitted a shift to oxidising conditions within the porous oxide, this must have been an effect, and not a cause, of the accelerated oxidation, since the oxidation rate increased before the hydrogen uptake rate [121]. That a large fraction of this deuterium may have been absorbed from the gas annulus side of these pressure tubes is an additional confounding factor in attempts to understand these observations.

Johnson observed identical effects in both  $\text{NH}_4\text{OH}$  and  $\text{LiOH}$  in the ETR loop tests, and the similarities between N-reactor ( $\text{NH}_4\text{OH}$ ) [528] and Pickering ( $\text{LiOH}$ ) [121] pressure tube oxidation have been alluded to previously. Since  $\text{NH}_4\text{OH}$  has no effect on the laboratory corrosion of the Zircalloys, these similarities are a major problem for any hypothesis explaining his in-reactor effects on the basis of  $\text{LiOH}$  concentration. Occam's Razor tells us that we should prefer the simplest hypothesis that explains the most observations, this is clearly the thick-film hypothesis, but this hypothesis seems to be fatally flawed based on our present understanding of the post-transition corrosion mechanism for the Zircalloys. Do we then need a completely new hypothesis or is there an irradiation effect on the chemistry of concentrated  $\text{NH}_4\text{OH}$  or an interaction with some other impurity in the water that can cause a similar effect on Zircaloy oxidation to the laboratory effect of  $\text{LiOH}$ . Although the results of Garzaroli [523] suggest that the concentration of  $\text{NH}_4\text{OH}$  may be as bad as  $\text{LiOH}$  for increasing Zircaloy corrosion, the appearance of an effect only in nickel autoclaves makes another explanation more probable. Knowing the autocatalytic effects of cuprammonium ion on the stress corrosion cracking of copper alloys in ammoniacal environments, one is tempted to suspect some involvement of the equivalent nickel ammonium complex ion in the autoclave results.

## 9 2 1 2 BWR corrosion

The enhanced nodular corrosion in BWR-type water chemistries was shown to require both a high fast neutron flux and the presence of radiolysis products in the water for its observation. As a result of this an hypothesis was proposed claiming that, in order to see large increases in corrosion rate in-reactor, both the ionic diffusion processes and the electronic transport processes in the oxide had to be accelerated. The acceleration of only one of these processes was insufficient, since the other one would then become rate limiting [26]. This hypothesis predicted certain shifts in the electrochemical polarisation curves of Zircaloy specimens undergoing enhanced corrosion that were not observed when experiments were set up to measure such effects using an accelerator as a radiation source [529]. Errors introduced in the polarisation curves by the 20 mA proton beam current, while not entirely negligible, did not affect the overall conclusion that increases in ionic conductivity (and oxidation rate) were influenced primarily by the oxygen content of the coolant [529]. In the light of these results, and subsequent evidence showing that enhanced corrosion seemed to be primarily a phenomenon of post-transition Zircaloy corrosion and was associated with the porosity of the oxide and processes going on in the pores, the above hypothesis was abandoned [530].

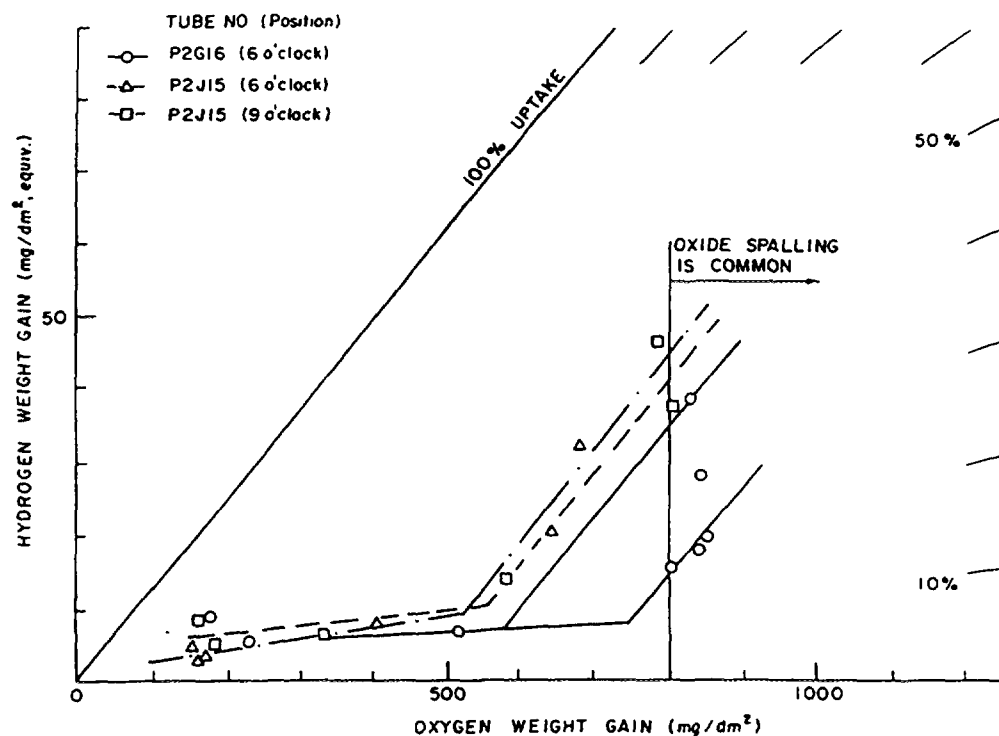


FIG. 9.20. Change in fractional uptake rate for hydrogen in oxide films  $>30 \mu\text{m}$  on Zircaloy-2 [535].

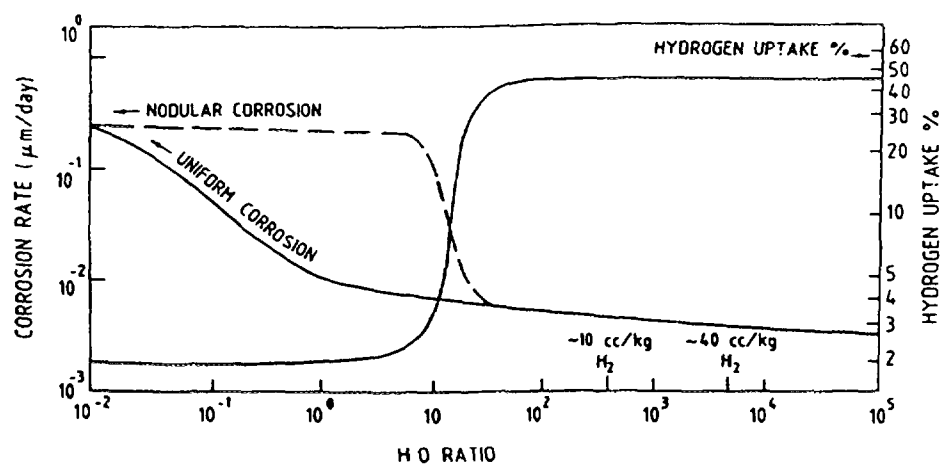


FIG. 9.21. Effect of H:O ratio in water on corrosion and hydrogen uptake in-reactor [527].

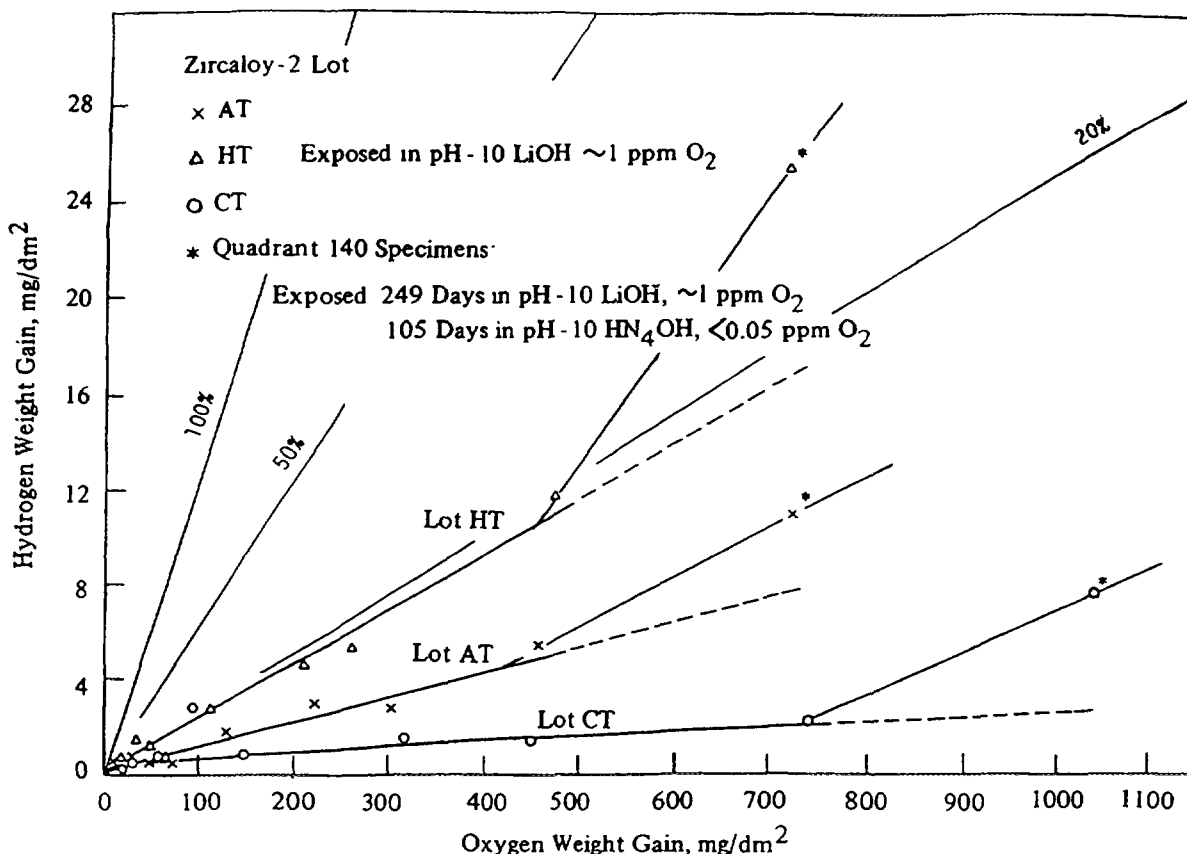


FIG 9.22. In-flux hydrogen weight gain as a function of in-flux oxygen weight gain [449]

At present the absence of any agreed site for nodule nucleation in the Zircaloys has limited our understanding of the phenomenon (see section 4. 3.). Amelioration of the effects of nodular corrosion have been achieved almost entirely by careful control of the second phase particle size during fabrication of the alloy. A fine particle size, achieved by late  $\beta$ -quenching, and subsequent control of precipitate size, by maintaining a low integrated annealing parameter during all subsequent heat treatments, gives the best results. This improved cladding, coupled with improved water chemistry control (especially for impurities that are concrete (Zeolite) formers (Ca, Mg, Si, Al)), and reductions in Cu content (by eliminating copper alloy feed water heaters and condensers) seem to have eliminated the serious aspects of nodular corrosion in BWRs without any clear mechanistic understanding

Before concluding, it should be pointed out that the hypothesis that explains nodular corrosion in BWRs as a direct effect of oxidising species in the water produced by radiolysis is flawed. While such an hypothesis may explain the initiation of nodules (although this too is doubtful as we have no agreed site for their initiation and hence no agreed mechanism for initiation), once formed, a nodule is merely another area of porous zirconium oxide, hydrogen pickup fractions are very low, and therefore any water or steam in the pores of this oxide must be highly hydrogenated. This should suppress the oxygen concentration from radiolysis in the pores, although arguments to the contrary have been raised [80,456]. In general, the rapid catalytic recombination of oxidising and reducing species on ZrO<sub>2</sub> surfaces has not been considered by these authors. Even in the presence of hard crud layers a steam filled crack is necessary, either in the crud or the oxide, to permit temperatures at the oxide/metal interface to come anywhere near to those of the 500°C steam test that in the laboratory shows such similar nodular corrosion to the in-reactor behaviour. Are we again

missing some vital step in the mechanism that can get us to this situation? Obviously the proposed CILC mechanisms [149,159,531] function logically once conditions in the oxide become similar to a 500°C steam test, and a radiolytic species hypothesis may satisfy the (unknown) conditions for nodule initiation, although it lacks a detailed micromechanism for relating the radiolytic species to nodule initiation. In fact, so long as a protective oxide is present, and oxidation is controlled by anion vacancy diffusion, radiolytic species can only change the surface potential as a route to affecting oxidation. The overall hypothesis breaks down in bridging the gap between nodule initiation and the onset of gross CILC failure. If an embryonic nodular oxide becomes filled with hydrogenated water immediately after initiation, when the oxide is still thin and temperatures at the oxide-metal interface are still close to 300°C, then conditions in the pores in the oxide will be no different chemically from those in a PWR, the initiation site should not develop into a visible nodule, and the whole subsequent development of the nodule should be stifled. Clearly there is some critical component of the process that is not understood.

The factor that is least often considered mechanistically, although its effects are well known practically in reactor operations, is the chemistry or electrochemistry of other species in the water. Of these the one that appears most prominently to affect the corrosion is the copper content of the water [532]. While copper was recognised early [531] as a major factor in the formation of the hard crud layers leading to the grosser forms of CILC failure, its importance in the early nodule nucleation and growth stages is not well documented. Nevertheless, it appears to be equally important at this stage of nodule growth, even at low concentrations in the crud (Figure 9.23). Since copper is close to its redox potential in 300°C water the initial state of the copper (soluble or insoluble) and small changes in water chemistry that can change this state may be important. The only other commonly occurring transition metal that is easily reducible in 300°C water is nickel. Additionally, the reduction of soluble cupric or nickelous ions to metallic copper or nickel at some intermetallic sites on the Zircalloys may provide a permanent cathode for the zirconium oxidation process that could locally enhance the anodic process (i.e. oxide growth) and might maintain the proton reduction reaction (cathodic process) on the surface of a porous film, thus preventing the water in the pores from becoming highly hydrogenated. However, experiments to test such an hypothesis failed to result in any nodules being produced in 300°C aqueous solutions [31].

Features that might be described as embryonic nodules were seen to start at flaws (second-phase particles?) in zirconium samples that were short-circuited during oxidation (Figure 9.24), but not in normally oxidised specimens [29]. Perhaps one contribution of irradiation to such initiation

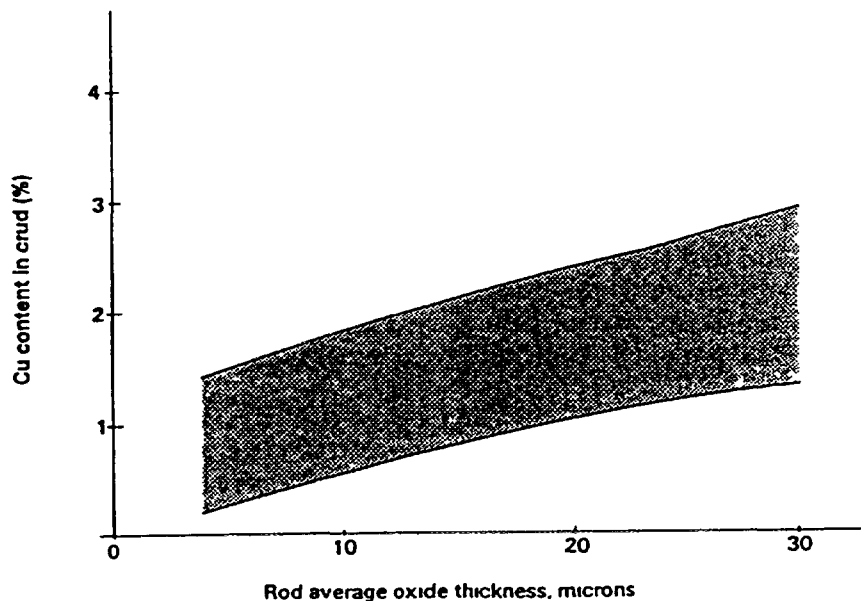
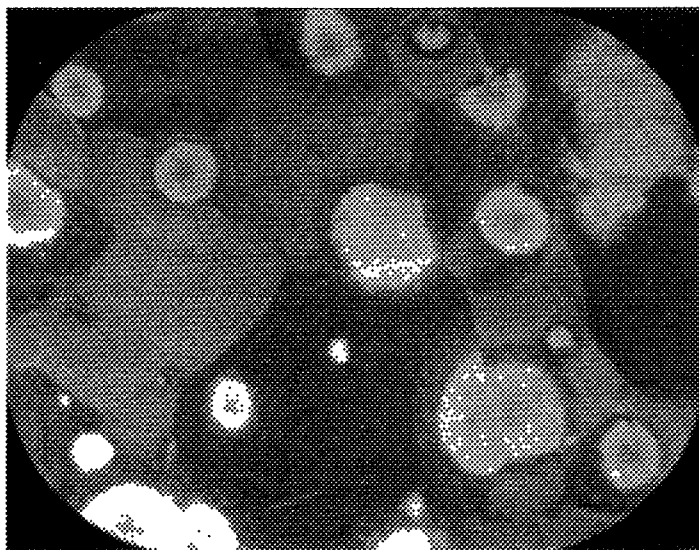


FIG 9.23 Correlation between Cu content in the crud and oxide thickness in Barsebeck-1 [532]





*FIG. 9. 24. Localised oxidation at second phase particles resulting from short-circuiting the oxide film during oxidation [29].*

steps is to effectively short-circuit the oxide by producing large numbers of electron-hole pairs. This is clearly speculative at present and represents an area of investigation that has not been pursued. Perhaps such studies could provide a micromechanism that could bridge the gap between nodule initiation in 300°C water and the later stage of CILC failures where conditions in the oxide become more like a 500°C steam test. There is certainly evidence for copper deposition within cracks in the zirconia film during CILC failures [150], but the chemical form of it is unknown, as is its role as either cause or effect of the cladding degradation. The recent in-reactor mini-autoclave tests have served to confuse the picture regarding effects of copper rather than clarifying it [533,534]. However, evidence is beginning to appear that the Si impurity in most Zircaloy-2 may be associated with nodule initiation, depending upon its location in the alloy as a result of prior heat treatment [152].

#### **9. 2. 2. Open questions on micromechanisms for in-reactor corrosion**

At present the development of our understanding of the in-reactor corrosion of zirconium alloys is restricted by our lack of well authenticated micromechanisms for the basic processes accompanying the development of porous oxide films as follows.

- (i) We do not know whether the porosity that develops at the rate transition originates at the outer surface of the oxide and grows in towards the metal-oxide interface, or whether it initiates randomly within the oxide and links up to finally form a network connected with the outside surface [87].
- (ii) The development of oxide porosity in reactor is closely linked to observations of enhanced corrosion. Recent evidence [128] suggests that it may originate much earlier than would be expected from the laboratory observations. Does this arise by an acceleration of the laboratory process for generating porosity in the pre-transition oxide, or is a new process such as dissolution of primary knock-on tracks followed by reprecipitation on the oxide surface [117,118] participating in the effect under irradiation? Quantities of zirconia appear at a variety of locations in a reactor system; however, it has always appeared to be impossible to establish whether they arrive there as species in solution or as particles of oxide that could be released from the alloy surface by fretting or spalling. In some situations it appears that only transport in solution could explain the observations; however, careful study of these circumstances has not been possible, and so it remains impossible to say whether or not an in-reactor solution and

reprecipitation of  $\text{ZrO}_2$  is a realistic micro-mechanism. Only observations of thin films formed in reactor, showing that they are porous well before the expected rate transition [128], support such a mechanism.

- (iii) We still know virtually nothing about the electrochemistry of zirconium alloys in 300°C water, and in particular about variations in surface electrochemical potential at intermetallic sites, and the extent to which local redox potentials vary with small changes in water chemistry. Recent studies [80] have not resolved these questions since the enhanced currents under  $\beta$ -irradiation were not identified as being ionic rather than electronic currents in the oxide. Until we understand this aspect of the process more clearly we will be unable to factor in the galvanic or electrochemical effects that seem to be involved in the in-reactor corrosion process in BWRs.

### 9 2 3 Present status of mechanistic studies

After many years of studying in-reactor corrosion of zirconium alloys we are still without any scientifically sound hypothesis that explains what is going on. Progress in our understanding of the processes, and improvements in the future performance of zirconium alloys in reactor, clearly need sound micromechanistic hypotheses whose predictions can be tested. At present we seem to be doing little experimentation that will resolve this, and recent advances in the performance of fuel cladding have usually resulted from an "ad hoc" engineering development approach.

### 9 2 4 Recommendations for future work

Throughout the above discussion, gaps in our knowledge that should be considered for future investigation have been identified. On considering the field as a whole, it is our opinion that the following areas are most in need of concerted experimental efforts to resolve them -

- a Studies of the local electrochemistry of oxidized Zircaloy surfaces at elevated temperature, and preferably either in-reactor or in a high  $\gamma$ -radiation field. In such tests, measurements of the electrochemical currents must be correlated with accurate oxide growth measurements (by NRA<sup>2</sup>) to distinguish ionic from electronic transport in the oxide. This requirement has been absent from recent studies. Tests such as those of Isobe [148] in which the intermetallic and the precipitate free alloy are connected through an external circuit would possibly achieve this.
- b Polarisation studies, of the type performed by Norfolk et al [529] using proton irradiation should be carried out in-reactor (or an in-reactor loop) in conditions typical of a BWR.
- c A detailed study of radiation chemistry, and the behaviour of impurity species in porous zirconia systems should be initiated. This would need to be combined with studies of the recombination rates of oxidising and reducing species on  $\text{ZrO}_2$  surfaces.
- d A concerted effort is needed to understand the nature of the porosity in zirconium oxide films and the mechanisms that generate it.
- e Mechanism of stress build-up in the oxide versus distance from the oxide-metal interface needs more investigation.
- f Measurements of solubilities of tetragonal and monoclinic zirconia in  $\text{LiOH}$  and boric acid solutions at elevated temperatures.
- g Mechanistic studies of the interaction of hydride at the oxide/metal interface with the corrosion reaction.

## APPENDIX

It is assumed that a deep crack or pore with a constant area of cross section (S) is under irradiation in a thick oxide layer on Zircaloy, and that hydrogen is sufficiently supplied outside the pore (concentration  $y_0$ ) and diffuses inside the pore where it is depleted by reaction (14). Attention is paid only to the OH radical as a reactive transient species for simplicity. Mass balance equations are expressed as follows, assuming one-dimensional diffusion

$$Sdx \frac{\partial y}{\partial t} = -SD_y \frac{\partial y}{\partial x} + g_y Sdx + SD_y \left[ \frac{\partial y}{\partial x} + (\partial^2 y / \partial x^2) dx \right] - kzy Sdx \quad (A1)$$

$$Sdx \frac{\partial z}{\partial t} = -SD_z \frac{\partial z}{\partial x} + g_z Sdx + SD_z \left[ \frac{\partial z}{\partial x} + (\partial^2 z / \partial x^2) dx \right] - k'z^2 Sdx - kyz Sdx \quad (A2)$$

Where  $y$  and  $z$  refer to the concentrations of  $H_2$  and OH at a distance  $x$  from the inlet of the pore, respectively,  $D_y$  and  $D_z$  are diffusion constants for  $H_2$  and OH,  $g_y$  and  $g_z$  are the production rates of  $H_2$  and OH by radiolysis, and  $k$  and  $k'$  are the rate constants of reaction (19) and the second order decay constant of OH, respectively. In this treatment the surface reactions in which the OH radical may be involved and the hydrogen formation in the course of the corrosion process, reaction (13), are neglected.

At steady state, equations (A1) and (A2) are reduced to equations (A3) and (A4)

$$d^2 y / dx^2 - (k/D_y)zy + g_y/D_y = 0 \quad (A3)$$

$$d^2 z / dx^2 - (k'/D_z)z^2 - (k/D_z)yz = g_z/D_z = 0 \quad (A4)$$

A very simple approximation is introduced here to derive a rough concentration profile for hydrogen in the pore, i.e. if the concentration of OH, ( $z$ ), is assumed to be constant and independent of distance  $x$  and an average value,  $z_{av}$ , is taken, then equation (A3) may be solved straightforwardly. The boundary conditions and the final solution are given below

$$x = 0 \quad y = y_0$$

$$x = \infty \quad dy/dx = 0$$

$$y = (y_0 - g_y/kz_{av}) \exp(-\sqrt{kz_{av}/D_y} x) + g_y/kz_{av} \quad (A5)$$

The value of  $y_0$  is estimated to be  $1 \times 10^{-3} \text{ mol dm}^{-3}$  (corresponding to PWR conditions) and  $g_y$  is calculated to be approximately  $2 \times 10^{-3} \text{ mol dm}^{-3} \text{ s}^{-1}$  (assuming an average primary G value of 0.65 for  $H_2$  and an average dose rate of  $4.3 \times 10^4 \text{ Gy/s}$  in the core) [192]. The rate constant of reaction (19),  $k$ , and the diffusion constant of  $H_2$ ,  $D_y$ , in water, at  $300^\circ\text{C}$  are estimated to be  $1.3 \times 10^9 \text{ dm}^{-3} \text{ mol}^{-1} \text{ s}^{-1}$  [193,194] and  $5.7 \times 10^{-6} \text{ dm}^2 \text{ s}^{-2}$  [178], respectively, assuming an activation energy of 12.5 kJ/mol for the latter. The value of  $z_{av}$  is taken to be a parameter, and the ratios  $y/y_0$  ( $[H_2]/[H_2]_0$ ) calculated using the above estimated values are shown as a function of distance  $x$  in Table A.1 for two values of  $z_{av}$ ,  $1 \times 10^{-7}$  and  $1 \times 10^{-6} \text{ mol dm}^{-3}$ . As seen from the Table, the ratio  $[H_2]/[H_2]_0$  is largely dependent on parameter  $z_{av}$ . The values used here are very close to those estimated in a computer simulation of a BWR core [192].

Table A. 1. Calculated profiles of hydrogen in a pore

Distance, x, $\mu\text{m}$	$\frac{[\text{H}_2]}{[\text{H}_2]_0}$ $z_{\text{av}}=1 \times 10^{-7} \text{ mol} \cdot \text{dm}^{-3}$	$\frac{[\text{H}_2]}{[\text{H}_2]_0}$ $z_{\text{av}}=1 \times 10^{-6} \text{ mol} \cdot \text{dm}^{-3}$
0	1.0	1.0
1	0.95	0.86
5	0.79	0.46
10	0.62	0.21
15	0.49	0.098
20	0.39	0.046
25	0.30	0.021

The Table shows that the concentration of hydrogen is reduced two order of magnitude at the distance of 25  $\mu\text{m}$  from the inlet of the pore, if  $z_{\text{av}}$  is assumed to be  $1 \times 10^{-6} \text{ mol} \cdot \text{dm}^{-3}$ , and it is too low to maintain the suppression effect of hydrogen on Zircaloy corrosion there.

## REFERENCES

- [1] INTERNATIONAL ATOMIC ENERGY AGENCY, Corrosion of zirconium alloys in nuclear power plants, IAEA-TECDOC-684, IAEA, Vienna (1993).
- [2] INTERNATIONAL ATOMIC ENERGY AGENCY, Fundamental aspects of corrosion of zirconium base alloys in water reactor environments, Proc. of Tech. Comm. Mtg., Portland, OR., IWGFPT/34, IAEA, Vienna (1989).
- [3] Zirconium in the Nuclear Industry: 9th Int. Symp., ASTM-STP-1132, (EUCKEN, C. M., GARDE, A. M., Eds.), American Society for Testing and Materials, W. Conshohocken, PA. (1991).
- [4] TRICOT, R., Le zirconium et ses alliages, Métallurgie et applications au nucléaire, Rev. Gen. Nucl. Jan./Fev. (1990) 8-20.
- [5] MOULIN, L., RESCHKE, S., TENCKHOFF, E., "Correlation between fabrication parameters, microstructure and texture in Zry tubings", Zirconium in Nuclear Industry: 6th Int. Symp., ASTM-STP-824, (FRANKLIN, D., ADAMSON, R. B., Eds.), American Society for Testing and Materials, W. Conshohocken, PA. (1984) 225-243.
- [6] LUSTMAN, B., KERZE, F., The metallurgy of Zr, McGraw Hill, N.Y. (1955).
- [7] HOLT, R. A., CAUSEY, A. R., The effects of intergranular constraints in irradiation growth of Zry2 at 320°C, J. Nucl. Mater. **150** (1987) 306-318.
- [8] CHARQUET, D., HAHN, R., ORTLIEB, E., GROS, J. P., WADIER, J. F., "Solubility limits and formation of intermetallic precipitates in Zr-Sn-Fe-Cr alloys", Zirconium in the Nuclear Industry: 8th Int. Symp., ASTM-STP-1023, (VAN SWAM, L. F. P., GARDE, A. M., Eds.), American Society for Testing and Materials, W. Conshohocken, PA. (1989) 405-422.
- [9] CHARQUET, D., ALHERITIERE, E., "Second phase particles and matrix properties on Zircalloys", Proc. workshop on second phase particles in Zircalloys, Erlangen FRG, Kern Tech. Gesell. (1985) 5-11.
- [10] WILLIAMS, C. D., GILBERT, R. W., Tempered structure of a Zr-2.5%Nb alloy, J. Nucl. Mater. **18** (1966) 161-166.
- [11] CHEADLE, B. A., ALDRIDGE, S. A., Transformation and age hardening behaviour of Zr-19% Nb, J. Nucl. Mater. **47** (1973) 255-258.
- [12] URBANIC, V. F., GILBERT, R. W., "Effect of microstructure on the corrosion of Zr-2.5%Nb alloy", Proc. Tech. Comm. Mtg. on Fundamental Aspects of Zr Based Alloys in Water Reactor Environment, IWGFPT/34, International Atomic Energy Agency, Vienna, (1990) 262-272.
- [13] TENCKHOFF, E., "Deformation mechanisms, texture and anisotropy in zirconium and Zircalloys", ASTM-STP-966, American Society for Testing and Materials, W. Conshohocken, PA. (1988).
- [14] NUMAKURA, H., MINONISHI, Y., KOIWA, M.,  $[1\ 1\ 23]\{101\ 1\}$  Slip in zirconium, Phil. Mag. **63** (1991) 1077-1084.
- [15] CABRERA, N., MOTT, N. F., Repts. Prog. in Phys., **12** (1949) 163.
- [16] HAUFFE, K., Oxidation of metals, Plenum, N.Y. (1965).
- [17] FROMHOLD, A. T., Jr., Theory of Metal Oxidation-vol. I, Fundamentals, North-Holland, Amsterdam, (1976).
- [18] TAMMANN, G., Zeitschrift fur anorganische und allgemeine Chem., **111** (1920) 78.
- [19] COX, B., ROY, C., Transport of oxygen in oxide films on zirconium determined by the nuclear reaction  $O^{17}(He^3, \alpha)O^{16}$ , Electrochem. Tech., **4** (1966) 121-127.
- [20] COX, B., PEMSLER, J. P., Diffusion of oxygen in growing zirconia films, J. Nucl. Mater. **28** (1968) 73-78.
- [21] HUSSEY, R. J., SMELTZER, W. W., The oxidation kinetics of zirconium in the temperature range 400-600°C, J. Electrochem. Soc., **111** (1964) 564-568.
- [22] COX, B., Hydrogen absorption by Zircaloy-2 and some other alloys during corrosion in steam, J. Electrochem. Soc., **109** (1962) 6-12.
- [23] COX, B., DONNER, A., The morphology of thick oxide films on Zircaloy-2, J. Nucl. Mater. **47** (1973) 72-78.

- [24] ROY, C , DAVID, G , X-ray diffraction analyses of zirconia films on zirconium and Zircaloy-2, *J Nucl Mater* **37** (1970) 71-81
- [25] DAVID, G , GESCHIER, R , ROY, C , Etude de la croissance de l'oxyde sur le zirconium et le Zircaloy-2, *J Nucl Mater* **38** (1971) 329-339
- [26] COX, B , "Oxidation of zirconium and its alloys", *Adv in Corr Sci and Tech* , Vol 5, (FONTANA, M G , STAEHLE, R W , Eds ), Plenum, N Y (1976) 173-391
- [27] SPEIGHT, M V , HARRIS, J E , *Acta Met* **26** (1978) 1043
- [28] WANKLYN, J N , "L'influence de l'hydrogene sur la corrosion du zirconium dans l'eau a haute temperature", *Proc 3me Colloque de Metallurgie-Corrosion*, Saclay, France, (29-30 June, 1959), North Holland Publ Co , Amsterdam (1960) 127-136, and *J Appl Chem* **8** (1958) 496-504
- [29] COX, B , Rate controlling processes during the pretransition oxidation of zirconium alloys, *J Nucl Mater* **31** (1969) 48-66
- [30] URQUHART, A W , VERMILYEA, D A , ROCCO, W A , A mechanism for the effect of heat treatment on the acceleration of corrosion of Zircaloy-4 in high temperature high pressure steam, *J Electrochem Soc* , **125** (1978) 199-204
- [31] COX, B , WONG Y-M , QUON, C , Cathodic polarisation of corroding Zircaloy-4, *J Nucl Mater* **223** (1995) 321-326
- [32] COX, B , Mechanism of oxide film growth and breakdown on zirconium and Zircaloy-2, *J Electrochem Soc* , **108** (1961) 24-30
- [33] SHIRVINGTON P J , Electron conduction through oxide films on Zircaloy-2, *J Nucl Mater* **37** (1970) 177-202
- [34] WAGNER, C *Z Phys Chemie, B* , **21** (1933) 25-
- [35] JOST, W , *Diffusion in Solids, Liquids and Gases*, Academic Press Inc , New York, (1962)
- [36] DOUGLASS, D L , WAGNER, C , The oxidation of oxygen-deficient zirconia and its relationship to the oxidation of zirconium, *J Electrochem Soc* , **113** (1966) 671
- [37] KROGER, F A , Electronic conductivity of calcia-stabilized zirconia, *J Amer Ceram Soc* **49** (1966) 215
- [38] KUMAR, A , RAJDEV, D , DOUGLASS, D L , Effect of oxide defect structure on the electrical properties of  $ZrO_2$ , *J Amer Ceram Soc* , **55** (1972) 439
- [39] TAYLOR, D , CHENG, B , ADAMSON, B R , "Nodular corrosion mechanisms and their application to alloy development", *Proc IAEA Tech Comm Mtg IWGFPT/34*, Portland, IAEA, Vienna, Austria, (1990) 27-35
- [40] PORTE, H A , SCHNIZLEIN, J G , VOGEL, R C , FISCHER, D F , Oxidation of zirconium and zirconium alloys, *J Electrochem Soc* , **107** (1960) 506-511
- [41] MISCH, R D , VAN DRUNEN, C , "The oxidation of zirconium binary alloys in 700°C oxygen for times up to 200 days", *Proc USAEC Symp on Zr Alloy Development* Castlewood, CA , (1962), GEAP-4089, Vol II, Paper 15, (General Electric Co , San Jose, CA )
- [42] PECHEUR, D , LEFEBVRE, F , MOTTA, A T , LEMAIGNAN, C , WADIER, J F , Precipitate evolution in the Zircaloy-4 oxide layer, *J Nucl Mater* **189** (1992) 318-332
- [43] PECHEUR, D , LEFEBVRE, F , MOTTA, A T , LEMAIGNAN, C , CHARQUET, D , "Oxidation of intermetallic precipitates in Zircaloy-4 Impact of irradiation", *Zirconium in the Nuclear Industry 10th Int Symp* , ASTM-STP-1245, (GARDE, A M , BRADLEY, E R , Eds ), American Society for Testing and Materials, W Conshohocken, PA (1994) 687-705
- [44] KOMAREK, K L , SILVER, M , "Thermodynamic properties of zirconium-oxygen, titanium-oxygen and hafnium-oxygen alloys" *Thermodynamics of nuclear materials*, *Proc Int Conf* , IAEA, Vienna, (1962) 749-774
- [45] ZHANG, C-S , FLINN, B J , MITCHELL, I V , NORTON, P R , The initial oxidation of Zr (0001), 0 to 0.5 monolayers, *Surf Sci* , **245** (1991) 373-379
- [46] TAPPING, R L , X-ray photoelectron and ultraviolet photoelectron studies of the oxidation and hydriding of zirconium, *J Nucl Mater* **107** (1982) 151-158
- [47] AMSEL, G , DAVID, D , BERANGER, G , BOISOT, P , DE GELAS, B , LACOMBE, P , Analyse a l'aide d'une methode nucleaire des impuretes introduites dans les metaux par leurs

- préparations d'état de surface: application au zirconium, J. Nucl. Mater. **29** (1969) 144-153.
- [48] DOERFFLER, W. W., "A contribution to the mechanism of dissolution and diffusion of oxygen in zirconium", Proc. Conf. on Thermodynamics of Nuclear Materials and Atomic Transformations in Solids, IAEA, Vienna, (July 1965) (SM66/18); and Swiss Rep. EIR-82, Wurenlingen, (1965).
- [49] WANKLYN, J. N., "Recent studies of the growth and breakdown of oxide films on zirconium and zirconium alloys", Corrosion of Zirconium Alloys, ASTM-STP-368, American Society for Testing and Materials, W. Conshohocken, PA. (1964) 58-75.
- [50] COX, B., The zirconium-zirconia interface, J. Aust. Inst. Met. **14** (1969) 123-131.
- [51] KASS, S., "The development of the Zircalloys", Corrosion of Zirconium Alloys, ASTM-STP-368, American Society for Testing and Materials, W. Conshohocken, PA. (1964) 3-27.
- [52] COX, B., "Recent developments in zirconium alloy corrosion technology", Progress in Nuclear Energy, Series IV, Technology, Engineering and Safety, Vol. 4, Ch. 3-3, (NICHOLLS, C. M., Ed.), Pergamon, Oxford, (1961) 166-188.
- [53] PLOC, R. A., Transmission of electron microscopy of thin ( $<2000\text{\AA}$ ) thermally formed  $\text{ZrO}_2$  films, J. Nucl. Mater. **28** (1968) 48-60.
- [54] PLOC, R. A., Electron diffraction analysis of  $\text{ZrO}_2$  on  $\alpha\text{-Zr}$  (1120), J. Nucl. Mater. **113** (1983) 75-80.
- [55] PLOC, R. A., A theoretical treatment of  $\text{Zr}/\text{ZrO}_2$  epitaxy, Can. Rep. AECL 2751, Atomic Energy of Canada Ltd., Chalk River Nuclear Laboratories, (1967).
- [56] GODLEWSKI, J., GROS, J.-P., LAMBERTIN, M., WADIER, J.-F., WEIDINGER, H., "Raman spectroscopy study of the tetragonal-to-monoclinic transition in zirconium oxide scales and determination of overall oxygen diffusion by nuclear microanalysis of  $^{18}\text{O}$ ", Zirconium in the Nuclear Industry: 9th Int. Symp., ASTM-STP-1132, (EUCKEN, C. M., GARDE, A. M., Eds.), American Society of Testing and Materials, W. Conshohocken, PA. (1991) 416-436.
- [57] GODLEWSKI, J., "How the tetragonal zirconia is stabilised in the oxide scale formed on zirconium alloys corroded at  $400^\circ\text{C}$  in steam", Zirconium in the Nuclear Industry: 10th Int. Symp., ASTM-STP-1245, (GARDE, A. M., BRADLEY, E. R., Eds.), American Society for Testing and Materials, W. Conshohocken, PA. (1994) 663-683.
- [58] DONALDSON, A. T., EVANS, H. E., Oxidation-induced creep in Zircaloy-2, Pts. I-III, U.K. Reports RD/T/N4855, 4952 and 4976, Central Electricity Generating Board, Berkeley Nuclear Laboratories, (1980).
- [59] COX, B., Low temperature ( $<300^\circ\text{C}$ ) oxidation of Zircaloy-2 in water, J. Nucl. Mater. **25** (1968) 310-321.
- [60] PETERS, H. R., "Improved characterisation of aqueous corrosion kinetics of Zircaloy-4", Zirconium in the Nuclear Industry: 6th Int. Symp., ASTM-STP-824, (FRANKLIN, D., ADAMSON, R. B., Eds.), American Society for Testing and Materials, W. Conshohocken, PA. (1984) 507-518.
- [61] DAWSON, J. K., LONG, G., SEDDON, W. E., WHITE, J. F., The kinetics and mechanism of the oxidation of Zircaloy-2 at  $350\text{-}500^\circ\text{C}$ , J. Nucl. Mater. **25** (1968) 179.
- [62] GRIGGS, B., MAFFEI, H. P., SHANNON, D. W., Multiple rate transitions in the aqueous corrosion of Zircaloy, J. Electrochem. Soc., **109** (1962) 665-668.
- [63] COX, B., Processes occurring during the breakdown of oxide films on zirconium alloys, J. Nucl. Mater. **29** (1969) 50-66.
- [64] BRADHURST, D. H., HEUER, P. M., The influence of oxide stress on the breakaway oxidation of Zircaloy-2, J. Nucl. Mater. **37** (1970) 35.
- [65] COX, B., Comments on the paper, The influence of oxide stress on the breakaway oxidation of Zircaloy-2, J. Nucl. Mater. **41** (1971) 96-100.
- [66] CORIOU, H., GRALL, L., WILLERMOZ, H., Influence du cyclage thermique sur la corrosion du Zircaloy-2 dans l'eau ou la vapeur à  $360^\circ\text{C}$  et sur l'absorption de l'hydrogène par le métal, Rep. DM1005, Commissariat à l'Energie Atomique, Saclay, France (1961).
- [67] GÖHR, H., SCHALLER, J., RUHMANN, H., GARZAROLLI, F., "Long term in situ investigation of Zr alloys in simulated PWR environment by electrochemical

- measurements", Zirconium in the Nuclear Industry: 11th Int. Symp., Garmisch-Partenkirchen, (1995), ASTM-STP-1295, (BRADLEY, E. R., SABOL, G. P., Eds.), American Society for Testing and Materials, W. Conshohocken, PA., (1996) 181-202
- [68] AMBARTSUMYAN, R. S., KISELEV, A. A., GREBENNIKOV, R. V., MYSHKIN, V. A., TSUPRUN, L. J., NIKULINA, A. V., "Mechanical properties and corrosion resistance of zirconium and its alloys in water, steam and gases at elevated temperatures", Proc. 2nd Int. Conf. on the Peaceful Uses of Atomic Energy, Geneva, CH, (Aug. 1958), Vol. 6, p. 12, United Nations, New York.
- [69] VRTILKOVA, V., VALACH, M., MOLIN, L., "Oxidizing and hydriding properties of Zr-Nb cladding material in comparison with Zircalloys", Proc. Tech. Comm. Mtg. on Influence of Water Chemistry on Fuel Cladding Behaviour, Rez, Czech. Rep., (Oct. 4-8, 1993), IAEA-TECDOC-927, Vienna (1997) 227-251.
- [70] COX, B., Long-term oxidation of Zr-2.5wt% Nb alloy, Canadian Report, AECL-5610, Atomic Energy of Canada Ltd., Chalk River, (Sept. 1976).
- [71] COX, B., Some observations of the oxidation of Zr-Nb alloys at relatively low temperatures (~300°C) in water, Canadian Report, RM1-10, Atomic Energy of Canada Ltd., Chalk River, (Oct. 1964).
- [72] AMAEV, A. D., AMBARTSUMYAN, R. S., ANISIMOVA, I. A., DUBROVIN, K. P., IONOVA, L. M., SEDOVA, A. V., "Validation of choice of Zr alloy as fuel cladding material for commercial power reactors VVER-440", CMA, Proceedings of Scientific-Technical Conference, Atomic Power Fuel Cycles, Radiation Materials Science, USSR, Ul'yanovsk, (Oct. 1970), Moscow, Vol. II (1971) 503-545.
- [73] COX, B., WU, C., Dissolution of zirconium oxide films in 300°C LiOH, J. Nucl. Mater. **199** (1993) 272-284.
- [74] SABOL, G. P., KILP, G. R., BALFOUR, M. G., ROBERTS, E., "Development of a cladding alloy for high burnup", Zirconium in the Nuclear Industry 8th Int. Symp., ASTM-STP-1023, (VAN SWAM, L. F. P., EUCKEN, C. M., Eds.), American Society for Testing and Materials, W. Conshohocken, PA. (1989) 227-244.
- [75] SHIRVINGTON, P. J., COX, B., A study of charge transport processes during the oxidation of zirconium alloys, J. Nucl. Mater. **35** (1970) 211-222.
- [76] PLOC, R. A., Oxidation kinetics and Auger microprobe analysis of some oxidised zirconium alloys, Zirconium in the Nuclear Industry: 8th Int. Symp., (VAN SWAM, L. F. P., EUCKEN, C. M., Eds.), ASTM-STP-1023, American Society for Testing and Materials, W. Conshohocken, PA. (1989) 498-514.
- [77] SAWICKI, J. A., MAREST, G., COX, B., JULIEN, S. R., Mossbauer spectroscopy of iron implanted and doped in ZrO<sub>2</sub>, Nucl. Instrum. Methods **B32** (1988) 79-84.
- [78] GARZAROLLI, F., SEIDEL, H., TRICOT, R., GROS, J. P., "Oxide growth mechanisms on zirconium alloys", Zirconium in the Nuclear Industry: 9th Int. Symp., ASTM-STP-1132, (EUCKEN, C. M., GARDE, A. M., Eds.), American Society for Testing and Materials, W. Conshohocken, PA. (1991) 395-415.
- [79] PECHEUR, D., LEFEBVRE, F., LEMAIGNAN, C., Oxidation processes in Zircaloy, J. de Physique IV, C7, (1993) 503-507.
- [80] ILTIS, X., SALOT, R., LEFEBVRE, F., LEMAIGNAN, C., "Irradiation enhancement of water corrosion of Zr alloys: Material (Zr, ZrO<sub>2</sub>) and water radiochemistry aspects of oxide growth", ANS Int. Topical Mtg. on LWR Fuel Performance, West Palm Beach, Florida, American Nuclear Society, (April 16-19, 1994) 594-600.
- [81] WARR, B. D., RASILE, E. M., BRENNENSTUHL, A. M., "Electron microscopical analyses of oxides on Zr-2.5wt% Nb", Proc. IAEA Tech. Comm. Mtg. on the Fundamental Aspects of Corrosion on Zirconium Base Alloys in Water Reactor Environments, Portland, OR., USA, IWGFPT/34, IAEA, Vienna, Austria, (1989) 124-134.
- [82] WARR, B. D., ELMOSELI, M. B., NEWCOMB, S. B., McINTYRE, N. S., BRENNENSTUHL, A. M., LICHTENBERGER, P. C., "Oxide characteristics and their relationship to hydrogen uptake in zirconium alloys", Zirconium in the Nuclear Industry 9th Int. Symp., ASTM-STP-1132, (EUCKEN, C. M., GARDE, A. M., Eds.), American Society for Testing and Materials, W. Conshohocken, PA. (1991) 740-757.



- [83] NEWCOMB, S. B., WARR, B. D., STOBBS, W. M., "The TEM characterisation of oxidation-reduction processes in Zr-Nb alloys", Proc. EMAG 91 Conference, Bristol, UK, Inst. of Physics, London, Conf. Ser. No. 119: Section 6, (1991) 221-224.
- [84] COX, B., YAMAGUCHI, Y., The development of porosity in thick zirconia films, *J. Nucl. Mater.* **210** (1994) 303-317.
- [85] COX, B., A porosimeter for determining the sizes of flaws in zirconia or other insulating films 'in situ', *J. Nucl. Mater.* **27** (1968) 1-11.
- [86] COX, B., "Factors controlling the corrosion behaviour of zirconium alloys under irradiation", Reactor Materials Science (Proc. Int. Conf., Alushta, Crimea) Vol. 5, Atominform, Moscow, (1978) 90-131.
- [87] COX, B., Are zirconia corrosion films a form of partially stabilised zirconia (PSZ)?, Rept. AECL 9382, Atomic Energy of Canada Ltd., Chalk River Nuclear Laboratories, (1987).
- [88] KASS, S., Corrosion of prefilmed Zircaloy, *Corrosion*, **23** (1967) 374.
- [89] ROY, C., BURGESS, B., A study of the stresses generated in zirconia films during the oxidation of zirconium alloys, *Oxidation of Metals*, **2**, (1970) 235-261.
- [90] COX, B., Some effects of pressure on the oxidation of Zircaloy-2 in steam and oxygen, *J. Less-Common Met.* **5** (1963) 325-336.
- [91] WANKLYN, J. N., BRITTON, C. F., SILVESTER, D. R., WILKINS, N. J. M., The influence of the environment on the corrosion of zirconium and its alloys in high temperature steam, *J. Electrochem. Soc.*, **110** (1963) 856-866.
- [92] GEBHARDT, O., Investigation of in-pile formed corrosion films on Zircaloy fuel rod cladding by impedance spectroscopy and galvanostatic anodisation, *J. Nucl. Mater.* **203** (1993) 17-26.
- [93] GEBHARDT, O., A phase reference procedure for interpretation of impedance spectroscopy experiments, *Electrochim. Acta.*, **38** (1993) 633-641.
- [94] COX, B., WONG, Y-M., Simulating porous oxide films on zirconium alloys, *J. Nucl. Mater.* **218** (1995) 324-334.
- [95] COX, B., GASCOIN, F., WONG, Y-M., Properties of thin (<0.5  $\mu\text{m}$ ) oxide films on zirconium alloys, *J. Nucl. Mater.* **218** (1995) 113-128.
- [96] BEIE, H. J., MITWALSKY, A., GARZAROLLI, F., RUHMANN, H., SELL, H. J., "Examination of the corrosion mechanism of zirconium alloys", Zirconium in the Nuclear Industry: 10th Int. Symp., ASTM-STP-1245, (GARDE, A. M., BRADLEY, E. R., Eds.), American Society for Testing and Materials, W. Conshohocken, PA. (1994) 615-643.
- [97] PLOC, R. A., "Existence of cubic  $\text{ZrO}_2$  at 300°C on bulk zirconium", Proc. 27th Ann. EMSA Conf., St. Paul, MN., Electron Microscopical Society of America, (1969) 166-167.
- [98] COX, B., Pore structure in oxide films on irradiated and unirradiated zirconium alloys, *J. Nucl. Mater.* **148** (1987) 332-343.
- [99] GRITTI, O., Thesis, "Etude de l'alumine renforcée par dispersion de zircone, influence de l'oxyde de cérium", University of Limoges, French Report, CEA-R-5426 (Oct. 30, 1987), Commissariat à l'Energie Atomique, Paris, France.
- [100] RAMASUBRAMANIAN, N., PREOCANIN, N., LING, V. C., "Lithium uptake and the accelerated corrosion of zirconium alloys", Zirconium in the Nuclear Industry: 8th Int. Symp., ASTM-STP-1023, (VAN SWAM, L. F. P., EUCKEN, C. M., Eds.), American Society for Testing and Materials, W. Conshohocken, PA. (1989) 187-201.
- [101] CORIOU, H., GRALL, L., MEUNIER, J., PELRAS, M., WILLERMOZ, J., Corrosion du Zircaloy dans divers milieux alcalins à haute température, *J. Nucl. Mater.* **7** (1962) 320-327.
- [102] HILLNER, E., CHIRIGOS, J. M., The effect of lithium hydroxide and related solutions on the corrosion rate of Zircaloy-2 in 680°F water, U.S. Rep. WAPD-TM-307, Bettis Atomic Power Laboratory, W. Mifflin, PA. (1967).
- [103] MURGATROYD, R. A., WINTON, J., Hydriding Zircaloy-2 in lithium hydroxide solutions, *J. Nucl. Mater.* **23** (1967) 249, and U.K. Report, TRG Rep. 1439(C), (1967), U.K. Atomic Energy Authority, Reactor Group, Risley.

- [104] McDONALD, S G , SABOL, G P , SHEPPARD, K D , "Effect of lithium hydroxide on the corrosion behaviour of Zircaloy-4", Zirconium in the Nuclear Industry 6th Int Symp , ASTM-STP-824, (FRANKLIN, D , ADAMSON, R B , Eds ), American Society for Testing and Materials, W Conshohocken, PA (1983) 519-530
- [105] RAMASUBRAMANIAN, N , BALAKRISHNAN, P V , "Aqueous chemistry of lithium hydroxide and boric acid and corrosion of Zircaloy-4 and Zr-2.5wt% Nb alloy", Zirconium in the Nuclear Industry 10th Int Symp ASTM-STP-1245, (GARDE, A M , BRADLEY, E R , Eds ), American Society for Testing and Materials, W Conshohocken, PA (1994) 378-399
- [106] POLLEY, M V , EVANS, H E , "Review of effect of lithium on PWR fuel cladding corrosion", Proceedings of Water Chemistry of Nuclear Reactor Systems 6, British Nuclear Energy Society, London, (1992) 61-66
- [107] RAMASUBRAMANIAN, N , PRECOANIN, N , LING, V C , "Lithium uptake and the accelerated corrosion of zirconium alloys", Zirconium in the Nuclear Industry 8th Int Symp , ASTM-STP-1023, (VAN SWAM, L F P , EUCKEN, C M , Eds ), American Society for Testing and Materials, W Conshohocken, PA (1989) 187-201
- [108] SABOL, G P , McDONALD, S G , "Structural aspects of oxide film growth on zirconium based alloys", Stress Effects and the Oxidation of Metals (CATHCART, J V , Ed ), AIME (1975) 352
- [109] RAMASUBRAMANIAN, N , "Lithium uptake and the corrosion of zirconium alloys in aqueous lithium hydroxide solutions", Zirconium in the Nuclear Industry 9th Int Symp , ASTM-STP-1132, (EUCKEN, C M , GARDE, A M , Eds ), American Society for Testing and Materials, W Conshohocken, PA (1991) 613-627
- [110] COX, B , WU, C , Transient effects of lithium hydroxide and boric acid on Zircalov corrosion, J Nucl Mater **224** (1995) 169-178
- [111] COX, B , UNGURELU, M , WONG, Y-M , WU, C , "Mechanisms of LiOH degradation and  $H_2BO_3$  repair of  $ZrO_2$  films", Zirconium in the Nuclear Industry 11th Int Symp , Garmisch-Partenkirchen, Germany, (1995), ASTM-STP-1295, (BRADLEY, E R , SABOL, G P , Eds ), American Society for Testing and Materials, W Conshohocken, PA , (1996) 114-136
- [112] SOMIYA, S , Hydrothermal reactions for materials science and engineering, Elsevier Applied Sci Publ , London, (1989)
- [113] ILTIS, X , LEFEBVRE, F , LEMAIGNAN, C , "Iron redistribution in the Zircalov oxide layer Driving force and influence of irradiation", Zirconium in the Nuclear Industry 11th Int Symp , Garmisch-Partenkirchen, Ger , (1995), ASTM-STP-1295, (BRADLEY, E R , SABOL, G P , Eds ), American Society for Testing and Materials, W Conshohocken, PA (1996) 242-263
- [114] TICE, D R , HUDDART, G , BRAMWELL, I L , "Corrosion of Zircaloy-4 fuel cladding in high concentration lithium and boron conditions simulating extended burnup in PWR" Proc Conf , Materials for Nuclear Core Applications, British Nuclear Energy Society, London, (1987) 57-63
- [115] BRAMWELL, I L , PARSONS, P D , TICE, D R , "Corrosion of Zircaloy-4 PWR fuel cladding in lithiated and borated water environments", Zirconium in the Nuclear Industry 9th Int Symp , ASTM-STP-1132, (EUCKEN, C M , GARDE, A M , Eds ) American Society for Testing and Materials, W Conshohocken, PA (1991) 628-642
- [116] FIDLERIS, V , The irradiation creep and growth phenomenon J Nucl Mater **159** (1988) 22
- [117] COX, B , "Modelling the corrosion of zirconium alloys in nuclear reactors cooled by high temperature water", Proc NATO Adv Research Workshop on Modelling Aqueous Corrosion, RNEC, Manadon, Plymouth, U K , (TRETHERWEY, K , ROBERGE, P R , Eds ), NATO, ASI Series E, Vol 266, Kluwer Acad Pub Dordrecht, (1993) 183-200
- [118] COX, B , "A new model for the in-reactor corrosion of zirconium alloys", Proc IAEA Tech Comm Mtg on the Influence of Water Chemistry on Fuel Cladding Behaviour, Rez, Czech Rep , (Oct 1993), IAEA-TECDOC-927 Vienna (1997) 91-110

- [119] DING, Y , NORTHWOOD, D O , Effects of LiOH on the microstructure of the oxide formed during the aqueous corrosion of Zr-2.5wt% Nb alloy, *J Nucl Mater* **202** (1993) 180-192
- [120] JEONG, Y H , RUHMANN, H , GARZAROLLI, F , "Influence of alkali metal hydroxides on corrosion of Zr-based alloys", IAEA Technical Mtg on the Influence of Water Chemistry on Fuel Cladding Behaviour, Rez, Czech Republic, (4-8 Oct , 1993), IAEA-TECDOC-927 Vienna (1997) 161-192
- [121] URBANIC, V F , COX, B , FIELD, G J , "Long-term corrosion and deuterium uptake in CANDU-PHW pressure tubes", Zirconium in the Nuclear Industry 7th Int Symp , ASTM-STP-939, (ADAMSON, R B , VAN SWAM, L F P , Eds ), American Society for Testing and Materials, W Conshohocken, PA (1987) 189-205
- [122] KNIGHTS, C F , PERKINS, R , The effect of applied tensile stress on the corrosion behaviour of Zircaloy-2 in steam and oxygen", *J Nucl Mater* , **36** (1970) 180
- [123] BUTLER, E P , BONANOS, N , The characterisation of ZrO<sub>2</sub> engineering ceramics by A C impedance, *Mater Sci Eng* , **71** (1985) 49-56
- [124] GARZAROLLI, F , HOLZER, R , Waterside corrosion performance of light water power reactor fuel, *Nucl Energy*, **31** (1992) 65-86
- [125] GARZAROLLI, F , POHLMAYER, S , TRAPP-PRITSCHING, S , WEIDINGER, H G "Influence of various additions to water on Zircaloy-4 corrosion in autoclave tests at 350°C", Proc Technical Committee Mtg on Fundamental Aspects of Corrosion of Zirconium Base Alloys in Water Reactor Environments, Portland, OR, USA, IWGFPT-34, IAEA, Vienna, (1989) 65-72
- [126] GRAS, J M , NOEL, D , "Corrosion behaviour of Zircaloy-4 in lithiated-boricated water at 360°C", Poster Session, Zirconium in the Nuclear Industry 9th Int Symp , French Report HT-45/COM, 1187A (1991), Electricité de France
- [127] BILLOT, P H , ROBIN, J C , GIORDANO, A , PEYBERNES, J , THOMAZET, J , "Experimental and theoretical studies of parameters that influence corrosion of zirconium-based alloys in pressurised water", Zirconium in the Nuclear Industry 10th Int Symp , ASTM-STP-1245, (GARDE, A M , BRADLEY, E R , Eds ), American Society for Testing and Materials, W Conshohocken, PA (1994) 351-377
- [128] COX, B , FIDLERIS, V , "Enhanced low temperature oxidation of Zr alloys under irradiation", Zirconium in the Nuclear Industry 8th Int Symp , ASTM-STP-1023, (VAN SWAM, L F P , EUCKEN, C M , Eds ), American Society for Testing and Materials, W Conshohocken, PA (1990) 245-265
- [129] URQUHART, A W , VERMILYEA, D A , A preliminary correlation between the accelerated corrosion of Zircaloy in BWRs and in high temperature high pressure steam *J Nucl Mater* **62** (1976) 111-114
- [130] CHENG, B , ADAMSON, R B , U S Patent 4440862, (3 April 1984)
- [131] RUDLING, P , MACHIELS, A J , "Corrosion performance ranking of Zircaloy-2 for BWR applications", Zirconium in the Industry Industry 8th Int Symp , ASTM-STP-1023, (VAN SWAM, L F P , EUCKEN, C M , Eds ), American Society for Testing and Materials, W Conshohocken, PA (1989) 315-333
- [132] Papers on nodular corrosion, Zirconium in the Nuclear Industry 7th Int Symp , ASTM-STP-939, (ADAMSON, R B , VAN SWAM, L F P , Eds ), American Society for Testing and Materials, W Conshohocken, PA (1987) 243-447
- [133] Papers on nodular corrosion, Zirconium in the Nuclear Industry 8th Int Symp , ASTM-STP-1023, (VAN SWAM, L F P , EUCKEN, C M , Eds ), American Society for Testing and Materials, W Conshohocken, PA (1989) 291-402
- [134] CHARQUET, D , "Corrosion nodulaire du Zircaloy-4 en vapeur d'eau a 500°C", Proc 8th Congres Europeen de Corrosion, Nice, Vol 2, Societe de chimie industrielle et Centre Francais de la corrosion, Paris, (1985) P10-1-6
- [135] SABOL, G , McDONALD, S G , NURMINEN, J I , JACOBSEN, W A , "Laser-beam beta heat treatment of Zircaloy", Zirconium in the Nuclear Industry 7th Int Symp ASTM-

- STP-939, (ADAMSON, R. B., VAN SWAM, L. F. P., Eds.), American Society of Testing and Materials, W. Conshohocken, PA. (1987) 168-186.
- [136] DEMARS, H., GIVORD, J. P., ARMAND, M., Influence de la structure du Zircaloy-2 sur sa résistance à la corrosion par la vapeur d'eau, *Mem. Sci. Rév. Métall.* **62** (1965) 269
  - [137] BENTLEY, M. J., Out-of-reactor studies of the nodular oxidation of zirconium alloys, U.K. Rep. TRG-3001(S), United Kingdom Atomic Energy Authority, Reactor Fuel Element Laboratory, Springfield, (1977).
  - [138] BROWN, A., HARDIE, D., The effect of dissolved oxygen on the terminal solubility of hydrogen in alpha zirconium, *J. Nucl. Mater.* **4** (1961) 110-112.
  - [139] ROY, C., Hydrogen distribution in oxidized zirconium alloys by autoradiography, Can Rep AECL-2085, Atomic Energy of Canada Ltd., Chalk River Nuclear Laboratories, (1964).
  - [140] RAMASUBRAMANIAN, N., "Nodule nucleation at and away from intermetallics", Proc Tech. Comm. Mtg. on Fundamental Aspects of Corrosion on Zirconium Base Alloys in Water Reactor Environments, Portland, OR., USA, IWGFPT/34, IAEA, Vienna, Austria, (1989) 36-44.
  - [141] RAMASUBRAMANIAN, N., Out-reactor nodular corrosion behaviour of Zircalloys, *J. Nucl. Mater.* **119** (1983) 208-218.
  - [142] KUWAE, R., SATO, K., HIGASHINAKAGAWA, E., KAWASHIMA, E., NAKAMURA, S., Mechanism of Zircaloy nodular corrosion, *J. Nucl. Mater.* **119** (1983) 229-239.
  - [143] GARZAROLLI, F., STEHLE, H., STEINBERG, E., WEIDINGER, H., "Progress in the knowledge of nodular corrosion", Zirconium in the Nuclear Industry: 7th Int. Symp., ASTM-STP-939, (ADAMSON, R. B., VAN SWAM, L. F. P., Eds.), American Society for Testing and Materials, W. Conshohocken, PA. (1987) 417-430.
  - [144] SUMERLING, R., GARLICK, A., STUTTARD, A., HARTOG, J. M., TROWSE, F. W., SIMS, P., "Further evidence of Zircaloy corrosion in fuel elements irradiated in a steam generating heavy water reactor", Zirconium in the Nuclear Industry: 4th Int. Symp., ASTM-STP-681, (PAPAZOGLU, T. P., Ed.), American Society for Testing and Materials, W. Conshohocken, PA (1979) 107-121.
  - [145] ADAMSON, R. B., CHENG, B., LEVIN, H. A., TUCKER, R. P., "Zircaloy corrosion in GE plants", Proc. EPRI Workshop on Zircaloy Corrosion, Charlotte, NC., Electric Power Research Institute, Palo Alto, (1986).
  - [146] FERRETT, D. J., BLACK, W. S. A., BLACKMAN, T. E., "Winfrith SGHWR operations experience", Nuclear Power Plant Thermal Hydraulics and Operations (Proc. 2nd Int. Topical Mtg., Tokyo), American Nuclear Society, (1986) 5-87.
  - [147] PLATONOV, P. A., EPERIN, A. P., IVANOV, A. N., FROLOV, I. A., RODCHENKO, B. S., VAROVIN, I. A., "Some results of investigating the deformation behaviour of Zr-2.5 wt% Nb pressure tubes in the MR reactor and the operating RBMK units", Zirconium in the Nuclear Industry: 8th Int. Symp., San Diego, CA. (1988), not in proceedings.
  - [148] ISOBE, T., MURAI, T., MAE, Y., "Anodic protection of precipitates in aqueous corrosion of Zircaloy", Zirconium in the Nuclear Industry: 11th Int. Symp., Garmisch-Partenkirchen, Germany, (1995), ASTM-STP-1295, (BRADLEY, E. R., SABOL, G. P., Eds.), American Society for Testing and Materials, W. Conshohocken, PA, (1996) 203-217
  - [149] GARLICK, A., SUMERLING, R., SHIRES, G. L., Crud-induced overheating defects in water reactor fuel pins, *J. British Nucl. Energy Soc.* **16** (1977) 77.
  - [150] MARLOWE, M. O., ARMIJO, J. S., CHENG, B., ADAMSON, R. B., "Nuclear fuel cladding localized corrosion", Light-Water Reactor Fuel Performance, (Proc. ANS Topical Mtg., Orlando, FL), Vol. 1, American Nuclear Society, (1985) 3-73.
  - [151] BURNS, W. G., MOORE, P. B., "Radiation enhancement of Zircaloy corrosion in boiling water systems: A study of simulated radiation chemical kinetics", Water Chemistry of Nuclear Reactor Systems, (Proc. BNES Conf., Bournemouth), British Nuclear Energy Society, London, (1977) 281.
  - [152] ITO, Y., FURUYA, T., The effect of annealing parameter on corrosion resistance of Zircaloy-2, *J. Nucl. Sci. and Tech.*, **32** (1995) 1118-1126.
  - [153] NELSON, H. G., WACHOB, H. F., Stress corrosion cracking of Zircaloy, U.S. Rep EPRI-NP-717, Section 6, Electric Power Research Institute, Palo Alto, CA. (1978).

- [154] COLEMAN, C. E., COX, B., "Cracking of zirconium alloys in hydrogen", Zirconium in the Nuclear Industry 6th Int. Symp., ASTM-STP-824, (FRANKLIN, D., ADAMSON, R. B., Eds.), American Society for Testing and Materials, (1984) 675-690.
- [155] COLEMAN, C. E., AMBLER, J. F. R., Delayed hydrogen cracking in Zr-2.5 wt% Nb alloys, *Revs. of Coatings and Corrosion* 3 (1979) 105-137 (YAHALOM, J., Ed.) Freund, Tel Aviv, (1979).
- [156] URBANIC, V. F., COX, B., Long-term corrosion and deuteriding behaviour of Zircaloy-2 under irradiation, *Can. Metall. Quart.* 24 (1985) 189-196.
- [157] PERRYMAN, E. C. W., Pickering pressure tube cracking experience, *Nucl. Energy*, 17 (1978) 95-105.
- [158] COX, B., Some factors which affect the rate of oxidation and hydrogen absorption of Zircaloy-2 in steam, U.K. Rep. AERE-R4348, United Kingdom Atomic Energy Authority, AERE, Harwell, Berks. (1963).
- [159] COX, B., ROY, C., The use of tritium as a tracer in studies of hydrogen uptake by zirconium alloys, Can. Rep. AECL-2519, Atomic Energy of Canada Ltd., Chalk River Nuclear Laboratories, (1965).
- [160] HILLNER, E., Hydrogen absorption in Zircaloy during aqueous corrosion, Effect of Environment, U.S. Rep. WAPD-TM-411, Bettis Atomic Power Lab., W. Mifflin, PA (1964).
- [161] RAMASUBRAMANIAN, N., Localized electron transport in corroding zirconium alloys, *J Nucl. Mater.* 55 (1975) 134-154.
- [162] KISELEV, A. A., MYSHKIN, V. A., KOZHEVNIKOVA, A. V., KOROLEV, S. I., SHORINA, G., "Investigation of Zr alloy corrosion in water and steam at high temperature and pressure", *Proc. Conf. on Corrosion of Reactor Materials*, Salzburg, Austria, STI/59, Vol. II, IAEA, Vienna, (1962) 67-104.
- [163] KASS, S., KIRK, W. W., Corrosion and hydrogen absorption properties of nickel-free Zircaloy-2 and Zircaloy-4, *ASM Trans. Quart.* 56 (1962) 77.
- [164] PLOC, R. A., DAVIDSON, R. D., "Auger electron analysis of oxides grown on dilute zirconium alloys", *Microstructural Science*, Vol. 13 (SHIELDS, S. A., BAGNALL, C., WITKOWSKI, R. E., VANDERVOORT, G. F., Eds.), International Metallographic Society, Columbus, OH. (1985) 131-141.
- [165] COX, B., WONG, Y.-M., HOANG, T., Electrically conducting paths in zirconia films, *J Nucl. Mater.* 223 (1995) 202-209.
- [166] MAEKAWA, T., TERADA, M., Infra-red spectra study on the oxidation film of zirconium, *Trans. Jpn. Inst. Met.* 4 (1963) 47.
- [167] ELMOSELHI, M., WARR, B. D., McINTYRE, N. S., "A study of the hydrogen uptake mechanism in zirconium alloys", Zirconium in the Nuclear Industry 10th Int. Symp., ASTM-STP-1245, (GARDE, A. M., BRADLEY, E. R., Eds.), American Society for Testing and Materials, W. Conshohocken, PA. (1994) 62-79.
- [168] SMITH, T., Mechanism of hydrogen permeation of oxide films on zirconium, *J Electrochem. Soc.* 112 (1965) 560.
- [169] SMITH, T., Kinetics and mechanism of hydrogen permeation of oxide films on zirconium, *J Nucl. Mater.* 18 (1966) 323-336.
- [170] KHATAMIAN, D., MANCHESTER, F. D., An ion beam study of H diffusion in oxides of Zr and Zr-Nb (2.5 wt%), *J. Nucl. Mater.* 166 (1989) 300-306.
- [171] KHATAMIAN, D., Diffusion of hydrogen in the oxides of Zr-1 Nb, Zr-2.5 Nb and Zr-20 Nb alloys, *Z. Phys. Chemie.* 181 (1993) 435-440.
- [172] LENNARD, W. N., MASSOUMI, G. R., ALKEMADE, P. F. A., MITCHELL, I. V., McINTYRE, N. S., DAVIDSON, R. D., Deuterium depth distribution investigations in Zr and ZrO<sub>2</sub>, *Nucl. Instr. and Meth.*, B73 (1993) 203-213.
- [173] CHARQUET, D., RUDLING, P., MIKES-LINDBACK, M., BARBERIS, P., "Hydrogen absorption kinetics during Zircaloy oxidation in steam", Zirconium in the Nuclear Industry 10th Int. Symp., ASTM-STP-1245, (GARDE, A. M., BRADLEY, E. P., Eds.), American Society for Testing and Materials, W. Conshohocken, PA (1994) 80-97.

- [174] ELLEMAN, T. S., VERGHESE, K., Surface effects on tritium diffusion in niobium, zirconium and stainless steel, *J. Nucl. Mater.* **53** (1974) 299-306.
- [175] AUSTIN, J. H., ELLEMAN, T. S., VERGHESE, K., Tritium diffusion in Zircaloy-2 in the temperature range 78-204°C, *J. Nucl. Mater.* **51** (1974) 321-329.
- [176] FREER, D. W., SILVESTER, D. R., WANKLYN, N. J., Hydrogen uptake of zirconium and its alloys during early stages of corrosion in steam, *Corrosion*, **21** (1965) 137-142.
- [177] COX, B., The effect of some alloying additions on the oxidation of zirconium in steam, U.K. Report, AERE-R4458, United Kingdom Atomic Energy Authority, AERE, Harwell, Berks. (1963).
- [178] YENISCAVICH, W., WOLFE, R. A., LIEBERMAN, R. M., Hydrogen absorption by nickel enriched Zircaloy-2, *J. Nucl. Mater.* **3** (1959) 271-280.
- [179] YENISCAVICH, W., WOLFE, R. A., LIEBERMAN, R. M., "Irradiation-induced hydrogen absorption by nickel-enriched Zircaloy-2", *Proc. AIMME Nucl. Eng. and Sci. Conf.*, Cleveland, OH., (April 1959), Paper V-III.
- [180] MCINTYRE, N. S., DAVIDSON, R. D., WEISNER, C. G., GOOD, G. M., MOUNT, G. R., WARR, B. D., ELMOSELI, M., Migration of hydrogen through thin films of ZrO<sub>2</sub> on Zr-Nb alloy, *J. Vac. Sci. & Technol.*, **A9** (1991) 1402-1405.
- [181] ARONSON, S., Some experiments on the permeation of hydrogen through oxide films on zirconium, *Bettis Technical Rev.*, U.S. Rep. WAPD-BT-19, Bettis Atomic Power Lab., W. Mifflin, PA. (1960) 75-81.
- [182] GULBRANSEN, E. A., ANDREW, K. F., Mechanism of the reaction of hydrogen with Zircaloy, I, role of oxide films, pretreatments and occluded gases, *J. Electrochem. Soc.* **101** (1954) 348-353.
- [183] GULBRANSEN, E. A., ANDREW, K. F., Reaction of hydrogen with preoxidized Zircaloy-2 at 300° to 400°C, *J. Electrochem. Soc.* **104** (1957) 709-712.
- [184] SHANNON, D. W., Role of oxidation rate on the hydriding of zirconium alloys in gas atmospheres containing hydrogen, *Corrosion* **67** (1963) 414T.
- [185] BOYLE, R. F., KISIEL, T. J., Hydrogen permeation of Zircaloy-2 corrosion films, *Bettis Tech. Rev.*, U.S. Rep. WAPD-BT-10, Bettis Atomic Power Lab., W. Mifflin, PA. (1958) 31.
- [186] UNE, K., Kinetics of reaction of zirconium alloy with hydrogen, *J. Less-Common Met.* **57** (1978) 93-101.
- [187] SMITH, T., Hydrogen permeation of oxide films on zirconium, U.S. Report NAA-SR-6267, (1962), North American Aviation, Thousand Oaks, CA.
- [188] PEMSLER, J. P., Diffusion of oxygen in zirconium and its relation to oxidation and corrosion, *J. Electrochem. Soc.* **105** (1958) 315-322.
- [189] COX, B., Mechanisms of hydrogen absorption by zirconium alloys, *Can. Rep. AECL-8702*, Atomic Energy of Canada Ltd., Chalk River Nuclear Laboratories, (1985).
- [190] COX, B., Oxide breakdown on arc-melted sponge zirconium, *Corrosion* **16** (1960) 380t-384t.
- [191] COX, B., MCINTOSH, A. B., The oxide topography on crystal-bar and reactor grade sponge zirconium, *Can. Rep. AECL-3223*, Atomic Energy of Canada Ltd., Chalk River Nuclear Laboratories, (1968).
- [192] WANKLYN, N. J., BRITTON, C. F., SILVESTER, D. R., WILKINS, N. J. M., The corrosion of zirconium and its alloys, Part III The influence of the environment on oxidation, U.K. Rep. AERE-4130, United Kingdom Atomic Energy Authority, AERE, Harwell, Berks. (1962).
- [193] COX, B., Examination of oxidized zirconium alloys with the photo-emission and scanning electron microscopes, *Can. Rep. PR-CMA-9*, Atomic Energy of Canada Ltd., Chalk River Nuclear Laboratories, (1969) 76-79.
- [194] PEMSLER, J. P., Studies of oxygen gradients in corroding zirconium alloys, *J. Nucl. Mater.* **7** (1962) 16-25.

- [195] JOHNSON, A B , Jr , "Aqueous corrosion and hydriding of zirconium alloys in nuclear reactor environments", *Metallic Corrosion*, (Proc 4th Int Cong Amsterdam), National Association of Corrosion Engineers, Houston, (1972) 168-177
- [196] JOHNSON, A B , Jr , LeSURF, J E , PROEBSTLE, R A , "Study of zirconium alloy corrosion parameters in the advanced test reactor", *Zirconium in the Nuclear Industry 3rd Int Symp*, ASTM-STP-551, American Society for Testing and Materials, W Conshohocken, PA (1974) 495-513
- [197] JOHNSON, A B , Jr , A review of corrosion phenomena on zirconium alloys, niobium, titanium, Inconel, stainless steel and nickel plate under irradiation, *Revs on Coatings and Corrosion 4* (Ed YAHALOM, J ) Freund, Tel Aviv, (1975) 299
- [198] URBANIC, V F , "Observations of accelerated hydriding in zirconium alloys", *Zirconium in the Nuclear Industry 6th Int Symp*, ASTM-STP-824, (FRANKLIN, D , ADAMSON, R B , Eds ), American Society for Testing and Materials, (1984) 554-571
- [199] SAWATZKY, A , Hydriding Zircaloy-2 by electrolysis, Canadian Report AECL-1046 (CRMet-924), Atomic Energy of Canada Ltd , Chalk River, (1960)
- [200] ATTERMO, R , SIETNIKS, A , Electrolytic hydriding of zirconium, *Electrochim Acta*, **14** (1969) 121
- [201] MacGILLIVRAY, G M , URBANIC, V F , Hydrogen charging of Zr-2.5wt%Nb and Zircaloy-2 pressure tubes in fused salts, Canadian Report, CRNL-2134, Atomic Energy of Canada Ltd , Chalk River, (1983)
- [202] COX, B , Low-temperature oxidation and hydriding of Zircaloys, Canadian Report, CNEUT-91-10, University of Toronto, Centre for Nuclear Engineering, Ont (1991)
- [203] SAMMARONE, D G , The galvanic behaviour of materials in reactor water, U S Report, WCAP-1844, Westinghouse, Pittsburgh, PA (1961)
- [204] ALEXANDER, W K , Hydriding of Hanford production reactor Zircaloy process tubes, U S Report, DUN-SA-34, Hanford Works, Wash (1967)
- [205] WINEGARDNER, W K , GRIGGS, B , Zirconium hydride formation in Hanford production reactor tubes, U S Report, BNWL-588, Battelle North-West Laboratories, Hanford, Wash (1967)
- [206] GRIGGS, B , Evaluation of Zircaloy-2 process tubes containing non-standard spacers, U S Report, BNWL-CC-1633, Battelle North-West Laboratories, Hanford, Wash (1968)
- [207] DILLON, R L , GRIGGS, B , U S quarterly progress report, July-Sept 1965, BNWL-166, Battelle North-West Laboratories, Hanford, Wash (1966)
- [208] SCHWARTZ, C M , VAUGHAN, D. A , Effect of hydrogen pickup on corrosion behaviour of zirconium in water, U S Report BMI-1120, Battelle Memorial Institute, Columbus, OH (1956)
- [209] YAMANAKA, S , TANAKA, T , MIYAKE, M , Effect of oxygen on hydrogen solubility in zirconium, *J Nucl Mater* **167** (1989) 231-237
- [210] ROY, C , An experiment to clarify the effect of dissolved oxygen on the terminal solubility of hydrogen in zirconium, *J Nucl Mater* **13** (1964) 275-277
- [211] ELLS, C E , Hydride precipitates in zirconium alloys, *J Nucl Mater* **28** (1968) 129-151
- [212] ASHER, R C , TROWSE, F E , The distribution of hydrogen in zirconium alloy fuel cladding The effects of heat flux, *J Nucl Mater* **35** (1970) 115-121
- [213] PULS, M P , On the consequences of hydrogen supersaturation effects in Zr alloys to hydrogen ingress and delayed hydride cracking, *J Nucl Mater* **165** (1989) 128-141
- [214] COATES, D E , Hydrogen supersaturation in zirconium and zirconium-2.5wt% niobium, Canadian Report AECL-2599, Atomic Energy of Canada Ltd , Chalk River, (1966)
- [215] WESTERMAN, R E , Charging Zircaloy-2 with hydrogen beyond the solubility limit, *J Nucl Mater* **18** (1966) 31-38, and U S Report HW73382, Hanford Works, Wash (1962)
- [216] MARINO, G P , Hydrogen behaviour in zirconium-based alloys, U S Report, WAPD-TM-759, Bettis Atomic Power Lab , W Mifflin, PA (1968)
- [217] MARINO, G P , Hydrogen supercharging in Zircaloy, *Mater Sci and Eng* **7** (1971) 335, and U S Report WAPD-T-2303 Bettis Atomic Power Lab , W Mifflin, PA (1969)

- [218] WESTLAKE, D. G., OCKERS, S. T., Hydrogen supercharging during thermal cycling of zirconium, *J. Nucl. Mater.* **37** (1970) 236-242.
- [219] HILLNER, E., KASS, J. N., KEARNS, J. J., Hydrogen supercharging during corrosion of Zircaloy, *J. Nucl. Mater.* **45** (1972/73) 175-178.
- [220] MALLET, M. W., ALBRECHT, W. M., Hydrogen supercharging during corrosion of Zircaloy, *J. Electrochem. Soc.*, **104** (1957) 142-146.
- [221] SAWATZKY, A., The diffusion and solubility of hydrogen in the alpha phase of Zircaloy-2, *J. Nucl. Mater.* **2** (1960) 62-68.
- [222] KEARNS, J. J., Diffusion coefficient of hydrogen in alpha zirconium, Zircaloy-2 and Zircaloy-4, *J. Nucl. Mater.* **43** (1972) 330-338.
- [223] GREGOR, G. U., MUNZEL, H., KUNZ, W., SCHWIERCZINSKI, A., Diffusion of tritium in Zircaloy-2, *J. Nucl. Mater.* **88** (1980) 15-22.
- [224] KASS, S., Corrosion and hydrogen pickup of Zircaloy in concentrated lithium hydroxide solutions, *Corrosion*, **25** (1969) 30; and U.S. Report WAPD-TM-656, Bettis Atomic Power Lab., W. Mifflin, PA. (1967).
- [225] ZREIBA, N. A., NORTHWOOD, D. O., The corrosion/hydriding behaviour of Zr-2.5wt% Nb nuclear reactor pressure tubing in pressurised lithiated water (pH 12.3) at 300°, *J. Mater. Ener. Syst.*, **7** (1985) 104-122.
- [226] SHILHAN, J. T., Rapid hydriding of Zircaloy-2 by LiOH method, Canadian Report HSEN-FCP-65-033, Hawker Siddeley Engineering, Malton, Ont. (1965).
- [227] COX, B., LING, V. C., Effect of thermal cycling on the movement of the ( $\alpha$ Zr +  $\delta$ ZrH<sub>1.6</sub>) phase boundary in Zr-2.5% Nb, Canadian Report AECL-6538, 73-78, Atomic Energy of Canada Ltd., Chalk River, (1979).
- [228] MARKOWITZ, J. M., Internal zirconium hydride formation in Zircaloy fuel element cladding under irradiation, U.S. Report WAPD-TM-351, Bettis Atomic Power Lab., W. Mifflin, PA. (1963).
- [229] GULBRANSEN, E. A., ANDREW, K. F., Kinetics of the reactions of zirconium with O<sub>2</sub>, N<sub>2</sub> and H<sub>2</sub>, *Trans. AIMME (Met. Trans.)*, **185** (1949) 515-525.
- [230] LAURSEN, T., LESLIE, J. R., TAPPING, R. L., Deuterium depth distributions in oxidised Zr-2.5%wt Nb measured by nuclear reaction analysis, *J. Less. Comm. Met.*, **172-174** (1991) 1306-1312.
- [231] STERN, A., KHATAMIAN, D., LAURSEN, T., WEATHERLY, G. C., PERZ, J. M., Hydrogen and deuterium profiling at the surface of zirconium alloys II. The effects of oxidation, *J. Nucl. Mater.* **148** (1987) 257-265.
- [232] COX, B., JOHNSTON, T., The oxidation and corrosion of zirconium and its alloys, IX: Observation of a second transition point during the oxidation of zirconium alloys, U.K. Report, AERE-R3256 (June 1960), United Kingdom Atomic Energy Authority, AERE, Harwell, Berks. (1960).
- [233] COX, B., Causes of a second transition point occurring during oxidation of zirconium alloys, *Corrosion*, **18** (1962) 33t-36t.
- [234] GARDE, A. M., "Enhancement of aqueous corrosion of Zircaloy-4 due to hydride precipitation at the metal-oxide interface", *Zirconium in the Nuclear Industry: 9th Int. Symp.*, ASTM-STP-1132, (EUCKEN, C. M., GARDE, A. M., Eds.), American Society for Testing and Materials, W. Conshohocken, PA. (1991) 566-594.
- [235] KIDO, T., "A study on enhancement of uniform corrosion of Zircaloy-4 cladding under high burnup operation in PWRs", *Proc. of EPRI-PWR Fuel Corrosion Workshop*, Washington, DC, USA, Ed. Bo Cheng, Electric Power Research Inst., Palo Alto, CA, USA. (1993).
- [236] KIDO, T., "A study on enhanced uniform corrosion of Zircaloy-4 cladding during high burnup operation in PWRs", *Environmental Degradation of Materials in Nuclear Power Systems-Water Reactors*, (6th Int. Symp.), San Diego, CA., USA, (R. E. GOLD, E. P. SIMONEN, Eds.), MMMS, 449-455.
- [237] COX, B., JOHNSTON, T., The oxidation and corrosion of zirconium and its alloys, XIII: Some observations of hydride in zirconium and Zircaloy-2 and its subsequent effect on corrosion, UK Report, AERE-R3881, United Kingdom Atomic Energy Authority, AERE, Harwell, Berks. (1992).



- [238] CHENG, B , KLEPPER, H H , GILMORE, "PWR Zircaloy fuel cladding performance, mechanisms and modelling", Zirconium in the Nuclear Industry 11th Int Svmp , Garmisch-Partenkirchen, Germany, (1995), ASTM-STP-1295, (BRADLEY, E R ,SABOL, G P , Eds ), American Society for Testing and Materials, W Conshohocken, PA, (1996) 137-159
- [239] STRASSER, A , BOYLE, D O , YANG, R , Reliability - the first priority in fuel performance, Proc of ANS Int. Topical Mtg on Light Water Reactor Fuel Performance, West Palm Beach, (April 1994) 3-11
- [240] GARZAROLLI, F , et al , "Corrosion experience with Zircaloy cladding tubes in high efficiency pressurized water reactors and perspectives for future improvements", Zirconium in the Nuclear Industry 9th Int Symp , Kobe, Japan, Nov 1990, American Society for Testing and Materials, not published in the proceedings
- [241] SEIBOLD, A , WOODS, K N , "Advanced PWR cladding", Proc of the Int Topical Mtg on Light Water Reactor Fuel Performance, West Palm Beach, American Nuclear Soc , La Grange Park, ILL (1994) 633-642
- [242] GARZAROLLI, F , BROY, Y , BUSCH, R A , "Comparison of the long time corrosion behaviour of certain zirconium alloys in PWR, BWR and laboratory tests", Zirconium in the Nuclear Industry 11th Int Symp , Garmisch-Partenkirchen, Sept 11-14, 1995, ASTM-STP-1295, (BRADLEY, E R , SABOL, G P , Eds ), American Society for Testing and Materials, (1996) 850-863
- [243] FUCHS, H P , GARZAROLLI, F , WEIDINGER, H G , BODMER, R P , MEIER, G , BESCH, O-A , LISDAT, R , "Cladding and structural material development for the advanced Siemens PWR fuel performance", Fuel for the 90's, Proc Int Topical meeting on LWR Fuel Performance, Avignon, France, American Nuclear Society/European Nuclear Society, (1991) 682-690,
- [244] TAKESHI, I , MASUTO, Y , "Development of highly corrosion resistant zirconium-base alloys", Zirconium in the Nuclear Industry 9th Int Symp , ASTM-STP-1132, (EUCKEN, C M , GARDE, A M , Eds ), American Society for Testing and Materials, (1991) 346-367
- [245] MARDON, J P , CHARQUET, D , SENEVAT, J . "Development of new zirconium alloys for fuel rod cladding", Proc of Int Topical Mtg on Light Water Fuel Performance, West Palm Beach, American Nuclear Society, La Grange Park, ILL (1994) 643-649.
- [246] VAN SWAM, L F , GARZAROLLI, F , STEINBERG, E , "Advanced PWR cladding", Proc of ANS Int Topical Mtg on Light Water Reactor Fuel Performance, West Palm Beach, American Nuclear Society, La Grange Park, ILL (1994) 303-308
- [247] RUDLING, P , LIMBACK, M , JOURDAIN, P , "Zircaloy-2 and Zircaloy-4 corrosion and hydriding in PWRs". SFEN/ENS Conference on Contribution of Materials Investigation to the Resolution of Problems Encountered in Pressurised Water Reactors, Fontevraud III Societe Francaise pour l'Energie Nucleaire, (1994) 666-675
- [248] SABOL, G P , CORREAL-PULVER, O A , WEINER, R A , STANUTZ, R N , McATEE, K R , COMSTOCK, R J , LEECH, W J , MILLER, R S , In-reactor corrosion performance of ZIRLO and Zircaloy-4 and related modelling, Paper presented at ANS 1994 Int Topical Mtg on LWR Performance, April 17-21, 1994, West Palm Beach, Florida, (not published in Proceedings)
- [249] GARZAROLLI, F , SCHUMANN, R , STEINBERG, E , "Corrosion of optimized Zircaloy for BWR fuel elements", Zirconium in the Nuclear Industry 10th Int Symp , 1993, ASTM-STP-1245, (GARDE, A M , BRADLEY, E R , Eds ), American Society for Testing and Materials, (1994) 709-723
- [250] WEIDINGER, H G., GARZAROLLI, F , EUCKEN, C M , BAROCH, E F , "Effect of chemistry on elevated temperature nodular corrosion", Zirconium in the Nuclear Industry 7th Int Symp , ASTM-STP-939, (ADAMSON, R B , VAN SWAM, L F P , Eds ), American Society for Testing and Materials, (1987) 364-368
- [251] LEMAIGNAN, C , MOTTA, A T , Material Science and Technology, Vol 10 B Chapter 7, "Zirconium in Nuclear Applications", Nuclear Materials, Part 2, Verlag Chemie Weinheim, (1993) C, p 11

- [252] STEINBERG, E., WEIDINGER, H. G., SCHAA, A., "Analytical approaches and experimental verification to describe the influence of cold work and heat treatment on the mechanical properties of Zircaloy cladding tubes", Zirconium in the Nuclear Industry 6th Int Symp., ASTM-STP-824, (FRANKLIN, D. G., ADAMSON, R. B., Eds.), American Society for Testing and Materials, (1984) 106-122.
- [253] CHARQUET, D., STEINBERG, E., MILLET, Y., "Influence of variations in early fabrication steps on corrosion, mechanical properties, and structure of Zircaloy-4 products", Zirconium in the Nuclear Industry 7th Int Symp., ASTM-STP-939, (ADAMSON, R. B., VAN SWAM, L. F. P., Eds.), American Society for Testing and Materials, (1987) 431-447
- [254] URBAN, P., Development of ATRIUM fuel-assemblies for boiling water reactors, Siemens Nuclear Fuel Report, March 1992, p. 11.
- [255] FORSTER, J. P. et al., "Influence of final recrystallisation heat treatment on Zircaloy-4 strip corrosion", J. Nucl. Mater., 173 (1990) 164-178.
- [256] ANDERSSON, T., et al., "Influence of thermal processing and microstructure on the corrosion behaviour of Zircaloy-4 tubing", IAEA SM 288/59, IAEA, Vienna, (1986).
- [257] RUDLING, P., PETTERSSON, H., ANDERSSON, T., THORVALDSSON, T., "Corrosion performance of Zircaloy-2 and Zircaloy-4 PWR fuel cladding", Zirconium in the Nuclear Industry: 8th Int. Symp., ASTM-STP-1023, (VAN SWAM, L. F. P., EUCKEN, C. M., Eds.), American Society for Testing and Materials, W. Conshohocken, PA, (1989) 213-226.
- [258] WEIDINGER, H. G., LETTAU, H., "Advanced material and fabrication technology for LWR fuel", IAEA SM 288/27, IAEA, Vienna, (1986).
- [259] GARZAROLLI, F., STEINBERG, E., WEIDINGER, H. G., "Microstructure and corrosion studies for optimized PWR and BWR Zircaloy cladding", Zirconium in the Nuclear Industry 8th Int. Symp., ASTM-STP-1023, (VAN SWAM, L. F. P., EUCKEN, C. M., Eds.), American Society for Testing and Materials, W. Conshohocken, PA, (1989) 202-212
- [260] GARZAROLLI, F., STEHLE, H., "Behaviour of structural materials for fuel and control elements in light water cooled power reactors", IAEA STI/PUB/721, International Atomic Energy Agency, Vienna, (1987) p. 387,
- [261] GARZAROLLI, F., STEINBERG, E., Further development of cladding and structural materials for boiling water reactors, Siemens Nuclear Fuel Report No 3, July 1993, p. 19
- [262] ANDERSSON, T., THORVALDSSON, T., WILSON, A., WARDLEY, A. M., "Improvements in water reactor fuel technology and utilization", Proceedings of the IAEA-Symposium, Stockholm, Sweden, International Atomic Energy Agency, Vienna, (1987) 434-449
- [263] THORVALDSSON, T., ANDERSSON, T., WILSON, A., WARDLEY, A., "Correlation between 400°C steam corrosion behaviour, heat treatment, and microstructure of Zircaloy-4 tubing", Zirconium in the Nuclear Industry: 8th Int. Symp., ASTM-STP-1023, (VAN SWAM, L. F. P., EUCKEN, C. M., Eds.), American Society for Testing and Materials, W. Conshohocken, PA, (1989) 128-140
- [264] MAUSSNER, G., STEINBERG, E., TENCKHOFF, E., "Nucleation and growth of intermetallic precipitates in Zircaloy-2 and Zircaloy-4, and correlation to nodular corrosion behaviour", Zirconium in the Nuclear Industry: 7th Int. Symp., ASTM-STP-939, (ADAMSON, R. B., VAN SWAM, L. F. P., Eds.), American Society for Testing and Materials, W. Conshohocken, PA, (1987) 307-320.
- [265] MAUSSNER, G., et al., "Basic properties of zirconium alloys with respect to mechanical and corrosion behaviour", Proc. British Nuclear Energy Society Conference, London, (1987) paper 9.
- [266] KAHLWEIT, M., et al., Ostwald ripening of precipitates, Proceedings of the 2nd Acta/Scripta Metallurgica Conf., (1983) 61-69.
- [267] GROS, J. P., WADIER, J. F., Precipitate growth kinetics in Zircaloy-4, J. Nucl. Mater. 172 (1990) 85-96.
- [268] VAN SWAM, L., SHANN, S. H., "The corrosion of Zircaloy-4 fuel cladding in pressurized water reactors", Zirconium in the Nuclear Industry: 9th Int. Symp., ASTM-STP-1132.

- (EUCKEN, C M , GARDE, A M , Eds ), American Society for Testing and Materials, W Conshohocken, PA, (1992) 758-781
- [269] SCHEMEL, J H , Zirconium alloy fuel clad tubing engineering guide, Sandvik Special Metals, Kennewick, WA , (1989)
  - [270] CHARQUET, D , TRICOT, R , WADIER, J F , "Heterogeneous scale growth during steam corrosion of Zircaloy-4 at 500°C", Zirconium in the Nuclear Industry 8th Int Symp , ASTM-STP-1023, (VAN SWAM, L F P , EUCKEN, C M , Eds ), American Society for Testing and Materials, W Conshohocken, PA, (1989) 374-391
  - [271] HERB, B , MCCARTHY, J M , WANG, C T , RUHMANN, H , "Correlation of TEM microstructure with nodular corrosion behaviour for Zircaloy-2", Zirconium in the Nuclear Industry 10th Int Symp , ASTM-STP-1245, (GARDE, A M , BRADLEY, E R , Eds ), American Society for Testing and Materials, (1994) 419-436
  - [272] KRITSKY, V G , PETRIK, N G., BEREZINA, I G , DOILNITSINA, V V , "Effect of water chemistry and fuel operation parameters on Zr-1% Nb cladding corrosion", Proc Tech Comm Mtg on Influence of Water Chemistry on Fuel Cladding Behaviour, Rez, Czech Rep , (Oct 4-8, 1993), IAEA-TECDOC-927, Vienna (1997) 23-43
  - [273] ZAIMOVSKY, A S , NIKULINA, A V , RESHETNIKOV, N G , Zr Alloys In Nuclear Power, Moscow, Energoizdat, (1981)
  - [274] MENG, X , NORTHWOOD, D O., "Intermetallic precipitates in zirconium-niobium alloys", Zirconium in the Nuclear Industry 8th Int Symp , ASTM-STP-1023, (VAN SWAM, L F P , EUCKEN, C M , Eds ), American Society for Testing and Materials W Conshohocken, PA (1989) 478-486
  - [275] URBANIC V F , WARR, B D , MANOLESCU, A , CHOW, C K , SHANAHAN, M W , "Oxidation and deuterium uptake of Zr-2.5Nb pressure tubes in CANDU-PHW reactors", Zirconium in the Nuclear Industry 8th Int Symp , ASTM-STP-1023, (VAN SWAM, L F P , EUCKEN, C M , Eds ), American Society for Testing and Materials, W Conshohocken, PA (1989) 20-34
  - [276] PERKINS, R A , BUSCH, R , "Corrosion of Zircaloy-4 fuel cladding", Environmental Degradation of Materials in Nuclear Reactor Systems - Water Reactors, Proc 4th Int Symp , Jekyll Island, GA , 1989, National Association of Corrosion Engineers, Houston TX (1991) 10-15 to 10-24
  - [277] LUNDE, L , VIDEM, K , "Effect of materials and environmental variables on localized corrosion of zirconium alloys", Zirconium in the Nuclear Industry 4th Int Symp , ASTM-STP-681, (PAPAZOGLOU, T P , Ed ), American Society for Testing and Materials W Conshohocken, PA (1979) 40-59
  - [278] BERRY, W E , "Effect of fluoride ions on the aqueous corrosion of zirconium alloys" Corrosion of Zirconium Alloys, ASTM-STP-368, American Society for Testing and Materials, W Conshohocken, PA (1964), 28-40
  - [279] LUNDE, L , VIDEM, K , "Effect of surface treatment on the irradiation enhancement of corrosion of Zircaloy-2 in HBWR", Zirconium in Nuclear Applications, ASTM-STP-551 American Society for Testing and Materials, W Conshohocken, PA (1974), 514-526
  - [280] GARZAROLLI, F , BODMER, R P , STEHLE, H , TRAPP-PRITSCHING, S , "Progress in understanding PWR fuel rod waterside corrosion", Proc ANS Topical Mtg on Light Water Reactor Fuel Performance, Orlando, American Nuclear Society, La Grange Park, ILL (1985) 3-55 to 3-72,
  - [281] WOOD C J , (Ed ), PWR primary water chemistry guidelines Revision 3, Electric Power Research Institute, Palo Alto, CA , Report EPRI TR-105714 (1995)
  - [282] LARSSON, J , "Fuel experience at Ringhals Nuclear Power Plant, units 1-4", Presented at the 20th International Utility Nuclear Fuel Performance Conference, New Orleans, LA 24-28 Sept , 1989
  - [283] POLLEY, M V , EVANS, H E , ANDERSSON, P O , LARSSON, J , "Effect of lithium hydroxide on Zircaloy corrosion in the Ringhals-3 PWR plant", Proc EPRI/Utility Fuel Corrosion Workshop, Washington, USA, 28-30 July, 1993, Electric Power Research Institute, Palo Alto, CA

- [284] CHURCH, K., Effect of elevated pH/LiOH on fuel corrosion at Oconee Nuclear Station, Electric Power Research Institute, Palo Alto, CA., Report TR-100389 (1992)
- [285] KELLER, H. W., Addressing today's operating needs, AEA Technology, UK Publication, Atom, No 424 (1992) 32-36
- [286] NIKULINA, A. V., BIBILASHVILI, Y. K., MARKELOV, P. P., PEREGUD, M. M., KOTREKHOV, V. A., LOSITSKY, A. F., KUZMENKO, N. Y., SHEVNIN, Y. P., SHAMARDIN, V. K., KOBLYANSKY, G. P., NOVOSELOV, A. E., "Zirconium alloy E635 (Zr-1.2Sn-1Nb-0.4 Fe) as fuel rod cladding and other components of VVER and RBMK cores", Zirconium in the Nuclear Industry 11th Int. Symp., Garmisch-Partenkirchen, Ger., (1995), ASTM-STP-1295, (BRADLEY, E. R., SABOL, G. P., Eds.), American Society for Testing and Materials, West Conshohocken, PA, (1996) 785-804
- [287] HENZEL, N., "Alternative water chemistry for the primary loop of PWR plants", IAEA Technical Committee Mtg. on Influence of Water Chemistry on Fuel Cladding Behaviour, Rez, Czech Republic, 4-8 October, 1993, IAEA-TECDOC-927, Vienna (1997) 421-432
- [288] COHEN, P., Water coolant technology of power reactors, American Nuclear Society, La Grange Park, ILL (1980)
- [289] BRUN, C., LONG, A., SAURIN, P., THIRY, M. C., LACOUDRE, N., "Radiolysis studies in Belleville (PWR 1300), water chemistry with low hydrogen concentration", Proc. SFEN International Conference on Chemistry in Water Reactors, Nice, France, Société Française pour l'Energie Nucléaire, (1994) 72-79,
- [290] BJORKNVIST, L., "Oxidation and hydriding of fuel assembly guide tubes", Presented at 1st Mtg. of PWR Working Sub-Group of the European Federation of Corrosion, St. Denis, France, 10-11 Sept., 1992.
- [291] BERRY, W. E., WHITE, E. L., FINK, F. W., Zirconium alloy corrosion in high temperature halide solutions, Corrosion, **19** (1963) 253t
- [292] ALLSOP, H. A., MILLER, D. G., GODIN, M. S., "The benefits of zinc addition to primary side coolant", Proc. SFEN International Conference on Chemistry in Water Reactors, Nice, France, Société Française pour l'Energie Nucléaire, (1994) 321-328,
- [293] BERGMANN, C. A., KUNIG, R. H., CORPORA, G. J., "Engineering aspects of zinc addition in a Westinghouse designed PWR", Proc. SFEN International Conference on Chemistry in Water Reactors, Nice, France, Société Française pour l'Energie Nucléaire, (1994) 80-81,
- [294] ALDER, H. P., SCHEMKER, E., "Advanced analytical techniques for boiling water reactor chemistry control", IAEA Technical Committee Mtg. on The Influence of Water Chemistry on Fuel Cladding Behaviour, Rez, Czech Republic, 4-8 October, 1993, International Atomic Energy Agency, Vienna.
- [295] P. FEJES, "Moving from ultra-pure water to plant-tailored water chemistry", Chemistry of Nuclear Reactor Systems 6, British Nuclear Energy Society, London, Vol. 2, (1992). 90-95
- [296] BWR Water Chemistry Guidelines - 1993 Revision Normal and Hydrogen Water Chemistry, Electric Power Research Institute, Palo Alto, CA., Report TR-103515, (1994)
- [297] COWAN, R. L., MARBLE, W. J., Hydrogen water chemistry effects on BWR radiation fields, Electric Power Research Institute, Palo Alto, CA., Report TR-101463, (1992).
- [298] MILLET, P. J., WOOD, C. J., Mediterranean Reflections, Nuclear Engineering International, August 1994, 14-15
- [299] MARCHL, T. F. J., REITZNER, U., "Chemistry parameters influencing the dose rate build-up in BWR plants", Water Chemistry of Nuclear Reactor Systems 6, British Nuclear Energy Society, London, Vol. 1, (1992) 33-38.
- [300] ISHIGURE, K., "State of the art of water chemistry in Japanese BWRs", Proc. International Conference on Chemistry in Water Reactors, Nice, France, Société Française pour l'Energie Nucléaire, Paris, (1994), 235-246.
- [301] HUDSON, M. J. B., KLISIEWICZ, J. W., "Utility approach to radiation field reduction by coolant chemistry control", Water Chemistry of Nuclear Reactor Systems 6, British Nuclear Energy Society, London, Vol. 2, (1992) 96-102.

- [302] KOBAYASHI, M., MAED, K., HASHIMOTO, H., ISHIBE, T., USUI, N., OSUMI, K., ISHIGURE, K., "Operational experience of water quality improvement accompanied by monitoring with on-line chromatograph", Proc. Technical Committee Mtg. on The Influence of Water Chemistry on Fuel Cladding Behaviour, Rez, Czech Republic, 4-8 October, (1993), IAEA-TECDOC-927, Vienna (1997) 315-330.
- [303] SHIMADA, S., ITO, K., LIN, C. C., CHENG, B., IKEDA, T., OGUMA, M., TAKEI, T., VITANZA, C., KARLSEN, T. M., "Parametric tests of the effects of water chemistry impurities on corrosion of Zr-alloys under simulated BWR conditions", IAEA Technical Committee Mtg. on The Influence of Water Chemistry on Fuel Cladding Behaviour, Rez, Czech Republic, 4-8 October, (1993), IAEA-TECDOC-927, Vienna (1997) 73-89.
- [304] HERMANSSON, H. S., ARVIDSSON, P., "Hide-out and micro-chemistry on the Oskarshamn 3 fuel cladding", Proc. International Conference on Chemistry in Water Reactors, Nice, France, Société Française pour l'Energie Nucléaire, Paris, Vol. I, (1994) 315-320.
- [305] TURÝNA, von R., KYSELA, J., Probleme der Chemie und Korrosion in den Kernkraftwerken der ehemaligen Tschechoslowakei, VGB Kraftwerkstechnik, 73 (1993) Heft 4, 389-393.
- [306] KYSELA, J., ZMITKO, M., YURMANOV, V. A., TIAPKOV, V. F., "Primary coolant chemistry in VVER units", Proc. International Conference on Chemistry in Water Reactors, Nice, France, Société Française pour l'Energie Nucléaire, Paris, Vol. I, (1994) 17-28.
- [307] BRUNNING, J., CAKE, P., HARPER, A., SIMS, H. E., "Some observations on hydrazine and ammonia based chemistries in PWRs", IAEA Technical Committee Mtg. on The Influence of Water Chemistry on Fuel Cladding Behaviour, Rez, Czech Republic, 4-8 October, (1993), IAEA-TECDOC-927, Vienna (1997) 455-464.
- [308] KYSELA, J., ZMITKO, M., VRTILKOVA, V., "VVER water chemistry related to fuel cladding behaviour", IAEA Technical Committee Mtg. on The Influence of Water Chemistry on Fuel Cladding Behaviour, Rez, Czech Republic, 4-8 October, (1993), IAEA-TECDOC-927, Vienna (1997) 473-488.
- [309] YURMANOV, V. A., MAMET, V. A., SHESTAKOV, Y. M., AMOSOV, M. M., "Water chemistry in WWER reactors", Proc. Technical Committee Mtg. on The Influence of Water Chemistry on Fuel Cladding Behaviour, Rez, Czech Republic, 4-8 October, (1993), IAEA-TECDOC-927, Vienna (1997) 433-453.
- [310] RIESS, R., "Control of water chemistry in operating reactors", Proc. Technical Committee Mtg. on The Influence of Water Chemistry on Fuel Cladding Behaviour, Rez, Czech Republic, 4-8 October, (1993), IAEA-TECDOC-927, Vienna (1997) 407-420.
- [311] PIACQUADIO, N. H., MAROTO, A. J. G., "Primary circuit chemistry of pressure vessel PHWRs" and "Primary circuit chemistry of pressure tube PHWRs", Coolant Technology of Water Cooled Reactors, Vol. I, Chemistry of Primary Coolant in Water Cooled Reactors, TECDOC-667, IAEA, Vienna, (1992) 33-49.
- [312] VENKATESWARLU, K. S., "Coolant chemistry in pressurised heavy water reactors - The Indian Experience", Coolant Technology of Water Cooled Reactors, Vol. I, Chemistry of Primary Coolant in Water Cooled Reactors, TECDOC-667, IAEA, Vienna. (1992) 87-89.
- [313] URBANIC, V. F., CHOUBEY, R., CHOW, C. K., "Investigation of variables that influence corrosion of zirconium alloys during irradiation", Zirconium in the Nuclear Industry: 9th Int. Symp., ASTM-STP-1132 (EUCKEN, C. M., GARDE, A. M., Eds.). American Society for Testing and Materials, W. Conshohocken, PA. (1990), 665-682.
- [314] LEISTIKOW, S., SCHANZ, G., BERG, H. V., ALY, A. E., "Comprehensive presentation of extended Zircaloy-4 steam oxidation results (600-1600°C)", OECD-NEA-CSNI/IAEA Specialists Mtg. on Water Reactor Fuel Safety and Fission Product Release in Off-Normal Accident Conditions, Riso, May 1983, European Nuclear Energy Agency.
- [315] ALI, A. E., HUSSEIN, A. G., EL-SAYED, A. E., EL RAGHY, S. M., EL BANNA, O. A., "Oxidation-induced embrittlement and structural changes of Zircaloy-4 tubing in steam at 700-1000°C", Proc. Technical Committee Mtg. on The Influence of Water Chemistry on Fuel Cladding Behaviour, Rez, Czech Republic, 4-8 October, (1993), IAEA-TECDOC-927, Vienna (1997) 253-265.

- [316] PAWEL, R E , CATHCART, J V , McKEE, R A , The kinetics of oxidation of Zircaloy-4 in steam at high temperatures, *J Electrochem Soc* , **126** (1979) 1105-1111
- [317] URBANIC, V F , HEIDRICK, T R , High temperature oxidation of Zircaloy-2 and Zircaloy-4 in steam, *J Nucl Mater* , **75** (1978) 251-261
- [318] COX, B , Accelerated oxidation of Zircaloy-2 in supercritical steam, Canadian Report, AECL-4448 (1973), Atomic Energy of Canada Ltd , Chalk River
- [319] BOHMERT, J , DIETRICH, M , LINEK, J , "Comparative studies on high-temperature corrosion of Zr-1 Nb and Zircaloy-4, *Nucl Eng and Design*, **147** (1993) 53-62
- [320] GARZAROLLI, F , JUNG, W , SCHOENFELD, H , GARDE, A M , PARRY G W SMERD P G , Waterside corrosion of Zircaloy fuel rods, U S Rep EPRI-NP-2789 Electric Power Research Institute, Palo Alto, CA (1982)
- [321] BILLOT, P , et al , "Developments of a mechanistic model to assess the external corrosion of the Zircaloy cladding in PWRs", *Zirconium in the Nuclear Industry 8th Int Symp ASTM-STP-1023*, (VAN SWAM, L F P , EUCKEN, C M , Eds ), American Society for Testing and Materials, W Conshohocken, Pa (1989) 165-184, and *Proc IAEA Tech Comm Mtg , Portland, OR , 1989, IWGFPT/34, International Atomic Energy Agency Vienna*, (1990) 173-179
- [322] KLEIN, A C , REYES, J N , Jr , MAGUIRE, M A , "Thermal gradient effects on the oxidation of Zircaloy fuel cladding", *Proc Technical Committee Mtg on Fundamental Aspects of Corrosion on Zirconium Based Alloys in Water Reactor Environments*, Portland OR, USA, IAEA, Vienna, (1989) 61-65
- [323] FRANKLIN, D , LI, C-Y , "Effects of heat flux and irradiation-induced changes in water chemistry on Zircaloy nodular oxidation", *Zirconium in the Nuclear Industry 7th Int Symp , ASTM-STP-939* (ADAMSON, R B , VAN SWAM, L F P , Eds ), American Society for Testing and Materials, W Conshohocken, PA (1987) 206-223
- [324] MOTTA, A T , LEFEBVRE, F , LEMAIGNAN, C , "Amorphisation of precipitates in Zircaloy under neutron and charged particle irradiation", *Zirconium in the Nuclear Industry 9th Int Symp , ASTM-STP-1132*, (EUCKEN, C M , GARDE, A M , Eds ), American Society for Testing and Materials, W Conshohocken, PA (1991) 718-739
- [325] WHEELER, C L STEWART, C W , CENA, R J , ROWE, D S , SUTLEY, A M COBRA-IV-1 An interim version of COBRA for thermal-hydraulic analysis of rod bundle and nuclear fuel elements and cores, U S Report BNWL-1962 (UC-32), Battelle (Pacific) Northwest Laboratories, Richland, WA (1976)
- [326] STEWART, C W , CUTA, J M , MONTGOMERY, S D , KELLY, J M , BASEHORE K L , GEORGE, T L , ROWE, D S , VIPRE-01 A Thermo-hydraulic Code for Reactor Cores, Vol 1 Mathematical Modelling (Revision 3), US Report NP-2511-CCM-A, Vol 1, Rev 3, Electric Power Research Institute, Palo Alto, CA (1989)
- [327] COLLIER, J G , "Single- and two-phase heat transfer", Ch 7, *Nuclear Reactor Safety Heat Transfer*, (JONES, O C , Jr, Ed ), Hemisphere Publ , Washington, (1981)
- [328] COX, B , ISHIGURE, K , JOHNSON, A B , Jr, LEMAIGNAN, C , NECHAEV, A F , PETRIK, N G , REZNICHENKO, E A , "Mechanistic understanding of irradiation corrosion of zirconium alloys in nuclear power plants stimuli, status, and outlook" *Proc Int Conf on Radiation Materials Science, Alushta, Crimea, USSR, Atominform, Moscow*, (1990)
- [329] GARZAROLLI, F , JORDE, D , MANZEL, R , PARRY, G W , SMERD, P G , Review of PWR Fuel Rod Waterside Corrosion Behaviour, US Report NP-1472, Electric Power Research Inst , Palo Alto, CA (1980)
- [330] MATPRO Version 10, A handbook of materials properties for use in the analysis of light water reactor fuel rod behaviour, US Report TREE-NUREG-1180, Nuclear Regulatory Commission, Wash , DC (1978)
- [331] SHANN, S H , VAN SWAM, F L , MARTIN, L A , "Effects of coolant lithium concentration on PWR cladding waterside corrosion", *Fuel for the 90's, Proc Int Topical Mtg on LWR Fuel Performance, Avignon, France, Vol 2, American Nuclear Society /European Nuclear Society*, (1991) 742-748

- [332] KARLSEN, T., VITANZA, C., "Effects of pressurised water reactor (PWR) coolant chemistry on Zircaloy corrosion behaviour", *Zirconium in the Nuclear Industry: 10th Int Symp*, ASTM-STP-1245, (GARDE, A. M., BRADLEY, E. R., Eds.), American Society for Testing and Materials, W. Conshohocken, PA. (1994) 779-789.
- [333] SHEPPARD, K. D., SPEYER, D. M., CHAN, Y. Y., FRANKL, I., STRASSER, A. A., Analysis of Zircaloy oxide thickness data from PWRs, US Report NP-6698, Electric Power Research Inst., Palo Alto, CA. (1990)
- [334] BILLOT, P., GIORDANO, A., "Comparison of Zircaloy corrosion models from the evaluation of in-reactor and out-of-pile loop performance, *Zirconium in the Nuclear Industry 9th Int. Symp.*, Kobe, ASTM-STP-1132, (EUCKEN, C. M., GARDE, A. M., Eds.), American Society for Testing and Materials, W. Conshohocken, PA. (1991) 539-565
- [335] FORSBERG, K., MASSIH, A. R., "A model for uniform zircaloy clad corrosion in pressurised water reactors", *Proc. Technical Committee Mtg on Fundamental Aspects of Corrosion of Zircaloy Base Alloys in Water Reactor Environments*, IWGFPT/34, IAEA, Vienna, (1989) 178-200.
- [336] FORSBERG, K., LIMBACK, M., MASSIH, A. R., A model for uniform Zircaloy clad corrosion in pressurised water reactors, *Nuclear Engineering and Design*, **154**, (1995) 157-168.
- [337] POLLEY, M. V., EVANS, H. E., A comparison of Zircaloy oxide thicknesses on Millstone-3 and North Anna-1 PWR fuel cladding, US Report TR-102826, Electric Power Research Institute, Palo Alto, CA. (1993).
- [338] POLLEY, M. V., Evaluation of possible lithium effects on Zircaloy-4 fuel clad oxidation in the Millstone-3 PWR, US Report TR-105662, Electric Power Research Institute, Palo Alto, CA. (1995).
- [339] POLLEY, M. V., "Assessment of zircaloy fuel clad oxidation under elevated lithium primary coolant chemistry at Millstone 3 PWR", *Proc. Conf. on Chemistry in Water Reactors*, Nice, France, April 24-27, Société Française pour l'Energie Nucléaire, (1994) 82-89.
- [340] COX, B., Assessment of PWR waterside corrosion models and data, US Report NP-4287, Electric Power Research Institute, Palo Alto, CA. (1985).
- [341] PECHEUR, D., GIORDANO, A., PICARD, E., BILLOT, Ph., THOMAZET, J., "Effect of elevated lithium on the waterside corrosion of Zircaloy-4: Experimental and predictive studies", *Proc. Technical Committee Mtg. on Influence of Water Chemistry on Fuel Cladding Behaviour*, Rez, Czech Republic, 4-8 October, (1993), IAEA-TECDOC-927, Vienna (1997) 111-130.
- [342] BILLOT, P., BESLU, P., ROBIN, J. C., "Consequences of lithium incorporation in oxide films due to irradiation effect", *Fuel for the 90's*, (Int. Topical Mtg. on LWR Fuel Performance), Avignon, France, Vol. 2, American Nuclear Soc/European Nuclear Soc (1991) 757-769.
- [343] BILLOT, P., ROBIN, J.-C., GIORDANO, A., PEYBERNES, J., THOMAZET, J., AMANRICH, H., "Experimental and theoretical studies of parameters that influence corrosion of Zircaloy-4", *Zirconium in the Nuclear Industry. 10th Int. Symp.*, ASTM-STP-1245, (GARDE, A. M., BRADLEY, E. R., Eds.), American Society for Testing and Materials, W. Conshohocken, PA. (1994) 351-375.
- [344] CHENG, B., GILMORE, P., KLEPFER, H. H., "PWR Zircaloy fuel cladding corrosion performance, mechanisms and modelling", *Zirconium in the Nuclear Industry: 11th Int Symp*, Garmisch-Partenkirchen, Germany, (1995), ASTM-STP-1295, (BRADLEY, E. R., SABOL, G. P., Eds.), American Society for Testing and Materials, W. Conshohocken, PA. (1996) 137-159.
- [345] KRITSKY, V. G., DOILNITSINA, V. V., SHMANTSAR, O. P., LEBEDEV, V. I., GARUSOV, Yu. V., Analiz Vliyaniya Parametrov V. Kh. R na otkazy TVS na AES Teploenergetika, Moskva, N7, (1995) 7-11.
- [346] HOBBS, L. W., CLINARD, F., ZINKLE, S., EWING, R., Radiation effects in ceramics, *J Nucl. Mater* **216** (1994) 291-321.

- [347] LANDAU, L A , LIFSHITZ, E M , Mécanique, Moscow, Les Editions MIR, (1969) 243
- [348] OEN, O S, Cross section for atomic displacements in solids by fast electrons, U S Rep ORNL 4897, Oak Ridge National Laboratory, TN (1973)
- [349] GRIFFITHS, M , Displacement energies for Zr measured in a HVEM, J Nucl Mater , **165** (1989) 315-317
- [350] KINCHIN, G H , PEASE, R S , The displacement of atoms in solids by radiation, Rep Prog Phys , **18** (1955) 1-48
- [351] ROBINSON, M T , The influence of the scattering law on the radiation damage displacement cascade, I Phil Mag **12** (1965) 741
- [352] ZIEGLER, J F , BIRSACK, J P , LITTMARK, U , The stopping and range of ions in solids, Pergamon Press, New York (1985)
- [353] ROBINSON, M T , Basic physics of radiation damage, J Nucl Mater , **216** (1994) 1-28
- [354] BACON, D J , DIAS DE LA RUBIA, T , Molecular dynamics computation simulation of displacement cascades in metals, J Nucl Mater , **216** (1994) 275-290
- [355] GRIFFITHS, M , GILBERT, R W , CARPENTER, G J C , Phase instability, decomposition and redistribution of intermetallic precipitates in Zircaloy-2 and 4 during neutron irradiation, J Nucl Mater , **150** (1987) 53-66
- [356] LEFEBVRE, F , "Thesis Etude des Effets d'Irradiation sur la Microstructure du Zircaloy-4", Grenoble, France, (1989)
- [357] GOLDBERG, M D , MUGHABGHAB, S F , MARGURNO, B A , MAY, V M , Neutron cross sections, Vol II-A Z=21 to 40, U S Rep BNL325, Brookhaven National Laboratory, N Y (1966)
- [358] Intermetallic compounds, (WESTBROOK, J H , FLEISCHER, R L , Eds ), Ch 34 Irradiation damage, L Howe, 791-825, J Wiley and Sons, New York, 1995
- [359] HOWE, L M , RAINVILLE, M H , A study of the irradiation behaviour of Zr<sub>3</sub>Al, J Nucl Mater **68** (1977) 215-234, and The nature of irradiation produced damaged regions in ordered Zr<sub>3</sub>Al, Phil Mag **A39** (1979) 195
- [360] SHARPE, J V , RUMBSY, D , Electron irradiation damage in magnesium oxide, Rad Effects **17** (1973) 65
- [361] SOULLARD, J , ALAMO, A , Etude du ralentissement des ions dans une cible diatomique, II Calcul du nombre d'atomes déplacés, Rad Effects **38** (1978) 133
- [362] CLINARD, F W , JR , HOBBS, L W , Physics of radiation effects in crystals, (JOHNSON, R A , ORLOV, A N , Eds ), Elsevier Science Pub B V (1986) 387
- [363] TOULEMONDE, M , BALANZAT, E , BOUFFARD, S , JOUSSET, J C , Structural modifications induced by electronic energy deposition during the slowing down of heavy ions in matter, Nucl Instrum Methods Phys Res **B39** (1989) 1
- [364] YUANXUN, Q , GRIFFITH, J E , TOMBRELLO, T A , Sputtering of Al<sub>2</sub>O<sub>3</sub> and LiNbO<sub>3</sub> in the electronic stopping region, Rad Effects **64** (1982) 111
- [365] VARLEY, J H O , Radiation damage in covalent and ionic solids, Prog Nucl Energy **5** (1956) 672
- [366] PELLIS, G P , Radiation induced degradation of intrinsic electrical conductivity of MgAl<sub>2</sub>O<sub>4</sub> and Al<sub>2</sub>O<sub>3</sub>, J Nucl Mater **184** (1991) 167-182
- [367] CLINARD, F W , Jr , ROHR, D L , RANKEN, W A , Neutron irradiation damage in stabilized ZrO<sub>2</sub>, J Amer Ceram Soc **60** (1977) 287
- [368] WITTELS, M C , SHERRILL, F A , Irradiation induced phase transformation in zirconia, J Appl Phys **27** (1956) 643-644
- [369] ADAM, J , COX, B , Neutron and fission fragment damage in zirconia, Phys Rev Letters **3** (1959) 543-544
- [370] ILTIS, X , LEFEBVRE, F , LEMAIGNAN, C , Microstructural study of the oxide layers formed on Zircaloy-4 in autoclaves in reactor, Part I, J Nucl Mater , **224** (1995) 109-120, Part II, *ibid* , **224** (1995) 121-130
- [371] BAIG, M R , MESSOLORAS, S , STEWART, R J , Absence of voids in fast neutron irradiated zirconium by small angle neutron scattering, Rad Effects and Defects in Sol **108** (1989) 355



- [372] GRIFFITHS, M., A review of microstructure evolution in zirconium alloys during irradiation, *J. Nucl. Mater.* **159** (1988) 190-218.
- [373] GRIFFITHS, M., Evolution of microstructure in hcp metals during irradiation, *J. Nucl. Mater.* **205** (1993) 225-241.
- [374] NORTHWOOD, D. O., Irradiation damage in zirconium and its alloys, *Atomic Energy Rev.* **15** (1977) 547.
- [375] NORTHWOOD, D. O., et al., Characterisation of neutron irradiation damage in zirconium alloys - An international "round-robin" experiment, *J. Nucl. Mater.* **79** (1979) 379-394.
- [376] HELLIO, C., DE NOVION, C. H., BOULANGER, L., Influence of alloying elements on the dislocation loops created by  $Zr^{+}$  or by electron irradiation in  $\alpha$ -zirconium, *J. Nucl. Mater.* **159** (1988) 368-378.
- [377] BUCKLEY, S. N., BULLOUGH, R., HAYNS, M. R., The direct observation of irradiation damage in zirconium and its alloys, *J. Nucl. Mater.* **89** (1980) 283-295.
- [378] HUANG, P. Y., MAHMOOD, S. T., ADAMSON, R., B., "Effects of thermomechanical processing on in-reactor corrosion and post-irradiation mechanical properties of Zircaloy-2", *Zirconium in the Nuclear Industry: 11th Int. Symp.*, Garmisch-Partenkirchen, FRG, (1995), ASTM-STP-1295, (BRADLEY, E. R., SABOL, G. P., Eds.), American Society for Testing and Materials, W. Conshohocken, PA, (1996) 726-756.
- [379] GRIFFITHS, M., GILBERT, R. W., The formation of c-component defects in zirconium alloys during neutron irradiation, *J. Nucl. Mater.* **150** (1987) 169-181.
- [380] HOLT, R. A., GRIFFITHS, M., GILBERT, R. W., c-component dislocations of Zr-2.5wt% Nb alloys, *J. Nucl. Mater.* **149** (1987) 51-56.
- [381] DE CARLAN, Y., REGNARD, C., GRIFFITHS, M., GILBON, D., LEMAIGNAN, C., "Influence of iron in the nucleation of <c> component dislocation loops in irradiated Zircaloy-4", *Zirconium in the Nuclear Industry: 11th Int. Symp.*, Garmisch-Partenkirchen, FRG, (1995), ASTM-STP-1295, (BRADLEY, E. R., SABOL, G. P., Eds.), American Society for Testing and Materials, W. Conshohocken, PA, (1996) 638-652.
- [382] GRIFFITHS, M., GILBON, D., REGNARD, C., LEMAIGNAN, C., HVEM study on the effect of alloying elements and impurities on radiation damage in Zr alloys, *J. Nucl. Mater.* **205** (1993) 273-283.
- [383] McEWEN, S. R., FABER, J. TURNER, A. P. L., The use of time of flight neutron diffraction to study grain interaction stresses, *Acta. Metall.* **5** (1983) 657.
- [384] HOLT, R. A., Mechanisms of irradiation growth of alpha-zirconium alloys, *J. Nucl. Mater.* **159** (1988) 310-338.
- [385] HOLT, R. A., CAUSEY, A. R., The effects of intergranular constraints on irradiation growth of Zircaloy-2 at 320 K, *J. Nucl. Mater.* **150** (1987) 306-318.
- [386] COX, B., Effects of irradiation on the oxidation of zirconium alloys in high temperature aqueous environments (A Review), *J. Nucl. Mater.* **28** (1968) 1-47.
- [387] KIM, Y. S., NOH, J. S., KWON, S. C., KUK, I. H., Effect of hoop stress on corrosion of Zircaloy-4 cladding tube, *J. Nucl. Mater.* **223** (1995) 163-168.
- [388] VERSACI, R. A., IPOHORSKI, M., Composition of  $Zr(Cr,Fe)_2$ -type precipitates in Zircaloy-2 and -4, *J. Nucl. Mater.* **116** (1983) 321-323.
- [389] VITIKAINEN, E., NENONEN, P., Transmission electron microscopy studies on intermetallics in some zirconium alloys, *J. Nucl. Mater.* **78** (1978) 362-373.
- [390] MENG, X. Y., NORTHWOOD, D. O., Intermetallic precipitates in Zircaloy-4, *J. Nucl. Mater.* **132** (1985) 80-87.
- [391] BANGARU, N. V., An investigation of the microstructure of heat treated Zircaloy-4, *J. Nucl. Mater.* **131** (1985) 280.
- [392] CHANG, B., KRUGER, R., ADAMSON, D., "Corrosion behaviour of irradiated Zircaloy", *Zirconium in the Nucl. Industry: 10th Int. Symp.*, ASTM-STP-1245, (GARDE, A. M., BRADLEY, E. R., Eds.), American Society for Testing and Materials, W. Conshohocken, PA, (1994) 400-418.
- [393] STRASSER, A. A., ANDREWS, M. G., "Relationship of precipitates, their composition, heat treatment and irradiation to corrosion resistance of Zircalloys", *Fundamental Aspects of*

- Corrosion on Zirconium Base Alloys in Water Reactor Environments, Proc Tech Comm Mtg , Portland, OR , 1989), IWGFPT/34, IAEA, Vienna (1990) 88-98
- [394] KUBO, T , WAKASHIMA, Y , IMAHASHI, H , NAGAI, M , Distribution of intermetallic particles and its effects on SCC of zirconium alloys, J Nucl Mater **138** (1986) 256-267
  - [395] SCHEMEL, J J , CHARQUET, D , WADIER, J F , "Influence of the manufacturing process on the corrosion resistance of Zircaloy-4 cladding, Zirconium in the Nuclear Industry 8th Int Symp, ASTM-STP-1023, (VAN SWAM, L F R , EUCKEN, C M , Eds ), American Society for Testing and Materials, W Conshohocken, PA (1990) 141-152
  - [396] GILBERT, R W , GRIFFITHS M , CARPENTER, G J C , Amorphous intermetallics in neutron irradiated Zircaloys after high fluences, J Nucl Mater **135** (1985) 265-268
  - [397] YANG, W J S , TUCKER, R P , CHENG, B , ADAMSON, R B , Precipitates in Zircaloy Identification and effect of irradiation and heat treatment, J Nucl Mater **138** (1986) 185-195
  - [398] PECHEUR, D , LEFEBVRE, F , MOTTA, A , LEMAIGNAN, C , CHARQUET, D , Effect of irradiation on the precipitate stability in Zr alloys, J Nucl Mater **205** (1993) 445-451
  - [399] GARZAROLLI, F , GOLL, W , SEIBOLD, A , RAY, I , "Effect of in-PWR irradiation on size, structure and composition of intermetallic precipitates of Zr alloys", Zirconium in the Nuclear Industry 11th Int Symp , Garmisch-Partenkirchen, FRG, (1995), ASTM-STP-1295, (BRADLEY, E R , SABOL, G P , Eds ), American Society for Testing and Materials, W Conshohocken, PA, (1996) 541-555
  - [400] GILBON, D , SIMONOT, C , "Effect of irradiation on the microstructure of Zry4", Zirconium in the Nuclear Industry 10th Int Symp., ASTM-STP-1245, (GARDE, A M , BRADLEY, E R , Eds ), American Society for Testing and Materials, W Conshohocken, PA (1994) 521-548
  - [401] GRIFFITHS, M , GILBERT, R W , FIDLERIS, V , TUCKER, R P , ADAMSON, R B Neutron damage in zirconium alloys during neutron irradiation, J Nucl Mater **150** (1987) 159-168
  - [402] YANG, W J S , Precipitate stability in neutron-irradiated Zircaloy-4, Nucl Mater **158** (1988) 71-80
  - [403] MOTTA, A , "Electron irradiation induced amorphization of precipitates in Zircaloy-2", 14th ASTM Mtg on the Effect of Irradiation on Materials, Andover, MS 1988
  - [404] LEFEBVRE, F , LEMAIGNAN, C , Heavy ion induced amorphisation of Zr(Fe,Cr) precipitates in Zircaloy-4, J Nucl Mater **165** (1989) 122-127
  - [405] LEFEBVRE, F , LEMAIGNAN, C , "Effect of irradiation on the microstructure of Zr4 Amorphous transformation and alloying element resolution", Fundamental Aspects of Corrosion on Zirconium Base Alloys in Water Reactor Environments Proc Tech Comm Mtg , Portland, OR , (1989), IWGFPT/34, IAEA, Vienna, (1990) 80-87
  - [406] BRADLEY, E R , PERKINS, R A , "Characterisation of Zircaloy corrosion films by analytical transmission electron microscopy", Fundamental Aspects of Corrosion on Zirconium Base Alloys in Water Reactor Environments, Proc Tech Comm Mtg , Portland, OR , (1989), IWGFPT/34, IAEA, Vienna, (1990) 101-106
  - [407] BLANK, H , On the original of different rates of inpile post-transition oxidation of Zr-based cladding alloys, Z Metallkd **85** (1994) 645-657
  - [408] JHA, K N , RYAN, T G , FREEMAN, G R , Radiolysis of H O and D O between 0 and 300°C, J Phys Chem **79** (1975) 868-870
  - [409] CHRISTENSEN, H , SEHESTED, K , Hydrated electron and its reactions at high temperatures, J Phys Chem **90** (1986) 186-190
  - [410] COX, B , The effect of fission fragment irradiation on the subsequent corrosion of two zirconium alloys, Rep AERE-R2875, United Kingdom Atomic Energy Authority, AERE Harwell, Berks (1959)
  - [411] LEE, Y S , HUANG, K Y , HUANG, C Y , KAI, J J , HSEIH, W F , Effect of proton irradiation on the microstructural evolution and uniform corrosion resistance of Zry, J Nucl Mater **205** (1993) 476-482

- [412] BUXTON, G V , "Radiation chemistry of the liquid state Water and homogeneous aqueous solutions". Radiation Chemistry, Principle and Applications (RODGERS, M A J Ed ), VCH Publishers Inc , New York, (1987) 312-350
- [413] BURNS, W G , MARSH, W R , Radiation chemistry of high temperature water (300-410°C), Part 1 Reducing products from gamma radiolysis, J Chem Soc Faraday Trans 177 (1981) 197-215
- [414] BURNS W G , Water chemistry of nuclear reactor systems, 2, BNES London, (1981) 373
- [415] SHIRAISHI, H , KATSUMURA, Y , HIROISHI, D , ISHIGURE, K , WASHIO M , Pulse-radiolysis study on the yield of hydrated electrons at elevated temperature, J Phys Chem 92 (1988) 3011-3017
- [416] SHIRAISHI, H , KATSUMURA, H , ISHIGURE, K , On the yield of hydrated electrons at elevated temperatures, Radiat Phys Chem 34 (1989) 705-710
- [417] KATSUMURA, Y , TAKEUCHI, Y , ISHIGURE, K . Radiation chemistry of high temperature water - 1 Degradation products in acid by gamma radiation, Rad Phys Chem 32 (1988) 259-263
- [418] BUXTON, G V , WOOD, N D , DYSTER, S , Ionisation constants of radical OH and HO radical in aqueous solutions up to 200°C A pulse radiolysis study, J Chem Soc , Faraday Trans 184 (1988) 1113-1121
- [419] SHIRAISHI, H , BUXTON, G V , WOOD, N O , Temperature dependence of the absorption spectrum of the methyl viologen cation radical and use of methyl viologen as a scavenger for estimating yields of the primary radicals in the radiolysis of high-temperature water, Radiat Phys Chem 33 (1989) 519-522
- [420] ELLIOT, A J , CHENIER, M P , OUELLETTE, D C , G-value for gamma-irradiated water as a function of temperature, Can J Chem 68 (1990) 712-718
- [421] ELLIOT, A J , CHENIER, M , OUELLETTE, D , Temperature dependence of G-values of H O and D O irradiated with low linear energy transfer radiation, J Chem Soc Faraday Trans 89 (1993) 1193-1197
- [422] KATSUMURA, Y , TAKEUCHI, Y , HIROISHI, D , ISHIGURE, K . Fast neutron radiolysis of acid water at elevated temperatures, Radiat Phys Chem 33 (1988) 299-306
- [423] HICKEL, B , Quelques problèmes concernant la radiolyse de l'eau liquide a haute temperature application aux réacteurs nucléaires, J Chim Phys 88 (1991) 1177-1193
- [424] JENKS, G H , Effects of reactor operation on HFIR coolant, ORNL-3848, Oak Ridge National Laboratory, (1965)
- [425] ELLIOT, A J , McCracken, D R , BUXTON, G V , WOOD, N D , Estimation of rate constants for near diffusion controlled reactions in water at high temperatures, J Chem Soc Faraday Trans 86 (1990) 1539-1547
- [426] ISHIGURE, K , TAKAGI, J , KATO, I , SHIGETO, T , FUJITA, N , "Computer simulation of reactor water chemistry in a BWR", Water Chemistry and Corrosion Problems in Nuclear Power Plants (Proc Symp Vienna, 1982), International Atomic Energy Agency, Vienna, (1983) 181
- [427] ISHIGURE, K , TAKAGI, J , SHIRAISHI, H , Hydrogen injection in BWR and related radiation chemistry, Radiat Phys Chem 29 (1987) 195-199
- [428] IBE, E , UCHIDA, S , Evaluation of the yields from the radiolysis of water in boiling water reactors by neutron and gamma radiation, Nucl Sci Eng 85 (1983) 339-349
- [429] CHRISTENSEN, H , Remodelling of the oxidant species during radiolysis of high temperature water in a pressurised water reactor, Nucl Tech 109 (1995) 373-382
- [430] SPIERS, F W , The influence of energy absorption and electron range in irradiated bone, Br J Radiol 22 (1951) 521-533
- [431] DUTRIEUX, J , BERNARD, M , Dosimetry at interfaces for high energy X and gamma rays, Br J Radiol 39 (1966) 205-210
- [432] AIREY, P L , The effect of radiation on electrode processes, Radiat Res Rev 5 (1973) 341
- [433] LEMAIGNAN, C , SALOT, R , "Corrosion in Zr alloys in nuclear reactors A model for irradiation induced enhancement by local radiolysis in the porous oxide", Proc Technical

- Committee Mtg on Influence of water chemistry on fuel cladding behaviour, Rez, Czech Rep., Oct. 8-4, 1993, IAEA-TECDOC-927, Vienna (1997) 131-142.
- [434] BURNS, W. G., MARSH, W. R., WALTERS, W. S., The gamma irradiation-enhanced corrosion of stainless and mild steels by water in the presence of air, argon and hydrogen, *Radiat. Phys. Chem.* **21** (1983) 259-279.
  - [435] HENGLEIN, A., LINDIG, B., WESTERHAUSEN, J., Radiation-electrochemistry of the colloidal platinum electrode. Reactions of oxidizing free radicals, *Radiat Phys Chem* **23** (1984) 199.
  - [436] BUXTON, G. V., RHODES, T., SELLERS, R. M., Radiation induced dissolution of colloidal haematite, *Nature* **295** (1982) 583-588.
  - [437] HENGLEIN, A., LILLIE, J., Storage of electrons in aqueous solution. the rates of chemical charging and discharging in colloidal silver electrode, *J. Am. Chem. Soc.* **103** (1989) 1059-1066
  - [438] WESTERHAUSEN, J., HENGLEIN, A., LILLIE, J., Radiation-electrochemistry of the colloidal gold micro-electrode hydrogen formation by organic free radicals, *Ber Bunsenges, Phys Chem* **85** (1981) 182-189
  - [439] TAKAGI, J., ISHIGURE, K., Thermal decomposition of hydrogen peroxide and its effect on reactor water monitoring of boiling water reactors, *Nucl. Sci. Eng* **89** (1985) 177-186
  - [440] HIROISHI, D., ISHIGURE, K., "Homogeneous and heterogeneous decomposition of hydrogen peroxide in high temperature water", *Water Chemistry of Nuclear Reactor Systems 5, Proc. Int. Conf., Vol. 1, British Nuclear Energy Society, London.* (1989) 311-312
  - [441] ULLBERG, M., ROTH, T., PERSSON, B., "Hydrogen peroxide in BWRs", *Water Chemistry of Nuclear Reactor Systems 5, Proc. Int. Conf., Vol. 2, British Nuclear Energy Society, London,* (1986) 67-73.
  - [442] LIN, C. L., SMITH, F. R., ICHIKAWA, N., BABA, T., ITOW, M., "Decomposition of hydrogen peroxide in aqueous solutions at elevated temperatures", *Water Chemistry of Nuclear Reactor Systems 5, Proc. Int. Conf., Vol. 1, British Nuclear Energy Society, London,* (1989) 145-151.
  - [443] REBENDORFF, B., WIKMARK, G., "Decomposition of hydrogen peroxide in high temperature waters: A laboratory study", *ibid.*, 153-158.
  - [444] GERISCHER, R., GERISCHER, H., Über die katalytische Zersetzung von Wasserstoffsuperoxyd an metallischen Platin, *Z. Phys. Chem., Neue Folge* **6(S)** (1956) 178-200
  - [445] AOKI, M., NAKAZATO, C., MASUDA, T., "Radiation of water absorbed on zeolite", *Radiation Research, Proc 8th Int. Congress, Edinburgh, (FIELDEN, E. M., FOWLER, J. F., HENDRY, J. H., SCOTT, D., Eds.), Taylor and Francis, London,* (1987) 28
  - [446] ALEXANDROV, A. B., NECHAEV, A. F., *J. Phys. Chem. (Sov.)* **58** (1984) 1108
  - [447] NECHAEV, A. F., "Radiation induced processes on solid surfaces: General approach and outlook", *Radiat Phys Chem* **28** (1986) 433-436.
  - [448] TAKAGI, J., ICHIKAWA, N., HEMMI, Y., "Evaluation of corrosion environment in BWR primary circuit by water radiolysis model", *Water Chemistry of Nuclear Power Plants, Proc. Int. Conf., Vol. 2, Japan Atomic Industrial Forum, Tokyo,* (1988) 517-522
  - [449] JOHNSON, A. B., Jr., Zirconium alloy oxidation and hydriding under irradiation. Review of Pacific Northwest Laboratory's Test Program Results, U.S. Rep. EPRI-NP-5132, Electric Power Research Institute, Palo Alto, CA. (1987).
  - [450] IBE, E., UCHIDA, S., A water radiolysis model in a circulating flow system with a boiling region and its application to H alternative chemistry of BWRs, *Nucl. Sci. and Engng.* **90** (1985) 140-157
  - [451] CHEN, J. S., ADAMSON, R., "Observation of shadow phenomena on Zr alloys", *Proc. Int. Topical Mtg. on Light Water Reactor Fuel Performance, West Palm Beach, American Nuclear Society, La Grange Park, ILL* (1995) 309-317
  - [452] PLATONOV, P. A., EPERIN, A. P., FROLOV, I. A., RYAZANTZEVA, R. V., "The operation experience with Zr 2.5% Nb alloy technological channels of the RBMK 1000 reactors", *Zirconium in the Nuclear Industry: 9th Int. Symp., Kobe, Japan, Nov. 1990, Poster Presentation Only, American Society for Testing and Materials.*
  - [453] GARZAROLLI, F., MANZEL, R., RESCHKE, S., TENCKHOFF, E., "Review of corrosion and dimensional behaviour of Zircaloy under water reactor conditions", *Zirconium in the*

- Nuclear Industry. 4th Int. Symp., American Society for Testing and Materials, ASTM-STP-681, (PAPAZOGLU, T., Ed.), American Society for Testing and Materials, W Conshohocken, PA. (1979) 91-106
- [454] LARRICK, A. P., Corrosion evaluation of N-Reactor pressure tube Z455, U S Report, BNWL-CC-2101, Pacific Northwest Laboratory, Richland, WA. (1969)
  - [455] COX, B., SPEIRS, D. L., Rectification by oxide films on zirconium alloys, Can Rep AECL-2690, Atomic Energy of Canada Ltd., Chalk River Nuclear Laboratories, (1967)
  - [456] LEMAIGNAN, C., Impact of  $\beta$ -radiolysis and transient products on irradiation enhanced corrosion of Zr alloys, J. Nucl. Mater. **187** (1992) 122-130
  - [457] NOE, M., FREJAVILLE, G., BESLU, P., Corrosion of fuel assembly materials, Note CEA-N 2440, Commissariat à l'Energie Atomique, Cadarache, (1985).
  - [458] SOLOMON, Y., Paper presented at Int Conf. on Decontamination of Nuclear Facilities, Niagara Falls, Canada, 1982, Electric Power Research Institute, Palo Alto, CA
  - [459] INTERNATIONAL ATOMIC ENERGY AGENCY, Coolant Technology of Water Cooled Reactors. An Overview, Tech. Rep. Series 347, , Vienna, (1993).
  - [460] EDF/CEA/FRAMATOME/WESTINGHOUSE, Joint Venture: PWS1-4 Final Report 2-9, (1984)
  - [461] HILLNER, E., "Corrosion of zirconium alloys - An overview", Zirconium in the Nuclear Industry 3rd Int. Symp., Quebec City, Quebec, ASTM-STP-633, (LOWE, A. L. JR., PARRY, G. W., Eds.), American Society for Testing and Materials, W Conshohocken, PA. (1977) 211-235
  - [462] BERGE, P., et al., "Experience française sur le contrôle chimique de l'eau et le contrôle des produits de corrosion des réacteurs à eau sous pression", (Proc Symp.), International Atomic Energy Agency, Vienna, (1982).
  - [463] THOMAZET, J., et al., "Power reactor experience and experimental program to control crud build-up on fuel", IAEA Specialists Mtg., San Miniato, Italy, International Atomic Energy Agency, Vienna, (1981).
  - [464] SMITH MAGOWAN, D., et al., Evaluation of the applicability of colloid studies to Cobalt-60 deposition in LWRs, Rep. EPRI-NP-3773, Electric Power Research Institute, Palo Alto, CA. (1984)
  - [465] BERGMANN, C. A., et al., The Role of Coolant Chemistry in PWR Radiation Field Buildup, U S. Reps EPRI-NP-3463 (1984) and EPRI-NP-4247, Electric Power Research Institute, Palo Alto, CA. (1985).
  - [466] BESLU, P., French experience on PWR chemistry, Nuclear Europe **78** (1989).
  - [467] ISHIGURE, K., et al., Water chemistry experience on nuclear power plants in Japan, J Nucl Sci and Technol. **26** (1989) 145.
  - [468] KOHSE, G. E., CABELLO, E. C., DOBOE, L., DRISCOLL, M. J., HARLING, O. K., HEMMI, Y., SHODA, Y., Proc. Conf on Water Chemistry of Nuclear Reactor Systems 6, British Nuclear Energy Society, London, UK, (1992).
  - [469] COWAN, R. L., et al., "Experience with hydrogen water chemistry in boiling water reactors", Water Chemistry for Nuclear Reactor Systems, BNES, London, (1986).
  - [470] CHENG, B., ADAMSON, R., MACHIELS, A. J., O'BOYLE, D., "Effect of hydrogen water chemistry on fuel performance at Dresden-2", Fuel for the 90's, Proc Int Topical Mtg on LWR Fuel Performance, Avignon, American Nuclear Society/European Nuclear Society (1991) 664-681.
  - [471] POTTS, G. A., PROEBSTLE, R. A., "Recent GE BWR fuel experience", Proc. Int. Topical Mtg on LWR Fuel Performance, West Palm Beach, American Nuclear Society, La Grange Park, ILL (1985) 87-95
  - [472] SMIRNOV, A., KUSMIN, V. I., SMIRNOV, V. P., DUBROVIN, K. P., BIBILASHVILY, YU. K., SALETNIH, B. A., "WWER 1000 and -440 fuel operation experience", Proc Int Topical Mtg on LWR Fuel Performance, West Palm Beach, American Nuclear Society, La Grange Park, ILL. (1995) 31-44.
  - [473] COX, B., READ, J. A., Oxidation of a Zr-2.5 Nb alloy in steam and air, U.K. Rep. AERE-R4459, United Kingdom Atomic Energy Authority, AERE, Harwell, Berks. (1963).
  - [474] CHOO, K. N., KANG, Y. H., PYUN, S. I., URBANIC, V. F., "Effect of composition and heat treatment on the microstructure and corrosion behaviour of Zr-Nb alloys", J Nucl Mater, **209** (1994) 226-235

- [475] INDIG, M E , GORDON, B M , DAVIS, R B , WEBER, J E , "Evaluation of in-reactor intergranular stress corrosion cracking via electrochemical measurements", Environmental Degradation of Materials in Nuclear Reactor Systems - Water Reactors, Proc 2nd Int Symp , Monterey, CA, American Nuclear Society, La Grange Park, ILL (1986) 411-418
- [476] INDIG, M E , "Recent advances in measuring ECPs in BWR systems", Environmental Degradation of Materials in Nuclear Reactor Systems - Water Reactors, Proc 4th Int Symp , Jekyll Island, GA , National Association of Corrosion Engineers, Houston, TX (1991) 4-111 to 4-132
- [477] BIBILASHVILY, YU, K , VASIL'CHENKO, I N , NIKULINA, A V , ONUFRIEV, V D , PROSELKOV, V N , "Improvements in technology of water cooled reactor fuel rod materials and experience in VVER fuel operation", Paper presented to the German Nuclear Engineering Society, Karlsruhe, November 1993
- [478] BELOKOPYTOV, V S , VOTINOV, S N , PAKHOMOV, Z I , DEREKIZOV, M D "Post-irradiation studies of fuel rods operated for 626 effective days in core of VVER-1 of NVNPP", CMA, Proceedings of Scientific-Technical Conference on Atomic Power, Fuel Cycles, Radiation Materials Science, USSR, Ul'yanovsk, October 1970, Moscow, (1971), Vol II, 260-266
- [479] TSYKANOV, V A , DAVYDOV, E F , "Irradiation stability of nuclear reactor fuel rods", Moscow, Atomizdat, 1977
- [480] SHAMARDIN, V K , POKROVSKY, A S , KOBLYANSKY, G N , STUPINA, L N , MAERSHINA, G I , "Results of studies into RBMK Zr-Nb, Zr-Nb-Sn-Fe and Zr-Sn-Fe clad fuel rods operated to lifetime burn-up", Preprint of SRIAR (NIIAR) - 8 (654)
- [481] WOLSEY, I S , MORRIS, J R , A study of Zircaloy-2 corrosion in high temperature water using ion beam methods, Corrosion **37** (1981) 575-585
- [482] WHITTON, J L , The measurement of ionic mobilities in the anodic oxides of tantalum and zirconium by a precision sectioning technique, J Electrochem Soc **115** (1968) 58
- [483] COX, B , HALLIDAY, J D , Atomic Energy of Canada Ltd , Chalk River Nuclear Laboratories, unpublished results
- [484] KHATAMIAN, D , Diffusion of hydrogen in the oxides of Zr-1 Nb, Zr-2.5 Nb and Zr-20 Nb alloys, Z Phys Chemie, **181** (1993) 435-440
- [485] SMITH, T , Diffusion coefficients and anion vacancy concentrations for the zirconium-zirconium dioxide systems, J Electrochem Soc **112** (1965) 560
- [486] BANTER, J G , Incorporation of ions in anodic oxide films on zirconium and their effect on film behaviour, J Electrochem Soc **114** (1967) 508-511
- [487] STERN, A , KHATAMIAN, D , LAURSEN, T , WEATHERLY, G C , PERZ, J M , Hydrogen and deuterium profiling at the surface of zirconium alloys, I The effects of surface preparation, J Nucl Mater **144** (1978) 35-42
- [488] RAMASUBRAMANIAN, N , TROTTIER, T , Electrical breakdown in anodic oxide films on Zircaloy-2, J Electrochem Soc **118** (1971) 1797-1804
- [489] RAMASUBRAMANIAN, N , An imaging technique for studying localized electronic conduction in valve metal-oxide systems, J Electrochem Soc **116** (1969) 1237-1240
- [490] RAMASUBRAMANIAN, N , Electrical switching in anodic films on Zircaloy-2, J Electrochem Soc **119** (1972) 649-652
- [491] PLOC, R A , COX, B , "Oxidation of some zirconium-based precipitates", Second Phase Particles in Zircaloys (Proc Workshop Conf Erlangen 1985), Kerntechnische Gesellschaft e V (KTG) Bonn, (1987) 59-62
- [492] BARR, T L , ESCA studies of naturally passivated metal foils, J Vac Sci and Technol **14** (1977) 660
- [493] SAENZ, J M , PALACIO, C , CASAS, Y , MARTINEZ-DUART, J M , An AES study of the oxidation of polycrystalline zirconium at room temperature and low oxygen pressures, Surface and Interface Anal **10** (1987) 177
- [494] PLOC, R A , "Physical changes in thin ZrO<sub>2</sub> films with thickening", Proc 7<sup>e</sup> Congres Int de Microscopie Electronique, Grenoble, (1970) 373-374
- [495] DRAPER, P H G , The structure of anodic films - I An electron diffraction examination of the products of anodic oxidation of tantalum, niobium and zirconium, Acta Metall **11** (1963) 873

- [496] PLOC, R. A., Breakaway oxidation of zirconium at 573 K, *J. Nucl. Mater.* **82** (1979) 411-418.
- [497] SABOL, G. P., MacDONALD, S. G., AIREY, G. P., "Microstructure of the Oxide Films Formed on Zirconium-Based Alloys", *Zr in Nucl Appl*, ASTM-STP-551, American Society for Testing and Materials, W. Conshohocken, PA. (1974) 435-448.
- [498] URQUHART, A., VERMILYEA, D. A., "Characterization of Zircaloy Oxidation Films", *Zr in Nucl. Appl.*, ASTM-STP-551, American Society for Testing and Materials, W. Conshohocken, PA. (1974) 463-478.
- [499] YUREK, G. J., CATHCART, J. V., PAWEL, R. E., Microstructure of the scales formed on Zircaloy-4 in steam at elevated temperatures, *J. Oxid. Metals* **10** (1976) 255-276.
- [500] PENELLE, R., BOISOT, P., BERANGER, G., LACOMBE, P., Influence de l'orientation des monocristaux de zirconium sur les textures de croissance de la zircone monoclinique, and Discussion de X-ray diffraction analysis of zirconium films on zirconium and Zircaloy-2, *J. Nucl. Mater.* **38** (1971) 340-342 and 343.
- [501] ROY, C., DAVID, G., Authors' reply to Note by LACOMBE, P., BERANGER, G., BOISOT, P., PENELLE, R. J., *Nucl. Mater.* **38** (1971) 344-346.
- [502] WANKLYN, J. N., SILVESTER, D. R., A study of corrosion films on zirconium and its alloys by impedance measurements, *J. Electrochem Soc.* **105** (1958) 647-654.
- [503] COX, B., The Use of Electrical Methods for Investigating the Growth and Breakdown of Oxide Films on Zirconium Alloys, *Can. Rep. AECL-2668*, Atomic Energy of Canada Ltd., Chalk River Nuclear Laboratories, (1967).
- [504] ROSECRANS, P. M., "Application of alternating current impedance measurements to characterise zirconium alloy oxidation films", *Zirconium in the Nuclear Industry: 6th Int. Symp.*, ASTM-STP-824, (FRANKLIN, D. G., ADAMSON, R. B., Eds.), American Society for Testing and Materials, W. Conshohocken, PA. (1984) 531-553.
- [505] COX, B., WONG, Y-M., "Effects of LiOH on pretransition zirconium oxide films", *Zirconium in the Nuclear Industry: 9th Int. Symp.*, ASTM-STP-1132, (EUCKEN, C. M., GARDE, A. M., Eds.), American Society for Testing and Materials, (1991), 643-662.
- [506] PAWEL, R. E., PERKINS, R. A., McKEE, R. A., CATHCART, J. V., ZUREK, G. J., DRUSCHEL, R. E., "Diffusion of oxygen in beta-zircaloy and the high temperature Zircaloy-steam reaction", *Zirconium in the Nuclear Industry: 3rd Int. Symp.*, ASTM-STP-633, (LOWE, A. L., PARRY, G. W., Eds.), American Society for Testing and Materials, W. Conshohocken, PA. (1977) 119-133.
- [507] RAMASUBRAMANIAN, R., Oxidation and polarization measurements on zirconium and Zircaloy-2 in molten nitrite and nitrates in 573 K, *J. Electrochem Soc.* **127** (1980) 2566-2572.
- [508] KNEPPEL, D. S., PEMSLER, J. P., Research on the Mechanism of Zirconium Alloy Corrosion in High-Temperature Steam, *U.S. Rep. NMI-1251 B*, Nuclear Metals inc., Concord, MA. (1961).
- [509] COX, B., Chemical dissolution of  $ZrO_2$  during oxide stripping, *J. Nucl. Mater.*, **202** (1993) 286-291.
- [510] WARR, B. D., RASILE, E. M., BRENNENSTUHL, A. M., ELMOSELHI, M. B., McINTYRE, N. S., NEWCOMB, S. B., "Microscopical and compositional analyses of oxides in Zr-2.5%wt% Nb following in- and out-reactor exposures", *Proc. Inst. of Met Conf. on Electron Microscopy of Metals*, Cambridge, UK, (1990).
- [511] SPITZNAGEL, J. A., FLEISCHER, L. R., CHOYKE, W. J., "The effect of ion bombardment on the thin film oxidation behaviour of Zircaloy-4 and Zr-1.0 Nb", *Applications of Ion Beams to Metals (Proc. Int. Conf., Albuquerque)*, (1973) 87.
- [512] JENKS, G. H., "Zircaloy-2 Corrosion In-Pile in Aqueous Homogeneous Reactor Solutions", *Corrosion of Zirconium Alloys*, ASTM-STP-368, American Society for Testing and Materials, W. Conshohocken, PA. (1964) 41-57.
- [513] ALCOCK, K., COX, B., The Effect of Neutron Irradiation on the Dissolution Rate of  $ZrO_2$ , *UK Rep. AERE-R3114*, United Kingdom Atomic Energy Authority, AERE, Harwell, Berks. (1959).
- [514] RUBIN, B., LYNAM, L., Behaviour of blanket-UO<sub>2</sub> fuel rods in Shippingport PWR core, *Nucl. Appl.* **2** (1966) 49.

- [515] NAYMARK, S., SPALARIS, C. N., "Oxide fuel fabrication and performance", *Peaceful Uses of Atomic Energy (Proc. 3rd Int. Conf., Geneva)*, Vol. 11, United Nations, (1964) 425.
- [516] NICHOLS, R. W., PICKLES, B. W., SHEPPARD, M. R., WOODS, D. S., ASHER, R. C., HESKETH, R., "Irradiation effects in zirconium-alloy pressure tubes", *Peaceful Uses of Atomic Energy (Proc. 4th Int. Conf., Geneva)*, Vol. 10, IAEA, Vienna, (1972) 549-561.
- [517] ASHER, R. C., DAVIES, D., HALL, A., KERSTEIN, T. B. A., MARRIOTT, J. W., WHITE, J. F., Effects of radiation on the oxidation and hydrogen absorption of zirconium alloys in steam, *Electrochem. Technol.* **4** (1966) 231-236.
- [518] CERRAI, E., GADDA, F., SCARONI, A., Further Experiments on the Corrosion Rate of Zircaloy-2 in Steam-Water Mixture Under Reactor Radiations, Italian Rep. CISE-R-290, Centro Informazioni Studi Esperienze, Milan, (1969).
- [519] HILLNER, E., "Long Term In-Reactor Corrosion and Hydriding of Zircaloy-2 Tubing", *Zirconium in the Nuclear Industry: 5th Int. Symp., ASTM-STP-754*, (FRANKLIN, D. G., Ed.), American Society for Testing and Materials, W. Conshohocken, PA. (1982) 450-478.
- [520] COX, B., AECL Experiments on the Corrosion of Zirconium Alloys under Irradiation, Can. Rep. AECL-2257, Atomic Energy of Canada Ltd., Chalk River Nuclear Laboratories, (1965).
- [521] KAISER, R. S., MILLER, R. S., MOON, J. E., PISANO, N. A., "Westinghouse high burnup experience at Farley 1 and Point Beach 2", *LWR Fuel Performance (Proc. Topical Mtg., Williamsburg, VA., 1988)*, American Nuclear Society, La Grange Park, ILL. (1988) 119-124.
- [522] COX, B., "What is wrong with current models for in-reactor corrosion", *Proc. of Tech. Comm. Mtg. on Fundamental Aspects of Corrosion on Zirconium Base Alloys in Water Reactor Environments*, Portland, OR., IAEA, Vienna, IWGFPT/34 (1990) 167-173.
- [523] GARZAROLLI, F., BECK, W., FUCHS, H. P., STEINBERG, E., PERKINS, R. A., Recent occurrences of abnormal increased fuel rod corrosion in PWRs, *Proc. EPRI-PWR Fuel Rod Corrosion Workshop*, Washington, DC., USA, July 28-30, 1993.
- [524] CAUSEY, A. R., URBANIC, V. F., COLEMAN, C. E., In-reactor oxidation of crevices and cracks in cold-worked Zr-2.5wt% Nb, *J. Nucl. Mater.*, **71** (1977) 25-35.
- [525] HOLZER, R., KNAAB, H., "Recent fuel performance and improved products", *LWR Fuel Performance (Proc. Topical Mtg., Williamsburg, VA.)*, American Nuclear Society, La Grange Park, ILL. (1988) 69-80.
- [526] SEIBOLD, A., GARZAROLLI, F., STEINBERG, E., "Optimized Zry-4 with enhanced Fe and Cr content and DUPLEX cladding: the answer to corrosion in PWRs", *Proc. Topfuel '95 Conference*, Vol. II, European Nucl. Soc., 117-121.
- [527] COX, B., Effect of Hydrogen Injection on Hydrogen Uptake by BWR Fuel Cladding, U.S. Rep. EPRI-NP-3146, Electric Power Research Institute, Palo Alto, CA. (1983).
- [528] LANNING, D. D., JOHNSON, A. B., Jr., TRIMBLE, D. J., BOYD, S. M., "Corrosion and hydriding of N-reactor pressure tubes", *Zirconium in the Nuclear Industry: 8th Int. Symp., ASTM-STP-1023*, (VAN SWAM, L. F. P., EUCKEN, C. M., Eds.), American Society for Testing and Materials, (1989) 153-164.
- [529] NORFOLK, D. J., BURNS, W. G., MARSH, W. R., Zircaloy-2 Oxidation Using 46 MeV Protons to Simulate a Reactor Environment, U.K. Rep. RD/B/N4368, Central Electricity Generating Board, Berkeley Nuclear Laboratories, (1987).
- [530] COX, B., "Mechanisms of corrosion of zirconium alloys in high temperature water, High Temp. Materials Chem.", *Proc. Symp. on High Temperature Materials Chem.*, (CUBICCIOTTI, D. D., HILDENBRAND, D. L., Eds.), Electrochem. Soc., N.Y., Vol. 82-1, (1982) 18-32.
- [531] LOCKE, D. H., Review of experience with water reactor fuels 1968-1973, *Nucl. Eng. and Design*, **33** (1975) 94-124.
- [532] RUDLING, P., MASSIH, A., "Corrosion of Zr-2 cladding tubes in boiling water reactor environment", *Proc. EPRI Workshop Zircaloy Corrosion*, Charlotte, NC. (SANTUCCI, J., Ed.) (1986).
- [533] SHIMADA, S., ITO, K., LIN, C. C., CHENG, B., IKEDA, T., OGUMA, M., TAKEI, T., VITANZA, C., KARLSEN, T. M., "Parametric tests of the effects of water chemistry impurities on corrosion of Zr-alloys under simulated BWR conditions", *Proc. Tech. Comm.*



- Mtg. on Influence of Water Chemistry on Fuel Cladding Behaviour, Rez, Czech Rep., Oct. 4-8, 1993, IAEA-TECDOC-927, Vienna (1997) 73-89.
- [534] ITO, K., SHIMADA, S., LEVIN, H. A., ADAMSON, R. B., CHEN, J-S. F., OGUMA, M., CHENG, B., IKEDA, T., TAKEI, K., ISHII, Y., "Effects of water chemistry impurities on corrosion of Zr-alloys under BWR conditions", Proc. Int. Topical Mtg. on Light Water Reactor Fuel Performance, W.Palm Beach, American Nuclear Society, La Grange Park, ILL. (1994) 273-285.
- [535] COX, B., Mechanism of oxidation and hydrogen uptake in zirconium alloys, Canadian Report, AECL-9018, Atomic Energy of Canada Ltd., Chalk River, (1985).
- [536] RIKAEV, A. K., KABACHI, S. A., EGOROV, A. F., Some radiation aspects of nuclear chemistry, Radiat. Phys. Chem., 31 (1988) 789-803.
- [537] MOTTA, A., LEMAIGNAN, C., A ballistic mixing model for the amorphisation of precipitates in Zircaloy under neutron irradiation, J. Nucl. Mater., **195** (1992) 277-285.
- [538] TYZACK, C., et al., SCANUK: A collaborative programme to develop new zirconium cladding alloys, J. Nucl. Mater., **66** (1977) 163-186.

**NEXT PAGE(S)  
left BLANK**

## BIBLIOGRAPHY

### Zirconium Conferences, Workshops and Monographs

- INTERNATIONAL ATOMIC ENERGY AGENCY, The Metallurgy of Zirconium, Atomic Energy Review, Supplement 7, D. L. Douglass, IAEA Vienna (1971) 464 pp.
- PROCEEDINGS OF THE INTERNATIONAL CONFERENCE, Corrosion of Reactor Materials, Salzburg, Austria, STI/59, IAEA, Vienna, (1962) 2 Volumes.
- ETUDE SUR LA CORROSION ET LA PROTECTION DU ZIRCONIUM ET SES ALLIAGES, Colloque de Metallurgie 9e, Saclay, 21-24 June 1965, CEA Saclay, France, (1966).
- SPECIALIST WORKSHOP ON SECOND PHASE PARTICLES AND MATRIX PROPERTIES OF THE ZIRCALOYS, 1-2 July 1985, Erlangen, Germany, KTG, Germany, (1985)
- ZIRCONIUM ALLOY FUEL CLAD TUBE, Engineering Guide, Sandvik Special Metals Corporation, Kennewick, Washington, USA, (1989).
- LE ZIRCONIUM, Matériau pour Industries Chimiques, ( Eds. G. Béranger, P. Lacombe and R. Tricot), Ecole Normale Supérieure de Lyon, 10-11 Oct. 1990, Les Editions de Physique, Les Ulis, France, (1992).
- PROCEEDINGS OF THE INTERNATIONAL CONFERENCE, Water Chemistry of Nuclear Reactor Systems 6, 12-15 Oct. 1992, Bournemouth, U.K., BNES (1992).
- PROCEEDINGS OF GERMAN NUCLEAR SOCIETY CONFERENCE, Material Development for Fuel Elements in Light Water Reactors, 29-30 Nov. 1993, Karlsruhe, Germany, KTG, Germany, (1993).
- PROCEEDINGS OF THE INTERNATIONAL CONFERENCE, Chemistry in Water Reactors: Operating Experience and New Developments, Palais des Congrès, Nice, 24-27 Apr. 1994, SFEN. Paris, France, (1994).
- PROCEEDINGS OF THE INTERNATIONAL SYMPOSIUM FONTEVRAUD III, Contributions of Materials Investigation to the Resolution of Problems Encountered in Pressurized Water Reactors, Abbaye Royale de Fontevraud, 12-16 Sept. 1994, SFEN. Paris, France, (1994).
- LE ZIRCONIUM, Propriétés -Microstructures, ( Eds. G. Caillaud and P. Lemoine), I.N.S.T.N. Saclay, 25-26 Apr. 1995, Les Editions de Physique, Les Ulis, France, (1996).

### Zirconium in the Nuclear Industry Series

- 1962 Symposium on zirconium alloy development, Castlewood, Pleasanton, CA, USAEC/GE, GEAP-4029, 2 vols.
- 1963 Corrosion of zirconium alloys, New York, NY, ASTM-STP-368.
- 1965 Symposium on zirconium and its alloys, Buffalo, N.Y. Electrochem. Soc., Electrochem. Tech., Vol 4, pp 81-377.
- 1968 Applications-related Phenomena in Zr and its alloys, Philadelphia, Pa, ASTM-STP-458.
- 1971 International Symposium on zirconium and its alloys, Montreal, PQ, Canada, CIMM, Can.Met.Quart.Vol. II(1972) 642 pp.
- 1973 Symposium on zirconium in nuclear applications, Portland, OR, ASTM-STP-551, 526 pp.
- 1976 3rd International Symposium on zirconium in the nuclear industry, Quebec City, PQ, Canada, ASTM-STP-633, 627 pp.
- 1978 4th International Symposium on zirconium in the nuclear industry, Stratford-upon-Avon, UK, ASTM-STP-681, 627 pp.
- 1980 5th International Symposium on zirconium in the nuclear industry, Boston, Mass.,ASTM-STP-754, 488 pp.
- 1982 6th International Symposium on zirconium in the nuclear industry, Vancouver, BC, Canada, ASTM-STP-824, 846 pp.
- 1985 7th International Symposium on zirconium in the nuclear industry, Strasbourg, France, ASTM-STP-939, 833 pp.
- 1988 8th International Symposium on zirconium in the nuclear industry, San Diego, CA, TM-STP-1023, 780 pp.

- 1990 9th International Symposium on zirconium in the nuclear industry, Kobe, Japan, ASTM-STP-1132, 795 pp.
- 1993 10th International Symposium on zirconium in the nuclear industry, Baltimore, MD, ASTM-STP-1245, 799 pp.
- 1995 11th International Symposium on zirconium in the nuclear industry, Garmisch-Partenkirchen, Germany, ASTM-STP-1295, 908 pp.

#### **Water Reactor Fuel Performance Series**

- 1975 Joint Topical Meeting on Commercial Nuclear Fuel Technology Today, Toronto, ON, Canada, 75-CNA/ANS-100.
- 1977 ANS Topical Meeting on Water Reactor Fuel Performance, St. Charles, Ill, American Nuclear Society.
- 1979 ANS Topical Meeting on Water Light Reactor Fuel Performance, Portland, OR, American Nuclear Society UC78.
- 1982 ANS Topical Meeting on LWR Extended Burnup-Fuel Performance and Utilization, St. Williamsburg, VG, 2 vols, American Nuclear Society.
- 1985 ANS Topical Meeting on Water Light Reactor Fuel Performance, Orlando, FL, 2 vols, American Nuclear Society, UC-78, DOE/NE/34130-1.
- 1988 ANS Topical Meeting on LWR Fuel Performance, Williamsburg, VG, American Nuclear Society, ISBN: 0-89448-032-4, ANS-700131.
- 1991 International Topical Meeting on LWR Fuel Performance - Fuel for the 90's, Avignon, France, ANS/ENS/SFEN, 2 vols.
- 1994 International Topical Meeting on Light Water Reactor Fuel Performance, West Palm Beach, FL, ANS/IAEA, ISBN: 0-89448-190-8, ANS-700200.
- 1995 TOPFUEL'95, International Topical Meeting on Nuclear Fuel, Wurzburg, Germany, KTG/ENS, ISBN3-926956-27-5, 2 Volumes.
- 1997 TOPFUEL'97, International Topical Meeting on Nuclear Fuel, Manchester, U.K., BNES/ENS, ISBN 0-7277-2619-6, 2 Volumes.
- 1997 International Topical Meeting on LWR Fuel Performance, ANS/AESJ/Chinese Nucl. Soc./KNS, ISBN: 0-89448-616-0, ANS-700236.

#### **IAEA-TECDOC and IWGFPT Series**

INTERNATIONAL ATOMIC ENERGY AGENCY, Fuel Cladding Interaction with Water Coolant in Power Reactors, IAEA-TECDOC-356, IAEA, Vienna (1985).

INTERNATIONAL ATOMIC ENERGY AGENCY, External Cladding Corrosion in Water Power Reactor, IWGFPT/24, IAEA, Vienna (1986).

INTERNATIONAL ATOMIC ENERGY AGENCY, Fundamental Aspects of Corrosion on Zirconium Base Alloys in Water Reactor Environments,, IWGFPT/34, IAEA, Vienna (1990).

INTERNATIONAL ATOMIC ENERGY AGENCY, Corrosion of Zirconium Alloys in Nuclear Power Plants, IAEA-TECDOC-684, IAEA, Vienna (1993).

INTERNATIONAL ATOMIC ENERGY AGENCY, Coolant Technology of Water Cooled Reactors, IAEA-TECDOC-667, IAEA, Vienna (1992) 3 Volumes.

INTERNATIONAL ATOMIC ENERGY AGENCY, Influence of Water Chemistry on Fuel Cladding Behaviour, IAEA-TECDOC-927, Vienna (1997).

INTERNATIONAL ATOMIC ENERGY AGENCY, Thermophysical Properties of Materials for Water Cooled Reactors, IAEA-TECDOC-949, IAEA, Vienna (1997).

## **LIST OF CONTRIBUTORS**

### **CONTRIBUTORS TO DRAFTING AND REVIEW**

Cox, B	University of Toronto, Canada
Kritsky, V.G.	VNIPIET, St Petersburg, Russian Federation
Lemaignan, C	Commissariat à l'énergie atomique, Grenoble, France
Polley, V	Nuclear Electric plc, Barnwood, United Kingdom
Ritchie, I G	International Atomic Energy Agency
Ruhmann, H	Siemens AG, Erlangen, Germany
Shishov, V N	VNIINM Research Institute of Inorganic Materials, Moscow, Russian Federation

\*Other authors who contributed to the VNIINM part of the review were

Bibilashvili, Yu K and Nikulina, A.V.

### **CONTRIBUTORS TO DRAFTING AND REVIEW OF IAEA-TECDOC-684**

Billot, P	Commissariat à l'énergie atomique, Cadarache, France
Cox, B	University of Toronto, Canada
Ishigure, K	University of Tokyo, Japan
Johnson Jr, A B	Battelle, Pacific Northwest Laboratories, USA
Lemaignan, C	Commissariat à l'énergie atomique, Grenoble, France
Nechaev, A F	International Atomic Energy Agency
Petrik, N G	All-Union Institute of Complex Power Technology, Russian Federation
Reznichenko, E.A.	Kharkov Institute of Technology, Ukraine
Ritchie, I G	International Atomic Energy Agency
Sukhanov, G I	International Atomic Energy Agency